Post−translational mechanisms of the ZIP family of zinc channels

A thesis submitted for the degree of
Philosophiae Doctor in Cardiff University

by

Thirayost Nimmanon

June 2016

Cardiff School of Pharmacy and Pharmaceutical Sciences
Cardiff University

Summary

Zinc is an essential trace metal involved in diverse cellular processes. Cellular zinc levels are controlled by three families of proteins, including ZIP channels, which facilitate zinc influx into the cytosol. Aberrant function of many ZIP channels has been associated with human diseases. However, their cellular mechanisms are relatively unclear. Importantly, our group have reported that ZIP7 function is triggered by CK2−mediated phosphorylation on residues S275 and S276, and have created a pZIP7 antibody that recognises this phosphorylated form of ZIP7. This project therefore aimed to decipher post−translational mechanisms of three ZIP channels: ZIP7, ZIP6, and ZIP10. Computational analysis of ZIP sequences revealed salient characteristics of ZIP channels, especially those belonging to the LIV−1 subfamily, and detected multiple potential phosphorylation sites in the cytosolic loop between TM3 and TM4 of ZIP3, ZIP4, ZIP6, ZIP7 and ZIP10. Characterisation of the pZIP7 antibody revealed that it specifically recognised ZIP7 when phosphorylated on S275 and S276 and accurately indicated increased or impaired function of the protein. Employing different antibody arrays, phosphorylation of multiple kinases by ZIP7 overexpression or zinc was demonstrated, introducing multiple signalling pathways as downstream cascades of ZIP7−mediated zinc release from intracellular stores. An investigation on ZIP6 detected that it was phosphorylated by CK2, CK1, GSK−3,β and PLK1 exclusively in mitotic cells. This led to a deeper discovery of the cellular mechanism of ZIP6 in mitosis involving its heteromer formation with ZIP10 and its binding to pS727 STAT3, which also bound to pStathmin, a protein required for microtubule reorganisation. Importantly, ZIP6 and ZIP10 antibody treatment successfully inhibited mitosis in multiple breast cancer cell lines, either nocodazole−induced or endogenous. Collectively, this project has provided a deeper insight into ZIP7, ZIP6 and ZIP10 cellular mechanisms, introduced pZIP7 antibody as a potential biomarker, and proposed ZIP6 and ZIP10 antibodies as promising mitosis−blocking agents.

Publications and presentations

Journal articles

- Taylor KM, Muraina I, Brethour D, Scmitt−Ulms G, **Nimmanon T**, Ziliotto S, Kille, P and Hogstrand, C. Zinc transporter ZIP10 forms a heteromer with ZIP6 which regulates embryonic development and cell migration. Biochem J. 2016.

- **Nimmanon T**, Burt A, Gee JMW, Andrews GK, Kille P, Hogstrand H, Maret W and Taylor K M. The zinc importer ZIP6:ZIP10 heteromer triggers mitosis. (In preparation)

- **Nimmanon T**, Morris S, Flanagan L, Ziliotto S and Taylor K M. Phosphorylation of zinc transporter ZIP7 activates growth and migration signalling. (In preparation)

Book chapters

- **Nimmanon T**, Taylor KM. Cellular Zinc Signalling Is Triggered by CK2. In: Ahmed K, Issinger O−G, Szyszka R, editors. Protein Kinase CK2 Cellular Function in Normal and Disease States. Switzerland: Springer International Publishing; 2015. p. 141−57.

- **Nimmanon T**, Taylor KM. Zinc signalling and cancer. In: Fukada T, Kambe T, editors. Zinc Signals in Cellular Functions and Disorders. Tokyo: Springer Japan; 2014. p. 285−313.

Oral presentation

- **Nimmanon T**, Taylor KM. Exploration of downstream effectors of ZIP7−mediated zinc release. The 10th Zinc−UK Meeting, Anglia Ruskin University, Cambridge, UK. (10th July 2015)

- **Nimmanon T**, Taylor KM. Zinc transporter−mediated zinc influx triggers mitosis. Post−graduate Research Day, Cardiff School of Pharmacy and Pharmaceutical Sciences, Cardiff, UK. (29th April 2014)

Poster presentation

- **Nimmanon T**, Taylor KM. Phosphorylation of ZIP channels explains their functional diversity. International Society for Zinc Biology Meeting 2014, Asilomar, California, USA. (14^{th}–19^{th} September 2014, poster prize)
- **Nimmanon T**, Taylor KM. Investigation of the mechanisms of ZIP channel phosphorylation. Post−graduate Research Day, Cardiff School of Pharmacy and Pharmaceutical Sciences, Cardiff, UK. (30^{th} April 2014)
- **Nimmanon T**, Taylor KM. Investigation of the mechanisms of ZIP transporter phosphorylation. The 8^{th} Zinc−UK Meeting, Rowett Institute of Nutrition and Health, Aberdeen, UK. (4^{th}–5^{th} July 2013, the first poster prize)
- **Nimmanon T**, Taylor KM. Exploration of phosphorylation sites in ZIP transporters and their predicted kinases. The 7^{th} Zinc−UK Meeting, UCL Institute of Ophthalmology, London, UK. (12^{th} November 2012)

Acknowledgment

I would like to express my sincerest gratitude to Dr. Kathryn Taylor for her invaluable support, guidance, and encouragement throughout this project. Her expertise greatly motivated me to pursue research in the field of zinc biology. I would like to thank Dr. Julia Gee, Dr. Stephen Hiscox, and Dr. Professor Arwyn Tomos Jones for their advice. I am also very much grateful to the Ministry of Science and Technology, the Royal Thai Government, for funding my PhD placement, and all the staff members of the Office of Educational Affairs, the Royal Thai Embassy, UK for advice, monitoring and financial coordination.

I would like to thank all the members of Breast Cancer Molecular Pharmacology group for their help throughout my project. In particular, I would like to acknowledge Richard McClelland, who taught me molecular biology techniques; Carol Dutkowski and Huw Mottram, who helped me with all essential cell culture works and provided precious cells for me; Lindy Goddard and Veronika Hölzlwimmer, who trained me to do immunoprecipitation and Western blotting and helped me troubleshoot problems; Lynne Farrow, who gave me an advice about statistical analysis; and Susan Kyme, Christopher Smith, and Pauline Finlay, who were always willing to provide practical supports. I extend many thanks to all my fellow PhD students and undergraduate students, especially Benyamin Ertefai and Silvia Ziliotto, for their contributions to various domains.

I would like to express my heart−felt gratitude to my dad and my mum for their love, concern, support, and strength. Most importantly, I would like to thank God for this abundant grace that helped me get through all the difficulties and discouragement, and for sending many lovely brothers and sisters, both in the Church in Cardiff and in the Network of Thai Christians, who faithfully shepherded me.

“For of him, and through him, and to him, are all things:
to whom be glory for ever. Amen.”
(Romans 11:36 KJV)

Table of contents

List of figures

List of tables

Abbreviations

µ− (unit prefix)	Micro
A (amino acid)	Alanine
A (nucleic acid)	Adenine
ADAM	A disintegrin and metalloproteinase
AM ester	Acetoxymethyl ester
AMPK	AMP−activated protein kinase
ANOVA	Analysis of variance
BGH	Bovine growth hormone
BSA	Bovine serum albumin
C (amino acid)	Cysteine
C (nucleic acid)	Cytosine
CD	Cluster of differentiation
CDK	Cyclin−dependent kinase
CHO cells	Chinese hamster ovary cells
CK	Casein kinase
CMV	Cytomegalovirus
CREB	cAMP response element binding protein
CRISPR	Clustered regularly−interspaced short palindromic repeats
C−terminus	Caboxy−terminus
D (amino acid)	Aspartate
Da (unit)	Dalton
DAPI	4',6−diamidino−2−phenylindole
DNA	Deoxyribonucleic acid
DNase	Deoxyribonuclease
DPP	Dipeptidyl peptidase
DTPA	Diethylenetriaminepentaacetic acid
E (amino acid)	Glutamate
E−cadherin	Epithelial cadherin
EDTA	Ethylenediaminetetraacetic acid
EGF	Epidermal growth factor
EGFR	Epidermal growth factor receptor
EGTA	Ethylene glycol tetraacetic acid

EMT	Epithelial−mesenchymal transition
ER	Endoplasmic reticulum
ERK	Extracellular signal−regulated kinase
ERK	Extracellular−signal−regulated kinases
FACS	Fluorescence−activated cell sorting
FAK	Focal adhesion kinase
FBS	Foetal bovine serum
FGFR	Fibroblast growth factor receptor
FRET	Fluorescence resonance energy transfer
G (amino acid)	Glycine
G (nucleic acid)	Guanine
g (unit)	Gram
G0 (cell cycle)	Gap 0
G1 (cell cycle)	Gap 1
G2 (cell cycle)	Gap 2
GAPDH	Glyceraldehyde 3−phosphate dehydrogenase
GSK	Glycogen synthase kinase
H (amino acid)	Histidine
HER2	Human epidermal growth factor receptor 2
HRP	Horseradish−peroxidase
HSP	Heat shock proteins
ICAM	Intercellular adhesion molecule
IGF−1R	Insulin−like growth factor 1 receptor
IRE	Iron−responsive element
JAK	Janus kinases
JNK	c−Jun N−terminal kinase
K (amino acid)	Lysine
k− (unit prefix)	Kilo
kb (unit)	Kilobase pair
Kd	Dissociation constant
KRH	KrebsRinger HEPES
L	Litre
L (amino acid)	Leucine
LB	Lysogeny broth
M (cell cycle)	Mitotic

m− (unit prefix)	Milli
M (unit)	Molar
m (unit)	Metre
MAPK	Mitogen−activated protein kinase
MAPKAPK	MAPK−activated protein kinase
MCF−7 cells	Michigan Cancer Foundation−7 cells
min (unit)	Minute
MMP	Matrix metalloproteinase
MSK	Mitogen− and stress−activated protein kinase
MTOR	Mammalian target of rapamycin
n− (unit prefix)	Nano
NCBI	National Center for Biotechnology Information
NMuMg cells	Normal murine mammary gland epithelial cell
N−terminus	Amino−terminus
ºC	Degree Celsius
OD	Optical density
P (amino acid)	Proline
PBS	Phosphate−buffered saline
PCR	Polymerase chain reaction
PDF	Peptide deformylase
PDGFR	Platelet derived growth factor receptor
PKB	Protein kinase B or AKT
PLA	Proximity ligation assay
PLK	Polo−Like Kinase
PRAS	Proline−rich AKT substrate
PrP^{C}	Cellular prion protein
pS or pSer (amino acid)	Phosphorylated serine
pY (amino acid)	Phosphorylated tyrosine
Q (amino acid)	Glutamine
RNA	Ribonucleic acid
RNase	Ribonuclease
ROC	Receiver operating characteristics
rpm (unit)	Revolutions per minute
RPMI	Roswell Park Memorial Institute
RSK	Ribosomal s6 kinase

RTK	Receptor tyrosine kinase
RYK	Receptor−like tyrosine kinase
S (amino acid)	Serine
S (cell cycle)	Synthesis
SDS−PAGE	Sodium dodecyl sulphate polyacrylamide gel electrophoresis
siRNA	Small interfering RNA
SLC	Solute−linked carrier
SOC	Super optimal broth with catabolite repression
STAT	Signal transducer and activator of transcription
T (amino acid)	Threonine
T (nucleic acid)	Thymine
TamR cells	Tamoxifen−resistant breast cancer cells
TBST	Tris−buffered saline with Tween
TCCF	Total corrected cellular fluorescence
TM	Transmembrane domain
TOR	Target of rapamycin
TPEN	N,N,N′,N′−Tetrakis(2−pyridylmethyl)ethylenediamine
UV	Ultraviolet
V (unit)	Volt
WT	Wild type
Y (amino acid)	Tyrosine
ZAP	Zeta−chain−associated protein kinase
ZIP	Zrt− and Irt−like protein
ZnT	Zinc transporters

Chapter 1:
Introduction

1.1 Zinc in human health and diseases

Zinc is nutritionally categorised as an essential trace element, which is the second most abundant in the human body, with iron being the most plentiful trace element in the body (McCall *et al.* 2000). The human body contains 2 g or 30 mmol of zinc, which is distributed throughout all tissues and fluids in the body with 60% of total body zinc in the skeletal muscle (King *et al.* 2000), and the highest concentration of zinc in the choroid region of the eye and the prostatic secretion (FAO/WHO 2002). In contrast to other metals, zinc is uniquely found associated with all classes of enzymes (Vallee and Galdes 1984). Using a bioinformatics approach, 2,800−3,200 human proteins, accounting for approximately 10% of the human proteome, are indicated as zinc proteins (Andreini *et al.* 2006; Passerini *et al.* 2007).

The necessity of zinc in human health had not been recognised until the profound description of a clinical syndrome attributed to zinc deficiency in a case series of 10 malnourished Iranian villagers (Prasad *et al.* 1961). In this report, these patients shared a common clinical history of geophagia, a form of pica characterised by craving for eating earth, soil, or clay. Upon physical examination, these patients were seen to have short stature, iron−deficiency anaemia, hepatosplenomegaly, and hypogonadism. The link of this clinical syndrome to zinc deficiency later became clearer a few years later when extensive biochemical studies in 16 stunted male Egyptian villagers with this clinical syndrome associated the condition with low plasma zinc levels (Prasad *et al.* 1963). Since the discoveries of cases with zinc deficiency, the importance of zinc in human health has been increasingly acknowledged and the knowledge of cause and pathogenesis of zinc deficiency syndrome has been increasingly understood (Roohani *et al.* 2013).

Zinc is involved in a vast variety of physiological processes (Kambe *et al.* 2015). It is therefore not surprising that the clinical syndrome of zinc deficiency in its severe form can be clinically characterised by abnormalities of virtually all the human organ systems (Hambidge 2000). The typical clinical manifestations of full−blown zinc deficiency include anorexia, pica, growth retardation, dermatopathy, hair loss, gonad dysfunction, delayed wound healing, compromised immune system, neuropsychiatric symptoms, glucose intolerance,

abnormal pregnancy, and increased risk of cardiovascular diseases and cancer (Yanagisawa 2008). The severest end of the spectrum of zinc deficiency is called acrodermatitis enteropathica, which has been described as a rare lethal autosomal recessive disorder characterised by intestinal malabsorption of zinc (Moynahan 1974). This condition of severe zinc deficiency manifests itself as a clinical syndrome of dermatitis (particularly in the acral, perioral, and periocular areas), alopecia, and diarrhoea, hence the proposal of the name acrodermatitis enteropathica by Danbolt and Closs (Danbolt and Closs 1942). The gene mutated in this condition has been mapped to chromosome 8q24.3, which encodes ZIP4 (SLC39A4), a member of the LIV−1 subfamily of ZIP channels responsible for intestinal absorption of zinc (Küry *et al.* 2002). Consequently, the ZIP4 gene has now been recognised as the gene defect responsible for the manifestation of acrodermatitis enteropathica (Andrews 2008).

It is noteworthy that regardless of the typical recognition of this condition as an inherited disease, an acquired form of acrodermatitis enteropathica has also been documented in adults. These patients have been reported to have the typical dermatologic presentation of the disease with a history of inadequate zinc intake in combination with chronic use of common anti−hypertensive drugs, which potentially enhances urinary loss of zinc (Macdonald *et al.* 2012), chronic alcoholism (Chaudhry *et al.* 2008), and surgical gastric bypass (Cunha *et al.* 2012). Additionally, transient neonatal zinc deficiency, an autosomal dominant disorder, has been known as a cause of hypozincaemia in infancy and classified as type 2 hypozincaemia in children (with the classical acrodermatitis enteropathica being classified as type 1) (Kumar *et al.* 2012). Pathogenetically, type 2 hypozincaemia has been attributed to a missense mutation of the gene of ZnT2 (SLC30A2), a zinc transporter responsible for zinc secretion from the mammary glands, resulting in impaired zinc secretion into the breast milk (Chowanadisai *et al.* 2006).

Regardless of the advancement of the insight into pathogenesis of zinc deficiency, this condition remains highly prevalent worldwide even today, with 17.3% of the population estimated to be at risk of inadequate zinc intake, based upon the bioavailability of absorbable zinc content in the national food supplies (Wessells and Brown 2012). Furthermore, both diagnosis of zinc deficiency and

determination of its prevalence are considered difficult particularly for cases with marginal or mild zinc deficiency, because of the non-specificity of clinical manifestations and the lack of a clinically-useful biomarker with undisprovable reliability for determining total body zinc status (Wieringa *et al.* 2015). A systematic review demonstrated that, out of 32 biomarkers investigated, only zinc levels in plasma, hair and urine successfully responded to a short-termed experimental manipulation of dietary zinc intake in a dose-dependent manner (Lowe *et al.* 2009). Nonetheless, accuracy of these three markers in determining body zinc status is yet to be proved, since the test results analysed in this systematic review could be interfered with by many factors. Moreover, the authors of this systemic review also suggested that body zinc homeostasis might be able to control the plasma zinc levels within the physiological range, thus limiting the use of this biomarker in cases with a long-termed change in dietary zinc intake. Additionally, metabolic redistribution of zinc from plasma to tissues, which may be triggered by various influences such as meals, infection, and other forms of stresses, can reduce plasma zinc levels, thereby confounding the interpretation of hypozincaemia (King 2011). Nowadays, diagnosis of individual cases solely depends on clinical evaluation and plasma zinc levels, the only test currently used in routine clinical practice (BMJ Best Practice). In contrast, for assessing a population-level zinc status, a combined use of three indicators was suggested, including the prevalence of inadequate zinc intakes according to the estimated average requirement, the prevalence of hypozincaemia, and the prevalence of children up to 5 years old who have low height-for-age (de Benoist *et al.* 2007). In as much as either subclinical or clinical zinc deficiency affects numerous people worldwide, both in developed and developing countries, and the detection is still a real challenge due to the lack of a reliable diagnostic test, zinc is inevitably considered as a micronutrient of remarkable significance both biologically and epidemiologically (Hambidge and Krebs 2007).

Beneficial effects of zinc in human health are widely-known nowadays. Zinc has positive effects on the immune system (Haase and Rink 2014b), the free radical scavenging mechanism (Oteiza 2012) and the wound healing process (Lansdown *et al.* 2007) as well as the intrinsic anti-microbial action of zinc against bacteria (David 2012) and fungi (Reeder *et al.* 2011). As a result,

zinc in its different forms is often included in various dietary supplements (Schwingshackl *et al.* 2015), topical therapeutic agents (Sadeghian *et al.* 2011), and even common everyday products such as anti-dandruff shampoos (Schwartz *et al.* 2013). A meta-analysis of 33 randomized clinical trials reported a significant positive effect of supplemental zinc in growth of prepubertal children, suggesting zinc supplementation as a means to improve the bodily zinc condition, and to prevent underweight and stunting in children who are at risk of zinc deficiency (Brown *et al.* 2002). Furthermore, zinc supplementation has also been approved to be used as a chemo-therapeutic means for acute diarrhoea (Walker *et al.* 2015) and common cold (Fashner *et al.* 2012) and proposed to benefit patients with early stages of age-related macular degeneration (Lawrenson and Grzybowski 2015).

1.2 Biological functions of zinc in the human body

Zinc plays indispensable roles in diverse biological processes. It plays important roles in different cellular mechanisms including, but not limited to, transcription, signal transduction, growth, proliferation, differentiation, apoptosis, and metabolism of carbohydrates, lipids, proteins, nucleic acids, and other micronutrients (FAO/WHO 2002; Hambidge and Krebs 2007). Not only does zinc help the body fight against infectious microorganisms by enhancing both the innate and the adaptive immune systems (Haase and Rink 2014b), but zinc also prevents cellular oxidative damage by exercising its properties as an antioxidant (Oteiza 2012), albeit it is more appropriately counted as a pro-antioxidant (Maret 2008). Furthermore, there has been increasing evidential support for zinc acting in the brain as a neuromodulator released by zincergic neurons, which are glutamatergic neurons that also secrete zinc (Kay and Tóth 2008; Takeda *et al.* 2013). Additionally, zinc is required for formation of water-insoluble crystals in pancreatic beta cell granules, which constitute hexamers of two zinc ions and four insulin molecules (Lemaire *et al.* 2009).

Intracellularly, zinc has been shown to indispensably function as a second messenger (Yamasaki *et al.* 2007), participating in various cellular signalling pathways, including those involved in carcinogenesis (Taylor *et al.* 2011). This notable role of zinc was experimentally demonstrated in mast cells after activation by an extracellular stimulus (Yamasaki et al. 2007). In this study,

mast cells were stimulated by cross-linking of the high affinity immunoglobulin E receptor, resulting in zinc release from the perinuclear region where the endoplasmic reticulum (ER) is located. This zinc release required both preceding calcium influx and MAPK activation, and the resulting increase in cytosolic zinc is known as a “zinc wave”. Furthermore, this zinc wave production was shown in the same study to mediate cellular signalling events at least partly through a direct inhibitory action of zinc on tyrosine phosphatase activity.

According to this study in mast cells (Yamasaki et al. 2007), zinc satisfies four out of five criteria for a second messenger that were proposed by Sutherland (Sutherland *et al.* 1968; Aley *et al.* 2013). These criteria consist of (1) inhibition of the extracellular messenger action by a second messenger antagonist; (2) demonstration of the extracellular messenger effect by application of the second messenger; (3) ability of the second messenger to be synthesised and metabolised; (4) changes of the second messenger level in response to the stimulus; and (5) presence of specific intracellular binding sites. In relation to these criteria, the study in mast cells demonstrated that TPEN, a zinc chelator, inhibited the extracellular messenger action in mast cells; application of zinc produced the effects the extracellular stimulus; the zinc level changed in response to the extracellular stimulus; and tyrosine phosphatases were identified as a target of zinc (Yamasaki et al. 2007). Even though the third criterion was not fully shown, because zinc was not synthesised in the cells, zinc was shown to be released from cellular stores. Altogether, these data have established the role of zinc as a second messenger. Noteworthy, evidence of zinc as a key signalling molecule has also been provided in T cells (Yu *et al.* 2011). However, the increase in cytosolic zinc levels following the activation of the T cell receptor was shown in this study to result from zinc influx mediated by zinc channel ZIP6, rather than zinc release from cellular stores.

Following the discovery of zinc acting as a second messenger, this similar role of zinc has also been detected in other non-immune cells. In Chinese hamster ovary cells, activation of the insulin-like growth factor 1 receptor (IGF-1R) was demonstrated to trigger zinc-mediated phosphorylation of extracellular-signal-regulated kinases 1 and 2 (ERK1/2) and protein kinase B (PKB or AKT) (Pandey *et al.* 2010). In addition to IGF-1R, activation of the

epidermal growth factor receptor (EGFR) was also shown in the same study to initiate the same zinc−mediated responses in vascular smooth muscle cells. Similarly, our group have revealed zinc−mediated phosphorylation of ERK1/2 and AKT in breast cancer cells following an extracellular stimulus of either zinc plus zinc ionophore pyrithione or the epidermal growth factor (EGF) plus calcium ionophore ionomycin (Taylor *et al.* 2012). Consistent with the proposed mechanism of the zinc−induced signalling events reported in mast cells (Yamasaki et al. 2007), the zinc−mediated responses seen in these non−immune cells were attributed to the zinc−induced inhibition of protein tyrosine phosphatases (Wilson *et al.* 2012).

In order for zinc to be classified as a second messenger, it is crucial that in response to cellular exposure to a first messenger, the zinc ions that produce a zinc wave and thereby modulate cellular signalling molecules originate from an intracellular compartment rather than an extracellular source (Bornfeldt 2006). Importantly, zinc has been shown to fulfil this criterion for a second messenger by inability of diethylenetriaminepentaacetic acid (DTPA), a membrane−impermeable zinc chelator, to inhibit zinc wave production in mast cells (Yamasaki et al. 2007). Furthermore, stimulation with EGF plus ionomycin was shown to produce a zinc wave in a similar manner to stimulation with zinc plus pyrithone in breast cancer cells (Taylor et al. 2012), proving an intracellular origin of the zinc ions that elicit the zinc wave. The role of zinc as a second messenger now provides an opportunity for zinc−mediated cellular effects to be observed within minutes independently of the transcriptional roles of zinc, which require hours or days to accomplish (Hirano *et al.* 2008). Furthermore, this also raises the importance of cellular zinc signalling to the level comparable to calcium signalling (Taylor et al. 2011). However, precise mechanistic details of zinc release control and relevance of zinc signalling to pathogenesis of human diseases are yet to be elucidated.

1.3 ZIP channels

Either too much or too little zinc adversely affects cellular homeostasis. Zinc excess causes cell death, either apoptosis (programmed cell death) or necrosis (Kim *et al.* 1999), whilst cellular zinc deprivation causes growth arrest (MacDonald 2000) and induces the apoptotic pathways (Fraker 2005). It is

therefore extremely crucial that a cell judiciously controls the concentration of free zinc in the cytosol where zinc ions are capable of efficiently activating numerous signalling molecules. Three families of proteins have been discovered to participate in this stringent regulation: ZIP channels (SLC39A, zinc importers), ZnT transporters (SLC30A, zinc exporters), and zinc−binding proteins such as the cysteine−rich metallothioneins (Lichten and Cousins 2009), which are also known to serve as an intracellular resource of zinc for redox signalling (Ruttkay-Nedecky *et al.* 2013). ZIP channels mobilise zinc into the cytosol either from extracellular space or from intracellular stores, thereby increasing cytosolic zinc bioavailability, whereas ZnT transporters reduce cytosolic zinc by transporting zinc in the opposite direction (Kambe et al. 2015). Noteworthy, in contrast to ZnT transporters, which are discovered to function as Zn^{2+}/H^{+} exchangers (Ohana *et al.* 2009), the underlying mechanistic detail of zinc transport by ZIP channels is relatively obscure.

ZIP channels are generally regarded in the literature as transporters; yet there are pieces of evidence supporting that they in fact transport zinc in a channel−like manner (Kambe et al. 2015). Firstly, ZIP proteins, like other ion channels, mobilise zinc down a transmembrane concentration gradient, given that the amount of free zinc ions in the cytosol is so small that it has been considered negligible by some authors (Alam and Kelleher 2012). Noteworthy, in spite of this negligible amount of free zinc ions the cytosol, it is by no means negligible in terms of the impact of zinc ions on cell physiology (Maret 2013). Secondly, a molecular characterisation of ZIPB, a ZIP homolog from *Bordetella bronchiseptica*, demonstrated that this primitive ZIP protein works as a non−saturable ion−selective electro−diffusional channel that facilitates passive uptake of zinc into the cell (Lin *et al.* 2010). These characteristics of ZIP7B are compatible with the salient biochemical properties of an ion channel, which include non−saturability with the ion substrate and passive transport of the ion that is dependent on the electrochemical properties of the ion (Nelson and Cox 2013). Nevertheless, the exact zinc transport mechanism of human ZIP channels is still largely unknown, and no investigation using electrophysiological methods, such as a patch clamp technique (Kornreich 2007), has been reported. Given these pieces of evidence suggesting that ZIP channels

potentially function as ion channels, zinc transport proteins in the ZIP family are referred to as ZIP channels throughout this thesis.

ZIP channels are classified according to the phylogenetic tree into four subfamilies, consisting of gufA, subfamily I, subfamily II, and the LIV−1 subfamily (Taylor *et al.* 2007) (Fig. 1.1). All ZIP channels are predicted to have eight transmembrane domains (TM) between a long N−terminus and a short C−terminus, which are both extracytosolically located (Guerinot 2000) (Fig. 1.2). A long variable region, which contains multiple histidine residues, is present in the cytosolic loop between TM3 and TM4 and thereby proposed to be a zinc−binding region (Guerinot 2000) (Fig. 1.2). Interestingly, many members of the LIV−1 subfamily have two additional regions that contain multiple histidine residues: The N−terminus and the extracytosolic loop between TM2 and TM3 (Taylor and Nicholson 2003) (Fig. 1.2). Importantly, in TM5 of the LIV−1 subfamily, there is a unique consensus motif HEXPHEXGD (H, histidine; E, glutamate; P, proline; D, aspartate; G, glycine; X, any amino acid), which is not seen in any other subfamilies of ZIP channels (Taylor and Nicholson 2003). Interestingly, this HEXPHEXGD consensus motif matches the region in zinc metallopeptidases (zincins) that binds zinc (Hooper 1994), suggesting that this HEXPHEXGD motif is a catalytic zinc−binding site for ZIP channels. Indeed, this region, which contains highly−conserved histidine residues, has been thought to be responsible for selective zinc transport (Guerinot 2000). This speculation has been further confirmed by the findings that ZIP8 and ZIP14, which have the initial histidine residue of the HEXPHEXGD motif replaced with a glutamate residue (Taylor et al. 2007), are capable of transporting metal ions other than zinc ions, such as cadmium, manganese (Girijashanker *et al.* 2008) and iron (Wang *et al.* 2012).

Figure 1.1 Classification of the ZIP family of zinc transport proteins

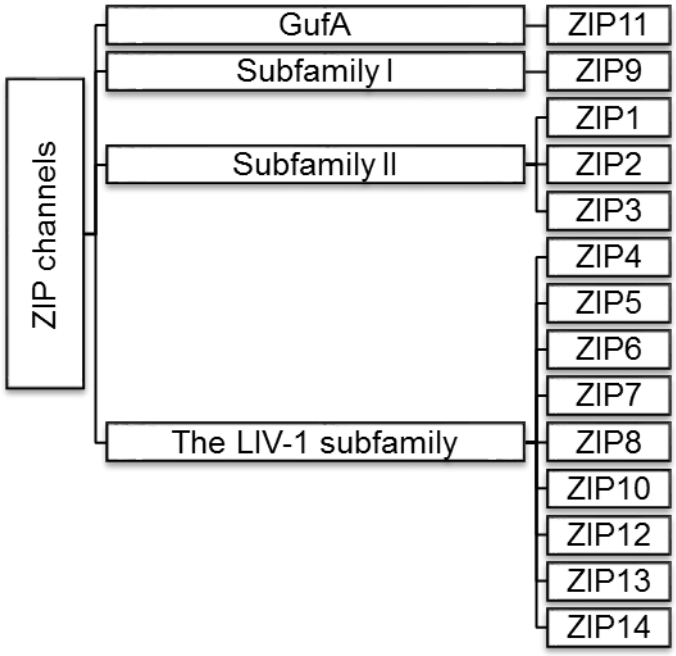

This diagram shows the classification of ZIP channels according to the phylogenetic tree (Nimmanon and Taylor 2015). ZIP channels can be grouped into four subfamilies: GufA (ZIP11), subfamily I (ZIP9), subfamily II (ZIP1, ZIP2 and ZIP3), and the most−recently characterised LIV−1 subfamily (ZIP4, ZIP5, ZIP6, ZIP7, ZIP8, ZIP10, ZIP12, ZIP13 and ZIP14).

Figure 1.2 Predicted structure of the LIV−1 subfamily members

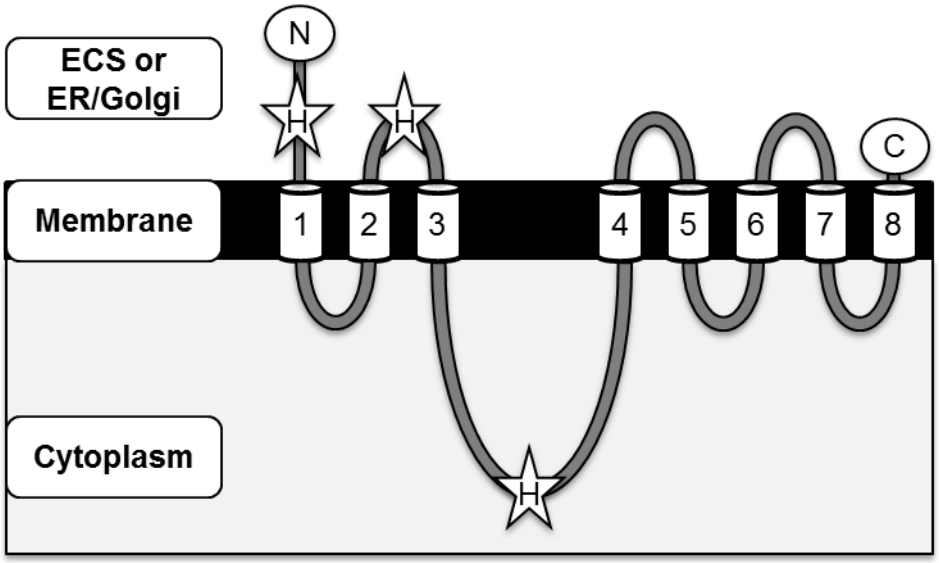

This figure illustrates the predicted structure of the LIV−1 subfamily according to a ZIP sequence computational analysis (Taylor and Nicholson 2003). Like other subfamilies of ZIP channels, the LIV−1 subfamily members are predicted to have eight transmembrane domains (TM), with extracytosolic N− and C−termini and a long histidine−rich intracytosolic loop between TM3 and TM4. Uniquely for the LIV−1 subfamily, they have additional histidine−rich regions at the amino−terminus and the region between TM2 and TM3.
ECS, the extracellular space; ER, the endoplasmic reticulum; H, the histidine−rich region.

The majority of the LIV-1 subfamily members of ZIP channels are located on the plasma membrane, and their function is therefore to import zinc into the cell (Hogstrand *et al.* 2009). Importantly, at least two members of this subfamily, namely ZIP7 and ZIP13, have been shown to be on intracellular membranes. Immunofluorescence imaging revealed co-localisation of recombinant ZIP7 with calreticulin, an ER marker (Taylor *et al.* 2004; Valentine *et al.* 2007) and recombinant ZIP13 with GM130, a Golgi marker (Bin *et al.* 2011). Instead of mediating cellular zinc influx from the extracellular space, ZIP7 and ZIP13 are therefore regulating zinc release from cellular stores. Besides the special cellular localisation of ZIP7, this ZIP channel is ubiquitously expressed throughout the human body (Taylor et al. 2004). Furthermore, ZIP7 activation by CK2-mediated phosphorylation on residues S275 and S276 (Taylor et al. 2012) results in activating phosphorylation of downstream effectors of zinc release from cellular stores, including tyrosine kinases that are involved in breast cancer progression (Taylor *et al.* 2008b). Hence ZIP7 is reasonably designated as “a gatekeeper for intracellular zinc release” and “a hub for tyrosine kinase activation” (Hogstrand et al. 2009).

Interestingly, chicken B cells (DT40) lack endogenous ZIP7 (Kambe *et al.* 2006), but have Golgi membrane-located ZIP9 functioning as a gatekeeper of zinc release from the stores instead of ZIP7 (Matsuura *et al.* 2009). Activation of ZIP9 in chicken B cells was shown to result in inhibition of protein tyrosine phosphatases and consequential activation of downstream activators of zinc release from cellular stores (Taniguchi *et al.* 2013), suggesting potential functional interchangeability of the intracellularly-located ZIP channels. Furthermore, these data also suggest that a prolonged ZIP7 functional defect in mammalian cells might be successfully compensated for by an increase in protein expression of other ZIP channels such as ZIP9.

1.4 The muffler model

Participating with zinc transport proteins in regulating free zinc levels in the cytosol, the metallothioneins facilitate the zinc−buffering reaction when cells are in a steady state, and the zinc−muffling reaction when zinc ions transiently flux into the cytosol (Colvin *et al.* 2010). Thanks to this highly effective cellular zinc−buffering system, the cytosolic free zinc levels are strictly maintained within the high picomolar to low nanomolar range, and only a small alteration can be observed following loading of micromolar levels of zinc (Krezel and Maret 2006).

To decipher this robust zinc−buffering system, a computational modelling study in correlation with experimental data was performed in cortical neuronal cells (Colvin *et al.* 2008). Among the three models investigated in this study, only the muffler model was able to predict the cellular free zinc and total zinc content in different conditions, including cellular exposure to exogenous zinc with or without pyrithione, and cellular exposure to ethylenediaminetetraacetic acid (EDTA), a metal chelator. This model incorporated a protein with high affinity for zinc ions, which was called the “muffler”, as well as sequestration and release of zinc into and from deep cellular stores into the equations. Notably, this “muffler” model is consistent with the role of zinc as a second messenger, which necessitates zinc being released from cellular stores in order to exert its action via activation of downstream effectors, as previously mentioned. Furthermore, this model highlights the importance of the cellular store−located ZIP channels through which zinc is released into the cytosol.

According to the muffler model (Colvin et al. 2010), when zinc ions flux into a cell from the extracellular space, the increase in free zinc levels is immediately modulated by the metallothionein−driven muffling reaction. The metallothioneins then shuttle the excess zinc ions to cellular stores such as the ER. Upon activation by an extracellular stimulus, zinc ions within the stores are released into the cytosol via a ZIP channel, leading to zinc−mediated cellular responses. A simplified schematic of the muffler model is shown in Fig. 1.3.

Figure 1.3 The muffler model

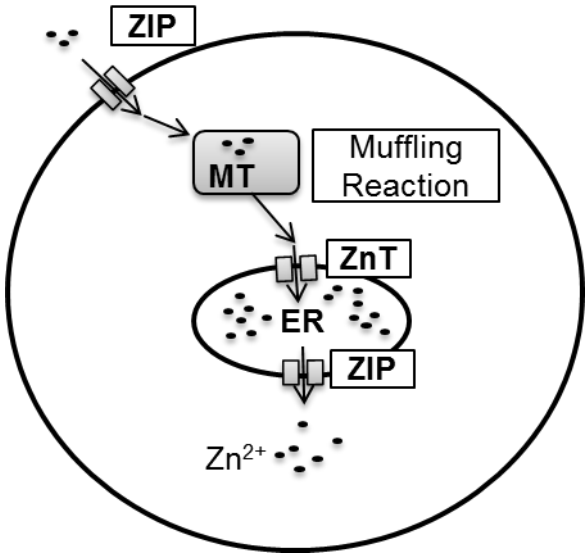

This schematic demonstrates intracellular zinc homeostasis with regard to the muffler model (Colvin et al. 2010). When zinc ions enter a cell via a ZIP channel, they are immediately bound to the muffler such as the cysteine−rich metallothioneins (MT) and shuttled to a cellular store such as the ER (Colvin et al. 2010). Upon activation, zinc ions are released from the store via a ZIP channel, leading to zinc−mediated cellular responses.

1.5 Zinc and cancer

According to the well−recognised action of zinc in promoting immunity and fighting against oxidative injuries, zinc is generally believed to be a promising dietary compound that prevents cancer (Dhawan and Chadha 2010). Regardless of lack of strong evidence from a clinical trial, many studies have supported the cancer−preventative effect of zinc. Epidemiologically, zinc deficiency, as judged by low serum zinc levels, is highly prevalent in patients with breast cancer (Arinola and Charles-Davies 2008; Gumulec *et al.* 2014) as well as cancers of the head and neck (Buntzel *et al.* 2007; Gumulec et al. 2014), the lungs (Gumulec et al. 2014), the digestive tract (Boz *et al.* 2005; Gumulec et al. 2014), the liver (Gumulec et al. 2014), the gallbladder (Gupta *et al.* 2005), the female reproductive organs (Martin-Lagos *et al.* 1997; Naidu *et al.* 2007), and the prostate (Gumulec et al. 2014). The high prevalence of zinc deficiency in breast cancer patients has also been confirmed by a decrease in hair zinc levels (Memon *et al.* 2007), which is another indicator of body zinc status with reliability comparable to serum zinc levels (Lowe et al. 2009). Noteworthy, there are still conflicting data regarding the correlation between serum zinc levels and cancer. A meta−analysis, which included 8,584 cases

and 14,153 controls from 114 various clinical observational studies, reported decreased serum zinc levels in patients with most types of cancer (Gumulec et al. 2014). In contrast, a more recent, but smaller, meta−analysis, which included 926 cases and 1324 controls from 21 studies, observed the association of breast cancer with low zinc levels only in the hair, but not in the serum (Wu *et al.* 2015). This discrepancy may be partly explained by the presence of many physiological or pathological factors that can confound serum zinc measurements (King 2011)

Experimentally, zinc deficiency in primary human lung fibroblasts, induced either by limitation of zinc supply or application of zinc chelator TPEN, was shown using DNA microarrays to upregulate genes that are involved in oxidative stress response, DNA damage and DNA repair, but downregulate expression of different DNA repair genes (Ho *et al.* 2003). An increase in oxidative DNA damage as a result of zinc deficiency was demonstrated using comet assays (single−cell gel electrophoresis) in both human lung fibroblasts (Ho et al. 2003) and rat glioma C6 cells (Ho and Ames 2002). Interestingly, although protein expression of P53 was significantly increased as a result of zinc deficiency (Ho et al. 2003), function of this DNA repair protein, which contains zinc and requires zinc for its site−specific DNA binding (Loh 2010), was shown to be markedly impaired without an adequate zinc supply (Bruinsma *et al.* 2002). These data have mechanistically indicated zinc deficiency as a cause of oxidative DNA damage, which cannot be effectively repaired, thereby predisposing cells to cancer development.

In addition, in vivo studies in mice and rats have provided evidence that zinc supplementation is able to prevent chemically induced cancers of the lungs (Satoh *et al.* 1993), the colon (Dani *et al.* 2007) and the oesophagus (Fong *et al.* 2001). Notwithstanding, clinical studies have been unable to provide agreeable data concerning the usefulness of zinc in cancer prevention, showing that zinc intake may either decrease (Kristal *et al.* 1999), have no association with (Leitzmann *et al.* 2003; Chang *et al.* 2004; Gonzalez *et al.* 2009) or increase (Kolonel *et al.* 1988) the risk of prostate cancer. Importantly, a randomised clinical trial in 5,141 men demonstrated a beneficial effect of zinc supplementation on prostate cancer prevention, even though the effect was not

distinguishable from effects of other vitamins and minerals that were taken together with zinc (Meyer *et al.* 2005). Noteworthy, the correlation between risk of cancer and body zinc status is to be interpreted with caution, given that there is no highly reliable indicator of the body zinc status available to date (Wieringa et al. 2015). Collectively, regardless of pieces of scientific evidence suggesting a potential role of zinc as a cancer chemo-preventive agent, further clinical studies are still needed to confirm this suggestion.

1.6 Zinc and ZIP channels in breast cancer

In so far as zinc is hypothesised to be an important element that prevents cancer, a tumour mass is expected to have zinc levels lower than its non-cancerous tissue counterpart. As expected, cancers of the prostate, the liver, the lungs and the thyroids have been shown to have low tissue levels of zinc (Huang *et al.* 2006). Surprisingly, in contrast to these cancers, breast cancer has been reported to have higher zinc concentrations in the tumour mass than in the normal breast tissue counterparts (Taylor et al. 2011). Emission spectrography, which is a sensitive chemical method for determining the amount of elements, was performed in eight breast cancer cases, revealing a 7-fold increase in mean zinc levels in breast cancerous tissues when compared to corresponding non-cancerous breast tissues (Mulay *et al.* 1971). This increase in zinc levels was further confirmed by two other studies using atomic absorption spectrophotometry, which, however, showed that the increase only ranged from 1.7- to 2-fold (Margalioth *et al.* 1983; Jin *et al.* 1999). Moreover, a recent investigation determined zinc levels in breast cancer tissues in a series of 59 cases, using synchrotron radiation micro probe x-ray fluorescence, which allows discrimination between zinc levels in cancerous and surrounding non-cancerous areas in the same specimens (Farquharson *et al.* 2009). Importantly, this investigation revealed that the tissue zinc levels were significantly increased only in oestrogen receptor-positive breast cancer cases (with a 1.5-fold increase), but not in oestrogen receptor-negative cases (with no increase), when compared to the adjacent non-cancerous breast tissue. Noteworthy, not only does the amount of zinc change, but the isotopic composition of zinc has also been reported to be lighter in breast cancer tumours compared to blood and normal breast tissue, introducing another potential biomarker for early detection of breast cancer (Larner *et al.* 2015).

Collectively, these data suggest that zinc levels in cancer tissues may not necessarily reflect body zinc status of the patients, and an abnormal increase in cellular zinc levels due to aberrant expression of a ZIP channel might in fact be contributory, rather than inhibitory, to breast carcinogenesis.

There has been increasing evidence of abnormal functioning of some ZIP channels in breast cancer cells (Taylor et al. 2011). Gene expression of ZIP6, the first ZIP channel to be associated with breast cancer, is positively correlated with oestrogen receptor positivity (Manning *et al.* 1993) and regional lymph node involvement (Manning *et al.* 1994). Interestingly, recent studies using a larger scale analysis in breast cancer specimens have proved that ZIP6 is a reliable marker of oestrogen receptor−positive breast cancer (Schneider *et al.* 2006; Tozlu *et al.* 2006). Another ZIP channel that has been implicated in breast carcinogenesis is ZIP10, which has also been shown using gene expression analyses in breast cancer samples to be associated with oestrogen receptor status (Taylor et al. 2007) and regional lymph node metastasis (Kagara *et al.* 2007). Importantly, our group have also reported apparently increased zinc levels in tamoxifen−resistant breast cancer cells when compared to tamoxifen−sensitive breast cancer cells, which is attributed to increased gene and protein expression of ZIP7 (Taylor et al. 2007). Furthermore, this increase in ZIP7 expression in tamoxifen−resistant breast cancer cells has been shown to contribute to aggressive behaviours in these cells (Taylor et al. 2008b). Given the links of ZIP6, ZIP10 and ZIP7 to breast cancer, mechanistic roles of these three ZIP channels in breast carcinogenesis will be discussed in more detail in the following sections.

1.6.1 ZIP7 in breast cancer

ZIP7, a member of the LIV1−subfamily of ZIP channels, is ubiquitously expressed throughout the human body (Taylor et al. 2004). ZIP7 has been proposed to play a crucial role in control of zinc release from cellular stores and thereby in regulation of cellular tyrosine kinase activation (Hogstrand et al. 2009). Interestingly, the ZIP7 gene, also recognised as SLC39A7 or HKE4, has been mapped to the human major histocompatibility complex II region on chromosome 6p21.3 (Ando *et al.* 1996), raising a possibility that this ZIP

channel might participate in zinc signalling involved in immunological responses, although no thorough investigation has been reported.

ZIP7 is uniquely localised to the ER, as confirmed by co-localisation of ZIP7 with calreticulin, an ER marker, in MCF-7 cells using the immunofluorescence technique (Taylor et al. 2004). This localisation has been further confirmed in Hela cervical cancer cells using the same method, demonstrating co-localisation of ZIP7 with ZnT5 variant B, a ZnT5 splice variant known to be specifically located in the ER (Thornton *et al.* 2011). However, it is noteworthy that one study proposed a subcellular location contrary to this, showing in human lung fibroblasts, prostate epithelial cells, erythroleukemia cells and breast cancer cells that ZIP7 was located in the Golgi (Huang *et al.* 2005). This proposal was based on a staining pattern of ZIP7 in these cells that resembled a cis-Golgi matrix protein according to a previous description (Nakamura *et al.* 1995). Moreover, in the same study, treatment with Brefeldin A, a reversible dissembler of the Golgi (Sciaky *et al.* 1997), was able to induce a reversible change in the staining pattern of ZIP7 in MCF-7 cells, consistent with ZIP7 being localised in the Golgi (Huang et al. 2005). However, this study did not directly demonstrate co-localisation of ZIP7 with a Golgi marker. Despite these conflicting pieces of evidence, it is indisputable that ZIP7 is located on intracellular membranes, the ER and/or the Golgi, and responsible for zinc release from cellular stores.

In breast cancer cells that have acquired resistance to tamoxifen (TAMR cells) (Knowlden *et al.* 2003), ZIP7 is overexpressed, resulting in a twofold increase in cellular zinc levels when compared to the parental tamoxifen-responsive MCF-7 cells (Taylor et al. 2008b). Noteworthy, TAMR cells not only grow in the presence of tamoxifen, but also manifest a more aggressive behaviour than the drug-sensitive progenitor (Hiscox *et al.* 2004). Given the strong inhibitory effect of zinc on protein tyrosine phosphatase 1B (Haase and Maret 2005; Bellomo *et al.* 2014), the increased zinc levels in TAMR cells explain the activation of signalling pathways that contribute to the aggressiveness of the cells. These signalling pathways involve the known substrates of protein tyrosine phosphatase 1B (Bourdeau *et al.* 2005), including EGFR (Knowlden et al. 2003), IGF-1R (Jones *et al.* 2004), and Src (Hiscox *et*

al. 2006). Consistent with these experimental findings, the Oncomine cancer microarray database (Rhodes *et al.* 2004) has revealed ZIP7 as an independent indicator of poor clinical outcome in breast cancer (Taylor et al. 2007). Our group have deciphered mechanistic involvement of ZIP7-mediated zinc signalling in TAMR cells, confirming that ZIP7-mediated zinc release from intracellular stores induces the activating phosphorylation of EGFR, IGF-1R, and Src (Taylor et al. 2008b), plausibly through the inhibition effect of zinc on protein tyrosine phosphatases (Haase and Maret 2005; Bellomo et al. 2014) (Fig. 1.4). The activation of these tyrosine kinases results in phosphorylation of their downstream effectors such as ERK1/2 and AKT, which in turn cause cell proliferation and migration (Taylor et al. 2008b) (Fig. 1.4). These findings have highlighted ZIP7-mediated zinc signalling as a potential target for control of breast cancer progression and for prevention of drug-resistance development.

Following the discovery of a role for ZIP7 in breast carcinogenesis, our group further investigated the functional control mechanism of ZIP7 in breast cancer cells and discovered a post-translational modification by phosphorylation on residues S275 and S276 as a ZIP7-triggering mechanism (Taylor et al. 2012). Both these residues of ZIP7, which are located in the cytosolic loop between TM3 and TM4, were shown in this investigation to be phosphorylated by protein kinase CK2, resulting in zinc release from intracellular stores, activation of ERK1/2 and AKT, and promotion of breast cancer cell migration. Given that CK2 is a key oncoprotein involved in carcinogenesis of various neoplasms with innumerable predicted substrates (Tawfic *et al.* 2001), ZIP7 might serve as a CK2 substrate that is responsible for the CK2-driven carcinogenic effects. Based upon this discovery, our group have developed a monoclonal antibody that recognises ZIP7 only when phosphorylated on residues S275 and S276, which is the activated form of ZIP7 (Taylor et al. 2012). Given the role of ZIP7 in breast carcinogenesis, particularly in the development of endocrine resistance (Taylor et al. 2008b), this antibody might be used as a biomarker predictive of tamoxifen treatment outcome. Furthermore, because there is no efficient biomarker of body zinc status (Wieringa et al. 2015), ZIP7 activity in blood cells as determined using this pZIP7 antibody might also become a useful indicator of body zinc status.

Figure 1.4 ZIP7−mediated zinc signalling

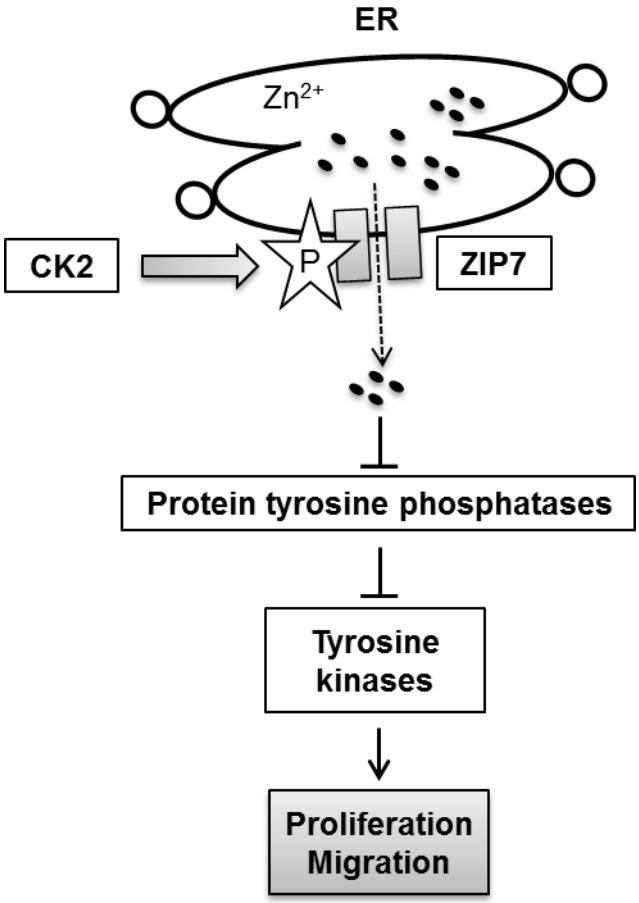

This schematic demonstrates a simplified ZIP7−mediated zinc−signalling pathway. ZIP7, which is located in the ER, is functionally activated by CK2−mediated phosphorylation on residues S275 and S276, which are located in the cytosolic loop between TM3 and TM4 (Taylor et al. 2012). This ZIP7 activation results in zinc release from cellular stores, with consequential inhibition of protein tyrosine phosphatases and activation of tyrosine kinases that contribute to a cancer phenotype such as cell proliferation and migration.

1.6.2 ZIP6 in breast cancer

ZIP6 (SLC39A6), another member of the LIV−1 subfamily of ZIP channels, was formerly known as LIV−1 (Taylor *et al.* 2003) or a 4.4 kb mRNA (Manning *et al.* 1988). An incomplete form of ZIP6 in mice, which lacks 245 residues in the N−terminus, was named “ermelin” (Suzuki and Endo 2002). The ZIP6 gene has been mapped to chromosome 18q12.2 according to the National Center for Biotechnology Information (NCBI) database. In contrast to ZIP7, which is ubiquitously expressed, a multiple−tissue expression array demonstrated that among 68 normal human tissues, the ZIP6 gene is preferentially expressed in brain tissue and tissues that are hormonally

regulated, such as the placenta, the breast and the prostate (Taylor et al. 2003). The ZIP6 gene is regulated by oestrogen, as supported by differential hybridisation identifying 4−fold and 8−fold increased ZIP6 expression in MCF−7 and ZR−75 breast cancer cells, respectively, as a result of oestrogen treatment (Manning et al. 1988). Furthermore, a Northern blot analysis in 118 primary breast cancer tumours revealed that the ZIP6 mRNA level was positively correlated with oestrogen−receptor positivity (Manning et al. 1993). This was also confirmed by another study in clinical breast cancer populations, which showed that ZIP6 expression was present in 50% of oestrogen receptor−positive cases, compared to 8% of oestrogen receptor−negative cases, with a positive correlation with oestradiol−inducible oestrogen receptor−positive cell lines (Manning *et al.* 1995).

The direct correlation between ZIP6 expression and oestrogen receptor status has been established by a large−scale real−time reverse transcription−PCR (Tozlu et al. 2006) and a microarray analysis (Schneider et al. 2006), which were performed in 36 and 56 clinical breast cancer specimens, respectively. Furthermore, our group investigated gene expression of multiple ZIP channels in a series of 74 breast cancer specimens using the reverse transcription PCR technique (Taylor et al. 2007). This investigation demonstrated a unique gene expression profile for ZIP6 with a significant positive correlation with the oestrogen receptor, erbB3, erbB4, and IGF−1R, and an inverse correlation with EGFR. Importantly, gene expression of ZIP6 is positively correlated not only with oestrogen receptor status in breast cancer specimens, but also with regional lymph node involvement. Using a Northern blotting analysis, ZIP6 gene expression was demonstrated to be significantly associated with regional lymph node involvement in oestrogen receptor−positive breast cancer (Manning et al. 1994). In this study, ZIP6 was expressed in 63% of the cases with lymph node metastasis, whereas only 13% of the cases without ZIP6 expression had lymph node involvement. Collectively, these data have identified ZIP6 as a potential biomarker for the hormone−responsive breast cancer that has now been molecularly classified as the luminal A subtype according to molecular classification of breast cancer (Schnitt 2010), with presence of regional lymph node metastasis. This luminal A molecular subtype is associated with good prognosis, having been shown to

have cumulative disease-free survival at 100 months of 95% in a series of 99 luminal A breast cancer patients (Kim *et al.* 2012). It is therefore not surprising that ZIP6 has been associated with a favourable outcome, including longer relapse-free and overall survival (Kasper *et al.* 2005).

Function of ZIP6 became known when the protein sequence was shown to match the LIV-1 subfamily of ZIP channels (Taylor and Nicholson 2003). The role of ZIP6 as a cellular zinc importer was further supported by increased cellular zinc uptake in CHO cells overexpressing recombinant ZIP6 using Newport Green diacetate, a zinc-sensitive dye, with FACS analysis (Taylor et al. 2003). This ZIP6-mediated zinc uptake was shown in the same study to be time- and temperature-dependent, suggesting a carrier-mediated process of zinc transport. Furthermore, the recombinant ZIP6 was shown using immunofluorescence to be located on the plasma membrane and the lamellipodia, which are membrane protrusions at the front of motile or migrating cells powered by actin polymerisation (Krause and Gautreau 2014), consistent with the role of ZIP6 as a zinc importer. Noteworthy, this intriguing localisation at the lamellipodia is reminiscent of the membrane-type 1 matrix metalloproteinase, which also contains an HEXXH motif and moves to the migration front where the protein promotes migration (Mori *et al.* 2002).

Currently, there is no available data directly indicating an increase in ZIP6 expression in breast cancer cells in general compared to normal mammary glandular cells. However, this assumption is supported by the fact that 73% of 3,030 breast cancer samples investigated in a study were classified as oestrogen receptor-positive using immunohistochemistry, which showed high concordance with Affymetrix U133A microarray data with the area under the receiver operating characteristics (ROC) curve of 0.949 (Karn *et al.* 2010). This fact implies that the majority of breast cancer cases are ZIP6-expressing, corresponding to the oestrogen receptor status, and therefore indirectly suggests that ZIP6 is a zinc channel responsible for the increased zinc levels in cancerous breast tissue (Mulay et al. 1971; Margalioth et al. 1983). Importantly, tissue zinc levels were shown to be exclusively increased in oestrogen receptor-positive cases, but not in oestrogen receptor-negative cases (Farquharson et al. 2009). This relationship between tissue zinc levels and

oestrogen receptor positivity is reminiscent of the aforementioned direct relationship between ZIP6 expression and oestrogen receptor status. Collectively, these data have attributed the increased zinc levels in breast cancer tissues, particularly the oestrogen receptor−positive cases, to the increased gene and protein expression of ZIP6.

The mechanism of ZIP6 in breast carcinogenesis had not become evident until it was firstly shown in embryonic development to be essential for the epithelial−mesenchymal transition (EMT) (Yamashita *et al.* 2004), which is a process whereby epithelial cells lose their epithelial phenotype and acquire a mesenchymal phenotype that enables them to migrate (Thiery *et al.* 2009). In this study, ZIP6 was shown to be a downstream target of the signal transducer and activator of transcription 3 (STAT3) during zebrafish gastrulation, leading to ZIP6−mediated nuclear retention of transcriptional repressor Snail, down−regulation of E−cadherin and cell migration (Yamashita et al. 2004). Importantly, the link between ZIP6 and STAT3 was also observed in breast cancer (Taylor et al. 2007), suggesting potential involvement of ZIP6 in breast cancer migration and metastasis, which also require EMT (Thiery et al. 2009). Our group recently demonstrated in MCF−7 cells that STAT3 induces transcription of ZIP6, and ZIP6 is produced as a pro−protein and stored in the ER (Hogstrand *et al.* 2013). In this study, Western blotting using antibodies that recognise ZIP6 at different regions suggested that the ZIP6 pro−protein undergoes an N−terminal cleavage before its relocation to the plasma membrane where it imports zinc into the cell. The imported zinc then induces inhibitory phosphorylation of GSK−3β, either directly (Ilouz *et al.* 2002) or indirectly via zinc−activated AKT (Lee *et al.* 2009; Ohashi *et al.* 2015), which in turn phosphorylates GSK−3β (Moore *et al.* 2013). Alternatively, given that GSK−3β is positively controlled by protein phosphatase 2A−mediated dephosphorylation on residue S9 (Zhou *et al.* 2009b), zinc may also induces this inhibitory of GSK−3β through its inhibitory action on this phosphatase (Xiong *et al.* 2015). Under normal circumstances, GSK−3β mediates phosphorylation of Snail (Zhou *et al.* 2004), resulting in cytoplasmic relocation and proteasomal degradation of Snail (Bauer *et al.* 2009). The inhibition of GSK−3β following ZIP6−mediated zinc influx therefore results in nuclear

retention of Snail and down−regulation of E−cadherin, enabling the cell to detach, migrate and metastasise (Hogstrand et al. 2013). The simplified schematic of this ZIP6 mechanism in EMT is shown in Figure 1.5. This mechanism of ZIP6 in breast cancer EMT clearly explains the direct relationship between ZIP6 and lymph node involvement in breast cancer.

Figure 1.5 The ZIP6 mechanism in the epithelial−mesenchymal transition

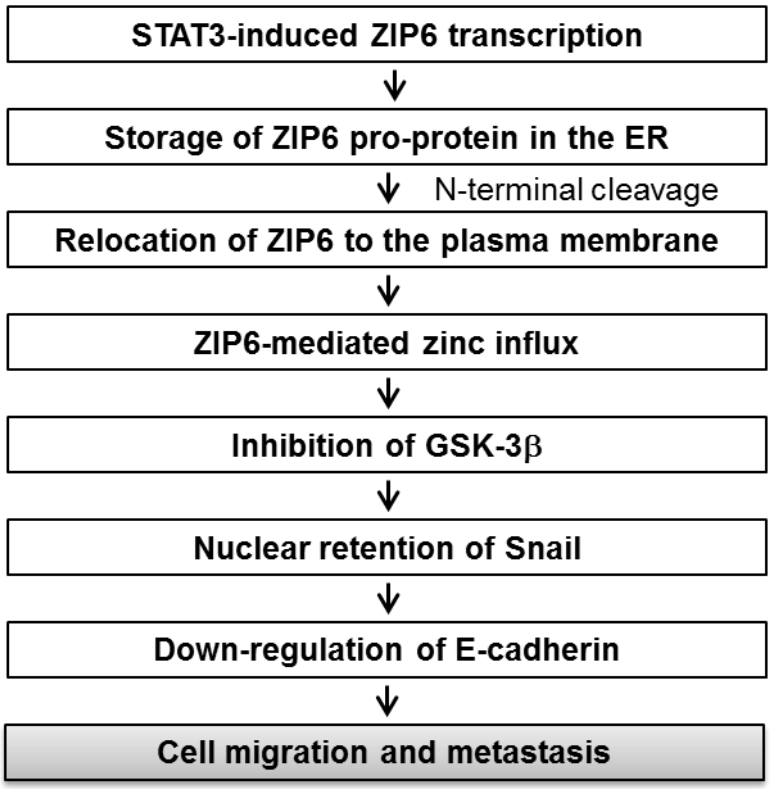

This schematic demonstrates a simplified mechanism of ZIP6 in the epithelial−mesenchymal transition (EMT) according to a previous study in our group (Hogstrand et al. 2013). When transcriptionally activated by STAT3, ZIP6 is produced as a pro−protein and stored in the ER. ZIP6 is activated by N−terminal proteolytic cleavage, and relocated to the plasma membrane, where it imports zinc ions into the cytosol, resulting in inhibitory phosphorylation on GSK−3β, nuclear accumulation of transcriptional repressor Snail, down−regulation of E−cadherin and cell migration and metastasis.

ZIP6 is involved in EMT not only in breast cancer, but also in other types of cancer. In Panc−1 pancreatic cancer cells, ZIP6 knockdown by siRNA transfection resulted in reduced nuclear localisation of Snail and increased gene and protein expression of E−cadherin when compared to an empty vector control (Unno *et al.* 2009), suggesting that ZIP6 enhances EMT in both breast

cancer and pancreatic cancer in a similar fashion. Interestingly, ZIP6 has also been shown to drive EMT even in prostatic cancer (Lue *et al.* 2011), tissue of which is known to be zinc-depleted (Huang et al. 2006). An investigation of the ZIP6 mechanism in prostate cancer EMT was performed in $ARCaP_E$ cells, which are a derivative of androgen-refractory prostate cancer cells with an epithelial phenotype (Lue et al. 2011). Interestingly, ZIP6 overexpression in these cells was shown to activate EMT via activation of matrix metalloproteinases 2 and 9, shedding of heparin binding-epidermal growth factor, phosphorylation of EGFR, and consequential triggering of the ERK signalling pathway, a pathway known to contribute to the EMT process. These data suggest that ZIP6 is mechanistically involved in EMT in a cancer type-specific manner.

1.6.3 ZIP10 in breast cancer

ZIP10, the closest paralogue of ZIP6, is another ZIP channel known to be involved in breast carcinogenesis. Its purified protein from brush border membrane of rat's kidneys was originally described as a zinc-binding protein that had high affinity and specificity for zinc binding (Kumar and Prasad 1999). This protein was confirmed shortly thereafter to be a zinc transport protein (Kumar and Prasad 2000). Using immunofluorescence, a later investigation demonstrated that this protein was localised to the plasma membrane (Kaler and Prasad 2007). Furthermore, the same investigation also showed using a ^{65}Zn uptake assay that this protein mediated zinc influx in a time-, temperature-, and concentration-dependent manner.

According to the NCBI database, the ZIP10 gene is mapped to chromosome 2q32.3. According to the Functional Annotation of the Mammalian Genome (FANTOM5) database (Lizio *et al.* 2015), the ZIP10 gene is seen to be widely expressed in human tissues, with preference for some organs, such as the brain, the spinal cord, the lungs, the kidneys, the intestines and the reproductive organs. Like ZIP6, a gene expression analysis using reverse transcription PCR demonstrated a positive correlation of ZIP10 gene expression with oestrogen receptor status in a series of 75 primary breast cancer samples (Taylor et al. 2007) and also with regional lymph node metastasis in a series of 177 primary breast cancer samples (Kagara et al. 2007).

Confirming the involvement of ZIP10 in breast cancer EMT, ZIP10 gene expression was significantly higher in cell lines with high capability to invade and metastasise, such as MDA−MB−231 and MDA−MB−435S, when compared to less aggressive cell lines, such as MCF−7, T47D, ZR75−1 and ZR75−30 (Kagara et al. 2007). Furthermore, the same study demonstrated using migration assays in the two highly invasive cell lines, MDA−MB−231 and MDA−MB−435S, that ZIP10 knockdown and zinc chelation resulted in decreased capability of the cells to migrate, proving essentiality of both ZIP10 and cellular zinc in breast cancer invasiveness. These data have introduced ZIP10 as another potential biomarker for prediction of breast cancer metastasis. Nevertheless, mechanistic details of ZIP10 involvement in EMT are still unclear and yet to be further investigated.

1.7 Post−translational modifications of ZIP channels

Regulation at the transcriptional level in various circumstances has been described for ZIP channels (Cousins *et al.* 2006). However, there is emerging evidence that ZIP channel proteins are also regulated by post−translational modifications. Given that ZIP channels have crucial roles in carcinogenesis, understanding of their post−translational modifications will provide opportunities to develop a chemo−therapeutic strategy for cancer treatment by modulating the modifications on these proteins that affect their function or cellular localisation. Two post−translational processes that have been implicated in the functional control of ZIP channels are phosphorylation and proteolytic cleavage, which will be further detailed in the following sections.

1.7.1 Phosphorylation of ZIP channels

Phosphorylation is the most extensively−studied reversible post−translational process in which a phosphoryl group is transferred from adenosine triphosphate (ATP) and covalently attached to a molecule, preferentially a serine (84%), threonine (15%) or tyrosine residue (less than 1%) (Humphrey *et al.* 2015). This process is mediated by a group of enzymes called kinases and reversed by phosphatase−mediated dephosphorylation (Cheng *et al.* 2011). It is undeniable that phosphorylation is mechanistically involved in almost all cellular aspects (Cohen 2002). Phosphorylation exerts its function as a modulator that controls enzyme activity and protein degradation, binding,

conformation, and translocation, and has biological crosstalk with other post-translational modifications, such as ubiquitination, acetylation, and methylation (Humphrey et al. 2015). Given that activity of a protein does not always reflect gene or protein expression levels of the protein, post-translation modifications, especially phosphorylation, constitute a key mechanism that causes this discrepancy (Lim 2005). It is therefore not surprising that disruption of phosphorylation control has been known as a key mechanism involved in pathogenesis of human diseases, including cancer.

The importance of phosphorylation in oncogenesis has been supported by identification of disruption of either phosphorylation sites or kinase functions in cancer. A high-throughput bioinformatics approach demonstrated that prevalence of the mutations that cause gain and loss of phosphorylatable residues was approximately 1.9% and 3.2%, respectively, which were both twice as high as control datasets (Radivojac *et al.* 2008). Furthermore, 164 out of 478 known eukaryotic protein kinases in human have been mapped to the amplicons that are commonly affected by cancer mutations (Manning *et al.* 2002). Importantly, some kinase inhibitors have been invented and successfully used for cancer treatment. Imatinib mesylate (Gleevec), a Bcr-Abl tyrosine kinase inhibitor, is one of the most successful targeted therapies, having become the first-line treatment for chronic myeloid leukaemia (Henkes *et al.* 2008). Trastuzumab (Herceptin), a monoclonal antibody against receptor tyrosine kinase erbB2 or HER2/neu, has also greatly benefitted patients with HER2-positive breast cancer (Pinto *et al.* 2013). These data highlight phosphorylation as a key cellular process that is essential for functional control of proteins, and when this mechanism is disrupted, dysregulated proteins may greatly contribute to pathogenesis of diseases. Additionally, given the crucial role of phosphorylation in regulation of protein functions, it is reasonable to raise the question whether ZIP channels may also be controlled by this mechanism.

Zinc is released from intracellular stores on the time scale of minutes in response to an extracellular stimulus, which has been observed in mast cells (Yamasaki et al. 2007) and breast cancer cells (Taylor et al. 2008b). This early response suggests that the process of zinc release might involve a post-translational mechanism that triggers ZIP channels in the cellular stores,

such as ZIP7, independently of transcriptional activation of the channels, which requires several hours to finish the process. Consistent with this suggestion, our group have proved the role of phosphorylation in functional control of ZIP7 (Taylor et al. 2012). In this study, ZIP7 was demonstrated to be phosphorylated by CK2 on residues S275 and S276, as previously mentioned in Section 1.6.1. This finding has specifically indicated residues S275 and S276 as potential sites for modulating the function of ZIP7. Furthermore, the association of ZIP7 with CK2 has introduced ZIP7 as a key substrate of this kinase that is responsible for the CK2−related cancer aggressiveness and poor clinical outcome (Ortega *et al.* 2014). Additionally, the discovery of ZIP7 control by phosphorylation also suggests a possibility that other ZIP channels, particularly those belonging to the LIV−1 subfamily, may also be post−translationally controlled in the same fashion. A number of phosphorylation sites, both serine/threonine and tyrosine residues, have been detected in online phosphorylation site databases for ZIP3, ZIP6, ZIP8 and ZIP10 (Hogstrand et al. 2009). However, these sites have not been confirmed by site−specific experiments other than mass spectrometry, and their roles as well as their responsible kinases are yet to be investigated.

1.7.2 Proteolytic cleavage of ZIP channels

In contrast to phosphorylation, proteolytic cleavage is an irreversible process in which protease−mediated hydrolysis breaks a protein into smaller pieces (Walsh *et al.* 2005). As a result, the proteolytic cleavage products have new termini, which are termed neo−N terminus and neo−C terminus (Marino *et al.* 2015). Proteolytic cleavage has been widely overlooked, despite its ubiquitous involvement not only in protein degradation, but also in protein activation or inactivation, localisation, maturation, and secretion (Rogers and Overall 2013). Some viruses have also been demonstrated to require this post−translational process for their infectivity, such as the 1918 influenza virus (Chaipan *et al.* 2009).

Proteases have been increasingly identified, with the MEROPS online peptidase database annotating 990 genes as human proteases, which account for 4−5% of the human genome (Rawlings *et al.* 2014). Based upon their catalysis mechanism, they can be classified into 5 classes: cysteine, serine, threonine, aspartic, and metalloproteases (Puente *et al.* 2003). The first 3

classes mediate covalent catalysis, employing an amino acid as the nucleophile of the catalytic site, whereas the last 2 classes mediate non−covalent catalysis, employing an activated water molecule as the nucleophile of the catalytic site (Turk 2006). Alternatively, these proteases can be divided based upon their modes of substrate cleavage into endopeptidases and exopeptidases (Barrett and McDonald 1986). Endopeptidases cleave their substrates in the middle of the molecules, whereas exopeptidases cleave their substrates at either the N−terminus (aminopeptidases) or the C−terminus (carboxypeptidases) (López-Otín and Bond 2008).

ZIP4 was the first ZIP channel to be established as post−translationally processed by proteolytic cleavage. Triggered by zinc deficiency, ZIP4 was shown to be proteolytically cleaved at the extracellular N−terminus immediately proximal to TM1 (Kambe and Andrews 2009). After this cleavage, an active 37−kDa fragment of ZIP4 on the apical plasma membrane of intestinal cells absorbs zinc from the intestinal lumen. This study therefore revealed that proteolytic cleavage is an important post−translational mechanism required for zinc−transport function of ZIP4. Intriguingly, quantitative interactome and bioinformatic analyses revealed in vivo spatial proximity of ZIP6 and ZIP10 to the cellular prion protein (PrP^C) (Watts *et al.* 2009). Furthermore, the PrP−like peptide sequence was detected in the extracellular N−terminus of ZIP6 and ZIP10, and ZIP5, which are grouped in the same sub−branch in the phylogenetic tree of ZIP channels (Schmitt-Ulms *et al.* 2009). These observations suggest mechanistic similarities of ZIP6, ZIP10, and ZIP5 to PrP^C, which has ecto−domain shedding as a crucial post−translational mechanism (Altmeppen *et al.* 2012). Importantly, the process of ecto−domain shedding has also been reported for both ZIP10 (Ehsani *et al.* 2012) and ZIP6 (Hogstrand et al. 2013). Triggered by deprivation of zinc or manganese, ZIP10 is cleaved at the N−terminus, shedding its PrP−like ecto−domain and the remained segment of ZIP10 is then enabled to transport zinc and manganese to maintain homeostasis of these metals (Ehsani et al. 2012). In a different context, N−terminal cleavage of the ER−located ZIP6 pro−protein enables the processed ZIP6 to relocate to the plasma membrane where ZIP6 imports zinc into the cytosol (Hogstrand et al. 2013), as described in Section 1.6.2 (Fig. 1.5). Collectively, these findings have established that proteolytic cleavage is a

crucial functional control mechanism and a requirement for zinc−transport capability for ZIP channels, particularly ZIP4, ZIP10, and ZIP6.

1.8 Zinc in the cell cycle

Zinc has been known for over 50 years to play a key role in cell proliferation, since EDTA, a chelating agent of divalent cations, was shown in a study to suppress DNA synthesis and this suppression was reversed by zinc (Fujioka and Lieberman 1964). Employing Fluozin−3, a zinc−sensitive fluorescent dye, the pivotal role of zinc in the cell cycle was further supported by a discovery of intracellular zinc fluctuations in a specific pattern during different cell cycle stages (Li and Maret 2009). Additionally, it was recently demonstrated in human hepatoblastoma cells that zinc deficiency caused transcriptional down−regulation of p21 (Wong *et al.* 2007), a potent cyclin−dependent kinase (CDK) inhibitor. Noteworthy, p21 is now known to promote cyclin D1 function by enhancing cyclin D1/CDK4/CDK6 complex formation (LaBaer *et al.* 1997). Repression of p21 transcription by different causes has been proved to reduce this complex formation, resulting in a block at the G1/S transition in vascular smooth muscle cells (Kavurma and Khachigian 2003) and endothelial cells (Noseda *et al.* 2004). These findings suggest that zinc deficiency might also inhibit cell cycle progression through this mechanism. However, the mitosis−inhibitory effect of zinc deficiency was shown to be independent of the reduction in p21 protein levels in human hepatoblastoma cells (Wong et al. 2007). Additionally, chronic zinc deprivation induced by exposure of neuronal precursor cells to TPEN was shown to induce the p53 pathway, resulting in impaired cell proliferation and eventually apoptosis (Corniola *et al.* 2008). Altogether, these data endorse the importance of zinc in normal cellular cell cycle machinery.

Confirming the pivotal role of zinc in DNA synthesis, thymidine incorporation, which is indicative of DNA synthesis, was shown to be markedly reduced by 90% after exposure of 3T3 fibroblast cells to diethylenetriamine pentaacetate, a divalent metal ion chelator, and this inhibition was specifically reversed by supplementation of zinc (Chesters *et al.* 1989). The need for zinc in proper DNA synthesis was shown in the same study to start from the mid−G1 phase when the proteins that are essential for initiation of DNA synthesis such

as thymidine kinase were produced. This finding was consistent with an observation that zinc deprivation by EDTA significantly suppressed enzyme activity of thymidine kinase (Lieberman *et al.* 1963). The requirement of zinc in the G1 phase was later supported by the prominent peaks of zinc concentrations observed in the early G1 phase and the late G1/S phase (Li and Maret 2009). Interestingly, even though DNA synthesis is known to be a zinc−dependent process, zinc is not required to be readily available during the process for its accomplishment (Chesters et al. 1989). However, it was shown in myoblasts that zinc was still needed during the S phase and also the G2 phase for subsequent cell passage through the G2/M phase and cell entry into the G1 phase (Chesters and Petrie 1999). The requirements of zinc during the pre−mitotic phases, which include the G1, S, and G2 phases, were shown to coincide with zinc−dependent increases in mRNA concentrations of the cyclins that are specifically required at different cell cycle stages (Chesters and Petrie 1999). Collectively, these findings suggest the pivotal role of zinc throughout the mitotic process. Nevertheless, the exact mechanism of zinc in the mitotic phase is still unknown.

1.9 STAT3

It has already been shown that ZIP6 is transcriptionally activated by STAT3 in zebrafish gastrula organizer cells (Yamashita et al. 2004) and breast cancer cells (Hogstrand et al. 2013), whereas ZIP10 expression is regulated by STAT3/STAT5 in B−cell lymphoma cells (Miyai *et al.* 2014). STATs, or signal transducers and activators of transcription, are known as a family of latent cytoplasmic transcription factors, which have a major role in defining destiny of a cell. They were originally recognised as a DNA−binding protein complex called interferon−stimulated gene factor 3, which was reported to be involved in interferon alpha−induced transcriptional activation (Schindler *et al.* 1992). This protein complex is now known to comprise STAT1, STAT2, and interferon regulatory factor 9 and becomes activated by Janus kinases (JAK), which is a family of receptor−bound non−receptor tyrosine kinases (Fink and Grandvaux 2013). Further investigations have indicated essential roles of this JAK/STAT pathway in diverse cellular processes, leading to identification of other members of the STAT family, namely STAT3 to STAT6, with STAT5 being divided into STAT5a and STAT5b (Schindler and Darnell 1995). Participation of this

JAK/STAT pathway in cell proliferation, cell differentiation, apoptotic cell death, inflammation and embryonic/foetal development has now been well established (Abroun *et al.* 2015).

The human STAT genes have been mapped to 3 clusters on chromosomes 2 (STAT1 and STAT4), 12 (STAT3, STAT5a and STAT5b), and 17 (STAT2 and STAT6) (Darnell 1997). Importantly, each STAT gene contains a conserved single tyrosine residue on the C−terminal tail around residue 700 (Schindler and Darnell 1995). Phosphorylation on this C−terminal tyrosine residue results in formation of either a homodimer or a heterodimer, which is a highly competent DNA−binding form of STATs that translocates to the nucleus and modulates STAT−dependent gene transcription (Rawlings *et al.* 2004). For example, STAT3 has been reported to form a dimer either with another molecule of STAT3 or with STAT1, STAT4, STAT5, and STAT6 in different contexts (Delgoffe and Vignali 2013). The formation of a STAT dimer is dependent upon intermolecular interaction of the phosphotyrosine of one STAT molecule with the Src Homology 2 domain of the other STAT molecule (Heim *et al.* 1995). Outstandingly, STAT3 and STAT5 are two major STATs that participate in promotion of tumour cell proliferation and prevention of tumour cell death (Walker *et al.* 2014). Furthermore, STAT3 is the only STAT that is involved in regulation of cancer immunity, thereby being appreciated as a potential target for cancer treatment (Yu *et al.* 2014). Additionally, the unique indispensable function of STAT3 is highlighted by early embryonic lethality that is exclusively found in mice deficient of STAT3, but not in mice deficient of any other STATs (Akira 1999).

Notably, a link between STAT3 and a ZIP channel became known for the first time when ZIP6 was demonstrated to be a gene that was transcriptionally activated by STAT3 during zebrafish gastrulation (Yamashita et al. 2004). Using morpholino injection as a means to modify gene expression in zebrafish embryos, this study showed that depletion of STAT3 abolished ZIP6 gene expression, and depletion of STAT3, ZIP6, or Snail1 prevented the organiser cells from undergoing a normal EMT process. These results have indicated ZIP6 as a STAT3 downstream target that is essential for EMT in zebrafish gastrulation, with Snail1 also involved in this pathway. Noteworthy, these

findings are consistent with the embryonic lethality in STAT3−deficient mice, which occurs in a stage requiring nutrient influx for cell migration (Akira 1999).

Importantly, all the three proteins that are associated with EMT in gastrulation, consisting of STAT3 (Devarajan and Huang 2009), ZIP6 (Manning et al. 1994), and Snail (Blanco *et al.* 2002), have also been associated with breast cancer metastasis. The role of this STAT3−ZIP6−Snail pathway in breast cancer EMT has been described in Section 1.6.2. Noteworthy, as a step in the EMT process, our group observed cell rounding and detachment as a result of the E−cadherin transcriptional repression by Snail (Hogstrand et al. 2013). This adoption of a spherical shape of cells is a prominent feature of the mitotic process (Thery and Bornens 2008). Given that both STAT3 (Abroun et al. 2015) and zinc (MacDonald 2000) are actively involved in mitosis, it is plausible that ZIP6 might be an intermediary between these two signalling molecules during the mitotic process. Furthermore, our group have also observed that cells expressing ZIP6 had decreased pY705 STAT3 and increased pS727 STAT3 (Hogstrand et al. 2013). This inverse relationship between pY705 STAT3 and pS727 STAT3 has also been observed in nocodazole−induced mitotic cells (Shi *et al.* 2006), and is consistent with direct binding of zinc to STAT3, which results in a structural change of STAT3 that disrupts its activation by JAK1−mediated tyrosine phosphorylation (Kitabayashi *et al.* 2010). In so far as ZIP6 plays a role in the cell rounding prior to mitosis, it is interesting to investigate whether ZIP6−mediated zinc influx is also responsible for the conversion of pY705 STAT3 to pS727 STAT3 during mitosis.

1.10 Aims of this project

The general aim of this project was to decipher post−translational mechanisms of ZIP7, ZIP6, and ZIP10, which play important roles in breast carcinogenesis. To attain this goal, the following objectives were pursued:

1. To define downstream pathways of ZIP7−mediated zinc release from intracellular stores
2. To explore potential phosphorylation sites in all ZIP channels
3. To investigate ZIP6 phosphorylation sites in mitosis
4. To determine a role for ZIP6 and ZIP10 in mitosis

Chapter 2:
Materials and methods

2.1 Cell preparation and treatments

2.1.1 Cell culture and cell seeding for experiments

MCF−7 (human breast carcinoma) cells were cultured in Roswell Park Memorial Institute (RPMI) medium (Gibco) supplemented with 5% foetal bovine serum (FBS) and antibiotics (10 IU/mL Penicillin, 10 µg/mL Streptomycin, and 2.5 µg/mL Amphotericin B). Tamoxifen−resistant MCF−7 (TAMR) cells (Knowlden et al. 2003), MDA−MB−231 (MDA−231) cells, and MDA−MB−436 (MDA−436) cells were cultured in phenol−red−free RPMI medium (Gibco) supplemented with 5% charcoal−stripped steroid−depleted FBS, and 200 mM L−glutamine, antibiotics (10 IU/mL Penicillin, 10 µg/mL Streptomycin, and 2.5 µg/mL Amphotericin B). Additionally, 10^{-7} M 4−hydroxytamoxifen was added to the medium for TAMR cells. NMuMg (mouse breast glandular) cells, either wild−type or ZIP6−knockout, were cultured in Dulbecco's Modified Eagle Medium (DMEM) with 4.5 g/L glucose supplemented with 10% FBS, 10 µg/mL bovine insulin, 200 mM L−glutamine, and antibiotics (10 IU/mL Penicillin, 10 µg/mL Streptomycin, and 2.5 µg/mL Amphotericin B).

For experiments, cells were trypsinised using 10 mL of 0.05% trypsin and 0.02% EDTA in PBS for up to 5 minutes at 37°C, which was neutralised using an equal amount of medium with serum. After resuspending the cell pellet in medium with serum, 100 µL of the cell suspension was added to 10 mL Isoton II balanced electrolyte solution (Beckman Coulter). The number of cells present was determined using a Coulter counter (Beckman Coulter), and $1.5x10^5$ cells were seeded onto 35 mm dishes, either with 22x22 mm ultra−thin glass coverslips (0.17 mm thick) for immunofluorescence or without coverslips for Western blotting. For proximity ligation assay, $0.5x10^5$ cells were seeded into each well of an 8−well chamber slide (Lab−Tek, Fisher), which has a removable chamber with a gasket on a standard microscope slide. For growth assays, $0.2x10^5$ cells were seeded into each well of a 24−well plate. MCF−7 cells were nourished with phenol−red−free RPMI medium (Gibco) that was supplemented with 5% FBS, 200 mM L−glutamine and antibiotics (10 IU/mL Penicillin, 10 µg/mL Streptomycin, and 2.5µg/mL Amphotericin B). Other cell lines were grown in regular medium with supplements as mentioned earlier. The medium was refreshed every 3−4 days.

2.1.2 Transfections

When MCF−7 cells were 60−90% confluent, they were transfected with plasmid DNAs using Lipofectamine−2000 transfection reagent (Invitrogen). The plasmid DNAs contained a CMV promoter and a carboxyl−terminal V5 tag in vector pcDNA3.1/V5−His−TOPO (Fig. 2.1).

Figure 2.1 Schematic of ZIP7 or ZIP6 gene inserted in a plasmid vector

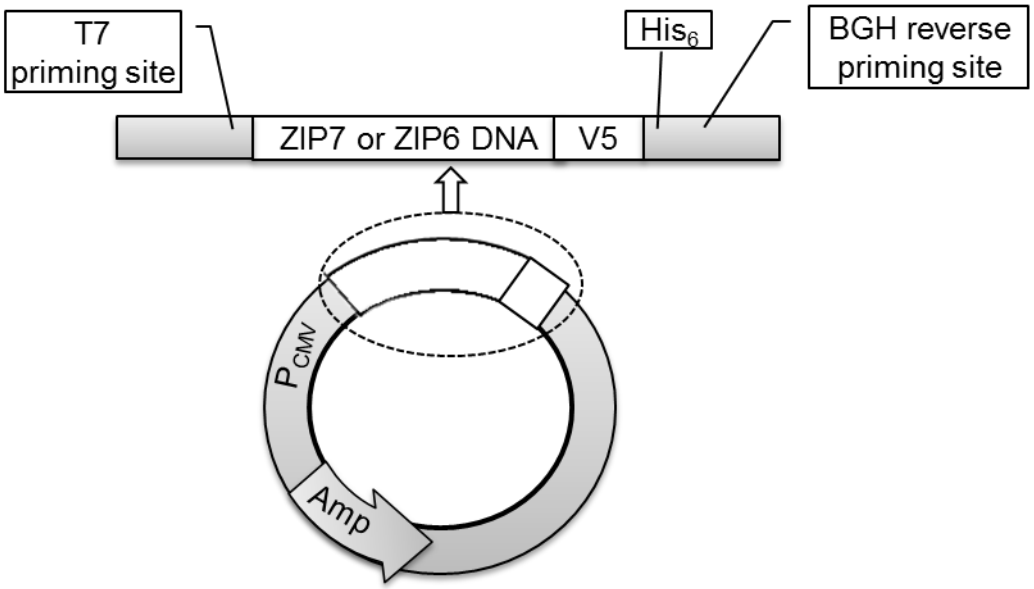

This schematic demonstrates a simplified structure of the pcDNA3.1/V5−His−TOPO plasmid. It contains a carboxyl−terminal V5 epitope with a T7 priming site and a BGH reverse priming site, which were used for verification of a DNA insert. This vector also contains a CMV promoter (P_{CMV}), an ampicillin−resistant gene (Amp), and a polyhistidine tag (His_6).

Either 3.5 µg ZIP7 plasmid DNA or 3.75 µg ZIP6 plasmid DNA, and 7.5 µL Lipofectamine 2000 reagent were separately diluted in 188 µL phenol−red−free RPMI medium (Gibco) without serum and antibiotics (either antibacterial or antifungal drugs). Within 5 minutes of dilution at room temperature, diluted DNA and diluted Lipofectamine 2000 were mixed together and incubated at room temperature for 20 minutes. The transfection reaction was added into a dish that contains cells in phenol−red−free RPMI medium (Gibco) with FBS and L−glutamine, making a final volume of 1.5 mL. For transfection a ZIP6 construct, 3 mM sodium butyrate was added for 16 hours to upregulate the CMV promoter and thereby enhance expression of the

recombinant proteins (de Poorter *et al.* 2007). The cells were incubated in the transfection mixture at 37°C for 16–24 hours for ZIP7 and 16 hours for ZIP6.

2.1.3 Treatments

For short-term zinc treatment (up to 20 minutes), cells were incubated in either 20 µM zinc plus 10 µM sodium pyrithione in phenol-red-free RPMI medium with glutamine, but without serum and antibiotics (either antibacterial or antifungal drugs), at 37°C. For short-term zinc treatment (up to 30 minutes) in live cell experiments, 100 µM zinc plus 10 µM sodium pyrithione in phenol-red-free RPMI medium with serum and glutamine, but without antibiotics (either antibacterial or antifungal drugs), at 37°C. For nocodazole treatment, cells were incubated with 100 nM nocodazole in RPMI medium with serum, glutamine, and antibiotics (antibacterial and antifungal drugs) at 37°C for 20 hours. For antibody treatment, a ZIP6 or ZIP10 antibody (Table 2.1) was added to RPMI medium with serum, glutamine, and antibiotics (antibacterial and antifungal drugs). For zinc chelation, 50 µM TPEN, a membrane-permeable zinc chelator, was added to the medium.

For ZIP6 experiments that require separation of the adherent and the non-adherent cells, cells were collected using the mitotic shake-off technique (Izawa and Pines 2015). Briefly, the medium, which contained some non-adherent cells, was transferred to a collection tube, and 1 mL of phenol-red-free RPMI medium with FBS and L-glutamine, but without antibiotics (either antibacterial or antifungal drugs), was gently added to the dish. The cells were agitated by gently tapping on the side of the dish 3 times. The loosely-attached non-adherent cells that had been detached were directly collected and transferred to the corresponding collection tube. The monolayer adherent cells in the bottom was trypsinised using 1 mL of 0.05% trypsin and 0.02% EDTA in PBS for up to 5 minutes at 37ºC, which was then neutralised with 1 mL of the medium with serum before being collected.

Table 2.1 ZIP antibodies

Antibody	Sp	Type	Company	Catalogue number	Dilutions				Ab Rx
					IF	WB	PLA	FACS	
pZIP7 [a]	m	mAb	Biogenes	–	1:100	1:1000	–	–	–
Total ZIP7 [b]	r	pAb	Biogenes	–	1:200	1:1000	–	–	–
ZIP6 E–20 [c]	r	pAb	SCBT	SC84875	–	1:1000	1:100	1:25	–
ZIP6 M [d]	m	mAb	Biogenes	–	–	–	–	–	✓
ZIP6 Y [e]	m	mAb	Biogenes	–	1:20	1:1000	–	1:25	✓
ZIP10 [f]	r	pAb	Sigma	SAB2102209	–	–	–	–	✓
ZIP10 [g]	m	mAb	Sigma	SAB1401780	–	1:1000	1:100	–	–
ZIP10 [h]	r	pAb	Abcam	Ab83947	–	1:1000	1:100	–	–
ZIP10 R [i]	r	pAb	Biogenes	–	–	–	1:100	–	✓

[a] **pZIP7 (S275/S276) mAb.** The epitope is TKEKQ pS pS EEEEK (residues 270–281, the cytosolic loop between TM3 and TM4).
[b] **Total ZIP7 pAb.** The epitope is GRQERSTKEKQSSE (residues 264–277, the cytosolic loop between TM3 and TM4).
[c] **ZIP6 E–20 pAb.** The epitope is in the cytosolic loop between TM3 and TM4.
[d] **ZIP6 M7 mAb.** The epitope is HHDHDHHSDHEHHSD (residues 93–107, the N–terminus).
[e] **ZIP6 Y3 mAb.** The epitope is VSEPRKGFMYSRNTNEN (residues 238–254, the N–terminus).
[f] **ZIP10 (SAB2102209) pAb.** The epitope is LHRQHRGMTELEPSKFSKQAAENEKKYYIEKLFE RYGENGRLSFFGLEKL (residues 36–85, the N–terminus).
[g] **ZIP10 (SAB1401780) pAb.** The epitope is CIRMFKHYKQQRGKQKWFMKQNTEESTIGRKLSDHK LNNTPDSDWLQLKPLAGTDDSVVSE DRLNETELTDLEGQQESPPKNYLCIEEEKIIDHSHSDGLHTIHEHDL (residues 514–621, from TM3 to the cytosolic loop between TM3 and TM4).
[h] **ZIP10 (Ab83947) pAb.** The epitope is in the cytosolic loop between TM3 and TM4.
[i] **ZIP10 R (animal 25) pAb.** The epitope is LEPSKFSKQAAENE (residues 46–59, the N–terminus).
Sp, species; IF, immunofluorescence; WB, Western blot; PLA, proximity ligation assay; FACS, fluorescence–activated cell sorting; Ab Rx, antibody treatment experiments; m, mouse; r, rabbit; Biogenes, Biogenes GmbH; CST, Cell Signaling Technology; SCBT, Santa Cruz Biotechnology; Sigma, Sigma–Aldrich; mAb, monoclonal antibody; pAb, polyclonal antibody.

2.2 Bacterial transformation and plasmid preparation

The process of bacterial transformation, plasmid preparation, transfection, and characterisation of DNA constructs is illustrated in Fig. 2.2 and 2.3. Each process will be further explained in individual sections. Briefly, competent bacteria were transformed with a pcDNA3.1/V5–His–TOPO plasmid that contained a ZIP7 or ZIP6 construct. Presence and orientation of the insert was confirmed by PCR using a specific ZIP7 or ZIP6 primer and a BGH reverse primer (Fig. 2.2). A clone that contained the correctly–orientated DNA insert was purified using a HiSpeed or EndoFree Plasmid Maxi Kit (Fig. 2.2).

Figure 2.2 An experimental strategy for plasmid preparation

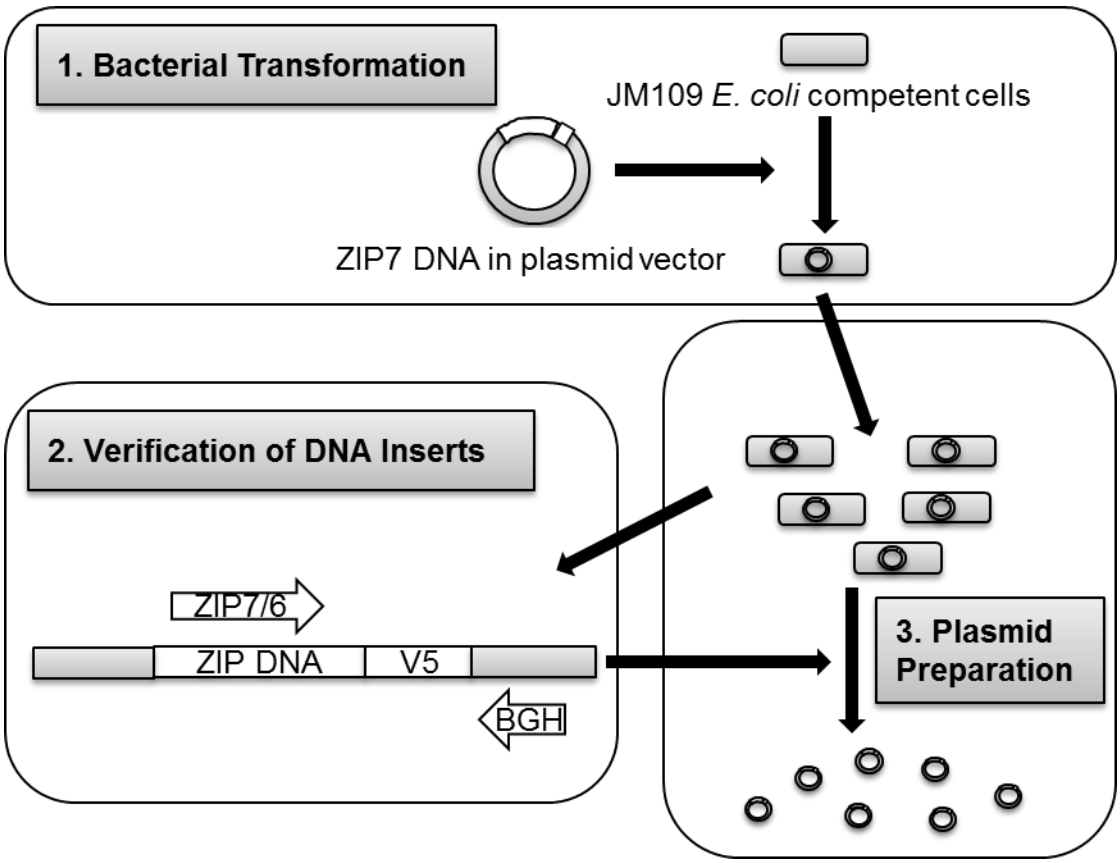

1. Competent bacteria are transformed with a pcDNA3.1/V5−His−TOPO plasmid that contains a ZIP7 or ZIP6 construct.
2. Presence and orientation of the insert are confirmed by PCR using a specific ZIP7 or ZIP6 primer and a BGH reverse primer.
3. A clone that contains the correctly−orientated DNA insert is selected for plasmid preparation, using either a HiSpeed or EndoFree Plasmid Maxi Kit.

For characterisation of a DNA construct, a transfection was performed using Lipofectamine 2000 (Fig. 2.3). Cells were then treated with zinc plus zinc ionophore sodium pyrithione or nocodazole (Fig. 2.3). Immunofluorescence, Western blotting, flow cytometry or proteome profiler antibody array procedure was performed for determination of protein expression or modification such as phosphorylation (Fig. 2.3). Furthermore, cellular zinc levels were determined by fluorescence microscopy or flow cytometry using zinc−sensitive dyes, consisting of Fluozin−3, Newport Green and Zinquin, whereas protein binding was determined by immunoprecipitation or proximity ligation assay (Fig. 2.3). All the antibodies that were used in these experiments are listed in Tables 2.1−2.3.

Figure 2.3 An experimental strategy for investigations in this project

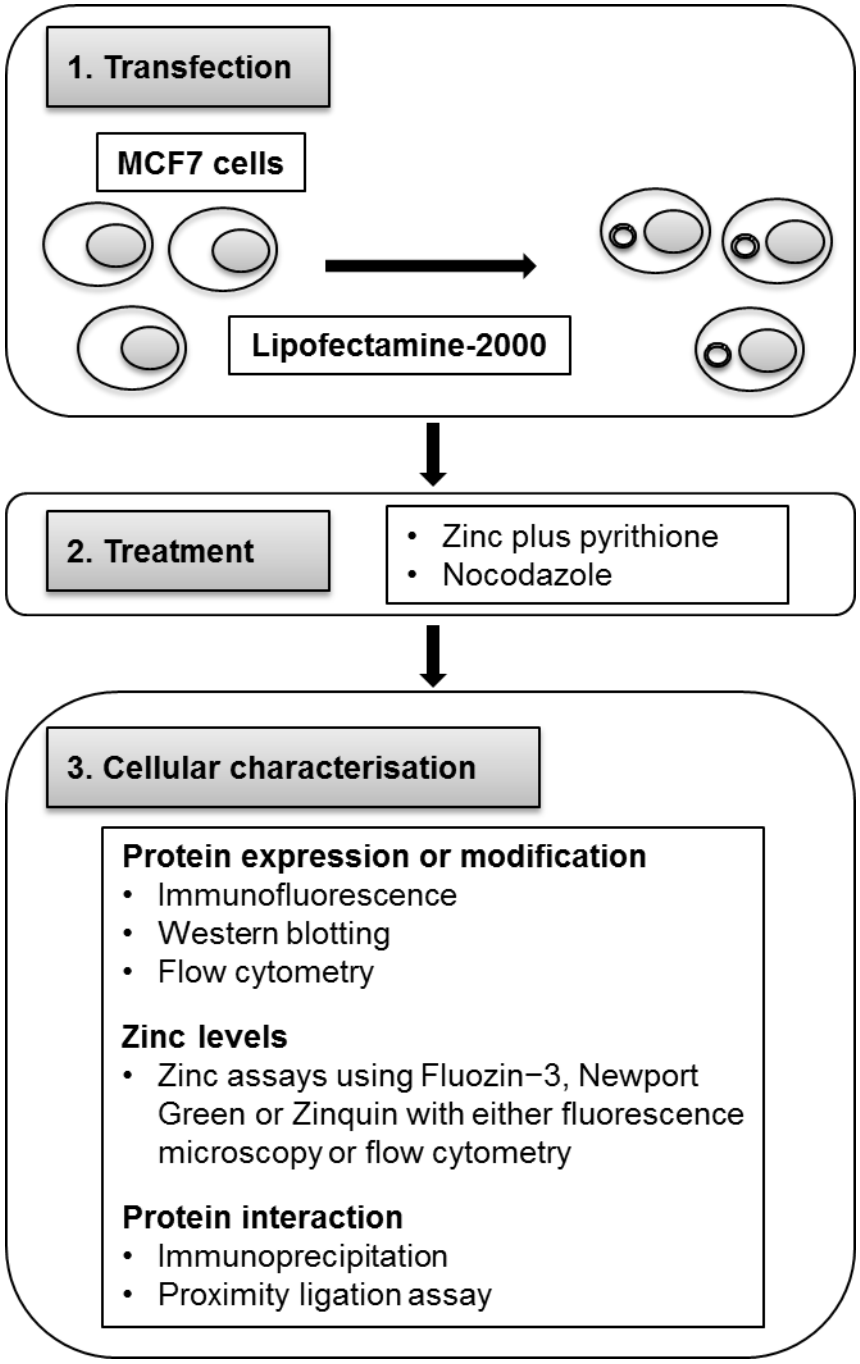

1. For experiments in transfected cells, purified plasmids are transfected into MCF−7 cells using Lipofectamine 2000.
2. Cells are treated with zinc plus zinc ionophore sodium pyrithione. For experiments on mitosis, cells are treated with nocodazole to increase the number of mitotic cells.
3. Cellular effects are determined using various techniques. Protein expression or modification (phosphorylation) is determined using immunofluorescence, Western blotting, flow cytometry and proteome profiler antibody arrays. Zinc levels are determined using a zinc−sensitive fluorescence dye (Fluozin−3, Newport Green, or Zinquin) with either fluorescence microscopy or flow cytometry. Protein interaction or binding is determined using immunoprecipitation or proximity ligation assay.

Table 2.2 Primary antibodies other than ZIP antibodies

Antibody	Sp	Type	Company	Catalogue number	Dilutions			
					IF	WB	PLA	FACS
β−actin−peroxidase	m	mAb	Sigma	A3854	−	1:50000	−	−
β−catenin	m	mAb	Sigma	C7082	1:100	1:1000	−	−
CK1a	m	mAb	SCBT	SC74582	−	1:1000	1:100	−
CK2a	m	mAb	SCBT	SC12738	−	1:1000	1:100	−
GAPDH−peroxidase	m	mAb	CST	SC32233	−	1:50000		−
GSK−3β	m	mAb	Abcam	Ab93926	−	1:1000	1:100	−
pAKT (S473)	r	pAb	CST	9271	−	1:1000	−	−
pCREB (S133)	r	pAb	CST	9198	−	1:1000	−	−
pGSK−3β (S9)	r	pAb	CST	9336	−	1:1000	−	−
pHistone H3 (S10)	m	mAb	CST	9706S	−	−	−	1:10
pHistone H3 (S10)	r	pAb	CST	3377S	1:500	1:1000	−	1:10
pP70 S6 (T421/S424)	r	pAb	CST	9204	−	1:1000	−	−
pSer	m	mAb	SCBT	SC81514	−	1:1000	−	−
pStathmin (S38)	r	pAb	CST	4191S	−	−	1:200	−
pSTAT3 (S727.49)	m	mAb	SCBT	SC136193	−	1:1000	1:200	−
pSTAT5a/b (S726)	r	pAb	SCBT	SC12893R	−	1:1000	−	−
V5	r	pAb	Abcam	Ab15828	1:1000	1:1000	−	−
V5	r	pAb	SCBT	SC83849R	1:1000	−	−	−

Sp, species; IF, immunofluorescence; WB, Western blot; PLA, proximity ligation assay; FACS, fluorescence−activated cell sorting;
m, mouse; r, rabbit;
CST, Cell Signaling Technology; SCBT, Santa Cruz Biotechnology; Sigma, Sigma−Aldrich;
mAb, monoclonal antibody; pAb, polyclonal antibody.

Table 2.3 Secondary antibodies

Antibody	Sp	Company	Catalogue number	Dilutions		
				IF	WB	FACS
Alexa Fluor−488	GAM	MP	A11029	1:1000	−	1:100
Alexa Fluor−488	GAR	MP	A11034	1:1000	−	1:100
Alexa Fluor−594	GAM	MP	A11032	1:1000	−	1:100
Alexa Fluor−594	GAR	MP	A11037	1:1000	−	1:100
Alexa Fluor−647	GAM	MP	A21237	1:1000	−	1:100
Alexa Fluor−647	GAR	MP	A21246	1:1000	−	1:100
HRP−linked IgG	GAM	Fisher	10094724	−	1:10000	−
HRP−linked IgG	GAR	CST	7074	−	1:10000	−

Sp, species; IF, immunofluorescence; WB, Western blot; FACS, fluorescence−activated cell sorting;
GAM, goat anti−mouse; GAR, goat anti−rabbit; HRP, horseradish−peroxidase;
Fisher, Fisher Scientific; MP, Molecular Probe; CST, Cell Signaling Technology

2.2.1 Site−directed mutagenesis

Site−directed mutagenesis was performed by Mutagenex Inc, and the mutations were confirmed by DNA sequencing. Individual serine, threonine, or tyrosine residues were mutated to alanine (codon GCA, GCT or GCC) for a phosphoablative (null) mutant or aspartate (codon GAC) for a phosphomimetic mutant (Table 2.4).

Table 2.4 DNA sequences of ZIP7 and ZIP6 mutants

Construct	Wild−type DNA sequence	Mutant DNA sequence
ZIP7 S275A S276A	CAG**AGCTCA**GAG	CAG**gcCgCA**GAG
ZIP7 S275D S276D	CAG**AGCTCA**GAG	CAG**gaCgac**GAG
ZIP6 S471A	CAGTTG**TCC**AAGTAT	CAGTTG**gCC**AAGTAT
ZIP6 Y473A	TCCAAG**TAT**GAATCT	TCCAAG**gct**GAATCT
ZIP6 S475A	TATGAA**TCT**CAACTT	TATGAA**gCT**CAACTT
ZIP6 S478A	CAACTT**TCA**ACAAAT	CAACTT**gCA**ACAAAT
ZIP6 T479A	CTTTCA**ACA**AATGAG	CTTTCA**gCA**AATGAG

2.2.2 Bacterial transformation

DNA constructs were inserted into an ampicillin-resistant pcDNA3.1/V5-His-TOPO plasmid vector and were amplified by transformation of single-use JM109 *E. coli* competent cells (Promega) according to the manufacturer's instructions. Briefly, 1 µL plasmid solution in Tris-EDTA (TE) buffer, which contained 3.0-3.3 µg plasmid DNA, and 50 µL competent cells were mixed and incubated on ice for 30 minutes. The bacteria were then heat-shocked at 40 ºC for 20 seconds, replaced on ice for 2 minutes, supplemented with 450 µL super optimal broth with catabolite repression (SOC) medium, and incubated at 37ºC with shaking for 60 minutes. Eventually, 100 µL of the transformation reaction was plated on a Luria-Bertani (LB) agar plate with 100 µg/mL ampicillin at 37ºC for 18 hours. The transformed bacteria on an agar plate were kept at 4 ºC for less than one month.

Presence and orientation of DNA inserts in the plasmid vector were verified by PCR using a forward primer specific to either ZIP7 (MWG Biotech AG, sequence: 5'-TTGTTGCCTTTCTTGTCGTG-3') or ZIP6 (MWG Biotech AG, sequence: 5'-GTCTAACAGCTCTAGGAGGC-3') and a BGH reverse primer (MWG Biotech AG, sequence: 5'-TAATACGACTCACTATAGGG-3'). Noteworthy, the BGH reverse primer was complementary to the BGH reverse priming site of the pcDNA3.1/V5-His-TOPO vector (Fig. 2.1). Each 25 µL PCR mixture contained 1x NH4 reaction buffer [16 mM $(NH_4)_2SO_4$, 67 mM Tris-HCl (pH 8.8)] (Bioline), 1.5 mM of $MgCl_2$ (Bioline), 200 µM of dNTP mix, 0.2 µM of each primer, and 1 U of BIOTAQ DNA polymerase (Bioline), and a bacterial colony from the LB agar plate. Twenty cycles of PCR were programmed to perform the following thermal cycling conditions: the denaturation step at 94 ºC for 10 seconds, the annealing step at 55 ºC for 30 seconds, and the extension step at 72 ºC for 2 minutes. An initial denaturation at 94 ºC for 10 minutes and a final extension at 72 ºC for 10 minutes were also added to the PCR settings. Five µL of each PCR product was separated by 1% agarose gel electrophoresis, along with 0.6 µg/lane 1 kb DNA Step Ladder (Promega) at 100 V for 45 minutes, and visualised with a UV transilluminator.

2.2.3 Plasmid preparation

The correctly-orientated plasmids obtained within the competent cells were purified using the HiSpeed Plasmid Maxi Kit (Qiagen) for ZIP7 constructs or the EndoFree Plasmid Maxi Kit (Qiagen) for ZIP6 constructs according to the manufacturer's instructions. Briefly, a colony of the transformed competent cells was inoculated in 5 mL LB medium with 100 µg/mL ampicillin at 37ºC with vigorous shaking for 8 hours. The starter culture was diluted 1/500 into 250 mL LB medium with 100 µg/mL ampicillin, and further grown at 37ºC with vigorous shaking for 16 hours. After centrifugation at 6,500 rpm at 4 °C for 15 minutes and resuspension of the pellet with 10 mL buffer P1 with 100 µg/mL RNAse and 1x LyseBlue added, the competent cells were lysed with 10 mL buffer P2 for 5 minutes. The bacterial lysate was then neutralised with 10 mL buffer P3 and cleared by filtration using a QIAfilter Cartridge.

For the HiSpeed Plasmid Maxi Kit, the plasmid DNA was purified using a HiSpeed Maxi Tip, from which the DNA was eluted with 15 mL buffer QF. The DNA obtained was further purified by precipitations with isopropanol and 70% ethanol, employing the QIAprecipitator Module provided in the kit. The purified DNA was finally dissolved in 500 µL endotoxin-free Buffer TE.

For the EndoFree Plasmid Maxi Kit, endotoxin was removed from the filtrate by incubation in 2.5 mL buffer ER on ice for 30 minutes. The plasmid DNA was purified using a QIAGEN-tip 20 anion-exchange tip, from which the DNA was eluted with 15 mL buffer QN. The DNA obtained was further purified by precipitations with isopropanol and 70% ethanol. Finally, the purified DNA was re-dissolved in 200 µL endotoxin-free Buffer TE.

The plasmid DNA solution was analysed with a UV spectrophotometer for concentration and purity, which were determined by the absorbance at 260 nm (OD260) and the ratio of the absorbance at 260 nm to the absorbance at 280 nm (OD260/OD280 ratio), respectively. Additionally, the plasmid DNA was also analysed with 1% agarose gel electrophoresis along with 0.6 µg of 1 kb DNA Step Ladder (Promega) at 100 V for 45 minutes and visualised with a UV transilluminator. Eventually, the plasmid was verified using immunofluorescence stained with the anti-V5 antibody, which will be shown in the corresponding chapters.

2.3 Immunofluorescence

Cells on a 22x22 mm 0.17 mm thick glass coverslip or an 8-well chamber slide (Lab-Tek, Fisher) were fixed with 4% formaldehyde in PBS for 15 minutes and washed with PBS twice. For the 8-well chamber slide, the chamber was removed after fixing, leaving a gasket on the slide. The cells either on the coverslip or on the slide were blocked and permeabilised with 1% bovine serum albumin (Sigma-Aldrich) and 0.4% saponin (Sigma-Aldrich) in PBS for 15 minutes, with additional blocking with 10% normal goat serum (DAKO) in the blocking/permeabilisation solution for 15 minutes. The cells were then probed with primary antibodies (Tables 2.1 and 2.2) for 60 minutes. After washing, the cells were incubated with either a mixture of 2 µg/mL Alexa Fluor goat anti-mouse 594 and goat anti-rabbit 488 antibodies (Molecular Probes) or a mixture of 2 µg/mL Alexa Fluor goat anti-mouse 488 and goat anti-rabbit 594 antibodies (Molecular Probes) (Table 2.3) for 30 minutes, with light protection. The coverslip was mounted on a slide with VECTASHIELD Mounting Media (Vector Laboratories) containing 1.5 µg/mL 4,6-diamidino-2-phenylindole (DAPI) and sealed with nail varnish. For the 8-well chamber slide, the gasket was removed, and a 22x50 mm 0.17 mm thick glass coverslip was mounted on the slide with the mounting media with DAPI and sealed with nail varnish. The stained slides were stored at 4ºC in the dark until they were visualised on a Leica RPE automatic microscope using a 63x oil immersion lens with a multiple bandpass filter for DAPI, Texas Red and fluorescein. Images were acquired using Openlab modular imaging software for Macintosh operating system with one-level deconvolution. Brightness and contrast adjustments were performed using GIMP 2.8.4 (GNU Image Manipulation Program) open-source software.

2.4 Western blotting and co-immunoprecipitation

2.4.1 Cell harvesting and sample preparation

Cells in a 35 mm dish were lysed with 100 µL lysis buffer pH 7.6 (50 mM Tris, 150 mM NaCl, 5 mM EGTA, and 1% Triton X-100) with 10% (v/v) protease inhibitor cocktail for mammalian cells (Sigma-Aldrich) and additional phosphatase inhibitors (2 mM sodium orthovanadate and 50 mM sodium fluoride). The lysate was incubated on ice with occasional mixing for 60 minutes to allow maximal separation of the plasma membrane proteins from the

membrane and centrifuged at 12,000 rpm for 12 minutes at 4ºC. Concentration of the supernatant was analysed with a UV spectrophotometer, using a Bio-Rad/Bradford dye-binding protein microassay. The sample was diluted in Laemmli sample buffer (Laemmli 1970), to make a final concentration of 1 µg/µL, boiled at 100 ºC for 5 minutes and stored at −20ºC.

2.4.2 Co-immunoprecipitation

Four-hundred µg cell lysate was incubated with either 0.4 µg rabbit LIV-1 E-20 antibody (Santa Cruz Biotechnology, SC-84875) or 4.0 µg rabbit V5 polyclonal antibody (Abcam, Ab9116) at 4ºC overnight. On the following day, the sample was mixed with 20 µl of EZview Red Protein A Affinity Gel beads (Sigma-Aldrich, P6486) at 4 ºC for 4 hours. The beads were washed with lysis buffer containing protease inhibitors 4 times and eventually resuspended in 20 µL lysis buffer with 20 µL Laemmli sample buffer (Laemmli 1970). The precipitated proteins were separated from the beads by boiling at 100 ºC for 5 minutes and centrifuging at 9600 rpm for 30 seconds. The supernatant was collected for analysis by Western blotting.

2.4.3 Polyacrylamide gel electrophoresis-sodium dodecyl sulphate (SDS-PAGE) and immunodetection

Proteins were separated by 7.5-12% SDS-PAGE at 120 V for 90 minutes and transferred onto a nitrocellulose membrane at 100 V for 60 minutes. Proteins on the membrane were reversibly stained with 0.1% (w/v) Ponceau S in 5% acetic acid to image bands, before washing off with Tris Buffered Saline with Tween-20 (TBST). Non-specific proteins were blocked with 5% non-fat dried milk (Marvel) in TBST for 60 minutes. The blot was then incubated with a primary antibody at 4 ºC overnight. The primary antibodies used are shown in Tables 2.1 and 2.2. After incubation with the primary antibody, the membrane was incubated with either horseradish-peroxidase (HRP)-labelled goat anti-mouse or anti-rabbit antibodies (1:10,000) (Table 2.3) at room temperature for 60 minutes. Either a β-actin peroxidase-conjugated antibody or a GAPDH peroxidase-conjugated antibody (Table 2.2) was used as a standard, with which the membrane was incubated at room temperature for 15 minutes. Combinations of Pierce ECL Western blotting detection reagents (Thermo Scientific), Clarity Western ECL substrate

(Bio-Rad), SuperSignal West Dura Substrate (Thermo Scientific), and SuperSignal West Femto Substrate (Thermo Scientific) were used for the chemiluminescence-based immunodetection. To visualise the protein bands, the blot was exposed to a high-resolution blue sensitive X-ray film (Photon Imaging Systems) in a dark room. Densitrometric data were acquired using Alpha DigiDoc version 4.10, and the results were analysed with Microsoft Excel 2010 or 2013 program, using β-actin, GAPDH, or V5 for normalisation.

2.5 Flow cytometry

2.5.1 Immunostaining

Cells in a 35 mm dish were trypsinised using 1 mL of 0.05% trypsin and 0.02% EDTA in PBS for up to 5 minutes at 37ºC and centrifuged at 1000 rpm for 5 minutes. The cells were washed in 1 mL ice-cold PBS, and incubated with 50 µL of primary antibodies (Tables 2.1 and 2.2) in blocking/permeabilisation solution (1% BSA and 0.4% saponin in KRH buffer) on ice for 60 minutes. The cells were washed again in 1 mL ice-cold PBS and then incubated with 50 µL of 20 µg/mL Alexa Fluor goat anti-mouse 647 plus 20 µg/mL Alexa Fluor goat anti-rabbit 488 antibodies (Molecular Probes) (Table 2.3) in the blocking/permeabilisation solution on ice for 30 min. The cells were then fixed with 500 µL 4% formaldehyde at room temperature for 15 min, centrifuged at 1000 rpm for 10 min and resuspended in 500 µL PBS. Fluorescence intensity was measured with BD FACSVerse Flow Cytometer. Data were analysed using Flowing Software version 2.50 (Turku Centre for Biotechnology).

2.5.2 Cell cycle analysis

Cells in a 35 mm dish were trypsinised using 1 mL of 0.05% trypsin and 0.02% EDTA in PBS for up to 5 minutes at 37ºC, washed in PBS and fixed in 70% ethanol at −20 ºC overnight or longer. After centrifuging at 2000 rpm for 10 minutes, the fixed cells were washed in ice-cold PBS twice and incubated with the staining solution (20 µg/mL propidium iodide, 0.2 µg/mL DNase-free RNase A, and 0.1% Triton X-100 in PBS) at 37ºC for 20 minutes. The cell suspension was filtered through a cell strainer (12x75 mm; mesh size: 35 µm) to collect the single cells. Fluorescence intensity was measured with BD FACSVerse Flow Cytometer. Cell cycle analysis was performed with FlowJo Software version 10, using the Watson pragmatic algorithm (Watson *et al.* 1987).

2.6 Zinc assays

Cells were loaded with 5 µM Fluozin-3 (Invitrogen), 25 µM Zinquin (Santa Cruz Biotechnology) or 5 µM Newport Green diacetate DCF (Invitrogen) in phenol-red-free RPMI medium with glutamine and serum, but without antibiotics (either antibacterial or antifungal drugs), at 37ºC for 30 minutes in the dark. The cells were washed and incubated in the same medium without dye for at least 30 minutes to allow complete de-esterification of intracellular AM esters. For determination of cellular zinc using fluorescence microscopy, the cells were fixed after treatment. The coverslip was mounted on a glass slide, and the cells were visualised as described for immunofluorescence. At least 6 images were taken from each coverslip using the same exposure time for each experiment. Fluorescence intensity was determined using ImageJ Software version 1.49 (Schneider *et al.* 2012), and the total corrected cellular fluorescence was calculated by subtracting integrated density with background intensity, which equals area of selected cell multiplied by mean fluorescence of average background readings (McCloy *et al.* 2014). For determination of cellular zinc using flow cytometry, fluorescence intensity was measured with BD FACSVerse Flow Cytometer. Mean fluorescence was calculated using Flowing Software version 2.50 (Turku Centre for Biotechnology).

2.7 Proximity ligation assays (PLA)

The process of PLA is illustrated in Fig 2.4. Treated and/or transfected cells on an 8-well chamber slide (Lab-Tek, Fisher) were fixed with 4% formaldehyde in PBS for 15 minutes. After washing with PBS twice, the chamber was removed, leaving the hydrophobic well borders on the slide to accommodate 100 mL volumes. The cells were blocked and permeabilised with a 50/50 mixture of the blocking/permeabilisation solution and the Duolink blocking solution (Sigma-Aldrich) for 15 minutes. The blocking/permeabilisation solution contains 1% bovine serum albumin (Sigma-Aldrich) and 0.4% saponin (Sigma-Aldrich) in PBS. The cells were then incubated with primary antibodies (Tables 2.1 and 2.2) in the blocking/permeabilisation solution at room temperature for 60 minutes. The slide was placed in a water chamber to prevent drying, and the cells were then probed with a mixture of Duolink II anti-rabbit MINUS and anti-mouse PLUS probes (Sigma-Aldrich), which contain oligonucleotides, in the blocking/permeabilisation solution at 37ºC for 60

minutes. Utilising Duolink In Situ Detection Reagents Red (Sigma−Aldrich), signals were produced by further incubating the cells with ligase in the ligation buffer at 37ºC for 30 minutes to hybridise the PLA probes and generate a closed circle and polymerase in the amplification buffer at 37ºC for 100 minutes to enhance rolling circle amplification in the water chamber.

Figure 2.4 Proximity ligation assays (PLA)

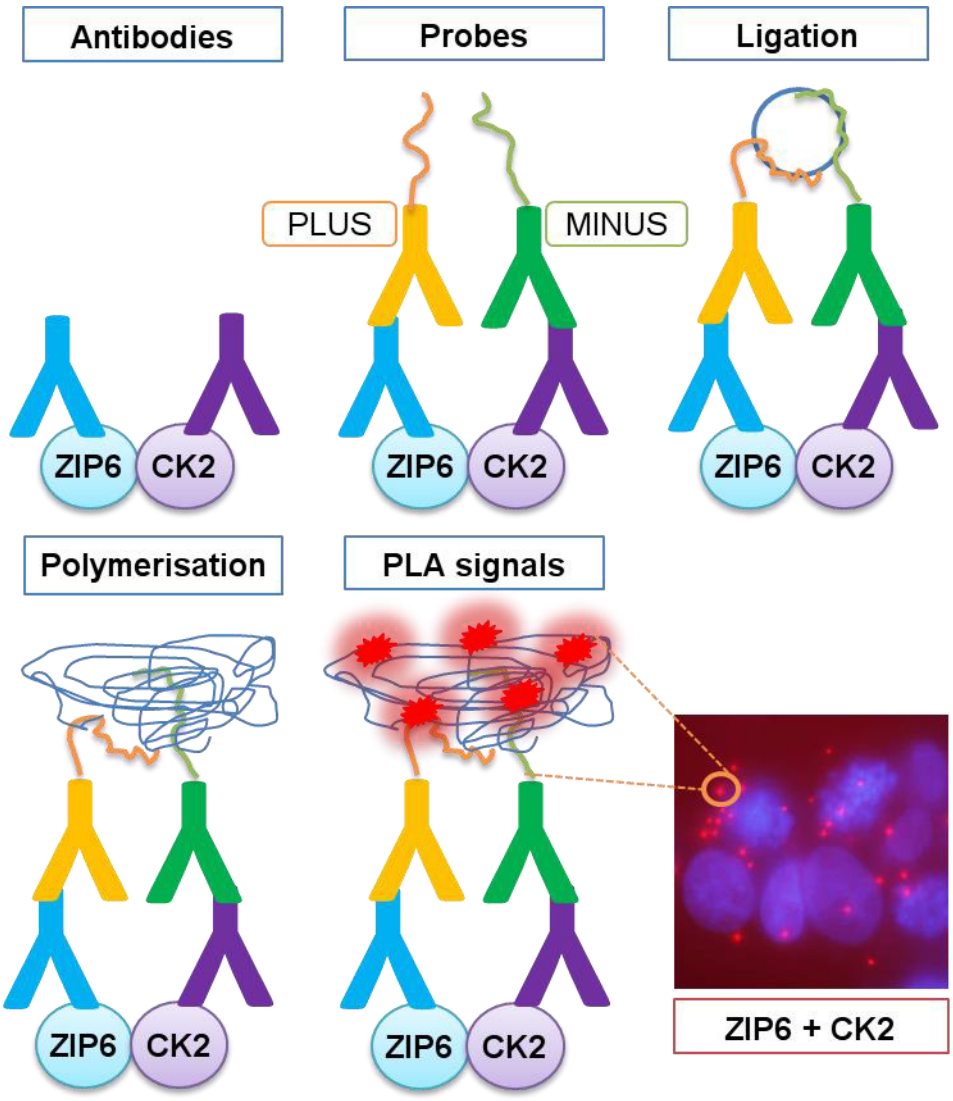

This schematic shows the process of PLA. Cells are incubated with two antibodies against the proteins of interest. These antibodies are raised from two different animal species. PLA probes, plus and minus, bind to the primary antibodies corresponding to the animal species from which they are raised. Enzymes ligase and polymerase are applied to enhance ligation and amplification of the oligonucleotide attached to the probes, resulting in ring DNA circle formation and rolling circle amplification. A red fluorescent probe that is added during the amplification step hybridises with the amplified DNA. Provided the two target proteins are in close proximity, the binding is detected as red fluorescent dots.

After the gasket was completely removed, a 22x50 mm 0.17 mm thick glass coverslip was mounted on the slide using VECTASHIELD Mounting Media (Vector Laboratories) containing DAPI and sealed with nail varnish. The slide was visualized on a Leica RPE automatic microscope using a 63x oil immersion lens with a multiple bandpass filter for DAPI and Texas Red. The images were acquired and presented as maximal projections of 25 stacks taken 0.3 µm apart using Openlab modular imaging software for Macintosh operating system. The numbers of dots per cell were determined using Duolink ImageTool software (Olink Bioscience). Brightness and contrast adjustments were performed using GIMP 2.8.4 software.

2.8 Growth assays

Cells were grown in a 24−well plate and treated with either a ZIP6 or a ZIP10 antibody (Table 2.1) at 24 hours. The cells were collected every day until day 4. The medium was refreshed on day 3. To collect the cells, they were trypsinised using 1 mL of 0.05% trypsin and 0.02% EDTA in PBS for 5 minutes at 37°C, and 3 mL Isoton II balanced electrolyte solution (Beckham Coulter) was added to each well. To prepare single cells, the cell suspension was drawn up into a 5 mL syringe through a 25G needle and transferred to a Coulter Counter counting cups containing 6 mL Isoton II balanced electrolyte solution (Beckham Coulter). The amount of the single cells was determined using a Beckham Coulter counter (Beckham Coulter).

2.9 Proteome profiler antibody array procedures

The human phospho−receptor tyrosine kinase (RTK) (R&D Systems, ARY001B), phospho−mitogen−activated protein kinase (MAPK) (R&D Systems, ARY002B), phospho−kinase (R&D Systems, ARY003B), and protease (R&D Systems, ARY021B) antibody arrays were used. The strategies of array signal detection are illustrated in Fig. 2.5 and 2.6.

After transfection and zinc treatment, cells in a 35 mm dish with 90% confluence were lysed in either 100 µL Lysis Buffer 17 with 10 µg/mL Aprotinin, 10 µg/mL Leupeptin, and 10 µg/mL Pepstatin (for the phosphor−RTK and the protease arrays) or 100 µL Lysis Buffer 6 (for the phospho−kinase and the

phospho−MAPK arrays). The rest of the procedures were performed according to the manufacturer's instruction utilising the reagents supplied with the arrays.

For the phospho−RTK array, each membrane was blocked in Array Buffer 1 at room temperature for 60 minutes and incubated in 300 µg lysate diluted in the blocking buffer at 4 ºC overnight. On the following day, the array was incubated with the Anti−Phospho−Tyrosine−HRP Detection Antibody in Array Buffer 2 at room temperature for 2 hours.

Figure 2.5 Human phospho−receptor tyrosine kinase (RTK) arrays

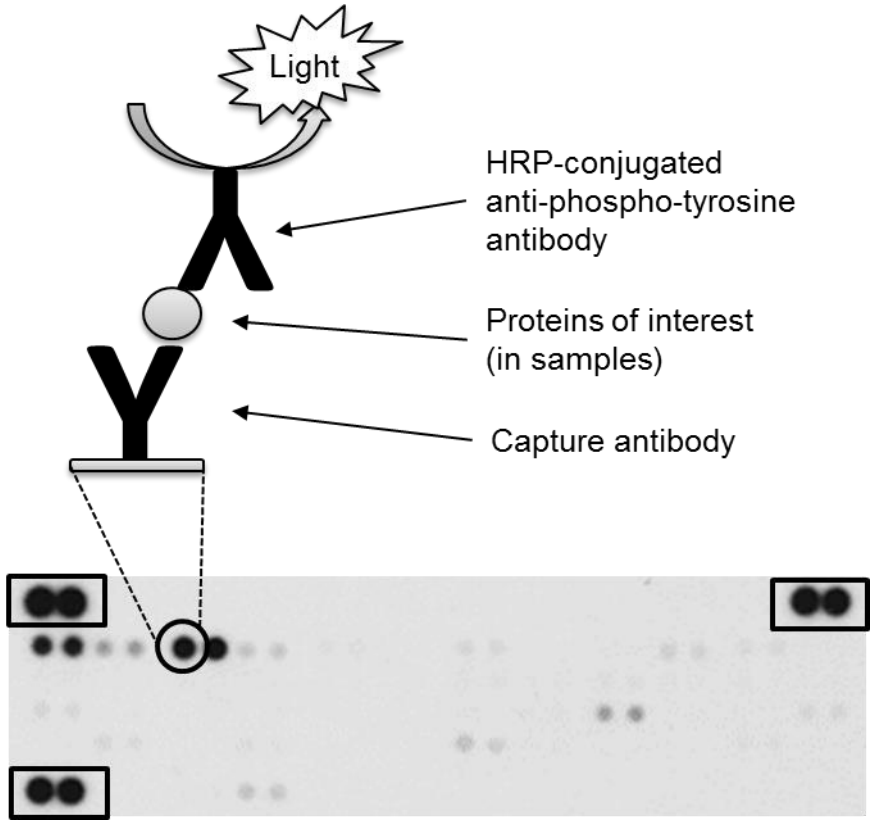

This schematic illustrates the signal detection strategy for phospho−RTK arrays. Three pairs of reference spots are present on the left upper, right upper, and left lower corners of each array. Capture antibodies are blotted on the membrane in duplicate and bind to RTKs that are present in cell lysates. Tyrosine phosphorylation of particular RTKs is determined by application of an HRP−conjugated anti−phospho−tyrosine antibody. Signals are detected using a standard chemiluminescence procedure.

For the phospho−kinase array, each of Part A and Part B of the membrane was blocked in Array Buffer 1 at room temperature for 60 minutes and incubated in 300 µg lysate diluted in the blocking buffer at 4 ºC overnight. On the following day, the array was incubated with either Detection Antibody Cocktail A (for Part A) or B (for Part B) in Array Buffer 2/3 (Array Buffer 2 diluted in Array Buffer 3) at room temperature for 2 hours and with Streptavidin−HRP (1:2,000) in Array Buffer 2/3 at room temperature for 30 minutes.

Figure 2.6 Human phospho−kinase, phospho−mitogen−activated protein kinase (MAPK), and protease arrays

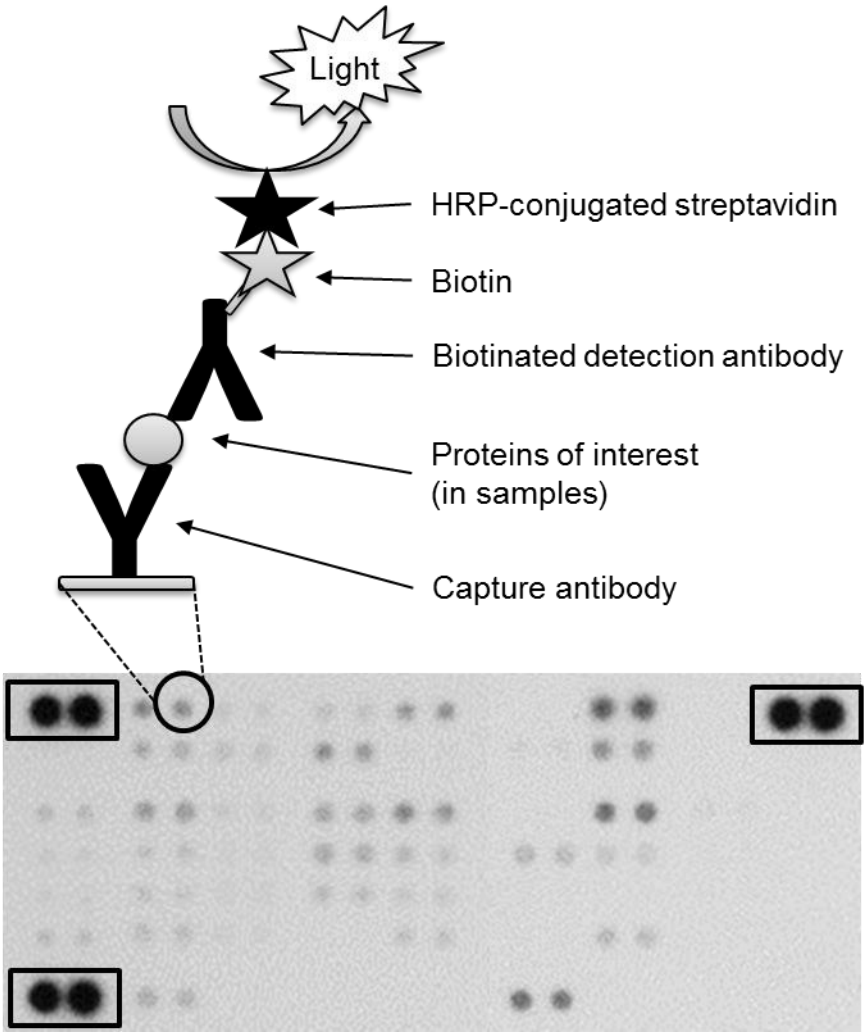

This schematic illustrates the signal detection strategy for phospho−kinase, phospho−MAPK, and protease arrays. Three pairs of reference spots are present on the left upper, right upper and left lower corners of each array. Capture antibodies are blotted on the membrane in duplicate and bind to kinases or proteases that are present in the cell lysates. Phosphorylation of particular kinases on specific sites or presence of particular proteases is determined by application of biotin−conjugated detection antibodies and HRP−conjugated streptavidin. Signals are detected using a standard chemiluminescence procedure.

For the phospho-MAPK and the protease arrays, each membrane was blocked in either Array Buffer 5 (the phospho-MAPK array) or Array Buffer 6 (the protease array) at room temperature for 60 minutes. The membrane was then incubated in 300 µg (the phospho-MAPK array) or 200 µg (the protease array) of the lysate that had been pre-incubated with Detection Antibody Cocktail at room temperature for 60 minutes. On the following day, the array was incubated with Streptavidin-HRP (1:2,000) in the blocking buffer at room temperature for 30 minutes.

All the arrays were applied with Chemi Reagent Mix and exposed to film for 10 minutes. Signal intensities were determined by densitometric analysis using Alpha DigiDoc version 4.10. Heat maps were generated using a GENE-E matrix visualization and analysis platform (The Board Institute).

2.10 Statistical analysis

Statistical analysis was performed using either independent t-test or analysis of variance (ANOVA) with Dunnett's test. The change was considered significant when $p<0.05$. Statistical significance was assumed with $* = p<0.05$, $** = p<0.01$, $*** = p<0.001$. Error bars shown represent standard errors.

2.11 Materials

All the materials that were used in this project are shown in Table 2.5.

Table 2.5 Materials

Reagent	Company	Catalogue number
Acrylamide/bis−acrylamide (30% solution (v/v), 29:1 ratio)	Sigma−Aldrich, Poole, Dorset, UK	A3699
Agarose	Bioline Ltd, London, UK	BIO−41025
Alpha Digidoc RT Densitometry software	Alpha Innotech Corp, California, USA	
Amersham Protran 0.45µm nitrocellulose	Fisher Scientific UK Ltd, Loughborough, UK	10087970
Ammonium persulphate (APS)	Sigma−Aldrich, Poole, Dorset, UK	A3678
Amphotericin B (Fungizone)	Invitrogen, Paisley, UK	15290
Amplification red (5x)	Olink Bioscience, Uppsala, Sweden	82011
Aprotinin	Sigma−Aldrich, Poole, Dorset, UK	10820
BD FACSVerse	Becton, Dickinson UK Ltd, Oxford, UK	
Bio−Rad protein assay dye reagent concentrate	BioRad Laboratories Ltd, Hertfordshire, UK	500−0006
Blue sensitive X-ray film (18x24 cm)	Photon Imaging Systems, Swindon, UK	FM024
Bovine serum albumin (BSA)	Sigma−Aldrich, Poole, Dorset, UK	A2153
Bovine trypsin	Lorne Laboratories Ltd, Reading, UK	
Bromophenol blue	BDH Chemicals Ltd, Poole, Dorset, UK	
Cecil CE 2041 spectrophotometer	CECIL, Cambridge, UK	
Cell scrapers	Greiner Bio−One Ltd, Gloucestershire, UK	
Class II biological safety cabinet	MDH Intermed Airflow from Bioquell, Andover, UK	
Coulter Counter counting cups and lids	Sarstedt AG and Co., Nümbrecht, Germany	
DAPI dilactate	Invitrogen, Paisley, UK	D3571
Denly BA852 autoclave	Thermoquest Ltd, Basingstoke, UK	

Reagent	Company	Catalogue number
Dimethyl sulphoxide (DMSO)	Sigma−Aldrich, Poole, Dorset, UK	D8418
Disposable cuvettes	Fisher Scientific UK Ltd, Loughborough, UK	FB55143
Di−thiothreitol (DTT)	Sigma−Aldrich, Poole, Dorset, UK	43815
DNase−free RNase A (Ribonuclease A from bovine pancreas)	Sigma−Aldrich, Poole, Dorset, UK	R5503
dNTPs (dGTP, dCTP, dATP, dTTP; 100 mM)	Amersham, Little Chalfont, UK	28−4065−52
Dulbecco's Modified Eagle Medium (DMEM) with 4.5 g/L glucose	Fisher Scientific UK Ltd, Loughborough, UK	11960044
Duolink ImageTool software	Olink Bioscience, Uppsala, Sweden	
Duolink II PLA probe (Anti−mouse, plus)	Olink Bioscience, Uppsala, Sweden	82001
Duolink II PLA probe (Anti−rabbit, minus)	Olink Bioscience, Uppsala, Sweden	82005
Eppendorf tubes	Eppendorf, Hamburg, Germany	
Ethanol	Fisher Scientific UK Ltd, Loughborough, UK	10428671
Ethidium bromide (EtBr)	Sigma−Aldrich, Poole, Dorset, UK	E8751
Ethylene diamine tetraacetic acid (EDTA)	Sigma−Aldrich, Poole, Dorset, UK	59815
EZview Red Protein A Affinity Gel	Sigma−Aldrich, Poole, Dorset, UK	P6486
Falcon tube with cell strainer cap (12x75 mm; mesh size: 35 µm)	Fisher Scientific UK Ltd, Loughborough, UK	10585801
FlowJo data analysis 10 software	FlowJo LLC, Oregon, USA	
Fluozin−3	Invitrogen, Paisley, UK	F24195
Foetal bovine serum (FBS)	Invitrogen, Paisley, UK	26140
Formaldehyde	Fisher Scientific UK Ltd, Loughborough, UK	10041040
Glass coverslips (thickness no. 1, 22x22 mm and 22x50 mm)	BDH Chemicals Ltd, Poole, Dorset, UK	

Reagent	Company	Catalogue number
Glass slides	Fisher Scientific UK Ltd, Loughborough, UK	
Glycerol	Fisher Scientific UK Ltd, Loughborough, UK	10152970
Glycine	Fisher Scientific UK Ltd, Loughborough, UK	G/P460/53
Hoechst 33342	Fisher Scientific UK Ltd, Loughborough, UK	62249
Improvision OpenLab 4.04 software	Improvision, Coventry, UK	
Insulin solution from bovine pancreas (10 mg/mL)	Sigma−Aldrich, Poole, Dorset, UK	I0516
Isopropanol	Fisher Scientific UK Ltd, Loughborough, UK	10723124
Isoton II azide−free balanced electrolyte solution	Beckman, High Wycombe, UK	
Lab−Tek chamber slide system, 8−well glass slide	Sigma−Aldrich, Poole, Dorset, UK	177402
Leica DM−IRE2 inverted microscope	Leica Microsystems Imaging, Solutions Ltd, Cambridge, UK	
Leupeptin	Sigma−Aldrich, Poole, Dorset, UK	L0649
L−glutamine	Invitrogen, Paisley, UK	25030
Ligase	Olink Bioscience, Uppsala, Sweden	82027
Ligation (5x)	Olink Bioscience, Uppsala, Sweden	82009
Lipofectamine 2000 transfection reagent	Invitrogen, Paisley, UK	11668019
Lower buffer for SDS−PAGE gels (Tris 1.5 M, pH 8.8)	BioRad Laboratories Ltd, Hertfordshire, UK	161−0798
Magnesium chloride ($MgCl_2$)	Sigma−Aldrich, Poole, Dorset, UK	M8787
Magnetic stirrer	Fisher Scientific UK Ltd, Loughborough, UK	
Methanol	Fisher Scientific UK Ltd, Loughborough, UK	10499560
Micro−centrifuge tubes (0.5 mL and 1.5 mL)	Elkay Laboratory Products, Basingstoke, UK	

Reagent	Company	Catalogue number
Mini−Protean 3 electrophoresis apparatus	BioRad Laboratories Ltd, Hertfordshire, UK	
N,N,N',N'−tetramethylene−diamine (TEMED)	Fisher Scientific UK Ltd, Loughborough, UK	BPE150−20
N,N,N′,N′−Tetrakis(2−pyridylmethyl) ethylenediamine (TPEN)	Sigma−Aldrich, Poole, Dorset, UK	P4413
Newport Green DCF	Invitrogen, Paisley, UK	N7991
Nikon Eclipse TE200 phase contrast microscope	Nikon, Kingston−upon Thames, UK	
Olympus 8 MP digital camera	Olympus, Oxford, UK	
Penicillin/Streptomycin	Invitrogen, Paisley, UK	15140
Pepstatin A	Sigma−Aldrich, Poole, Dorset, UK	P5318
Pierce ECL Western Blotting Substrate	Pierce and Warriner Ltd, Cheshire, UK	32106
Pipette Tips	Greiner Bio−One Ltd, Gloucestershire, UK	
Platform rocker STR6	Stuart Scientific, Bibby Sterilin Ltd, Stone, UK	
Polymerase	Olink Bioscience, Uppsala, Sweden	82028
Polyoxyethylene−sorbitan monolaurate (Tween 20)	Sigma−Aldrich, Poole, Dorset, UK	93774
Precision Plus protein blue standards	BioRad Laboratories Ltd, Hertfordshire, UK	161−0393SP
Propidium iodide solution	Sigma−Aldrich, Poole, Dorset, UK	P4864
Protease inhibitor cocktail (in DMSO)	Sigma−Aldrich, Poole, Dorset, UK	P8340
Proteome Profiler Human Phospho−Kinase Array Kit	Bio-Techne EMEA, Abingdon, UK	ARY003B
Proteome Profiler Human Phospho−Mitogen−activated Protein Kinase (MAPK) Antibody Array Kit	Bio-Techne EMEA, Abingdon, UK	ARY002B
Proteome Profiler Human Phospho−Receptor Tyrosine Kinase (RTK) Array Kit	Bio-Techne EMEA, Abingdon, UK	ARY001B
Proteome Profiler Human Protease Array Kit	Bio-Techne EMEA, Abingdon, UK	ARY021B

Reagent	Company	Catalogue number
PTC−100 Thermocycler	MJ Research Ltd, Massachusetts, USA	
Roller platform	Stuart Scientific, Bibby Sterilin Ltd, Stone, UK	
Roswell Park Memorial Institute (RPMI) medium 1640	Fisher Scientific UK Ltd, Loughborough, UK	11875093
Roswell Park Memorial Institute (RPMI) medium, phenol−red−free 1640	Fisher Scientific UK Ltd, Loughborough, UK	32404014
Sanyo 950 W microwave	Sanyo Europe, Loughborough, UK	
Sanyo MCO−17AIC incubator	Sanyo E&E Europe BV, Loughborough, UK	
Sodium butyrate	Sigma−Aldrich, Poole, Dorset, UK	B5887
Sodium chloride (NaCl)	Sigma−Aldrich, Poole, Dorset, UK	S3014
Sodium dodecyl sulphate (SDS)	Sigma−Aldrich, Poole, Dorset, UK	L3771
Sodium fluoride (NaF)	Sigma−Aldrich, Poole, Dorset, UK	919
Sodium molybdate (Na_2MoO_4)	Sigma−Aldrich, Poole, Dorset, UK	243655
Sodium orthovanadate (Na_3VO_4)	Sigma−Aldrich, Poole, Dorset, UK	S6508
Sterile disposable pipettes (5 mL, 10 mL and 25 mL)	Sarstedt AG and Co., Nümbrecht, Germany	
Sterile Falcon tubes (15 mL and 50 mL)	Sarstedt AG and Co., Nümbrecht, Germany	
Sterile phosphate buffered saline (PBS)	Invitrogen, Paisley, UK	
Sterile universal containers (30 mL)	Greiner Bio−One Ltd, Gloucestershire, UK	
Sub−cell agarose electrophoresis system	BioRad Laboratories Ltd, Hertfordshire, UK	
SuperSignal West Dura Extended Duration Substrate	Pierce and Warriner Ltd, Cheshire, UK	34075
SuperSignal West Femto Maximum Sensitivity Substrate	Pierce and Warriner Ltd, Cheshire, UK	34095
Syringes (5 mL and 10 mL)	Sherwood Medical Davis and Geck, Gosport, UK	

Reagent	Company	Catalogue number
Tissue culture plasticware (24−well plates, filter flasks, 35 mm, 60 mm and 100 mm dishes)	Nunc Int., Roskilde, Denmark	
Triton X−100	Sigma−Aldrich, Poole, Dorset, UK	93443
Trizma (Tris) base	Sigma−Aldrich, Poole, Dorset, UK	T1503
Upper buffer for SDS−PAGE gels (Tris 0.5M, pH 6.8)	BioRad Laboratories Ltd, Hertfordshire, UK	161−0799
UV transilluminator	Alpha Innotech Corp, California, USA	
VectorShield mounting medium with DAPI	Vector Laboratories Inc, Peterborough, UK	H−1200
Western blocking reagent	Roche Diagnostics, Mannheim, Germany	11921673001
Zinquin	Santa Cruz Biotechnology, Heidelberg, Germany	SC 222427

Chapter 3:
Computational sequence analysis of ZIP channels

3.1 Introduction

The link between increases in function of many ZIP channels, particularly those belonging to the LIV−1 subfamily (Taylor and Nicholson 2003), and human diseases including cancer, has been well established (Taylor et al. 2011). For example, ZIP7, a gatekeeper of zinc release from cellular stores and a hub for tyrosine kinase activation (Hogstrand et al. 2009), has been implicated in development of tamoxifen resistance and aggressive phenotypes of breast cancer cells (Taylor et al. 2008b). However, functional control of ZIP channels is still unclear. Importantly, our group have proposed a post−translational control mechanism for ZIP7, showing that ZIP7 function is triggered by phosphorylation on residues S275 and S276, which are located in the histidine−rich intracytosolic loop between TM3 and TM4 (Taylor et al. 2012). Knowing that ZIP7 is functionally controlled by phosphorylation, it was hypothesised that there could also be other phosphorylation sites in ZIP7 as well as in other ZIP channels. The aims of this chapter were therefore to analyse peptide sequences of ZIP channels and to explore potential phosphorylation sites as well as discover candidate kinases. To achieve these aims, a computational analysis of the amino acid sequences of all the ZIP channels was performed. Furthermore, employing different online databases, we focused the search for the potential phosphorylation sites on the intra cytosolic loop between TM3 and TM4 in which the phosphorylation sites in ZIP7 are located.

3.2 Materials and methods

Online databases and platforms that were used are shown in Table 3.1. Amino acid sequences of ZIP channels in a text−based FASTA format were retrieved from the gene database of the National Center for Biotechnology Information (NCBI) and aligned into a ClustalW format using the TCoffee multiple sequence alignment program (Swiss Institute of Bioinformatics) (Notredame *et al.* 2000). The multiple aligned sequences were then shaded for identical or similar residues using the BoxShade 3.21 online program (Swiss Institute of Bioinformatics) (Hofmann and Baron 1996) and a phylogenetic tree was generated using the Phylogeny.fr web service (Dereeper *et al.* 2008). Potential proteolytically−cleaved PEST motifs were identified using the Emboss Pestfind platform (Rogers *et al.* 1986).

Table 3.1 Online databases and platforms used for the sequence analysis

Data	Database or platform	Reference
Peptide sequences	NCBI [a]	–
Sequence alignment	TCoffee [b]	(Notredame et al. 2000)
Alignment formatting	BoxShade [c]	(Hofmann and Baron 1996)
Phylogenetic tree generation	Phylogeny.fr [d]	(Dereeper et al. 2008)
PEST motif analysis	EMBOSS: Pestfind [e]	(Rogers et al. 1986)
Phosphorylation sites	HPRD [f]	(Keshava Prasad *et al.* 2009)
	PHOSIDA [g]	(Gnad *et al.* 2011)
	Phospho.ELM [h]	(Dinkel *et al.* 2011)
	PhosphoNET [i]	–
	PhosphoSitePlus [j]	(Hornbeck *et al.* 2015)
Protein functions	UniprotKB [k]	(The UniProt Consortium 2015)

[a] **NCBI**, National Center for Biotechnology Information. http://www.ncbi.nlm.nih.gov/gene
[b] **TCoffee**. http://www.tcoffee.org
[c] **Boxshade**. http://www.ch.embnet.org/software/BOX_form.html
[d] **Phylogeny.fr**. http://www.phylogeny.fr
[e] **EMBOSS: Pestfind**. http://emboss.bioinformatics.nl/cgi-bin/emboss/epestfind
[f] **HPRD**, Human Protein Reference Database. http://www.hprd.org
[g] **PHOSIDA**. http://www.phosida.com
[h] **Phospho.ELM**, Phospho Eukaryotic Linear Motif. http://phospho.elm.eu.org
[i] **PhosphoNET**. http://www.phosphonet.ca
[j] **PhosphoSitePlus**. http://www.phosphosite.org
[k] **UniProtKB**, UniProt Knowledgebase. http://www.uniprot.org/help/uniprotkb

Potential phosphorylation sites were searched for using gene names of human ZIP channels (SLC39A1−14) in 3 different online phosphorylation site databases: PhosphoNET (Kinexus Bioinformatics Corporation), PHOSIDA (Max Planck Institute of Biochemistry) (Gnad et al. 2011) and PhosphoSitePlus (PSP) (Hornbeck et al. 2015). The peptide sequences and residue numbers reported for the phosphorylation sites and their locations were confirmed with those retrieved from the UniProtKB/Swiss−Prot database (The European Bioinformatics Institute) (The UniProt Consortium 2015). Only the sites that had been experimentally confirmed in mammalian cells by mass spectrometry and that resided in the cytosolic loop between TM3 and TM4 were selected. Data from all these databases were combined together. Predicted kinases with the

highest prediction scores were selected, and their functions were searched for in the UniProt Knowledgebase (UniProtKB) (The UniProt Consortium 2015). Additionally, predicted phosphorylation sites and kinases according to amino acid sequences were searched for in the Human Protein Reference Database (Keshava Prasad et al. 2009).

3.3 Results and discussion

3.3.1 Analysis of amino acid sequences of ZIP channels

To demonstrate evolutionary relationships and molecular similarities among different human ZIP channels, a phylogram was created from their peptide sequences. Supporting the established classification of ZIP channels (Taylor and Nicholson 2003), the phylogenetic tree showed that ZIP channels could be grouped into four subfamilies: subfamily II (ZIP1−ZIP3), subfamily I (ZIP9), GufA (ZIP11), and the LIV−1 subfamily (ZIP4−ZIP8, ZIP10, and ZIP12−ZIP14) (Fig. 3.1).

Figure 3.1 A phylogenetic tree of human ZIP channels

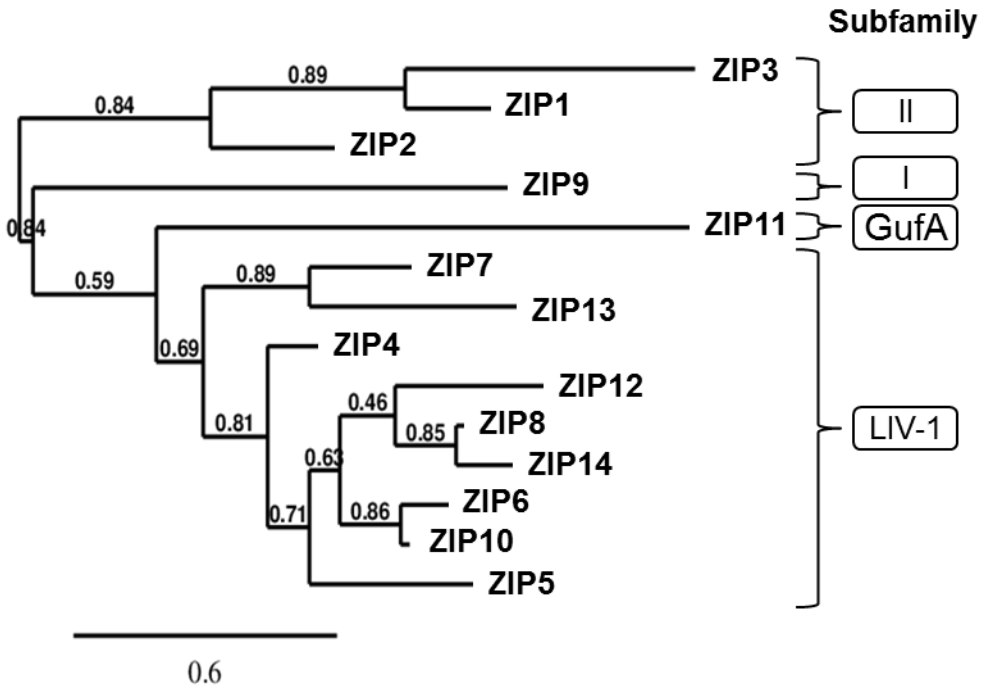

This phylogram was generated using Phylogeny.fr web service (Dereeper et al. 2008). The bar at the bottom provides a scale for the degree of genetic changes as represented by the horizontal dimension of the phylogram. The numbers next to each node indicate a measure of support for the nodes. According to this phylogram, human ZIP channels can be grouped into four subfamilies: subfamily II, subfamily I, GufA subfamily, and the LIV−1 subfamily.

According to the phylogenetic tree (Fig. 3.1), three pairs of the ZIP channels in the LIV−1 subfamily were grouped together, and each pair has been shown to have some prominent characteristics in common. ZIP7 and ZIP13, which were grouped separately from the rest of the LIV−1 subfamily with the statistical support for the node of 0.89 (Fig. 3.1), have been reported to be intracellularly located. ZIP7 has been reported to be located in the ER (Taylor et al. 2004) and/or the Golgi (Huang et al. 2005), whereas ZIP13 has been reported to be located in the Golgi (Bin et al. 2011). ZIP6 and ZIP10 are also grouped together with the statistical support for the node of 0.86 (Fig. 3.1). Both ZIP6 and ZIP10 contain peptide sequences in the N−terminus that indicate their evolutionary link to prion genes (Schmitt-Ulms et al. 2009), undergo an N−terminal cleavage upon activation (Ehsani et al. 2012; Hogstrand et al. 2013), and play important roles in carcinogenesis, particularly the EMT process (Kagara et al. 2007; Hogstrand et al. 2013). Additionally, ZIP8 and ZIP14 are grouped together in the same sub−branch with the statistical support for the node of 0.85 (Fig. 3.1). Interestingly, even though ZIP8 and ZIP14 are recognised as zinc channels, they are capable of transporting other metals such as cadmium and manganese (Girijashanker et al. 2008) as well as iron (Zhao *et al.* 2014). The ability of ZIP8 and ZIP14 to transport metal ions other than zinc might be at least partially attributed to the lack of the initial histidine residue, a known zinc−binding amino acid, in the consensus motif of the LIV−1 subfamily in TM5, HEXPHEXGD, which will be discussed further in Section 3.3.2.3.

The peptide sequences of all the human ZIP channels were then aligned according to their similarities (Fig. 3.2 and 3.3). All the TM regions were identified according to a previous computational sequence analysis (Taylor and Nicholson 2003) (Fig. 3.3). General features that were observed in all the ZIP channels included the presence of eight TMs, a very short C−terminus and a long intracytosolic loop between TM3 and TM4 (Fig. 3.3). This particular intracytosolic loop was shown to be a histidine−rich region, which is defined as a region containing consecutive HX repeats (H, histidine; X, any amino acid) (Guerinot 2000). The TM regions were highly conserved across different types of the ZIP channels, whereas the N−terminus (Fig. 3.2) and the loops between the TM regions (Fig. 3.3) were highly variable.

Figure 3.2 Alignment of all human ZIP channels (N-terminus)

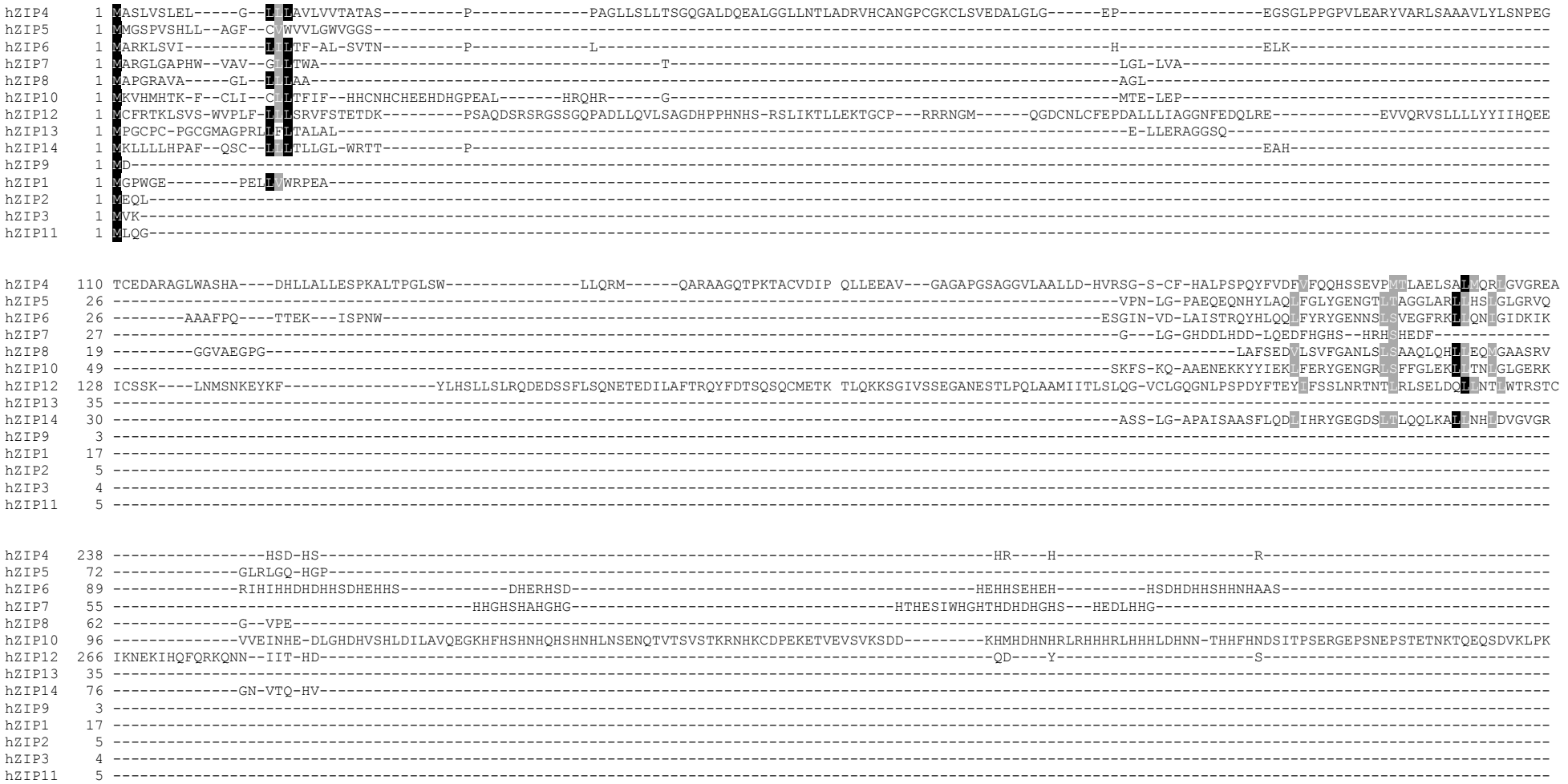

Figure 3.2 Alignment of all human ZIP channels (N-terminus) (continued)

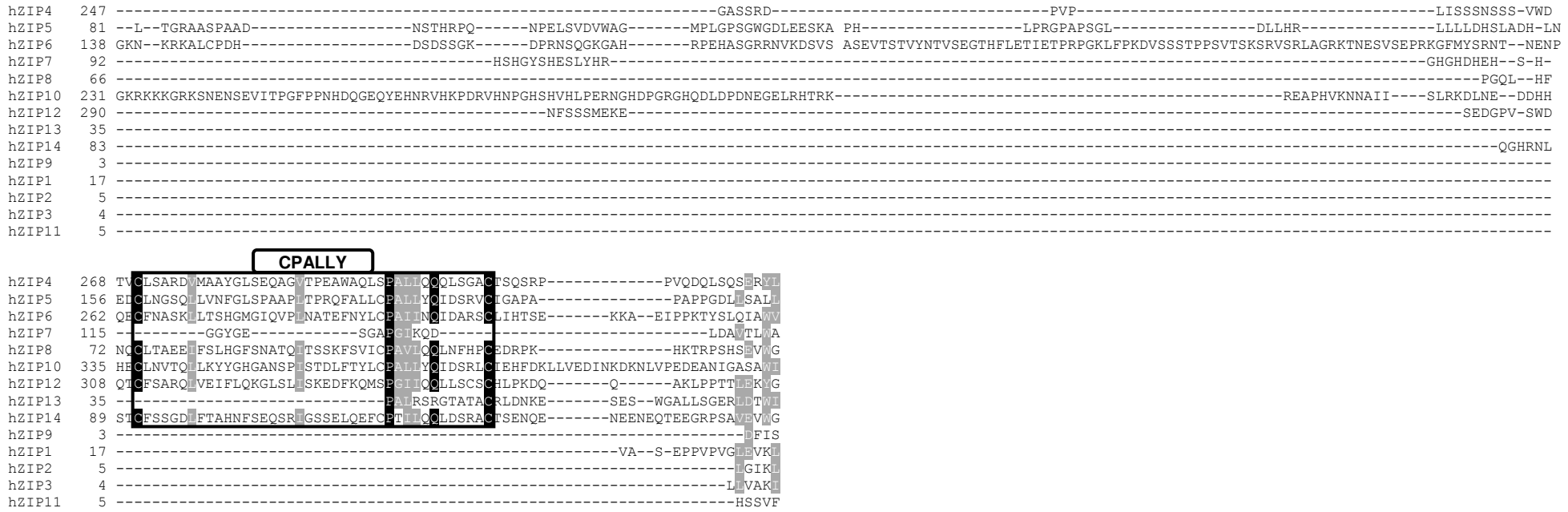

Amino acid sequences in the N−terminus of all human ZIP channels were aligned using the TCoffee multiple sequence alignment program. Residues that were at least 50% identical (black) and complementary (grey) were shaded using the BoxShade 3.21 online program. The CPALLY motif, which contains three conserved cysteine residues, is indicated in a box with a black border. This motif is uniquely seen in the N−terminus of the LIV−1 subfamily, except ZIP7 and ZIP13.

Figure 3.3 Alignment of all human ZIP channels (from TM1 to C−terminus)

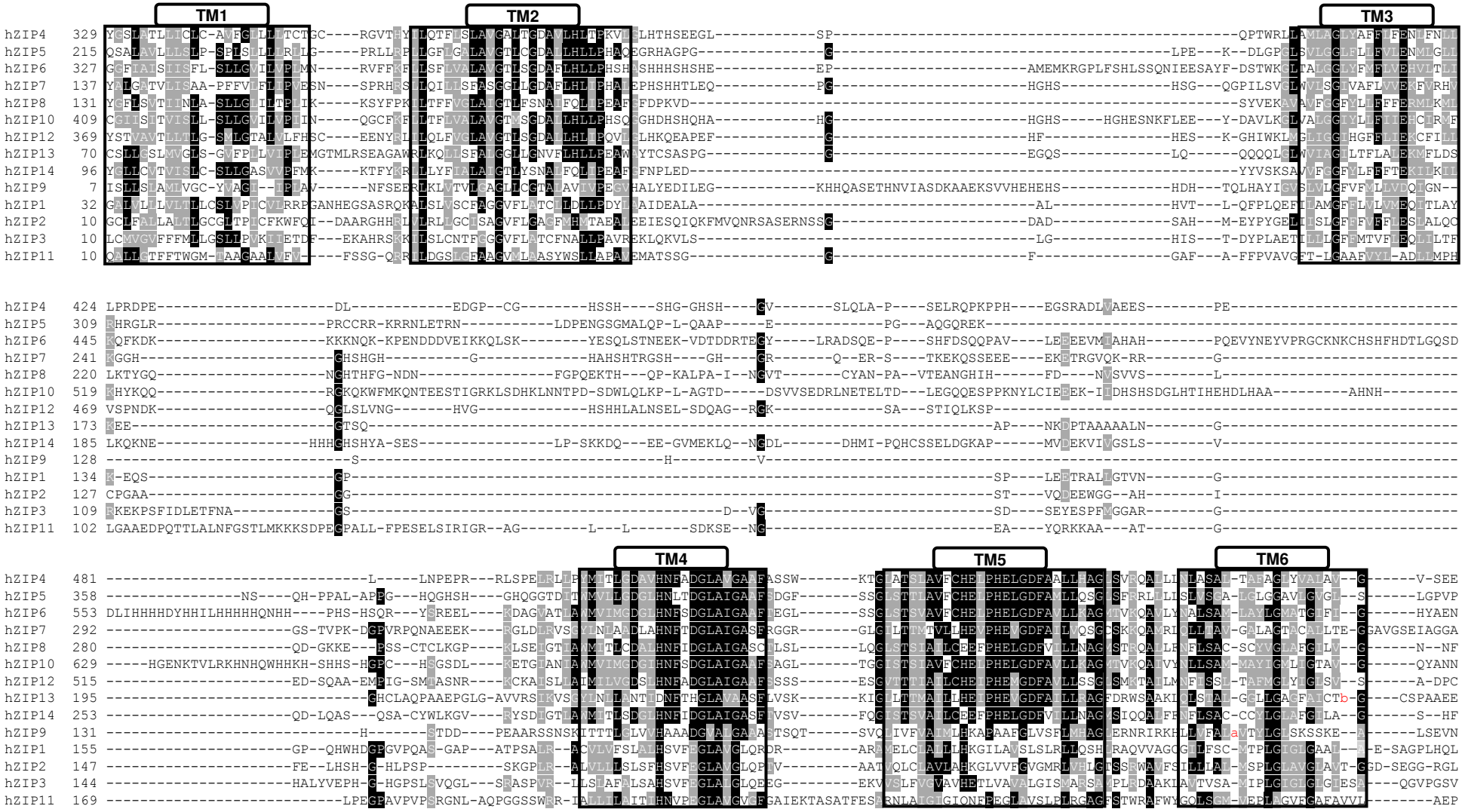

Figure 3.3 Alignment of all human ZIP channels (from TM1 to C−terminus) (continued)

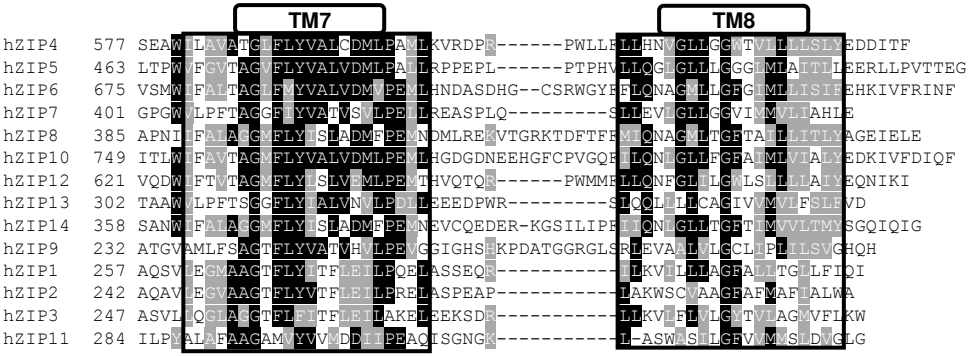

Amino acid sequences between TM1 and the C−terminus of all human ZIP channels were aligned using the TCoffee multiple sequence alignment program. Residues that were at least 50% identical (black) and complementary (grey) were shaded using the BoxShade 3.21 online program. The predicted TM regions (Taylor and Nicholson 2003) are indicated in boxes with black borders.
a (ZIP9, TM6), AAPVMSM; b (ZIP13, TM6), QSPKGVV

3.3.2 Identification of unique characteristics of the LIV−1 subfamily

When comparing the LIV−1 subfamily with all the other ZIP channels, the LIV−1 subfamily demonstrated some unique characteristics. These included a longer N−terminus (Fig. 3.4 and 3.5); a CPALLY motif (Fig. 3.6); PEST motifs in ZIP6 and ZIP10 (Fig. 3.7); additional histidine−rich regions in the N−terminus (Fig. 3.4 and 3.8) and the extracytosolic loop between TM2 and TM3 (Fig. 3.4 and 3.9); and a HEXPHEXPHGD motif within TM5 (Fig. 3.9). These salient features were individually analysed.

3.3.2.1 A long N−terminus containing a CPALLY motif

Amino acid residues in the N−terminus of each ZIP channel were counted (Fig. 3.5). The LIV−1 subfamily members had a long N−terminus, with an average of 230 amino acids, ranging from 68 amino acids in ZIP13 to 408 amino acids in ZIP10 (Fig. 3.5). In contrast, the N−terminus of the other ZIP channels was 18 times shorter than the LIV−1 subfamily, having an average of 13 amino acids and ranging from 6 amino acids in ZIP9 to 31 amino acids in ZIP1 (Fig. 3.5). These data confirmed that a long N−terminus is a prominent characteristic of the LIV−1 subfamily. Furthermore, this characteristic also suggested a more complex post−translational mechanism of the LIV−1 subfamily than the other subfamilies, since signal sequences are contained in the N−terminus (Coleman *et al.* 1985), and post−translational modifications in the N−terminus have been shown to participate in functional control of proteins (Lai *et al.* 2015). Noteworthy, a signal sequence is a 20−25 amino acid sequence that plays an important role in targeting a protein into a secretory pathway or integrating a protein into cellular membranes. A potential ER−retention signal peptide ARGL (residues 2−5) has been detected in the N−terminus of ZIP7, consistent with the unique localisation of ZIP7 in the ER (Taylor et al. 2004). Another potential ER−retention signal peptide with sequence RKLS (residues 3−6) is present in the N−terminus of ZIP6 (Taylor et al. 2003) and might explain the ER localisation of the pro−protein form of ZIP6 prior to its plasma membrane relocation (Hogstrand et al. 2013). Additionally, a potential cleavage site was seen in the N−terminus of ZIP6 and ZIP10, and this will be discussed in Section 3.3.3.

Figure 3.4 Structure of the LIV−1 subfamily of ZIP channels

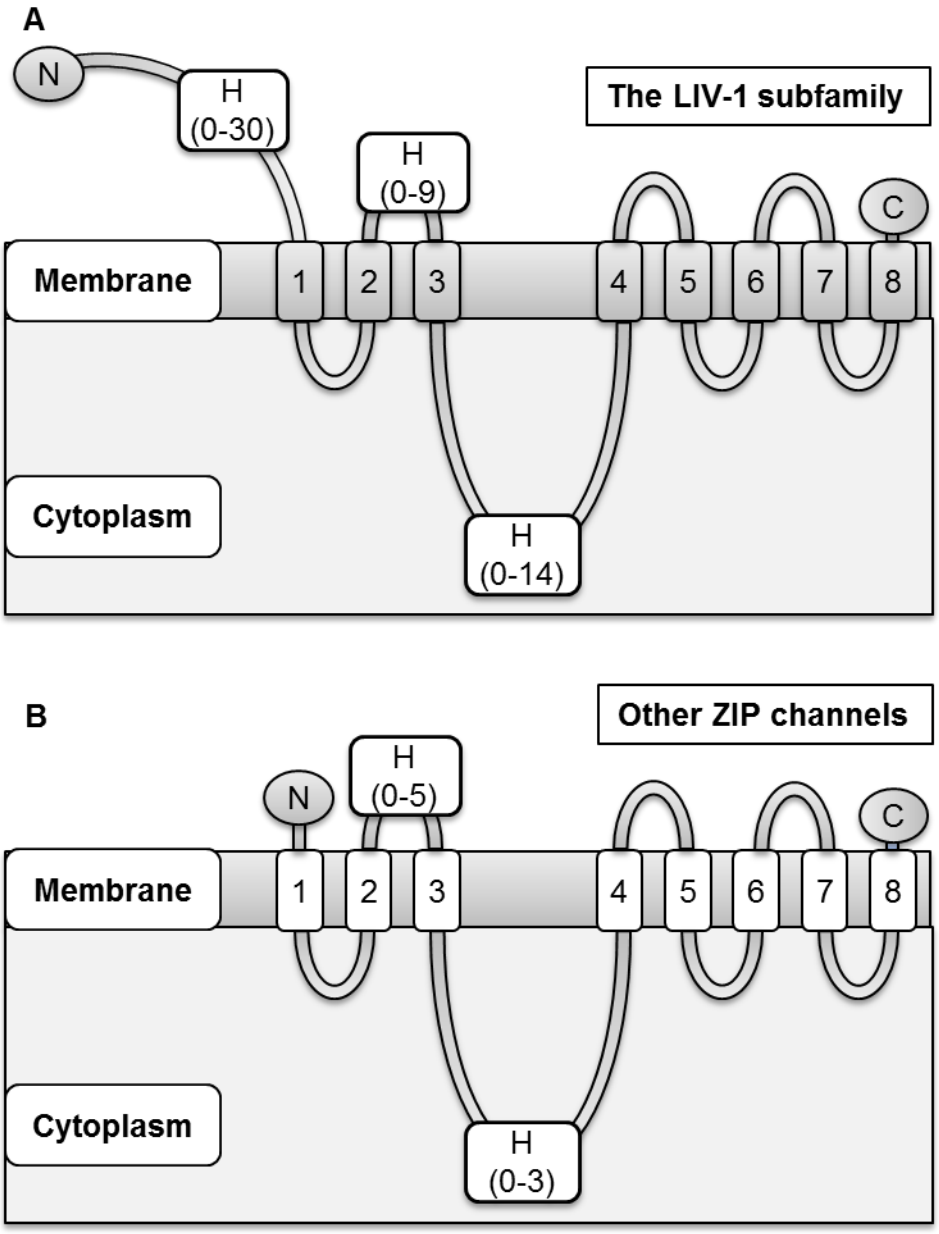

This schematic illustrates a simplified structure of the LIV−1 subfamily members (A), compared to other ZIP channels (B). Distinctive features of this subfamily include a longer N−terminus and additional histidine−rich regions in the N−terminus and the extracytosolic loop between TM2 and TM3. Numbers of the HX repeats detected in particular regions are indicated in brackets. These numbers represent combined numbers of consecutive HX motifs, where H stands for histidine and X stands for any amino acid.
N, the amino−terminus; C, the carboxyl−terminus; H, the histidine−rich region.

Figure 3.5 Numbers of residues in the N−terminus of ZIP channels

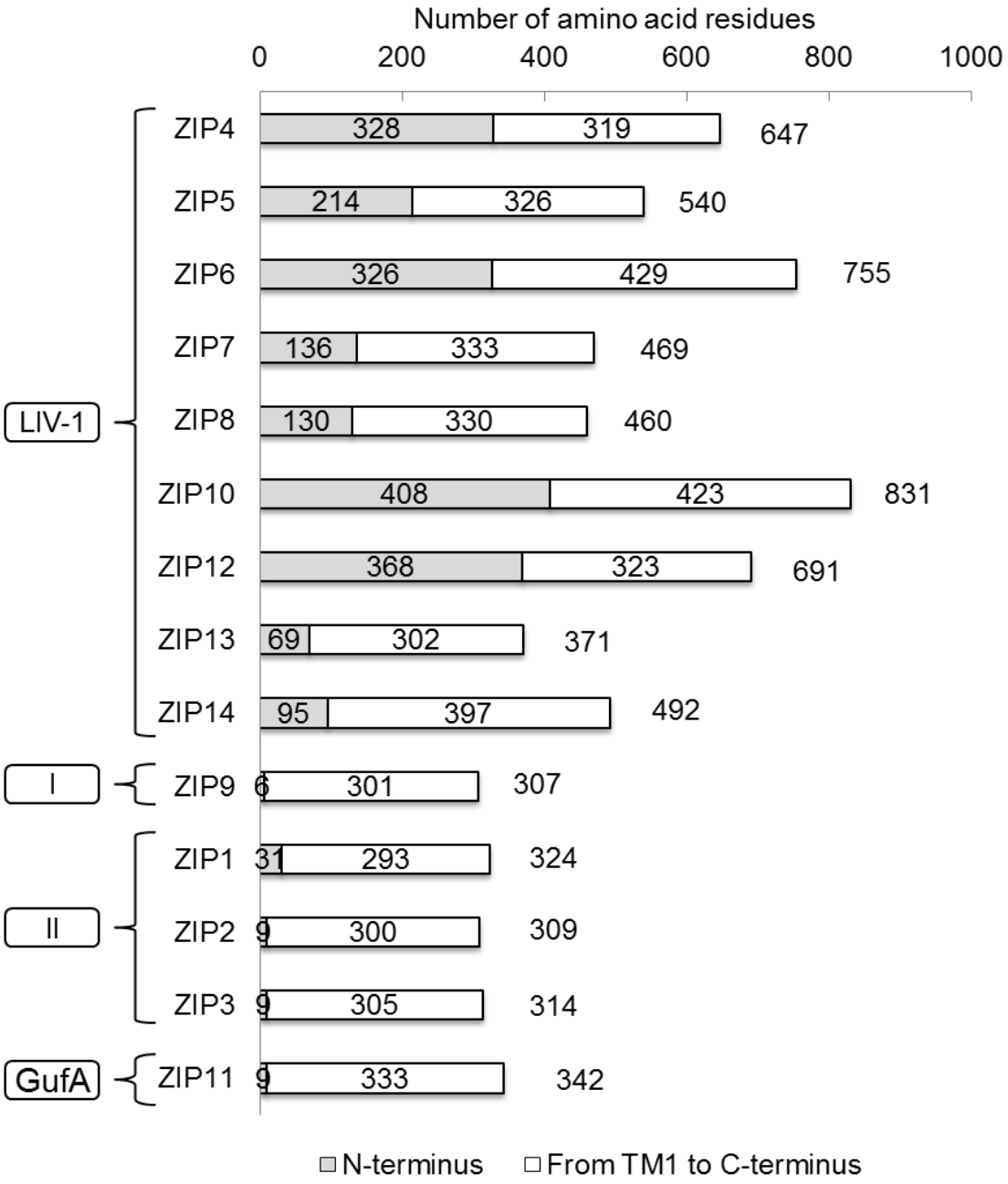

This bar chart reveals sizes of all human ZIP channels. Numbers inside the bars indicate amounts of amino acid residues in the N−terminus and in the rest of the molecules (from the TM1 to the C−terminus). Numbers outside the bars indicate full lengths of the proteins.
LIV−1, the LIV−1 subfamily; I, subfamily I; II, subfamily II

Another unique characteristic of the LIV−1 subfamily is the CPALLY motif, which is located in the N−terminus immediately proximal to TM1 (Taylor and Nicholson 2003). This motif consisted of three highly conserved cysteine residues and a proline residue, which was 100% identical across this subfamily (Fig. 3.2 and 3.6). This motif was present in the majority of the LIV−1 subfamily members (Fig. 3.2 and 3.6), but absent in all the other subfamilies (Fig. 3.2). Importantly, ZIP7 and ZIP13 were the only two ZIP channels in the LIV−1 subfamily that did not have this motif (Fig. 3.6). ZIP7 did not have any cysteine residue in this region, whereas ZIP13 had only one cysteine residue at the distal end of this region (Fig. 3.6). Even though this motif was present in ZIP4 and ZIP12, the second cysteine residue in the middle of this region was replaced with a serine residue (Fig. 3.6), which is structurally similar to cysteine but have a sulphur atom in the thiol group replaced with an oxygen atom.

Figure 3.6 The CPALLY motif in the LIV−1 subfamily of ZIP channels

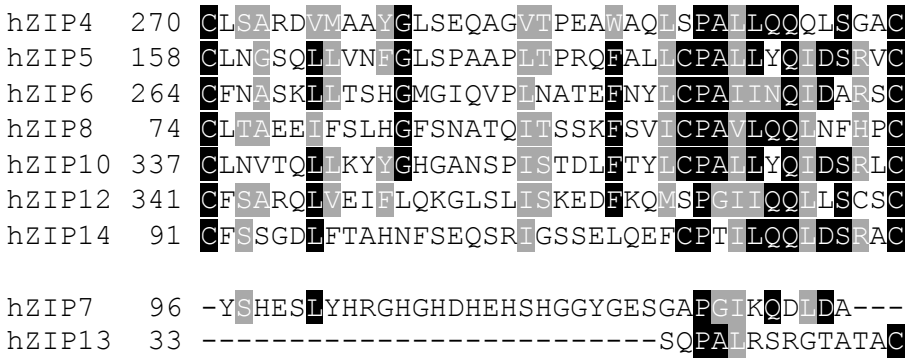

The CPALLY motif of ZIP4, ZIP5, ZIP6, ZIP8, ZIP10, ZIP12, and ZIP14 were aligned using the TCoffee multiple sequence alignment program, with the equivalent region in ZIP7 and ZIP13 shown separately. Residues that were at least 70% identical (black) and complementary (grey) were shaded using the BoxShade 3.21 online program. This CPALLY motif is a region in the N−terminus upstream of TM1 that contains three consensus cysteine residues (Taylor and Nicholson 2003). This motif is absent in ZIP7 and ZIP13.

The CPALLY motif has been proposed to provide substantial structural support for the LIV−1 subfamily members, given that cysteine residues in the CPALLY motif contain thiol groups needed for formation of disulphide bonds (Taylor and Nicholson 2003), which normally stabilise the tertiary structure of proteins (Lodish *et al.* 2000). Furthermore, there was a highly conserved

cysteine residue in TM5 immediately proximal to the HEXPHEXGD motif (Fig. 3.10). This cysteine residue was present in all the LIV−1 subfamily members, but it was exceptionally replaced with a leucine residue in ZIP7 and ZIP13 (Fig. 3.10). The binding of the cysteine residues in the CPALLY motif to this additional cysteine residue in TM5 might provide a control mechanism for zinc movement through the pores of the ZIP channels (Taylor et al. 2007). The absence of these cysteine residues both in the CPALLY motif and in TM5 of ZIP7 and ZIP13 therefore suggested that these zinc channels might employ a different mechanism for controlling the pores without a need for these cysteine residues.

A Hispanic American, who presented with a phenotype of acrodermatitis enteropathica, has been reported to have two homozygous mutations of the ZIP4 gene, C309T and P84L (Wang *et al.* 2002). Interestingly, residue C309 is the third cysteine residue in the CPALLY motif of human ZIP4 (Wang et al. 2002). This report therefore further highlights the importance of this motif in the function of ZIP channels. Plausibly, the functional impairment of ZIP4 in this patient might be partly attributed to the disruption of the tertiary structure of ZIP4 caused by the lack of the cysteine residue in this motif. Nevertheless, the effect of the lack of the second cysteine in this motif in normal human ZIP4 and ZIP12 (Fig. 3.6) on their function was not evident. This might be due to the presence of multiple additional cysteine residues in the N−terminus far proximal to the CPALLY motif (Fig. 3.2), which might provide sufficient thiol groups for structural support and pore control for ZIP4 and ZIP12.

3.3.2.2 A PEST site in the N−terminus of ZIP6 and ZIP10

A PEST motif is a hydrophilic region comprising a 12 amino-acid cluster that is rich in proline (P), glutamate (E), serine (S), and threonine (T), in the absence of positively−charged residues such as arginine, histidine, and lysine (Rogers et al. 1986; Rechsteiner and Rogers 1996). The PEST motif has been recognised as a potential target for ubiquitination−mediated proteolytic cleavage (Meyer *et al.* 2011; Ramakrishna *et al.* 2011). The PEST motif was searched for in all human ZIP channels. Strong PEST motifs with PEST scores above the threshold score of +5 were uniquely detected in ZIP6 and ZIP10 (Fig. 3.7), which were not present in any other ZIP channels in the LIV−1 subfamily. ZIP6

had only one strong PEST motif in its N-terminus upstream of the CPALLY motif, with a PEST score of +5.07 (Fig. 3.7, the sequence underneath a green solid line). ZIP10 had two PEST motifs: one in the N-terminus proximal to the CPALLY motif and the other in the cytosolic loop between TM3 and TM4, with PEST scores of +16.60 and +7.97, respectively (Fig. 3.7, the sequences above green dashed lines). Noteworthy, there were also many other PEST motifs present that were reported as poor PEST motifs, with PEST scores ranging from −5.77 to −23.57 in ZIP6 and from +2.38 to −25.86 in ZIP10, which were assumed to be negative.

Generally, a PEST motif is linked to a shortened half-life of a protein since it predestines the protein to be proteolytically degraded through a ubiquitination-mediated mechanism (Meyer et al. 2011; Ramakrishna et al. 2011). However, in contrast to this general role in negatively regulating a protein by enhancing proteolytic degradation, a PEST motif in the CaVβ3 subunit of voltage-gated calcium channels is required for calcium/calpain-mediated cleavage that leads to activation of the channels (Sandoval *et al.* 2006). Consistent with this finding, both ZIP6 (Hogstrand et al. 2013) and ZIP10 (Ehsani et al. 2012) undergo N-terminal cleavage or ectodomain shedding, which triggers zinc transport function of these zinc channels. For ZIP6, this N-terminal proteolytic cleavage in breast cancer cells results in relocation of ZIP6 to the plasma membrane, ZIP6-mediated zinc influx, inhibitory phosphorylation of GSK-3β, nuclear retention of Snail, and down-regulation of E-cadherin, triggering the epithelial-mesenchymal transition (EMT), a process necessary for migration and metastasis (Hogstrand et al. 2013). This N-terminal cleavage or ecto-domain shedding mechanism is also required for activation of ZIP10 in zinc- or cadmium-deprived condition (Ehsani et al. 2012), even though the involvement of this mechanism in EMT has not been reported. Given the fact that both ZIP6 and ZIP10 are associated with breast cancer metastasis (Kagara et al. 2007; Hogstrand et al. 2013) and are activated by proteolytic cleavage (Ehsani et al. 2012; Hogstrand et al. 2013), inhibition of this post-translational event in these ZIP channels might become a new strategy for breast cancer treatment.

Figure 3.7 Alignment of ZIP6 and ZIP10 with analysis of the PEST motifs

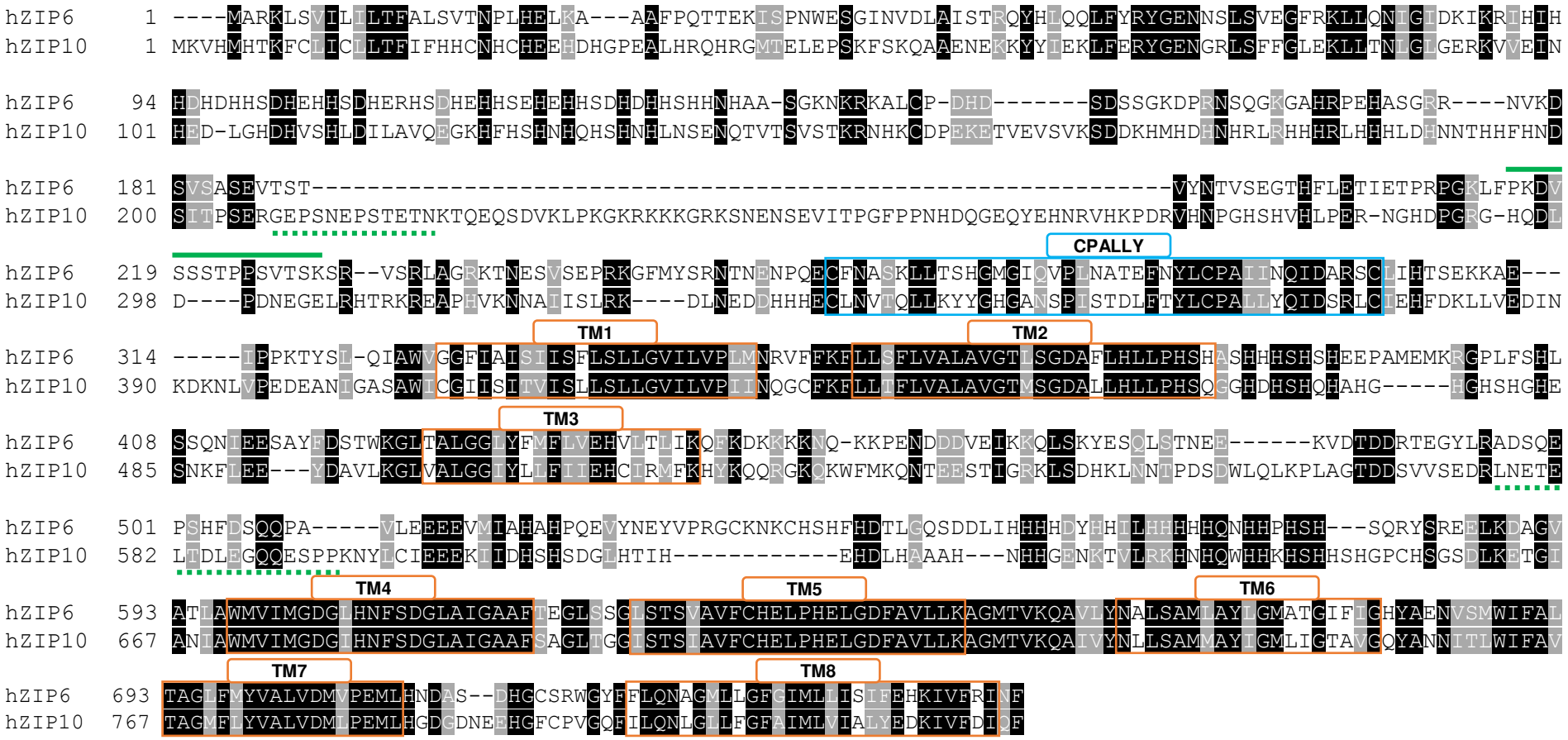

Amino acid sequences of ZIP6 and ZIP10 were aligned using the TCoffee multiple sequence alignment program. Residues that were at least 70% identical (black) and complementary (grey) across all the LIV−1 subfamily members were shaded using the BoxShade 3.21 online program. The predicted TM regions (Taylor and Nicholson 2003) (orange boxes), the CPALLY motif (a blue box), and the PEST motifs (the ZIP6 motif beneath a green continuous line, and the ZIP10 motifs above green dashed lines) are indicated. The PEST motifs were analysed using Emboss Pestfind platform (Rogers et al. 1986).

It is also noteworthy that ZIP4, another member of the LIV-1 subfamily, has been reported to be activated by an N-terminal cleavage during zinc deficiency (Kambe and Andrews 2009), regardless of the absence of a strong PEST motif in this ZIP channel. Additionally, ZIP1 was the only ZIP channel in all the other subfamilies that also had a PEST motif, with sequence KEQSGPSPLEETR (positions 134 to 146, PEST score +11.14), which was located in the cytosolic loop between TM3 and TM4. A PEST motif in the human calcium receptor predestines the protein to lysosomal degradation (Zhuang *et al.* 2012). Furthermore, a PEST motif is present in a cytosolic loop of a pathological protein in Tangier disease called ABCS1 with a high PEST prediction score, and this motif was shown to be responsible for Calpain-mediated degradation of this pathological protein (Wang *et al.* 2003). These findings therefore implied that the presence of a PEST site in the cytosolic loop between TM3 and TM4 of ZIP1 and ZIP10 might be responsible for the lysosomal degradation of these ZIP channels, consistent with a report of ZIP1 being degraded through lysosomal degradation (Huang and Kirschke 2007). However, the exact contribution of this site to the degradation of either ZIP1 or ZIP10 has not been investigated.

3.3.2.3 Histidine-rich regions in the N-terminus and cytosolic loops

The presence of a histidine-rich region in the long variable cytosolic loop between TM3 and TM4 has been recognised as a common characteristic of the ZIP family (Taylor and Nicholson 2003). This region has been proposed to be a potential zinc-binding domain of the ZIP channels (Guerinot 2000). Interestingly, histidine-rich areas were also detected in the N-terminus and the extracytosolic loop between TM2 and TM3 of many members of the ZIP family, particularly those belonging to the LIV-1 subfamily (Fig. 3.2 and 3.3). We therefore investigated the numbers of histidine residues as well as the HX repeats, with the generic formula of $(HX)_n$ (H, histidine; X, any amino acid; n, number of consecutive HX motifs) in the whole sequences of the ZIP channels. The numbers of both histidine residues and the HX repeats were also individually determined in the N-terminus, the extracytosolic loop between TM2 and TM3, and the intracytosolic loop between TM3 and TM4.

Overall, the LIV−1 subfamily members had an average of 35 histidine residues and 9 HX repeats, which was 3.5 times and 5 times higher than other ZIP channels, respectively (Fig. 3.8A), suggesting a higher zinc−binding capacity of the LIV−1 subfamily than other subfamilies. In the N−terminus of the LIV−1 subfamily members, there were up to 52 histidine residues (in ZIP10) and up to 30 HX repeats (in ZIP10), with an average of 17 histidine residues and 8 HX repeats (Fig. 3.8B). However, no histidine residue was present in the N−terminus of ZIP13, and no HX repeat was present in the N−terminus of ZIP5, ZIP8, ZIP13 and ZIP14 (Fig. 3.8B). There was neither histidine residue nor HX repeat present in the N−terminus of all the other ZIP channels, except ZIP11, which had a histidine residue with no HX repeat (Fig. 3.8B).

Figure 3.8 Histidine residues and the HX repeats in the N−terminus

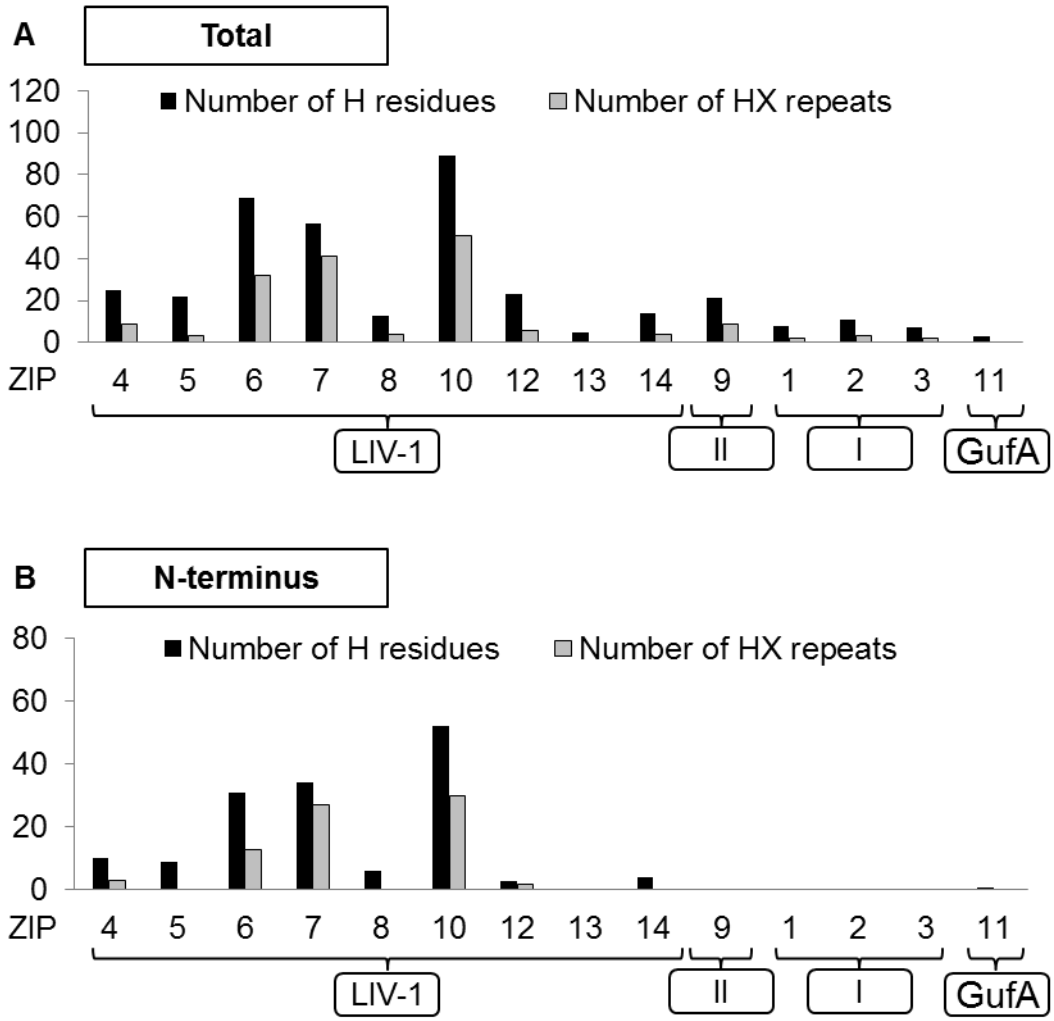

These bar charts reveal numbers of histidine residues and the HX repeats in the whole sequence (A) and in the N−terminus (A) for each ZIP channel. The numbers of the HX repeats represent combined numbers of consecutive HX motifs, where H stands for histidine and X stands for any amino acid. LIV−1, the LIV−1 subfamily; I, subfamily I; II, subfamily II

In the region between TM2 and TM3, an average of 3 histidine residues and 2 HX repeats were present in the LIV−1 subfamily, yet many members of this subfamily, including ZIP5, ZIP8, ZIP13 and ZIP14, did not have an HX repeat (Fig. 3.9A). Among the other ZIP channels, the HX repeats were present only in ZIP9, which had 5 HX repeats in this region (Fig. 3.9A). Provided that ZIP9 is a gatekeeper of zinc release from cellular stores in chicken cells, which lacked endogenous ZIP7 (Taniguchi et al. 2013), the presence of the HX repeats in this extracytosolic loop of ZIP9 suggested that this region might be used for sensing zinc in cellular stores and thereby controlling zinc release from the stores. To confirm the histidine−rich cytosolic loop as a shared feature of the ZIP family, the LIV−1 subfamily members were demonstrated to contain an average of 6 HX repeats in the intracytosolic loop between TM3 and TM4, whereas the other ZIP channels had an average of 2 HX repeats in this cytosolic loop (Fig. 3.9B). The 2 exceptions in which no HX repeat was present in this region were ZIP13 and ZIP11 (Fig. 3.9B).

Even though the additional presence of the HX repeats in the N−terminus and the extracytosolic loop between TM2 and TM3 was shown to be a prominent characteristic of the LIV−1 subfamily, many exceptions were observed. This particular characteristic was therefore considered to be highly variable and rather non−specific to this subfamily. Nevertheless, the presence of the HX repeats could by no means be overstated. Investigations of the role of the histidine−rich repeats have been extensively performed in metal tolerance proteins of *Arabidopsis thaliana* (AtMTP), which, like ZnT transporters, belong to the cation diffusion facilitator family. The histidine−rich loop in AtMTP1 has been shown to function as a cytosolic zinc sensor (Kawachi *et al.* 2008; Tanaka *et al.* 2013; Tanaka *et al.* 2015), a regulator of zinc transport (Tanaka et al. 2013), and a determinant of metal selectivity (Podar *et al.* 2012), supporting the role of histidine residues in zinc selectivity (Hoch *et al.* 2012).

Figure 3.9 Histidine residues and the HX repeats in the cytosolic loops between TM2 and TM3, and between TM3 and TM4

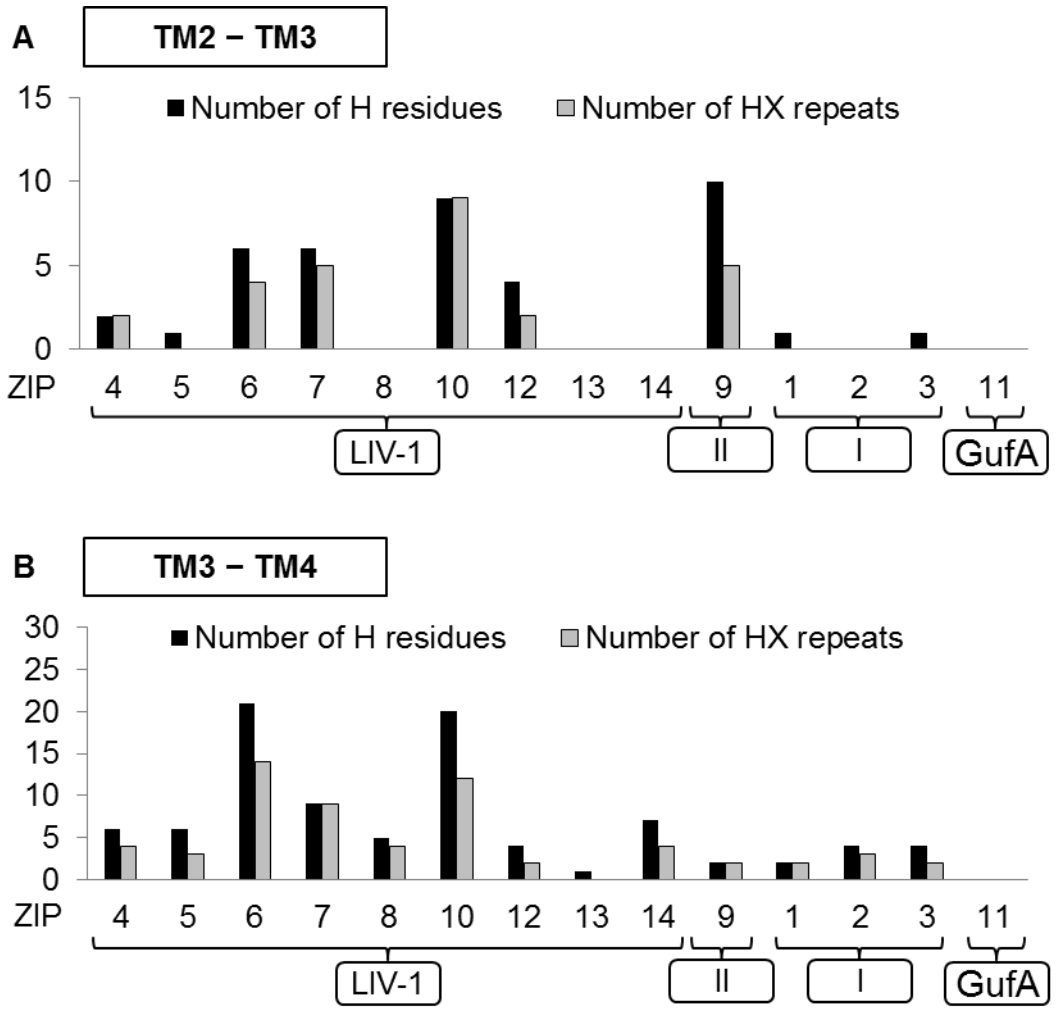

These bar charts reveal numbers of histidine residues and the HX repeats in the region between TM2 and TM3 (A) and the region between TM3 and TM4 (B) for each ZIP channel. The numbers of the HX repeats represent combined number of consecutive HX motifs, where H stands for histidine and X stands for any amino acid.
LIV−1, the LIV−1 subfamily; I, subfamily I; II, subfamily II

In ZnT5, a mammalian ZnT transporter, the histidine−rich loop has also been shown to play a major role in zinc binding (Suzuki *et al.* 2005). Importantly, ZnT5 contains histidine−rich regions on both sides of the plasma membrane (Kambe et al. 2015) and has been reported to bi−directionally transport zinc (Valentine et al. 2007). The unprecedented presence of histidine−rich regions on both sides of the membrane in the majority of the LIV−1 subfamily therefore suggested a possibility that these ZIP channels might also be capable of facilitating zinc transport bi−directionally. Supporting this suggestion, yeast KE4, an ER−located ZIP7 ortholog, was shown to be capable

of facilitating bidirectional zinc transport in *Saccharomyces cerevisiae* (Kumánovics *et al.* 2006). Nevertheless, this notable bidirectional zinc transport has yet to be proved for human ZIP channels.

Additionally, the absence of the HX repeats in ZIP11 and ZIP13 was a remarkable finding, making the role of these two channels as zinc transport proteins questionable. Nevertheless, there are pieces of evidence proving the role for both ZIP11 (Yu *et al.* 2013) and ZIP13 (Jeong *et al.* 2012) in zinc transport. These observations suggested that the presence of individual histidine residues anywhere in the protein might be sufficient for zinc transport function of these ZIP channels, thereby making the role of the HX repeats in zinc transport, rather than the function of these ZIP channels, questionable.

3.3.2.4 A HEXPHEXGD consensus motif in TM5

In TM5, the motif HEXPHEXGD was prominently conserved across the LIV−1 subfamily members, with apparently low similarity in all the other ZIP channels (Fig. 3.3), consistent with a proposal of this motif as a consensus motif for this subfamily (Taylor and Nicholson 2003). This consensus motif matches the region that is reported to be zinc−binding in zinc metallopeptidases (zincins) (Hooper 1994), suggesting that this region could be a catalytic zinc−binding site of the ZIP channels. In the LIV−1 subfamily, the two glutamate residues (E), the proline residue (P), the second histidine residue (H), the glutamine residue (G), and the aspartate residue (D) in this motif showed 100% identity (Fig. 3.10). The two X residues (any amino acids) also showed a relatively high degree of identity and similarity across the LIV−1 subfamily (Fig. 3.10). Collectively, these observations supported the HEXPHEXGD motif as a consensus motif for the LIV−1 subfamily.

Notably, the initial histidine residue (H) of the HEXPHEXGD motif was replaced with a glutamate residue (E) in ZIP8 and ZIP14 (Fig. 3.10), the two ZIP channels which were grouped together in the same sub−branch of the phylogenetic tree (Fig. 3.1). Furthermore, these two ZIP channels did not have the additional HX repeats either in the N−terminus (Fig. 3.8B) or in the extracellular loop between TM2 and TM3 (Fig. 3.9A). Both the histidine residues (Hoch et al. 2012) and the HX repeats (Podar et al. 2012) are needed for zinc selectivity of the ZIP channels over other metals. The lack of these components

in ZIP8 and ZIP14 might therefore explain their ability to also facilitate the cellular uptake of bivalent metals other than zinc, such as cadmium (Dalton *et al.* 2005; Girijashanker et al. 2008), manganese (He *et al.* 2006; Girijashanker et al. 2008), and iron (Liuzzi *et al.* 2006; Wang et al. 2012; Zhao et al. 2014). Interestingly, ZIP14 has been shown to participate in pathogenesis of iron overload in hepatocytes of hemochromatotic mice (Jenkitkasemwong *et al.* 2015). Ironically, according to a metal cation competition assay in ZIP8-retrovirally-transfected cells, cadmium uptake via ZIP8 is most effectively inhibited by manganese, followed by mercury, lead, copper, zinc and then caesium, suggesting exceptionally high affinity of ZIP8 for manganese even in preference to zinc (He et al. 2006). Not surprisingly, these two zinc channels have now become known as canonical manganese importers in the nervous system (Chen *et al.* 2015).

Figure 3.10 TM5 of ZIP channels in the LIV-1 subfamily

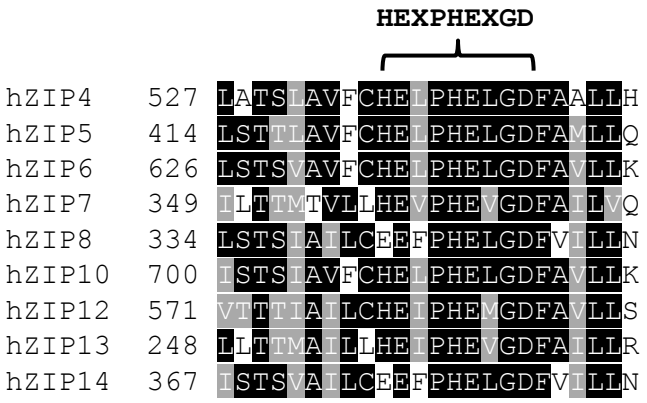

Amino acid sequences of TM5 of all the LIV-1 subfamily members were aligned using the TCoffee multiple sequence alignment program. Residues that were at least 70% identical (black) and complementary (grey) were shaded using the BoxShade 3.21 online program. The consensus motif of the LIV-1 subfamily with sequence HEXPHEXGD is indicated.

3.3.3 ZIP channel phosphorylation site discovery with kinase prediction

Since ZIP7 was discovered to be activated by CK2-mediated phosphorylation on residues S275 and S276 (Taylor et al. 2012), it was hypothesised that other phosphorylation sites either in ZIP7 or in other ZIP channels might also be involved in post-translational regulation of ZIP channels. We therefore comprehensively explored the phosphorylation sites in

all the ZIP channels using multiple online databases, including PhosphoNET (Kinexus Bioinformatics Corporation), PHOSIDA (Gnad et al. 2011) and PhosphoSitePlus (Hornbeck et al. 2015). To reduce the huge number of the phosphorylation sites to a manageable level and to exclude the less likely sites, only the sites that had been experimentally confirmed in mammalian cells by mass spectrometry were selected and listed along with their kinase prediction (Table 3.2; Fig. 3.11). Only the residues located in the cytosolic loop between TM3 and TM4 were included, given the presence of a conserved mixed-charged area in this cytosolic loop immediately proximal to TM4 (Taylor and Nicholson 2003), which indicated this cytosolic loop as a reactive region likely to interact with other proteins (Zhu and Karlin 1996). Furthermore, the two experimentally-confirmed phosphorylated residues in ZIP7, S275 and S276, are also located in this particular cytosolic loop (Taylor et al. 2012).

A total of 29 such phosphorylation sites were detected in the cytosolic loop between TM3 and TM4 of ZIP3, ZIP4, ZIP6, ZIP7, and ZIP10 (Table 3.2; Fig. 3.11). Residues S275 and S276 of ZIP7 (Sharma *et al.* 2014) were the only sites that had already been confirmed by site-specific methods (Taylor et al. 2012), whereas all the other residues have been detected only by mass spectrometry-based proteomics. In ZIP3, 7 sites were detected, including residues S125, S129, S131, Y133, Y147, S156, and S163 (Table 3.2; Fig. 3.11). In ZIP4, only one residue, S490, was reported by a study to be phosphorylated (Table 3.2; Fig. 3.11). In ZIP6, residues S471, Y473, S478, T479, Y493, Y528, and Y531 were detected (Table 3.2; Fig. 3.11). In ZIP7, besides S275 and S276, phosphorylation on residues S293 and T294 had also been reported (Table 3.2; Fig. 3.11). In ZIP10, as many as 10 residues were detected to be phosphorylated, including residues T536, S539, T540, S546, T553, S570, S573, T583, S591, and Y596 (Table 3.2; Fig. 3.11). Interestingly, the sites that were predicted to be phosphorylated by CK2 with the highest prediction scores for the individual sites were present not only in ZIP7, but also in ZIP3 (S129), ZIP6 (S478), and ZIP10 (S583 and T583) (Table 3.2; Fig. 3.11). It is therefore plausible that CK2 might also phosphorylate ZIP3, ZIP6, and ZIP10 on these potential sites, thereby triggering cellular zinc influx and replenishing zinc into the stores.

Table 3.2 Phosphorylation sites in the cytosolic loop between TM3 and TM4 of ZIP channels with predicted kinases (updated 10th August 2015)

ZIP	Site	Sequence	Reference (mass spectrometry) [a]	No. of rec. [b]	Predicted kinase (gene symbol)	Function of the predicted kinase [c]
ZIP3	**S125**	LETFNAG**S**DVGSDSE	(Franz-Wachtel *et al.* 2012)	15	Rho-associated protein kinase 1 (ROCK)	N/A
	S129	NAGSDVG**S**DSEYESP	(Weber *et al.* 2012)	13	Protein kinase CK2 (CSNK2)	Cell cycle progression, apoptosis, transcription, viral infection
	S131	GSDVGSD**S**EYESPFM	(Phanstiel *et al.* 2011)	3	Inhibitor of nuclear factor kappa-B kinase epsilon (IKBKE)	Protection against DNA damage-induced cell death.
	Y133	DVGSDSE**Y**ESPFMGG	(Phanstiel et al. 2011)	1	Mast/stem cell growth factor receptor Kit (KIT)	Cell survival and proliferation, haematopoiesis, stem cell maintenance, gametogenesis, mast cell development, migration and function
	Y147	GARGHAL**Y**VEPHGHG	(Palacios-Moreno *et al.* 2015)	184	Tyrosine-protein kinase FRK (FRK)	Negative regulation of cell proliferation
	S156	EPHGHGP**S**LSVQGLS	(2010) CST Curation Set 10170 [d]	5	Serine/threonine-protein kinase mTOR (MTOR)	Cellular metabolism, growth and survival.
	S163	SLSVQGL**S**RASPVRL	(2009) CST Curation Set 6183 [d]	1	None	
ZIP4	**S490**	NPEPRRL**S**PELRLLP	(Brill *et al.* 2009)	1	Mitogen-activated protein kinase 13 (MAPK13)	Cell proliferation, differentiation, transcription and development

ZIP	Site	Sequence	Reference (mass spectrometry) [a]	No. of rec. [b]	Predicted kinase (gene symbol)	Function of the predicted kinase [c]
ZIP6	**S471**	VEIKKQL**S**KYESQLS	(Zhou *et al.* 2013)	2	Calcium/calmodulin-dependent protein kinase type II gamma (CAMK2G)	N/A
	Y473	IKKQLSK**Y**ESQLSTN	(Wu *et al.* 2010)	1	N/A	N/A
	S478	SKYESQL**S**TNEEKVD	(Sharma et al. 2014)	15	Protein kinase CK2 (CSNK2)	Cell cycle progression, apoptosis, transcription, viral infection
	T479	KYESQLS**T**NEEKVDT	(Wu et al. 2010)	4	DNA-dependent protein kinase (PRKDC)	Molecular sensor for DNA damage
	Y493	TDDRTEG**Y**LRADSQE	(Palacios-Moreno et al. 2015)	10	DNA-dependent protein kinase (PRKDC)	Molecular sensor for DNA damage
	Y528	HAHPQEV**Y**NEYVPRG	(Palacios-Moreno et al. 2015)	122	Tyrosine-protein kinase Lck (LCK)	Host-virus interaction
	Y531	PQEVYNE**Y**VPRGCKN	(Palacios-Moreno et al. 2015)	61	N/A	N/A
ZIP7	**S275**	RSTKEKQ**S**SEEEEKE	(Sharma et al. 2014)	13	Protein kinase CK2 (CSNK2)	Cell cycle progression, apoptosis, transcription, viral infection
	S276	STKEKQS**S**EEEEKET	(Sharma et al. 2014)	14	Protein kinase CK2 (CSNK2)	Cell cycle progression, apoptosis, transcription, viral infection
	S293	VQKRRGG**S**TVPKDGP	(Olsen *et al.* 2010)	1	MAP kinase-activated protein kinase-2-3 (MAPKAPK2-3)	Cytokines production, endocytosis, cell migration, chromatin remodelling and transcriptional
	T294	QKRRGGS**T**VPKDGPV	(2008) CST Curation Set 4745 [d]	1	Serine/threonine-protein kinase pim-1-3 (PIM1-3)	Cell survival, cell proliferation

ZIP	Site	Sequence	Reference (mass spectrometry) [a]	No. of rec. [b]	Predicted kinase (gene symbol)	Function of the predicted kinase [c]
ZIP10	**T536**	KWFMKQN**T**EESTIGR	(Shiromizu *et al.* 2013)	4	Serine/threonine-protein kinase ATR (ATR)	DNA damage response
	S539	MKQNTEE**S**TIGRKLS	(Kettenbach *et al.* 2011)	7	Serine/threonine-protein kinase pim-1 (PIM1)	Cell survival, Cell proliferation
	T540	KQNTEES**T**IGRKLSD	(Sharma et al. 2014)	3	Leucine-rich repeat serine/threonine-protein kinase 2 (LRRK2)	Regulation of dardarin production (mutation involved in pathogenesis of Parkinson's disease)
ZIP10	**S546**	STIGRKL**S**DHKLNNT	(Sharma et al. 2014)	5	Serine/threonine-protein kinase pim-1-3 (PIM1-3)	Cell survival, Cell proliferation
	T553	SDHKLNN**T**PDSDWLQ	(Sharma et al. 2014)	5	Mitogen-activated protein kinase 8-10 (MAPK8-10)	Cell proliferation, differentiation, migration, transformation and programmed cell death.
	S570	PLAGTDD**S**VVSEDRL	(Sharma et al. 2014)	2	Serine/threonine-protein kinase pim-1-2 (PIM1-2)	Cell survival, Cell proliferation
	S573	GTDDSVV**S**EDRLNET	(Sharma et al. 2014)	1	Protein kinase CK2 (CSNK2)	Cell cycle progression, apoptosis, transcription, viral infection
	T583	RLNETEL**T**DLEGQQE	(Sharma et al. 2014)	1	Protein kinase CK2 (CSNK2)	Cell cycle progression, apoptosis, transcription, viral infection
	S591	DLEGQQE**S**PPKNYLC	(Sharma et al. 2014)	13	Cyclin-dependent kinase 1-2 (CDK1-2)	Cell cycle
	Y596	QESPPKN**Y**LCIEEEK	(Sharma et al. 2014)	9	Tyrosine-protein kinase SYK (SYK)	Immunity

[a] For the sites where there is more than one reference, only the latest one is shown as a representative for each site.
[b] **No. of rec.**, number of records, representing the number of proteomic studies that detected phosphorylation at the individual residues using mass spectrometry.
[c] Functions of the kinases were retrieved from the UniProt Knowledgebase (UniProtKB, The UniProt Consortium) (The UniProt Consortium 2015)
[d] **CST curation set**, curation sets from Cell Signaling Technology, Inc.

Figure 3.11 Potential phosphorylation sites and kinases for ZIP channels

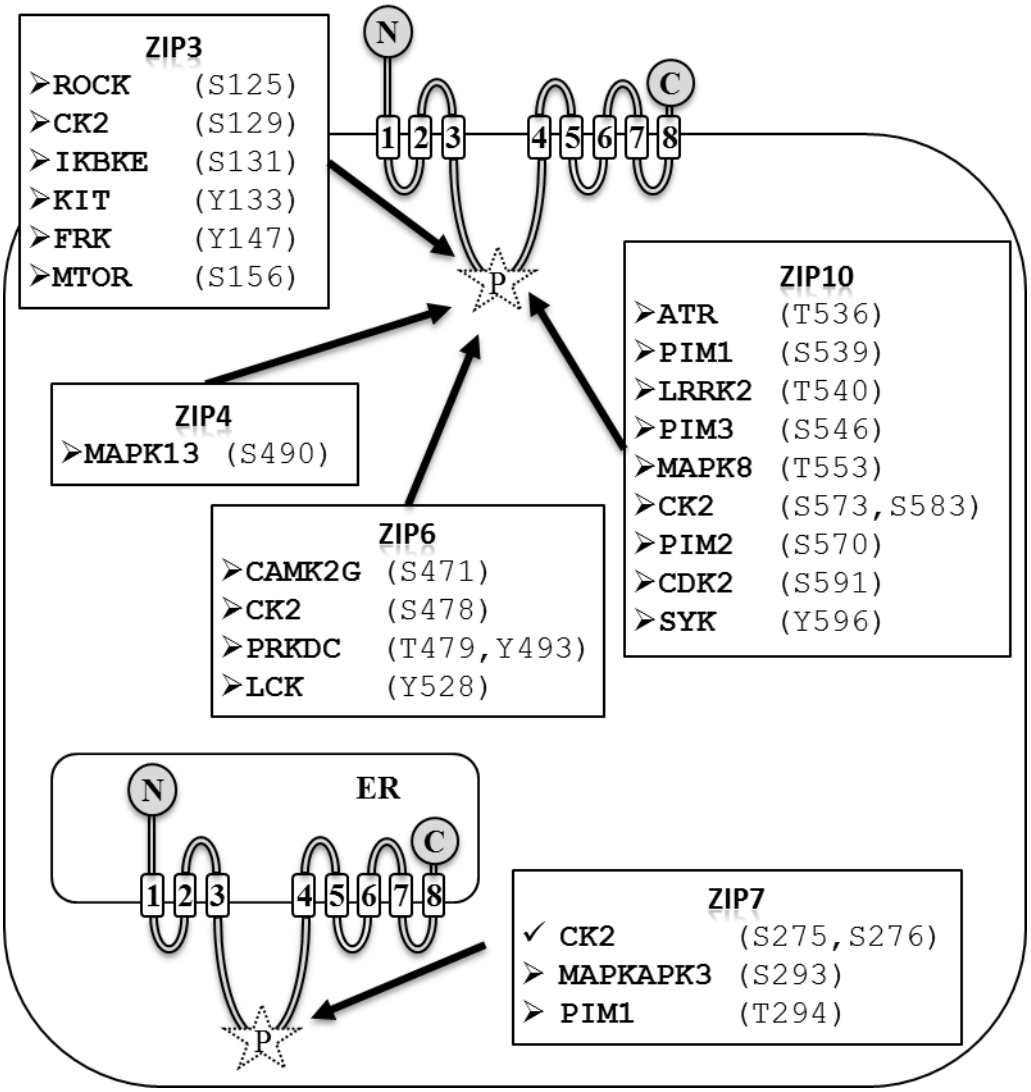

Phosphorylation sites with kinase prediction of all ZIP channels were searched for in the PhosphoNET (Kinexus Bioinformatics Corporation), the PHOSIDA (Gnad et al. 2011), and the PhosphoSitePlus (Hornbeck et al. 2015) databases. The sites that had been experimentally confirmed by mass spectrometry in mammalian cells and that located in the cytosolic loop between TM3 and TM4 were selected. Predicted kinases with the highest prediction scores are shown. The potential phosphorylation sites are found in ZIP3, ZIP4, ZIP6, ZIP7, and ZIP10. ZIP7 S275 and S276 are the only two sites that have been confirmed using site-specific methods (Taylor et al. 2012).

The hallmarks of cancer comprise six biological features that cancer cells need to acquire during carcinogenesis: sustained proliferation, growth suppressor evasion, cell death resistance, immortality, angiogenesis, and invasion/metastasis (Hanahan and Weinberg 2011). Considering the predicted kinases for ZIP3, ZIP4, ZIP6, ZIP7, and ZIP10 (Table 3.2; Fig. 3.11), in correlation with the hallmarks of cancer, all these ZIP channels had at least one predicted kinase whose function was contributory to some of these hallmarks.

The kinases predicted for ZIP3 included CK2, which promotes proliferation; KIT, which promotes proliferation and migration; and MTOR, which promotes proliferation and survival (Table 3.2 and 3.3; Fig. 3.11). The kinase predicted for ZIP4 included MAPK13, which promotes proliferation (Table 3.2 and 3.3; Fig. 3.11). Besides CK2, ZIP7 was predicted to be phosphorylated by MAPKAPK2−3, which promote cell migration, and PIM1−3, which promote cell proliferation and migration, whereas ZIP10 was predicted to be phosphorylated by PIM1−3, as well as MAPK8−10, which promote cell proliferation and migration, and CDK1−2, which promote cell proliferation (Table 3.2 and 3.3; Fig. 3.11). It is noteworthy that the functions of these kinases were obtained from UniProt Knowledgebase (The UniProt Consortium 2015), which might not have included all their functions in the literature. Moreover, because none of the potential phosphorylation sites, except residues S275 and S276 of ZIP7, had been confirmed using site−specific methods, the roles of these ZIP channels in carcinogenesis still need further investigations.

Table 3.3 Association of the kinases predicted for the phosphorylation sites in ZIP channels with carcinogenesis

ZIP channels	Hallmarks of cancer associated with predicted kinases		
	Proliferation	Survival	Migration
ZIP3	✓	✓	✓
ZIP4	✓		
ZIP6	✓		
ZIP7	✓	✓	✓
ZIP10	✓	✓	✓

Phosphorylation sites with kinase prediction for all the ZIP channels were searched for in the PhosphoNET (Kinexus Bioinformatics Corporation), the PHOSIDA (Gnad et al. 2011), and the PhosphoSitePlus (Hornbeck et al. 2015) databases. Functions of the predicted kinases with the highest prediction scores for all the phosphorylation sites in each ZIP channel were looked for in the UniProt Knowledgebase (The UniProt Consortium 2015). In correlation with the proposed hallmarks of cancers (Hanahan and Weinberg 2011), every ZIP channel has at least one predicted kinase that contributes to some of these hallmarks of cancer.

3.3.4 Analysis of potential phosphorylation sites in ZIP7

To determine evolutionary conservation of residues S275 and S276 in ZIP7, which might imply potential importance of these residues in ZIP7 post−translational control, ZIP7 amino acid sequences in different animal species were aligned. ZIP7 sequences had been reported in mammals (human, Sumatran orang-utan, chimpanzee, gorilla, rhesus monkey, dog, cat, rabbit, bovine, horse, pig, sheep, panda, mouse, and rat), an amphibian (African clawed frog), fishes (zebrafish, Atlantic salmon, and trout), and a plant (maize) (Fig. 3.12). Evolutionary conservation of the protein sequences was clearly seen across the eukaryotic species (Fig. 3.12). Importantly, the two consecutive serine residues equivalent to S275 and S276 in human ZIP7 were highly conserved across the mammalian species (Fig. 3.12 and 13, the red box). Furthermore, these two residues were located in a region that had a sequence consistent with the consensus motif for CK2−binding site, **S**/**T**−X−X−E (S, serine; T, threonine; E, glutamine; X, any amino acid) (Fig. 3.12 and 13, the red box). Additionally, multiple acidic amino acids were present distal to these sites (Fig. 3.12 and 13, the red box). These features collectively increased the possibility for CK2−mediated phosphorylation (Pinna 1990; Meggio and Pinna 2003), which has already been confirmed using site−specific methods (Taylor et al. 2012).

Figure 3.12 Alignment of ZIP7 in various animal species

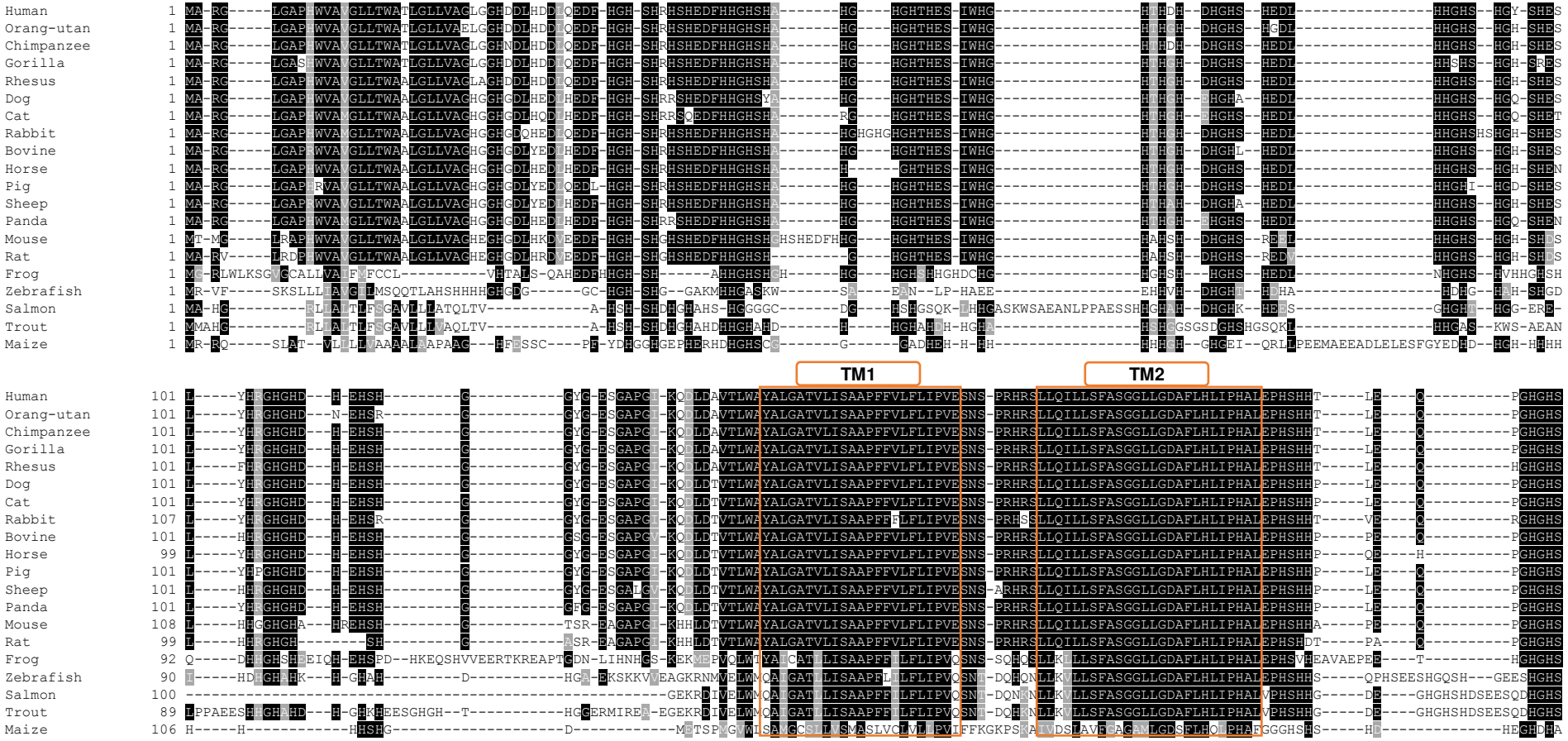

Figure 3.12 Alignment of ZIP7 in various animal species (continued)

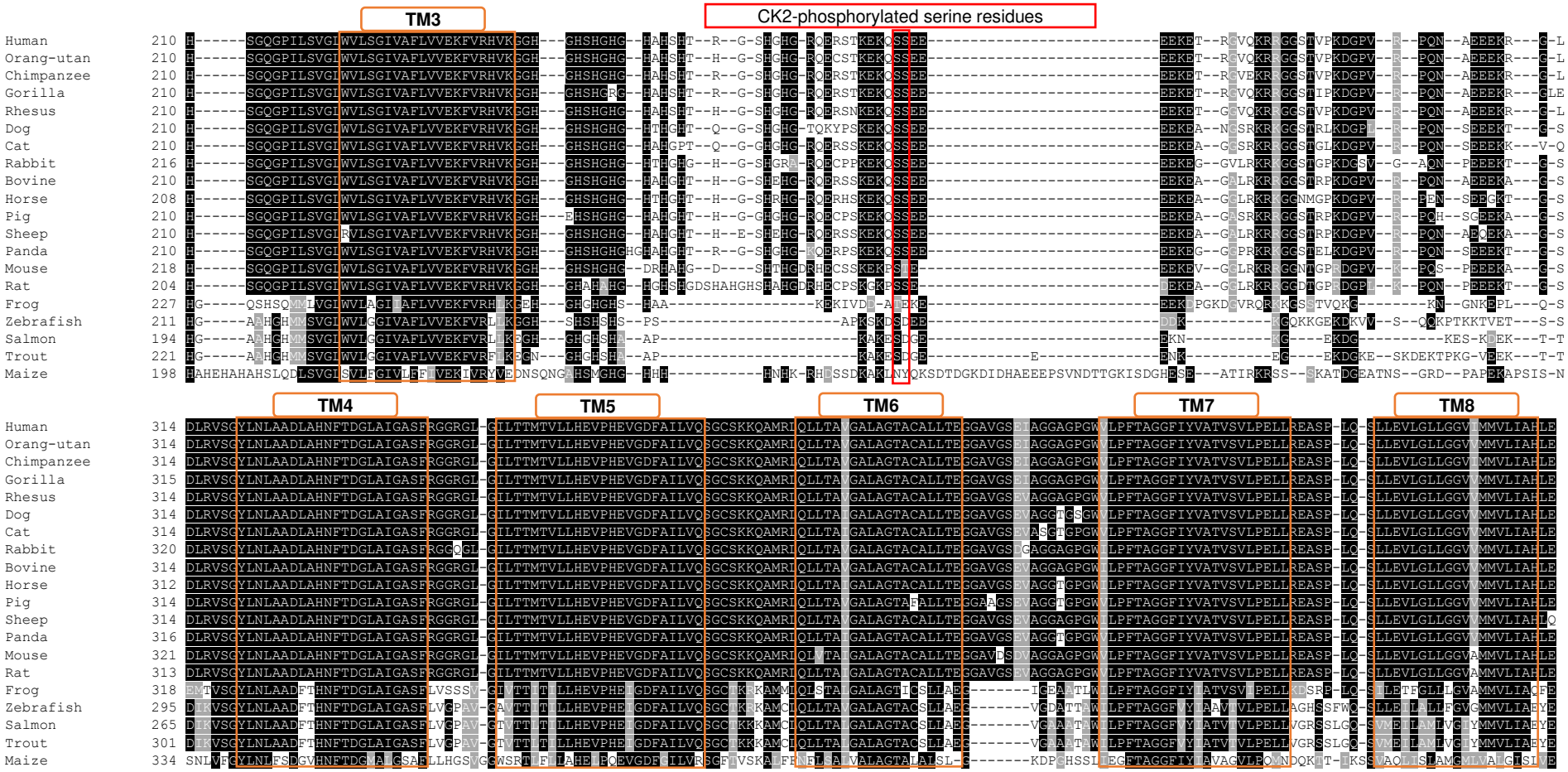

Amino acid sequences of ZIP7 from mammals (human, Sumatran orang-utan, chimpanzee, gorilla, rhesus monkey, dog, cat, rabbit, bovine, horse, pig, sheep, panda, mouse and rat), an amphibian (African clawed frog), fishes (zebrafish, Atlantic salmon and trout), and a plant (maize) were aligned using the TCoffee multiple sequence alignment program. Residues that were at least 70% identical (black) and complementary (grey) were shaded using the BoxShade 3.21 online program. The regions equivalent to the TM regions (orange box) and the serine residues S275 and S276 (red box) in hZIP7 are indicated.

Figure 3.13 The CK2−phosphorylated sites in ZIP7

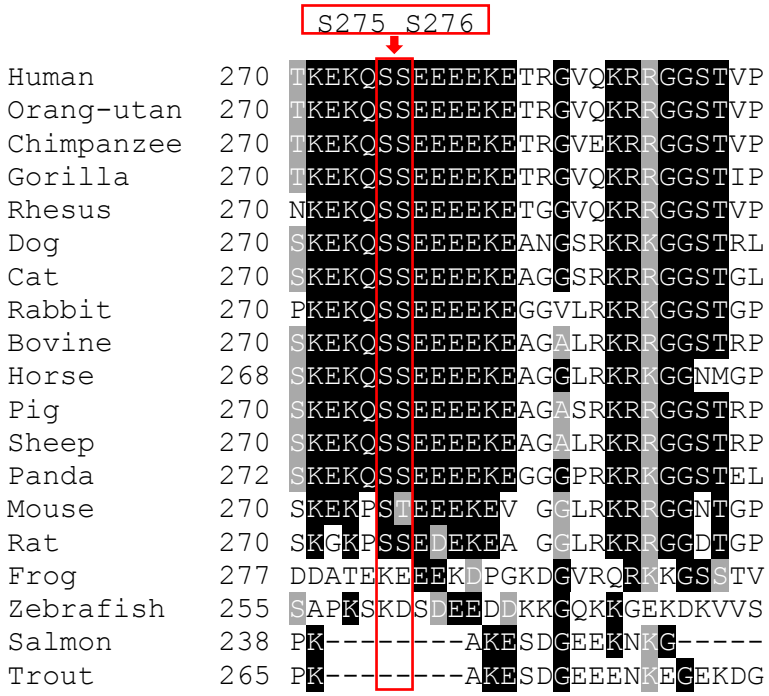

Amino acid sequences of ZIP7 from mammals (human, Sumatran orang−utan, chimpanzee, gorilla, rhesus monkey, dog, cat, bovine, horse, pig, sheep, panda, mouse, and rat), an amphibian (African clawed frog), and fishes (zebrafish, Atlantic salmon and trout) were aligned using the TCoffee multiple sequence alignment program. The region equivalent to residues 270−296 of human ZIP7 is shown. Residues that were at least 70% identical (black) and complementary (grey) were shaded using the BoxShade 3.21 online program. The serine residues equivalent to S275 and S276 of ZIP7 are indicated in a red box.

3.3.5 Analysis of potential phosphorylation sites in ZIP6

To explore the possibility that ZIP6 was post−translationally regulated by phosphorylation like ZIP7, all available ZIP6 sequences in different animal species were aligned. ZIP6 sequences were found in mammals (human, chimpanzee, Sumatran orang−utan, marmoset, gibbon, Tasmanian Devil, cat, dog, mouse, and rat) and zebrafish (Fig. 3.14). The sites that had been reported to be phosphorylated by mass spectrometry were investigated for their evolutionary conservation, focusing on residue S478, which was predicted to be phosphorylated by CK2, and the sites in the vicinity, including residues S471 and T479 (Fig. 3.14 and 3.15). Additionally, even though phosphorylation on residue S475 had not been experimentally confirmed, the sequence in this region matched established consensus motifs for multiple kinases. The residue S475 was therefore listed as a predicted phosphorylation site, according to the Human Protein Reference Database (Keshava Prasad et al. 2009).

Figure 3.14 Alignment of ZIP6 in various animal species

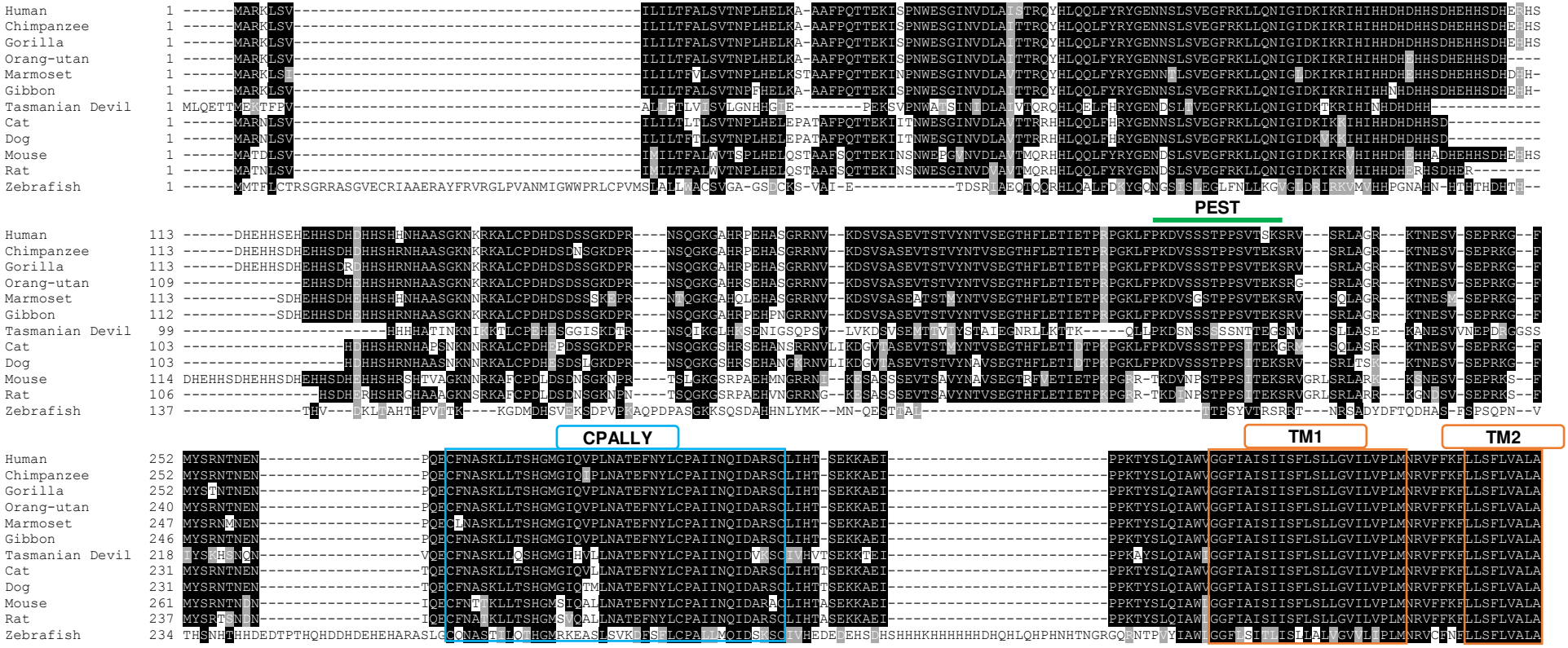

Figure 3.14 Alignment of ZIP6 in various animal species (continued)

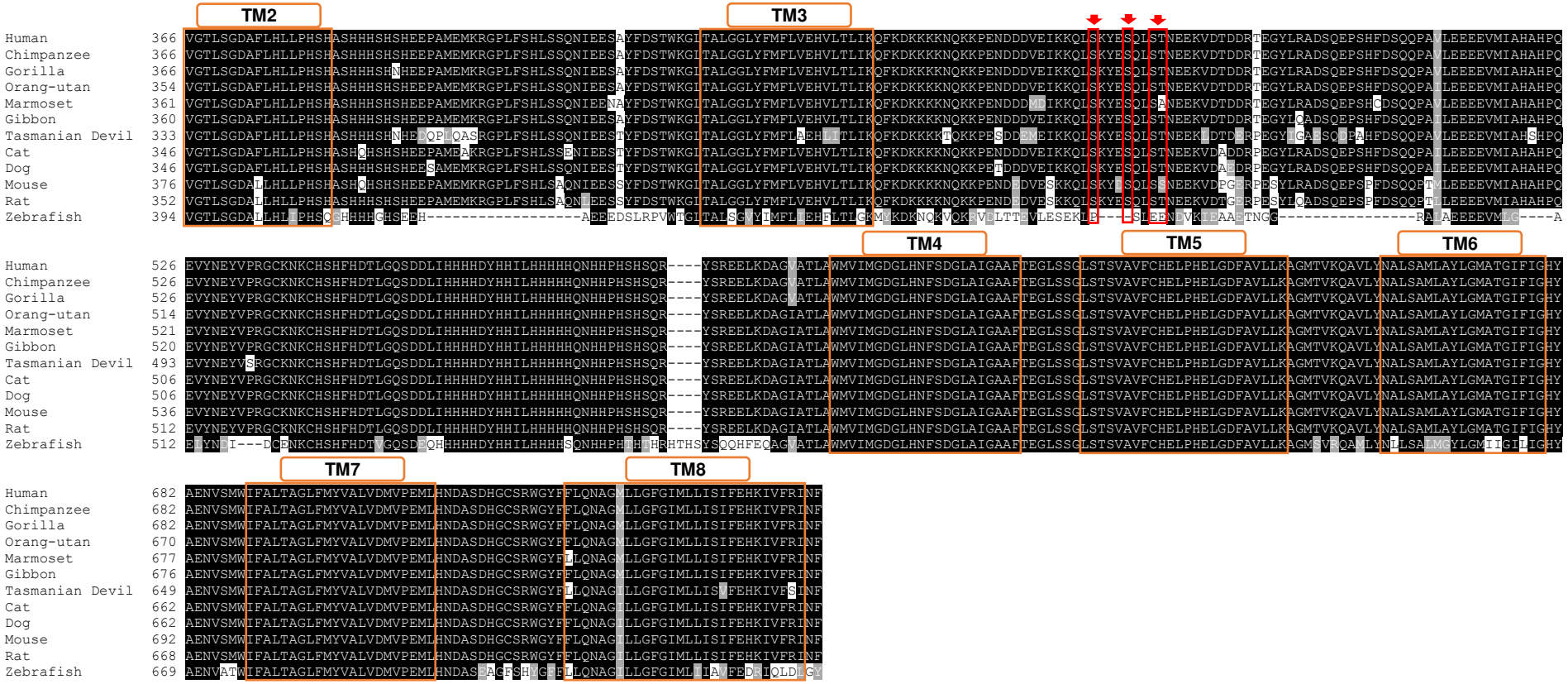

Amino acid sequences of ZIP6 from mammals (human, chimpanzee, Sumatran orang−utan, marmoset, gibbon, Tasmanian Devil, cat, dog, mouse, and rat) and zebrafish were aligned using the TCoffee multiple sequence alignment program. Residues that were at least 70% identical (black) and complementary (grey) were shaded using the BoxShade 3.21 online program. The regions equivalent to the PEST site (the motifs underneath a green continuous line), the CPALLY motif (a blue box), the predicted TM regions (orange boxes), and the potential phosphorylation sites (red boxes with red arrows) in human ZIP6 are indicated. The PEST motifs were analysed using Emboss Pestfind platform (Rogers et al. 1986).

Figure 3.15 The potential phosphorylation sites in ZIP6

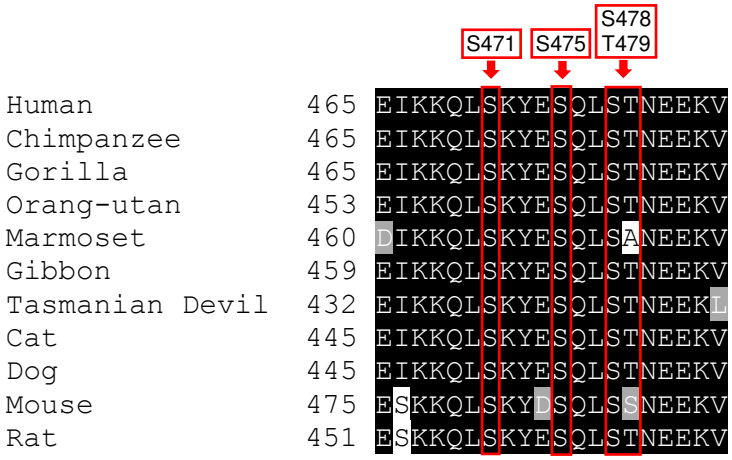

Amino acid sequences of ZIP6 from mammals (human, chimpanzee, Sumatran orang−utan, marmoset, gibbon, Tasmanian Devil, cat, dog, mouse, and rat) were aligned using the TCoffee multiple sequence alignment program. The region equivalent to residues 465−484 of human ZIP6 is shown. Residues that were at least 70% identical (black) and complementary (grey) were shaded using the BoxShade 3.21 online program. The serine and threonine residues equivalent to S471, S475, S478 and T479 of human ZIP6, which are potential phosphorylation sites in this region, are indicated in red boxes.

Like ZIP7, a high degree of evolutionary conservation was observed in ZIP6 across different mammal species (Fig. 3.14). Residues S471, S475, and S478 were 100% identical, whereas residue T479 was 83.33% identical (Fig. 3.14 and 3.15). The high conservation of these potential phosphorylation sites identified these sites as important residues for ZIP6 functional control.

3.4 Chapter summary

The computational sequence analysis of ZIP channels confirmed the unique characteristics of the LIV−1 subfamily among all the ZIP channels, as proposed in a previous study (Taylor and Nicholson 2003). The LIV−1 subfamily members had an apparently longer N−terminus than the other subfamilies (Fig. 3.5), suggesting a more complex post−translational control for these ZIP channels. Furthermore, the N−terminus of the LIV−1 subfamily members, except ZIP7 and ZIP13, contained a CPALLY motif, a sequence upstream of TM1 containing 3 consensus cysteine residues (Fig. 3.6). The presence of the cysteine residues in the CPALLY motif as well as another cysteine residue in TM5 might explain a mechanism whereby these ZIP channels control zinc movement through their pores (Taylor et al. 2007). Uniquely for the N−terminus of ZIP6 and ZIP10, there is a PEST motif (Rogers et al. 1986; Rechsteiner and Rogers 1996) (Fig. 3.7), consistent with the previous reports that highlight proteolytic cleavage as a key post−translational mechanism for ZIP6 and ZIP10 (Ehsani et al. 2012; Hogstrand et al. 2013). Moreover, the HX repeats, which are generally detected in the cytosolic loop between TM3 and TM4, were notably present in the N−terminus and the extracytosolic loop between TM2 and TM3 of the majority of the LIV−1 subfamily (Fig. 3.8 and 3.9). Importantly, a HEXPHEXPHGD motif in TM5 was uniformly present in the LIV−1 subfamily and totally absent in all the other subfamilies, confirming its uniqueness for this subfamily (Taylor and Nicholson 2003) (Fig. 3.10).

Furthermore, the exploration of phosphorylation sites revealed multiple sites in the cytosolic loop between TM3 and TM4 of ZIP3, ZIP4, ZIP6, ZIP7, and ZIP10, which had been confirmed by mass spectrometry in mammalian cells (Table 3.2; Fig. 3.11). The two adjacent serine residues in ZIP7, S275 and S276, were shown to be highly likely sites for CK2−mediated phosphorylation, and this has recently been confirmed using site−specific experiments (Taylor et al. 2012). Importantly, residue S478 on ZIP6 was predicted to be a CK2−phosphorylated site (Table 3.2; Fig. 3.11). This serine residue on ZIP6 and the nearby residues, including S471, S475 and T479, were proved to be highly conserved across different mammal species (Fig. 3.14 and 3.15), implying that these residues might be important for the ZIP6 functional control. These potential sites on ZIP6 will be further investigated in Chapter 6

Chapter 4:
Characterisation of pZIP7 antibody

4.1 Introduction

In the previous chapter, the computational analysis demonstrated a number of different potential phosphorylation sites in ZIP3, ZIP4, ZIP6, ZIP7, and ZIP10. Among these sites, only the two residues in ZIP7, S275 and S276, have been experimentally confirmed by site-specific procedures to be phosphorylated by CK2, resulting in activation of ZIP7-mediated zinc release from the stores (Taylor et al. 2012). ZIP7 has been proposed to be involved in development of tamoxifen resistance in breast cancer cells and contributory to aggressive behaviours in the tamoxifen-resistant cells (Taylor et al. 2008b). Furthermore, ZIP7 gene expression is independently predictive of poor clinical outcome of breast cancer (Taylor et al. 2007; Nimmanon and Taylor 2015). An indicator of ZIP7 activity could therefore become clinically useful. Our group have developed a monoclonal antibody that recognises ZIP7 only when phosphorylated on residues S275 and S276. This chapter therefore aims to characterise this antibody by investigating the specificity of this antibody to this phosphorylated form of ZIP7 and its potential usefulness in determining ZIP7 function.

Firstly, to determine the specificity of this antibody, immunofluorescence was performed in the cells that were transfected with wild-type ZIP7, a ZIP7 phosphomimetic mutant (S275D/S276D), and a ZIP7 phosphoablative mutant (S275A/S276A). Secondly, using immunofluorescence and Western blotting, the ability of this antibody to detect a ZIP7-mediated zinc wave following zinc treatment was investigated. Thirdly, its potential usefulness in recognising the increase in ZIP7 function in tamoxifen-resistant MCF-7 cells, or TAMR cells (Knowlden et al. 2003), was examined. Finally, the antibody was used to investigate two ZIP7 mutants, ZIP7 P190A and E363K, which have been reported in two patients suffering from an immunodeficiency disease.

4.2 Materials and methods

DNA constructs of ZIP7 S275A/S276A, P190A, and E363K had been inserted into an ampicillin-resistant pcDNA3.1/V5-His-TOPO plasmid vector, and were amplified by transformation of the single-use JM109 *E. coli* competent cells (Promega). Polymerase chain reaction (PCR) using a forward primer specific to ZIP7 and a BGH reverse primer confirmed the presence of the

correctly−orientated ZIP7 DNA in 1 out of 10 clone for ZIP7 S275A/S276A (Fig. 4.1A) and all clones for P190A and E363K (Fig. 4.1B). The plasmids of ZIP7 WT, S275A/S275A, S275D/S275D, P190A, and E363K were purified using the HiSpeed Plasmid Maxi Kit (Qiagen). The plasmid DNA solution was analysed with a UV spectrophotometer, showing OD260/OD280 ratios within a desirable range of 1.8−2.0, signifying the purity of the DNAs, and concentrations ranging from 0.74−3.50 µg/µL (Table 4.1). Additionally, the plasmid DNA was analysed with 1% agarose gel electrophoresis, showing a strong band between 5000-7000 bp (expected size = 6283 bp) (Fig 4.2).

Figure 4.1 Bacterial transformation for ZIP7 mutants

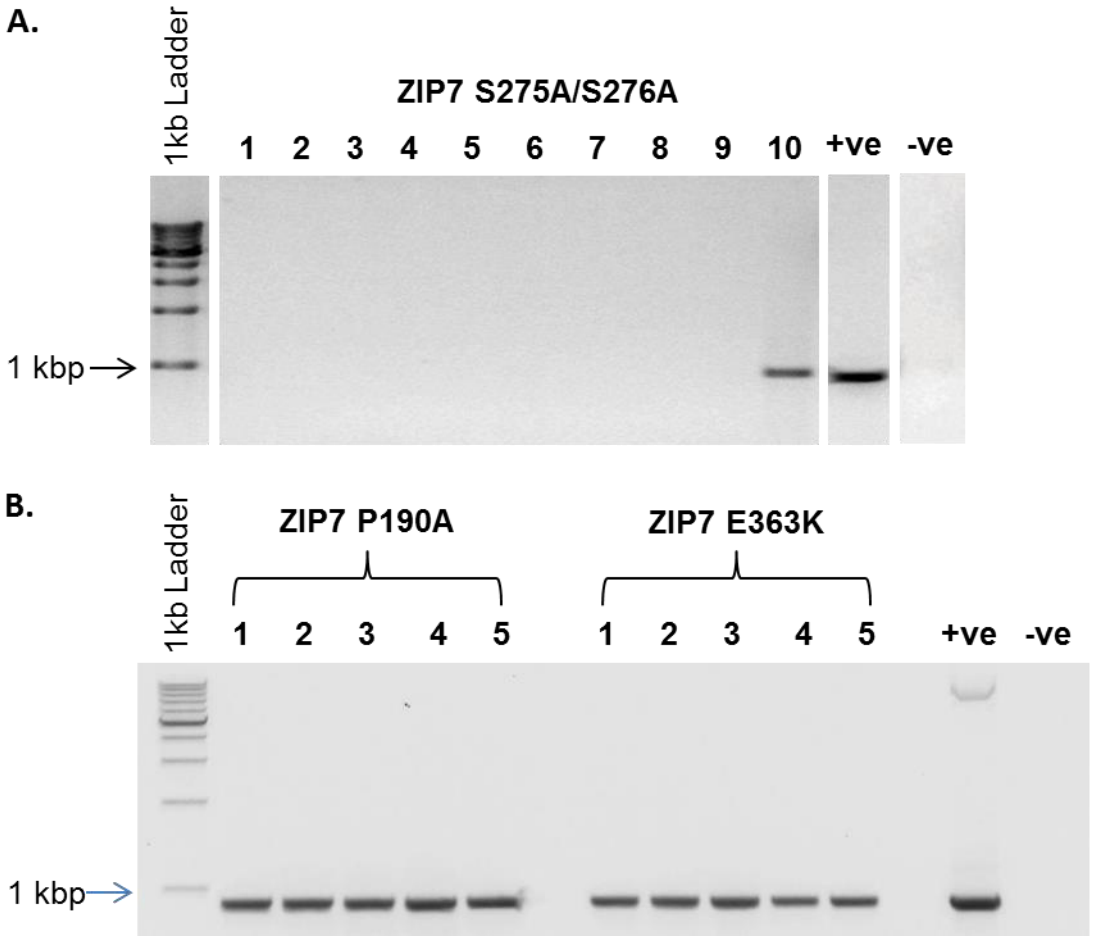

The JM109 E. coli competent cells were transformed with the pcDNA3.1/V5-His-TOPO that contains the DNA of ZIP7 S275A/S276A (A), and ZIP7 clinical mutants, P190A and E363K (B). Presence of the DNA inserts and their orientation in the plasmid vector were verified by PCR using a specific ZIP7 forward primer and a BGH reverse primer. The PCR products were separated by 1% agarose gel electrophoresis, revealing a band of approximately 900 bp (expected size = 903 bp), which was approximately the same size as the positive control. Clone 10 of the S275A/S276A mutant, clone 1 of the P190A mutant, and clone 1 of the E363K mutant were selected for plasmid preparation.

Table 4.1 Concentrations and OD260/280 ratios of prepared plasmids

Plasmid	Concentration (µg/µL)	OD260/280 Ratio
ZIP7 WT	1.12	1.931
ZIP7 S275A S276A	3.50	2.000
ZIP7 S275D S276D	0.74	1.900
ZIP7 P190A	1.22	1.937
ZIP7 E363K	1.16	1.966

Figure 4.2 Plasmid preparation for wild−type and mutant ZIP7 constructs

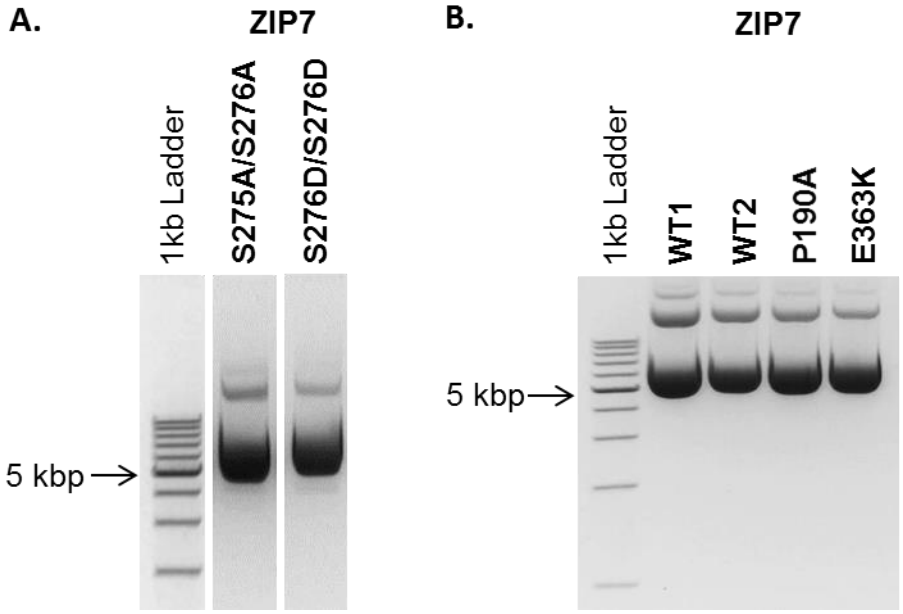

Plasmids of ZIP7 S275A/S276A and S275D/S276D mutants (A), as well as wild−type ZIP7 (WT) and the clinical mutants, P190A and E363K (B), were purified using the HiSpeed Plasmid Maxi Kit (Qiagen). The purified plasmid DNAs were analysed with 1% agarose gel electrophoresis, showing a strong band of between 5000-7000 bp (expected size = 6283 bp).

Please refer to Chapter 2 for the methods of transfection and treatments (Section 2.1), immunofluorescence (Section 2.3), Western blotting (Section 2.4), flow cytometry (Section 2.5), and zinc assays (Section 2.6).

4.3 Results and discussion

4.3.1 Wild−type and mutant ZIP7 constructs are robustly transfected

To verify the purified plasmids of ZIP7 constructs, immunofluorescence using a V5 antibody was performed. The V5 antibody targets the C−terminal V5 tag of the plasmid constructs. Immunofluorescence images revealed that

20−30% of cells transfected with the ZIP7 S275A/S275A, S275D/S275D (Fig. 4.3A), P190A, and E363K (Fig. 4.4A) mutants expressed V5, suggesting a transfection rate of 20−30%. This transfection rate was comparable to that of wild−type ZIP7 (Fig. 4.3A and 4.4A). An ER−like localisation pattern of the recombinant proteins was observed in enlarged images of the transfected cells (Fig. 4.3B and 4.4B). This staining pattern was consistent with two previous studies in which wild−type ZIP7 recombinant protein was demonstrated to co−localise with Calreticulin, an ER marker, in CHO cells (Taylor et al. 2004) and the ER−located variant B of ZnT5 in HeLa cells (Thornton et al. 2011), confirming the ER localisation of ZIP7.

Figure 4.3 A robust transfection of ZIP7 S275A/S276A and S275D/S276D

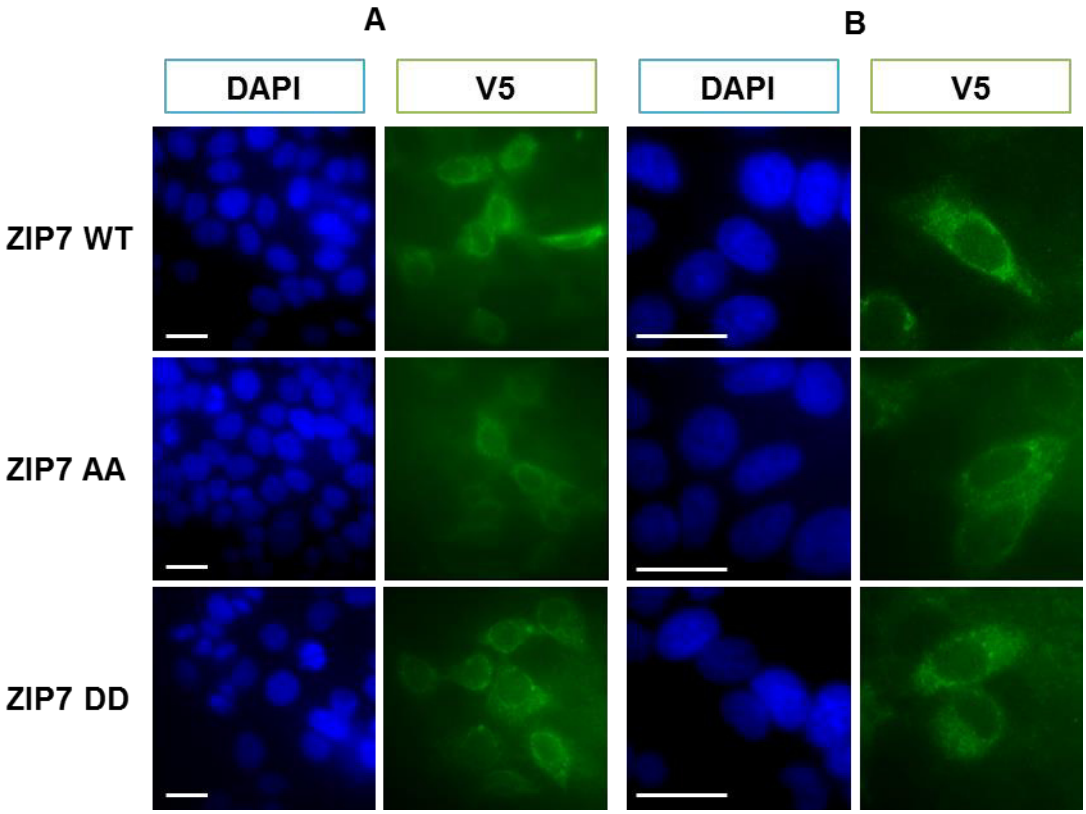

MCF−7 cells were transfected with wild−type ZIP7 (WT) and ZIP7 mutants, S275A/S276A (AA) and S275D/S276D (DD). Immunofluorescence was performed using a V5 antibody, which was conjugated to Alexa Fluor 488 (green), with DAPI nuclear staining (blue). Representative microscopic views were captured using a 63x magnification lens. The images reveal that 20%−30% of the cells are transfected with the ZIP7 mutants, as judged by positive V5 staining, which is comparable to the transfection with wild−type ZIP7 (A). Closer views of the transfected cells (B) reveal a robust expression of the recombinant proteins, with a typical ER−like localisation of ZIP7.
Scale bar, 25 µm.

Figure 4.4 A robust transfection of ZIP7 P190A and E363K

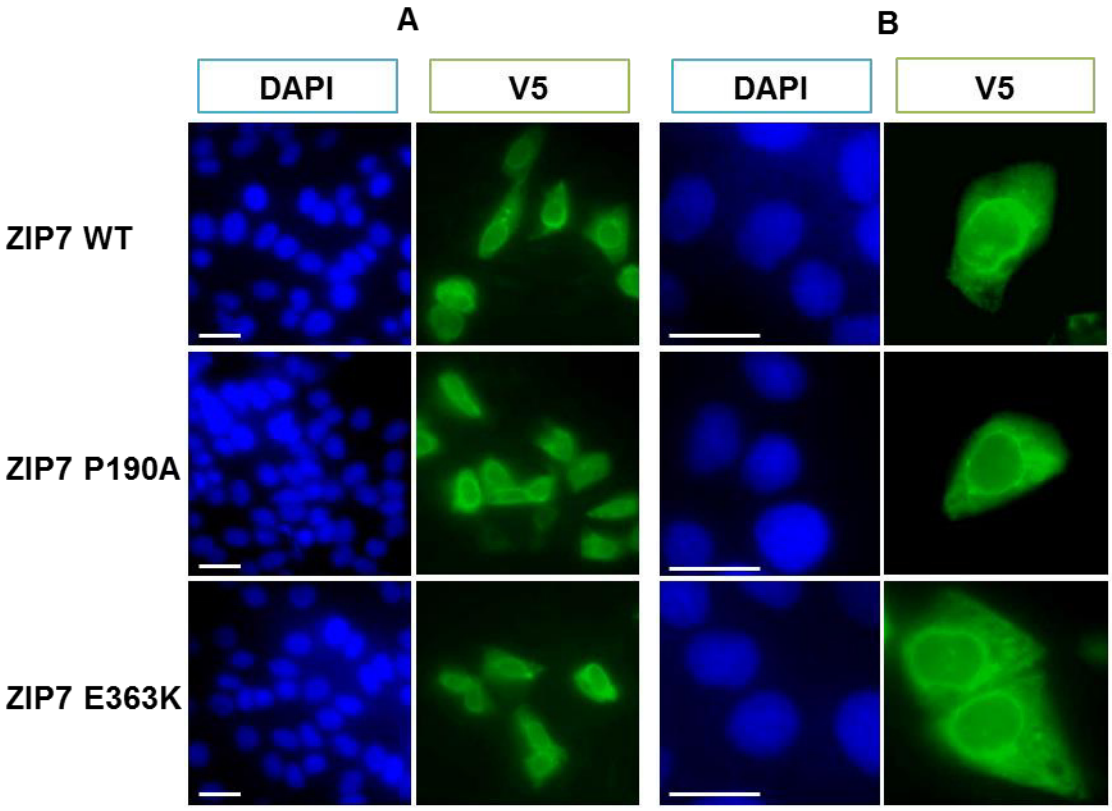

MCF−7 cells were transfected with wild−type ZIP7 (WT) and the ZIP7 clinical mutants, P190A and E363K. Immunofluorescence was performed using a V5 antibody, which was conjugated to Alexa Fluor 488 (green), with DAPI nuclear staining (blue). Representative microscopic views were captured using a 63x magnification lens. The images reveal that 20%−30% of the cells are transfected with the ZIP7 mutants, as judged by positive V5 staining, which is comparable to the transfection with wild−type ZIP7 (A). Closer views of the transfected cells (B) reveal a robust expression of the recombinant proteins, with a typical ER−like localisation of ZIP7.
Scale bar, 25 µm.

4.3.2 pZIP7 antibody binds ZIP7 when phosphorylated on S275/S276

The pZIP7 antibody has been generated by the Biogenes GmbH Company against peptide TKEKQ pS pS EEEEK (positions 270−281) (Fig. 4.5). To determine the specificity of the antibody to this phosphorylated form of ZIP7, immunofluorescence was performed in cells transfected with different ZIP7 constructs, including wild−type ZIP7, a ZIP7 phosphoablative mutant (ZIP7 S275A/S276A), or a phosphomimetic mutant (ZIP7 S275D/S276D). Noteworthy, in the ZIP7 phosphoablative mutant, residues S275 and S276 were substituted for alanine to prevent phosphorylation, whereas in the phosphomimetic mutant, these two residues were substituted for aspartate, which structurally mimics phosphoserine (Nordle Gilliver *et al.* 2010). A V5 antibody was used to identify the recombinant proteins.

Figure 4.5 The peptide epitope of the pZIP7 antibody

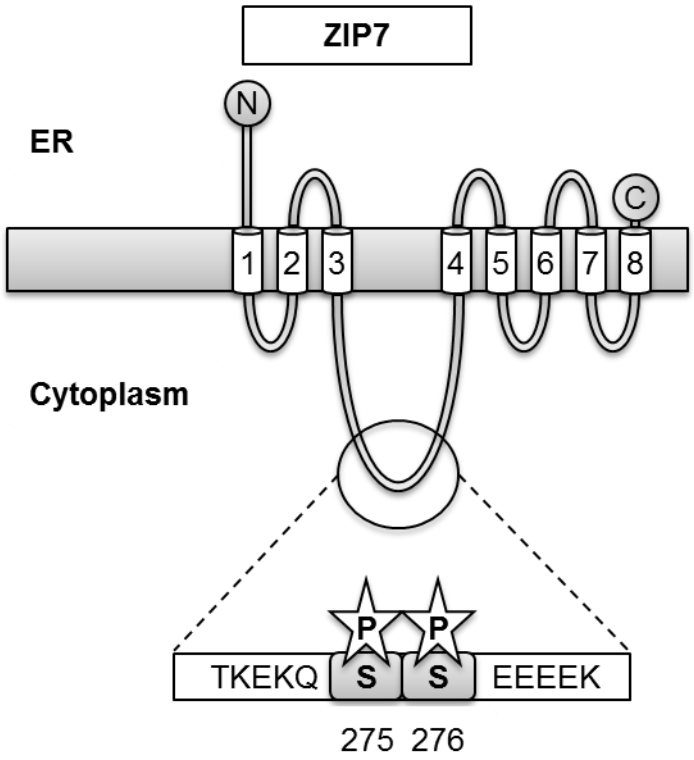

This schematic illustrates the predicted structure of ZIP7, which is located in the ER (Taylor and Nicholson 2003; Taylor et al. 2004) and activated by CK2−mediated phosphorylation on residues S275 and S276 (Taylor et al. 2012). A monoclonal antibody that recognises ZIP7 when residues S275 and S276 are phosphorylated have been developed. The epitope sequence of the antibody is TKEKQ pS pS EEEEK (positions 270−281).
ER, the endoplasmic reticulum.

The result revealed that 40% of the cells transfected with wild−type ZIP7 (V5−positive cells) were positive for pZIP7 (Fig. 4.6). Percentage of the pZIP7−positive cells increased to virtually 100% in the cells transfected with the ZIP7 phosphomimetic mutant, but decreased to 0% in the cells transfected with the ZIP7 phosphoablative mutant (Fig. 4.6). The presence of some non−transfected cells with strong pZIP7 staining confirmed the negative pZIP7 staining for the phosphoablative mutant (Fig. 4.6). Additionally, overlay images of the cells transfected with wild−type ZIP7 and the ZIP7 phosphomimetic mutant that were pZIP7−positive demonstrated that pZIP7 and V5 were co−localised, with an ER−like staining pattern (Fig. 4.6). Altogether, these findings suggested that the pZIP7 antibody could bind to either the phosphorylated form of wild−type ZIP7 or the phosphomimetic construct, but could not recognise the phosphoablative construct, indicating the specificity of this antibody to ZIP7 when residues S275 and S276 were phosphorylated.

Figure 4.6 pZIP7 antibody recognition of ZIP7 when phosphorylated

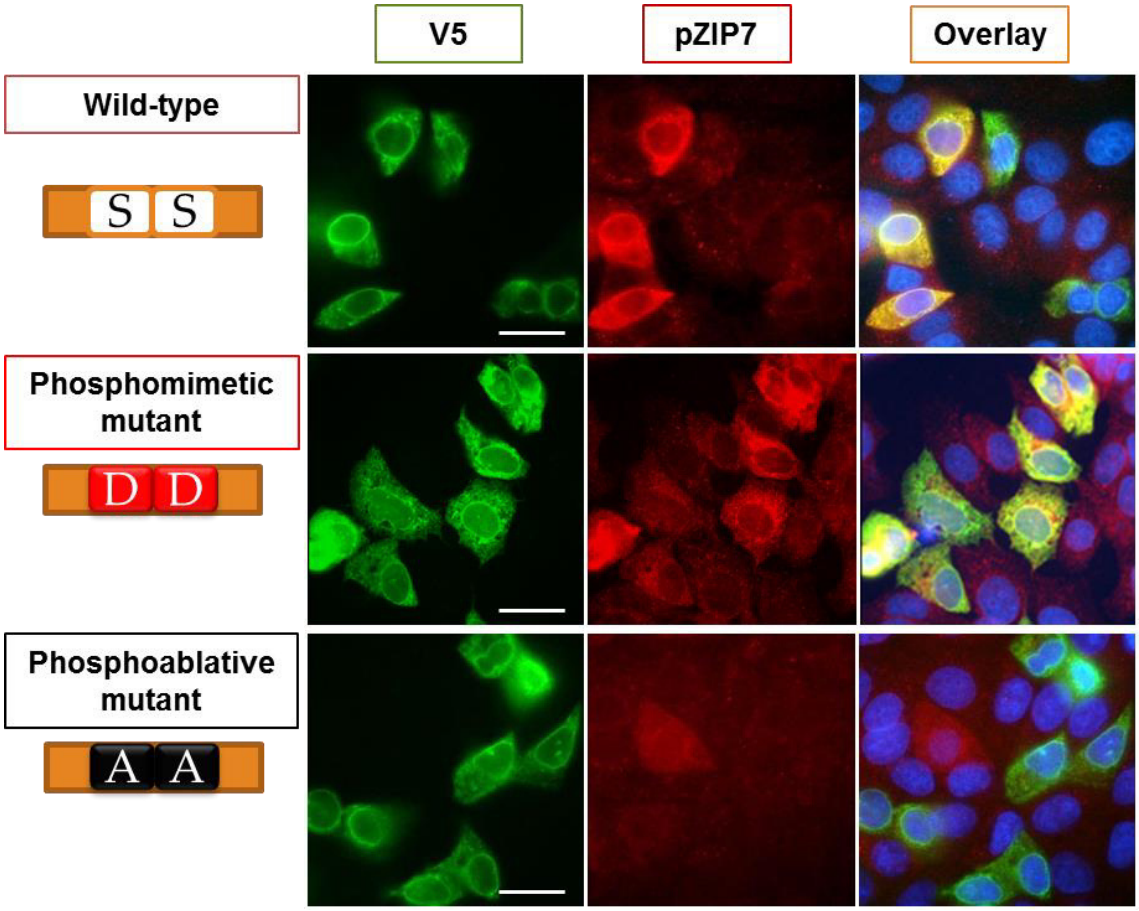

MCF−7 cells were transfected with wild−type ZIP7, a ZIP7 phosphomimetic mutant (S275D/S276D), and a ZIP7 phosphoablative mutant (S275A/S276A). Immunofluorescence was performed using V5 and pZIP7 antibodies, which were conjugated to Alexa Fluor 488 (green) and Alexa Fluor 594 (red), respectively, with DAPI nuclear staining (blue). Representative microscopic views were captured using a 63x magnification lens.
Scale bar, 25 μm.

4.3.3 pZIP7 antibody detects zinc−induced ZIP7 activation

To investigate the ability of the antibody to recognise a ZIP7-mediated zinc wave after external zinc stimulation, immunofluorescence and Western blotting were performed in cells transfected with wild−type ZIP7. Using immunofluorescence, approximately 40% of the cells transfected with wild−type ZIP7, probed with V5, overexpressed pZIP7 before zinc treatment (Fig. 4.7). Percentage of the pZIP7−positive cells significantly increased to 58% as a result of 10−minute external zinc stimulation (Fig. 4.7). Zinc ionophore pyrithione was also added to the treatment to enhance ZIP7 activation, given that zinc pyrithione, not zinc alone, produced effects comparable to an external zinc stimulation at the same treatment duration (Taniguchi et al. 2013).

Figure 4.7 Increased ZIP7 phosphorylation after zinc stimulation

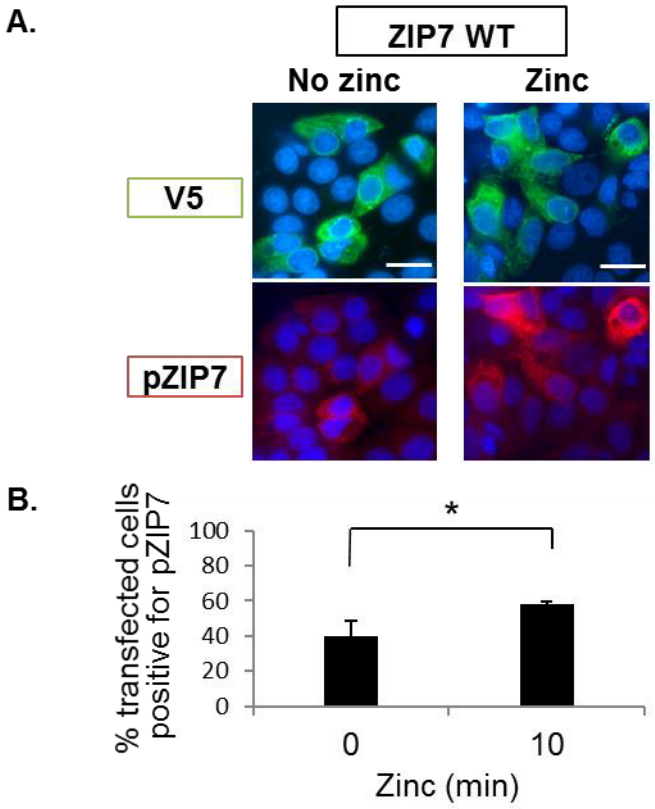

MCF−7 cells were transfected with wild−type ZIP7 (WT) and were treated with 20 μM zinc plus 10 μM sodium pyrithione for 10 minutes. Immunofluorescence was performed using V5 and pZIP7 antibodies, which were conjugated to Alexa Fluor 488 (green) and Alexa Fluor 594 (red), respectively, with DAPI nuclear staining (blue). A representative microscopic view captured using a 63x magnification lens is shown (A) with percentages of the transfected cells that are positive for pZIP7 demonstrated in a bar graph as mean of 4 representative fields ± standard error (B). Statistical significance is compared between the cells with and without zinc treatment. Scale bar, 25 μm. * $p < 0.05$.

Using Western blotting, the total ZIP7 antibody (Taylor et al. 2008b) recognised protein bands at 40 and 35 kDa (Fig. 4.8), which were predicted to represent the recombinant ZIP7 containing a 5−kDa C−terminal V5 tag and the endogenous ZIP7, respectively. In contrast, the pZIP7 antibody recognised a distinct band at 48 kDa (Fig. 4.8). A 4−kDa change in size has been reported for phosphorylation on two serine residues in a protein molecule (Bin et al. 2011). The difference in size of the pZIP7 band from the upper total ZIP7 band by 8 kDa (Fig. 4.8) therefore supported the presence of other phosphorylation sites in ZIP7 in addition to residues S275 and S276. Importantly, residues S293 and T294 were detected as potential phosphorylation sites in ZIP7 (Table 3.2; Fig. 3.11). Hypothetically, simultaneous phosphorylation on these two residues could be responsible for this big mobility shift on the blot (Fig. 4.8).

Figure 4.8 pZIP7 antibody detection of a distinct band at 48 kDa

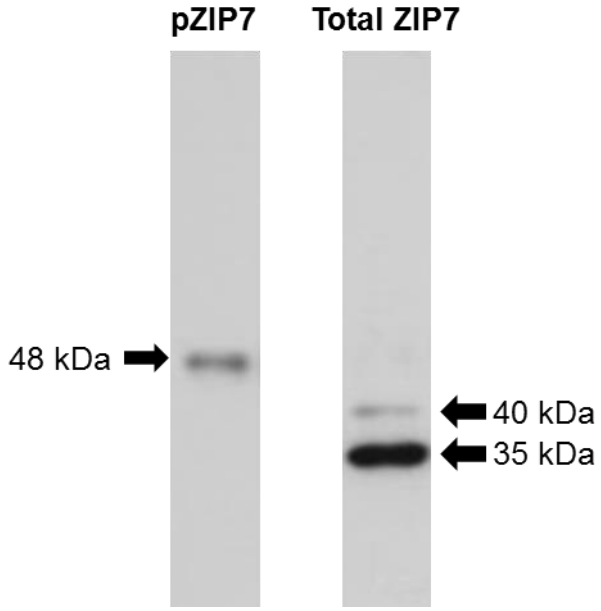

MCF−7 cells were transfected with wild−type ZIP7. Immunoblotting was performed using the pZIP7 and the total ZIP7 antibodies. A protein band of 48 kDa was detected with the pZIP7 antibody, whereas protein bands of 40 and 35 kDa were detected with the total ZIP7 antibody.

To confirm the immunofluorescence results, which demonstrated the ability of the pZIP7 antibody to detect zinc−activated ZIP7 (Fig. 4.7), a course of zinc treatment was performed in cells transfected with wild−type ZIP7. To verify the samples, Western blotting of pS473 AKT was performed first. AKT is a direct downstream effector of zinc release from cellular stores, which has been shown to be phosphorylated on S473 at 5 minutes after zinc treatment in MCF−7 cells transfected with wild−type ZIP7 (Taylor et al. 2012). This AKT activation is compatible with early CK2−mediated ZIP7 phosphorylation on residues S275 and S276, which was detected at 2 minutes after zinc treatment (Taylor et al. 2012). Given the instantaneous activation of AKT after zinc treatment, AKT phosphorylation was considered as a good indicator of the ZIP7−mediated zinc release from cellular stores. Consistent with the previous study, AKT activation was detected at 5 minutes after zinc treatment and became markedly increased at 10 minutes after zinc treatment (Fig. 4.9A). Probing with a V5 antibody confirmed the constant transfection levels in all the samples, and densitometric data normalised to V5 statistically confirmed the AKT activation at 5 minutes after zinc treatment (Fig. 4.9A). These data verified ZIP7 activation in these samples of zinc−treated cells.

Figure 4.9 pZIP7 antibody detection of zinc−activated ZIP7

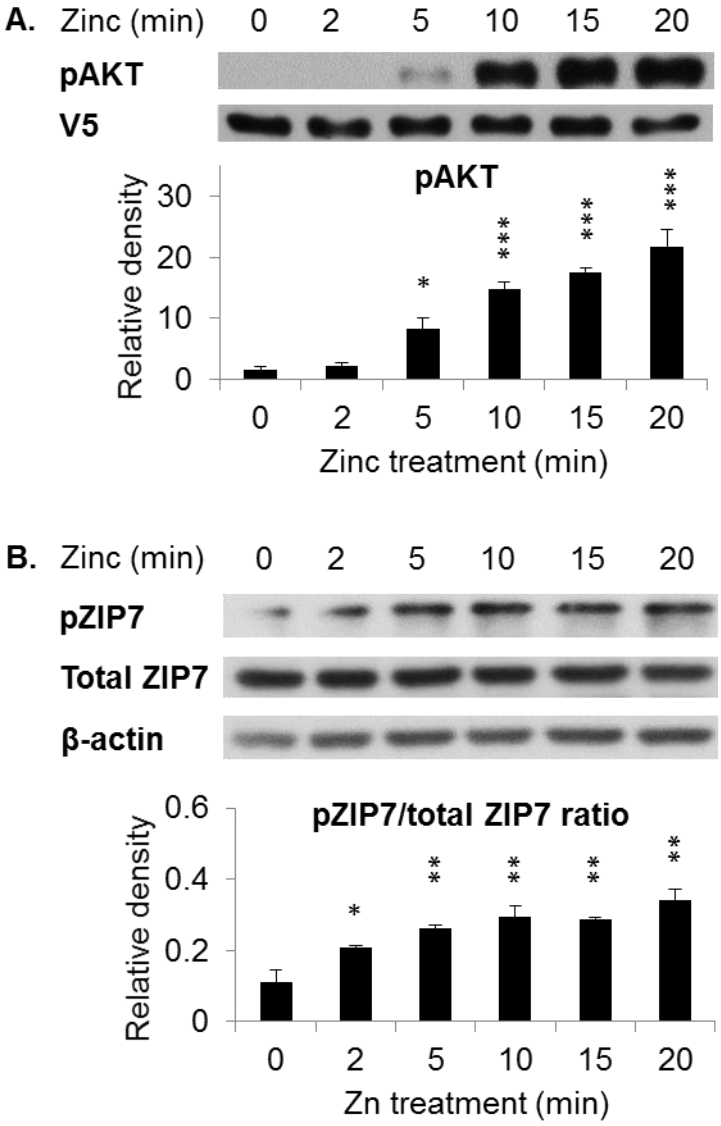

A. MCF−7 cells were transfected with wild−type ZIP7 and treated with 20 μM zinc plus 10 μM sodium pyrithione. Immunoblotting was performed using a pS473 AKT antibody. Protein bands of pS473 AKT (60 kDa) and β−actin (45 kDa) are demonstrated. Densitometric data normalised to V5 are shown in a bar graph as mean ± standard error (n = 3). Statistical significance is compared to time 0.
* $p < 0.05$, *** $p < 0.001$.

B. MCF−7 cells were transfected with wild−type ZIP7 and treated with 20 μM zinc plus 10 μM sodium pyrithione. Immunoblotting was performed using the pZIP7 and the total ZIP7 antibodies. Protein bands of pZIP7 (48 kDa), total ZIP7 (40 kDa) and β−actin (45 kDa) are demonstrated. Densitometric data are shown in a bar graph as mean of pZIP7/total ZIP7 ratios ± standard error (n = 2). Statistical significance is compared to time 0.
* $p < 0.05$, ** $p < 0.01$.

Using these verified samples, Western blotting analysis of pZIP7 and total ZIP7 was performed. The Western blot showed a gradual increase in pZIP7 levels after zinc treatment (Fig. 4.9B). In contrast to the pZIP7 levels, total ZIP7 levels staged the same throughout the 20-minute course of zinc stimulation (Fig 4.9B). Densitometric data presented as pZIP7/total ZIP7 ratios detected significant ZIP7 phosphorylation at 2 minutes after zinc treatment (Fig. 4.9B). This ZIP7 activation at 2 minutes was compatible with the AKT activation at 5 minutes after zinc treatment (Fig. 4.9A). Collectively, these results demonstrated that the pZIP7 antibody was able to recognise ZIP7 activation by phosphorylation on residues S275 and S276 after zinc stimulation, and was potentially useful for determination of ZIP7 activity.

4.3.4 pZIP7 antibody detects increased ZIP7 activation in TAMR cells

It has already been established that TAMR (tamoxifen-resistant) breast cancer cells, which derive from endocrine-sensitive MCF-7 cells (Knowlden et al. 2003), have increased cellular zinc levels, corresponding to the increase in ZIP7 protein levels in TAMR cells when compared to MCF-7 cells (Taylor et al. 2008b). Exploiting this cell model, we examined the ability of the pZIP7 antibody to detect the increase in ZIP7 activity. We firstly tested three different zinc-selective dyes that had been widely used by zinc biologists, consisting of Zinquin (Kd for Zn^{2+} = 370nM, UV light), Fluozin-3 (Kd for Zn^{2+} = 15nM, green fluorescence), and Newport Green (Kd for Zn^{2+} = 1μM, green fluorescence). MCF-7 cells were transfected with wild-type ZIP7, treated with zinc for 30 minutes, and analysed using FACS analysis in live cells.

Using Zinquin, the fluorescence intensity gradually increased throughout the 30-minute course of zinc treatment (Fig. 4.10A). However, TPEN treatment failed to reverse the change and the difference in fluorescence intensity was not apparent between the transfected and the non-transfected cells (Fig. 4.10A), suggesting that Zinquin was neither specific nor sensitive to zinc. On the contrary, the fluorescence intensity of Fluozin-3 increased at 5 minutes after zinc treatment in both the transfected and the non-transfected cells, and the levels remained constantly high after 5 minutes (Fig. 4.10B). The fluorescence intensity was apparently higher in the transfected cells than in the non-transfected cells throughout the course of zinc treatment (Fig. 4.10B). The

rises in the intensity were completely abolished by zinc chelation (Fig. 4.10B). These data suggested that Fluozin-3 was both sensitive and specific to zinc and was potentially useful for future investigations. On the other hand, the fluorescence intensity of Newport Green slightly increased at 10 minutes after zinc stimulation for wild-type ZIP7 (Fig. 4.10C). The Newport Green fluorescence intensity apparently decreased to even below the baseline levels after zinc chelation (Fig. 4.10C). However, no remarkable change in fluorescence intensity of Newport Green was detected in the non-transfected control (Fig. 4.10C). The findings for Newport Green therefore suggested that this fluorescent dye was specific, but not sensitive, to zinc, consistent with its relatively high dissociation constant for zinc.

Fluozin-3 is structurally related to calcium fluorescent probes fluo-3 and fluo-4, having chelator structure resembling calcium chelator BAPTA (Kikuchi *et al.* 2004). It has excitation and emission peaks at 494 nm and 518 nm, which are not altered by addition of zinc or any other transition metals, and its detection of zinc is not perturbed by high amounts of calcium or magnesium (Zhao *et al.* 2008). Weak fluorescence was induced by a high amount of calcium at 40 μM, with substantially lower sensitivity reported for other metals (Gee *et al.* 2002). Given the specificity and sensitivity of Fluozin-3, it was selected for further investigation.

To confirm the increased zinc levels in TAMR cells compared to MCF-7 cells, TAMR cells were loaded with Fluozin-3 and imaged using fluorescence microscopy. All the microscopy and camera settings, particularly the exposure time, were kept the same for all the images in each experiment, to validate the comparison between different samples. TAMR cells were shown to have a slight increase in green fluorescent intensity, which signified a mild increase in cellular free zinc levels in the cells, when compared to MCF-7 cells (Fig. 4.11A). To semi-quantitatively compare the fluorescence intensity in these images, the total corrected cellular fluorescence (TCCF) was calculated using the equation TCCF = integrated density – (area of selected cell x mean background fluorescence) (McCloy et al. 2014). This calculation proved statistical significance of the small increase in the Fluozin-3 fluorescence intensity in TAMR cells when compared to MCF-7 cells (Fig. 4.11B).

Figure 4.10 Zinc measurement using different dyes

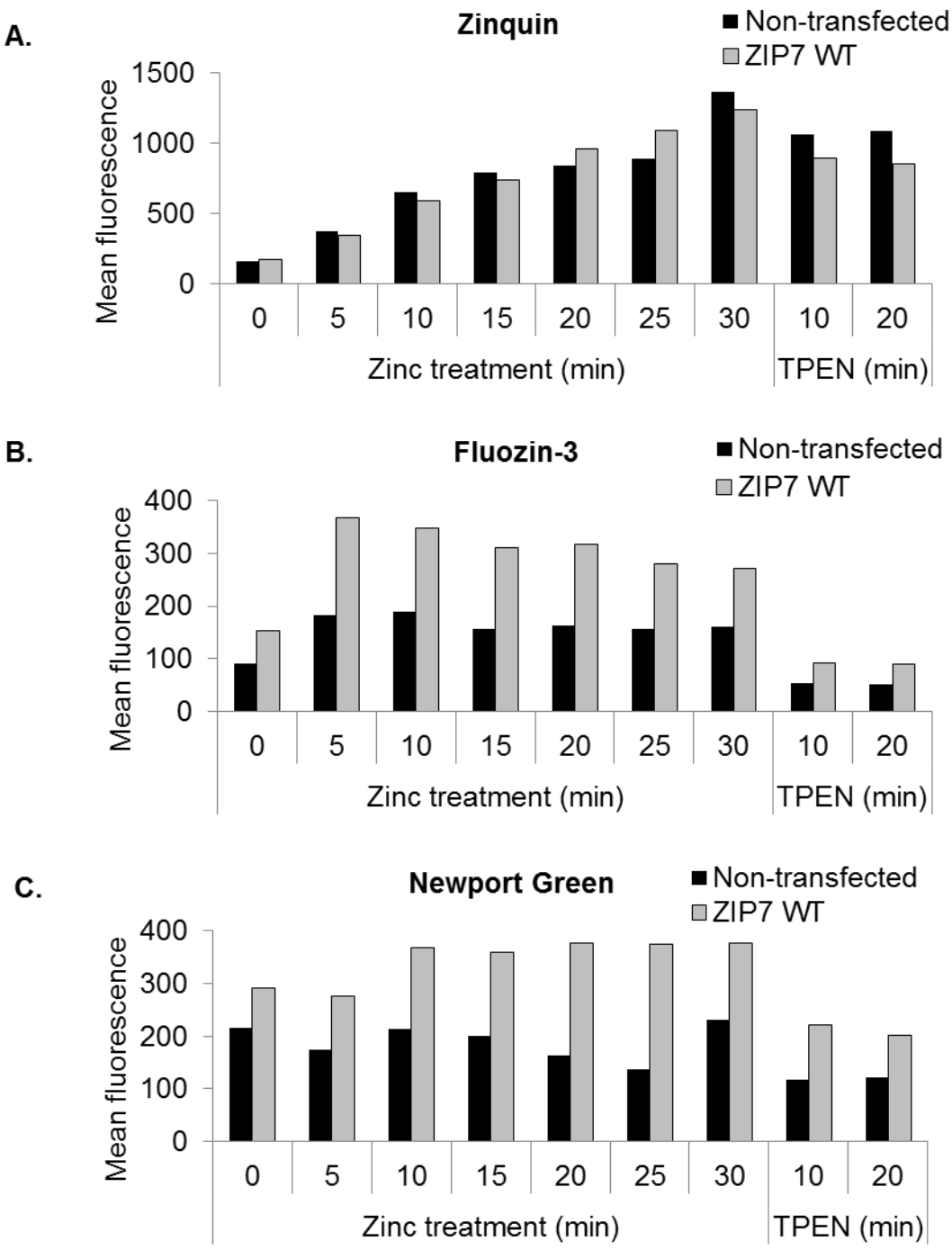

MCF−7 cells were transfected with wild−type ZIP7 and loaded with Zinquin, Fluozin−3, or Newport Green. The cells were treated with 100 μM zinc plus 10 μM sodium pyrithione in the medium with full serum. Fluorescence intensity was measured in live cells using FACS analysis. TPEN was added after the 30−minute course of zinc treatment. Geometric mean fluorescence intensities of Zinquin (A), Fluozin−3 (B), and Newport Green (C) in the transfected cells are demonstrated and compared to the non−transfected cells.

Figure 4.11 Increased zinc in TAMR cells suggested by zinc imaging

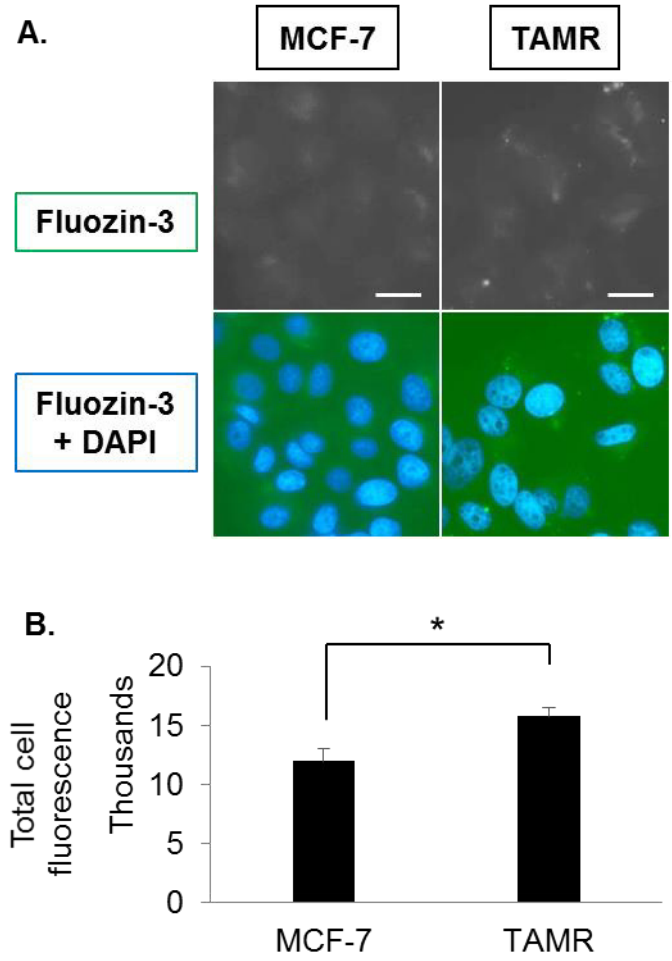

MCF−7 cells and tamoxifen−resistant MCF−7 cells (TAMR cells) were loaded with Fluozin−3 (green) and fixed in 4% formaldehyde. The nuclei were stain with DAPI (blue). A representative microscopic view was captured with a 63x magnification lens using the same exposure time and other settings (A). Fluorescence intensity was determined in at least 4 representative images using ImageJ software (Schneider et al. 2012). The total corrected cell fluorescence was calculated by subtracting the integrated density with the background intensity (McCloy et al. 2014) and presented in a bar graph as mean ± standard error (B).
Scale bar, 25 µm. * $p < 0.05$.

To confirm the increased zinc levels in TAMR cells as shown using fluorescence microscopy, the fluorescent intensity was also measured using FACS analysis. Live cells were treated with zinc and TPEN, and zinc levels were presented as Fluozin−3 saturation, which was calculated using the equation Fluozin−3 saturation (%) $= \frac{F-F0}{Fmax-F0} x100$, where F = basal fluorescence intensity, F0 = minimum fluorescence intensity after TPEN treatment, and Fmax = maximum fluorescence intensity after zinc treatment (Qin *et al.* 2013). Fluozin−3 saturation in TAMR cells was 16%, which was 3 times as high as MCF−7 cells (Fig. 4.12A). A course of zinc treatment was then performed. An increase in zinc levels as a result of zinc release from cellular

stores by ZIP7 was detected at 5 minutes after zinc treatment in both TAMR and MCF−7 cells, and the increase was reversed by zinc chelation, verifying the specificity of the dye to zinc (Fig. 4.12B). Furthermore, the Fluozin−3 fluorescence intensity was higher in TAMR cells than in MCF−7 cells throughout the 30-minute course of zinc treatment (Fig. 4.12B). The results of zinc assays, both using fluorescence microscopy and FACS, therefore agreeably confirmed the significant increase in zinc levels in TAMR cells when compared to MCF-7 cells. Nevertheless, zinc imaging was shown to be less effective than FACS in detection of the increased zinc levels in TAMR cells.

Figure 4.12 Increased zinc in TAMR cells confirmed by FACS analysis

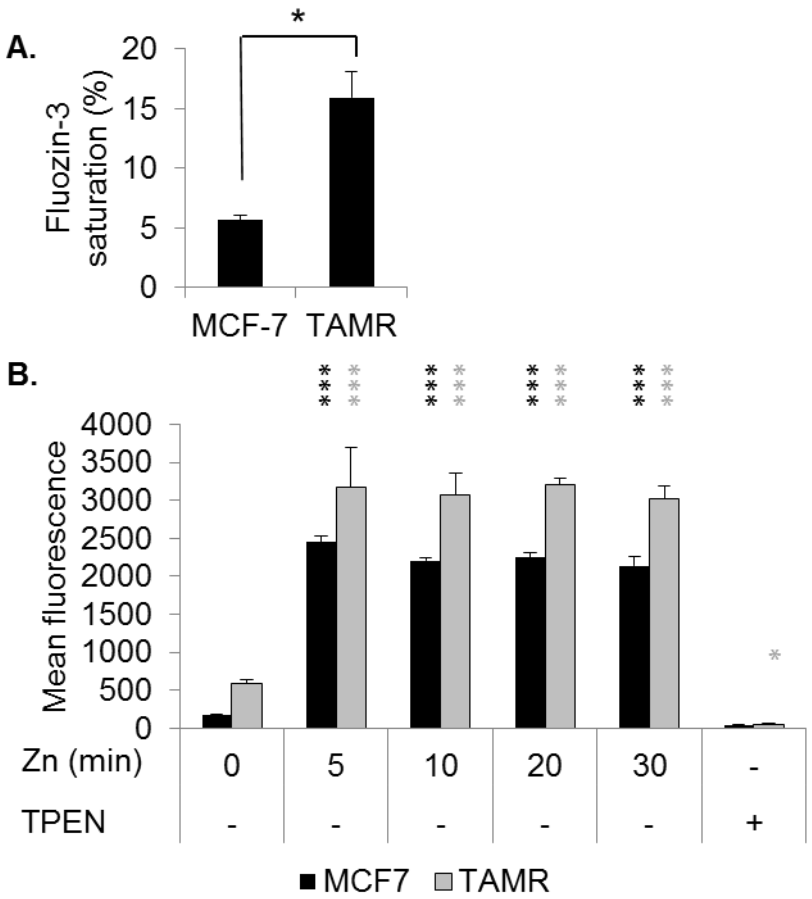

MCF−7 cells and tamoxifen−resistant MCF−7 cells (TAMR cells) were loaded with fluozin−3 (green), and treated with 20 μM zinc plus 10 μM sodium pyrithione. Fluorescence intensity was measured using FACS analysis. The cells were treated with TPEN at the end of the 30−minute course of zinc treatment, and the fluorescence intensity was measured at 10 minutes after TPEN treatment. Zinc levels are presented as saturation percentages, calculated using the equation Fluozin−3 saturation (%) $= \frac{F-F0}{Fmax-F0} x100$ (Qin et al. 2013) (A). Mean fluorescence intensities throughout the course of treatment are demonstrated as mean ± standard error (n = 3) (B). Statistical significance is compared either between cell types (A) or to time 0 (B).
* $p < 0.05$, *** $p < 0.001$.

This result was confirmed by another student in the group, Silvia Ziliotto, who compared ZIP7 activation in different cell lines, including TAMR cells and MCF-7 cells, using the pZIP7 antibody. Immunofluorescence of pZIP7 demonstrated that virtually 100% of TAMR cells were positive for pZIP7, whereas only 8% of MCF-7 cells were seen to be pZIP7-positive (Fig. 4.13A). Confirming this increase in ZIP7 activation, Western blotting was performed. AKT activation was used as an indicator of ZIP7 activation, given that AKT is a direct downstream effector of ZIP7-mediated zinc release from cellular stores (Taylor et al. 2012). The Western blot of pAKT demonstrated a twofold increase in AKT activation when compared to MCF-7 cells (Fig. 4.13B). This increased AKT activation was compatible with the 3-fold increased zinc levels in TAMR cells observed in the Fluozin-3 assays using FACS (Fig. 4.12A) and suggestive of an increase in ZIP7 activity in TAMR cells when compared to MCF-7 cells. Importantly, the Western blot of pZIP7 showed that pZIP7 levels were significantly increased 8-fold in TAMR cells when compared to MCF-7 cells (Fig. 4.13C). Collectively, these data showed that the pZIP7 antibody was able to detect the increase in ZIP7 activation, and reflect the high zinc levels in TAMR cells.

4.3.5 pZIP7 antibody detects impaired function of ZIP7 clinical mutants

Two siblings who suffered from a blistering skin condition in the first few days of life have been observed with failure to thrive, (Hambleton S., personal communication). Family history indicated childhood blistering conditions on both sides of the family, and their maternal grandmother had been diagnosed with zinc deficiency. The blood profile of the patients revealed a marked increase in T-cell population with predominance of CD4-positive cells, and absence of B cells. The profile was compatible with Bruton agammaglobulinemia. A genetic test was performed at Newcastle University, showing a compound heterozygous mutation of ZIP7; one allele harboured a P190A mutation, and the other an E363K mutation. As part of collaboration with Newcastle University, recombinant ZIP7 DNA with each mutation was created from our wild-type ZIP7 plasmid construct and sent to our laboratory group for further experimentation.

Figure 4.13 Detection of increased ZIP7 activity in TAMR cells

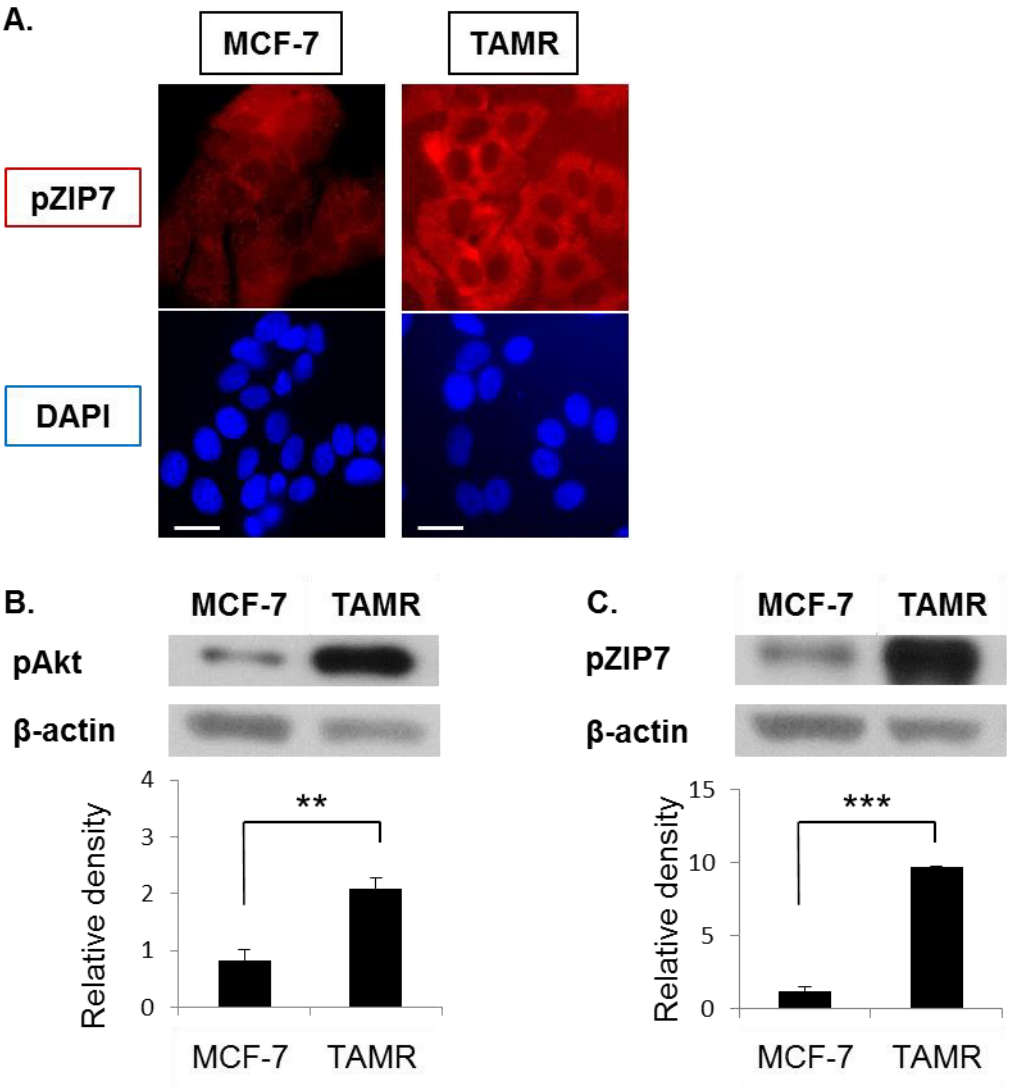

As a part of Silvia Ziliotto's project, immunofluorescence of pZIP7 (A) and immunoblotting of pAKT (B) and pZIP7 (C) were performed in MCF−7 cells and tamoxifen−resistant MCF−7 cells (TAMR cells). For immunofluorescence, the cells were immunostained using the pZIP7 antibody, which was conjugated to Alexa Fluor 593 (Red), and the nuclei were stained with DAPI (blue). A representative microscopic view of MCF−7 and TAMR cells was captured using a 63x magnification lens (A), showing that 8.3% of MCF−7 cells and virtually 100% of TAMR cells are positive for pZIP7. For immunoblotting, protein bands of pS473 AKT (60 kDa), pZIP7 (48 kDa), and β−actin (45 kDa) are demonstrated (B−C). Densitometric data of pAKT and pZIP7, normalised to β−actin, are presented in bar graphs as mean ± standard error (n = 3). Statistical significance is compared between the two cell types.
Scale bar, 25 μm. ** $p < 0.01$, *** $p < 0.001$. Courtesy of Silvia Ziliotto.

The mutations of P190A and E363K are located in TM2 and TM5, respectively (Fig. 4.14). Both of these TMs are highly conserved across the LIV-1 subfamily of ZIP channels (Fig. 3.3). The E363K mutation interestingly involves the LIV-1 subfamily consensus motif HEXPHEXGD in TM5, which is also a potential zinc-binding region that is essential for zinc transport (Taylor and Nicholson 2003) (Fig. 4.14). The potential effect of the E363K mutation on the zinc transport function of ZIP7 is therefore reasonable. Glutamate (E) is a negatively charged amino acid that has a high affinity towards zinc ions, whereas lysine (K) is a positively charged amino acid that cannot bind to zinc (Trzaskowski *et al.* 2008). In as much as the zinc-binding amino acid glutamate is located in the potential zinc-transport region (Taylor and Nicholson 2003), its substitution for a non-zinc-binding amino acid lysine would reasonably interfere with the zinc-transport function of the channel. In contrast to the E363K mutation, the P190 mutation does not directly affect the notable zinc-binding site in TM5. Nevertheless, according to an amino acid sequence analysis comparing the sequences of the ZIP channels to the haemagglutininesterase-fusion glycoprotein of influenza C virus, TM2 was predicted to interact with TM5 in maintaining the pore region in the tertiary structure of the ZIP channels in the LIV-1 subfamily (Taylor and Nicholson 2003). Moreover, transmembrane helix kinks, which are crucial for membrane protein structure, typically occur at proline residues (Yohannan *et al.* 2004). As a result, a mutation affecting the residue P190 could have some negative effect on the conformation and the pore generation of ZIP7, thereby adversely influencing the function of ZIP7 in mobilising zinc across the ER membrane.

The purified plasmids of ZIP7 P190A and E363K were verified for their transfection efficiency and their expression within the cells by immunofluorescence using a V5 antibody. The result revealed that both these mutant constructs were robustly transfected into cells (Fig. 4.4). Furthermore, an ER-like staining pattern was also observed for these mutant constructs, suggesting that the mutations did not affect ZIP7 in terms of its protein production, stability, or delivery to the ER membrane.

Figure 4.14 Locations of the ZIP7 P190A and E363K mutations

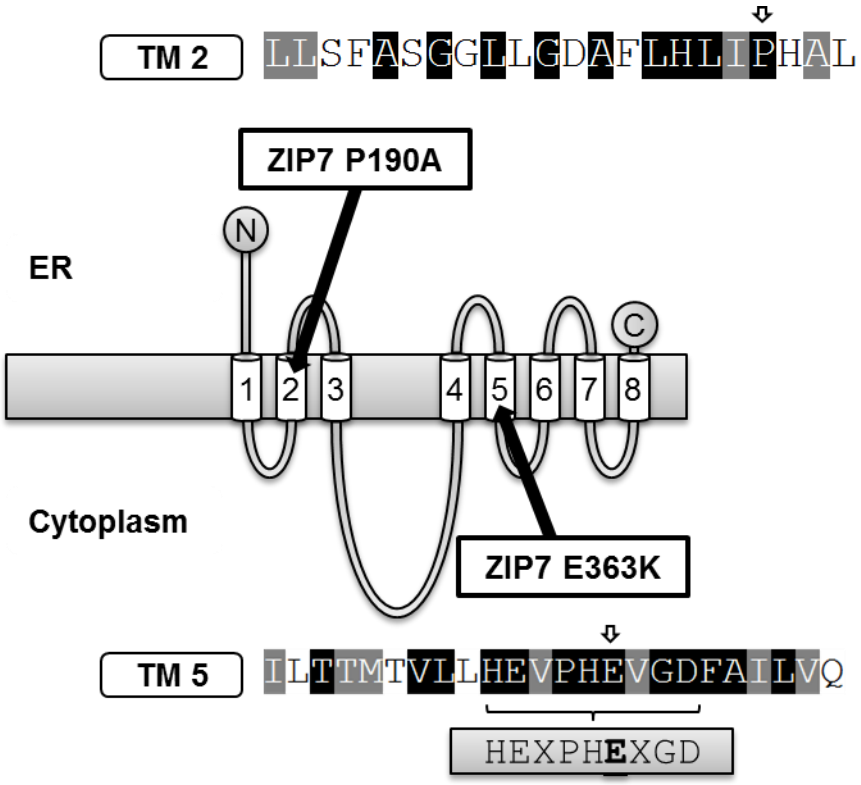

This figure illustrates the predicted structure of ZIP7, with mutation sites and amino acid sequences of the ZIP7 clinical mutants, P190A and E363K, indicated. The mutations are located in TM2 and TM5, respectively. Importantly, both the residues P190 and E363 are 100% identical across the LIV−1 subfamily of ZIP channels, and the residue E363 involves the second glutamate residue of the LIV−1 subfamily consensus motif HEXPHEXGD.
ER, the endoplasmic reticulum; N, the amino−terminus; C, the carboxyl−terminus.

4.3.5.1 Both ZIP7 P190A and E363K are able to produce a zinc wave

To investigate the effects of the ZIP7 clinical mutants on zinc homeostasis, free zinc levels in the cytosol after stimulation of ZIP7−mediated zinc release from cellular stores were determined. MCF−7 cells were transfected with ZIP7 P190A and E363K, and loaded with Fluozin−3. The fluorescence intensity was determined using FACS analysis. The Fluozin−3 fluorescence intensity in the cells transfected with wild−type ZIP7 was significantly increased at 5 minutes after zinc stimulation (Fig. 4.15), consistent with the ZIP7−mediated zinc release from cellular stores (Taylor et al. 2012). The rise in fluorescence intensity was successfully abolished by zinc chelation (Fig. 4.15). The cells transfected with either mutant also demonstrated a dramatic increase in fluorescence intensity, which was comparable to wild−type ZIP7 and responsive to zinc chelation (Fig 4.15). However, the increase did not

show a statistical significance, except for ZIP7 P190A at 10 minutes after zinc stimulation (Fig 4.15). In contrast, the non-transfected cells showed a slight increase in zinc levels with no statistical significance, and zinc chelation resulted in an apparent decrease in zinc levels (Fig 4.15). These findings therefore suggested that the two ZIP7 mutants were able to transport zinc in a manner comparable to wild-type ZIP7. However, because of the variability of the zinc levels before zinc treatment, a statistically significant increase was seen only at 10 minutes for ZIP7 P190A, and was not detected at any time point for ZIP7 E363K (Fig 4.15). This might imply that regardless of the increase in zinc levels after zinc treatment, both these mutants had impaired zinc release function compared to wild-type ZIP7, and ZIP7 P190A functioned better than ZIP7 E363K.

Figure 4.15 Zinc wave production by the ZIP7 P190A and E363K mutants

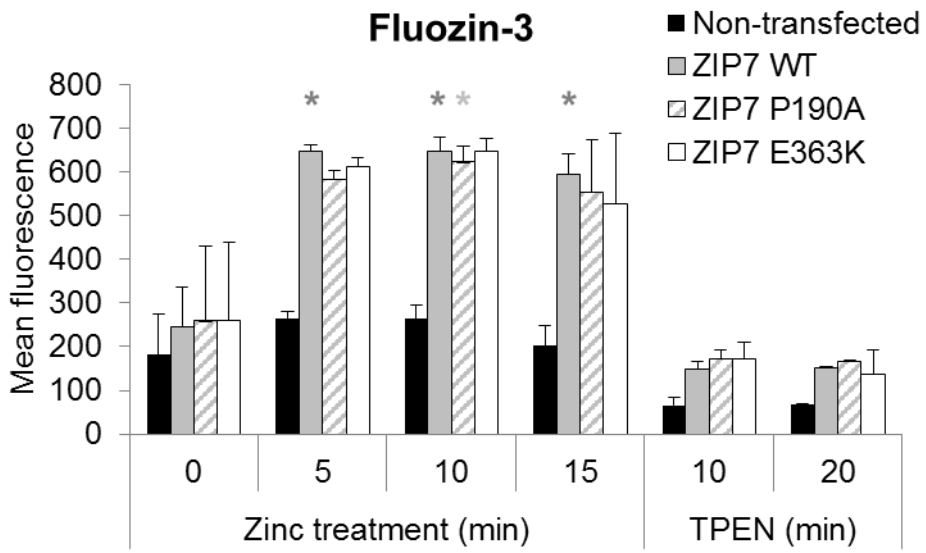

MCF-7 cells were transfected with wild-type ZIP7 (WT) and the ZIP7 clinical mutants, P190A and E363A. The cells were loaded with Fluozin-3, and treated with 100 μM zinc plus 10 μM sodium pyrithione in the medium with full serum. Fluorescence intensity was measured in live cells using FACS analysis. TPEN was added at the end of the 15-minute course of zinc treatment. Geometric mean fluorescence intensities are demonstrated in a bar graph as mean ± standard error (n = 3). Statistical significance is compared to time 0.
* $p < 0.05$.

Additionally, immunofluorescence in cells transfected with the ZIP7 P190A and E363K mutants and loaded with Fluozin−3 was also performed to image the transfected cells, expecting to visualise the difference in zinc levels between the transfected and the non−transfected cells in the same fields (Fig 4.16). Nevertheless, no change in fluorescence intensities of Zinquin and Fluozin−3 could be seen in either the cells transfected with wild−type ZIP7 or the ZIP7 mutants, when compared to the adjacent non−transfect cells in the same visual fields (Fig 4.16). One possible explanation was that the dyes were leaked out from the cells during the immunostaining steps, which required a permeabilising agent to allow the V5 antibody to bind the recombinant proteins.

4.3.5.2 ZIP7 E363K shows less AKT activation than ZIP7 P190A

AKT activation was detected in MCF−7 cells that had been transfected with wild−type ZIP7 at 5 minutes after zinc treatment (Taylor et al. 2012). This AKT activation was delayed to 10 minutes after zinc treatment in the cells transfected with ZIP7 S275A/S276A, a phosphoablative mutant which cannot be phosphorylated on residues S275 and S276 (Taylor et al. 2012). This delay in the AKT activation suggests that the ZIP7 phosphoablative mutant did not activate AKT, and that the endogenous ZIP7 did after 10 minutes. The AKT activation was again employed as an indicator of ZIP7 activity in the investigation of the effects of the Z190A and E363K mutations on ZIP7−mediated zinc release from cellular stores, using Western blotting.

In the cells transfected with wild−type ZIP7, pAKT levels started to increase at 2 minutes after zinc treatment (Fig. 4.17A, B). The levels reached the peak at 10 minutes and remained constantly high until 20 minutes after zinc treatment (Fig. 4.17A, B). For ZIP7 S275A/S276A, which was used as a negative control, the transfected cells demonstrated a gradual increase in pAKT levels at 2 and 5 minutes after zinc stimulation (Fig. 4.17A, B). The levels were unexpectedly higher than that for wild−type ZIP7 (Fig. 4.17A, B). Interestingly, although high variability was observed, the pAKT levels for ZIP7 S275A/S276A slightly decreased at 10 minutes and dramatically decreased, becoming significantly less than wild−type ZIP7, at 15 and 20 minutes after zinc stimulation, (Fig. 4.17A, B).

Figure 4.16 Zinc imaging in cells transfected with ZIP7 P190A and E363A

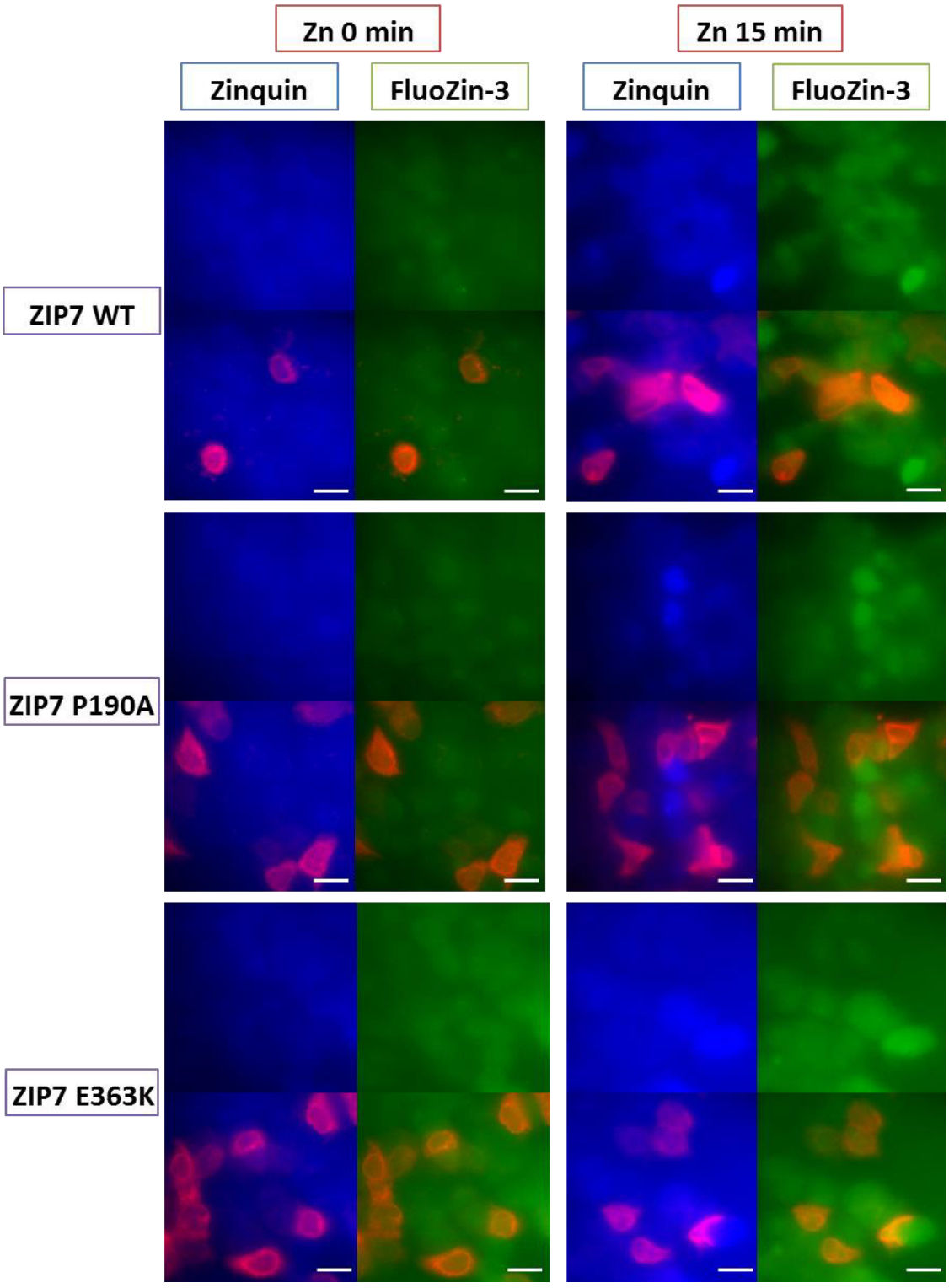

MCF-7 cells were transfected with wild−type ZIP7 (WT) and the ZIP7 clinical mutants, P190A and E363A. These ZIP7 constructs contained a C−terminal V5 tag. The cells were loaded with Zinquin (25μM, blue) and Fluozin-3 (5μM, green), treated with 20 μM zinc plus 10 μM sodium pyrithione, and fixed in 4% formaldehyde. Immunofluorescence was performed using a V5 antibody, which was conjugated to Alexa Fluor 594 (red). Representative microscopic views were captured using a 63x magnification lens. The result reveals no definite alteration in zinc content in the transfected (V5−positive) cells.
Scale bar, 25 μm.

Like wild−type ZIP7, both the clinical mutants showed marked increases in pAKT levels up to 10 minutes after zinc stimulation (Fig. 4.17A, B). The pAKT levels for the ZIP7 P190A mutant did not change after 10 minutes, whereas, like the ZIP7 S275A/S276A mutant, the pAKT levels for the ZIP7 E363K mutant dramatically decreased and became significantly lower than the levels for wild−type ZIP7 (Fig. 4.17A, B).

Figure 4.17 Ability of the ZIP7 P190A and E363K mutants to activate AKT

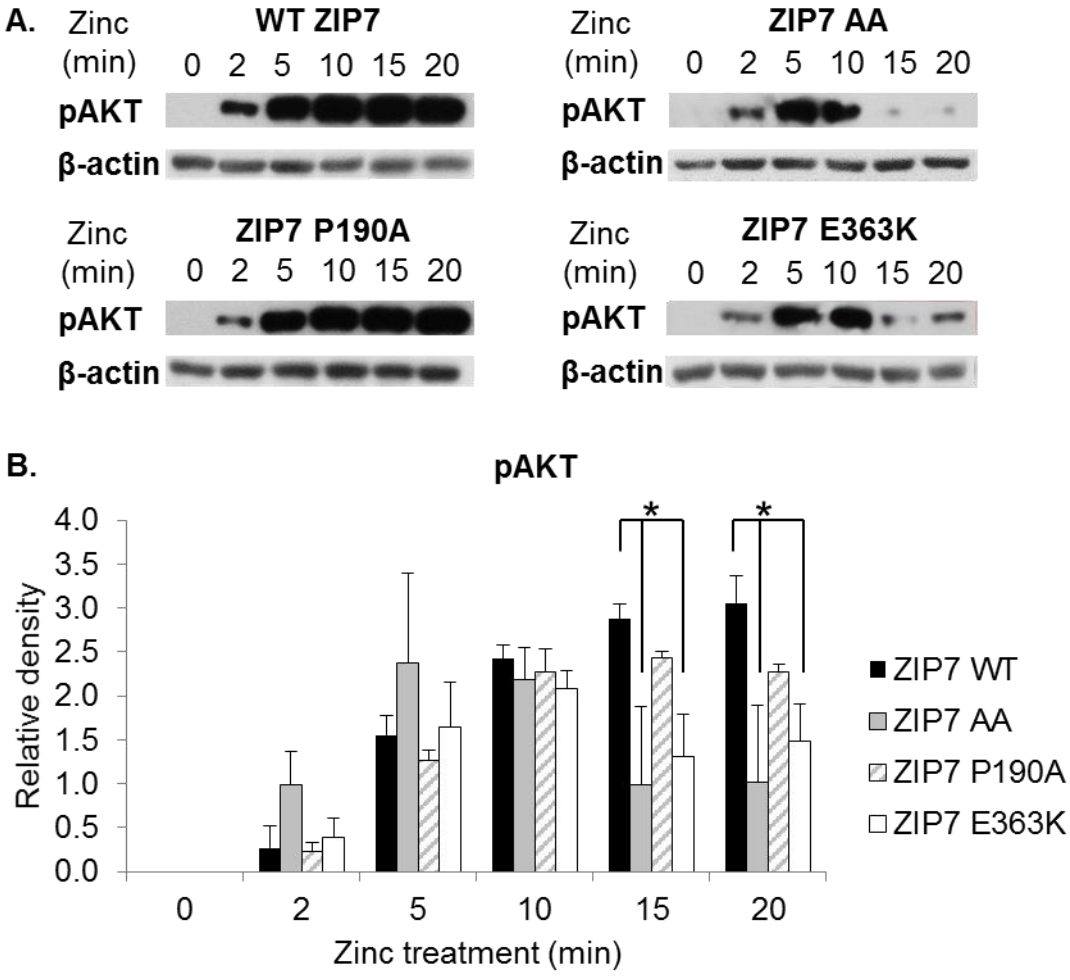

MCF−7 cells were transfected with wild−type ZIP7 (WT) and ZIP7 mutants S275A/S276A (AA), P190A, and E363K. The cells were treated with 20 μM zinc plus 10 μM sodium pyrithione. Immunoblotting was performed using a pS473 pAKT antibody with a β−actin antibody for normalisation. Protein bands of pS473 pAKT (60 kDa) and β−actin (45 kDa) are demonstrated as representative results of 3 independent experiments (A). Densitometric data normalised to β−actin are demonstrated in a bar graph as mean ± standard error (n = 3) (B). Statistical significance is compared to wild−type ZIP7.
* $p < 0.05$.

In summary, this experiment demonstrated that the ZIP7 P190A mutant, which showed an AKT activation pattern comparable to wild-type ZIP7, could transport zinc more effectively than the ZIP7 E363K mutant, which showed an AKT activation pattern similar to the ZIP7 S275A/S276A mutant. Noteworthy, no bands were detected at time 0 at the exposure times used to detect the signals because of the tremendous AKT activation as a result of zinc treatment, and the very low basal levels of AKT activation at time 0 in comparison with the zinc-activated levels. The pAKT levels during the course of zinc treatment were therefore compared to wild-type ZIP7 at the same time points rather than comparing to time 0. Moreover, there was a discrepancy between the representative blot and the densitometric data shown in the figure because of the high variability of the results.

4.3.5.3 pZIP7 antibody detects halted ZIP7 P190A and E363K activation

Residues P190 and E363 are not in the same region as residues S275 and S276. Nevertheless, a conformational change caused by the P190A and E363K mutations might interfere with CK2 binding and thereby prevent ZIP7 phosphorylation on residues S275 and S276. To investigate whether the mutations adversely affected ZIP7 phosphorylation after zinc treatment, Western blotting using the pZIP7 antibody was performed in the cells transfected with the ZIP7 S275A/S276A, P190A, and E363K mutants. Confirming a previous experiment in this chapter (Fig. 4.9B), a typical activation pattern of ZIP7 was seen in the cells transfected with wild-type ZIP7 (Fig. 4.18A, B). A similar pattern of ZIP7 activation was also detected for ZIP7 P190A, but with no statistical significance (Fig. 4.18A, B). In contrast, both ZIP7 E363K and S275A/S276A failed to demonstrate an increase in pZIP7 levels after zinc stimulation (Fig. 4.18A, B). These findings suggested that the E363K mutation interfered with the CK2-mediated phosphorylation on the residues S275 and S276 to an extent comparable to the S275A/S276A mutation, whereas the P190A mutation affected this CK2-mediated phosphorylation to a lesser extent. Importantly, the Western blotting of pZIP7 was consistent with the Western blotting of pAKT, showing the impaired function for both of ZIP7 P190A and E363K, with the P190A mutant working better than the E363K mutant did, thereby further suggesting the potential usefulness of this antibody.

Figure 4.18 Activation of the ZIP7 P190A and E363K mutants by zinc

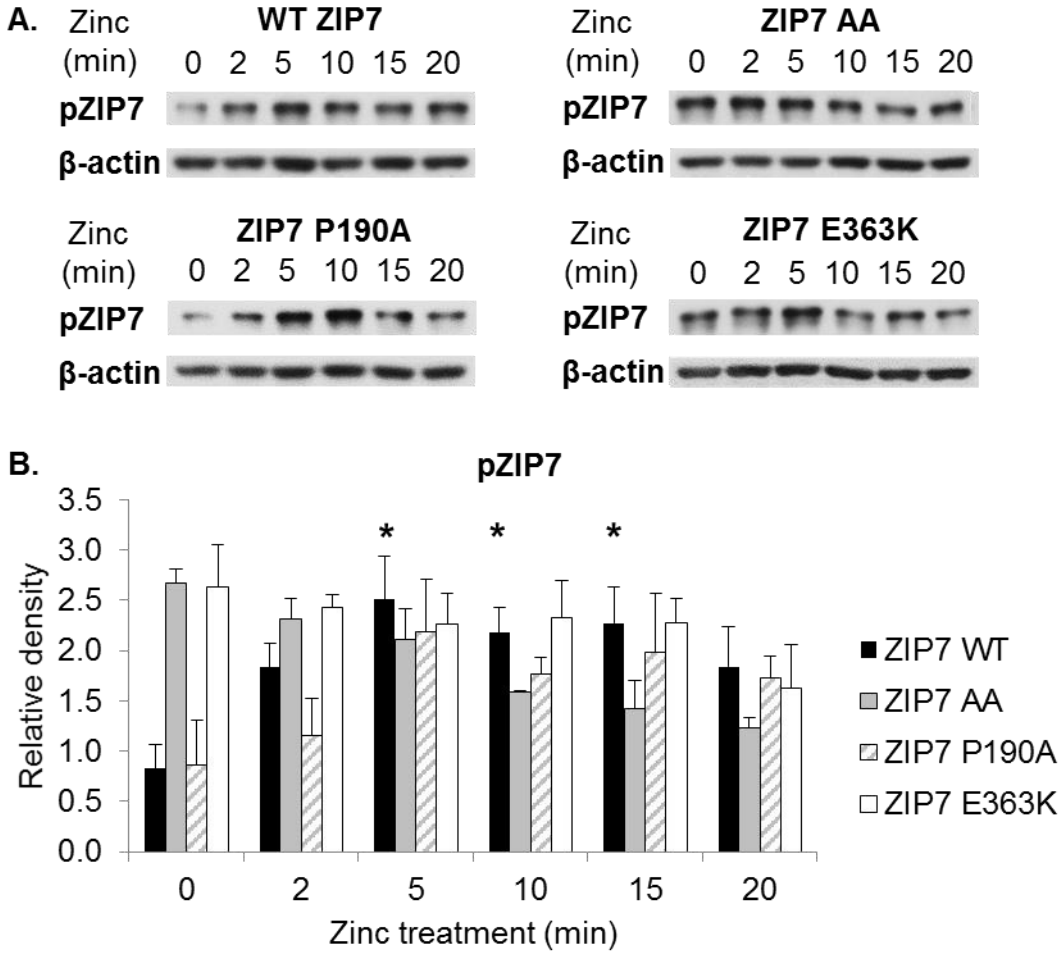

MCF−7 cells were transfected with wild−type ZIP7 (WT) and ZIP7 mutants S275A/S276A (AA), P190A, and E363K. The cells were treated with 20 μM zinc plus 10 μM sodium pyrithione. Immunoblotting was performed using the pZIP7 antibody with a β−actin antibody for normalisation. Protein bands of pZIP7 (48 kDa) and β−actin (45 kDa) are demonstrated as representative results of at least 3 independent experiments (A). Densitometric data normalised to β−actin are demonstrated in a bar graph as mean ± standard error (n = 3) (B). Statistical significance is compared to time 0.
* $p < 0.05$.

It is noteworthy that without zinc treatment, the pZIP7 levels for ZIP7 E363K and S275A/S276A were consistently higher than the levels for wild−type ZIP7 and ZIP7 P190A. This surprisingly high basal ZIP7 activation for either ZIP7 S275A/S276A or E363K was consistent with a previous study that showed apparently high phospho−serine levels in the cells transfected with ZIP7 S275A/S276A at time 0 (Taylor et al. 2012). One plausible explanation was that the prolonged overexpression of these non−functioning ZIP7 mutants during the overnight transfection might have resulted in an increase in transcription of the endogenous ZIP7 as a compensatory mechanism.

To confirm the Western blotting of pZIP7 in the cells expressing wild-type ZIP7 and the ZIP7 clinical mutants, immunofluorescence using the anti-pZIP7 antibody was performed in the transfected cells with 10-minute zinc treatment. A V5 antibody was also applied for identification of the transfected cells. For wild-type ZIP7, percentage of the transfected cells that were positive for pZIP7 increased from 40% before zinc treatment to 58% after zinc treatment (Fig. 4.19A). In contrast, only 8% and 3% of the cells transfected with ZIP7 S275A/S276A were pZIP7-positive before and after zinc stimulation respectively (Fig. 4.19B). Noteworthy, the ZIP7 positivity in the cells overexpressing ZIP7 S275A/S276A was comparable to the basal ZIP7 activation in the non-transfected non-treated MCF-7 cells (Fig. 4.13A).

For the clinical mutants, 38% of the cells overexpressing ZIP7 P190A (Fig. 4.19C) and 37% of the cells overexpressing ZIP7 E363K were positive for pZIP7 (Fig. 4.19D). The positivity rates in the clinical mutants were comparable to the cells transfected with wild-type ZIP7, which had 40% positivity (Fig. 4.19C). However, neither of the mutants showed an increase in pZIP7 positivity after zinc stimulation (Fig. 4.19C, D). These data suggested that the clinical mutants could be recognised by the pZIP7 antibody. However, the mutations significantly interfered with the zinc-induced CK2-mediated phosphorylation on residues S275 and S276 of ZIP7. Importantly, given that the antibody did not detect the ZIP7 activation in these mutants, it might be implied that this antibody was able to indicate the impairment of ZIP7 function, even though it was not able to detect the difference between the two clinical mutants. The discrepancy between the results from the immunofluorescence and the Western blotting might be due to the less sensitivity and the non-quantitative nature of the immunofluorescence technique.

Figure 4.19 Impaired activation for the ZIP7 P190A and E363K mutants

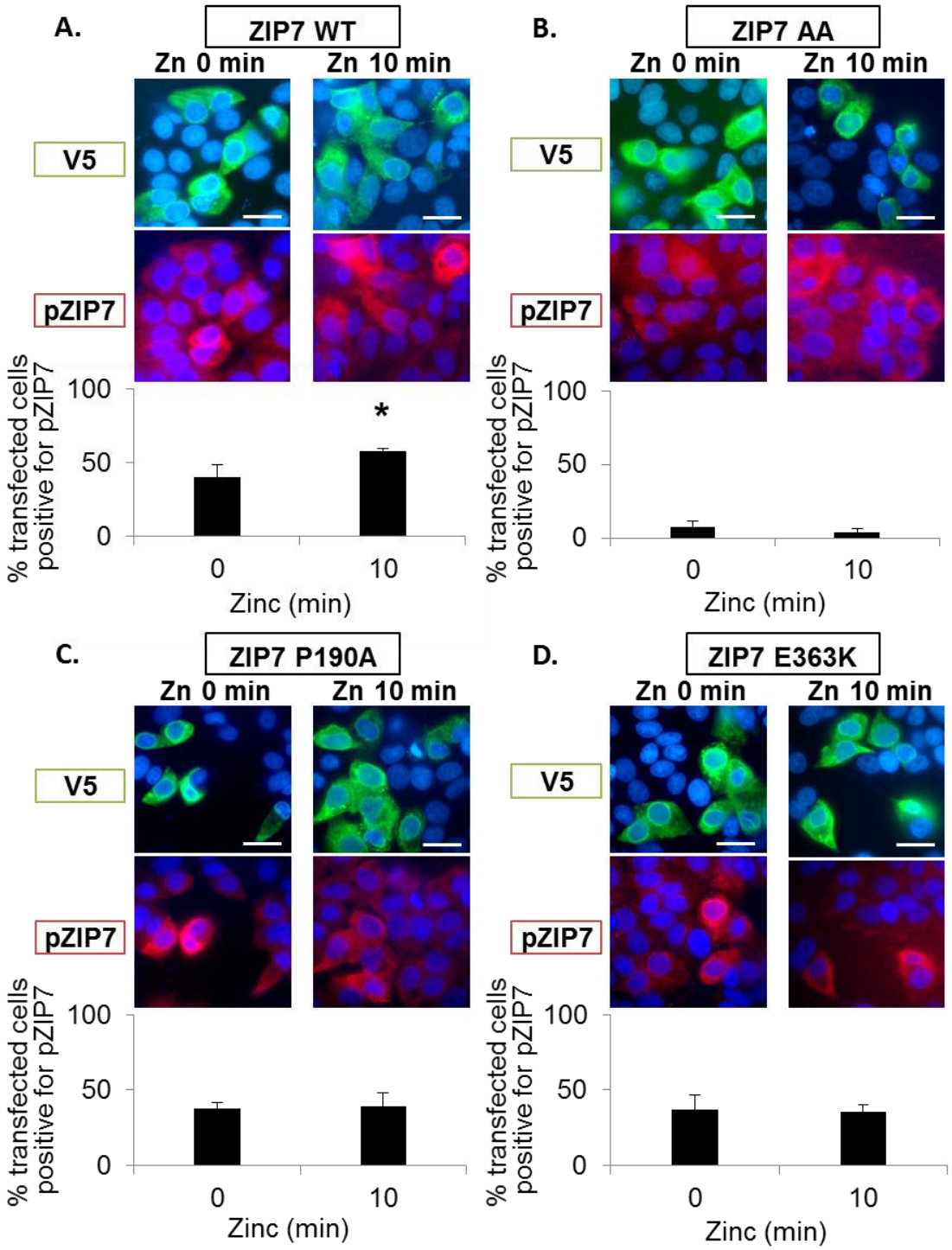

MCF−7 cells were transfected with wild−type ZIP7 (WT) and ZIP7 mutants ZIP7 S275A/S276A (AA), P190A, and E363K. The cells were treated with 20 μM zinc plus 10 μM sodium pyrithione. Immunofluorescence was performed using V5 (green) and pZIP7 (red) antibodies, which was conjugated to Alexa Fluor 488 (green) and Alexa Fluor 594 (red), respectively, with DAPI nuclear staining (blue). A representative microscopic view of wild−type ZIP7 (A), ZIP7 AA (B), ZIP7 P190A (C), and ZIP7 E363K (D) captured using a 63x magnification lens is presented. The percentages of the transfected cells that are positive for pZIP7 are shown in bar graphs as mean of 4 representative fields ± standard error. Statistical significance is compared to time 0. Scale bar, 25 μm. * $p < 0.05$.

All the results for the ZIP7 clinical mutants, P190A and E363K, are summarised in Table 4.2. Both of the clinical mutants were able to mobilise zinc ions from the stores and able to produce a zinc wave, although the increase in zinc levels was not significant. However, the ZIP7 E363K mutant showed impaired ZIP7 activation by phosphorylation on residues S275 and S276. This impaired ZIP7 activation by the E363K mutation was consistent with a significant decrease in AKT activation when compared to wild-type ZIP7 at 15 minutes after zinc treatment. In contrast, the ZIP7 P190A mutant could be phosphorylated on residues S275 and S276 after zinc stimulation, although no statistical significance was observed. Moreover, the P190A mutant could activate AKT after zinc stimulation to the extent comparable to wild-type ZIP7. These results collectively suggested that the ZIP7 P190A mutant had less functional impairment than the ZIP7 E363K mutant, further supporting the crucial involvement of the HEXPHEXGD motif in TM5 in the zinc transport (Taylor and Nicholson 2003). Importantly, the pZIP7 antibody was able to reflect the functional impairment of these two mutants, and when using the Western blotting technique, this antibody could even demonstrate the superior functionality of ZIP7 P190A over E363K. These data therefore further supported the potential usefulness of this antibody in determining ZIP7 function.

Table 4.2 Result summary for ZIP7 P190A and E363K

Changes after zinc stimulation	ZIP7 constructs			
	WT	P190A	E363K	AA
Increase in zinc level	✓✓✓	✓✓	✓✓	–
AKT activation	✓✓✓	✓✓	✓	✓
ZIP7 activation (by Western blotting)	✓✓✓	✓✓	×	×
ZIP7 activation (by immunofluorescence)	✓✓✓	×	×	×

✓✓✓ The changes for wild-type ZIP7 as reference.
✓✓ The changes comparable to wild-type ZIP7.
✓ The changes significantly less than wild-type ZIP7.
× No change detected.
– Not investigated

4.4 Chapter summary

This chapter has provided pieces of evidence supporting that our pZIP7 antibody is both specific to the S275/S276−phosphorylated form of ZIP7 and potentially useful for determining ZIP7 function. Using an immunofluorescence technique, the specificity of the antibody was confirmed by its ability to recognise ZIP7 when residues S275 and S276 were mutated to aspartate, which structurally mimics phosphoserine (Fig. 4.6). In contrast, the mutation of these residues to alanine, a non−phosphorylatable amino acid, could prevent the binding of the antibody (Fig. 4.6). Using the same technique, there was a significant increase in the percentage of cells transfected with wild−type ZIP7 that were pZIP7−positive, suggesting the ability of the antibody to detect ZIP7 activation upon 10−minute zinc treatment (Fig. 4.7).

Employing the Western blotting technique, an 8 kDa mobility shift of the pZIP7 band (at 48 kDa) when compared to the total ZIP7 band (at 40 kDa) was observed (Fig. 4.8). Furthermore, the pZIP7 levels were significantly increased at 2 minutes after zinc treatment when normalised to the total ZIP7 levels (Fig. 4.9), confirming that the antibody could detect a zinc wave. The ZIP7 activation at 2 minutes after zinc treatment was consistent with a previous report (Taylor et al. 2012) and compatible with the AKT activation at 5 minutes after zinc treatment both in this project (Fig. 4.9) and in the previous report (Taylor et al. 2012). The ability of the antibody to determine ZIP7 activity was further highlighted by the finding that the pZIP7 levels were significantly increased in TAMR cells when compared to the parental MCF−7 cells (Fig. 4.12 and 4.13), consistent a previous report of an increase in pZIP7 activity in TAMR cells (Taylor et al. 2008b). Additionally, this antibody was also able to detect impaired ZIP7 function in the two ZIP7 clinical mutants, P190A and E363K (Fig. 4.15−4.19; Table 4.2). Collectively, the data in this chapter confirmed the potential usefulness of this pZIP7 antibody for determining ZIP7 activity.

Chapter 5:
Exploration of downstream effectors of ZIP7-mediated zinc release

5.1 Introduction

ZIP7 is ubiquitously expressed, ER membrane-located, and functionally triggered by phosphorylation (Taylor et al. 2004; Taylor et al. 2008b; Taylor et al. 2012). ZIP7 has therefore been designated as a gatekeeper for zinc release from cellular stores and a hub of cellular tyrosine kinase activation (Hogstrand et al. 2009). The activation of cellular tyrosine kinases is thought to be mainly through the inhibitory effect of zinc ions that have been released from cellular stores on protein tyrosine phosphatases, such as protein tyrosine phosphatase 1B (Haase and Maret 2005; Bellomo et al. 2014). Notably, protein tyrosine phosphatases are strongly inhibited even by the physiologically-relevant nanomolar levels of zinc ions (Wilson et al. 2012).

Our group have previously revealed that 20-min zinc treatment in tamoxifen-resistant MCF-7 breast cancer cells resulted in activating phosphorylation of both receptor tyrosine kinases (RTKs), namely EGFR (ErbB1), ErbB2, ErbB3, ErbB4, and IGF-1R, and a non-receptor tyrosine kinase, namely Src (Taylor et al. 2008b). Importantly, ZIP7 knockdown by transfection with ZIP7 siRNA was shown in the same study to prevent the phosphorylation of EGFR, IGF-1R, and Src, proving the ZIP7 dependency of the activation of these signalling molecules. All of these downstream effectors of ZIP7-mediated zinc release from cellular stores are among the known substrates of protein tyrosine phosphatase 1B (Bourdeau et al. 2005), and responsible for the aggressive behaviours of breast cancer cells that have acquired tamoxifen resistance (Taylor et al. 2008b). The activation of these tyrosine kinases in turn results in activation of ERK1/2 and AKT, which have been shown to be phosphorylated when ZIP7 is triggered by CK2-mediated ZIP7 phosphorylation on residues S275 and S276 (Taylor et al. 2012).

To gain a deeper understanding of the role of ZIP7-mediated zinc signalling, this chapter aimed to explore other cellular kinases that are potential downstream effectors of ZIP7-mediated zinc release from cellular stores, employing antibody arrays for tyrosine phosphorylation of human receptor tyrosine kinases and site-specific phosphorylation of multiple cellular kinases.

5.2 Materials and methods

The antibody arrays that were used consisted of the human phospho-receptor tyrosine kinase (RTK) (R&D Systems, ARY001B), phospho-mitogen-activated protein kinase (MAPK) (R&D Systems, ARY002B) and phospho-kinase (R&D Systems, ARY003B) antibody arrays. Increases in phosphorylation of some kinases according to the array signals were confirmed using Western blotting. Please refer to Chapter 2 for the methods of transfection and treatments (Section 2.1), antibody array procedures (Section 2.9) and Western blotting (Section 2.4). The antibodies used for Western blotting are listed in Tables 2.1 and 2.2.

5.3 Results and discussion

To explore potential target molecules of ZIP7-mediated zinc release from cellular stores, ZIP7 was overexpressed in MCF-cells by wild-type ZIP7 transfection. Furthermore, ZIP7 was also activated by treating the cells with exogenous zinc. This zinc treatment has been shown to trigger ZIP7-mediated zinc release from cellular stores, resulting in activation of cellular kinases (Taylor et al. 2012). According to this previous study, CK2 binds to ZIP7 and induces ZIP7 activation by phosphorylation on residues S275 and S276 at 2 minutes after zinc treatment, resulting in AKT activation at 5 minutes in cells transfected with wild-type ZIP7 and at 10 minutes in cells transfected with ZIP7 S275A/S276A, which is a ZIP7 null mutant. The same study also showed that the activation at 10 minutes in the cells transfected with the ZIP7 null mutant is attributed to the action of endogenous ZIP7 in the cells. To allow adequate time for zinc release from cellular stores and phosphorylation of kinases with limited activation of downstream pathways triggered by zinc-activated kinases, the treatment was performed for 10 minutes.

Three different types of antibody arrays were utilised: the phospho-RTK arrays, the phospho-kinase arrays, and the phospho-MAPK arrays. Using these arrays, phosphorylation of as many as 49 RTKs (the phospho-RTK arrays), 43 cellular kinases with 2 related total proteins (the phospho-kinase arrays), and 26 MAPKs with related kinases (the phospho-MAPK arrays) could be simultaneously investigated. For each type of array, the data are presented in four figures and a table. These four figures include (1) images of the signals

on the arrays (Fig. 5.1, 5.5 and 5.9), (2) a bar graph showing densitometric values of the pairs of corresponding duplicate dots for all the kinases detected (Fig. 5.2, 5.6 and 5.10), (3) a heat map generated from the densitometric data (Fig. 5.3, 5.7 and 5.11), and (4) a bar graph showing densitometric values for the kinases that were classified as “marked increase” (see definition below) (Fig. 5.4, 5.8 and 5.12). Noteworthy, a heat map graphically presents relative values of different types of samples for individual kinases as colours, where blue colour represents the lowest value in the row and red colour represents the highest value in the row according to the indicated scale (Fig. 5.3, 5.7 and 5.11). However, the values in the rows do not give any representation of abundance.

In addition, the table for each type of the arrays indicates the kinases that are phosphorylated as a result of either wild−type ZIP7 transfection or zinc treatment (Table 5.1−5.3). In each table, the kinases were arbitrarily divided into 2 groups, based on the differences in signal density: marked increase (> 10,000 density units) and mild increase (2,000−10,000 density units). To reduce false positive results due to the variability of background intensity, the differences by less than 2,000 units were considered negative.

5.3.1 Multiple RTKs are phosphorylated by ZIP7 overexpression or zinc

The phospho−RTK arrays detected only the presence of tyrosine phosphorylation of different RTKs, with no specific phosphorylated residues identified. In MCF−7 cells without treatment or transfection, the arrays detected tyrosine phosphorylation of ErbB3 (Fig. 5.1−5.3). ZIP7 overexpression was shown to decrease tyrosine phosphorylation of ErbB3, but caused a 18−fold increase in tyrosine phosphorylation of EGFR (Fig. 5.1−5.4, Table 5.1). Confirming a previous study in our group (Taylor et al. 2008b), 10−minute zinc treatment induced tyrosine phosphorylation of EGFR, ErbB2, ErbB3, and ErbB4 (Fig. 5.1−5.4, Table 5.1). Furthermore, the treatment also caused marked increases (>10,000 density units) in ALK, EphA1, and RYK tyrosine phosphorylation (Fig. 5.1−5.4, Table 5.1), whereas only mild increases (2,000−10,000 density units) were seen for Axl, c−Ret, EphA4, EphA7, Flt−3, FGFR3, IGF−1R, and Tie−1 tyrosine phosphorylation (Fig. 5.1−5.4, Table 5.1).

Figure 5.1 Phospho−RTK arrays in MCF−7 stimulated with ZIP7 and zinc

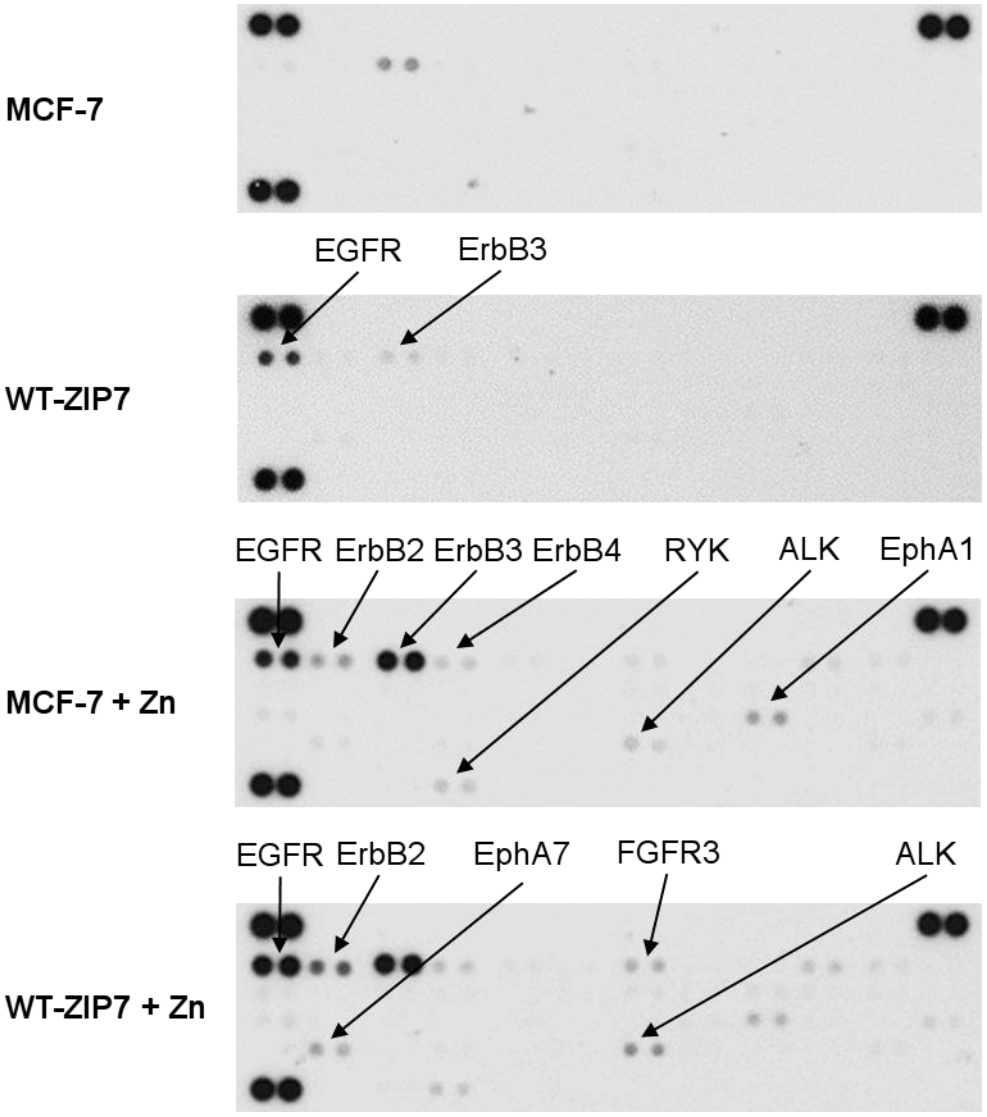

MCF−7 cells were transfected with wild−type ZIP7 and treated with 20 μM zinc plus 10 μM sodium pyrithione for 10 minutes. Tyrosine phosphorylation of selected receptor tyrosine kinases (RTKs) was determined using the human phospho−RTK antibody arrays (R&D Systems). Signals for each tyrosine kinase are presented as a pair of duplicate spots, with three pairs of dark reference spots on the upper left, upper right, and lower left corners for alignment. The kinases that show conspicuous changes in tyrosine phosphorylation (>10,000 density units) in the non−transfected zinc−treated cells (MCF−7 + Zn) or the transfected non−treated cells (WT−ZIP7) when compared to the non−transfected non−treated cells (MCF−7) are indicated. In addition, the kinases that show increases in tyrosine phosphorylation in the transfected zinc−treated cells (WT−ZIP7 + Zn) when compared to the non−transfected zinc−treated cells (MCF−7 + Zn) are also indicated.

Figure 5.2 Densitometric analysis of phospho−RTK arrays in MCF−7 stimulated with ZIP7 and zinc

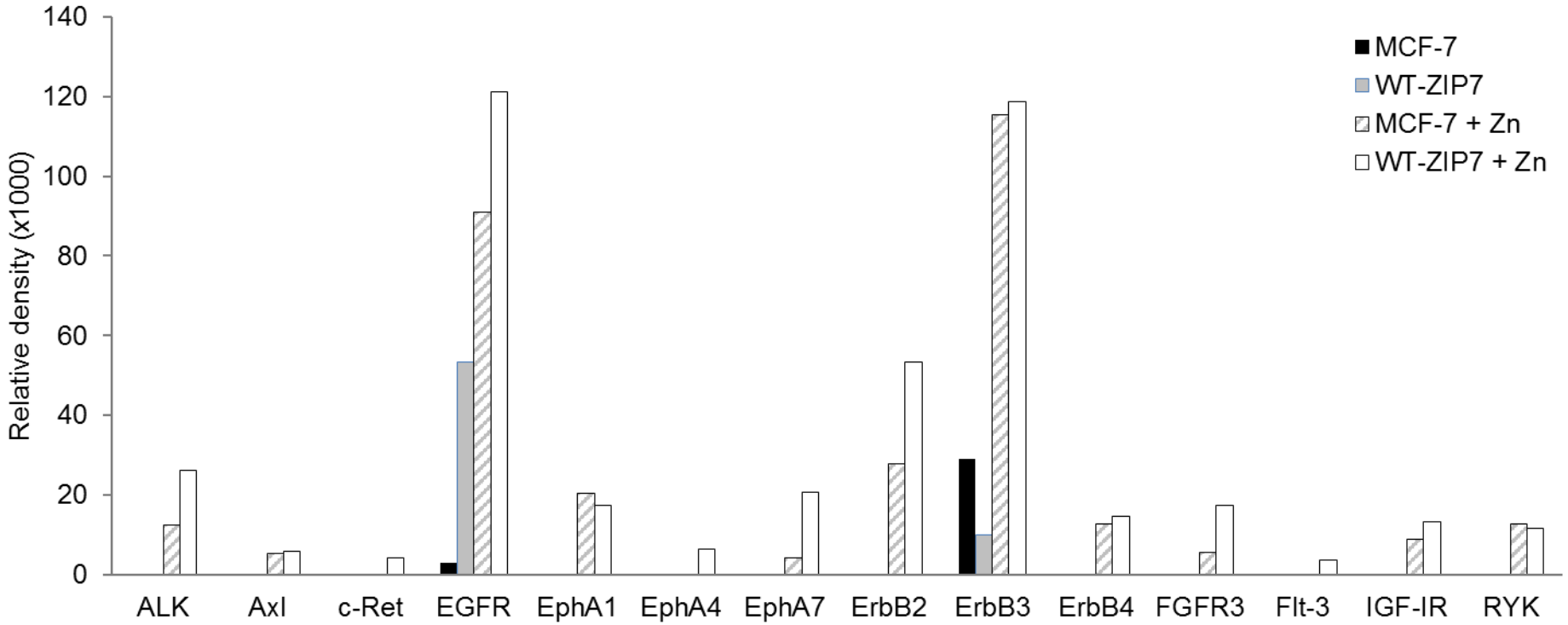

MCF−7 cells were transfected with wild−type ZIP7 and treated with 20 μM zinc plus 10 μM sodium pyrithione for 10 minutes. Tyrosine phosphorylation of selected receptor tyrosine kinases (RTKs) was determined using the human phospho−RTK antibody arrays (R&D Systems). Densitometric data are presented as mean of the duplicate dots for each kinase.

Figure 5.3 A heat map of phospho−RTKs activated by ZIP7 or zinc

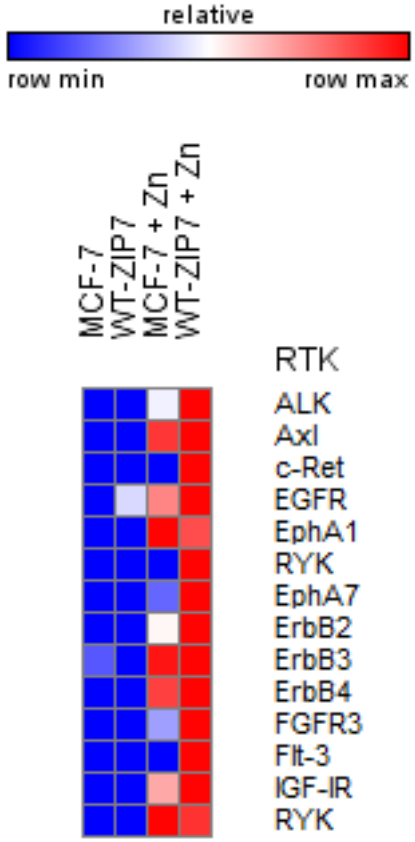

MCF−7 cells were transfected with wild−type ZIP7 and treated with 20 μM zinc plus 10 μM sodium pyrithione for 10 minutes. Phosphorylated receptor tyrosine kinases (RTKs) were determined using the human phospho−RTK antibody arrays (R&D Systems). The heat map was generated using a GENE−E matrix visualization and analysis platform (The Board Institute). Densitometric values in relation to other samples for each kinase are presented as a spectrum of colour where blue colour represents the lowest value in the row and red colour represents the highest value in the row according to the indicated scale, irrespective of the absolute signal intensities.

Wild−type ZIP7 transfection plus zinc treatment resulted in marked increases in tyrosine phosphorylation (>10,000 density units) of ALK, EGFR, ErbB2, EphA7, and FGFR3, with mild increases in tyrosine phosphorylation (2,000−10,000 density units) of c−Ret, IGF−1R, and Flt−3, when compared to the zinc−treated MCF−7 cells (Fig. 5.1−5.4, Table 5.1). These increases in tyrosine phosphorylation further confirmed the involvement of ZIP7 in the tyrosine phosphorylation of these kinases. On the contrary, the dependency upon ZIP7 function of tyrosine phosphorylation of Axl, ErbB3, ErbB4, EphA1, EphA4, RYK, and Tie−1 could not be confirmed, suggesting the possible presence of an alternative pathway that could activate these kinases without a

need for ZIP7−mediated zinc release from cellular stores. Collectively, these results detected activation of eight RTKs as a result of both ZIP7 overexpression and zinc treatment. Importantly, three of these RTKs, namely EGFR, ErbB2, and IGF−1R, had been experimentally demonstrated to be downstream effectors of ZIP7−mediate zinc release from cellular stores (Taylor et al. 2008b).

Figure 5.4 RTKs activated by ZIP7 or zinc (increases by >10,000 units)

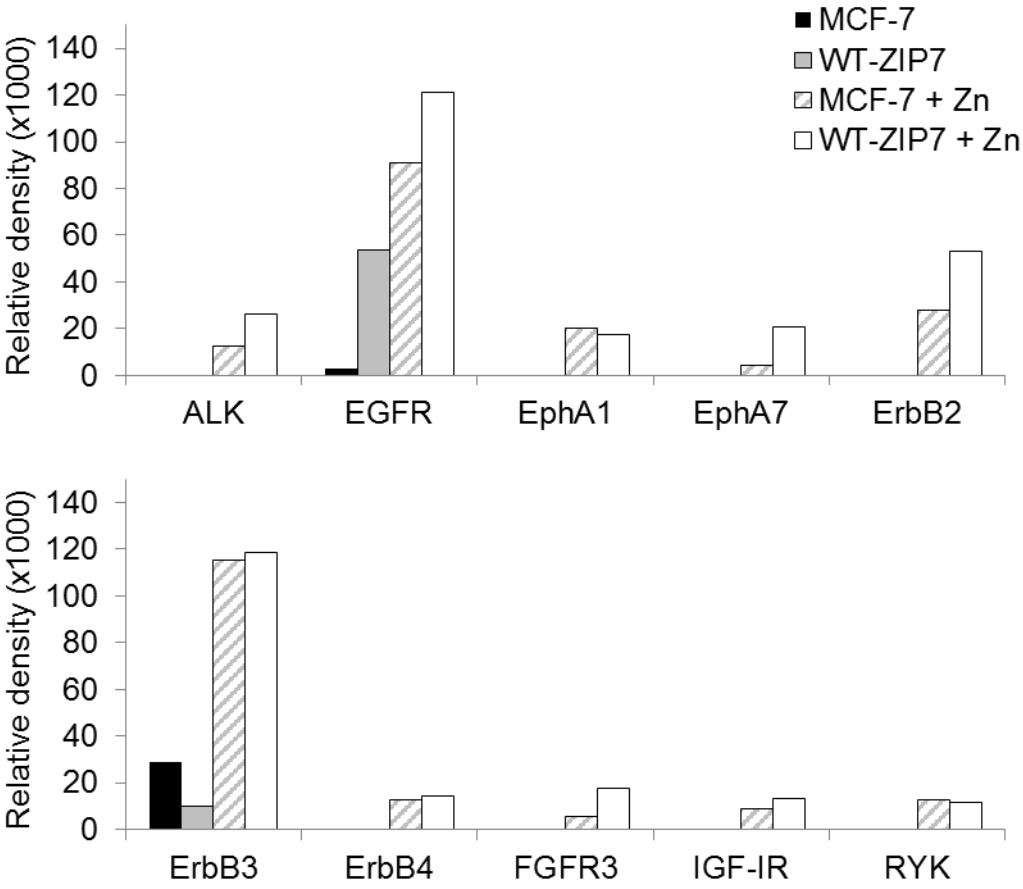

MCF−7 cells were transfected with wild−type ZIP7 (WT−ZIP7) and treated with 20 μM zinc plus 10 μM sodium pyrithione for 10 minutes. Tyrosine phosphorylation of selected receptor tyrosine kinases (RTKs) was determined using the human phospho−RTK antibody arrays (R&D Systems). Average densities of the duplicate spots for the kinases that show conspicuous increases in tyrosine phosphorylation (>10,000 density units) in the non−transfected zinc−treated cells (MCF−7 + Zn) or the transfected non−treated cells (WT−ZIP7) when compared to the non−transfected non−treated cells (MCF−7) are demonstrated. In addition, the kinases that show increases in tyrosine phosphorylation in the transfected zinc−treated cells (WT−ZIP7 + Zn) when compared to the non−transfected zinc−treated cells (MCF−7 + Zn) are also included.

Table 5.1 RTKs phosphorylated by ZIP7 overexpression or zinc

RTKs phosphorylated by ZIP7 overexpression [a]		
Marked increase: (> 10,000 units)	ALK	EphA7
	EGFR	FGFR3
	ErbB2	
Mild increase: (2,000−10,000 units)	c−Ret	Flt−3
	IGF−1R	

RTKs phosphorylated by zinc [b]		
Marked increase: (> 10,000 units)	ALK	ErbB4
	EGFR	EphA1
	ErbB2	RYK
	ErbB3	
Mild increase: (2,000−10,000 units)	Axl	FGFR3
	c-Ret	IGF−1R
	EphA4	Tie−1
	EphA7	
	Flt−3	

MCF−7 cells were transfected with wild−type ZIP7 and treated with 20 μM zinc plus 10 μM sodium pyrithione for 10 minutes. Tyrosine phosphorylation of selected receptor tyrosine kinases (RTKs) was determined using the human phospho−RTK antibody arrays (R&D Systems). Average densities of the duplicate spots for the kinases were determined.

[a] "Marked increase" and "mild increase" are arbitrarily judged by the increases in tyrosine phosphorylation in the transfected zinc−treated cells when compared to the non−transfected zinc−treated cells according to densitometric analysis as indicated. In addition, the kinases that show increases in tyrosine phosphorylation in the transfected non−treated cells when compared to the non−transfected non−treated cells are also included.
[b] "Marked increase" and "mild increase" are arbitrarily judged by the increases in tyrosine phosphorylation in the non−transfected zinc−treated cells when compared to the non−transfected non−treated cells according to densitometric analysis as indicated.
The kinases that are underlined are tyrosine−phosphorylated by either zinc alone.
The kinases that are shown in regular formatting are tyrosine−phosphorylated by both zinc and ZIP7 overexpression.

5.3.2 Multiple kinases are phosphorylated by ZIP7 overexpression or zinc

To extend the exploration to cellular kinases other than RTKs, we employed the phospho-kinase arrays to determine activation of up to 43 different cellular kinases with 2 related total proteins. In contrast to the phospho-RTK arrays, the phospho-kinase arrays also indicated specific phosphorylated residues in the kinases. Many kinases were already phosphorylated in MCF-7 cells without zinc treatment or ZIP7 overexpression (Fig. 5.5). As a result of transfection with wild-type ZIP7, the arrays revealed apparent increases in phosphorylation (>10,000 density units) of c-Jun (S63), CREB (S133), p70 S6 (T421/S424), STAT2 (Y689), STAT5a (Y694), and WNK1 (T60), when compared to the MCF-7 cells without transfection (Fig. 5.5-5.8, Table 5.2). Furthermore, mild decreases in phosphorylation (2,000-10.000 density units) were also observed for p53 (S392), p38α MAPK (T180/Y182), Chk-2 (T68), HSP27 (S78/S82), STAT6 (Y641), PDGFRβ (Y751), Hck (Y411), JNK (T183/Y185, T221/Y223), and PRAS40 (T246), when compared to the MCF-7 cells without transfection (Fig. 5.5-5.8, Table 5.2). Among these increases, either marked or mild, statistical significance compared to the MCF-7 cells without transfection was detected only for the HSP27 (S78/S82) phosphorylation (Fig. 5.8). Noteworthy, a replicate revealed an increase in AMPKα1 phosphorylation by 40,014 density units as a result of ZIP7 overexpression. However, this increase was not reproducible, since the other batch directly contradicted this increase by instead showing a marked decrease.

As a result of zinc treatment, phosphorylation of AKT (S473), AMPKα2 (T172), CREB (S133), GSK-3α/β (S21/S9), HSP27 (S78/S82), JNK (T183/Y185, T221/Y223), p38α MAPK (T180/Y182), p70 S6 (T421/S424), STAT2 (Y689), STAT5a (Y694), STAT5a/b (Y694/Y699), and STAT5b (Y699) was markedly increased (>10,000 density units) (Fig. 5.5-5.8, Table 5.2). On the contrary, only mild increases in phosphorylation (2,000-10.000 density units) were observed for c-Jun (S63), EGFR (Y1086), ERK1/2 (T202/Y204, T185/Y187), FAK (Y397), Fgr (Y412), MSK1/2 (S376/S360), Lck (Y394), PRAS40 (T246), RSK (S380/S386/S377), STAT6 (Y641), and TOR (S2448) (Fig. 5.5-5.8, Table 5.2). Among these kinases, only the increases in GSK-3α/β, HSP27, JNK, p38α MAPK, and STAT5a phosphorylation were statistically significant (Fig. 5.8).

To investigate whether the increases following zinc treatment were mediated by ZIP7, cells were both transfected with wild-type ZIP7 and treated with zinc. Among the kinases activated by zinc, phosphorylation levels of CREB (S133), GSK-3α/β (S21/S9), HSP27 (S78/S82), p70 S6 (T421/S424), PRAS40 (T246), and WNK1 (T60) were markedly increased (>10,000 density units) when compared to the non-transfected zinc-treated MCF-7 cells. On the contrary, phosphorylation levels of AKT (S473), c-Jun (S63), ERK1/2 (T202/Y204, T185/Y187), FAK (Y397), JNK (T183/Y185, T221/Y223), and STAT5a (Y694) were mildly increased (2,000-15,000 density units) when compared to the non-transfected zinc-treated MCF-7 cells (Fig. 5.5-5.8, Table 5.2). These increases confirmed that the phosphorylation of these kinases was ZIP7-dependent. However, only the increase in STAT5a (Y694) phosphorylation was statistically significant (Fig. 5.8). Unexpectedly, p38α MAPK (T180/Y182), which showed a marked increase in phosphorylation following ZIP7 overexpression in the cells without zinc treatment, revealed a marked decrease in phosphorylation in the ZIP7-overexpressing zinc-treated cells when compared to the non-transfected zinc-treated cells (Fig. 5.8). However, due to the high variation of the data between the duplicates, this decrease was not statistically significant (Fig. 5.8).

Interestingly, multiple kinases were shown to be phosphorylated as a result of ZIP7 overexpression in the zinc-treated cells, with no discernible increases in phosphorylation as a result of zinc treatment alone. Among these notable kinases, p53 (S46) and p53 (S392) were markedly phosphorylated (>10,000 density units), whilst AKT (T308), Chk-2 (T68), Hck (Y411), HSP60, Lyn (Y397), p70 S6 (T421/S424), and Yes (Y426) were mildly phosphorylated (2,000-10,000 density units) (Fig. 5.5-5.8, Table 5.2). Unexpectedly, total β-Catenin levels were also markedly increased (>10,000 density units) as a result of ZIP7 transfection plus zinc treatment, when compared to zinc treatment alone (Fig. 5.5-5.8, Table 5.2). These data therefore revealed not only the kinases that were phosphorylated through the ZIP7-mediated zinc-dependent mechanism, but also the kinases that might be phosphorylated through an alternative ZIP7-mediated pathway independently of zinc. Noteworthy, because of the high variability between the two batches of the phospho-kinase arrays, the statistical analysis was rather limited.

Figure 5.5 Phospho−kinase arrays in MCF−7 stimulated with ZIP7 and zinc

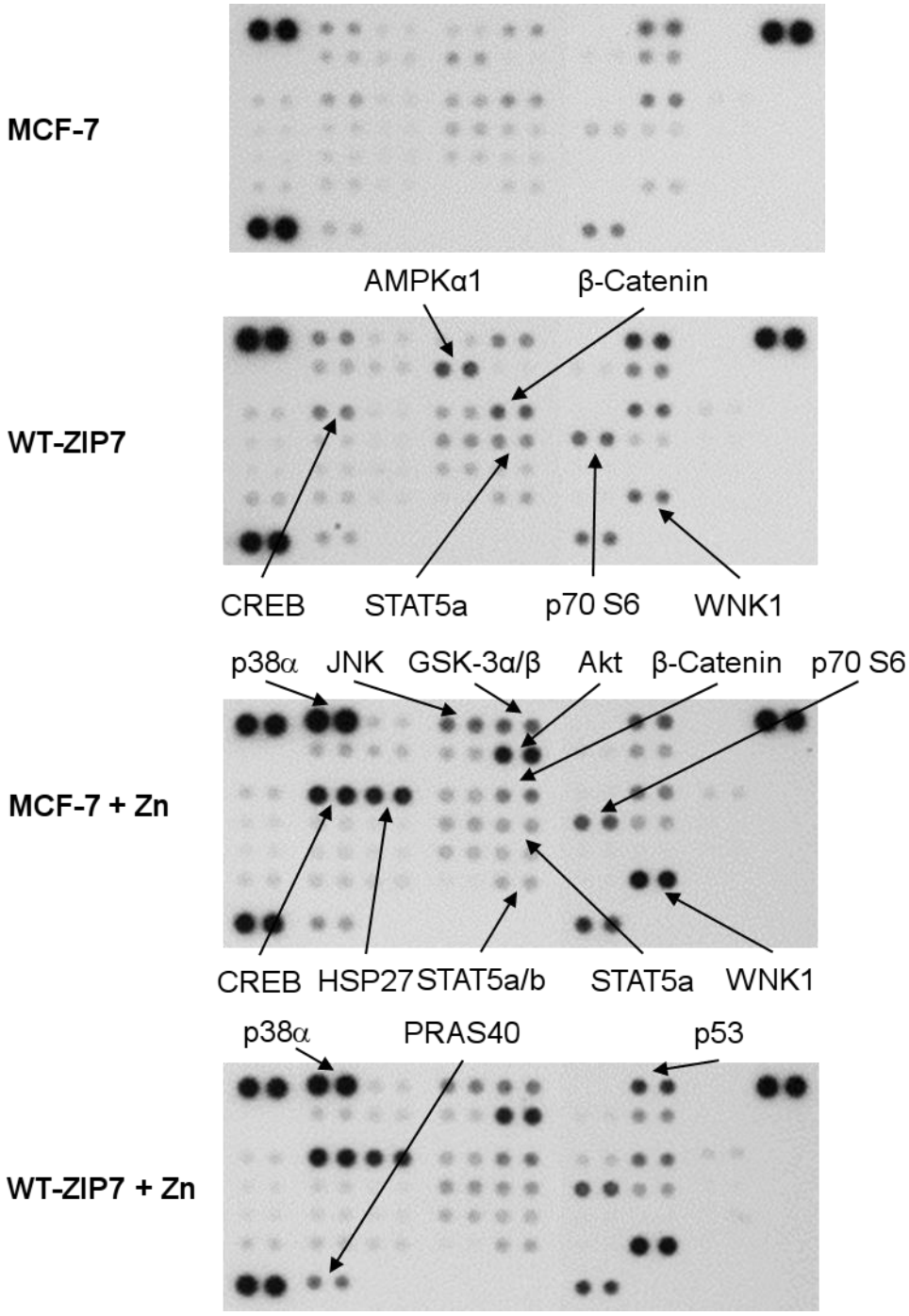

MCF−7 cells were transfected with wild−type ZIP7 and treated with 20 µM zinc plus 10 µM sodium pyrithione for 10 minutes. Phosphorylation of selected kinases was determined using the human phospho−kinase antibody arrays (R&D Systems). Signals for each kinase are presented as a pair of duplicate spots, with three pairs of dark reference spots on the upper left, upper right, and lower left corners for alignment. The kinases that show conspicuous changes in phosphorylation (>10,000 density units) in the non−transfected zinc−treated cells (MCF−7 + Zn) or the transfected non−treated cells (WT−ZIP7) when compared to the non−transfected non−treated cells (MCF−7) are indicated. In addition, the kinases that show increases in phosphorylation in the transfected zinc−treated cells (WT−ZIP7 + Zn) when compared to the non−transfected zinc−treated cells (MCF−7 + Zn) are also indicated.

Figure 5.6 Densitometric analysis of phospho−kinase arrays in MCF−7 stimulated with ZIP7 and zinc (1/3)

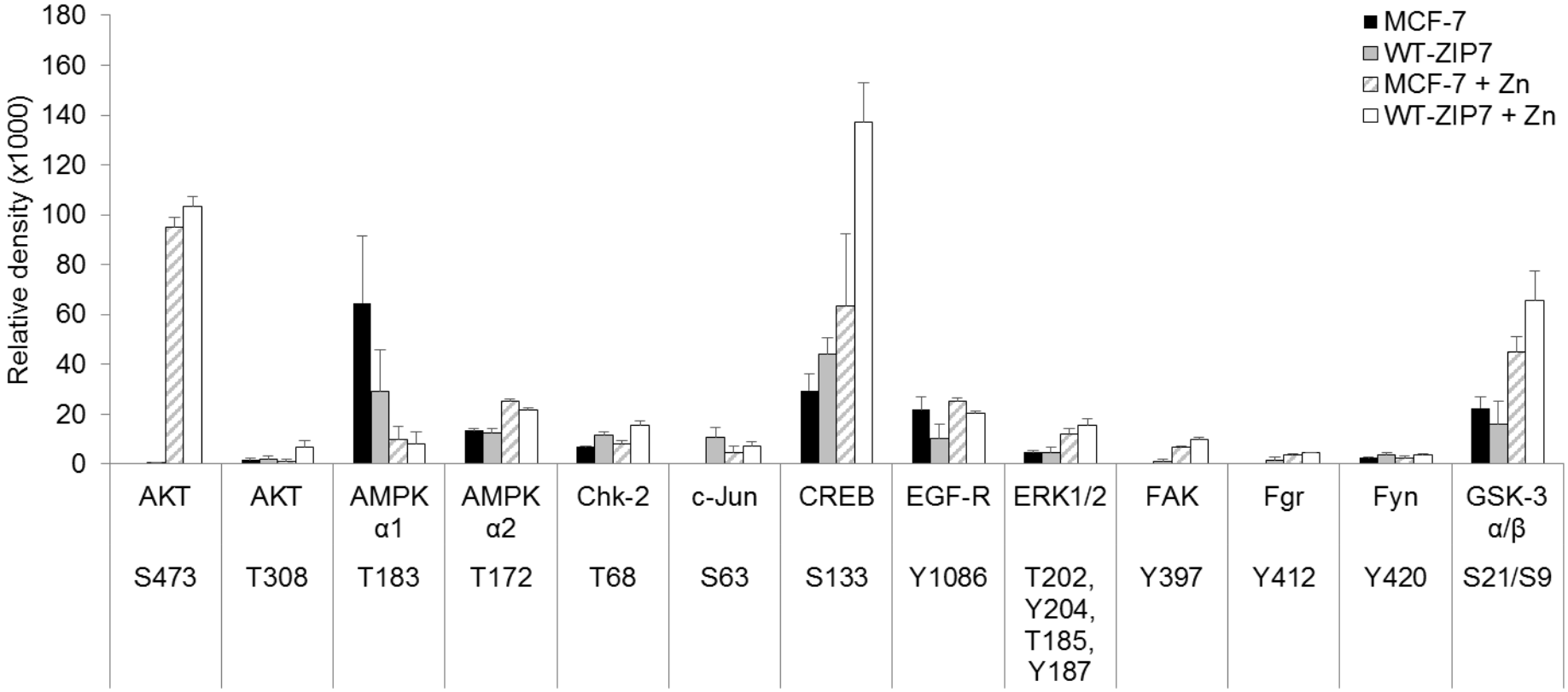

MCF−7 cells were transfected with wild−type ZIP7 and treated with 20 μM zinc plus 10 μM sodium pyrithione for 10 minutes. Phosphorylation of selected kinases at the residues indicated below the names of the kinases was determined using the human phospho−kinase antibody arrays (R&D Systems). Densitometric data are presented as mean of the duplicate dots for each kinase ± standard error (n=2).

Figure 5.6 Densitometric analysis of phospho−kinase arrays in MCF−7 stimulated with ZIP7 and zinc (continued, 2/3)

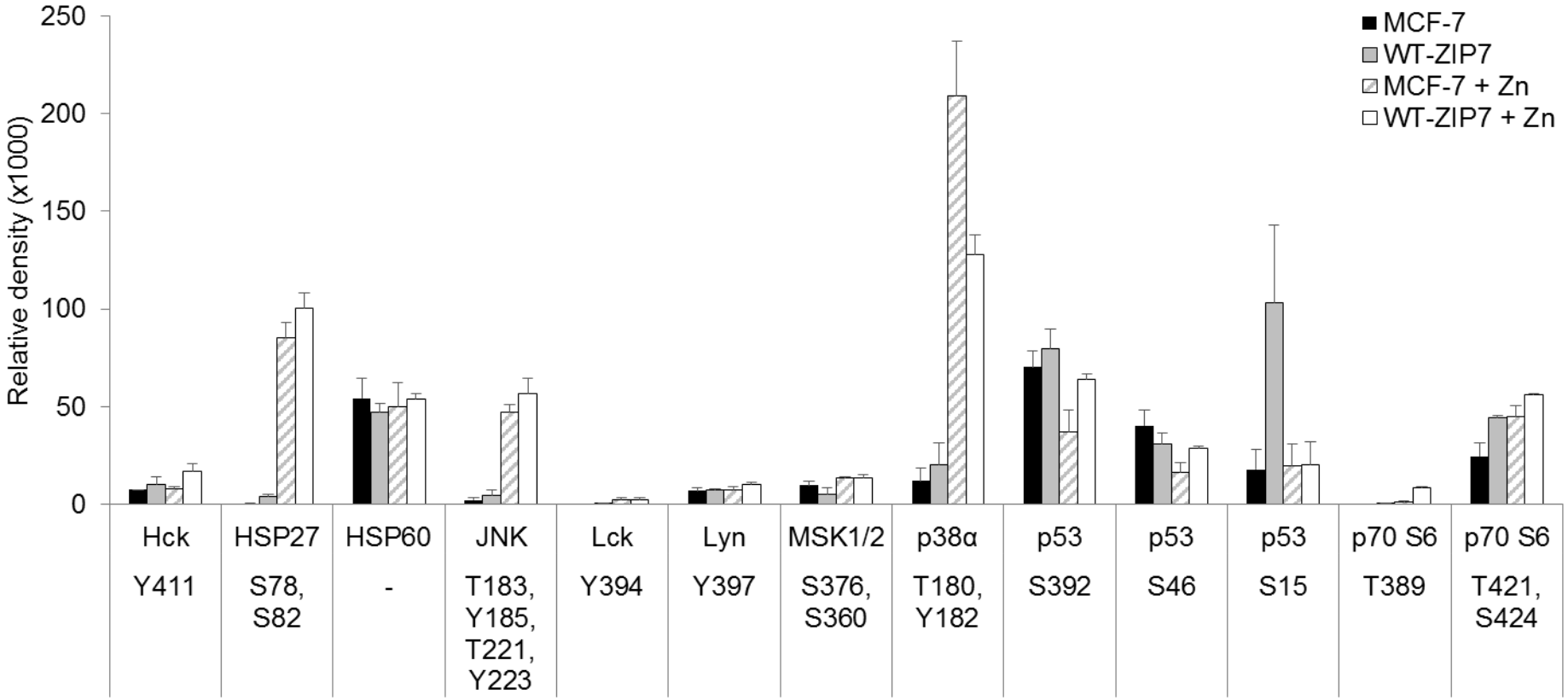

MCF−7 cells were transfected with wild−type ZIP7 and treated with 20 μM zinc plus 10 μM sodium pyrithione for 10 minutes. Phosphorylation of selected kinases at the residues indicated below the names of the kinases was determined using the human phospho−kinase antibody arrays (R&D Systems). Densitometric data are presented as mean of the duplicate dots for each kinase ± standard error (n=2).

Figure 5.6 Densitometric analysis of phospho−kinase arrays in MCF−7 stimulated with ZIP7 and zinc (continued, 3/3)

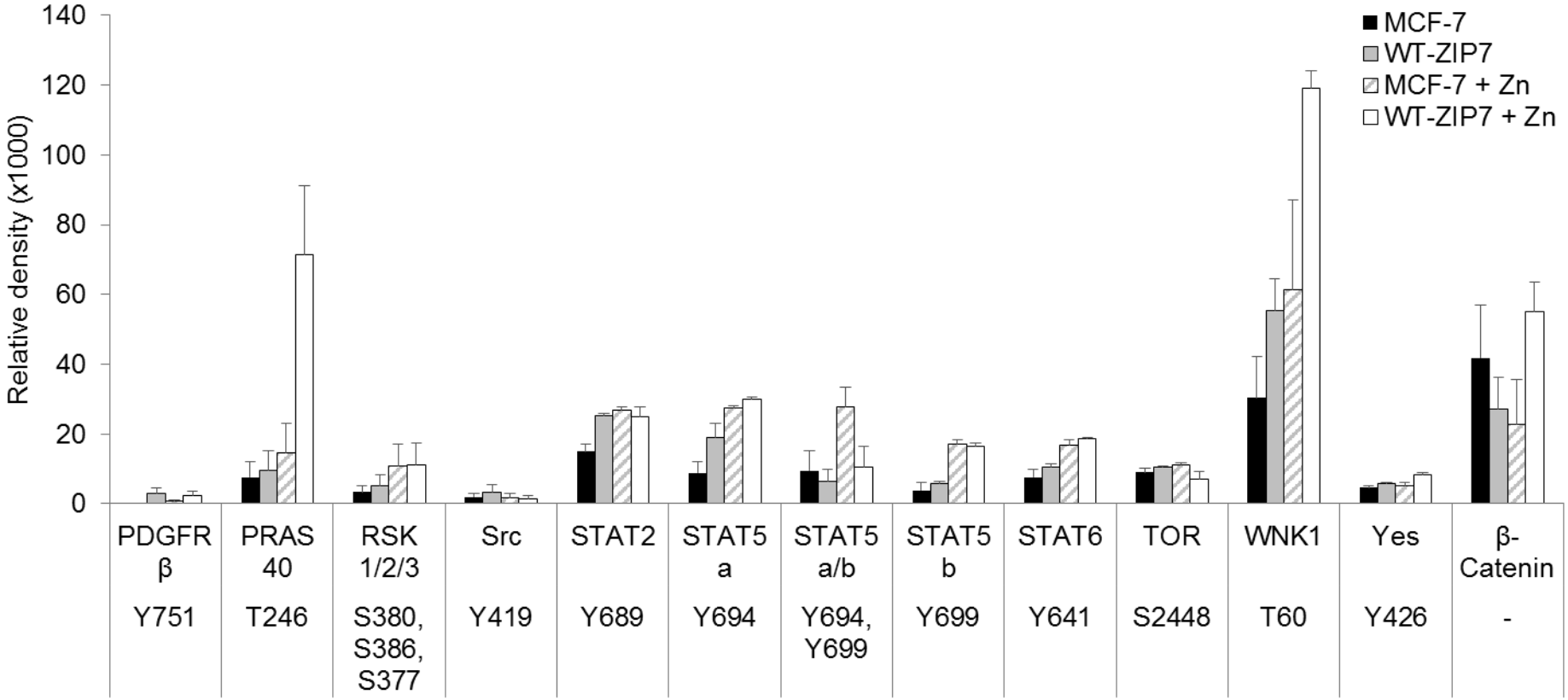

MCF−7 cells were transfected with wild−type ZIP7 and treated with 20 μM zinc plus 10 μM sodium pyrithione for 10 minutes. Phosphorylation of selected kinases at the residues indicated below the names of the kinases was determined using the human phospho−kinase antibody arrays (R&D Systems). Densitometric data are presented as mean of the duplicate dots for each kinase ± standard error (n=2).

Figure 5.7 A heat map of phospho−kinases activated by ZIP7 or zinc

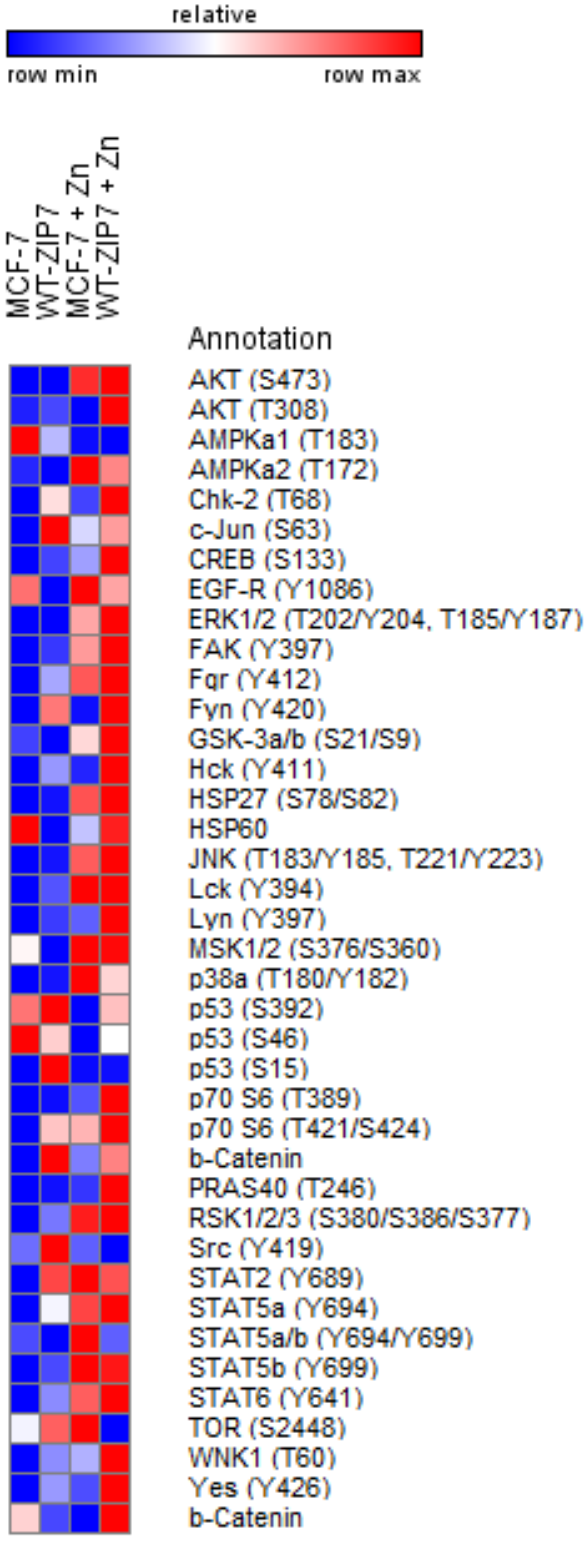

MCF−7 cells were transfected with wild−type ZIP7 and treated with 20 μM zinc plus 10 μM sodium pyrithione for 10 minutes. Phosphorylation of selected kinases at the residues indicated was determined using the human phospho−kinase antibody arrays (R&D Systems). The heat map was generated using a GENE-E matrix visualization and analysis platform (The Board Institute). Densitometric values in relation to other samples for each kinase are presented as a spectrum of colour where blue colour represents the lowest value in the row and red colour represents the highest value in the row according to the indicated scale, irrespective of the absolute signal intensities.

Figure 5.8 Kinases activated by ZIP7 or zinc (increases by >10,000 units)

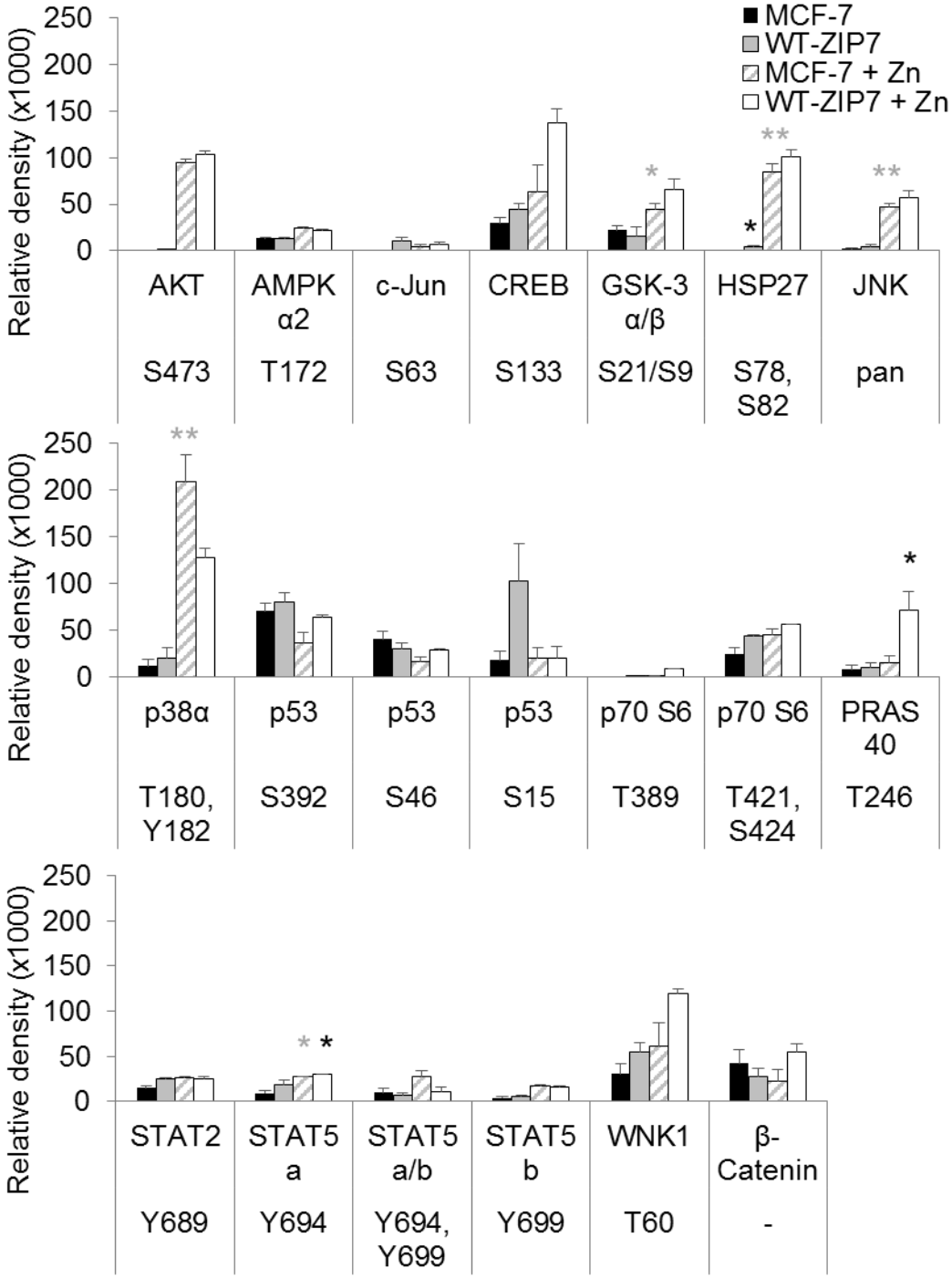

MCF−7 cells were transfected with wild−type ZIP7 and treated with 20 μM zinc plus 10 μM sodium pyrithione for 10 minutes. Phosphorylation of selected kinases at the residues indicated below the names of the kinases was determined using the human phospho−kinase antibody arrays (R&D Systems). Average densities of the duplicate spots for the kinases that show conspicuous increases in phosphorylation (>10,000 density units) in the non−transfected zinc−treated cells (MCF−7 + Zn) or the transfected non−treated cells (WT−ZIP7) when compared to the non−transfected non−treated cells (MCF−7) are demonstrated. In addition, the kinases that show increases in phosphorylation in the transfected zinc−treated cells (WT−ZIP7 + Zn) when compared to the non−transfected zinc−treated cells (MCF−7 + Zn) are also included. Densitometric data are presented as mean ± standard error (n=2).
* $p < 0.05$, ** $p < 0.01$

Table 5.2 Kinases phosphorylated by ZIP7 overexpression or zinc

Kinases phosphorylated as a result of ZIP7 overexpression [a]		
Marked increase: (> 10,000 units)	c−Jun (S63)	p70 S6 (T421/S424)
	CREB (S133)	PRAS40 (T246)
	GSK−3α/β (S21/S9)	STAT2 (Y689)
	HSP27 (S78/S82)	STAT5a (Y694)
	p53 (S15)	WNK1 (T60)
	p53 (S46)	**β−Catenin**
	p53 (S392)	
Mild increase: (2,000−10,000 units)	AKT (S473)	JNK (T183/Y185,T221/Y223)
	AKT (T308)	**Lyn (Y397)**
	Chk−2 (T68)	p38α MAPK (T180/Y182)
	ERK1/2 (T202/Y204,T185/Y187)	**p70 S6 (T389)**
	FAK (Y397)	**PDGFRβ (Y751)**
	Hck (Y411)	STAT6 (Y641)
	HSP60	**Yes (Y426)**

Kinases phosphorylated as a result of zinc treatment [b]		
Marked increase: (> 10,000 units)	AKT (S473)	p38α MAPK (T180/Y182)
	AMPKα2 (T172)	p70 S6 (T421/S424)
	CREB (S133)	STAT2 (Y689)
	GSK−3α/β (S21/S9)	STAT5a (Y694)
	HSP27 (S78/S82)	STAT5a/b (Y694/Y699)
	JNK (T183/Y185,T221/Y223)	STAT5b (Y699)
		WNK1 (T60)
Mild increase: (2,000−10,000 units)	c-Jun (S63)	MSK1/2 (S376/S360)
	EGFR (Y1086)	Lck (Y394)
	ERK1/2 (T202/Y204,T185/Y187)	PRAS40 (T246)
		RSK (S380/S386/S377)
	FAK (Y397)	STAT6 (Y641)
	Fgr (Y412)	TOR (S2448)

MCF−7 cells were transfected with wild−type ZIP7 and treated with 20 µM zinc plus 10 µM sodium pyrithione for 10 minutes. Phosphorylation of selected kinases was determined using the human phospho−kinase antibody arrays (R&D Systems). Average densities of the duplicate spots for the kinases were determined.

[a] "Marked increase" and "mild increase" are arbitrarily judged by the increases in phosphorylation in the transfected zinc−treated cells when compared to the non−transfected zinc−treated cells according to densitometric analysis as indicated. In addition, the kinases that show increases in phosphorylation in the transfected non−treated cells when compared to the non−transfected non−treated cells are also included.
[b] "Marked increase" and "mild increase" are arbitrarily judged by the increases in phosphorylation in the non−transfected zinc−treated cells when compared to the non−transfected non−treated cells according to densitometric analysis as indicated.
The kinases that are in bold are phosphorylated by ZIP7 overexpression alone.
The kinases that are underlined are phosphorylated by zinc alone.
The kinases that are shown in regular formatting are phosphorylated by both zinc and ZIP7 overexpression.

The phosphorylation of AKT (S473) and ERK1/2 (T202/Y204) as a result of ZIP7 overexpression or zinc treatment (Fig. 5.5−5.8, Table 5.2) has previously been shown to result from ZIP7−mediated zinc release from cellular stores (Taylor et al. 2008b), which is triggered by CK2−mediated phosphorylation of ZIP7 on residues S275 and S276 (Taylor et al. 2012). The zinc−induced phosphorylation or p70 S6 (T421/S424), ERK1/2 (T202/Y204), JNK (T183/Y185), and p38α MAPK (T180/Y182) (Fig. 5.5−5.8, Table 5.2) has also been reported in SH-SY5Y neuroblastoma cells using Western blotting in a previous study that linked this phosphorylation to the pathogenesis of Alzheimer's disease (An *et al.* 2005). Importantly, the phospho−kinase array data further suggested that this phosphorylation of p70 S6, ERK1/2, JNK, and p38α MAPK was mediated by ZIP7. Noteworthy, the zinc−induced phosphorylation of AKT on T308, which was reported in the previous study (An et al. 2005), was not detected by the phospho−kinase arrays (Fig. 5.5−5.8, Table 5.2). However, this phosphorylation was shown to be induced by ZIP7 overexpression using these arrays (Fig. 5.5−5.8, Table 5.2).

The phosphorylation of p38α MAPK as a result of zinc treatment and HSP27 as a result of both zinc treatment and ZIP7 overexpression (Fig. 5.5−5.8, Table 5.2) needs to be considered because of the fact that these proteins are related to cell stress (Coulthard *et al.* 2009; Vidyasagar *et al.* 2012). Their activation might suggest cell stress caused by the procedure of transfection or zinc treatment. Nevertheless, these two stress−related proteins

have also been reported to play important roles in other cellular processes. Importantly, both p38α MAPK (Hong *et al.* 2014) and HSP27 (Wei *et al.* 2011) have been reported to promote breast cancer migration and metastasis. Given that ZIP7 is a zinc channel that contributes to breast cancer aggressiveness particularly in endocrine-resistant cell lines (Taylor et al. 2008b), these two kinases might in fact be involved in the carcinogenetic pathways that were triggered by ZIP7-mediated zinc release from cellular stores, rather than the experimentally-induced cell stress.

Interestingly, the phosphorylation of p53 on S15, S46, and S392 was shown to be solely ZIP7-dependent, with no any effect from zinc treatment (Fig. 5.5-5.8, Table 5.2). S46-phosphorylated p53 has been associated with its ability to bind to apoptosis-related genes (Smeenk *et al.* 2011) and S15-phosphorylated p53 has been shown to be triggered preceding the p53 phosphorylation on S46 in the apoptotic process (Perfettini *et al.* 2005). This finding from the phospho-kinase arrays might therefore imply an ongoing apoptotic process induced by ZIP7 overexpression, which might or might not be confounded by the transfection procedure. In contrast to the phosphorylation on S46 and S15, the p53 phosphorylation on S392 has been controversially reported both to suppress and to promote tumorigenesis, and is under ongoing investigations (Dai and Gu 2010), supporting the involvement of ZIP7-mediated zinc signalling in cancer pathogenesis.

5.3.3 Multiple MAPKs are phosphorylated by ZIP7 overexpression or zinc

To confirm the activation of various cellular kinases and to explore the activation of more isoforms of MAPKs, the phospho-MAPK arrays were employed. Like the phospho-kinase arrays, the phospho-MAPK arrays not only indicated phosphorylation of kinases, but also specified the residues in the kinases that were phosphorylated. In the resting state, phosphorylation of GSK-3α/β (S21/S9), HSP27 (S78/S82), and p70 S6 (T421/S424) was detected (Fig. 5.9). Outstandingly, ZIP7 overexpression alone could markedly induce phosphorylation of GSK-3α/β (S21/S9) and p70 S6 (T421/S424) with increases in signal intensity by >10,000 density units. Furthermore, ZIP7 overexpression also mildly induced phosphorylation of HSP27 (S78/S82), CREB (S133), and

ERK1 (T202/Y204) with increases in signal intensity by 2,000−10,000 density units (Fig. 5.9−5.12, Table 5.3).

Consistent with the phospho−kinase array data, the phospho−MAPK arrays revealed many kinases that were phosphorylated as a result of zinc treatment. AKT (S473, S474, S472), AKT1 (S473), AKT2 (S474), CREB (S133), ERK1 (T202/Y204), GSK−3α/β (S21/S9), HSP27 (S78/S82), JNK (T183/Y185, T221/Y223), and p70 S6 (T421/S424) were shown to have marked increases in phosphorylation (>10,000 density units) when compared to the MCF−7 cells without treatment or transfection (Fig. 5.9−5.12, Table 5.3). On the contrary, ERK2 (T185/Y187), JNK2 (T183/Y185), MSK2 (S360), and p38α (T180/Y182) were shown to have mild increases in phosphorylation (2,000−10,000 density units) when compared to the MCF−7 cells without treatment or transfection (Fig. 5.9−5.12, Table 5.3). Among these kinases, all the kinases that were markedly phosphorylated as a result of ZIP7 overexpression in the non−treated cells again revealed marked increases (>10,000 density units) in phosphorylation as a result of ZIP7 overexpression in the zinc−treated cells, except ERK1 (T202/Y204), which showed only a mild increase (2,000−10,000 density units) (Fig. 5.9−5.12, Table 5.3). In addition, mild increases in phosphorylation (2,000−10,000 density units) of ERK2 (T185/Y187), JNK (T183/Y185, T221/Y223) and JNK2 (T183/Y185) were also seen in the ZIP7−overexpressing zinc−treated cells when compared to the non−transfected zinc−treated cells (Fig. 5.9−5.12, Table 5.3). Collectively, these data confirmed substantial ZIP7 involvement in the phosphorylation of these kinases on the particular sites.

Agreeing with the phospho−kinase data, the phosphorylation of p53 (S46) was induced specifically by wild−type ZIP7 transfection with no changes observed as a result of zinc treatment (Fig. 5.9−5.12, Table 5.3), again raising the question of whether the transfection procedure confounded the experiment. Moreover, the phosphorylation of the cell stress−related proteins, p38α MAPK and HSP27 (S78/S82), which resulted from zinc treatment or ZIP7 overexpression, was also confirmed (Fig. 5.9−5.12, Table 5.3). Cell stress induced by the experiments therefore needed to be carefully considered.

Figure 5.9 Phospho-MAPK arrays in MCF−7 stimulated with ZIP7 and zinc

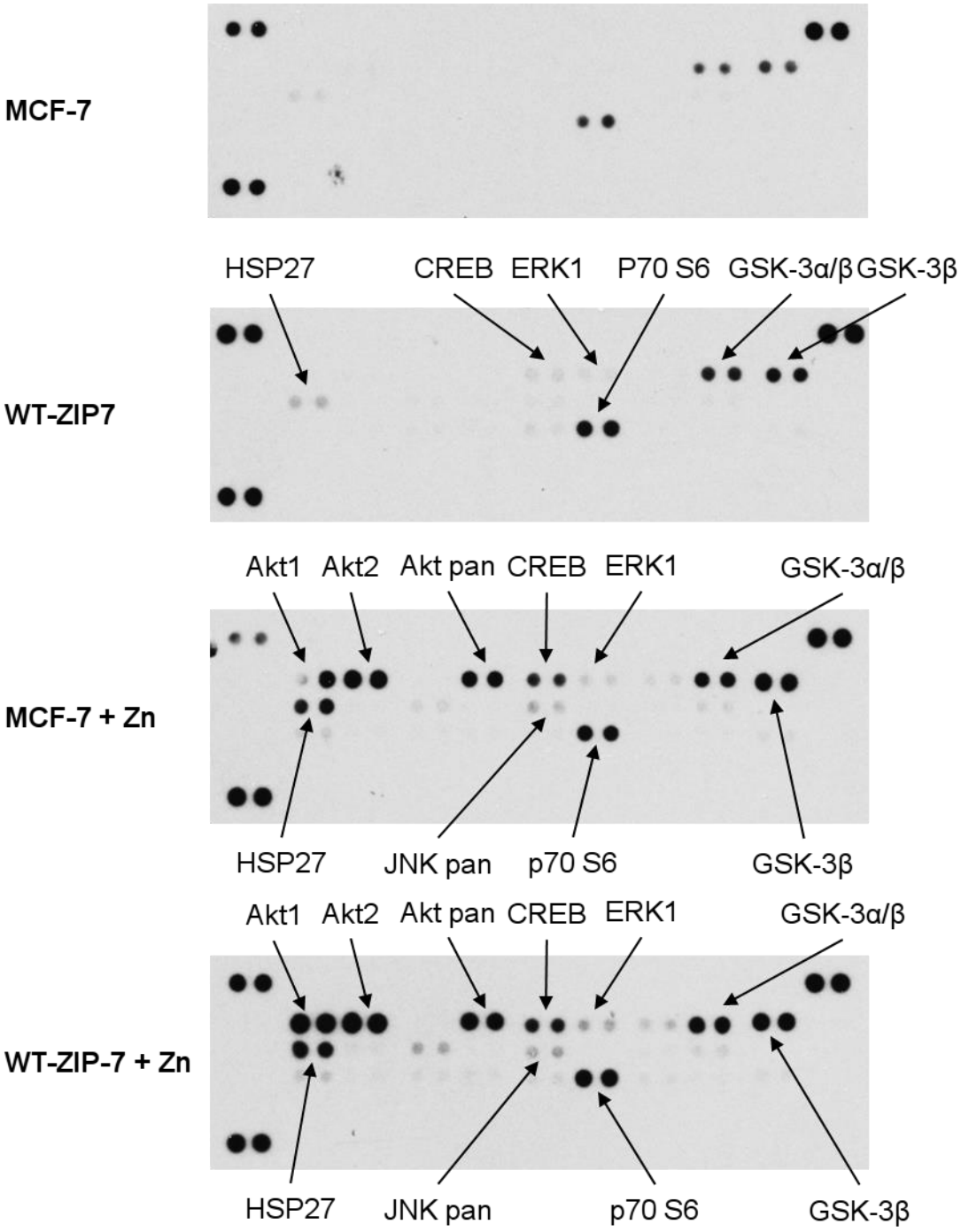

MCF−7 cells were transfected with wild−type ZIP7 and treated with 20 μM zinc plus 10 μM sodium pyrithione for 10 minutes. Phosphorylation of selected mitogen−activated protein kinases (MAPKs) was determined using the human phospho−MAPK antibody arrays (R&D Systems). Signals for each kinase are presented as a pair of duplicate spots, with three pairs of dark reference spots on the upper left, upper right, and lower left corners for alignment. The kinases that show conspicuous changes in phosphorylation (>10,000 density units) in the non−transfected zinc−treated cells (MCF−7 + Zn) or the transfected non−treated cells (WT−ZIP7) when compared to the non−transfected non−treated cells (MCF−7) are indicated. In addition, the kinases that show increases in phosphorylation in the transfected zinc−treated cells (WT−ZIP7 + Zn) when compared to the non−transfected zinc−treated cells (MCF−7 + Zn) are also indicated.

Figure 5.10 Densitometric analysis of phospho−MAPK arrays in MCF−7 stimulated with ZIP7 and zinc

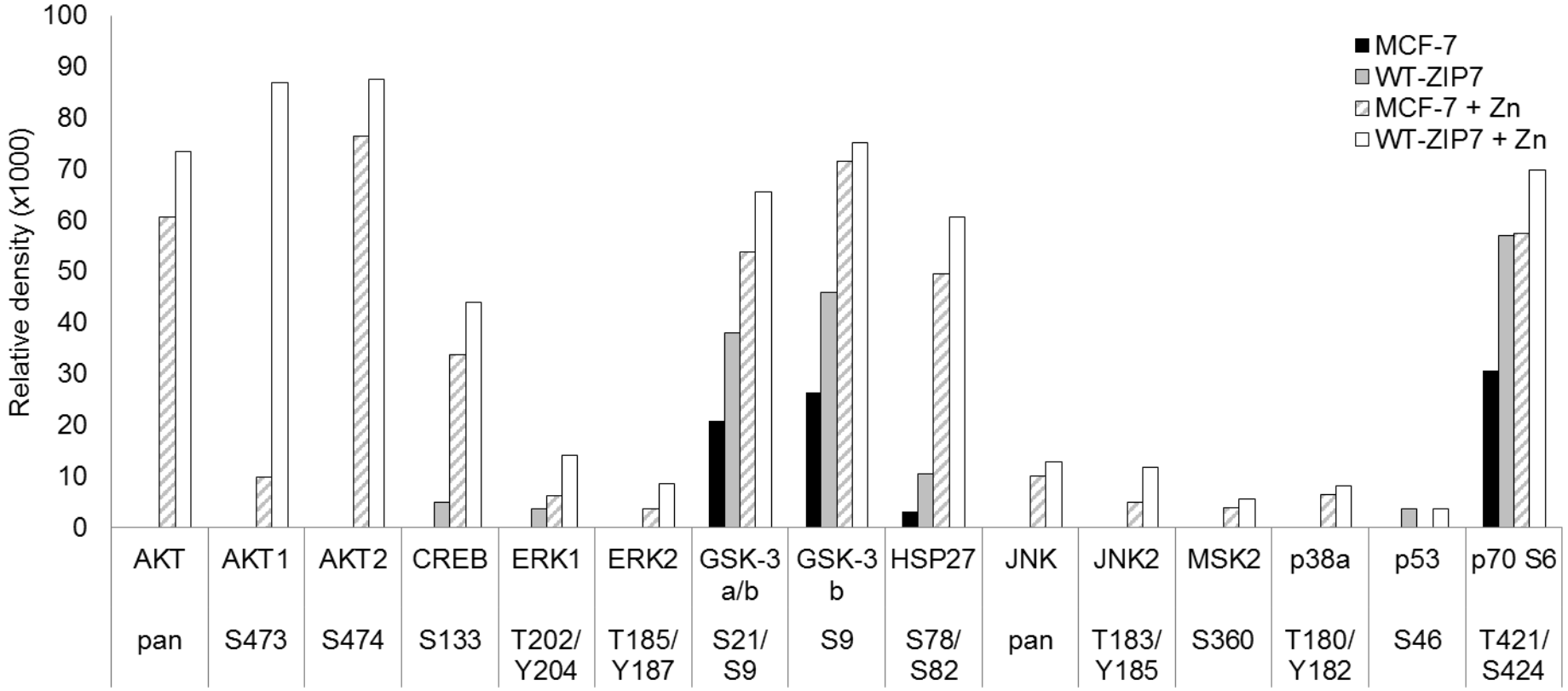

MCF−7 cells were transfected with wild−type ZIP7 and treated with 20 µM zinc plus 10 µM sodium pyrithione for 10 minutes. Phosphorylation of selected mitogen−activated protein kinases (MAPKs) at the residues indicated below the names of the kinases was determined using the human phospho−MAPK antibody arrays (R&D Systems). Densitometric data are presented as mean of the duplicate dots for each kinase.

Figure 5.11 A heat map of phospho−MAPKs activated by ZIP7 or zinc

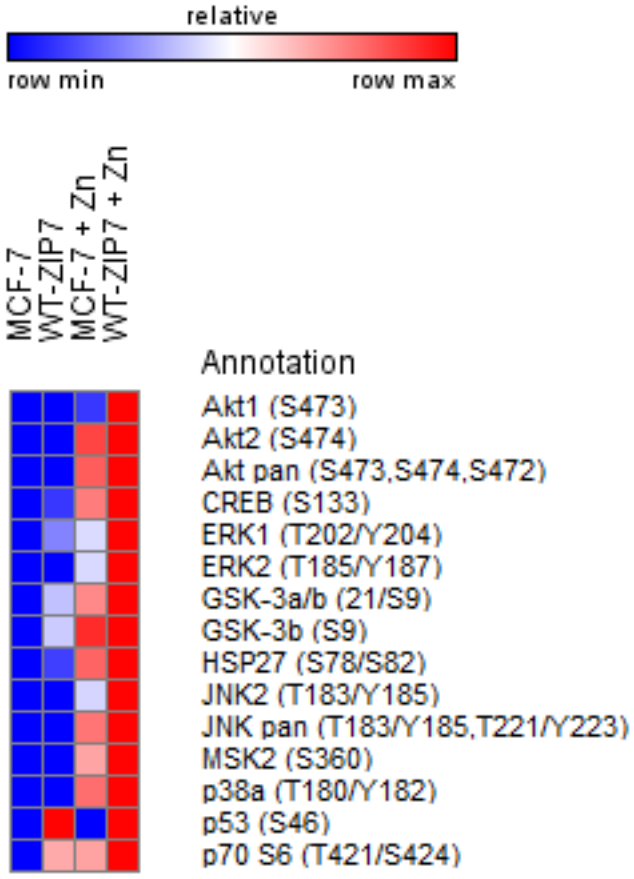

MCF−7 cells were transfected with wild−type ZIP7 and treated with 20 µM zinc plus 10 µM sodium pyrithione for 10 minutes. Phosphorylation of selected mitogen−activated protein kinases (MAPKs) at the residues indicated was determined using the human phospho−MAPK antibody arrays (R&D Systems). The heat map was generated using a GENE-E matrix visualization and analysis platform (The Board Institute). Densitometric values in relation to other samples for each kinase are presented as a spectrum of colour where blue colour represents the lowest value in the row and red colour represents the highest value in the row according to the indicated scale, irrespective of the absolute signal intensities.

Figure 5.12 MAPKs activated by ZIP7 or zinc (increases by >10,000 units)

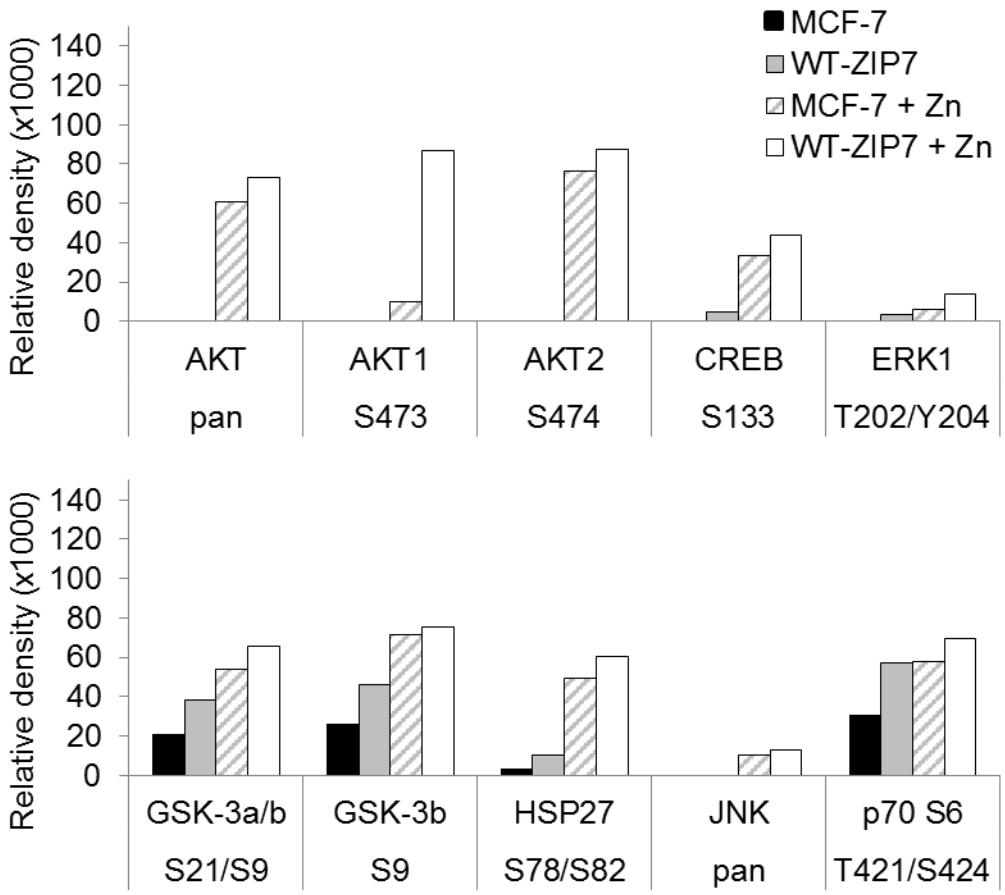

MCF−7 cells were transfected with wild−type ZIP7 and treated with 20 μM zinc plus 10 μM sodium pyrithione for 10 minutes. Phosphorylation of selected mitogen−activated protein kinases (MAPKs) at the residues indicated below the names of the kinases was determined using the human phospho−MAPK antibody arrays (R&D Systems). Average densities of the duplicate spots for the kinases that show conspicuous increases in phosphorylation (>10,000 density units) in the non−transfected zinc−treated cells (MCF−7 + Zn) or the transfected non−treated cells (WT−ZIP7) when compared to the non−transfected non−treated cells (MCF−7) are demonstrated. In addition, the kinases that show increases in phosphorylation in the transfected zinc−treated cells (WT−ZIP7 + Zn) when compared to the non−transfected zinc−treated cells (MCF−7 + Zn) are also included.

Table 5.3 MAPKs phosphorylated by ZIP7 overexpression or zinc

MAPKs phosphorylated as a result of ZIP7 overexpression [a]		
Marked increase: (> 10,000 units)	AKT (S473,S474,S472)	ERK1 (T202/Y204)
	AKT1 (S473)	GSK−3α/β (S21/S9)
	AKT2 (S474)	HSP27 (S78/S82)
	CREB (S133)	p70 S6 (T421/S424)
Mild increase: (2,000−10,000 units)	ERK2 (T185/Y187)	JNK2 (T183/Y185)
	JNK (T183/Y185,T221/Y223)	**p53 (S46)**

MAPKs phosphorylated as a result of zinc treatment [b]		
Marked increase: (> 10,000 units)	AKT (S473,S474,S472)	GSK−3α/β (S21/S9)
	AKT1 (S473)	HSP27 (S78/S82)
	AKT2 (S474)	JNK (T183/Y185,T221/Y223)
	CREB (S133)	p70 S6 (T421/S424)
	ERK1 (T202/Y204)	
Mild increase: (2,000−10,000 units)	ERK2 (T185/Y187)	MSK2 (S360)
	JNK2 (T183/Y185)	p38α MAPK (T180/Y182)

MCF−7 cells were transfected with wild−type ZIP7 and treated with 20 μM zinc plus 10 μM sodium pyrithione for 10 minutes. Phosphorylation of selected mitogen−activated protein kinases (MAPKs) was determined using the human phospho−MAPK antibody arrays (R&D Systems). Average densities of the duplicate spots for the kinases were determined.

[a] "Marked increase" and "mild increase" are arbitrarily judged by the increases in phosphorylation in the transfected zinc−treated cells when compared to the non−transfected zinc−treated cells according to densitometric analysis as indicated. In addition, the kinases that show increases in phosphorylation in the transfected non−treated cells when compared to the non−transfected non−treated cells are also included.
[b] "Marked increase" and "mild increase" are arbitrarily judged by the increases in phosphorylation in the non−transfected zinc−treated cells when compared to the non−transfected non−treated cells according to densitometric analysis as indicated.
The kinases that are in bold are phosphorylated by ZIP7 overexpression alone.
The kinases that are underlined are phosphorylated by zinc alone.
The kinases that are shown in regular formatting are phosphorylated by both zinc and ZIP7 overexpression.

5.3.4 Western blotting verifies kinase activation by zinc or ZIP7

To confirm the phosphorylation of the potential kinases as a result of zinc treatment or ZIP7 overexpression, Western blotting was performed. Given that zinc treatment more effectively induced phosphorylation of the majority of the kinases according to the antibody array results, the treatment was performed first to verify the activation using Western blotting. The kinases that could be confirmed to be zinc−activated would then be further investigated with wild−type ZIP7 transfection. This initial investigation included only the kinases that were shown to be apparently phosphorylated as a result of both ZIP7 overexpression and zinc treatment by either the phospho−kinase arrays or the phospho−MAPK arrays. The kinases selected for this investigation consisted of CREB (S133), p70 S6 (T421/S424), and WNK1 (T60). Given that the increase in STAT5 phosphorylation was shown to be significant following both zinc treatment and ZIP7 overexpression regardless of the low amplitudes of the changes (Fig. 5.8), this kinase was also investigated. Phosphorylation of AKT and GSK−3β was included as positive controls, because they have previously been confirmed to be phosphorylated as a result of zinc treatment (An et al. 2005; Taylor et al. 2008b), with a link to ZIP7 (Taylor et al. 2008b) and ZIP6 (Hogstrand et al. 2013), respectively.

Using our pZIP7 antibody, Western blotting demonstrated a significant increase in ZIP7 phosphorylation on residues S275 and S276 (Fig 5.13A). Confirming the previous studies (An et al. 2005; Taylor et al. 2008b) and the phospho−kinase array results, AKT (Fig 5.13B) and GSK−3β (Fig 5.13C) were shown to be significantly phosphorylated on residues S473 and S9, respectively, as a result of zinc treatment. Furthermore, a 3−fold increase in CREB phosphorylation (Fig 5.13D) and a 2−fold increase in p70 S6 phosphorylation (Fig 5.13E) were also shown to be statistically significant, supporting the findings of the phospho−kinase arrays. On the contrary, only a mild increase in STAT5 phosphorylation was detected without statistical significance (Fig 5.13F). Noteworthy, no band was detected on the Western blot of WNK1, possibly due to the relatively high molecular weight of WNK1 (250 kDa), which might have been lost during the transfer process when using the current Western blotting conditions.

Figure 5.13 Confirmation of zinc stimulation of kinase phosphorylation

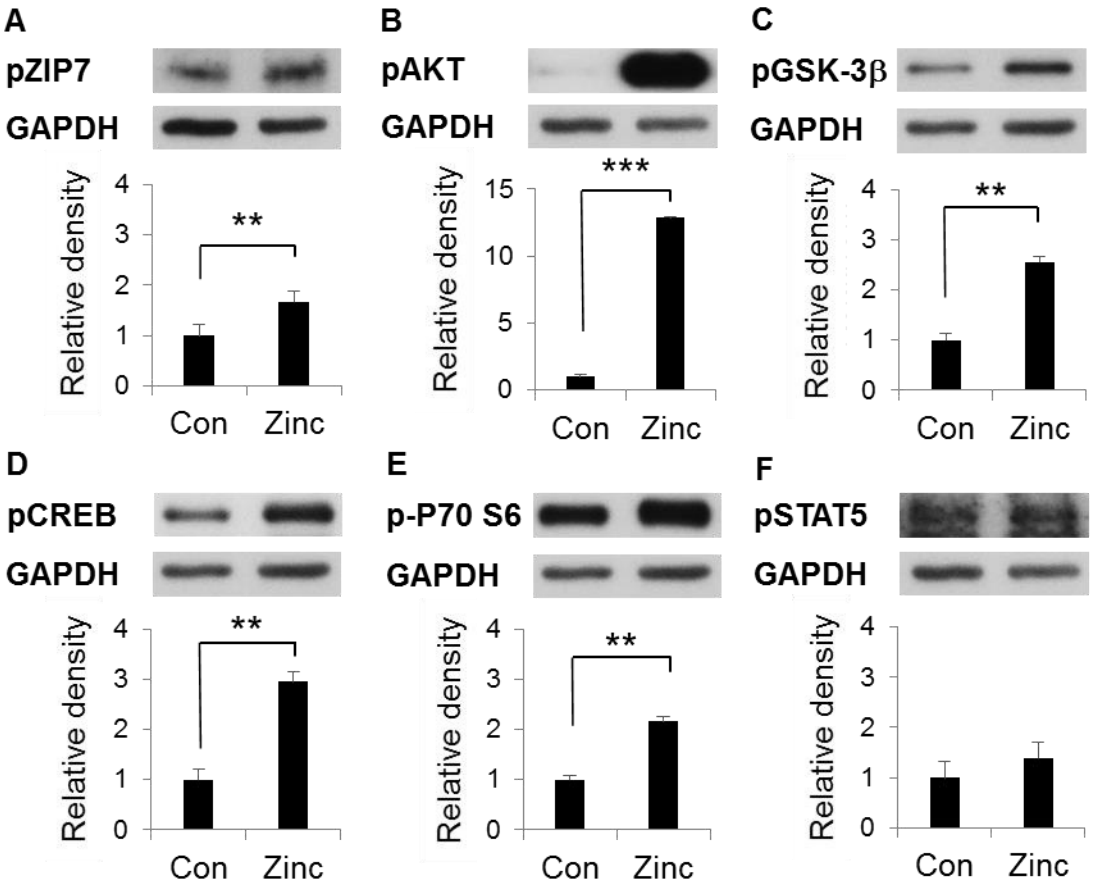

Representative blots are shown of the MCF−7 cells treated with 20 μM zinc plus 10 μM sodium pyrithione for 10 minutes, harvested, lysed, and probed for pS275/S276 ZIP7 (A), pS473 AKT (B), pS9 GSK−3β (C), pS133 CREB (D), pT421/S424 p70 S6 (E), and pS726 STAT5 (F). Densitometric data normalised to GAPDH are shown as mean ± standard error (n = 3). Statistical significance is compared between the zinc−treated cells (Zinc) and the non−treated cells (Con).
** $p < 0.01$, *** $p < 0.001$

To determine the link of ZIP7 to the phosphorylation of these kinases, Western blotting was performed in cells transfected with wild−type ZIP7. Because the increase in STAT5 phosphorylation could not be confirmed, STAT5 was not included in this experiment. Confirming the robustness of ZIP7 transfection, the pZIP7 levels were significantly increased (Fig 5.14A). Mild increases in the levels of pAKT (Fig 5.14B) and pGSK−3β (Fig 5.14C) were also displayed and were also shown to be significant, proving the relationship of AKT phosphorylation with ZIP7 (Taylor et al. 2008b) and introducing ZIP7 to the pathways involved in GSK−3β phosphorylation, in addition to ZIP6 (Hogstrand et al. 2013). No change in phosphorylation was observed for CREB (Fig 5.14D).

In contrast, a significant 1.8−fold increase in phosphorylation was detected for P70 S6 as a result of ZIP7 overexpression (Fig 5.14E), proving the ZIP7 dependency of the phosphorylation of P70 S6 and agreeing with the phospho−kinase and phospho−MAPK array data.

Figure 5.14 Confirmation of ZIP7 stimulation of kinase phosphorylation

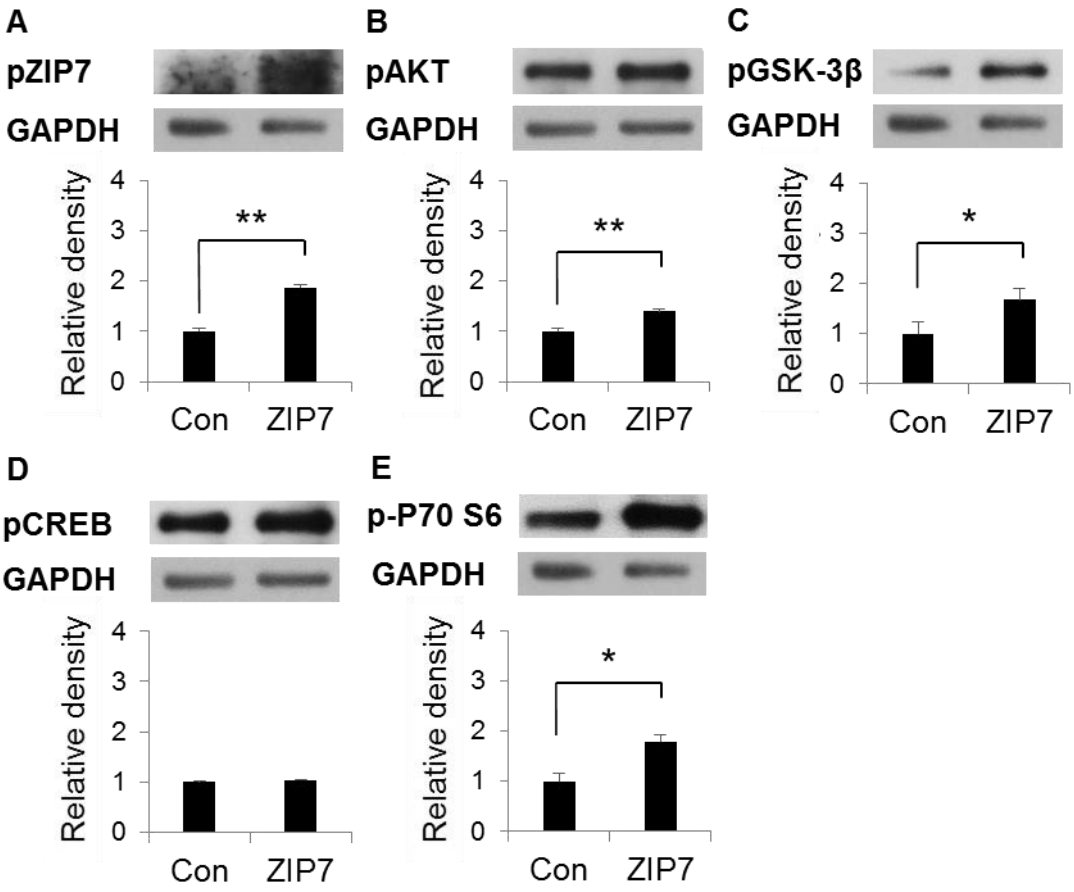

Representative blots are shown of the MCF−7 cells transfected with wild−type ZIP7 for 16−24 hours, harvested, lysed, and probed for pS275/S276 ZIP7 (A), pS473 Akt (B), pS133 CREB (C), pS9 GSK−3β (D), and pT421/S424 p70 S6 (E). Densitometric data normalised to GAPDH are shown as mean ± standard error (n = 3). Statistical significance is compared between the transfected cells (ZIP7) and the non−transfected cells (Con).
* $p < 0.05$, ** $p < 0.01$

5.4 Chapter summary

The antibody arrays demonstrated activation of various kinases, which was either dependent on or independent of ZIP7−mediated zinc mobilisation. Compatible with a previous investigation (Taylor et al. 2008b), the phospho−RTK arrays demonstrated tyrosine phosphorylation of EGFR, ErbB2, and IGF−1R as a result of ZIP7 overexpression or zinc treatment, with further discovery of tyrosine phosphorylation of ALK, EphA7, FGFR3, c−Ret, and Flt−3 (Fig. 5.1−5.4, Table 5.1). Furthermore, using the phospho−kinase arrays (Fig. 5.5−5.8, Table 5.2) and the phospho−MAPK arrays (Fig. 5.9−5.12, Table 5.3), multiple kinases were detected to be phosphorylated on specific residues as a result of zinc treatment or ZIP7 overexpression. These kinases included AKT, c−Jun, CREB, ERK1/2, GSK−3α/β, HSP27, JNK, JNK2, p38α MAPK, p70 S6, PRAS40, STAT2, STAT5a, STAT6, and WNK1. Using Western blotting, the phosphorylation of CREB (S133) and p70 S6 (T421/S424) as a result of both ZIP7 overexpression and zinc treatment was verified (Fig. 5.13 and 5.14). These data provided an insight into functional diversity of ZIP7−mediated zinc signalling through activation of a vast variety of downstream signalling pathways.

Chapter 6:
ZIP6 mechanisms in mitosis

6.1 Introduction

With the molecular link of ZIP6 to STAT3 and Snail, ZIP6 has been shown to play an indispensable role in the epithelial–mesenchymal transition (EMT) in physiological processes such as zebrafish gastrulation (Yamashita et al. 2004). Recently, ZIP6 has also been associated with EMT during invasion and metastasis of human malignant neoplasms, including breast cancer (Hogstrand et al. 2013), pancreatic cancer (Unno et al. 2009), cervical cancer (Zhao *et al.* 2007), and prostate cancer (Lue et al. 2011). Mechanistically, ZIP6–mediated zinc influx into the cytosol results in inhibitory phosphorylation of GSK–3β, nuclear accumulation of Snail, down–regulation of E–cadherin, cell rounding, and thereby EMT (Hogstrand et al. 2013) (Section 1.6.2). Importantly, mitosis is another biological process that also requires cell rounding (Thery and Bornens 2008). ZIP6 was therefore hypothesised to cause cell rounding not only in EMT, but also in mitosis.

Our group have discovered that ZIP7 is post–translationally activated by CK2–mediated phosphorylation on residues S275 and S276 (Taylor et al. 2012). According to the screening for phosphorylation sites in all ZIP channels (Section 3.3.5), multiple potential phosphorylation sites were also detected in the cytosolic loop between TM3 and TM4 of ZIP6. Interestingly, CK2 was listed as a potential kinase that phosphorylated ZIP6 on residue S478 (Sharma et al. 2014) with the highest prediction score according to different online phosphorylation site databases (Section 3.3.5; Fig. 6.1). There were also two other potential phosphorylation sites located in the same region, consisting of residues S471 (Zhou et al. 2013) and T479 (Wu et al. 2010) (Fig. 6.1). Even though CK2 was not ranked as the kinase most likely responsible for the phosphorylation on residues S471 and T146 of ZIP6, the sequences of these two residues also matched the consensus CK2–binding motif. Furthermore, residue S475 was also predicted to be phosphorylated with a sequence matching the consensus motifs of multiple kinases, including GSK–3β and CK1 (Keshava Prasad et al. 2009; Horn *et al.* 2014), yet without mass spectrometry data support. Additionally, GSK–3β was also predicted to phosphorylate residue S471 (Fig. 6.1). Interestingly, a STAT3–binding motif with sequence YESQ (residues 473–476) (Fig. 6.1) was detected in the same region as these potential phosphorylation sites.

Figure 6.1 Potential phosphorylation and STAT3-binding sites in ZIP6

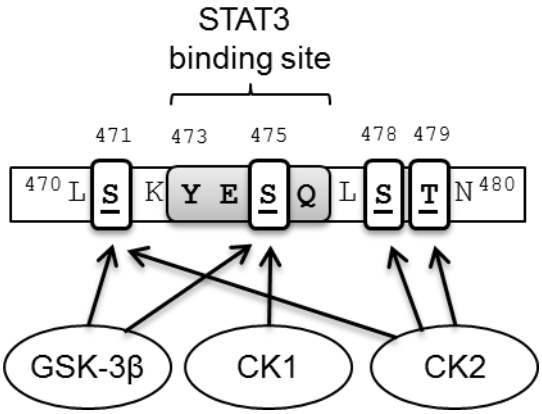

This schematic demonstrates the amino acid sequence of human ZIP6 between residues 470 and 480, which is located in the intra cytosolic loop between TM3 and TM4. Potential phosphorylation sites (S471, S475, S478, and T479) with their predicted kinases and a predicted STAT3−binding site with sequence YESQ (positions 473−476, grey box) are indicated. The phosphorylation sites have been confirmed by mass spectrometry in mammalian cells according to PhosphoNET (Kinexus Bioinformatics Corporation), PHOSIDA (Gnad *et al.* 2007), and PhosphoSitePlus databases (Hornbeck *et al.* 2012), except S475, which has been suggested according to GSK−3β and CK1 consensus motifs (Keshava Prasad et al. 2009).

The alignment of mammalian ZIP6 sequences demonstrated that both the potential phosphorylation sites and the STAT3−binding motif were virtually 100% conserved across different species (Section 3.3.6; Fig. 6.2). The only non−identical residues were two residues in mouse ZIP6 equivalent to residues E474 (in the YESQ motif) and T479, which were replaced with the complementary residues aspartate (D) and serine (S), respectively, and a residue in marmoset ZIP6 equivalent to residue S479, which were replaced with alanine (A) (Fig. 6.2). This high degree of conservation implied the importance of these sites in ZIP6 functional control (Fig. 6.2). Plausibly, ZIP6 function might be regulated by phosphorylation on these sites, and STAT3 might interact with ZIP6 not only at the transcriptional level (Yamashita et al. 2004; Hogstrand et al. 2013), but also post−translationally. Noteworthy, a preliminary investigation in our group observed an N−terminal proteolytic cleavage during early mitosis in addition to the processing at the PEST site that had previously been reported (Hogstrand et al. 2013). This second N−terminal cleavage might therefore also participate in ZIP6 post−translational control in mitosis.

Figure 6.2 Conservation of ZIP6 potential phosphorylation and STAT3−binding sites in mammals

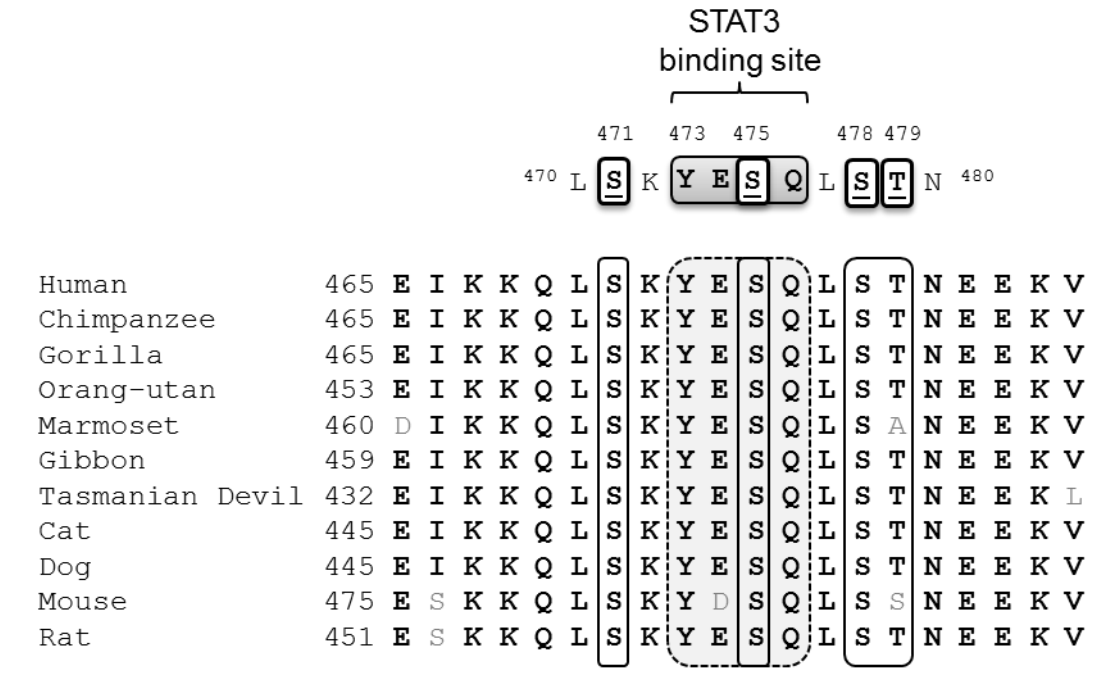

ZIP6 sequences from different mammals were aligned across the intracytosolic loop between TM3 and TM4 equivalent to residues 465 to 484 of human ZIP6. Potential phosphorylation sites (S471, S475, S478, and T479) are indicated in boxes with black solid borders, and a predicted STAT3−binding site (sequence YESQ, positions 473−476) is indicated in a grey box with a black dashed border. The phosphorylation sites have been confirmed by mass spectrometry in mammalian cells according to PhosphoNET (Kinexus Bioinformatics Corporation), PHOSIDA (Gnad et al. 2007), and PhosphoSitePlus (Hornbeck et al. 2012) databases, except S475, which has been suggested according to GSK−3β and CK1 consensus motifs (Keshava Prasad et al. 2009). Residues with at least 70% identity are shown in black bold letters, whereas residues with less than 70% identity are shown in grey regular letters.

This chapter aimed to decipher mechanisms of ZIP6 in mitosis. ZIP6 was firstly investigated for its interaction with pS727 STAT3, pStathmin and ZIP10 during mitosis. Furthermore, the protease antibody arrays were utilised to explore the proteases that were activated during mitosis, which might explain the extra cleavage that had been observed in the preliminary experiment. Additionally, phosphorylation on the potential phosphorylation sites in ZIP6 with the binding of their relevant kinases during mitosis was investigated.

6.2 Materials and methods

Site−directed mutagenesis was performed by the Mutagenex Inc in a wild−type ZIP6 construct that was contained in a pcDNA3.1/V5−His−TOPO plasmid vector to create ZIP6 mutants S471A, Y473A, S475A, S478A, and T479A, which were confirmed using DNA sequencing (Fig. 6.3). PCR was performed following bacterial transformation with the plasmid constructs to verify the presence and the orientation of the DNA insert (Fig. 6.4A). After plasmid preparation, agarose gel electrophoresis was performed to confirm the purity of the product (Fig. 6.4B), and UV spectrophotometry was performed to demonstrate the purity and concentrations of the plasmid DNA (Table 6.1).

Please refer to chapter 2 for the methods of transfection and treatments (Section 2.1), bacterial transformation and plasmid preparation (Section 2.2), immunofluorescence (Section 2.3), immunoprecipitation with Western blotting (Section 2.4), flow cytometry (Section 2.5), zinc assays (Section 2.6), and proximity ligation assays (Section 2.7). Additionally, the antibody arrays used were the human protease arrays (R&D Systems, ARY021B) (Section 2.9).

A schematic of the epitopes of different ZIP6 and ZIP10 antibodies used in chapters 6 and 7 is shown in Fig. 6.5. ZIP6 M, ZIP6 Y, and ZIP10 R antibodies bind to the N−terminus, whereas ZIP6 E−20 (Santa Cruz Biotechnology, SC−84875) and ZIP10 (Abcam, ab83947) antibodies bind to the cytosolic loop between TM3 and TM4 of the corresponding ZIP channels.

Table 6.1 Concentrations and OD260/280 ratios of ZIP6 plasmids

Plasmid	Concentration (µg/µL)	OD260/280 Ratio
ZIP6 WT	4.11	1.948
ZIP6 S471A	1.21	1.833
ZIP6 Y473A	3.29	1.982
ZIP6 S475A	0.99	1.904
ZIP6 S478A	0.62	1.938
ZIP6 T479A	1.02	1.925

Figure 6.3 DNA sequencing of ZIP6 mutant constructs

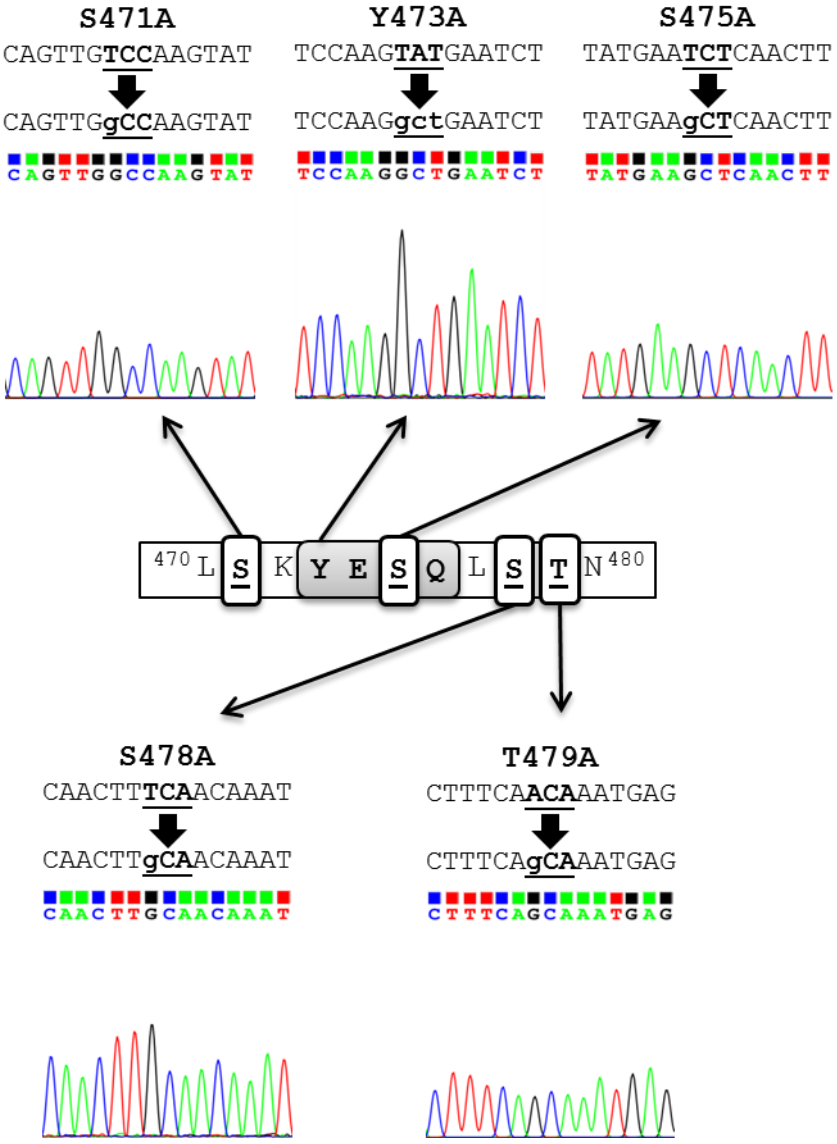

This schematic shows the DNA sequences of ZIP6 mutants that were created by the Mutagenex Inc using site−directed mutagenesis, consisting of S471A, Y473A, S475A, S478A, and T479A. The sequences reveal that the individual serine (codon TCA, TCC, or TCT), threonine (codon ACA), and tyrosine (codon TAT) residues at the potential phosphorylation and STAT3−binding sites were correctly substituted for alanine (codon GCA, GCC, or GCT).

Figure 6.4 Preparation of ZIP6 plasmids

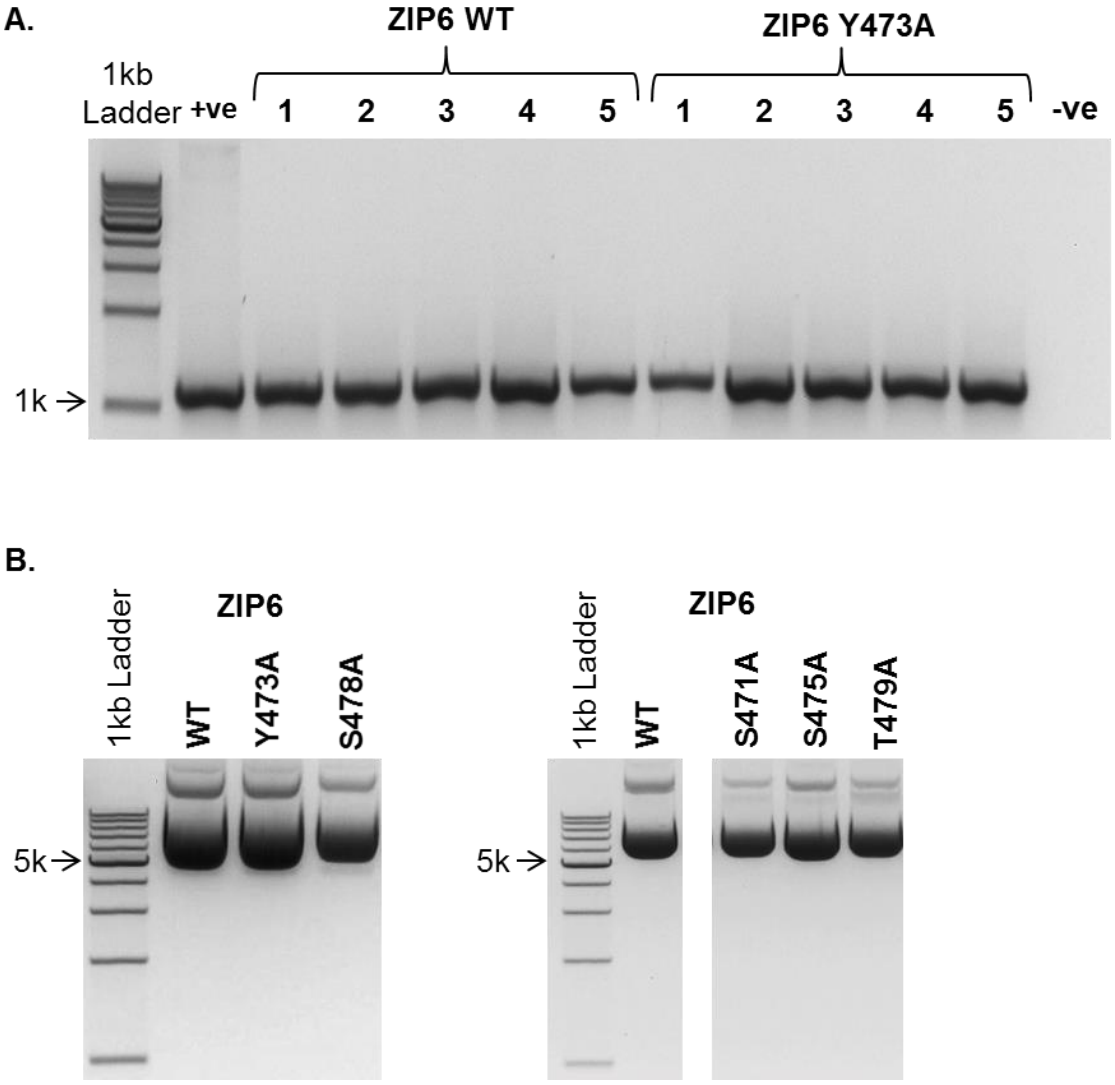

A. JM109 E. coli competent cells were transformed with pcDNA3.1/V5-His-TOPO containing DNAs of wild−type ZIP6 and a ZIP6 Y473A mutant. The presence of DNA inserts and their orientation in plasmid vector were verified by PCR using a specific ZIP6 forward primer and a BGH reverse primer. The PCR products were separated by 1% agarose gel electrophoresis. The result reveals a band of about 1100 bp (expected size = 1170 bp), approximately the same size as the positive control. A clone of each construct was selected for plasmid preparation.

B. The plasmids of wild−type ZIP6 and ZIP6 mutants (Y473A, S478A, S471A, S479A, and T479A) were prepared using the EndoFree Plasmid Maxi Kit (Qiagen). The plasmid DNAs were analysed with 1% agarose gel electrophoresis, which shows a strong band of between 5000-7000 bp (expected size = 6283 bp).

Figure 6.5 Locations of ZIP6 and ZIP10 antibody epitopes

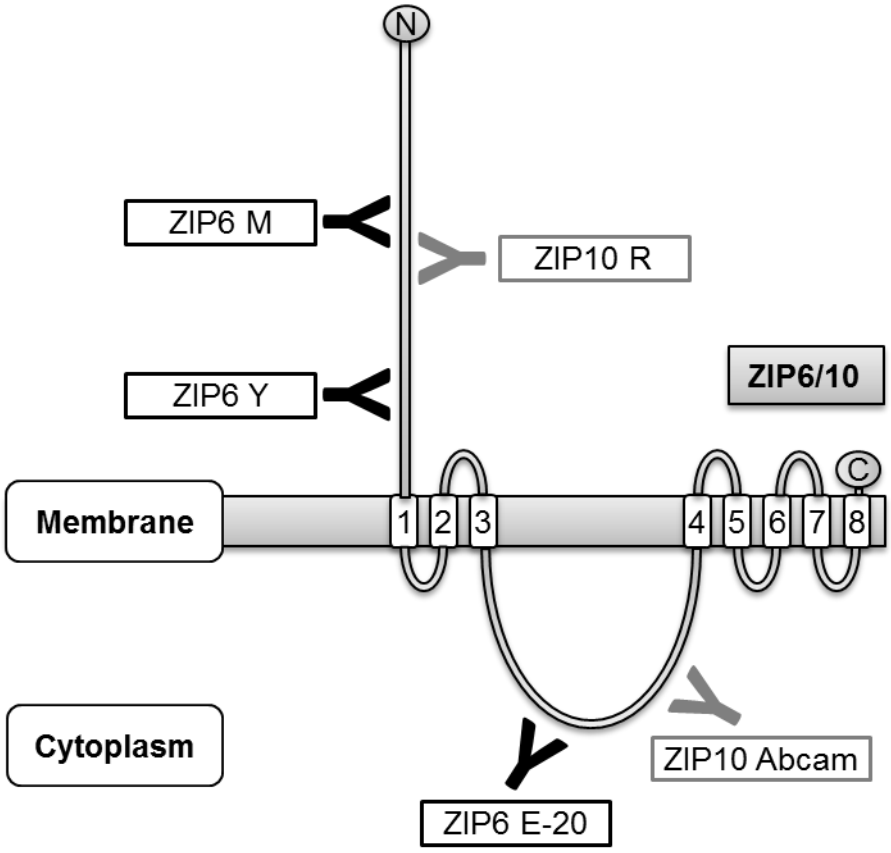

This schematic demonstrates the predicted structure of ZIP6 or ZIP10, according to a computational analysis of their sequences (Taylor and Nicholson 2003). ZIP6 M/Y and ZIP10 R antibodies, which were generated by the Biogenes GmbH Company, bind to the extracytosolic N−terminus of ZIP6 and ZIP10, respectively. On the contrary, ZIP6 E−20 (Santa Cruz Biotechnology, SC−84875) and ZIP10 (Abcam, ab83947) antibodies bind to the cytosolic loop between TM3 and TM4 of ZIP6 and ZIP10, respectively.

6.3 Results and discussion

6.3.1 ZIP6 mutants are robustly transfected

To verify the purified plasmids of ZIP6 constructs, consisting of wild−type ZIP6 and ZIP6 mutants (S471A, Y473A S475A, S478A, and T479A), MCF−7 cells were transfected with these constructs for 16 hours. The transfection was performed in the presence of butyrate, which activates the CMV promoter (Choi *et al.* 2005) and thereby enhances expression of the ZIP6 recombinant protein. Immunofluorescence was performed using a V5 antibody to detect the recombinant protein, which all had a C−terminal V5 tag. Approximately 50 transfected cells were seen on each coverslip (Fig. 6.6A). This notably low

expression of the recombinant ZIP6 protein has been constantly observed and attributed to the presence of a PEST site in the N−terminus and numerous pairs of consecutive arginine or lysine throughout the ZIP6 sequence, which predispose ZIP6 to proteolytic degradation (Taylor et al. 2003). Additionally, the V5−positive cells demonstrated an ER−like staining pattern (Fig. 6.6B), highlighting the pro−protein form of ZIP6 in the ER, which is much more commonly detected than the rare plasma membrane−located ZIP6 (Hogstrand et al. 2013). The similarity between the staining pattern of the wild−type and the mutant constructs of ZIP6 suggested that there was no change in ZIP6 processing caused by the mutations.

6.3.2 ZIP6 is increased and mediates zinc influx in mitosis

ZIP6 pro−protein in the ER was shown to be N−terminally cleaved before its relocation to the plasma membrane (Hogstrand et al. 2013). According to this previous study, this cleavage was concluded from different cellular localisation of ZIP6 detected using immunofluorescence and appearance of different bands on a Western blot when using different ZIP6 antibodies, consisting of ZIP6 M, ZIP6 Y, and ZIP6 E−20 antibodies. The in−house made ZIP6 M and ZIP6 Y antibodies target the N−terminus of ZIP6 at residues 93–107 and residues 238–254, respectively, whereas the commercially available ZIP6 E−20 antibody targets the cytosolic loop between TM3 and TM4 of ZIP6 at residues 500–550 (Table 2.1, Fig. 6.5). Using immunofluorescence, the ZIP6 M antibody stained only the ER−located ZIP6 pro−protein, whereas the ZIP6 Y antibody also detected the plasma membrane−located ZIP6 (Hogstrand et al. 2013), suggesting the cleavage between the epitopes of these two N−terminal antibodies. The cleavage was confirmed by a Western blot showing ZIP6 bands at 103 kDa (full−length ZIP6, detected by all the three antibodies), 68 kDa (N−terminally cleaved ZIP6, detected by the ZIP6 Y and the ZIP6 E−20 antibodies), and 35 kDa (an N−terminal fragment product of the cleavage, detected only by the ZIP6 M antibody).

Figure 6.6 A robust transfection of ZIP6 mutants

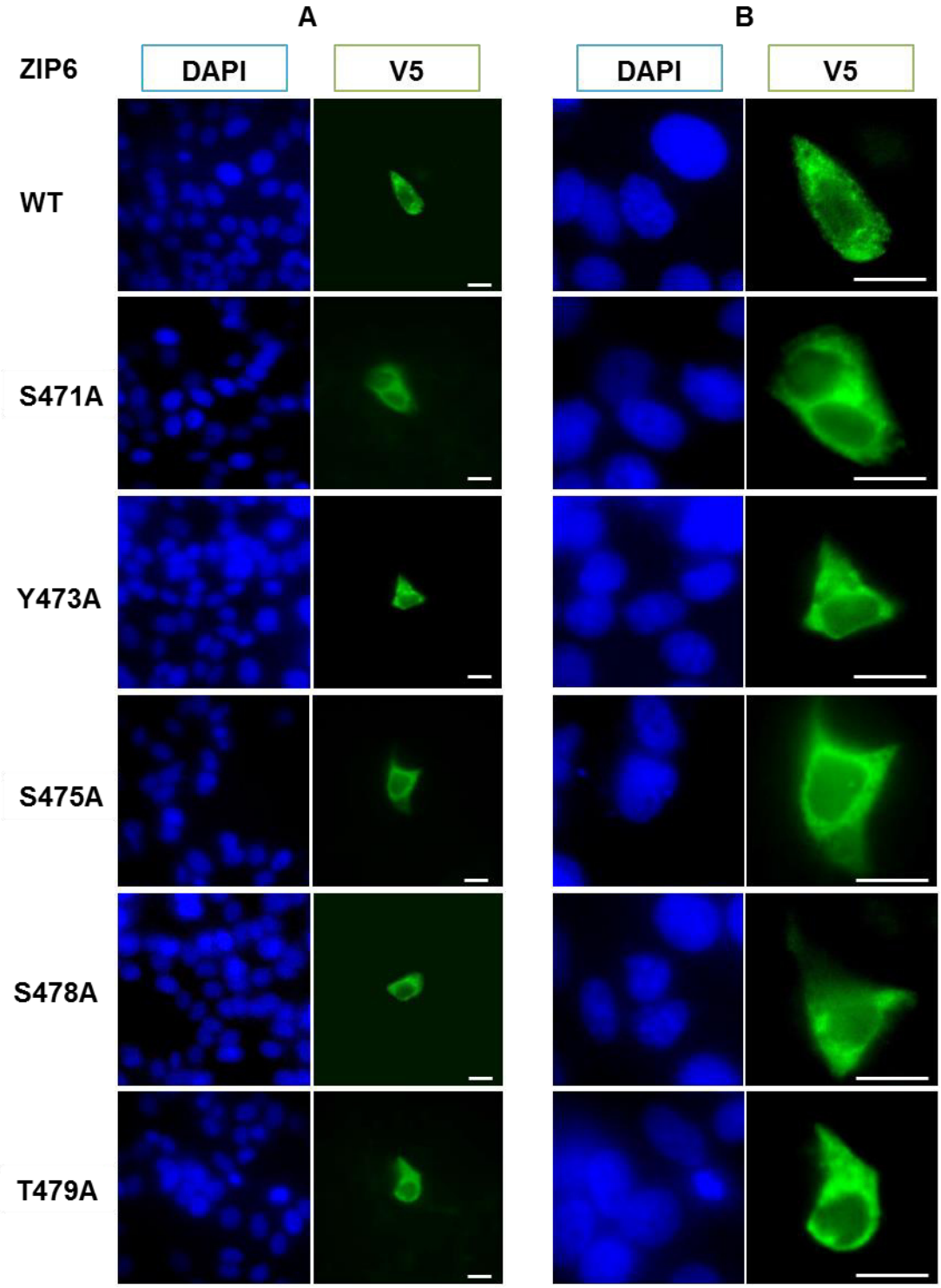

MCF−7 cells were transfected with wild−type ZIP6 and ZIP6 mutants (S471A, Y473A, S475A, S478A, and T479A) in the presence of butyrate for 16 hours. Immunofluorescence was performed using a rabbit V5 antibody, which was conjugated to Alexa Fluor 488 (green), with DAPI nuclear staining. Representative microscopic views captured with a 63x magnification lens (A) show one or two transfected cells per high power field, with a total of approximately 50 V5−positive cells in a coverslip for both the ZIP6 wild−type and mutant constructs. Closer views of the transfected cells (B) reveal an ER−like staining pattern, signifying the inactive form of ZIP6 (Hogstrand et al. 2013).
Scale bar, 25 μm.

To observe protein expression of ZIP6 in mitotic cells, immunofluorescence using the ZIP6 Y antibody was performed in MCF−7 cells treated with nocodazole for 20 hours. Noteworthy, nocodazole stabilises microtubule, inhibits microtubule polymerisation, and causes cell cycle arrest in early mitosis, thereby enriching the mitotic cell population (Vasquez *et al.* 1997; Rosner *et al.* 2013). A representative microscopic view demonstrated three mitotic cells, which were in prophase as judged by DAPI (blue, indicated by white arrows) (Fig. 6.7). ZIP6 was seen to be increased in these cells when compared to the adjacent non−mitotic cells in the same field (Fig. 6.7), suggesting that ZIP6 protein expression is enhanced during mitosis.

Figure 6.7 Increased ZIP6 protein expression in mitotic cells

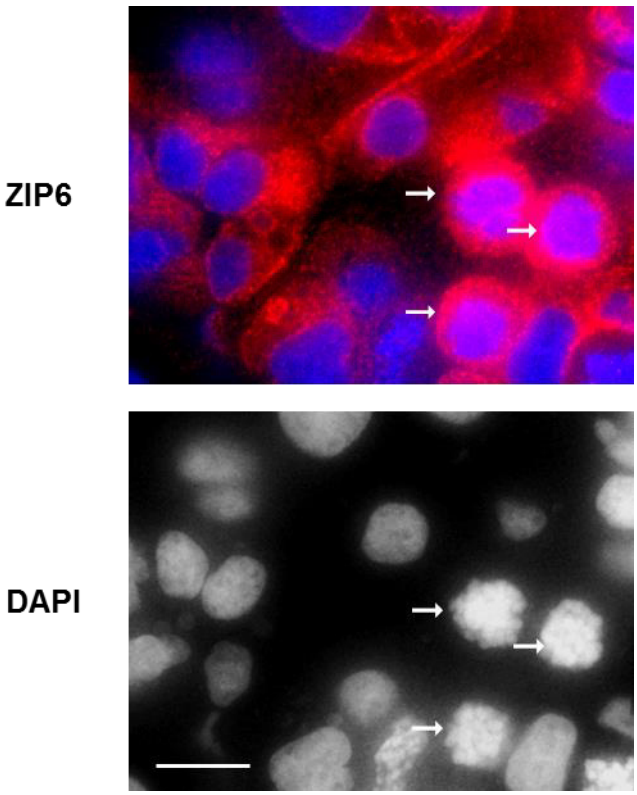

MCF−7 cells were treated with 100 nM nocodazole for 20 hours. Immunofluorescence was performed using the ZIP6 Y antibody, which was conjugated to Alexa Fluor 594 (red), with DAPI nuclear staining. Mitotic cells are indicated by white arrows. A representative microscopic view captured with a 63x magnification lens is shown.
Scale bar, 25 µm.

Noteworthy, no classic plasma membrane staining pattern was observed in mitotic cells (Fig. 6.7). Given that the ZIP6 Y antibody stains both the processed ZIP6 on the plasma membrane and the ZIP6 pro-protein in the ER (Hogstrand et al. 2013), this unexpected staining pattern might be due to the abundance of the newly-produced ZIP6 pro-protein in the ER, which obscured the staining of the plasma membrane-located ZIP6. Moreover, a conventional epifluorescence microscope, which was employed in this experiment, was not capable of eliminating out-of-focus fluorescence signals from the planes above and below the focal planes. A confocal microscope might therefore be required for the detection of the plasma membrane staining pattern of the ZIP6 protein.

To investigate ZIP6 processing in mitosis using Western blotting, different protein bands were firstly demonstrated and compared to the ZIP6 bands that have been reported in the previous study on ZIP6 processing (Hogstrand et al. 2013). MCF-7 cells were transfected with wild-type ZIP6 for 16 hours, and Western blotting was performed using a V5 antibody. Given that ZIP6 is enriched in the loosely-attached mitotic cells (Fig. 6.7), non-adherent cells in the medium were also collected and pooled together with adherent cells at the cell harvest. Unless otherwise specified, pooled samples were used in all the experiments for ZIP6 except immunofluorescence. Noteworthy, the pcDNA3.1/V5-His-TOPO plasmid vector in which the wild-type ZIP6 DNA was inserted contains a C-terminal V5-His tag, which is 5 kDa in size (Elomaa *et al.* 2001). The size of a recombinant ZIP6 band was therefore estimated to be 5 kDa larger than the corresponding band of endogenous ZIP6. Four bands of the ZIP6-V5 protein were present on the Western blot: 108 kDa, 73 kDa, 48 kDa, and 42 kDa (Fig. 6.8A). The 108 kDa and 73 kDa bands were consistent with the 103 kDa and 68 kDa bands of the endogenous ZIP6, which represent the whole ZIP6 and the N-terminally cleaved ZIP6, respectively (Fig. 6.8B). In the previous study (Hogstrand et al. 2013), two bands of the endogenous ZIP6 corresponding to the 48 kDa and 42 kDa bands of the recombinant ZIP6 were also present on a Western blot when using the ZIP6 E-20 antibody and were considered non-specific.

Figure 6.8 Protein bands of ZIP6

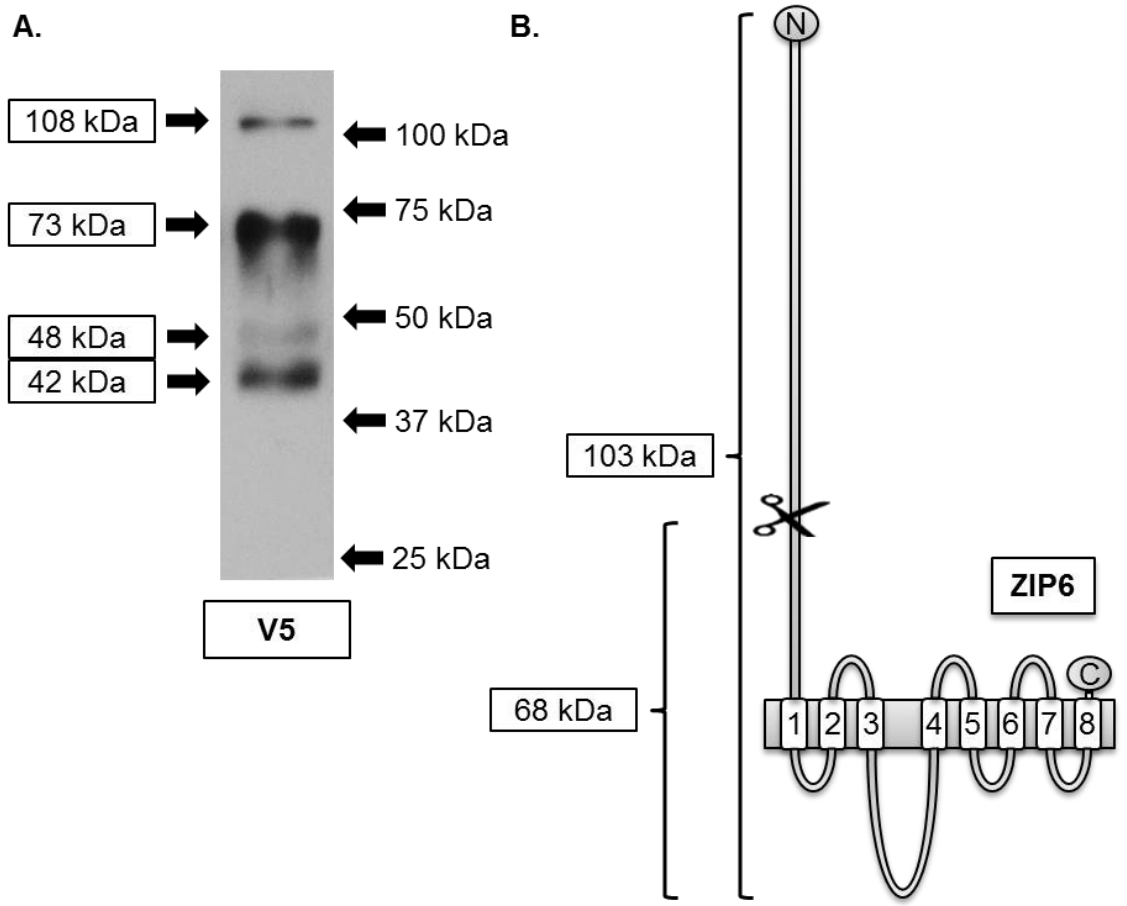

MCF−7 cells were transfected with wild−type ZIP6 in the presence of butyrate for 16 hours. Immunoblotting was performed in pooled samples of the adherent and the non−adherent cells using a V5 antibody. Protein bands of the recombinant ZIP6 are present at 108 kDa, 73 kDa, 48 kDa, and 42 kDa (A). Compared to the schematic of ZIP6 processing (B) according to a previous study in our group (Hogstrand et al. 2013), the 108 kDa and 73 kDa bands of the recombinant ZIP6 correspond to the whole ZIP6 (103 kDa) and the processed/activated ZIP6 (68 kDa), respectively.

To confirm the increase in endogenous ZIP6 during mitosis, Western blotting using the ZIP6 E−20 antibody was performed in MCF−7 cells that had been treated with nododazole for 20 hours. In contrast to the previous study that showed multiple bands when using the ZIP6 E−20 antibody (Hogstrand et al. 2013), only a clean band at 68 kDa was detected on the blot (Fig. 6.9), suggesting predominance of the processed ZIP6 protein in these samples. Importantly, density of the band at 68 kDa was much increased in the nocodazole−treated cells when compared to the control (Fig. 6.9). Densitometric data normalised to GAPDH demonstrated that the increase was 2.5−fold and statistically significant (Fig. 6.9). These data revealed a significant increase in the processed ZIP6 during mitosis.

Figure 6.9 Increased ZIP6 band at 68 kDa in nocodazole−treated cells

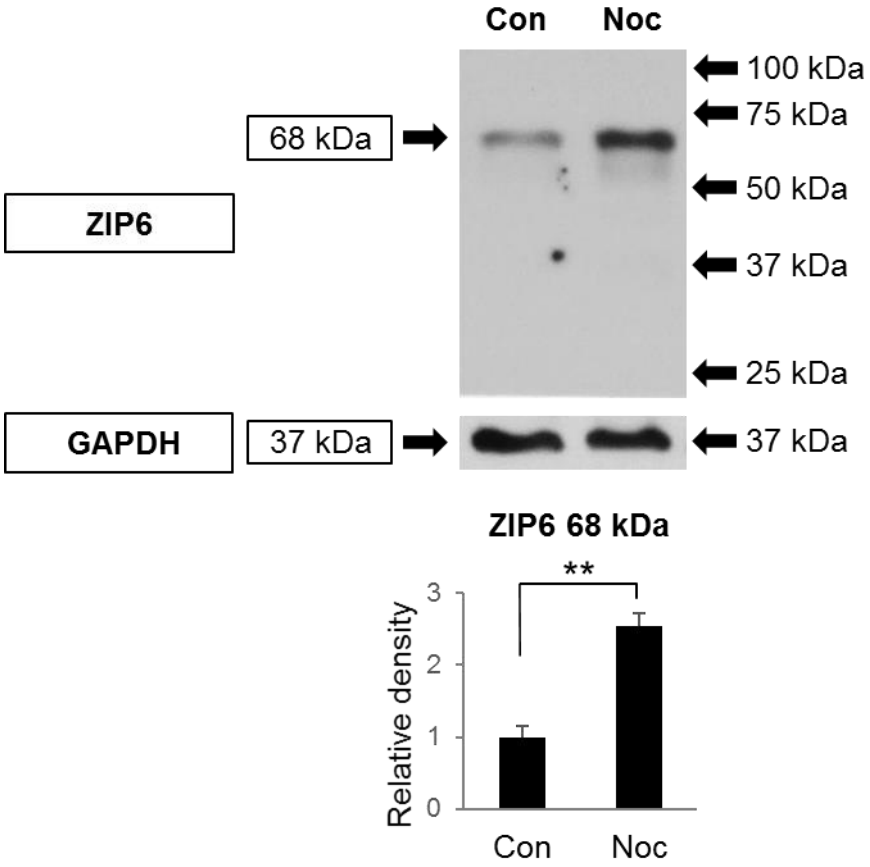

MCF−7 cells were treated with 100 nM nocodazole for 20 hours. Immunoblotting was performed using the ZIP6 E−20 antibody. Protein bands of ZIP6 E−20 at 68 kDa and GAPDH at 37 kDa are demonstrated as a representative result of 3 independent experiments. Densitometric data normalised to GAPDH are demonstrated in a bar graph as mean ± standard error (n = 3). Statistical significance is compared between the nocodazole−treated cells and the control without treatment.
** $p < 0.01$.

In order to confirm this Western blotting result, FACS analysis was performed in MCF−7 cells that had been treated with nocodazole for 20 hours, using ZIP6 E−20 and pS10 histone H3 antibodies. Noteworthy, histone H3 is N−terminally phosphorylated on residue S10 in early prophase (Sauve *et al.* 1999). This phosphorylation is maximally increased in metaphase, and decreased to the basal non−mitotic levels in telophase (Sauve et al. 1999). Therefore, pS10 histone H3 was used as a mitotic marker in this experiment. The cells in each sample were gated and divided into two groups: the pS10 histone H3−negative (non−mitotic) cells and the pS10 histone H3−positive (mitotic) cells. The fluorescence intensity of ZIP6 was separately determined in each group. The overlay histogram demonstrated a shift of the ZIP6 logarithmic

fluorescence intensity curve in the mitotic cells to the right, when compared to the non−mitotic cells (Fig. 6.10). The calculation of the mean fluorescence for each group demonstrated a significant 2−fold increase in ZIP6 intensity in the mitotic cells, compared to the non−mitotic cells in the same samples (Fig. 6.10). These data established the increased protein expression of ZIP6 during mitosis.

Figure 6.10 Increased ZIP6 levels in mitotic cells detected by FACS

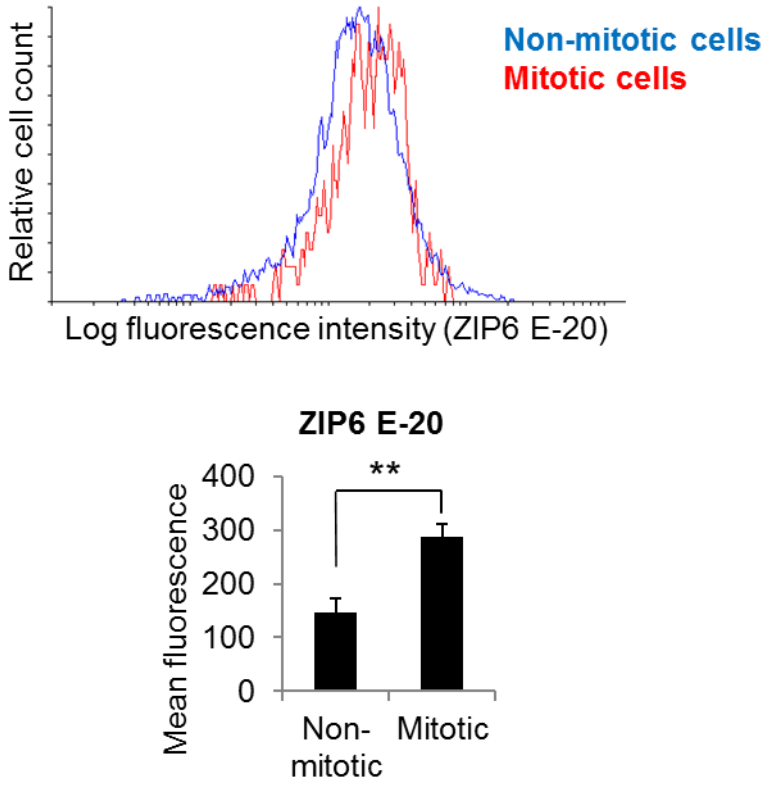

MCF−7 cells were treated with 100 nM nocodazole for 20 hours, and pooled samples of the adherent and the non−adherent cells were immunostained with ZIP6 E−20 and mouse pS10 Histone H3 antibodies, which were conjugated to Alexa Fluor 647 and 488, respectively. FACS analysis was performed. The cells were gated and divided into 2 groups: the cells that were positive for pS10 Histone H3 (mitotic cells) and the cells that were negative for pS10 Histone H3 (non−mitotic cells). Data are shown in an overlay histogram. The mean fluorescence intensity of ZIP6 E−20 for each population is presented in a bar graph as mean ± standard error (n = 3). Statistical significance is compared between the mitotic and the non−mitotic cells.
** $p < 0.01$.

To associate the increased ZIP6 in mitosis with its zinc-importing function, FACS analysis was performed in live MCF-7 cells that had been treated with nocodazole for 20 hours, and loaded with zinc-sensitive fluorescent dye Fluozin-3. The curve of the logarithmic fluorescent intensity of Fluozin-3 in the nocodazole-treated cells was shifted to the right when compared to the control (Fig. 6.11). The analysis of the mean fluorescent intensity revealed a 15.8% increase in zinc levels in the nocodazole-treated cells compared to the control, which was shown to be statistically significant (Fig. 6.11). The discrepancy between the 100% increase in ZIP6 levels (Fig. 6.10) and the only 15.8% increase in zinc levels might be because the whole cell population in the samples, both mitotic and non-mitotic, was measured in the Fluozin-3 assay (Fig. 6.11), whereas the mitotic cells were specifically examined in the ZIP6 measurement (Fig. 6.10).

Figure 6.11 Increased Fluozin-3 fluorescence in nocodazole-treated cells

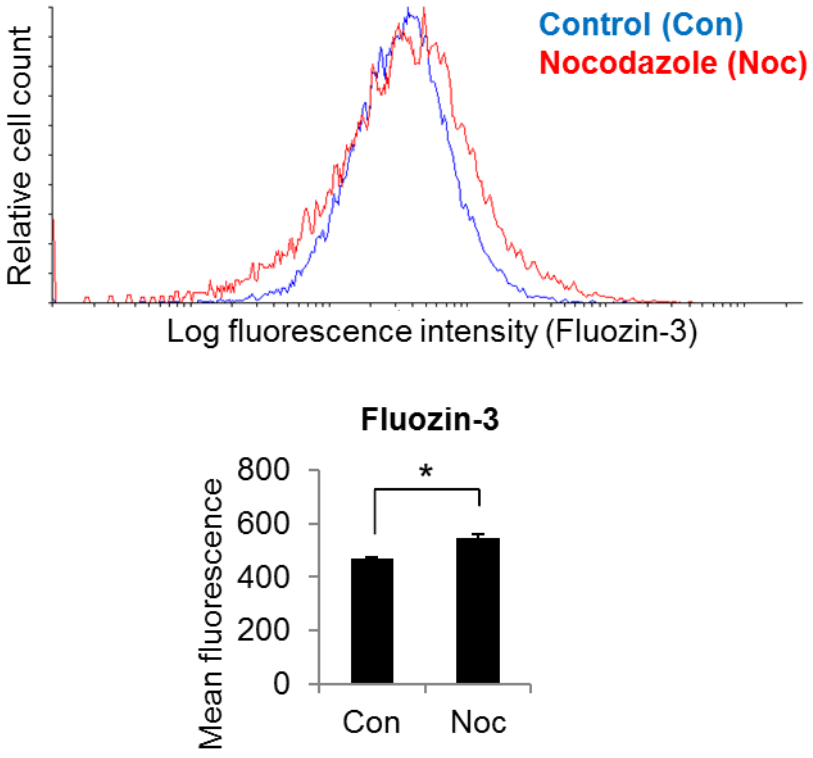

MCF-7 cells were treated with 100 nM nocodazole for 20 hours, and pooled samples of the adherent and the non-adherent cells were loaded with Fluozin-3. FACS analysis was performed. Data are shown in an overlay histogram. The mean fluorescence intensity of Fluozin-3 for each population is presented in a bar graph as mean ± standard error (n = 3). Statistical significance is compared between the nocodazole-treated cells (Noc) and the control without treatment (Con).
* $p < 0.05$.

To measure zinc levels precisely in the mitotic cells and contrast them to the non−mitotic cell population, a mitotic shake−off was performed (Izawa and Pines 2015) (Section 2.3). This technique allows a separate collection of the non−adherent or floating cells, which are predominantly mitotic, and the adherent cells, which are predominantly non−mitotic, from the same cell population, exploiting the loose adherence property of the mitotic cells. The abundance of mitotic cells in the non−adherent cell population was determined by cell cycle analysis using propidium iodide nuclear staining and FACS. The histogram of the adherent cells showed a high 2n peak (the left peak), which represented the cells in the G0/G1 phase, and a shorter 4n peak (the right peak), which represented the cells in the G2/M phase (Fig. 6.12A). In contrast, the non−adherent cells demonstrated a low 2n peak and a much taller 4n peak (Fig. 6.12A), suggesting predominance of the G2/M cell population. The analysis using the Watson Pragmatic algorithm showed that 90% of the non−adherent cells were in the G2/M phase, whereas only 48% of the adherent cells were in the G2/M phase (Fig. 6.12A). The difference in the percentages of the G2/M population was statistically significant (Fig. 6.12A).

To confirm that the majority of the non−adherent cells were mitotic, the adherent and the non−adherent cells were separately collected and stained with Hoechst 33342, a nucleic acid stain. The histogram of the adherent cells showed a prominent 2n peak with no identifiable 4n peak, whereas the histogram of the non−adherent cells showed a small 2n peak with a prominent 4n peak (Fig. 6.12B). The pattern of the histograms did not fit an algorithm for cell cycle analysis, and percentages of the G2/M cells could therefore not be determined. To compare the G2/M population between the adherent and non−adherent cells, the cells were gated and determined for percentages of the cells with high DNA content, which were in the area equivalent to the 4n peak of the non−adherent cells (Fig. 6.12B). It was assumed that the high DNA content group were equivalent to the cells in the G2/M phase and the low DNA content group were equivalent to the cells in the G0/G1 phase. The result revealed that 79% of the non−adherent cells had high DNA content, compared to 19% of the adherent cells with high DNA content (Fig. 6.12B). These findings suggested that the non−adherent cells were predominantly in the G2/M phase, whereas the adherent cells were predominantly in the G0, G1 or S phases.

Figure 6.12 Increased G2/M population in non−adherent cells

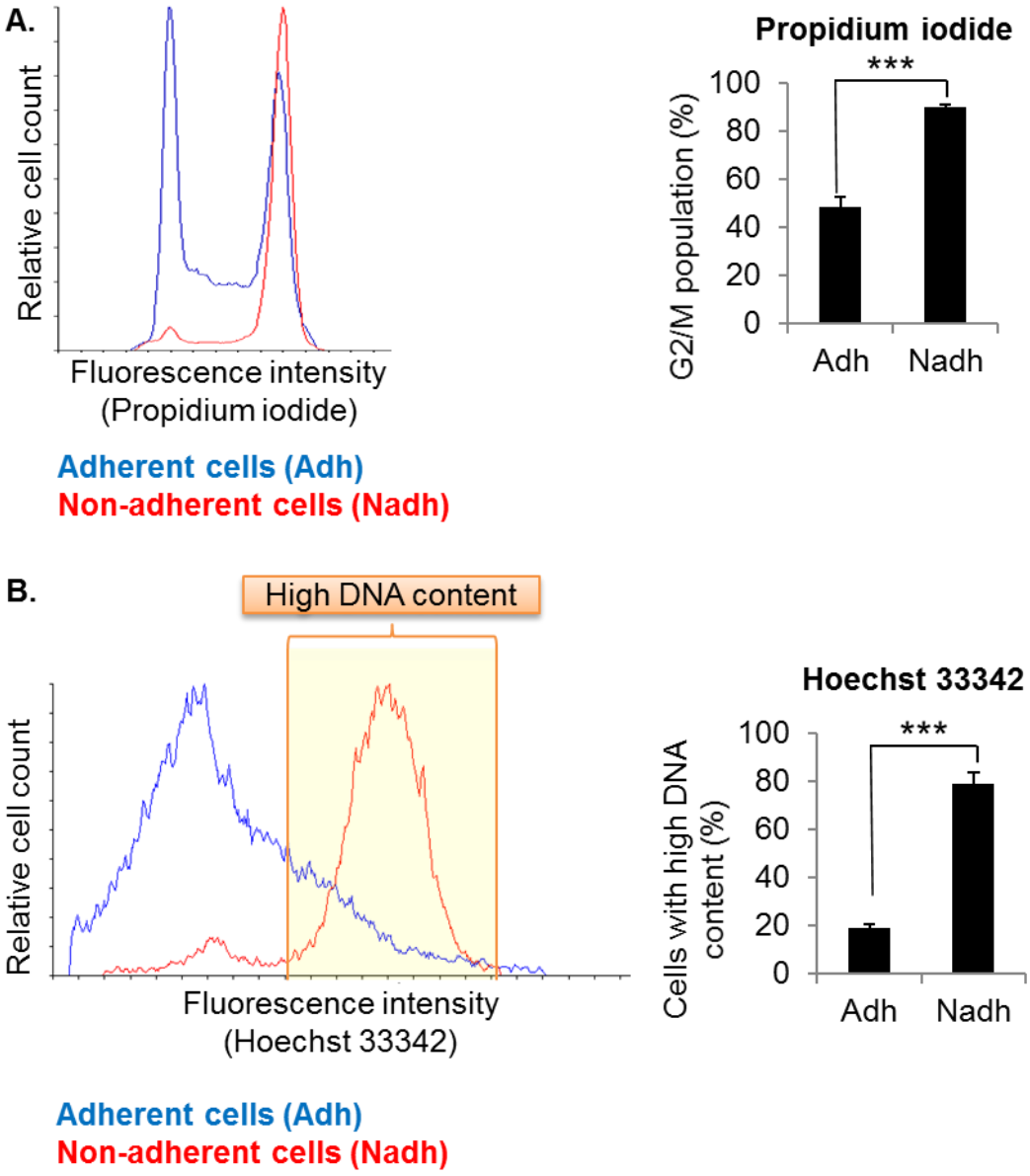

A. MCF−7 cells were treated with 100 nM nocodazole for 20 hours. Adherent (Adh) and non−adherent (NAdh) cells were separately collected using the mitotic shake−off technique. The nuclei were stained with propidium iodide, and cell cycle analysis was performed using FACS. Data are shown in an overlay histogram. The calculated G2/M population (%) is demonstrated in a bar graph as mean ± standard error (n = 3). Statistical significance is compared between the adherent and the non−adherent cells. *** $p < 0.001$.

B. MCF−7 cells were treated with 100 nM nocodazole for 20 hours. Adherent (Adh) and non−adherent (NAdh) cells were separately collected using the mitotic shake−off technique. The nuclei were stained with Hoechst 33342, a nucleic acid stain. FACS analysis was performed. Data are shown in an overlay histogram. The cells were gated and divided into a high DNA content group and a low DNA content group. The percentage of the cells with high DNA content, which are assumed to be equivalent to the G2/M population, is demonstrated in a bar graph as mean ± standard error (n = 3). Statistical significance is compared between the adherent and the non−adherent cells. *** $p < 0.001$.

To compare zinc levels between non−adherent cells and adherent cells, the cells were separately collected and loaded with Fluozin−3. The overlay histogram revealed that the Fluozin−3 logarithmic fluorescence intensity curve of the adherent cells was dramatically shifted to the right (Fig. 6.13), suggesting an increase in zinc levels in the non−adherent cells. The calculation of the mean fluorescence intensity revealed a 3.2−fold increase in the non−adherent cells compared to the adherent cells, which was shown to be statistically significant (Fig. 6.13). These data confirmed the significant increase of zinc levels in mitosis.

Figure 6.13 Increased Fluozin−3 fluorescence in non−adherent cells

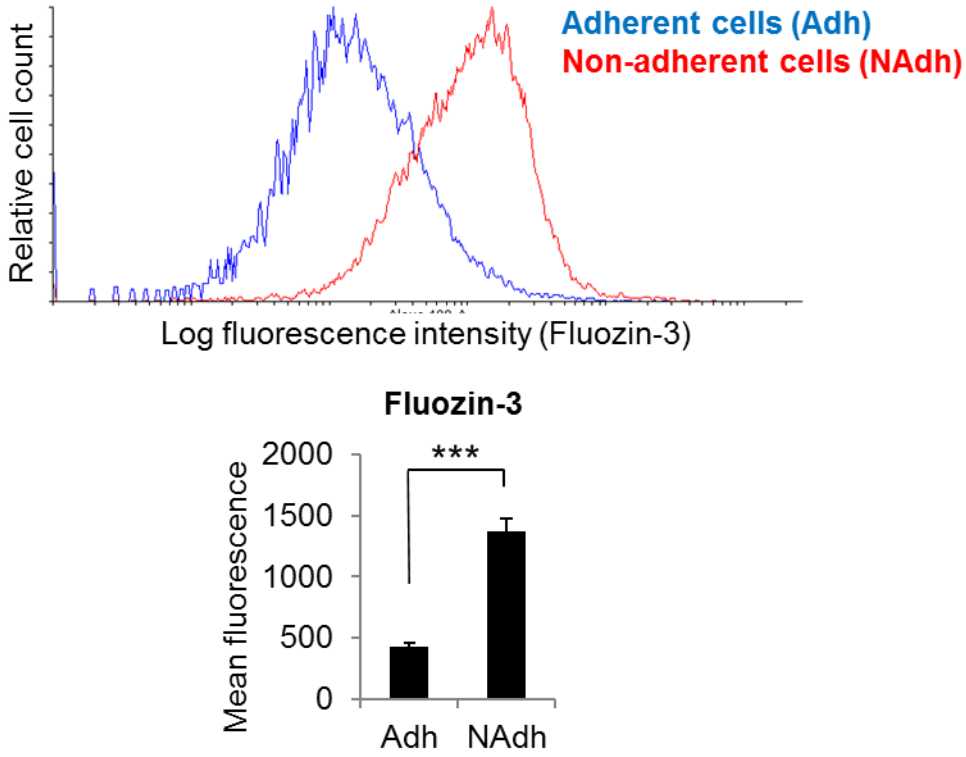

MCF−7 cells were treated with 100 nM nocodazole for 20 hours. Adherent (Adh) and non−adherent (NAdh) cells were separately collected using mitotic shake−off technique. The cells were loaded with Fluozin−3. FACS analysis was performed. Data are shown in an overlay histogram. The mean fluorescence intensity is demonstrated in a bar graph as mean ± standard error (n = 3). Statistical significance is compared between the adherent and the non−adherent cells.
*** $p < 0.001$.

To confirm the Fluozin−3 assay analysed by FACS and to determine the increase in zinc levels in different stages of mitosis, fluorescence microscopy was performed in cells loaded with Fluozin−3. Imaging demonstrated an increase in Fluozin−3 levels in mitotic cells compared to the adjacent non−mitotic cells in the same field (Fig. 6.14). The stages of mitosis were judged by morphology of the DAPI−stained nuclei. The corrected total cell fluorescence was individually calculated in the cells in each mitotic stage. Compared to the non−mitotic (interphase) cells, the zinc levels were significantly increased 5.1−fold, 3.9−fold, and 6.0−fold in prophase, metaphase, and anaphase, respectively (Fig. 6.14).

Figure 6.14 Increased Fluozin−3 fluorescence in different mitotic stages

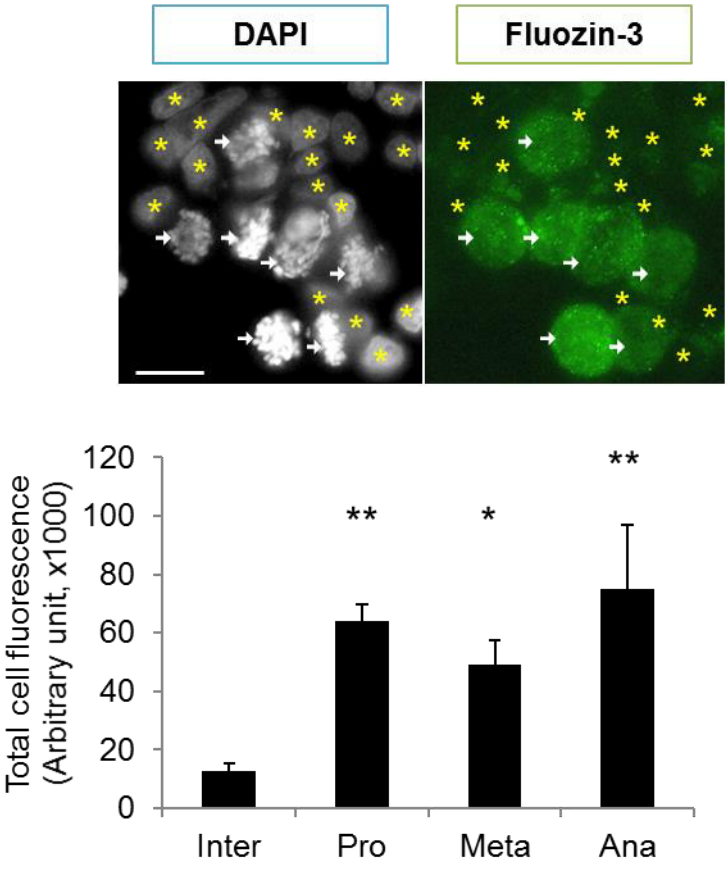

MCF−7 cells were treated with 100 nM nocodazole for 20 hours, loaded with Fluozin−3 (green), and fixed in 4% formaldehyde. The nuclei were stained with DAPI. A representative microscopic view captured with 63x magnification lens is shown. Mitotic cells are indicated by white arrows, and non−mitotic cells are indicated by yellow stars. Different cell cycle stages, including interphase (Inter), prophase (Pro), metaphase (Meta) and anaphase (Ana), were judged according to nuclear morphology. The corrected total cell fluorescence calculated from multiple images using ImageJ software (Schneider et al. 2012) is shown in a bar graph as mean ± standard error. Statistical significance is compared to the interphase (non−mitotic) cells.
Scale bar, 25 µm. * $p < 0.05$, ** $p < 0.01$.

Interestingly, the increases were still detected in this fluorescence microscopy experiment (Fig. 6.14), regardless of the fact that the cells were fixed in 4% formaldehyde, which might theoretically diminish the signals due to the potential chemically-induced crosslinking of the fluorescent dye. Noteworthy, telophase was excluded from the analysis due to the difficulty in distinguishing between telophase cells and interphase cells. Collectively, these data demonstrated that zinc levels were significantly increased throughout the mitotic process, compatible with the significant increase in protein expression of ZIP6 during mitosis.

6.3.3 pS727 STAT3 binds to ZIP6 on Y473 and to pStathmin in mitosis

Zinc has been reported to bind to STAT3 and inhibit the transcriptional activity of STAT3 by reducing its tyrosine-phosphorylated form, pY705 STAT3 (Kitabayashi et al. 2010). A preliminary work in our group using Western blotting demonstrated that zinc not only reduced the tyrosine-phosphorylated transcriptionally-active form of STAT3, but also enhanced serine phosphorylation of STAT3 on residue S727 (Nimmanon T *et al.*, manuscript in preparation), consistent with a previous report of an inverse relationship between pY705 STAT3 and pS727 STAT3 (Decker and Kovarik 2000). Our findings of enhanced ZIP6-mediated zinc influx during mitosis therefore additionally explained the predominance of pS727 STAT3 in mitotic cells, which was also observed in all stages of mitosis in both normal and cancer cells (Nimmanon T et al., manuscript in preparation). Noteworthy, cyclin-dependent kinase 1-induced pS727 STAT3 is required for maintenance of the M phase in nocodazole-treated cells (Shi et al. 2006). However, the mechanism of pS727 STAT3 in mitosis is still unknown.

To decipher any post-translational relationship of STAT3, specifically pS727 STAT3, with ZIP6, immunoprecipitation was performed using a V5 antibody in cells transfected with wild-type ZIP6. Normal rabbit IgG immunoprecipitation was used as a negative control. To ensure the presence of loosely-attached mitotic cells in the samples, non-adherent cells were also collected and pooled together with adherent cells. Western blotting using V5 and pS727 STAT3 antibodies in the V5-immunoprecipitated samples demonstrated 108 kDa and 73 kDa bands of the recombinant ZIP6 and a

88 kDa band of pS727 STAT3 (Fig. 6.15), confirming the robustness of the immunoprecipitation and the binding of pS727 STAT3 to the recombinant ZIP6, respectively. The binding was validated by the absence of either a ZIP6 or a pS727 STAT3 band in the IgG control (Fig. 6.15). Noteworthy, a strong band at 50 kDa, which appeared on the blot when probed for either V5 or pS727 STAT3, was consistent with the immunoglobulin heavy chain.

Figure 6.15 pS727 STAT3 binding to ZIP6

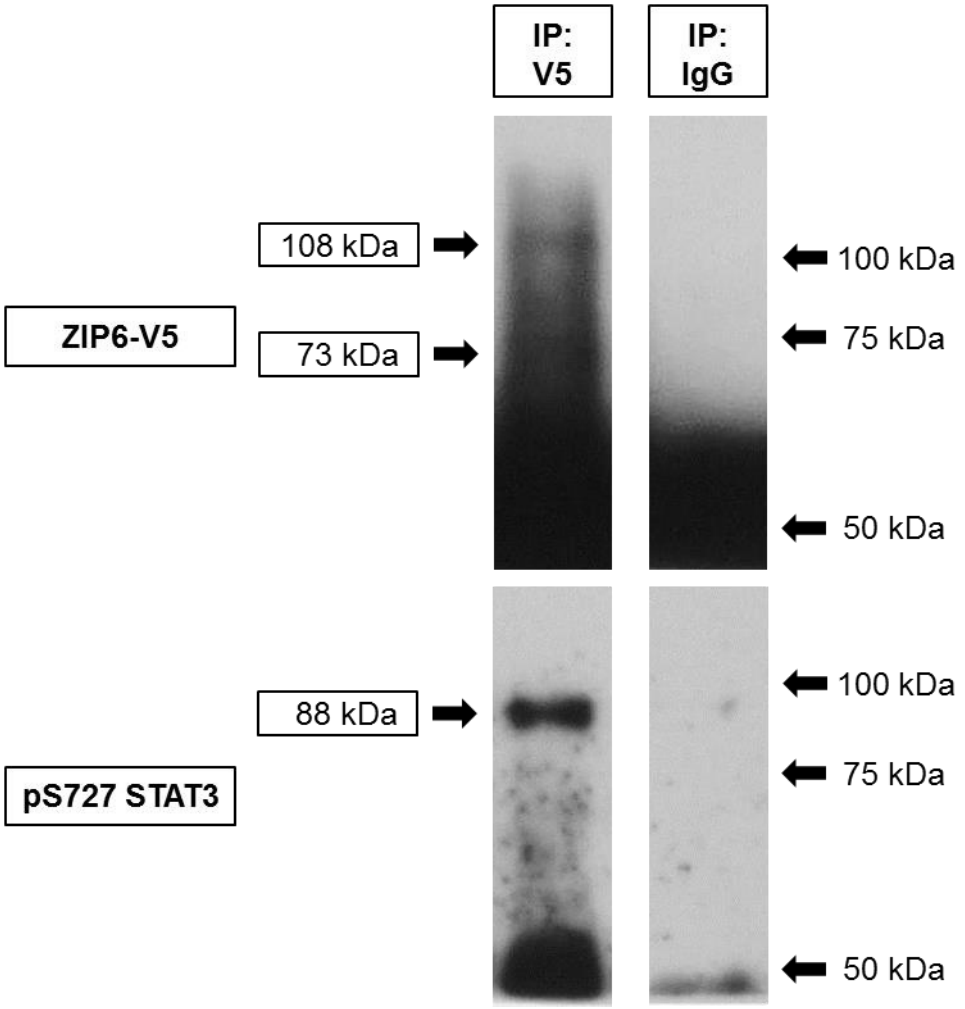

MCF−7 cells were transfected with wild−type ZIP6 in the presence of butyrate for 16 hours. Pooled samples of the adherent and the non−adherent cells were immunoprecipitated with V5 antibody and rabbit IgG (control). Immunoblotting was performed using V5 and pS727 STAT3 antibodies. Protein bands of recombinant ZIP6 at 108 kDa and pS727 STAT3 at 88 kDa are shown. The images of both the samples were taken from the same blot.

To confirm the binding of ZIP6 to pS727 STAT3 and to demonstrate whether the binding was specifically in mitotic cells, an in situ proximity ligation assay (PLA) was performed in nocodazole-treated cells using ZIP6 E-20 and pS727 STAT3 antibodies. Noteworthy, using this PLA technique, a protein-protein physical interaction can be visualised as fluorescent signals when 2 target molecules are localised in close proximity of up to 40 nm (Gullberg and Andersson 2010). A representative image and signal quantification demonstrated an average of 23 red fluorescent dots/cell in the mitotic cells, with only an average of one dot per cell in the non-mitotic cells (Fig. 6.16), signifying the binding between the two proteins predominantly in mitosis. The chance of false positive signals was eliminated by the presence of only a few PLA signals in the controls when using only the ZIP6 antibody or the pS727 STAT3 antibody (Fig. 6.16).

To interrogate a specific site in ZIP6 to which pS727 STAT3 bound, MCF-7 cells were transfected with ZIP6 constructs, consisting of wild-type ZIP6 and ZIP6 mutants (S478A, T479A, S471A, S475A, and Y473A). Because residues S478 and T479 of ZIP6 were located distant to the YESQ STAT3-binding motif, the S478A and T479A mutants were used as negative controls. Immunoprecipitation was performed using a V5 antibody. Probing for V5 demonstrated a 73 kDa band of the recombinant ZIP6 with a strong band of the immunoglobulin heavy chain at 50 kDa in all the samples (Fig. 6.17), proving that the immunoprecipitation was robust. However, the 73 kDa band was severely interfered by the immunoglobulin heavy chain band in the cells transfected with ZIP6 T479A, limiting the interpretation of the binding in this sample (Fig. 6.17). Probing for pS727 STAT3 showed a clean band of pS727 STAT3 at 88 kDa in the cells transfected with ZIP6 S478A with the signal intensity comparable to wild-type ZIP6 as expected (Fig. 6.17). An insignificant decrease in the pS727 STAT3 levels were observed for the T479A mutant, a negative control, which could be attributed to the interference of the immunoglobulin heavy chain band in one replicate (Fig. 6.17). Furthermore, the pS727 STAT3 levels were decreased in the cells transfected with ZIP6 S471A, the mutation of which affected a serine residue near the YESQ motif, but with no statistical significance (Fig. 6.17). On the contrary, the pS727 STAT3 levels were significantly reduced by 85% in the cells transfected with either

ZIP6 S475A or Y473A when compared to wild-type ZIP6 (Fig. 6.17). These data demonstrated the binding of pS727 STAT3 to ZIP6 on the predicted STAT3-binding motif. This binding might serve as a means whereby ZIP6 was functionally controlled during mitosis. Noteworthy, the decrease in the pS727 STAT3 binding to ZIP6 S475A could also suggest that residue S475 might need to be phosphorylated prior to the binding

Using an immunofluorescence technique, an investigation in our group initially observed an increase in pStathmin protein expression throughout the mitotic stages (Nimmanon T et al., manuscript in preparation). To determine the binding of pS727 STAT3 to pStathmin, PLA was performed in nocodazole-treated cells using pS727 STAT3 and pStathmin antibodies, revealing that the mitotic cells contained significantly higher PLA signals than the non-mitotic cells (Fig. 6.18). The signal quantitation confirmed the significant increase, showing 140 signals/cell in the mitotic cells, but only 10 signals/cell in the non-mitotic cells (Fig. 6.18). The negative controls using either of the antibodies revealed a considerably lower number of PLA signals, validating that the signals in the sample using both of the antibodies were produced by the binding between the two proteins (Fig. 6.18). These data proposed a novel role of pS727 STAT3 through its binding to pStathmin in facilitating the process of microtubule reorganisation (Rubin and Atweh 2004). Noteworthy, the relatively high PLA signals in this experiment when compared to the PLA using the ZIP6 and pS727 STAT3 antibodies could be due to the higher protein expression and the higher approachability to pS727 STAT3 of pStathmin than ZIP6. Alternatively, this might be due to the higher compatibility with the PLA technique of the pStathmin antibody than the ZIP6 antibody. Additionally, given that both the STAT3-binding site and the epitope of the ZIP6 E-20 antibody are located in the same cytosolic loop, the binding of pS727 STAT3 to ZIP6 might partially interfere with the binding of the ZIP6 E-20 antibody to its epitope, and as a result, the PLA signals were decreased.

Figure 6.16 pS727 STAT3 binding to ZIP6 in mitotic cells

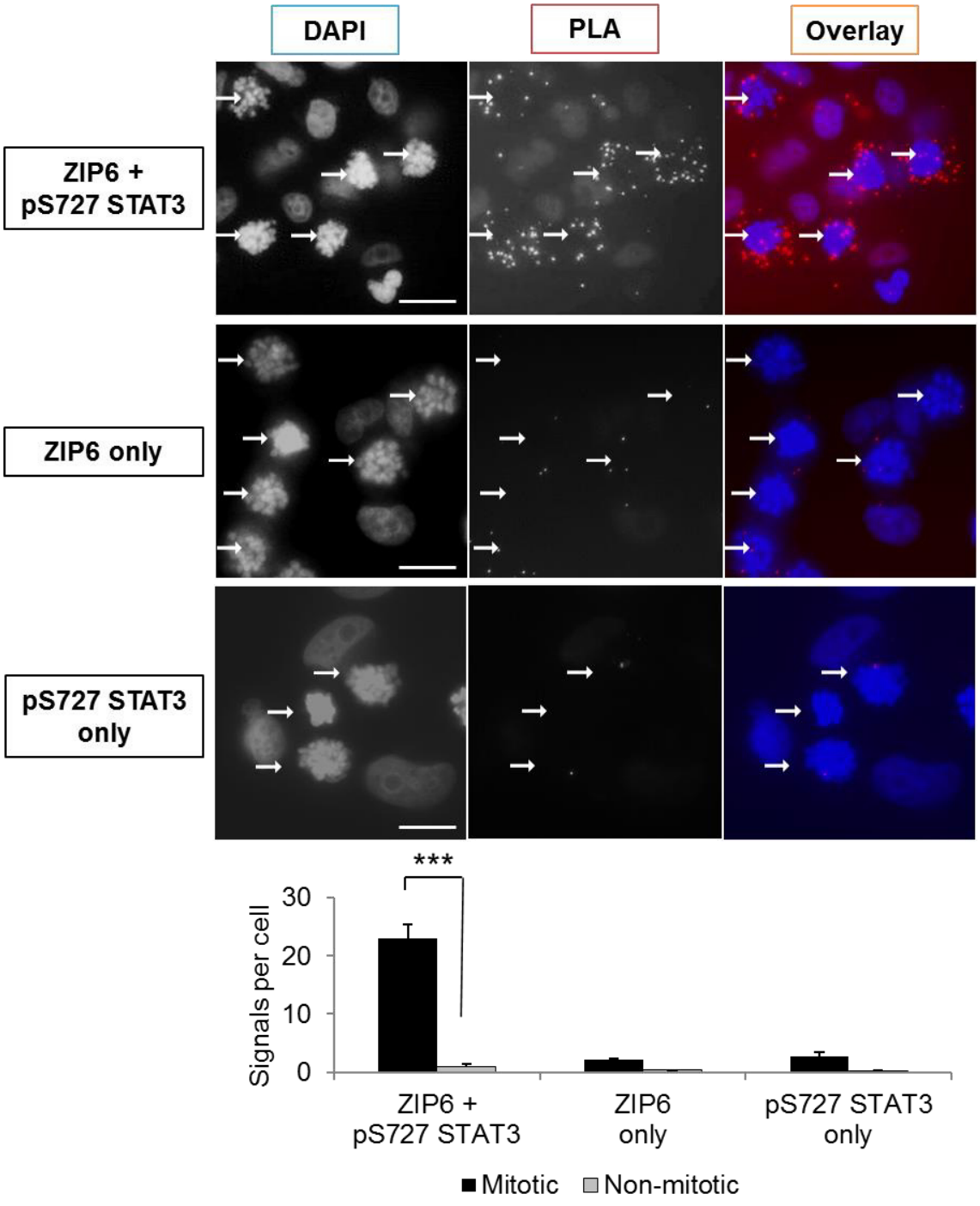

MCF−7 cells on 8−well chamber slides were treated with 100 nM nocodazole for 20 hours. A proximity ligation assay using ZIP6 E−20 and pS727 STAT3 antibodies was performed and compared to controls using either of the antibodies. Mitotic cells are indicated by white arrows. Quantitative measurements in at least 6 images of 25 stacks taken 0.3 µm apart from 3 independent experiments are demonstrated as mean ± standard error. Statistical significance is compared between the signals in the mitotic and the non−mitotic cells.
*** $p < 0.001$. Scale bar, 25 µm.

Figure 6.17 pS727 STAT3 binding to ZIP6 on the predicted binding site

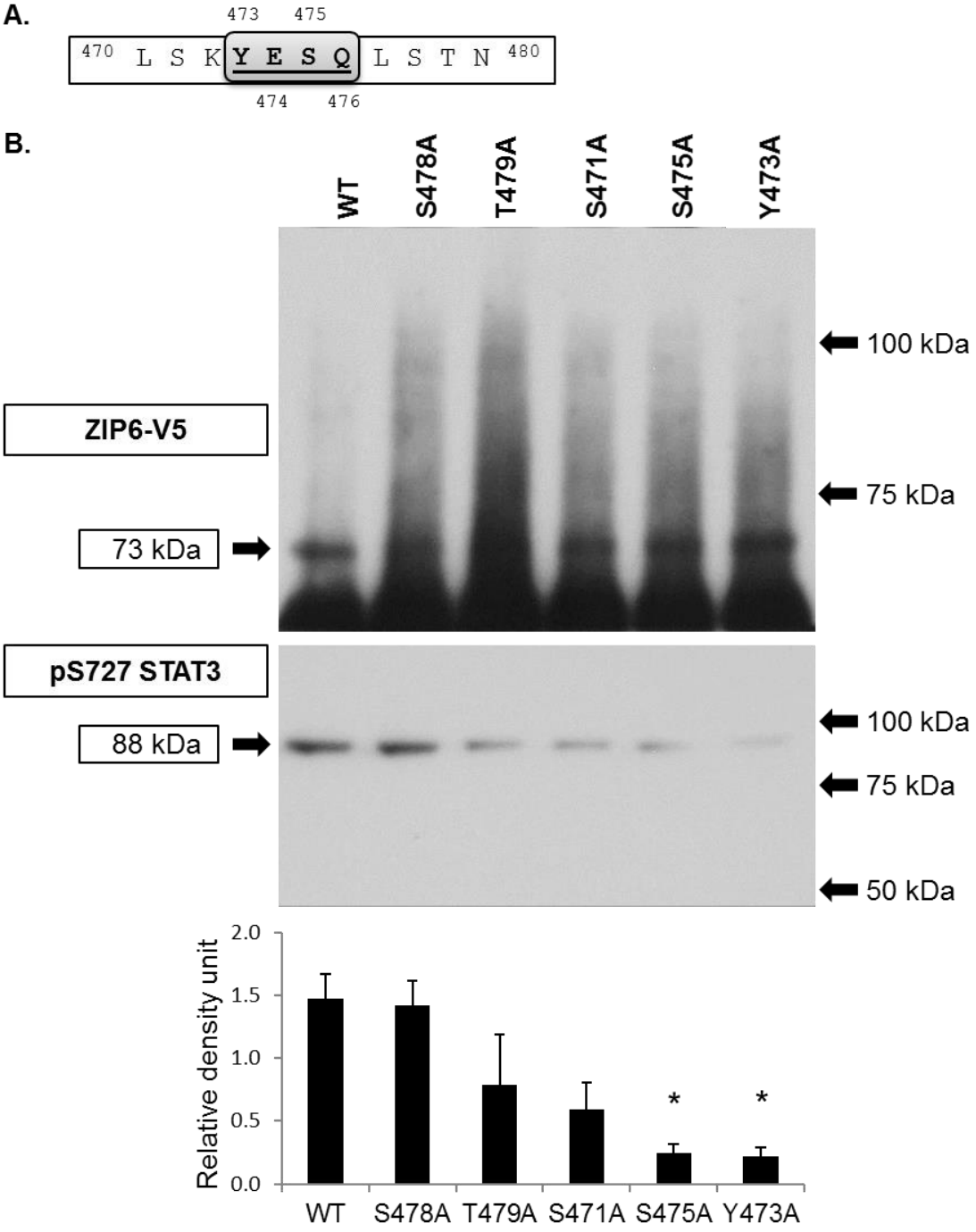

A. This schematic demonstrates the amino acid sequence of ZIP6 between residues 470 and 480 with a predicted STAT3−binding site (sequence YESQ, positions 473−476).

B. MCF−7 cells were transfected with wild−type ZIP6 and ZIP6 mutants (S478A, T479A, S471A, S475A, and Y473A) in the presence of butyrate for 16 hours. Pooled samples of the adherent and the non−adherent cells were immunoprecipitated with a V5 antibody. Immunoblotting was performed using V5 and pS727 STAT3 antibodies. Representative protein bands are shown. Densitometric data of the pS727 STAT3 bands (88 kDa) normalised to V5 (73 kDa) are presented in a bar graph as mean ± standard error (n = 3). Statistical significance is compared to wild−type ZIP6.
* $p < 0.05$.

Figure 6.18 pS727 STAT3 binding to pStathmin in mitotic cells

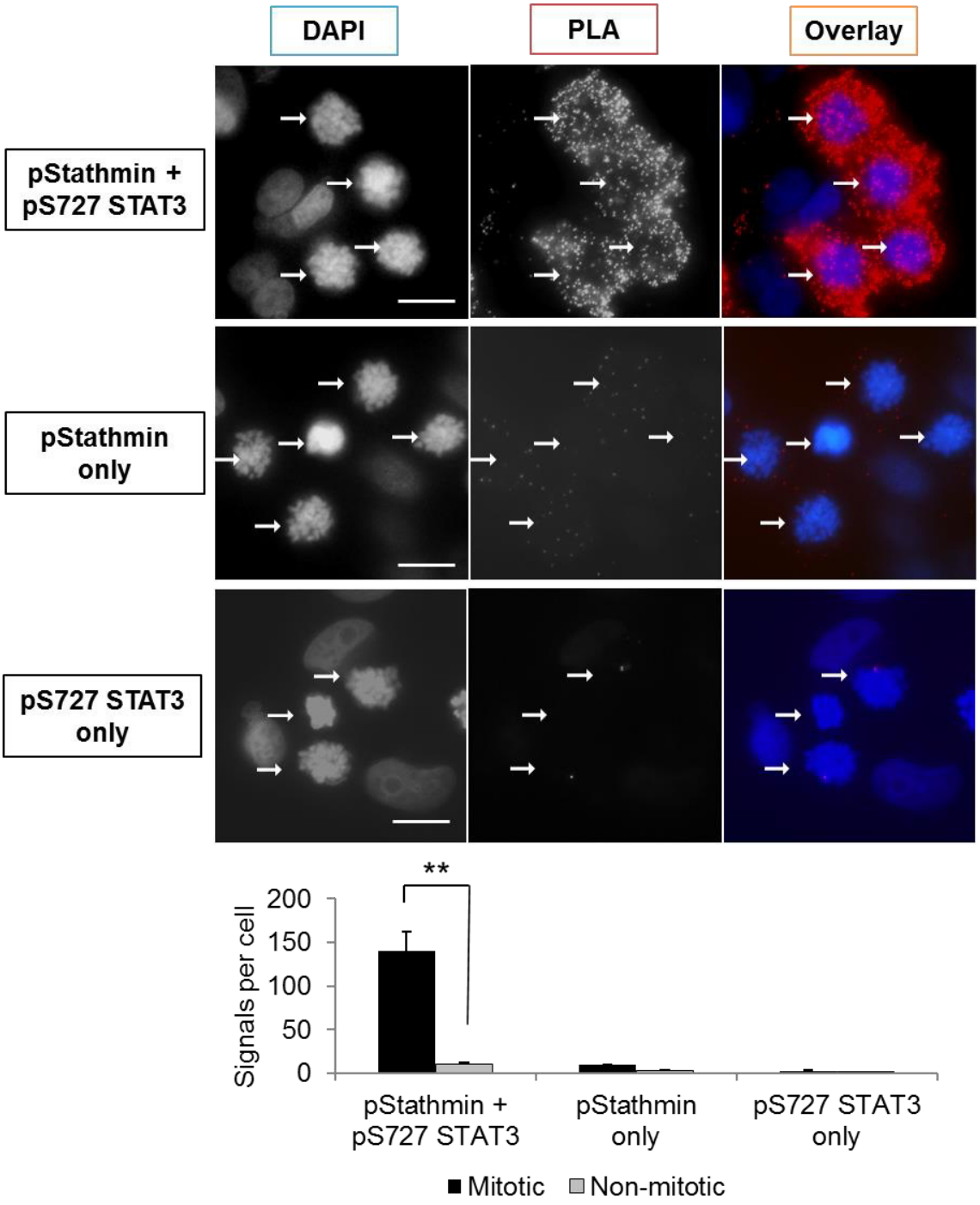

MCF−7 cells on 8−well chamber slides were treated with 100 nM nocodazole for 20 hours. A proximity ligation assay using pS38 Stathmin and pS727 STAT3 antibodies was performed and compared to controls using either of the antibodies. Mitotic cells are indicated by white arrows. Quantitative measurements in at least 6 images of 25 stacks taken 0.3 µm apart from 3 independent experiments are demonstrated as mean ± standard error. Statistical significance is compared between the signals in the mitotic and the non−mitotic cells.
*** $p < 0.001$. Scale bar, 25 µm.

6.3.4 ZIP10 binds to ZIP6 and pS727 STAT3 in mitosis

ZIP6 and ZIP10 are both members of the LIV-1 subfamily of zinc channels, which share the same sub-branch in the phylogenetic tree of ZIP channels (Taylor and Nicholson 2003) (Fig. 3.1). Consistent with their evolutionary closeness, their genes have many common characteristics, including their evolutionary link to prion genes (Schmitt-Ulms et al. 2009), presence of PEST proteolytic cleavage sites (Fig. 3.7), and presence of STAT3-binding motifs (Shao *et al.* 2004; Keshava Prasad et al. 2009). Biologically, both ZIP6 and ZIP10 have been associated with oestrogen-receptor positivity (Taylor et al. 2007) as well as an invasive phenotype (Kagara et al. 2007; Hogstrand et al. 2013) in breast cancer. Importantly, both ZIP6 and ZIP10 have been demonstrated to be enriched in the oocyte cortex and responsible for zinc influx during meiotic progression of oocytes (Kong *et al.* 2014), although no exact mechanism of ZIP6 and ZIP10 was investigated in the study. In so far as ZIP6 was involved in mitosis, it was interesting to investigate the association of ZIP10 with ZIP6 during mitosis.

To determine whether ZIP6 and ZIP10 form a heteromer during mitosis, immunoprecipitation was performed in cells transfected with wild-type ZIP6, using a V5 antibody and rabbit normal IgG. On the Western blot using the V5 antibody, the band at 68 kDa could not be visualised due to the interference of a strong immunoglobulin band at 50 kDa and the smearing pattern of the bands above 50 kDa. However, the 108 kDa band of the recombinant ZIP6, which represented the full length of ZIP6 (Hogstrand et al. 2013), could be recognised (Fig. 6.19). This 108 kDa band was absent in the IgG control, proving that it represented the recombinant ZIP6 and confirming the robustness of the immunoprecipitation (Fig. 6.19). The binding of ZIP10 to ZIP6 was proved by the presence of a faint 38 kDa band of ZIP10 in the V5-immunoprecipitated sample (Fig. 6.19). This ZIP10 band was not detected in the IgG-immunoprecipitated sample (Fig. 6.19), validating the binding. The result demonstrated a complex formation of ZIP6 and ZIP10, but did not distinguish whether the complex was present in mitotic or non-mitotic cells.

Figure 6.19 ZIP6 binding to ZIP10

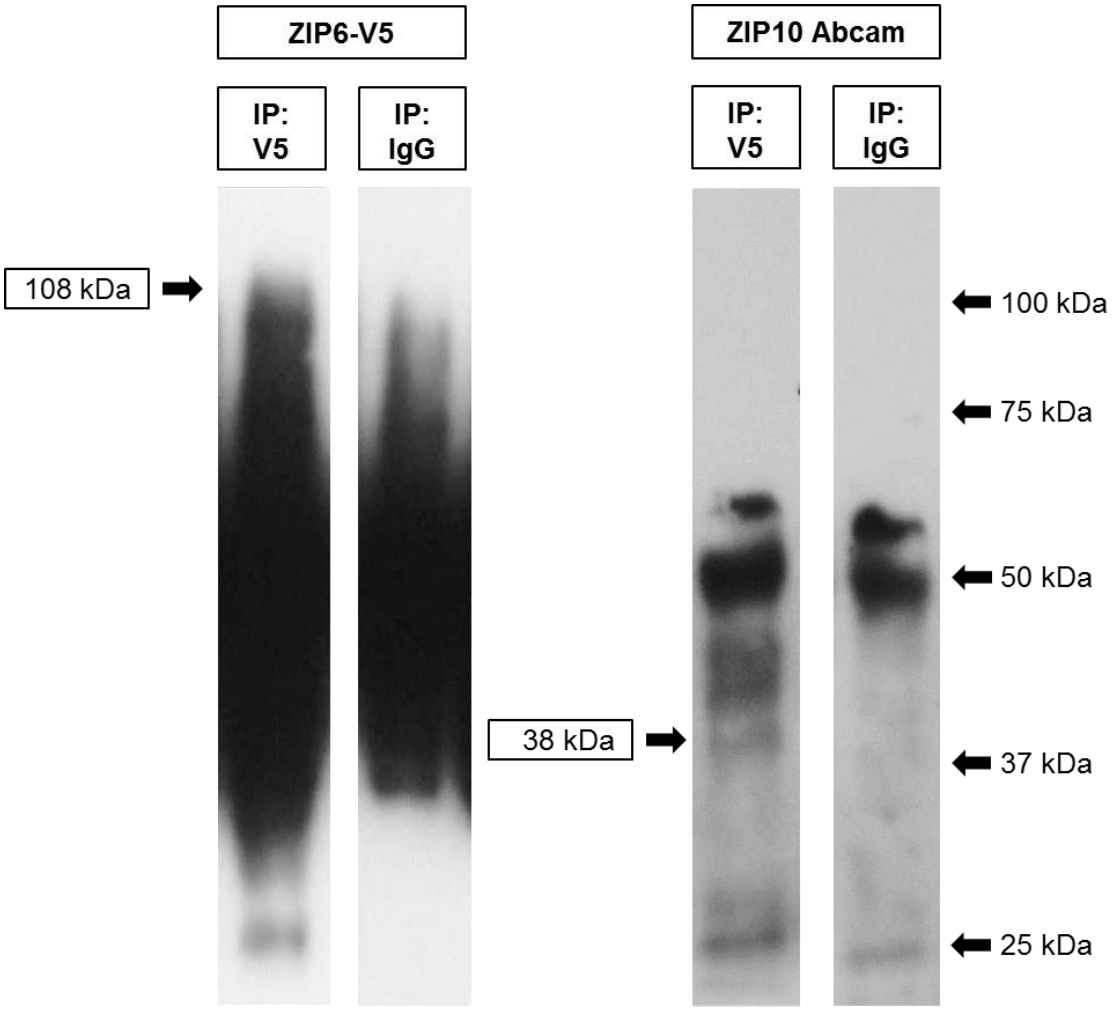

MCF−7 cells were transfected with wild−type ZIP6 in the presence of butyrate for 16 hours. Pooled samples of the adherent and the non−adherent cells were immunoprecipitated with V5 antibody and rabbit IgG (control). Immunoblotting was performed using V5 and ZIP10 Abcam antibodies. Protein bands of recombinant ZIP6 at 108 kDa and ZIP10 at 38 kDa are shown. The images of both the samples were taken from the same blot.

To determine ZIP6 binding to ZIP10 during mitosis, PLA was performed in nocodazole−treated cells using ZIP6 Y and ZIP10 R antibodies. Noteworthy, these two antibodies were made in−house and targeted ZIP6 and ZIP10 at their N−terminus (Table 2.1, Fig. 6.5). The mitotic cells contained 21 PLA signals/cell, which were significantly higher than the non−mitotic cells, which contained 6 signals/cell (Fig. 6.20), suggesting that ZIP6 formed a complex with ZIP10 preferentially in mitosis. Only a few background signals were observed in the controls using a single antibody (Fig. 6.20), supporting the genuineness of the signals produced.

Figure 6.20 ZIP6 binding to ZIP10 in mitotic cells

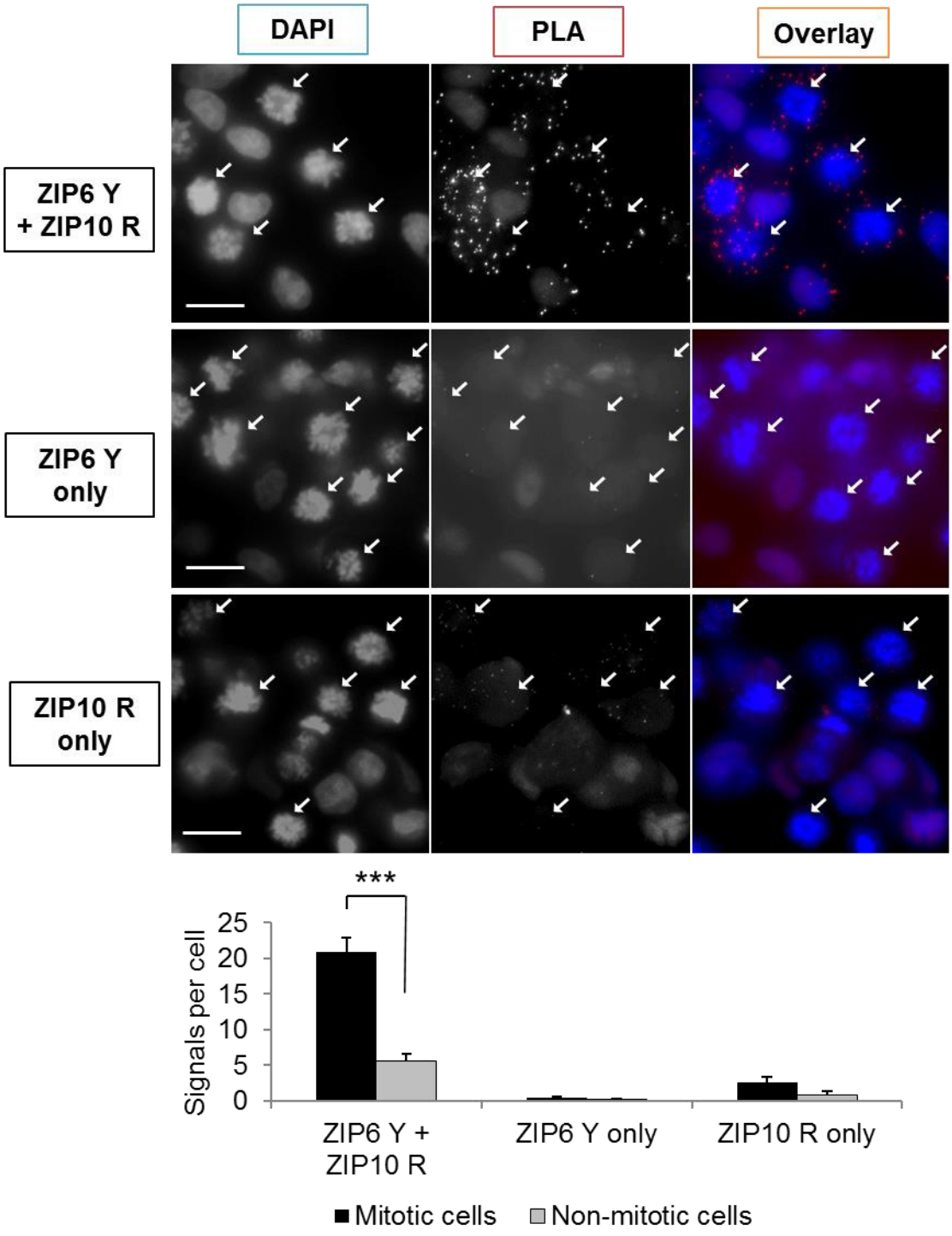

MCF−7 cells on 8−well chamber slides were treated with 100 nM nocodazole for 20 hours. A proximity ligation assay using ZIP6 Y and ZIP10 R antibodies was performed and compared to controls using either of the antibodies. Mitotic cells are indicated by white arrows. Quantitative measurements in at least 6 images of 25 stacks taken 0.3 µm apart from 3 independent experiments are demonstrated as mean ± standard error. Statistical significance is compared between the signals in the mitotic and the non−mitotic cells.
*** $p < 0.001$. Scale bar, 25 µm.

Heterodimerisation has been reported for some members of the ZnT family, such as ZnT5 and ZnT6 (Fukunaka *et al.* 2009). ZIP channels are believed to form a homodimer when transporting zinc through the pore (Kambe et al. 2015). The homodimer formation has been specifically reported for ZIP13 (Bin et al. 2011). However, no heterodimerisation of ZIP channels has been demonstrated. This ZIP6/ZIP10 complex formation (Fig. 6.19 and Fig. 6.20) provided evidence suggesting a possibility of heterodimerisation or heteromer formation for the ZIP family.

To determine pS727 STAT3 binding to ZIP10, PLA was performed in nocodazole−treated cells, using ZIP10 Abcam and pS727 STAT3 antibodies. Noteworthy, this ZIP10 antibody targets the cytosolic loop of ZIP10 (Table 2.1, Fig. 6.5). The result revealed a significant increase in binding in the mitotic cells, which had 93 PLA signals/cell, compared to the non−mitotic cells, which contained only 10 PLA signals/cell (Fig. 6.21). These data suggested that pS727 STAT3 might also bind to ZIP10 during mitosis. The more PLA signals observed when using the pS727 STAT3 antibody with the ZIP10 Abcam antibody (Fig. 6.21) than with the ZIP6 E−20 antibody (Fig. 6.16) suggested that pS727 STAT3 might bind to ZIP10 to a greater extent than ZIP6. However, this could in fact be because of the different antibodies used, which might have different capability to bind to the ZIP channels that had already complexed with pS727 STAT3. Moreover, the higher PLA signals when the ZIP10 antibody was added alone than when the ZIP6 antibody was added alone suggested that the difference might be partly due to the difference in background signals produced by the antibodies. Noteworthy, the specific binding site of pS727 STAT3 in ZIP10 was not investigated. Additionally, pS727 STAT3 might bind to ZIP10 directly or only bind to ZIP6 that had already formed a complex with ZIP10. If latter was the case, the false positive results rendered by the immunoprecipitation and the PLA experiments might have resulted from the presence of ZIP10 within the ZIP10/ZIP6/pS727 STAT3 complex and thereby the molecular proximity of ZIP10 and pS727 STAT3 within the complex.

Figure 6.21 pS727 STAT3 binding to ZIP10 in mitotic cells

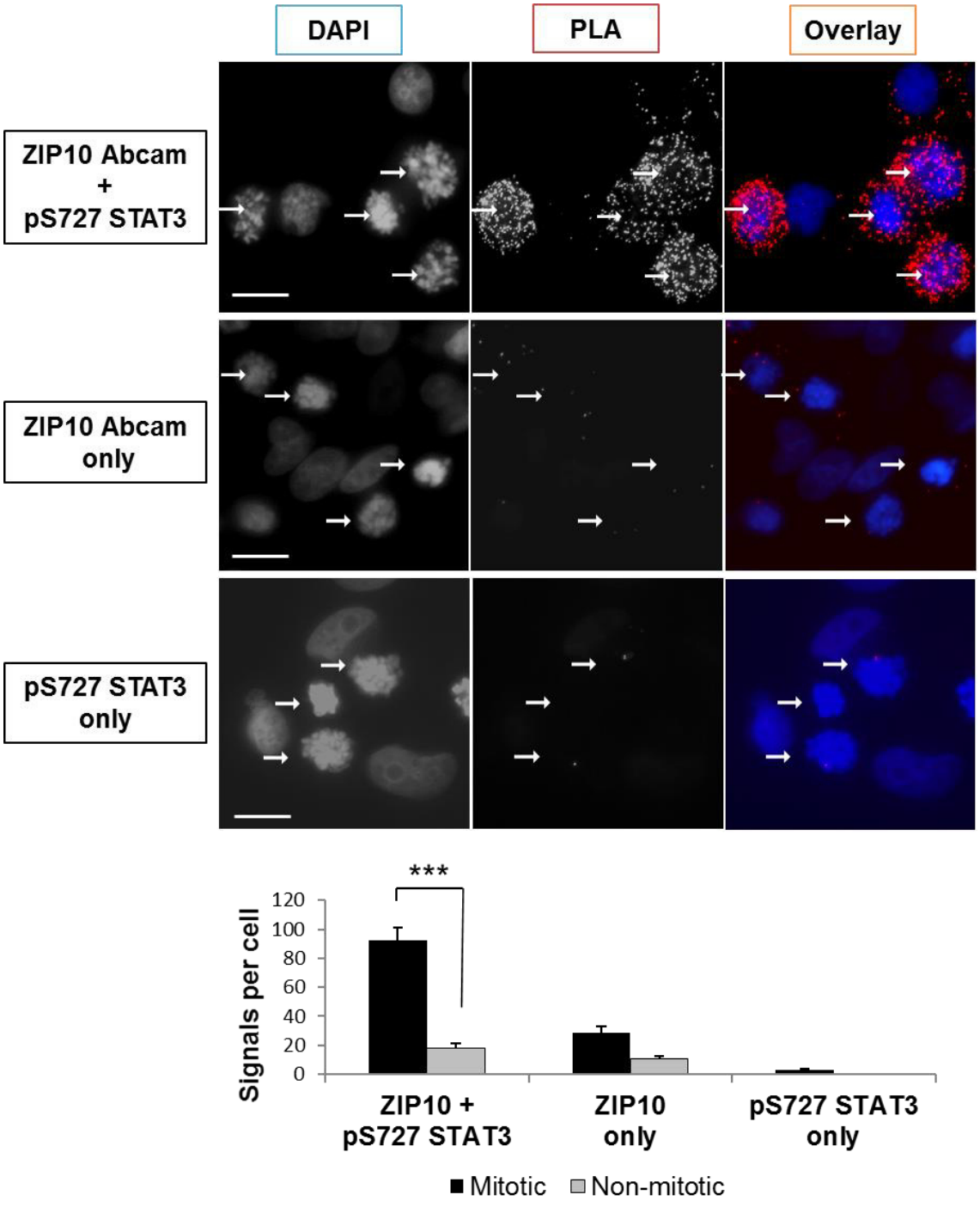

MCF−7 cells on 8−well chamber slides were treated with 100 nM nocodazole for 20 hours. A proximity ligation assay using ZIP10 Abcam and pS727 STAT3 antibodies was performed and compared to controls using either of the antibodies. Mitotic cells are indicated by white arrows. Quantitative measurements in at least 6 images of 25 stacks taken 0.3 µm apart from 3 independent experiments are demonstrated as mean ± standard error. Statistical significance is compared between the signals in the mitotic and the non−mitotic cells.
*** $p < 0.001$. Scale bar, 25 µm.

6.3.5 ZIP6 is processed in mitosis

In nocodazole−treated cells, an initial investigation in our group demonstrated two additional bands of ZIP6 at 48 kDa (detected by the ZIP6 E−20 antibody) and 15 kDa (detected by the ZIP6 Y antibody) (Nimmanon T et al., manuscript in preparation). These bands were compatible with products of a second cleavage in the plasma membrane−located ZIP6 at the N−terminus downstream of the ZIP6 Y epitope during mitosis. To support this second cleavage of ZIP6, immunofluorescence was performed using the N−terminal ZIP6 Y antibody in cells transfected with wild−type ZIP6. A V5 antibody was also used for identification of the recombinant ZIP6 protein. Agreeing with the previous study (Hogstrand et al. 2013), the V5−positive (transfected) interphase cells consistently expressed ZIP6 with an ER−staining pattern of the ZIP6 pro−protein (Fig 6.22A, the top row). In contrast, the V5−positive (transfected) cells that were mitotic did not express ZIP6, particularly those in metaphase and later stages (Fig 6.22A, the bottom row). Furthermore, FACS analysis was performed on nocodazole−treated cells using either the ZIP6 E−20 or the ZIP6 Y antibody with a pS10 histone H3 antibody, a mitotic marker. The cells were gated according to the levels of pS10 histone H3. Using the ZIP6 E−20 antibody, the curve of the mitotic cell population on the histogram was shifted to the right, when compared to the non−mitotic cell population (Fig 6.22B). Consistent with the histogram, the calculation of the mean fluorescence intensities demonstrated a 2−fold significant increase in ZIP6 in the mitotic cells when compared to the non−mitotic cells (Fig 6.22B), compatible with the increased ZIP6 in mitosis, as discussed previously (Section 6.3.2). In contrast to the ZIP6 E−20 antibody, a dramatic left shift of the curve of the mitotic cell population was shown using the ZIP6 Y antibody when compared to the non−mitotic cell population, with a 79% significant decrease in mean fluorescence intensity demonstrated (Fig 6.22B). This left shift observed when using the ZIP6 Y antibody suggested a loss of the N−terminal segment containing the ZIP6 Y epitope and further supported the second cleavage in mitotic cells.

Figure 6.22 A ZIP6 N−terminal cleavage during mitosis

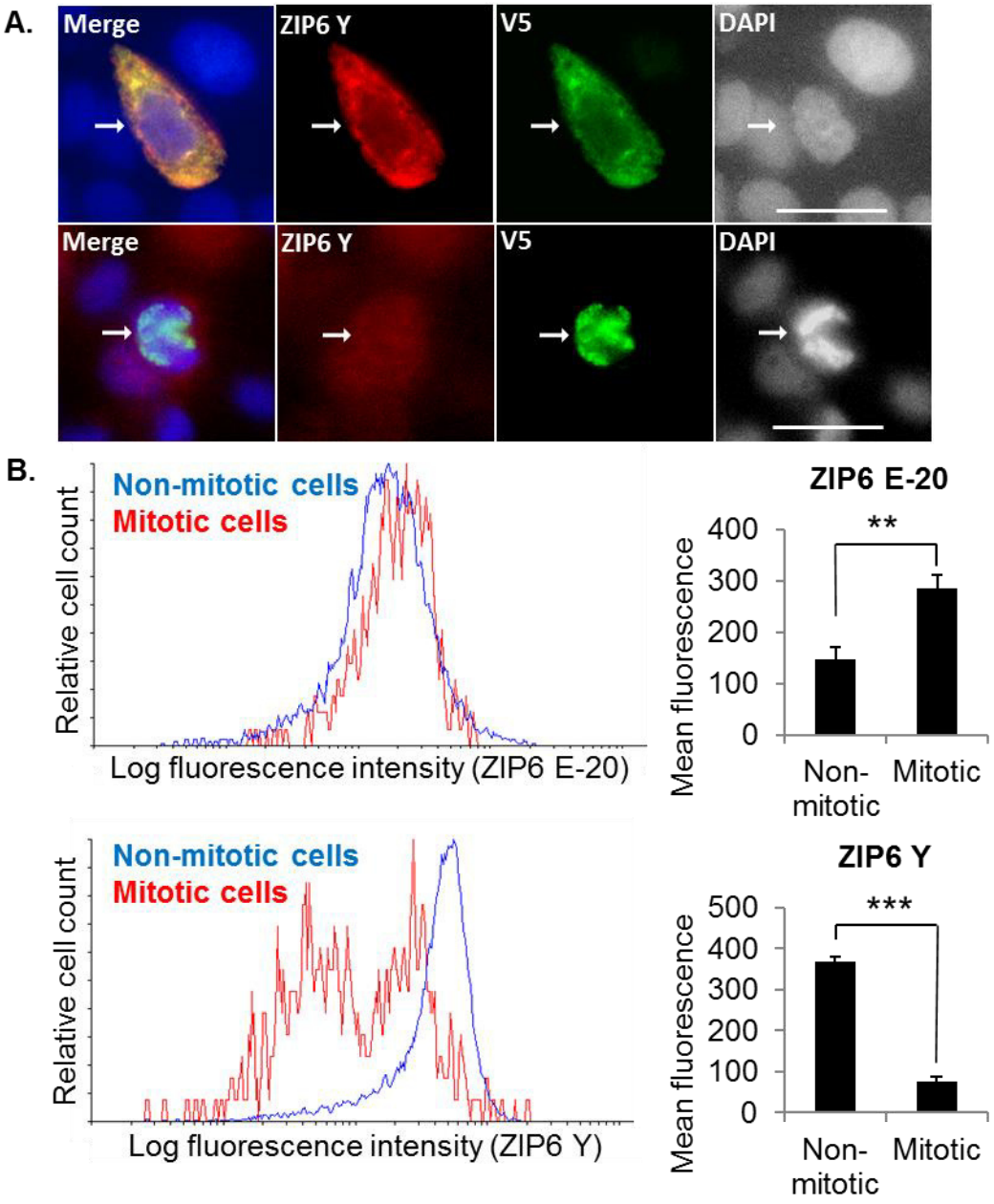

A. MCF−7 cells were transfected with wild−type ZIP6 in the presence of butyrate for 16 hours. Immunofluorescence was performed using ZIP6 Y and V5 antibodies, which were conjugated to Alexa Fluor 594 (red) and 488 (green), respectively. The nuclei were counterstained with DAPI. Representative images of the transfected cells (white arrow) that are non−mitotic (top) and mitotic (bottom), which were taken from the same slide, are presented.
Scale bar, 25 µm.

B. MCF−7 cells were immunostained with either ZIP6 (E−20) plus mouse pS10 Histone H3 antibodies or ZIP6 Y plus rabbit pS10 Histone H3 antibodies. FACS analysis was performed. The cells were gated and divided into 2 groups: the cells that are positive for pS10 Histone H3 (mitotic cells) and the cells that are negative for pS10 Histone H3 (non−mitotic cells). Data are presented in histograms. The mean fluorescence intensity of either ZIP6 Y or ZIP6 E−20 for each population is presented in a bar graph as mean ± standard error (n = 3). Statistical significance is compared between the mitotic and the non−mitotic cells.
** $p < 0.01$, *** $p < 0.001$.

To explore potential proteases that were activated during mitosis, the human protease antibody arrays were tested in cells treated with nocodazole with or without 1−hour or 2−hour recovery from the drug effects. Using these arrays, up to 34 proteases could be simultaneously detected in duplicate in a sample (Fig. 6.23). There are three pairs of reference dots on the left upper, right upper, and left lower corners (Fig. 6.23). Signal intensities were semi−quantitatively evaluated using densitometric analysis, and are shown in a bar graph (Fig. 6.24). To simplify the data, relative intensities of individual proteases across different samples are presented as a heat map, where blue colour represents the minimum value of the row and red colour represents the maximum value of the row, according to the indicated scale (Fig. 6.25).

In the cells without nocodazole treatment, signals of multiple proteases were detected, consisting of ADAM9, cathepsins (A, B, C, D, V, and X/Z/P), MMP−7, MMP−8, MMP−12, presenilin, and proprotein convertase. With 20−hour nocodazole treatment, ADAM9, MMP−7, presenilin, and proprotein convertase were shown to increase, whereas cathepsins B, V, and X/Z/P and MMP−8 were shown to decrease, and others were not changed when compared to the control (Fig. 6.23−6.25). With the progression of mitosis in the nocodazole−treated cells during the 1 hour and 2 hour recoveries, ADAM9, cathepsins (A, B, C, D, V, and X/Z/P), DPPIV/CD26, kallikrein 13, MMP−1, MMP−12, and presenilin were progressively increased when compared to the nocodazole−treated cells without drug recovery (Fig. 6.23−6.25). In contrast, MMP−7, MMP−8, and proprotein convertase were decreased during the recovery (Fig. 6.23−6.25). Given that the cleavage of ZIP6 occurred in early mitosis, the proteases that were increased in the nocodazole−treated cells were considered as the candidates likely to be activated during mitosis, including ADAM9, MMP−7, presenilin, and proprotein convertase (Fig. 6.23−6.25). Among these proteases, the increase in presenilin levels was shown to have the largest percentage change as a result of nocodazole treatment (Fig. 6.23 and 6.24), suggesting presenilin as the protease with the highest potential.

Figure 6.23 Protease arrays in nocodazole−treated cells

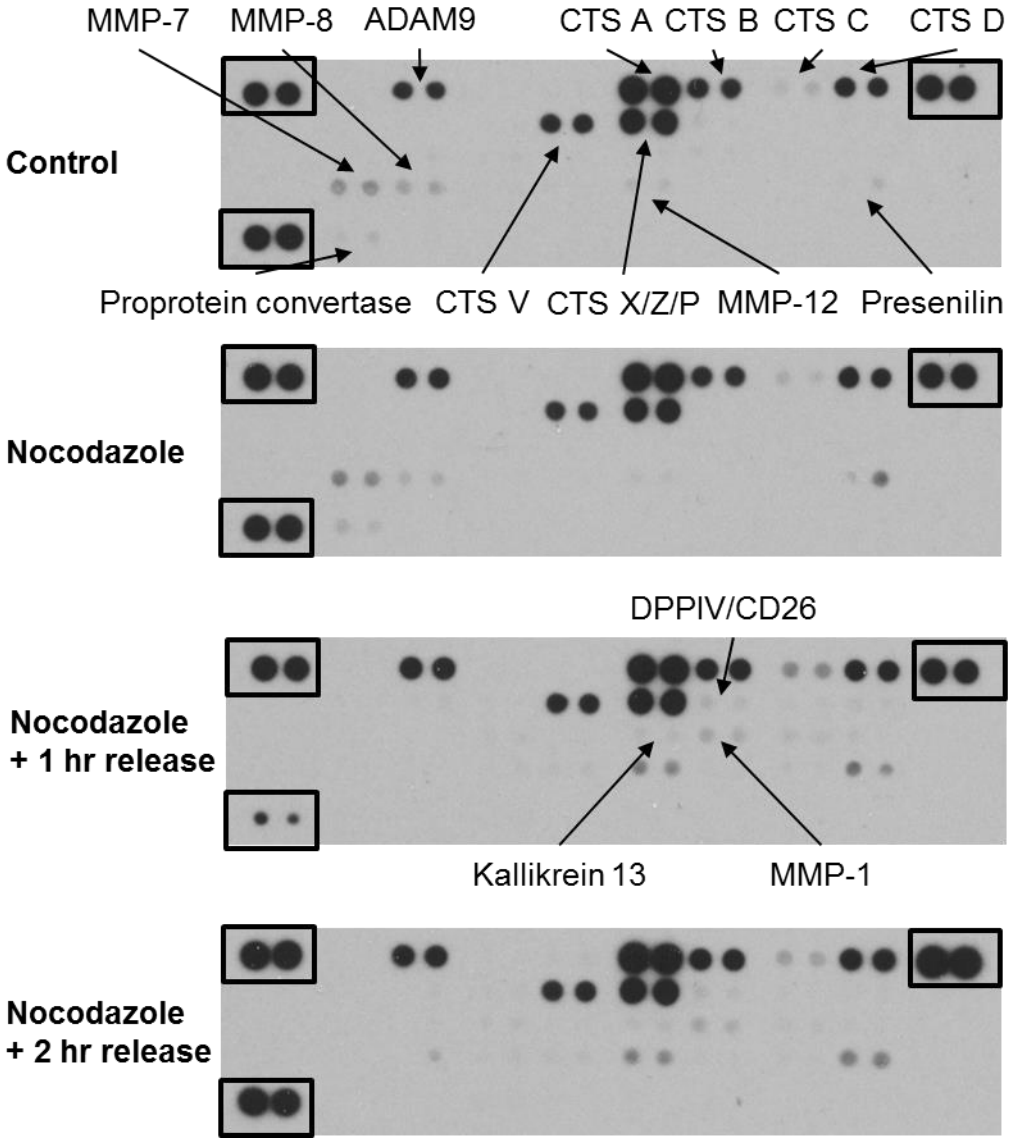

MCF−7 cells were treated with 100 nM nocodazole for 20 hours with 1−hour and 2−hour recovery. The changes in levels of selected proteases were determined using the protease antibody arrays (R&D Systems). The signal for each type of proteases is presented as a pair of duplicate spots, with three pairs of dark reference spots on the upper left, upper right, and lower left corners for alignment (purple boxes). The proteases that show signals on the arrays are indicated.

Figure 6.24 Densitometric analysis of protease arrays in nocodazole−treated cells

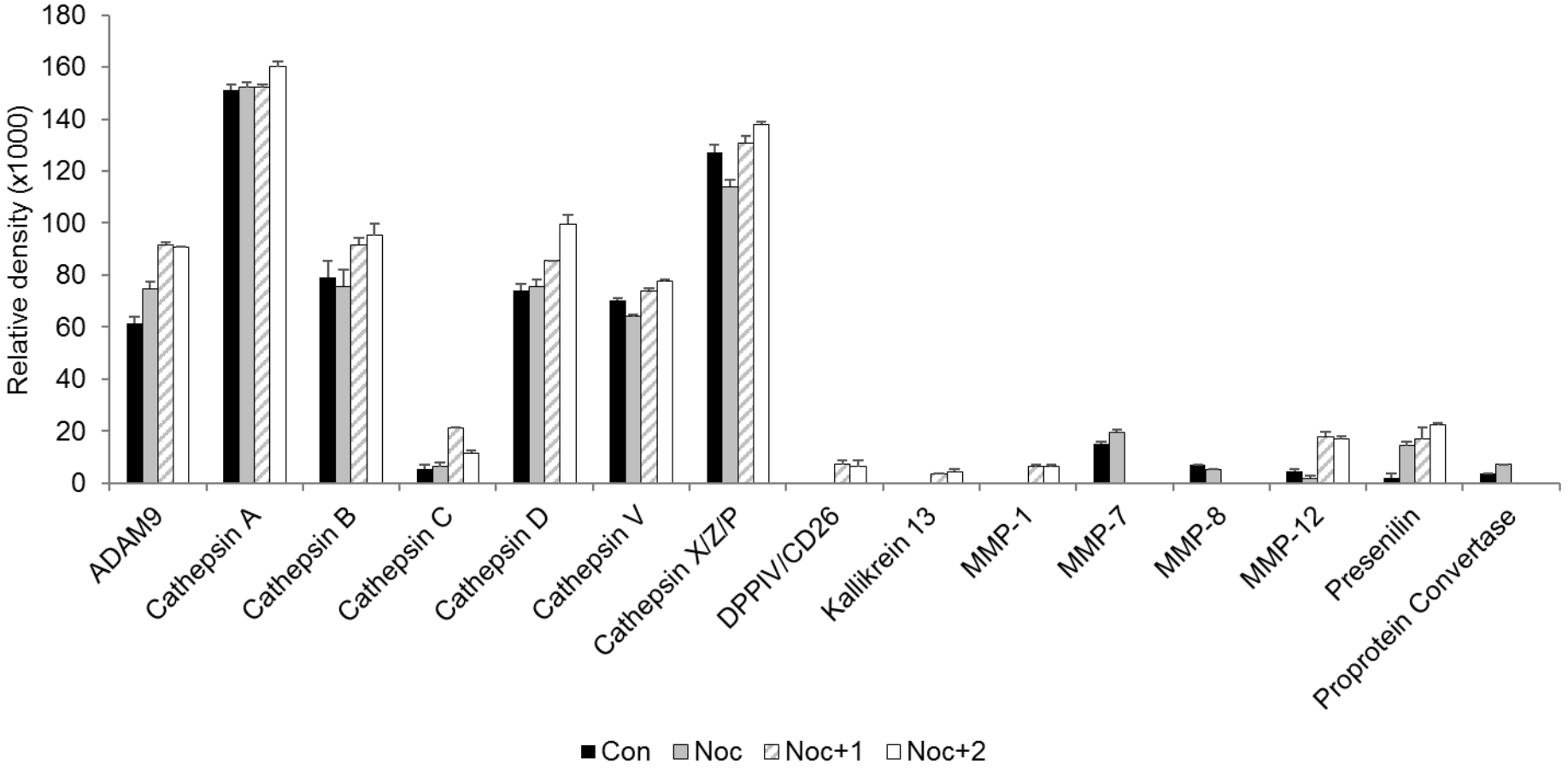

MCF−7 cells were treated with 100 nM nocodazole for 20 hours with 1−hour and 2−hour recovery. The changes in levels of selected proteases were determined using the protease antibody arrays (R&D Systems). Densitometric data are presented as mean of the duplicate dots ± standard error.

Figure 6.25 A heat map of the proteases that change during mitosis

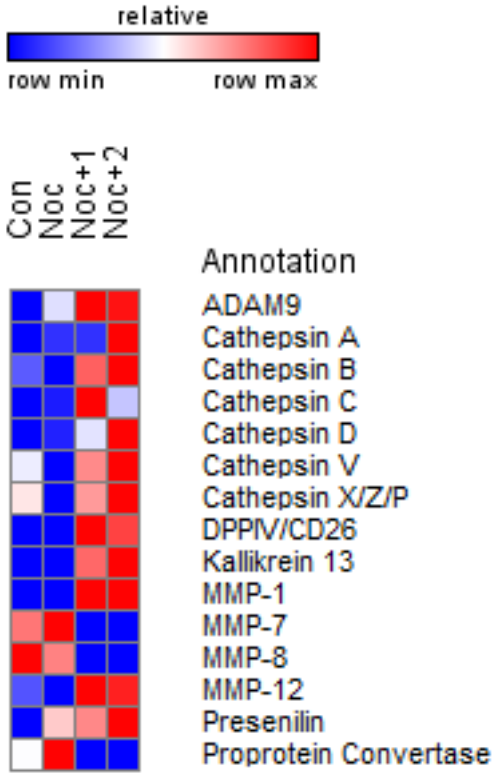

MCF−7 cells were treated with 100 nM nocodazole for 20 hours with 1−hour and 2−hour recovery. The changes in levels of selected proteases were determined using protease antibody arrays (R&D Systems). The heat map was generated using GENE−E matrix visualization and analysis platform (The Board Institute). Densitometric values in relation to other samples for each kinase are presented as a spectrum of colour where blue colour represents the lowest value in the row and red colour represents the highest value in the row according to the scale, irrespective of the absolute signal intensities.

6.3.6 ZIP6 is phosphorylated on S478 at 2 minutes after zinc treatment

Based on the finding that zinc−transport function of ZIP7 was triggered by CK2−mediated phosphorylation (Taylor et al. 2012), ZIP6 was hypothesised to be post−translationally controlled by the same mechanism. According to multiple phosphorylation site databases, CK2 has been predicted as a potential kinase that phosphorylates ZIP6 on residue S478 (Section 3.3.5; Fig. 6.1). Whether ZIP6 was also phosphorylated by CK2 on this potential site would now be investigated.

To determine whether ZIP6 was serine−phosphorylated, Western blotting using a pSer antibody was performed in cells transfected with wild−type ZIP6 for 18 hours in the presence of butyrate. The cells were treated with 20 µM zinc

plus 10 µM sodium pyrithione in serum free medium, the method which has been successfully used for inducing ZIP7 phosphorylation (Taylor et al. 2012) (Fig. 4.9, 4.18 and 5.13). Noteworthy, due to the process of zinc treatment, the non−adherent cells were not collected, and only the adherent cells remained in the samples. A gradual increase in intensity of the pSer bands at 73 kDa were observed as a result of zinc treatment (Fig. 6.26). The bands at 73 kDa were also observed on the blot when probed for V5 (Fig. 6.26), confirming that these pSer bands represented serine phosphorylation on the recombinant ZIP6. Noteworthy, the 73 kDa bands of the recombinant ZIP6 correspond to the active plasma membrane−located form of ZIP6 (Fig. 6.8). Densitometric data of the pSer bands normalised to the corresponding V5 bands demonstrated a 1.7−fold significant increase in pSer levels at 2 minutes after zinc treatment when compared to time 0 (Fig. 6.26). Even though the increase became 1.8−fold at 5 minutes and 3.0−fold at 10 minutes when compared to time 0, no statistical significance was demonstrated due to the high variability of the data at these time points (Fig. 6.26). These data suggested a role for serine phosphorylation in ZIP6 post−translational regulation.

To determine whether this serine phosphorylation of ZIP6 was on residue S478, Western blotting using the pSer antibody was also performed in cells transfected with the ZIP6 S478A mutant, in which residue S478 was mutated to alanine to prevent phosphorylation on this site. The cells were treated with zinc plus sodium pyrithione. The pSer and V5 bands at 73 kDa for wild−type ZIP6 are shown again for comparison (Fig. 6.27). In contrast to wild−type ZIP6, the pSer levels in the cells transfected with ZIP6 S478A remained steady throughout the 10−minute course of zinc treatment (Fig. 6.27). The pSer levels for ZIP6 S478A became significantly lower than wild−type ZIP6 at 2 minutes after zinc treatment (Fig. 6.27). Nonetheless, due to the high variability of the densitometric values for wild−type ZIP6 at 5 and 10 minutes after zinc treatment, a statistical difference between the two constructs was not detected after 2 minutes (Fig. 6.27).

Figure 6.26 ZIP6 serine−phosphorylation after zinc treatment

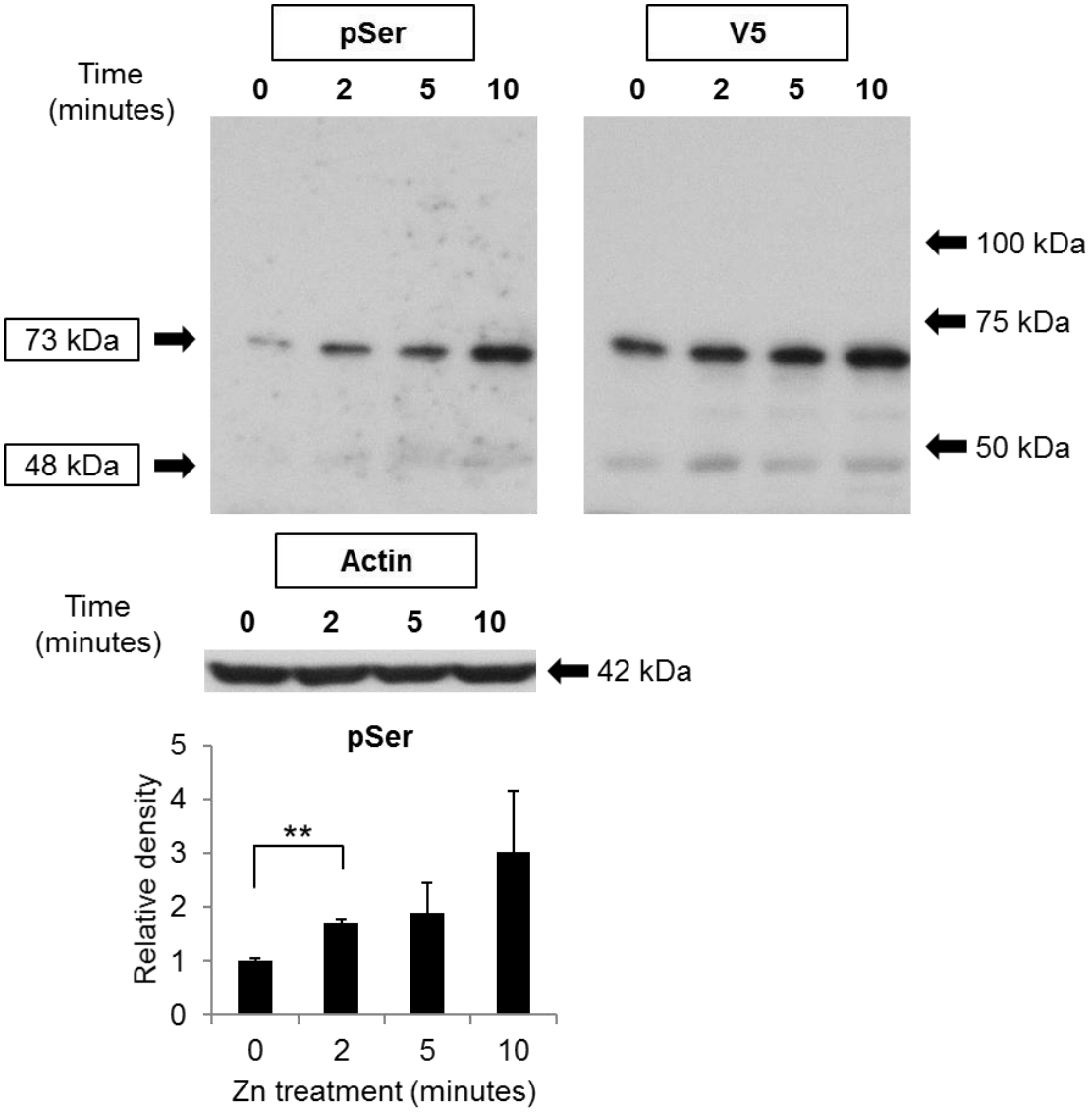

MCF−7 cells were transfected with wild−type ZIP6 in the presence of butyrate for 16 hours, and the adherent cells were treated with 20 µM zinc plus 10 µM sodium pyrithione. Immunoblotting was performed using pSer, V5 and β−actin antibodies. Protein bands of pSer, V5 and β−actin are shown as a representative result of 3 independent experiments. Densitometric data of the pSer bands (73 kDa) normalised to V5 (73 kDa) are shown in a bar graph as mean ± standard error (n = 3). Statistical significance is compared between different time points as indicated.
** $p < 0.01$.

The failure of the ZIP6 S478A mutant to be serine−phosphorylated suggested that residue S478 was an important serine residue phosphorylated as a result of zinc treatment. Interestingly, ZIP6 was shown to be serine−phosphorylated at 2 minutes after zinc treatment, which was as early as the serine phosphorylation of ZIP7 (Taylor et al. 2012). This finding suggested that both ZIP6 and ZIP7 might be simultaneously phosphorylated by CK2.

Whereas the phosphorylation of ZIP7 results in zinc release from cellular stores (Taylor et al. 2012), the phosphorylation of ZIP6 might result in cellular zinc import, supplying zinc to the stores and thereby synergistically working with ZIP7 in sustained activation of various tyrosine kinase signalling pathways.

Figure 6.27 ZIP6 serine−phosphorylation on S478 after zinc treatment

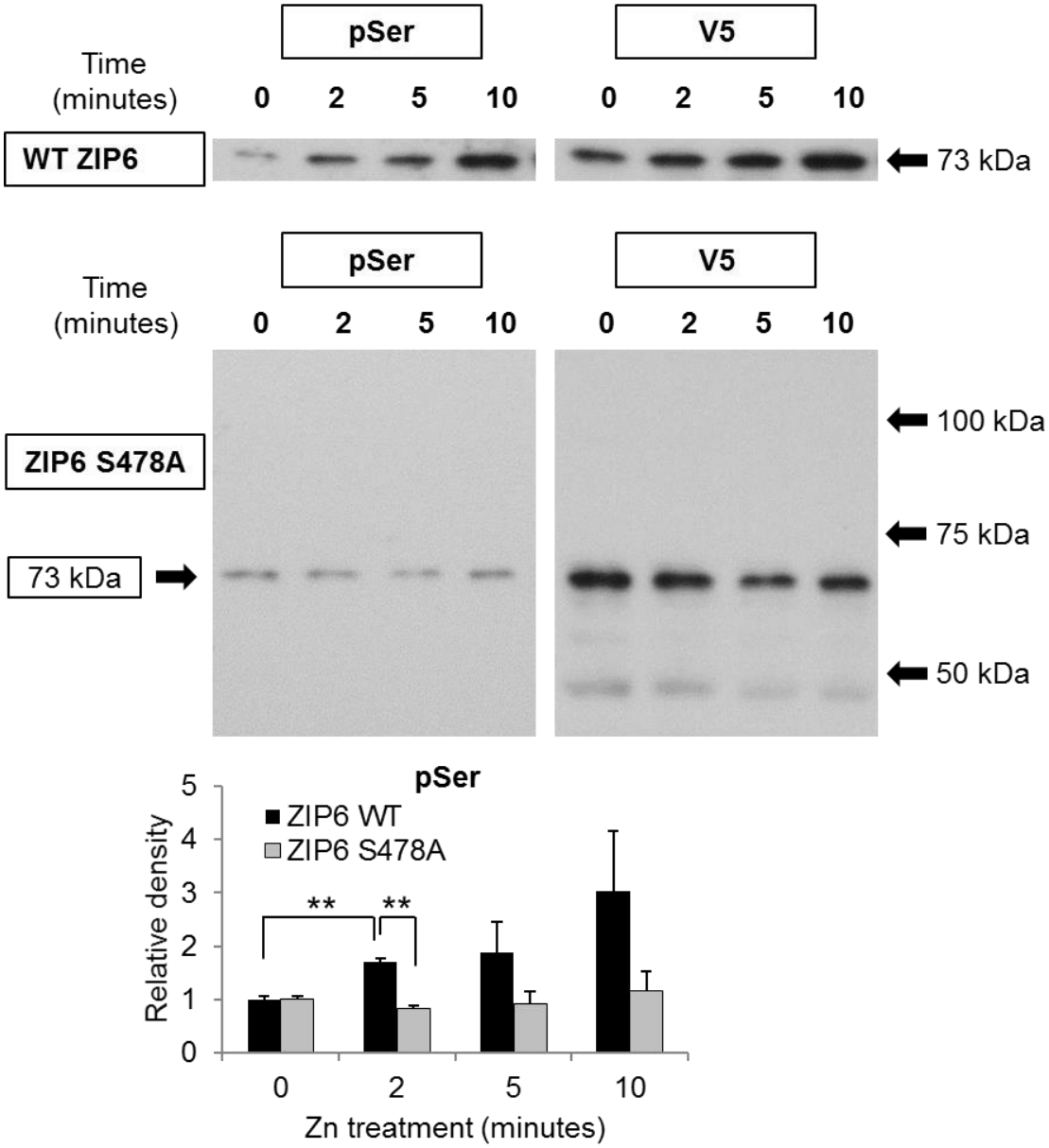

MCF−7 cells were transfected with wild−type ZIP6 and ZIP6 S478A in the presence of butyrate for 16 hours, and the adherent cells were treated with 20 µM zinc plus 10 µM sodium pyrithione. Immunoblotting was performed using pSer antibody and V5 antibody. Protein bands of pSer and V5 are demonstrated as a representative result of 3 independent experiments. Densitometric data of the pSer bands (68 kDa) normalised to V5 (68 kDa) are demonstrated in a bar graph as mean ± standard error (n = 3). Statistical significance is compared between different time points or different ZIP6 constructs as indicated.
* $p < 0.05$, ** $p < 0.01$.

6.3.7 ZIP6 is serine-phosphorylated by different kinases in mitosis

To determine whether ZIP6 was serine-phosphorylated during mitosis, Western blotting was performed in nocodazole-treated cells. A marked increase in levels of pS10 histone H3, a mitotic marker, was demonstrated in the nocodazole-treated cells when compared to the non-treated cells (Fig. 6.28A), confirming the successful induction of mitosis by the nocodazole treatment. Supporting the increase in ZIP6 protein expression in mitosis (Fig. 6.7, 6.9 and 6.10), the ZIP6 band at 68 kDa was significantly increased 2.6-fold in the nocodazole-treated cells when compared to the control (Fig. 6.28B). Furthermore, a significant 1.6-fold increase in intensity of the pSer band at 68 kDa, corresponding to the ZIP6 band, was also detected (Fig. 6.28B), revealing the serine phosphorylation of ZIP6 in mitosis. The higher percentage increase in ZIP6 levels than pSer levels in the nocodazole-treated cells implied that ZIP6 protein production outweighed the rate of its serine phosphorylation. The ZIP6 protein production might be markedly induced during mitosis, and the majority of ZIP6 that had been processed was serine-phosphorylated, leaving some ZIP6 on the plasma membrane non-phosphorylated. This amount of phosphorylated ZIP6 might be sufficient for the zinc influx required for mitotic progression.

To investigate the contribution of CK2 to the serine phosphorylation of ZIP6 in mitosis, immunoprecipitation using the ZIP6 E-20 antibody was performed. Cells were treated with nocodazole for enhancing mitosis and thereby ZIP6 protein expression. The non-adherent cells were also collected and pooled together with the adherent cells, to prevent loss of mitotic cells during cell harvest. Probing for ZIP6 in the ZIP6-immunoprecipitated sample demonstrated ZIP6 bands at 103 kDa and 68 kDa, which were partially obscured because of the smearing pattern of the bands (Fig. 6.29). These ZIP6 bands were equivalent to the full-length ZIP6 and the processed ZIP6, respectively (Fig. 6.8). The absence of the 103 kDa band and the presence of a barely-discernible smearing band at 68 kDa in the IgG control (Fig. 6.29) suggested that these ZIP6 bands truly represented ZIP6 and confirmed the robustness of the immunoprecipitation. The binding of CK2 to ZIP6 was demonstrated by the presence of a 42 kDa band when the sample was probed for CK2 (Fig. 6.29). The blot also revealed a few lower non-specific bands, and

a strong band at 37 kDa (Fig. 6.29), which was compatible with the immunoglobulin light chain present at the front line of protein migration on this blot. Importantly, the IgG control did not show the CK2 band at 42 kDa, but showed only the lower non−specific bands and the band of the immunoglobulin light chain (Fig. 6.29), validating the CK2 binding to ZIP6.

Figure 6.28 Serine phosphorylation of ZIP6 during mitosis

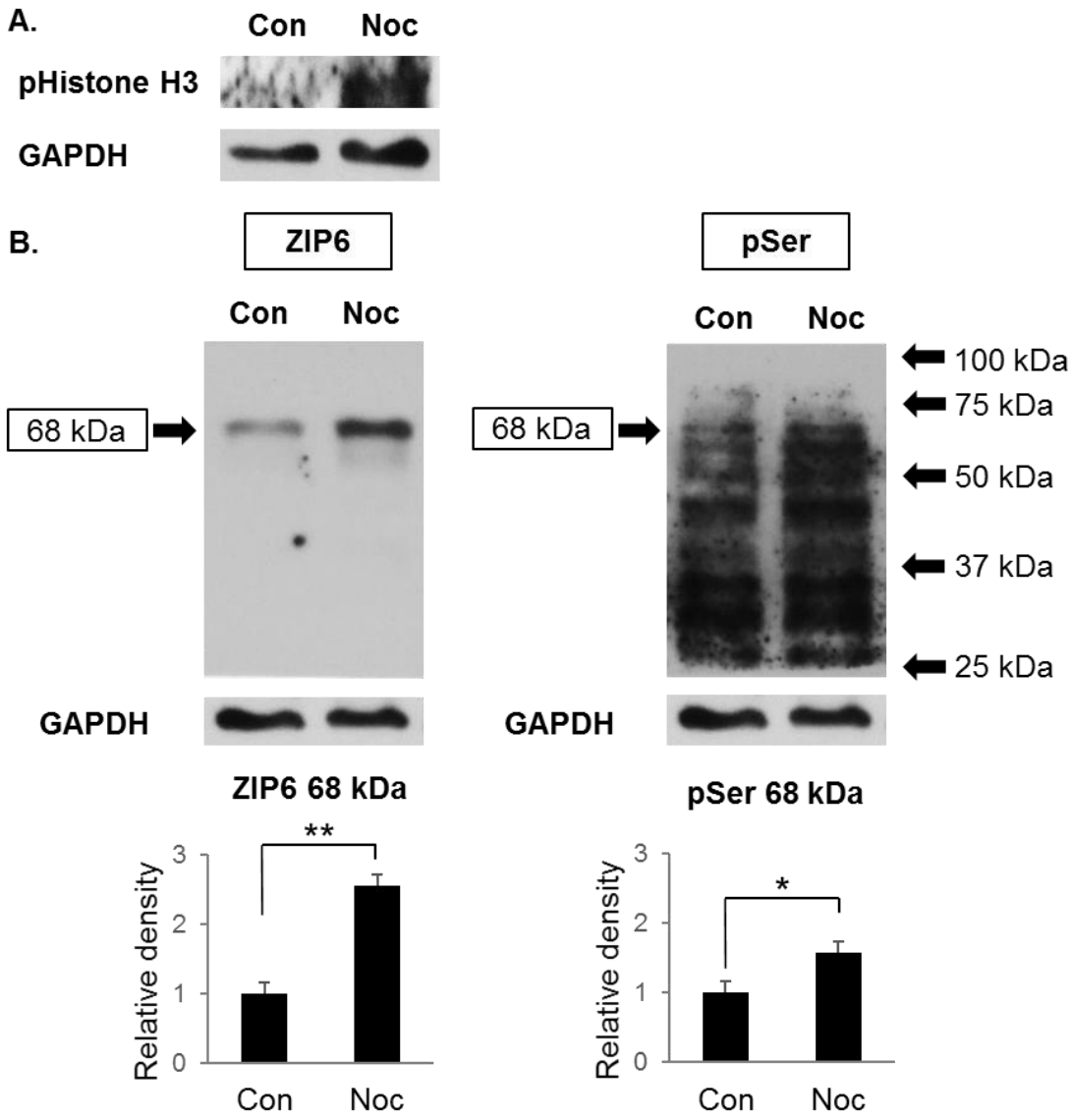

A. MCF−7 cells were treated with 100 nM nocodazole for 20 hours. Immunoblotting was performed using pS10 Histone H3 antibody. Protein bands of pS10 Histone H3 (15 kDa) are demonstrated as a representative result of 3 independent experiments.

B. MCF−7 cells were treated with 100 nM nocodazole for 20 hours. Immunoblotting was performed using pSer and ZIP6 E−20 antibody. Representative protein bands of pSer and ZIP6 are demonstrated. Densitometric data of the pSer bands at 68 kDa and the ZIP6 bands at 68 kDa normalised to GAPDH are demonstrated in bar graphs as mean ± standard error (n = 3). Statistical significance is compared between the nocodazole−treated cells (Noc) and the control without treatment (Con).
* $p < 0.05$, ** $p < 0.01$.

Figure 6.29 CK2 binding to ZIP6

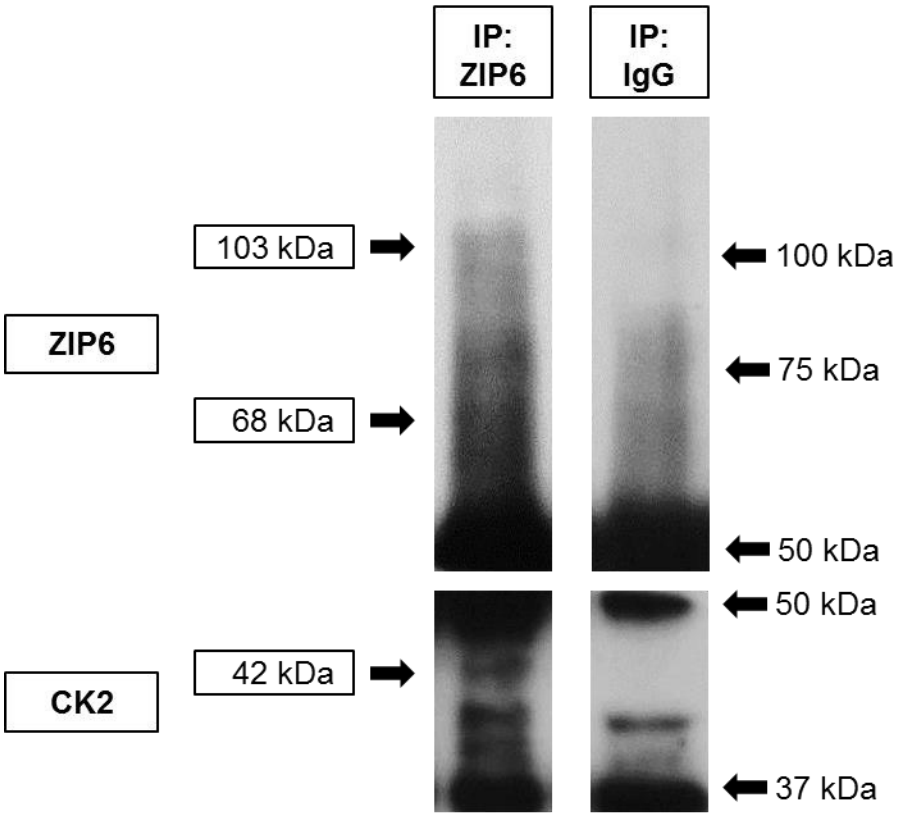

Pooled samples of the adherent and the non−adherent MCF−7 cells were immunoprecipitated with ZIP6 E−20 antibody and rabbit IgG (control). Immunoblotting was performed using ZIP6 E−20 and CK2 antibodies. The bands of ZIP6 at 103 kDa and 68 kDa and CK2 at 42 kDa are shown. The images of both the samples were taken from the same blot.

To identify a specific residue on ZIP6 that was phosphorylated by CK2, immunoprecitation using a V5 antibody was performed in cells that had been transfected with ZIP6 mutants (S471A, S475A, S478A, and T479A). Probing for V5 showed multiple bands of the recombinant ZIP6, including a band compatible with the full−length ZIP6 at 108 kDa (Fig. 6.30), which confirmed the robustness of the V5 immunoprecipitation. Probing for CK2 demonstrated a distinct band at 42 kDa, the predicted size of this protein kinase (Fig. 6.30). Nevertheless, the CK2 levels normalised to V5 did not show a decrease in CK2 binding in any of the ZIP6 mutant samples (Fig. 6.30). This could be explained by the presence of multiple predicted CK2−binding sites in ZIP6 (Fig. 6.1), and mutation of all these sites might be necessary to detect any decrease in binding. Noteworthy, a relatively faint band was consistently obtained for the wild−type ZIP6 sample (Fig. 6.30).

Figure 6.30 CK2 binding to ZIP6 with no specific sites identified

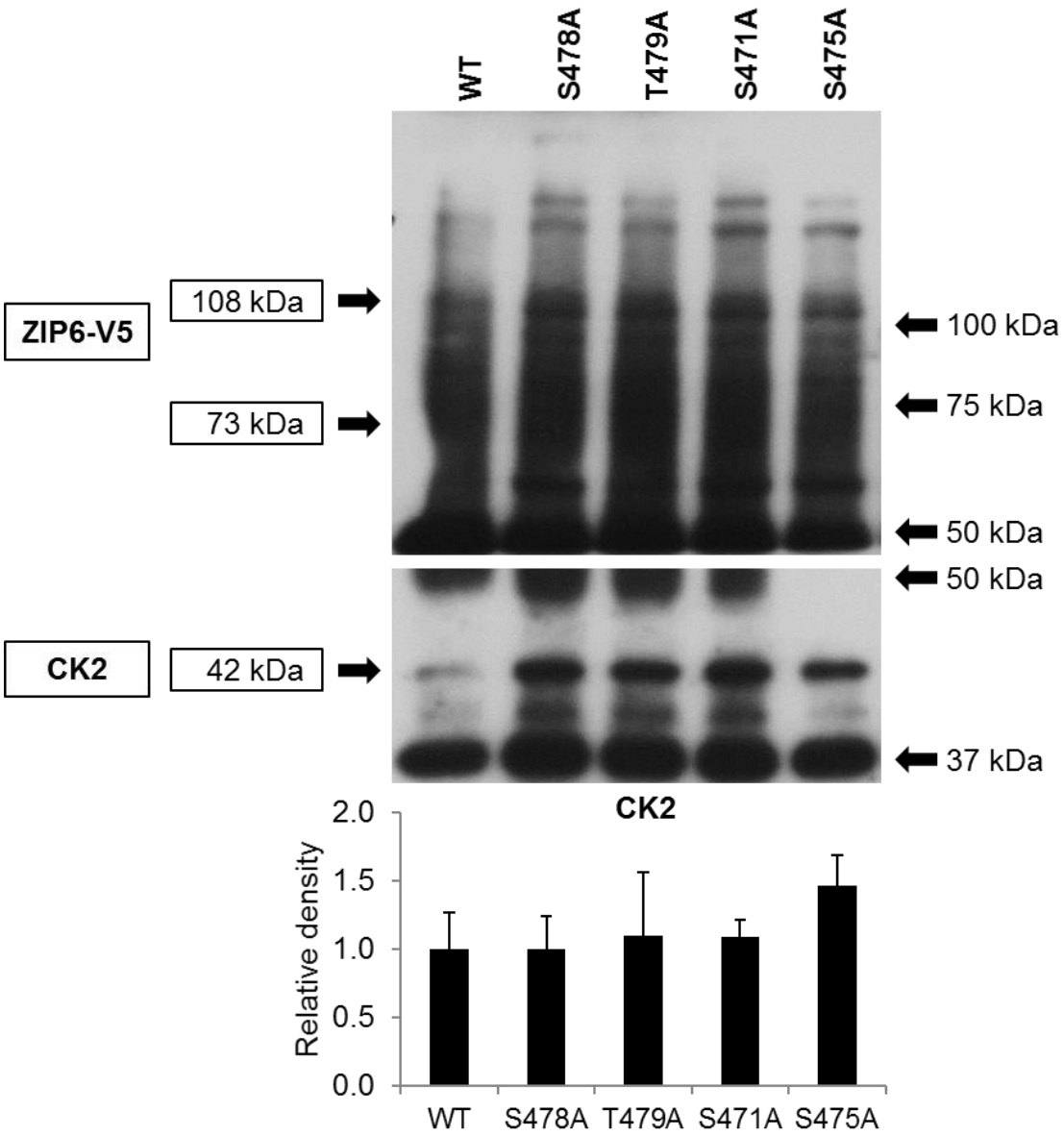

MCF−7 cells were transfected with wild−type ZIP6 and ZIP6 mutants (S478A, T479A, S471A, and S475A) in the presence of butyrate for 16 hours. Pooled samples of the adherent and the non−adherent cells were immunoprecipitated with V5 antibody. Immunoblotting was performed using V5 and CK2 antibodies. Representative protein bands of V5 and CK2 are shown. Densitometric data of the CK2 bands (42 kDa) normalised to V5 (108 kDa) are presented in a bar graph as mean ± standard (n = 4).

GSK-3β is one of the potential kinases that may be responsible for ZIP6 phosphorylation on residues S471 and S475 (Fig. 6.1). To investigate the binding of GSK-3β to ZIP6, immunoprecipitation using the ZIP6 E-20 antibody was performed in nocodazole-treated cells. However, a strong band appeared on the blot for the IgG control when probed for GSK-3β, nullifying the bands detected in the ZIP6-immunoprecipitated sample. Further attempts were therefore made using the V5 immunoprecipitation in cells transfected with wild-type ZIP6. The immunoprecipitated samples were probed for V5 and GSK-3β. A robust immunoprecipitation was shown by the presence of both the 108 kDa and 73 kDa bands of the recombinant ZIP6 (Fig. 6.31). The binding of GSK-3β to ZIP6 was proved by the presence of a faint yet clear band of GSK-3β at 47 kDa (Fig. 6.31). The binding was validated by the absence of a ZIP6 or a GSK-3β band demonstrable in the sample immunoprecipitated with rabbit normal IgG (Fig. 6.31).

To identify a specific residue targeted by GSK-3β, V5 immunoprecipitation was performed in cells that had been transfected with ZIP6 S471A, S475A, S478A, and T479A mutants for 16 hours in the presence of butyrate. The presence of a clear band of V5 at 108 kDa confirmed the robustness of the immunoprecipitation (Fig. 6.32). The presence of a 47 kDa band of GSK-3β was observed in both the wild-type and the mutant constructs, confirming the binding of this kinase to ZIP6 (Fig. 6.32). Importantly, a significant 44% reduction in the intensity of the GSK-3β band was detected for the S471A mutant when compared to wild-type ZIP6 (Fig. 6.32). These data strongly suggested the binding of the kinase to ZIP6 specifically on residue S471, a site predicted to be phosphorylated by GSK-3β (Fig. 6.32).

Figure 6.31 GSK−3β binding to ZIP6

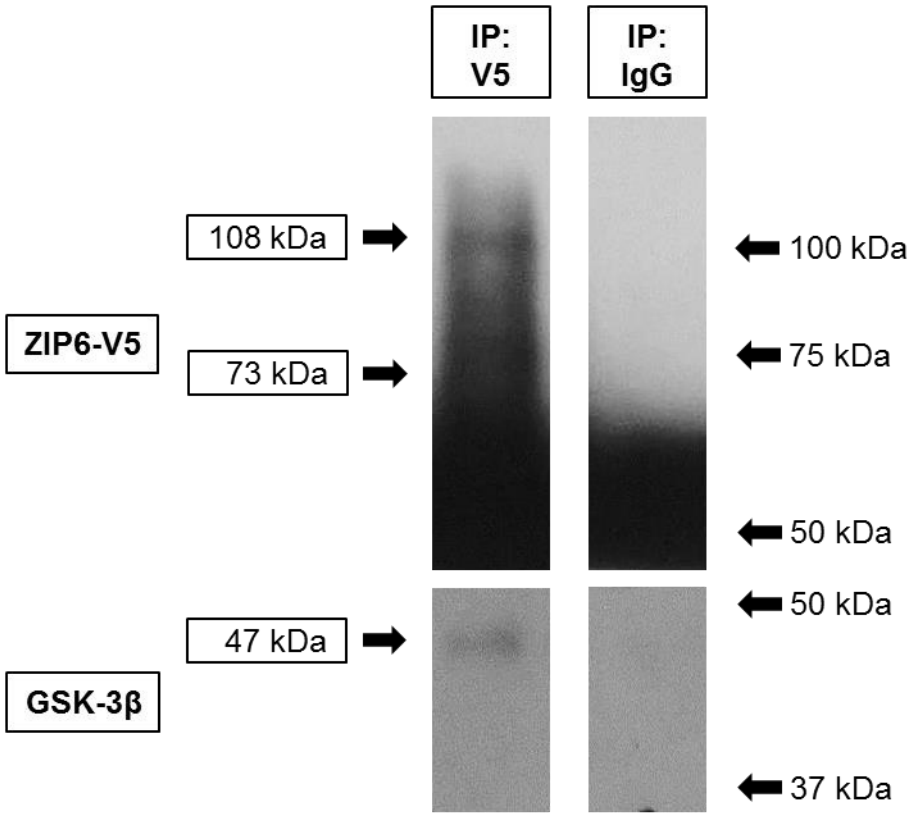

MCF−7 cells were transfected with wild−type ZIP6 in the presence of butyrate for 16 hours. Pooled samples of the adherent and the non−adherent cells were immunoprecipitated with V5 antibody and rabbit IgG (control). Immunoblotting was performed using V5 and GSK−3β antibodies. Protein bands of recombinant ZIP6 at 108 kDa and GSK−3β at 47 kDa are shown. The images of both the samples were taken from the same blot.

CK1 was predicted to phosphorylate ZIP6 on S475 (Fig. 6.1). To investigate the binding of CK1 to ZIP6, immunoprecipitation using the ZIP6 E−20 antibody was performed in cells treated with nocodazole for 20 hours. The probing for ZIP6 revealed the ZIP6 bands at 103 kDa and 68 kDa, confirming that ZIP6 was pulled down during the immunoprecipitation (Fig. 6.33). Probing for CK1 demonstrated a CK1 band at 38 kDa, confirming the binding of this kinase to ZIP6 (Fig. 6.33). The absence of any specific bands in the IgG−immunoprecipitated control verified the binding (Fig. 6.33).

Figure 6.32 GSK−3β binding to ZIP6 on S471

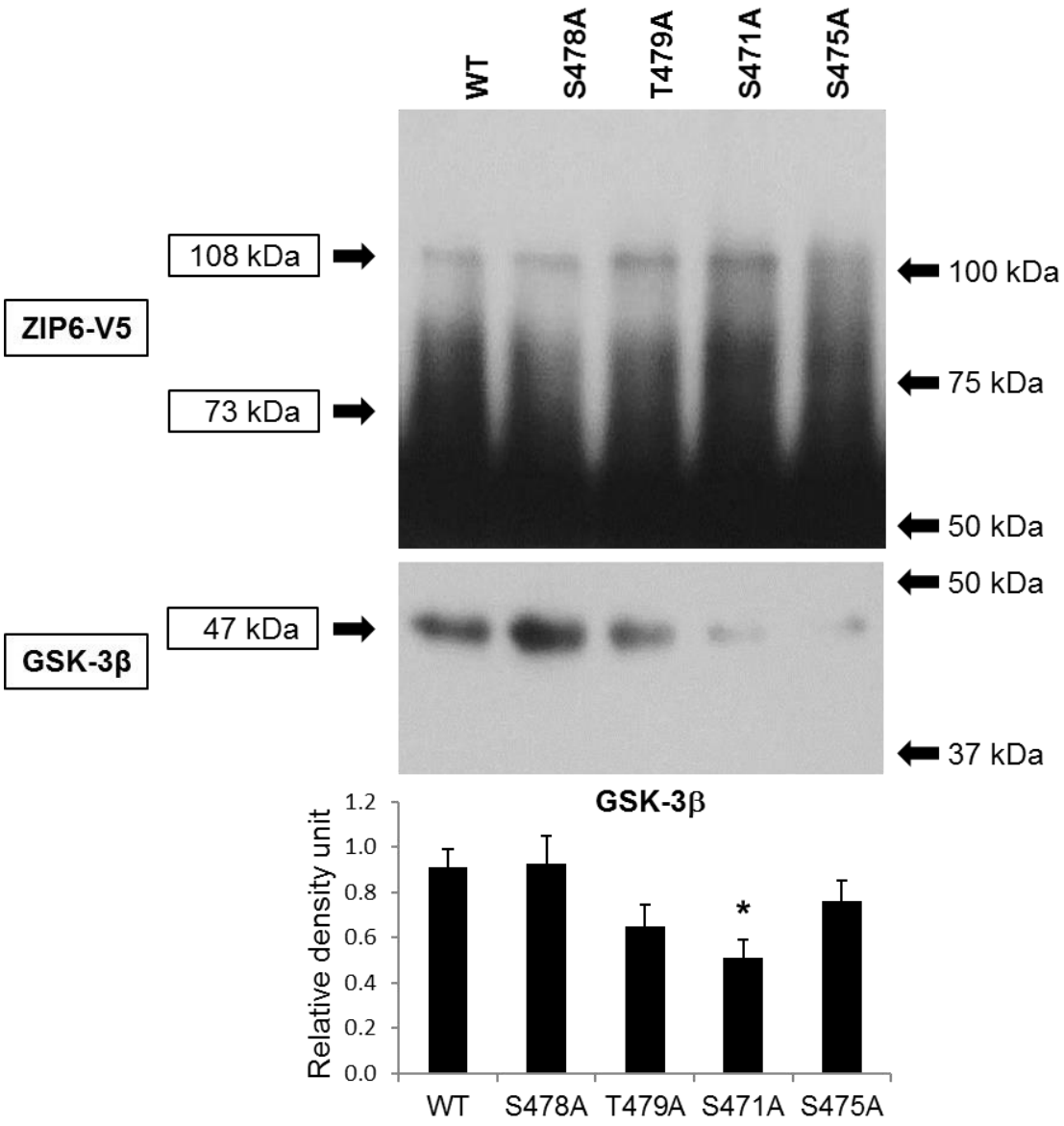

MCF−7 cells were transfected with wild−type ZIP6 and ZIP6 mutants (S478A, T479A, S471A, and S475A) in the presence of butyrate for 16 hours. Pooled samples of the adherent and the non−adherent cells were immunoprecipitated with V5 antibody. Immunoblotting was performed using V5 and GSK−3β antibodies. Representative protein bands of V5 and GSK−3β are shown. Densitometric data of the GSK−3β bands (47 kDa) normalised to V5 (108 kDa) are presented in a bar graph as mean ± standard (n = 4). Statistical significance is compared to wild−type ZIP6.
* $p < 0.05$.

Figure 6.33 CK1 binding to ZIP6

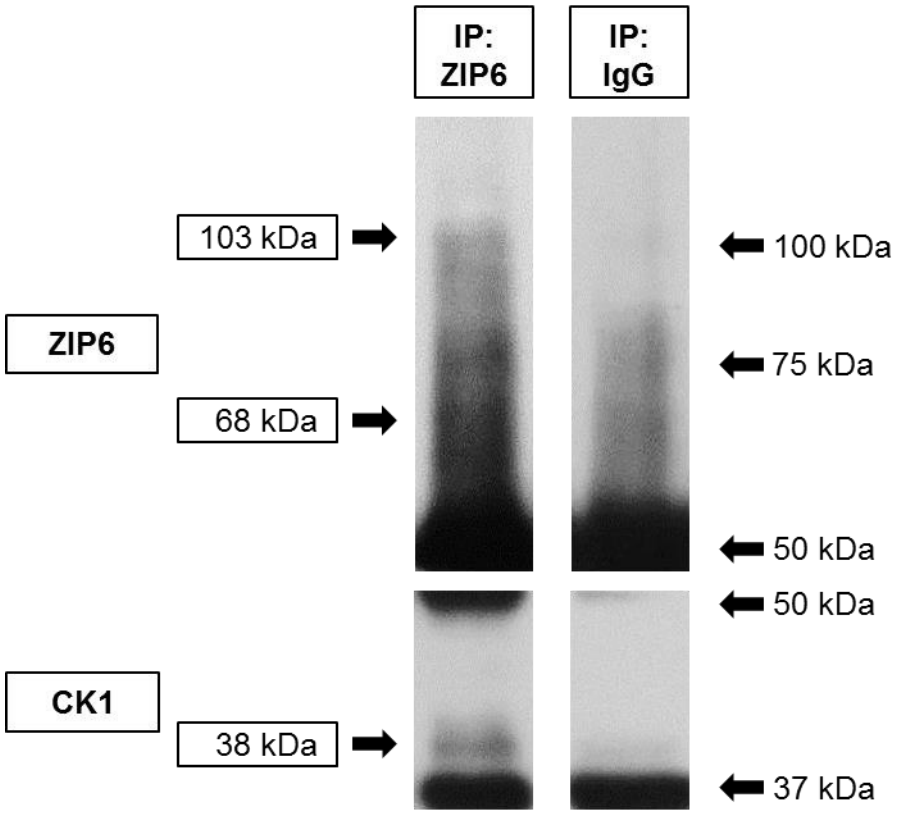

Pooled samples of the adherent and the non−adherent MCF−7 cells were immunoprecipitated with the ZIP6 E−20 antibody and rabbit IgG (control). Immunoblotting was performed using ZIP6 E−20 and CK1 antibodies. Protein bands of ZIP6 at 103 kDa and CK1 at 38 kDa are shown. The images of both the samples were taken from the same blot.

To identify a specific site to which CK1 bound, immunoprecipitation using the V5 antibody was performed in the cells transfected with the ZIP6 mutants. The probing for CK1 demonstrated a CK1 band at 38 kDa (Fig. 6.34). When normalised to V5, the binding was decreased in the cells transfected with the ZIP6 mutants (Fig. 6.34). However, due to the high variability of the data, no significant decrease in intensity could be statistically demonstrated (Fig. 6.34).

PLK1 has been predicted to phosphorylate ZIP6 on residues S471, S475, S478, and T479, although with low prediction scores. Interestingly, PLK1 is activated before and during the mitotic process (Lindqvist *et al.* 2009). To demonstrate the binding of PLK1 to ZIP6 during mitosis, immunoprecipitation was performed in nocodazole−treated cells using the ZIP6 E−20 antibody. The blot both for the nocodazole−treated cells and the control revealed the 103 kDa and 68 kDa bands of ZIP6 when probed with the ZIP6 E−20 antibody

(Fig. 6.35), suggesting the robustness of the immunoprecipitation. Interestingly, the 68 kDa band of PLK1 developed only on the blot of the nocodazole−treated cells, but not the control (Fig. 6.35), confirming the specific binding in the mitotic cells. The absence of any specific bands in the IgG immunoprecipitation control (Fig. 6.35) verified the binding of PLK1 to ZIP6 in the nocodazole−treated cells.

Figure 6.34 CK1 binding to ZIP6 with no specific sites identified

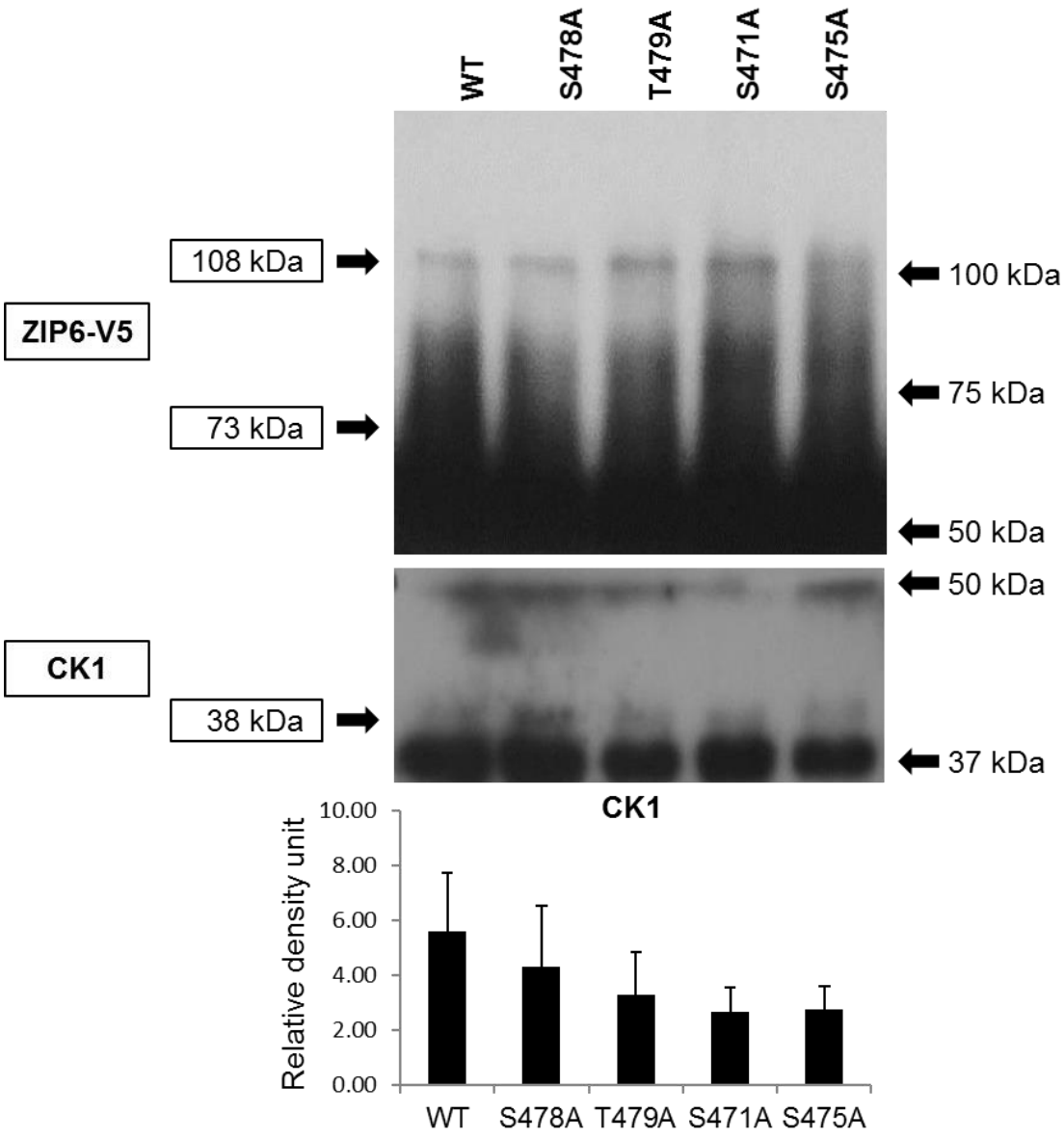

MCF−7 cells were transfected with wild−type ZIP6 and ZIP6 mutants (S478A, T479A, S471A, and S475A) in the presence of butyrate for 16 hours. Pooled samples of the adherent and the non−adherent cells were immunoprecipitated with V5 antibody. Immunoblotting was performed using V5 and CK1 antibodies. Representative protein bands of V5 and CK1 are shown. Densitometric data of the CK1 bands (38 kDa) normalised to V5 (108 kDa) are presented in a bar graph as mean ± standard (n = 4).

Figure 6.35 PLK1 binding to ZIP6 in nocodazole−treated cells

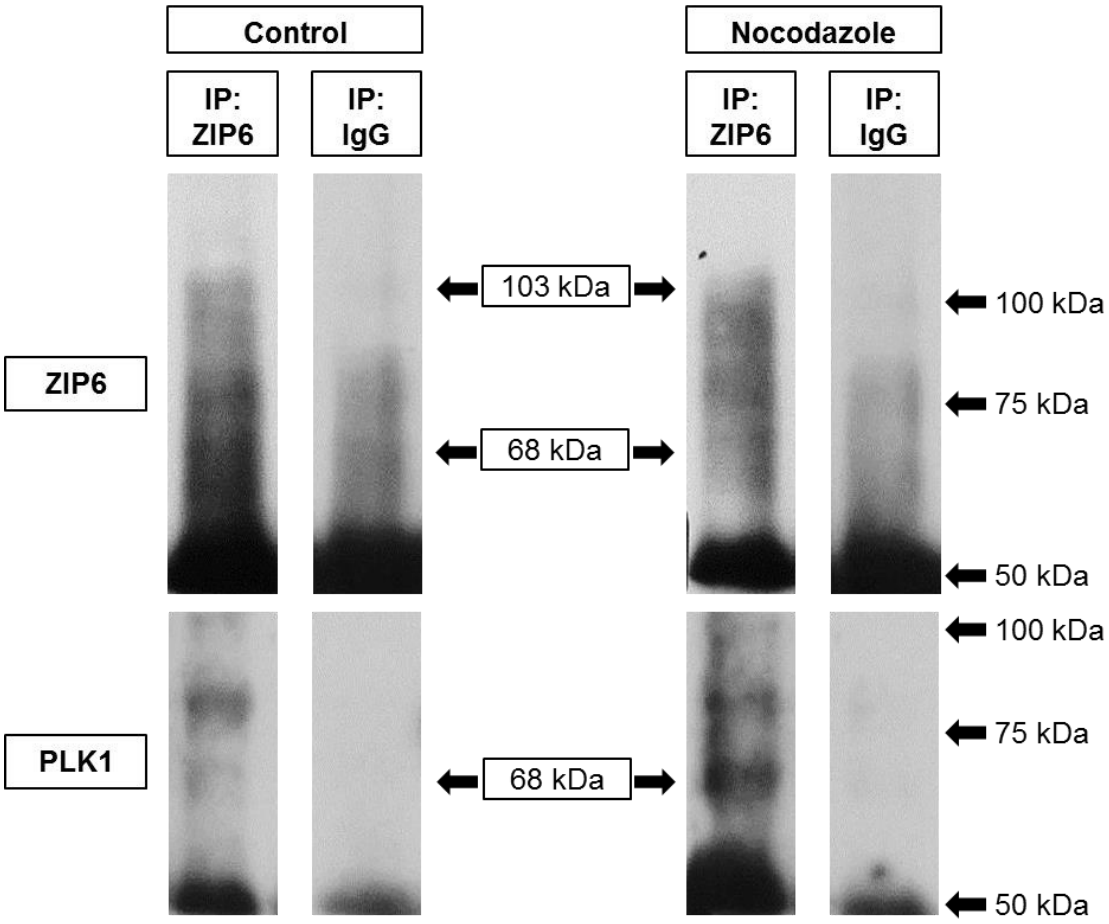

MCF−7 cells were treated with 100 nM nocodazole for 20 hours. Pooled samples of the adherent and the non−adherent cells with nocodazole treatment (nocodazole) and without nocodazole treatment (control) were immunoprecipitated with the ZIP6 E−20 antibody and rabbit IgG (control). Immunoblotting was performed using ZIP6 E−20 and PLK1 antibodies. Protein bands of ZIP6 at 103 kDa and PLK1 at 68 kDa are shown. The images of all the samples were taken from the same blot.

To determine a specific binding residue of PLK1, V5 immunoprecipitation was performed in cells transfected with the ZIP6 mutants. The PLK1 bands at 68 kDa were detected in all the immunoprecitated samples (Fig. 6.36), revealing the binding of PLK1 to all the ZIP6 mutants. However, the intensity of the PLK1 bands normalised to V5 did not show a significant decrease in binding for any of these mutants (Fig. 6.36), suggesting that PLK1 might be able to bind to ZIP6 on multiple sites.

Figure 6.36 PLK1 binding to ZIP6 with no specific sites identified

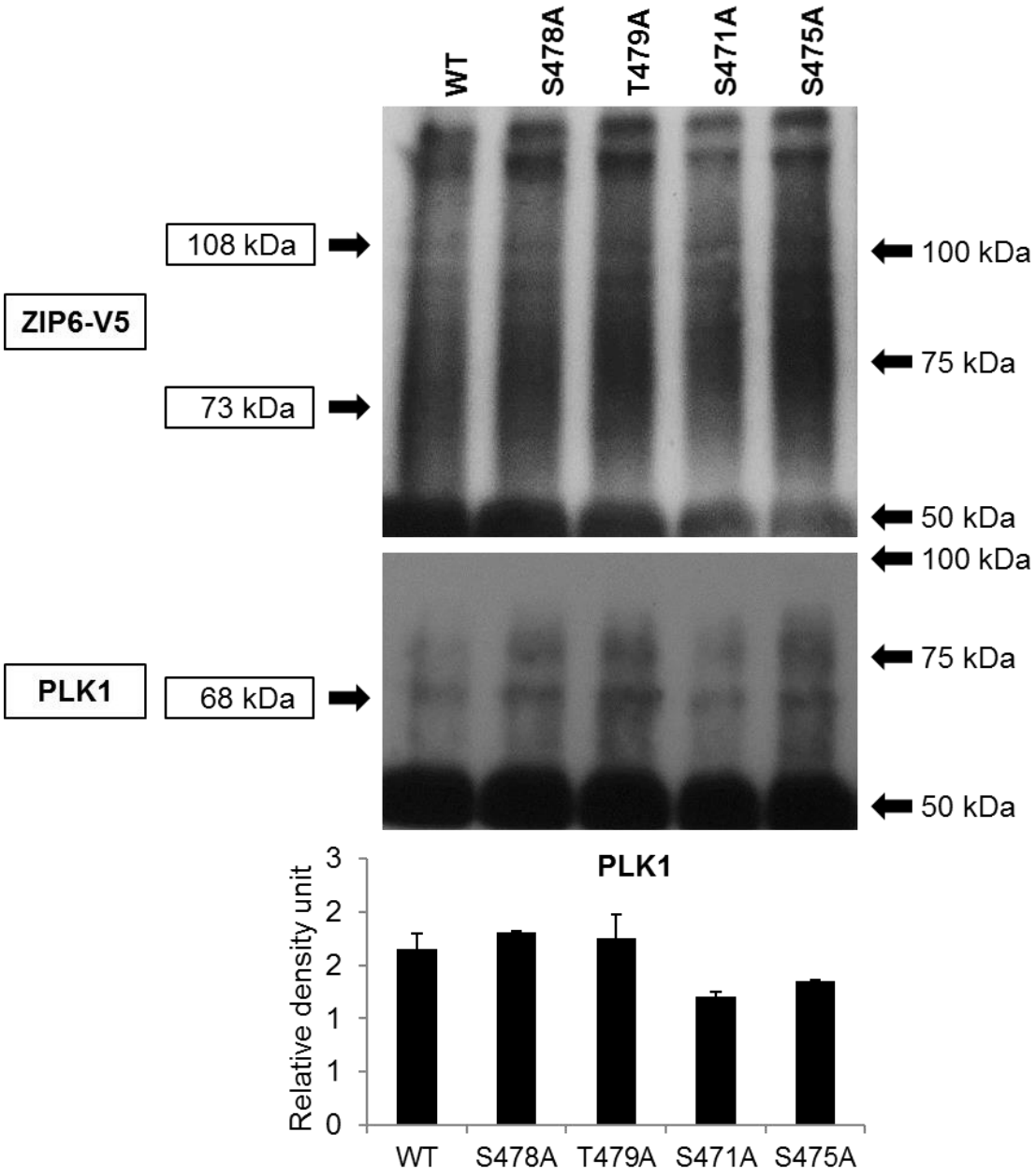

MCF−7 cells were transfected with wild−type ZIP6 and ZIP6 mutants (S478A, T479A, S471A, and S475A) in the presence of butyrate for 16 hours. Pooled samples of the adherent and the non−adherent cells were immunoprecipitated with V5 antibody. Immunoblotting was performed using V5 and PLK1 antibodies. Representative protein bands of V5 and PLK1 are shown. Densitometric data of the PLK bands (68 kDa) normalised to V5 (108 kDa) are presented in a bar graph as mean ± standard (n = 2).

Noteworthy, the immunoprecipitation in the cells transfected with ZIP6 mutants to determine specific residues to which individual kinases bound had limited implications due to the inability to demonstrate the 73 kDa bands of the recombinant ZIP6, which represent the active ZIP6 on the plasma membrane (Fig. 6.8). These 73 kDa bands were severely masked by the smearing pattern of the bands in the particular region. The bands of the kinases were therefore normalised to the 108 kDa bands of the recombinant ZIP6, which are equivalent to the ZIP6 pro-protein in the ER (Fig. 6.8). Alternatively, this might be implied that the kinases were able to bind to ZIP6 in its pro-protein form in the ER.

To visualise the binding of CK2, GSK-3β, CK1, and PLK1 to ZIP6 specifically in mitotic cells, PLA was performed in cells that had been treated with nocodazole for 20 hours, using the ZIP6 E-20 antibody with individual antibodies that target these kinases. PLA signals were observed predominantly in the mitotic cells when the ZIP6 antibody was used together with CK2, GSK-3β, CK1, or PLK1 antibody (Fig. 6.37). For CK2, the mitotic cells contained an average of 5.9 PLA signals/cell, compared to an average of 0.8 PLA signals/cell in the non-mitotic cells (Fig. 6.37). For GSK-3β, 8.8 signals/cell were detected in the mitotic cells, whereas the adjacent non-mitotic cells contained 1.0 signal/cell (Fig. 6.37). For CK1, averagely 4.5 PLA signals/cell were detected in the mitotic cells, compared to the adjacent non-mitotic cells, which contained 1.1 signals per cell (Fig. 6.37). For PLK1, the mitotic cells had 7.5 PLA signals/cell, compared to the adjacent non-mitotic cells with 0.5 PLA signals/cell (Fig. 6.37). When the PLA signals were compared between the mitotic cells and the non-mitotic cells, statistical significance was demonstrated for the binding of all the investigated kinases to ZIP6 (Fig. 6.37), signifying that this binding of these kinases was substantially increased in mitosis.

Figure 6.37 Binding of CK2, GSK−3β, CK1, and PLK1 to ZIP6 in mitosis

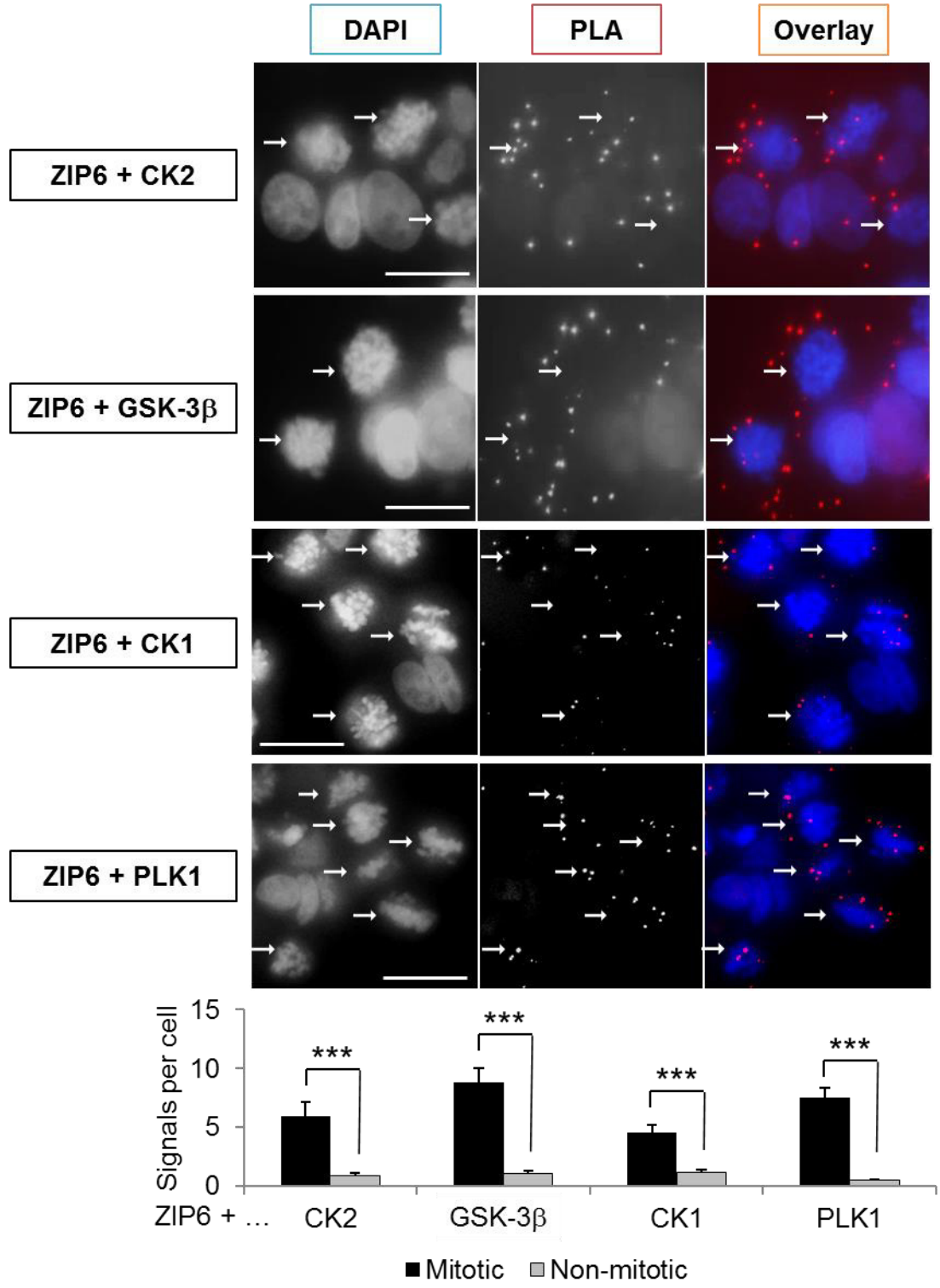

MCF−7 cells on 8−well chamber slides were treated with 100 nM nocodazole for 20 hours. Proximity ligation assays using the ZIP6 E−20 antibody plus either CK2, GSK−3β, CK1, or PLK1 antibody was performed. Mitotic cells are indicated by white arrows. Quantitative measurements in at least 6 images of 25 stacks taken 0.3 µm apart from 3 independent experiments are demonstrated as mean ± standard error. Statistical significance is compared between the signals in the mitotic and the non−mitotic cells.
*** $p < 0.001$. Scale bar, 25 µm.

To exclude the non-specific staining produced by PLA reagents or the antibodies, PLA was performed using individual ZIP6, CK2, GSK-3β, and CK1 antibodies, or without an antibody. The average signals when a single antibody was added were 0.9, 2.0, 1.7, and 1.0 PLA signals/cell for the ZIP6, CK2, GSK-3β and CK1 antibodies, respectively (Fig. 6.38). These signal levels were comparable to the PLA without antibody, which showed 1.5 PLA signals/cell (Fig. 6.38), suggesting that the non-specific signals were not attributed to the antibodies used. The PLA signals produced in these negative controls were significantly lower than when each pair of the antibodies was added, thereby validating the binding of the kinases to ZIP6.

The PLA signals detected in these experiments (Fig. 6.37) were relatively low, when compared to the PLA that determined the binding of pS727 STAT3 to ZIP6 (Fig. 6.16), pStathmin (Fig. 6.18) and ZIP10 (Fig. 6.21) and the binding of ZIP6 to ZIP10 (Fig. 6.20), which detected a range of 21 to 140 PLA signals/cell in mitotic cells. These low signals might suggest that CK2, GSK-3β, CK1, and PLK1 bound to ZIP6 to a lesser extent than pS727 STAT3 and ZIP10 did. Given that the STAT3-binding site is located in the same region as the phosphorylation sites (Fig. 6.1), the binding of pS727 STAT3 to ZIP6 could have interfered with the recognition of either ZIP6 or the kinases by the antibodies. Alternatively, the antibody recognition might also be masked by the complex formation of ZIP6 and ZIP10, which could hide the epitopes within the complex.

The GSK-3β binding to ZIP6 was notable, given that the PLA signals were the highest compared to the other kinases (Fig. 6.37), suggesting the greatest extent of the binding. Furthermore, this binding added a complexity to the previous finding of ZIP6 being an upstream inhibitor of GSK-3β (Hogstrand et al. 2013). A possible explanation was that when GSK-3β function was increased, the phosphorylation of ZIP6 by this kinase might provide a negative feedback loop to control the function of this kinase. Given that GSK-3β was inhibited during EMT, but active in phosphorylating ZIP6 during mitosis, this might also provide a switch mechanism that predestines whether a rounded cell should migrate or divide. Additionally, this GSK-3β-mediated ZIP6 phosphorylation might be needed before phosphorylation on other sites could occur (Ayuso *et al.* 2010).

Figure 6.38 Negative controls for proximity ligation assays

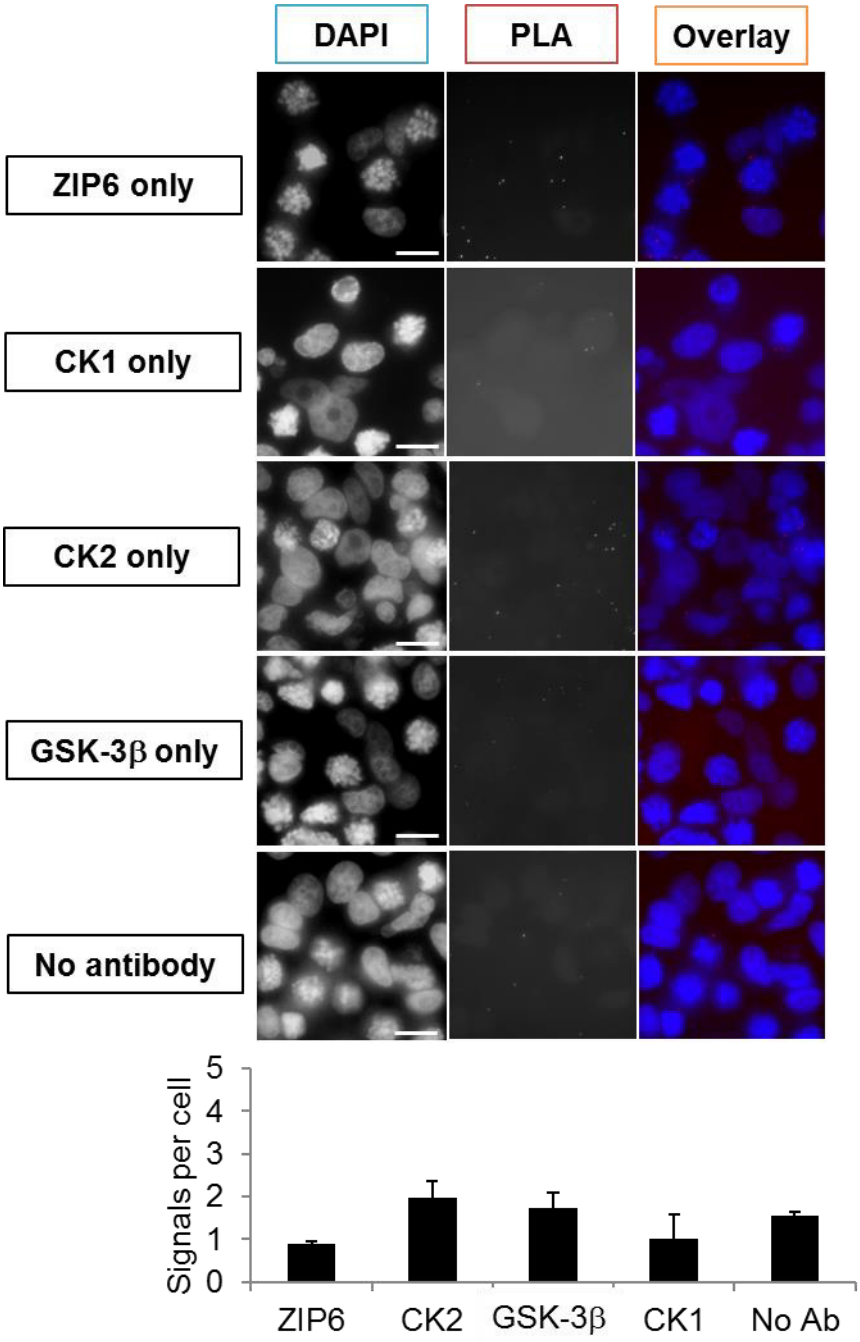

MCF−7 cells on 8−well chamber slides were treated with 100 nM nocodazole for 20 hours. Proximity ligation assays using individual ZIP6 E−20, CK2, GSK−3β, and CK1 antibodies or without a primary antibody (No Ab) was performed. Quantitative measurements in at least 4 images of 25 stacks taken 0.3 µm apart are demonstrated as mean ± standard error (n = 3).

Additionally, the binding of PLK1 to ZIP6 suggested that the mechanism of action of ZIP6 in mitosis might involve its association with PLK1 both before and during mitosis. In the light of the pivotal roles for PLK1 in successful mitosis, ZIP6 might help PLK1 facilitate cell entry into the mitotic phase, formation of the mitotic spindles, and division of the cytosol during cytokinesis at the end of the mitotic process (van Vugt and Medema 2005). Alternatively, it is also possible that ZIP6 might in fact be a downstream effector of PLK1, which facilitated the mitotic processes through zinc influx mediated by ZIP6, given that zinc is required for mitosis (Chesters and Petrie 1999).

6.4 Chapter summary

Our group have established that ZIP6 is required for cell rounding in EMT (Hogstrand et al. 2013). In this chapter, some evidence of ZIP6 involvement in cell rounding prior to mitosis was provided. ZIP6−mediated zinc influx was enhanced during mitosis, resulting in an increase in cellular zinc levels (Fig. 6.7−6.14). This increase in zinc levels in mitotic cells explained the presence of a particular modification of STAT3, pS727 STAT3, throughout mitosis, which is directly promoted by zinc (Nimmanon et al., manuscript in preparation). A twofold binding of pS727 STAT3 was also detected. Firstly, it bound to ZIP6 during mitosis on the predicted STAT3 binding site with sequence YESQ (positions 473−476) (Fig. 6.15 and 6.16), probably participating with ZIP6 in driving the mitotic process. Secondly, it was shown to bind to pStathmin (Fig. 6.18), linking the possible function of pS727 STAT3 to the role for pStathmin in microtubule reorganisation (Rubin and Atweh 2004). Importantly, the heteromer formation of ZIP6 and ZIP10 (Fig. 6.19 and 6.20) as well as the binding of pS727 STAT3 to ZIP10 was also observed in mitotic cells (Fig. 6.21), suggesting the close association of pS727 STAT3, ZIP6, and ZIP10 in mitosis. Additionally, N−terminal cleavage of ZIP6 was detected in early mitosis (Fig. 6.22). Potential proteases for this cleavage as suggested by the protease antibody arrays included ADAM9, MMP−7, presenilin, and proprotein convertase, with presenilin having the most potential due to the highest percentage increase in enzyme levels during mitosis (Fig. 6.23−6.25).

Additionally, ZIP6 was proved for the first time to be serine−phosphorylated. Interestingly, ZIP6 phosphorylation was shown to be enhanced not only as a result of zinc treatment (Fig. 6.26), but also during mitosis (Fig. 6.28). The kinases that were shown to bind to ZIP6 during mitosis, which might be responsible for the serine phosphorylation of ZIP6, were CK2, GSK−3β, CK1, and PLK1 (Fig. 6.29−6.38). Importantly, residue S471 of ZIP6 was shown to be the specific GSK−3β−binding site (Fig. 6.32), whereas the inability to indicate any specific residue that was phosphorylated by CK2, CK1, and PLK1 suggested the presence of more than one residue targeted by these kinases. These data provided a deeper insight into the post−translational mechanism of ZIP6 in mitosis.

Chapter 7:
Mitosis inhibitory effects of ZIP6 and ZIP10 antibody treatment

7.1 Introduction

In chapter 6, ZIP6 was shown to be actively involved in mitosis through its zinc−import function and its association with zinc−induced pS727 STAT3. Furthermore, it was shown to form a complex with its closest paralogue, ZIP10. To demonstrate whether ZIP6 and ZIP10 were needed for initiation of mitosis, we inhibited ZIP6 and ZIP10 function by treating cells with ZIP6 or ZIP10 antibodies that bound to these zinc channels at an extracellular epitope on the N−terminus. Additionally, NMuMg mouse mammary glandular cells with ZIP6 knockout using the clustered regularly interspaced short palindromic repeats (CRISPR) technique were received from Dr. Gerold Schmitt−Ulms, University of Toronto. The effects of this ZIP6 knockout on cell growth were therefore also investigated.

7.2 Materials and methods

Please refer to Chapter 2 for the details of the treatments (Section 2.1), immunofluorescence (Section 2.3), western blotting (Section 2.4), flow cytometry (Section 2.5), and zinc assays (Section 2.5). The ZIP6 and ZIP10 antibodies used for the treatments with their epitopes are listed in Table 2.1, and the schematic of their epitopes is shown in Fig. 6.5.

7.3 Results and discussion

7.3.1 ZIP6 Y antibody inhibits mitosis in MCF−7 cells

Two ZIP6 antibodies, ZIP6 M and ZIP6 Y, have been developed in our group and designed to recognise the N−terminus of ZIP6 at residues 93–107 and residues 238–254, respectively (Hogstrand et al. 2013) (Table 2.1). Exploiting these two ZIP6 antibodies, we determined the importance of ZIP6 in mitosis by performing treatment with either of the antibodies in the presence of nocodazole, hypothesising that the antibody binding was able to prevent ZIP6 function. This means of functional inhibition of a protein has been successfully employed for investigating Wnt−1 in different human cancer cell lines (He *et al.* 2004). In this study, a monoclonal Wnt−1 antibody successfully inhibited Wnt−1 signalling and triggered the apoptotic process, the same effects that were observed when Wnt−1 gene expression was silenced using Wnt−1 siRNA.

To determine whether treatment with the ZIP6 antibodies could inhibit mitosis, MCF-7 cells were treated with a 1:20 dilution of the ZIP6 Y or ZIP6 M antibody in the presence of nocodazole for 20 hours and stained with propidium iodide. Cell cycle analysis was then performed using flow cytometry. Noteworthy, the ZIP6 M epitope was shown to be cleaved off prior to relocation of ZIP6 to the plasma membrane (Hogstrand et al. 2013), whereas the ZIP6 Y epitope was shown to be cleaved off in early mitosis (Section 6.3.5). Based upon these findings of the ZIP6 proteolytic cleavage, only the epitope of ZIP6 Y, but not the epitope of ZIP6 M, should be present on cell surface in early mitosis. The ZIP6 M antibody treatment was therefore employed as a negative control. The histogram revealed that the treatment with the ZIP6 Y or ZIP6 M antibody resulted in an increase in the diploid (2n) cell population (the left peak of the histogram), which represents cells in the G0 or G1 phase, when compared to the nocodazole-treated cells without antibody treatment (Fig. 7.1A). In contrast, the tetraploid (4n) cell population (the right peak of the histogram), which represents cells in the G2 or M phase, was apparently decreased as a result of the antibody treatment when compared to the nocodazole-treated cells without antibody treatment (Fig. 7.1A). The increases in the G0/G1 population and the decreases in the G2/M population as a result of the antibody treatments were confirmed by the analysis using the Watson Pragmatic algorithm (Fig. 7.1B,C). This analysis revealed that the nocodazole treatment successfully increased the G2/M population from 22% to 41%, and the nocodazole-induced G2/M cells were significantly reduced by 12% as a result of the ZIP6 Y antibody treatment (Fig. 7.1B,C). A 9% decrease in the G2/M population was also observed as a result of the ZIP6 M antibody treatment when compared to the nocodazole-treated cells without antibody treatment, but with no statistical significance observed (Fig. 7.1B,C). The inability of the ZIP6 M antibody to suppress nocodazole-induced mitosis confirmed the N-terminal cleavage of ZIP6 at a PEST site distal to the ZIP6 M epitope prior to ZIP6 relocation to the plasma membrane (Hogstrand et al. 2013). Furthermore, this negative result for the ZIP6 M antibody treatment also validated that the decrease in the G2/M population as a result of the ZIP6 Y antibody treatment was due to the binding of the antibody to ZIP6 on the plasma membrane.

Figure 7.1 Decreased G2/M population by ZIP6 Y antibody

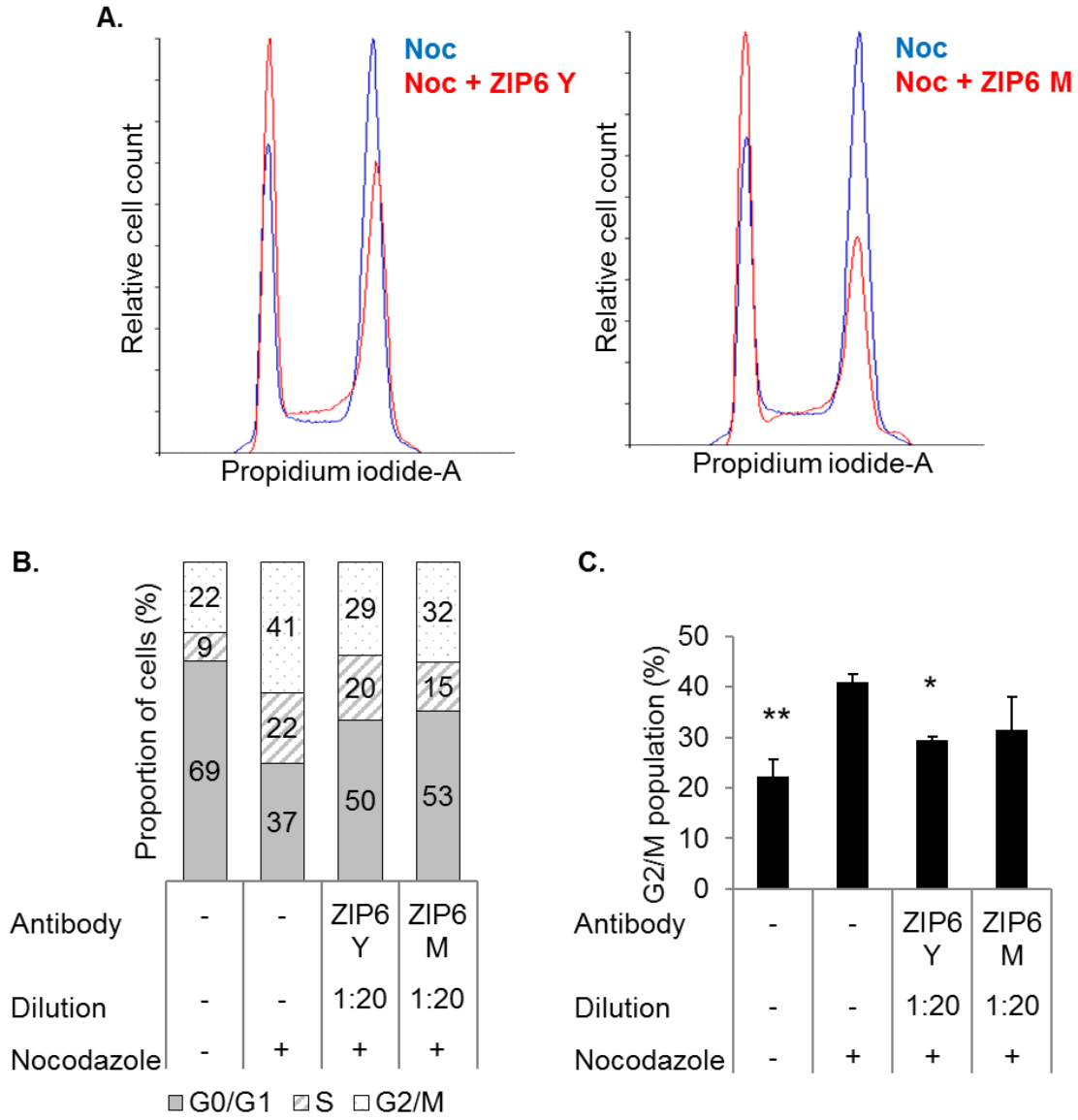

MCF−7 cells were treated with 100 nM nocodazole and incubated with the ZIP6 Y or ZIP6 M antibody for 20 hours. The cells were stained with propidium iodide. DNA content was measured using FACS analysis. Overlapping histograms for the nocodazole−treated cells without antibody treatment (Noc) and the nocodazole−treated cells incubated with either the ZIP6 Y (Noc + ZIP6 Y) or ZIP6 M (Noc + ZIP6 M) antibody were generated using Flowing Software (A). Percentages of the cells in the G0/G1, S and G2/M phases determined using FlowJo Software are presented as a 100% stacked column chart (B). The percentages of the G2/M population are also presented in a bar graph as mean ± standard error (n = 3) (C). Statistical significance is compared to the nocodazole−treated cells without antibody treatment.
* $p < 0.05$, ** $p < 0.01$.

The insignificant decrease in the G2/M population observed as a result of the ZIP6 M antibody treatment (Fig. 7.1) might be attributed to an off-target binding effect of the antibody. Using a BLAST analysis tool of the National Center for Biotechnology Information (NCBI) (Madden 2002), the epitope of the ZIP6 M antibody was detected in the Swissprot database to partially match the sequences of alpha-1G and alpha-1H subunits of the voltage-dependent T-type calcium channel. T-type calcium channels are highly expressed in tumour cells and involved in cell cycle progression (Taylor *et al.* 2008a). The partial affinity of the antibody to this calcium channel could therefore interfere with nocodazole-induced mitosis, explaining the insignificant yet observable decrease in mitosis as a result of the ZIP6 M antibody treatment. Alternatively, this decrease in the G2/M population could also be attributed to the ability of IgG to bind zinc (Yamanaka *et al.* 2016), which might result in cellular zinc deficiency and thereby mitosis inhibition. For these reasons, the ZIP6 M antibody would not be included in the following experiments.

To determine percentages of cells specifically in the M phase, immunofluorescence was performed in MCF-7 cells using a pS10 histone H3 antibody, a mitotic marker. Mitotic cells were counted in images taken from the immunofluorescence slides. In non-treated cells, 4% of the cells were mitotic (pS10 histone H3-positive) (Fig. 7.2). With nocodazole treatment, the mitotic cells were increased to 22% (Fig. 7.2). This nocodazole-induced mitosis was significantly reduced to 4% as a result of treatment with a 1:20 dilution of the ZIP6 Y antibody (Fig. 7.2). This decrease was demonstrated to be concentration-dependent (Fig. 7.2). These data confirmed that the treatment with the ZIP6 Y antibody successfully inhibited nocodazole-induced mitosis. Noteworthy, when compared to the percentages of the G2/M population as determined by FACS analysis (Fig. 7.1), the percentages of the mitotic cells that were stained positive for pS10 histone H3 (Fig. 7.2) were relatively small. In particular, when the cells were treated with a 1:20 dilution of the ZIP6 Y antibody in the presence of nocodazole, only 4% of the cells were positive for pS10 histone H3, accounting for 13% of the G2/M population as shown by FACS. According to these findings, it could be implied that 87% of the G2/M cells were in the G2 phase, consistent with a previous study that reported an increase in G2 cells as a result of cell cycle arrest (Luk *et al.* 2009).

Figure 7.2 Concentration−dependent mitosis inhibition by ZIP6 Y antibody

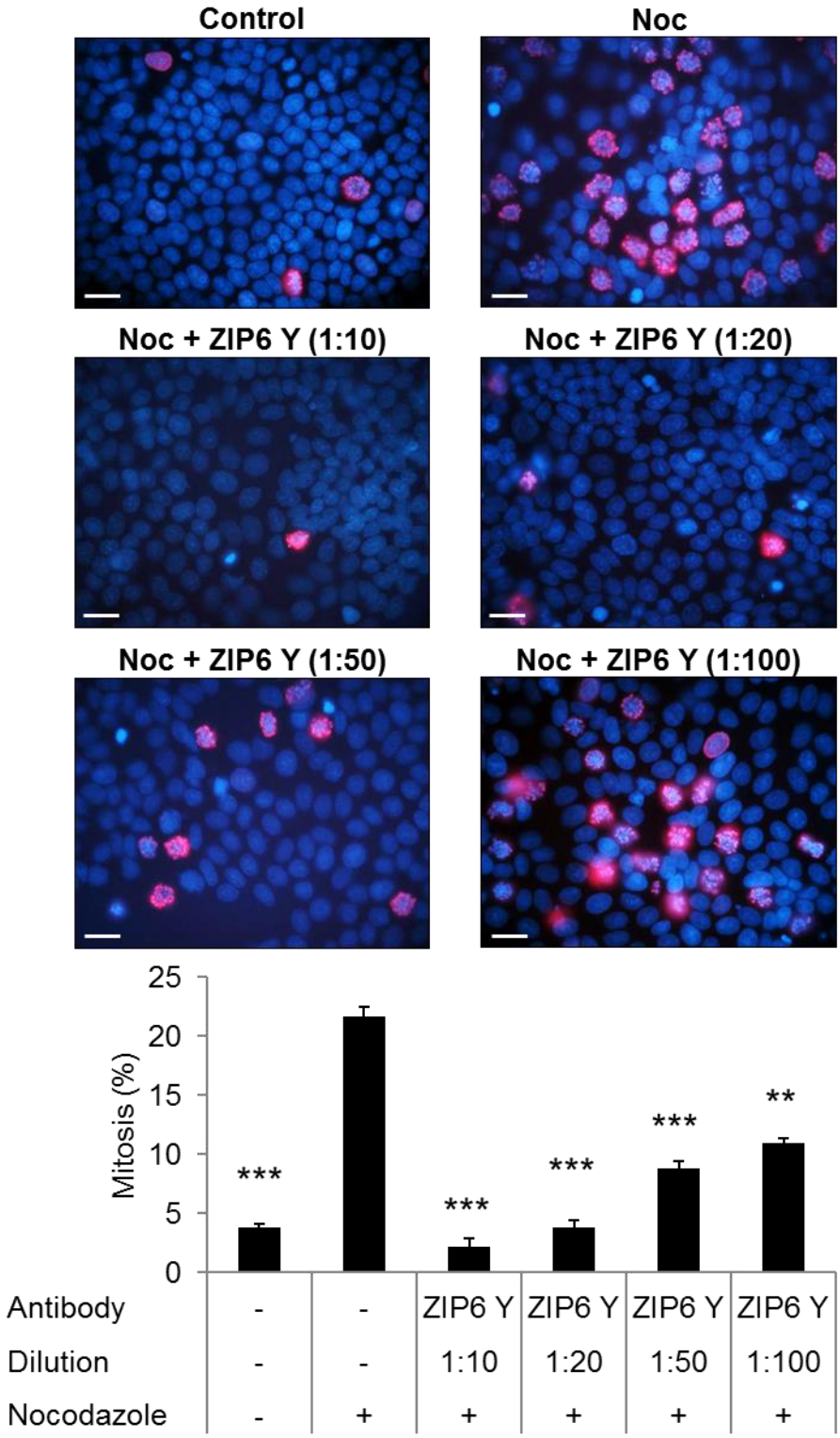

MCF−7 cells were treated with 100 nM nocodazole (Noc) and incubated with the ZIP6 Y antibody for 20 hours. The cells were immunostained with a rabbit pS10 histone H3 antibody, which was conjugated to Alexa Fluor 594 (red). The nuclei were stained with DAPI (blue). A representative image of each sample is shown. Percentages of mitotic cells are presented in a bar graph as mean ± standard error (n = 3). Statistical significance is compared to the nocodazole−treated cells without antibody treatment.
Scale bar, 25 µm. ** $p < 0.01$, *** $p < 0.001$.

To determine whether the effect of the antibody treatment could be observed for endogenous mitosis without any chemical induction, MCF-7 cells were synchronised using a serum deprivation technique. This technique limits exposure of the cells to mitogens or growth factors, thereby causing the cells to exit the cell cycle and enter the G0 phase (Rosner et al. 2013). Serum was withdrawn from the medium for 24 hours and added back to allow the cells to re-enter the G1 phase and progress through the following stages of the cell cycle. To determine the time when the serum-deprived cells reached the M phase following the serum repletion, the cells were harvested at different time points and immunofluorescence was performed using a pS10 histone H3 antibody. Mitotic cells were counted in images taken from the immunofluorescence slides and the mitotic cell numbers were compared to the control that had not been serum-deprived, which showed a basal mitotic rate of 3.8% (Fig. 7.3). Following serum replenishment, the mitotic rate in the cells previously deprived of serum started to increase at 27 hours, and a maximal increase was observed at 30 hours, with a mitotic rate of 7.2%, indicating this time point as the optimised time for cell entry into the mitotic phase (Fig. 7.3). After 30 hours, the mitotic rate reduced from the peak to 6.7% at 31 hours and 5.3% at 32 hours, implying the cells re-entering the G1 phase (Fig. 7.3). To determine the effect of the ZIP6 Y antibody treatment on endogenous mitosis, the antibody was added at 24 hours and the cells were harvested for immunofluorescence using the pS10 histone H3 antibody at 30 hours after serum replenishment. The mitotic count revealed that the mitotic rate was reduced from 8.2% to 4.4% as a result of the ZIP6 Y antibody treatment (Fig. 7.4). These data therefore confirmed the ability of the ZIP6 Y antibody to prevent not only the nocodazole-induced mitosis, but also the physiological cell cycle progression into the mitotic phase.

Figure 7.3 Maximum mitosis at 30 hours after serum replenishment

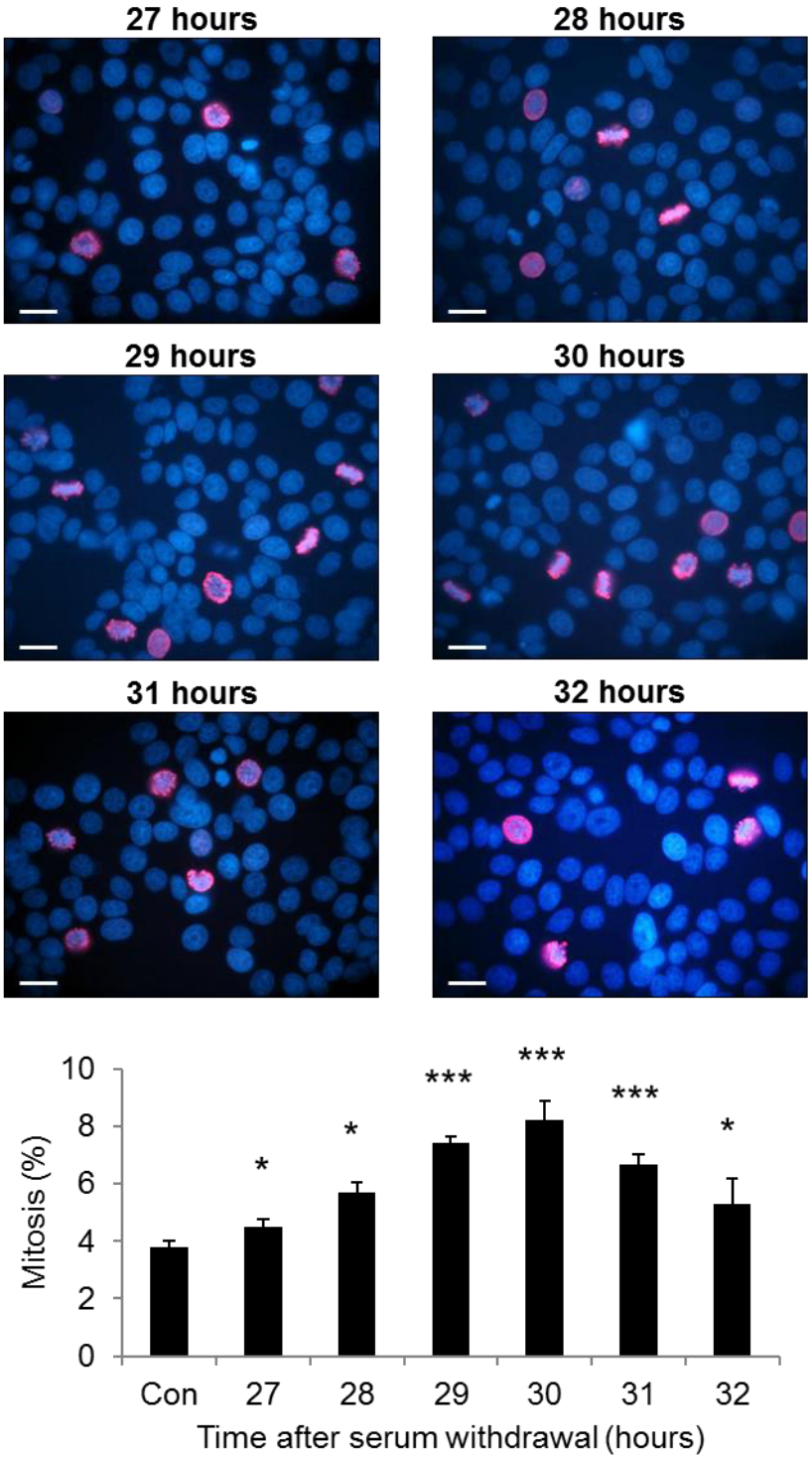

When MCF−7 cells were 50−70% confluent, they were grown in serum−free medium for 24 hours and fixed at 27−32 hours after serum replenishment. The cells were immunostained with a rabbit pS10 histone H3 antibody, which was conjugated to Alexa Fluor 594 (red). The nuclei were stained with DAPI (blue). A representative image of each of the samples that were harvested at 27−30 hours is shown. Percentages of mitotic cells are presented in a bar graph as mean ± standard error (n = 3). Statistical significance is compared to the control without serum starvation (Con).
Scale bar, 25 µm. * $p < 0.05$, *** $p < 0.001$.

Figure 7.4 Inhibition of endogenous mitosis by ZIP6 Y antibody

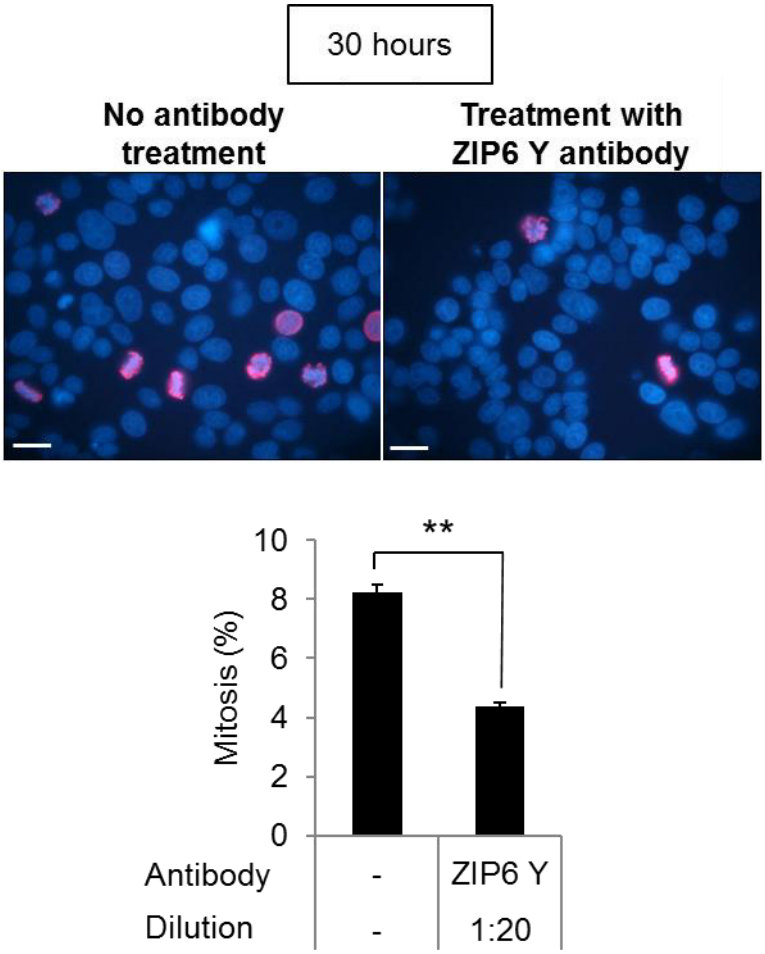

When MCF−7 cells were 50−70% confluent, they were grown in serum−free medium for 24 hours. They were incubated with a 1:20 dilution of the ZIP6 Y antibody at 24 hours and fixed in 4% formaldehyde at 30 hours after serum replenishment. The cells were immunostained with a rabbit pS10 histone H3 antibody, which was conjugated to Alexa Fluor 594 (red). The nuclei were stained with DAPI (blue). A representative image of each sample is shown. Percentages of mitotic cells are presented in a bar graph as mean ± standard error (n = 3). Statistical significance is compared between the samples with and without antibody treatment.
Scale bar, 25 μm. ** $p < 0.01$.

To observe the long−term effect of the ZIP6 Y antibody treatment on cell growth, MCF−7 cells were grown in a 24−well plate and allowed to attach to the surface for 24 hours, prior to the antibody treatment for 96 hours. Cell counting was performed every 24 hours to determine growth of the cells treated with the ZIP6 antibody compared to the control without antibody treatment. The medium with the antibody was refreshed on day 2 after the treatment, to ensure that the cells were not deprived of necessary nutrients and that the antibody was not degraded. MCF−7 cells demonstrated a typical exponential growth pattern, with cell numbers increasing 1.2−fold, 2.3−fold, 5.3−fold, and 7.8−fold at days 1, 2,

3, and 4 when compared to day 0, respectively (Fig. 7.5). With the ZIP6 Y antibody treatment at a 1:20 dilution, no change in cell number was observed at day 1, but a gradual increase in cell number could be observed at days 2, 3, and 4 (Fig. 7.5). A significant decrease in cell growth was seen at days 2, 3, and 4, with cell numbers reduced by 33.0%, 57.4%, and 69.36% when compared to the control, respectively (Fig. 7.5). These data suggested prolonged mitotic inhibition as a result of the ZIP6 Y antibody treatment. Noteworthy, a small degree of cell growth was still noticed, signifying that the inhibitory effect was not complete. This might be associated with a milder side effect of the antibody if used for cancer treatment, since normal cells in the body would be allowed to grow to some extent. Furthermore, in the light of the concentration−dependent manner of the ZIP6 antibody−induced mitosis inhibition (Fig. 7.2), this incomplete mitosis blockade could be an antibody concentration effect, and complete mitosis inhibition might therefore be clinically achieved when a higher concentration of the antibody was applied.

Figure 7.5 Long−term cell growth suppression by ZIP6 Y antibody

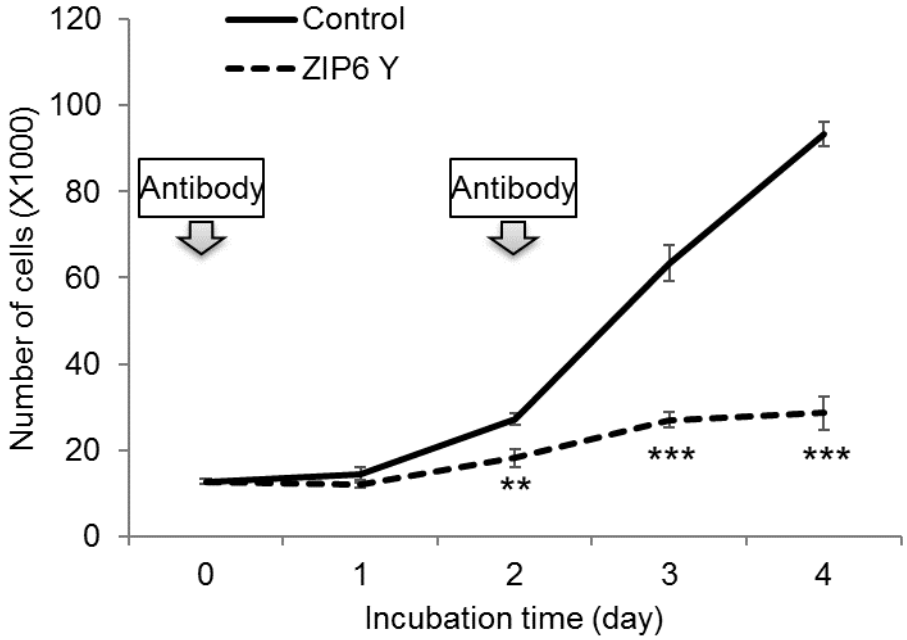

MCF−7 cells were seeded in a 24−well plate, and were treated with a 1:20 dilution of the ZIP6 Y antibody at 24 hours (day 0). The cells were counted every 24 hours for 4 days. The medium with the antibody was refreshed on day 2. The number of the cells from each counting is presented in a line graph as mean ± standard error (n = 3). Statistical significance is compared to the cells without antibody treatment (Control).
** $p < 0.01$, *** $p < 0.001$.

7.3.2 ZIP10 antibodies inhibit mitosis in MCF-7 cells

Hypothetically, in so far as ZIP6 and ZIP10 heteromer formation was required for their zinc transport function, inhibiting ZIP10 should also have the same mitosis inhibition effect as inhibiting ZIP6. The experiments that were performed using the ZIP6 Y antibody were therefore repeated, but using ZIP10 antibodies that specifically target the N-terminus of ZIP10 (Table 2.1). Using FACS in cells stained with propidium iodide, treatment with a 1:50 dilution of a ZIP10 antibody (Sigma-Aldrich, SAB2102209) (Table 2.1) was shown in an overlapping histogram to increase the 2n diploid cell population, but decrease the 4n tetraploid cell population (Fig. 7.6A). These changes in the cell cycle profile were confirmed by the analysis using the Watson Pragmatic algorithm (Fig. 7.6B,C). This analysis demonstrated an increase in the G2/M population from 22% in the control to 58% in the nocodazole-treated cells with a significantly decrease in the nocodazole-induced G2/M cells by 11% as a result of the antibody treatment (Fig. 7.6B,C).

To confirm the changes detected by FACS, immunofluorescence was performed using a pS10 histone H3 antibody. Nocodazole treatment significantly increased the mitotic cell population by 18% (Fig. 7.7). A significant reduction in the percentage of the mitotic cells by 15.5% was observed as a result of treatment with a 1:50 dilution of the ZIP10 antibody in the presence of nocodazole (Fig. 7.7). This inhibitory effect of the antibody on mitosis was shown to be concentration-dependent (Fig. 7.7). When using the same dilutions of the antibodies, the ZIP10 antibody was able to show a greater extent of mitosis inhibition than the ZIP6 Y antibody. For example, at a 1:50 dilution of the antibodies, the ZIP10 antibody was able to reduce the mitotic cells to 6.2% (Fig. 7.7), whereas the ZIP6 Y antibody decreased the mitotic cells to 8.8% (Fig. 7.2). The more potent cytostatic effect of the ZIP10 antibody suggested that ZIP10 might be more crucial in the mitotic process than ZIP6. Nevertheless, these two antibodies were made from different companies. The ZIP6 Y antibody was made in house and was not purified, whereas the ZIP10 antibody was commercially available and purified. The difference in cytostatic efficiency between these two antibodies could therefore be due to the difference in antibody concentrations.

Figure 7.6 Decreased G2/M population by ZIP10 antibody

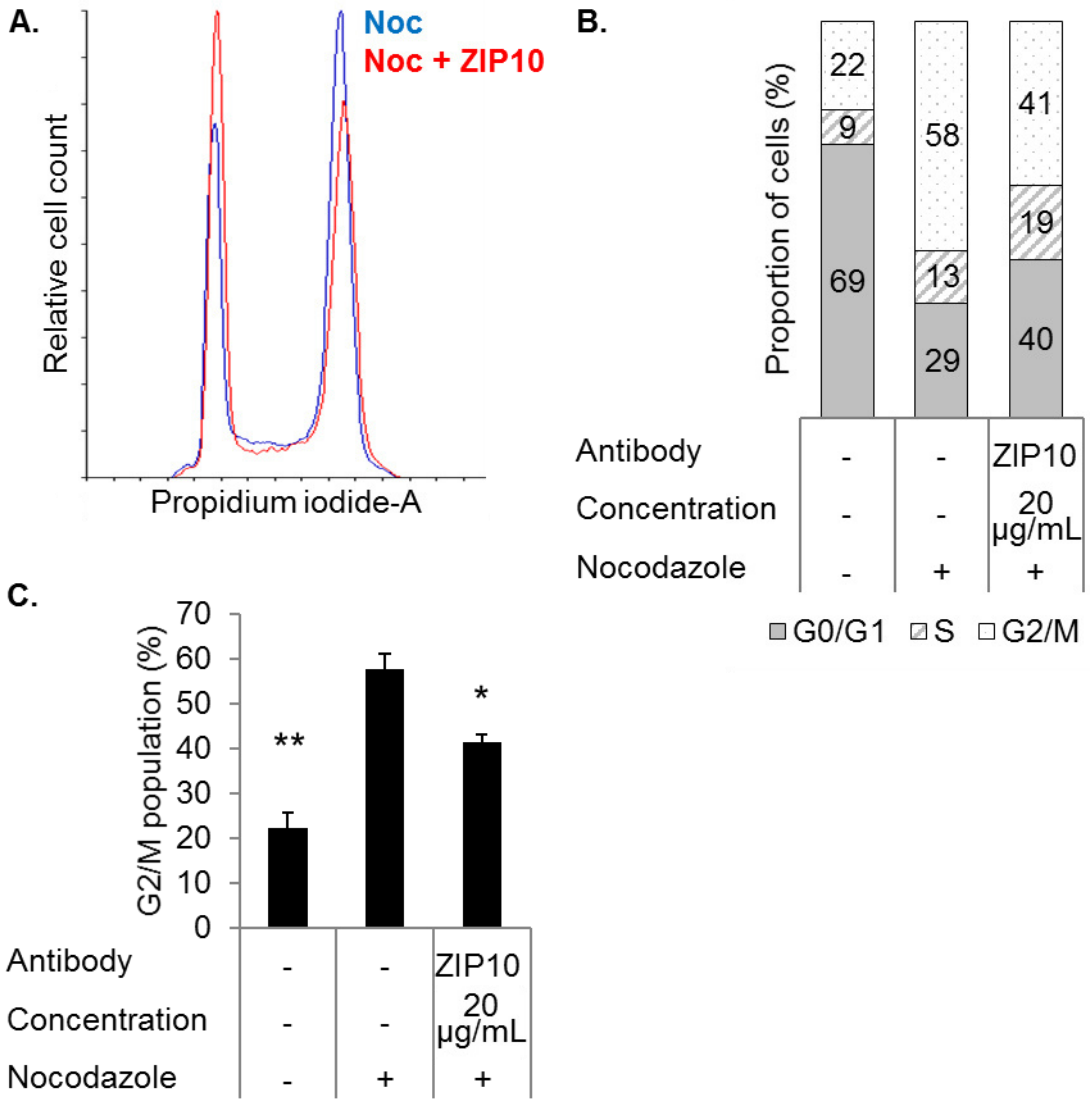

MCF−7 cells were treated with 100 nM nocodazole and incubated with a ZIP10 antibody (Sigma−Aldrich, SAB2102209) for 20 hours. The cells were stained with propidium iodide. DNA content was measured using FACS analysis. An overlapping histogram for the nocodazole−treated cells without antibody treatment (Noc) and the nocodazole−treated cells incubated with the ZIP10 antibody (Noc + ZIP10) was generated using Flowing Software (A). Percentages of the cells in the G0/G1, S and G2/M phases determined using FlowJo Software are presented as a 100% stacked column chart (B). The percentages of the G2/M population are also presented in a bar graph as mean ± standard error (n = 3) (C). Statistical significance is compared to the nocodazole−treated cells without antibody treatment.
* $p < 0.05$, ** $p < 0.01$.

Figure 7.7 Concentration−dependent mitosis inhibition by ZIP10 antibody

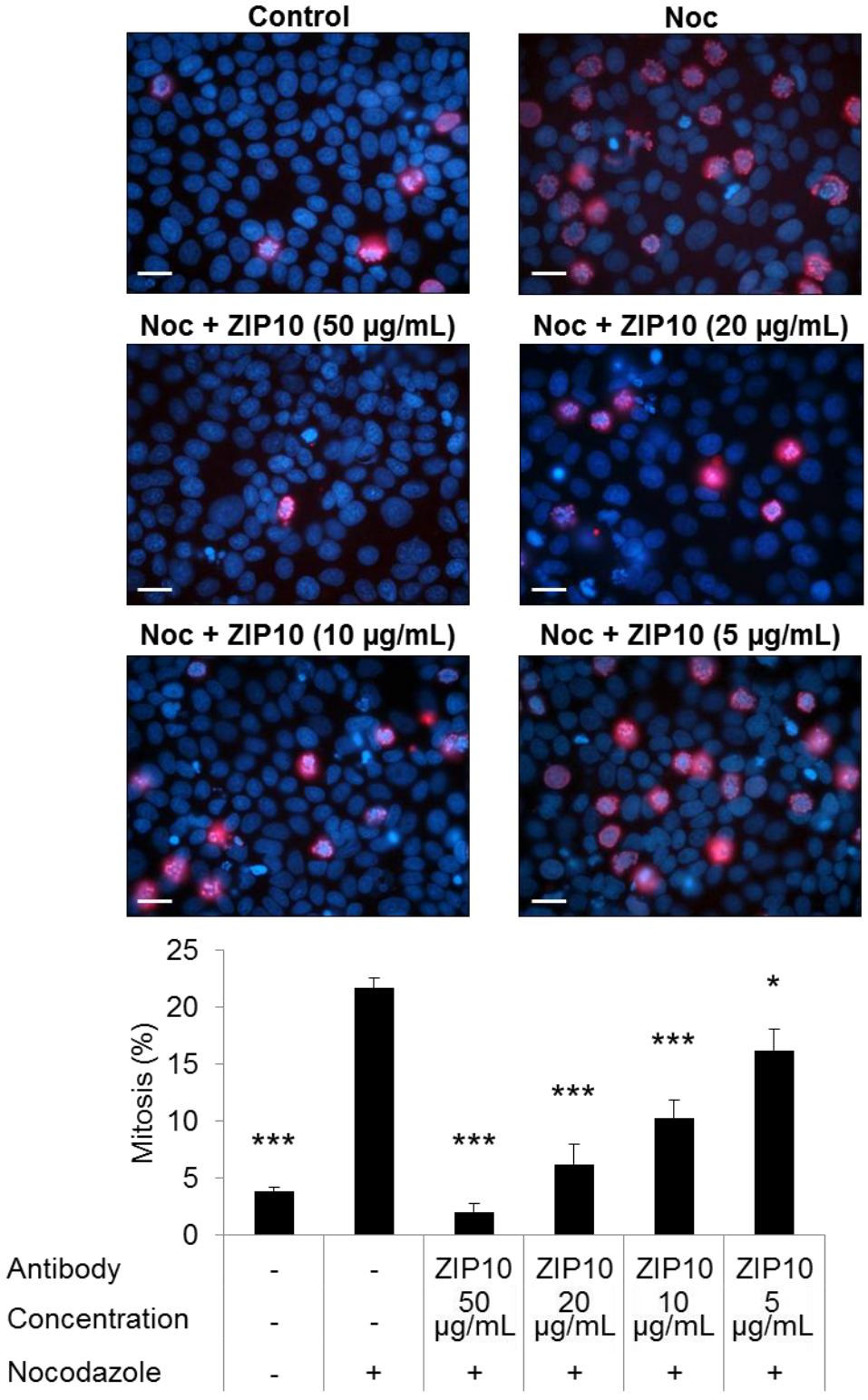

MCF−7 cells were treated with 100 nM nocodazole (Noc) and incubated with a ZIP10 antibody (Sigma−Aldrich, SAB2102209) for 20 hours. The cells were immunostained with a rabbit pS10 histone H3 antibody, which was conjugated to Alexa Fluor 594 (red). The nuclei were stained with DAPI (blue). A representative image of each sample is shown. Percentages of the mitotic cells are presented in a bar graph as mean ± standard error (n = 3). Statistical significance is compared to the nocodazole−treated cells without antibody treatment.
Scale bar, 25 µm. * $p < 0.05$, *** $p < 0.001$.

To validate the ZIP10 antibody treatment results (Fig. 7.6 and 7.7), FACS cell cycle analysis in cells stained with propidium iodide was performed again using the in-house made ZIP10 R antibody, which targets the N-terminus of ZIP10 similarly to the commercial ZIP10 antibody (Sigma-Aldrich, SAB2102209) (Table 2.1, Fig. 6.5). The overlapping histogram demonstrated a decrease in the 4n tetraploid peak as a result of the ZIP10 R antibody treatment when compared to the nocodazole-treated cells without antibody treatment, with no change in the 2n diploid peak observed (Fig. 7.8A). The G2/M cells were shown using the Watson Pragmatic algorithm to be significantly increased by 19% following the nocodazole treatment, and the ZIP10 R antibody treatment significantly reduced the percentage of the nocodazole-induced G2/M cell population by 12.5% (Fig. 7.8B), confirming that ZIP10 was required for initiation of nocodazole-induced mitosis.

To investigate the long-term effect of the ZIP10 R antibody treatment, a growth assay was performed for 96 hours. Exponential growth of MCF-7 cells was demonstrated and used as a control (Fig. 7.9). In contrast, the number of cells treated with the ZIP10 R antibody remained steady throughout the experiment, with a small decrease at day 1, a small increase at day 2, and inconspicuous decreases at day 3 and day 4 (Fig. 7.9). The difference between the numbers of the ZIP10 R antibody-treated cells and the control started to be significant at day 1 (Fig. 7.9). These data revealed a prolonged potent growth-inhibitory effect of the ZIP10 R antibody in MCF-7 cells. Noteworthy, both the FACS analysis and the growth assay agreeably demonstrated a stronger cytostatic effect of the ZIP10 R antibody than the ZIP6 Y antibody. For example, a greater percentage decrease in the G2/M population compared to the nocodazole-treated cells was observed when the cells were incubated with the ZIP10 R antibody (Fig. 7.8) than when they were incubated with the ZIP6 Y antibody at the same dilution of 1:20 (Fig. 7.1). Furthermore, the ZIP10 R antibody treatment could significantly suppress cell growth as early as day 1 (Fig. 7.9), whereas the ZIP6 Y antibody treatment still allowed the cells to slowly proliferate up to day 4 and did not show significant growth suppression until day 2 (Fig. 7.5). Both the ZIP10 R and ZIP6 Y antibodies were made in house and manufactured by the same company, with the same type of preservative added. However, exact concentrations of these antibodies were not known. The

comparison of the cytostatic effect between these two antibodies was therefore limited. The difference in their mitosis inhibition potency might be attributed to either the more important role of ZIP10 in zinc transport function of the ZIP6/ZIP10 heteromer or only the difference in antibody concentrations.

Figure 7.8 Decreased G2/M population by ZIP10 R antibody

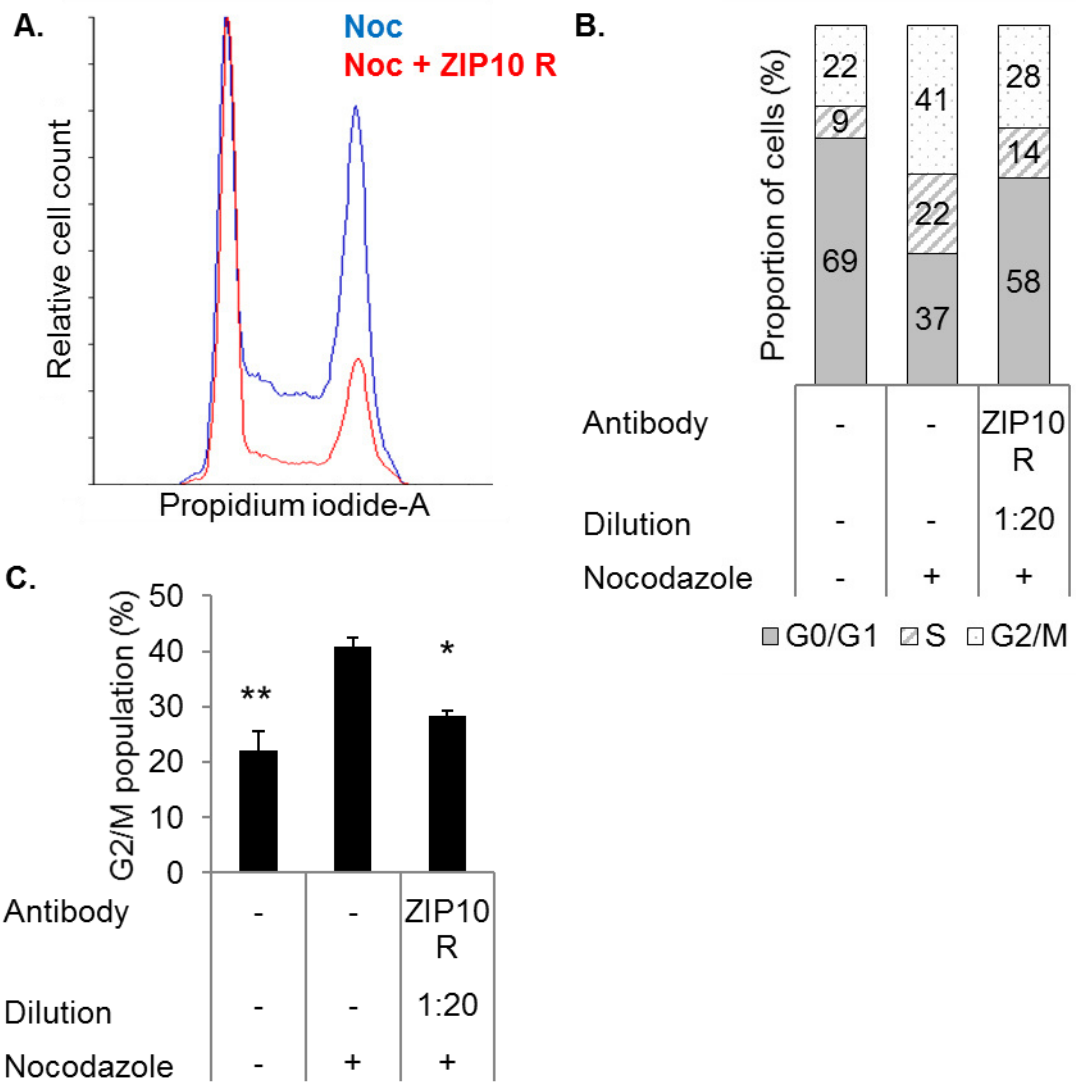

MCF−7 cells were treated with 100 nM nocodazole and incubated with ZIP10 R antibody for 20 hours. The cells were stained with propidium iodide. DNA content was measured using FACS analysis. An overlapping histogram for the nocodazole−treated cells without antibody treatment (Noc) and the nocodazole−treated cells incubated with ZIP10 R antibody (Noc + ZIP10 R) was generated using Flowing Software (A). Percentages of the cells in the G0/G1, S and G2/M phases determined using FlowJo Software are presented as a 100% stacked column chart (B). The percentages of the G2/M population are also presented in a bar graph as mean ± standard error (n = 3) (C). Statistical significance is compared to the nocodazole−treated cells without antibody treatment.
* $p < 0.05$, ** $p < 0.01$.

Figure 7.9 Long−term cell growth suppression by ZIP10 R antibody

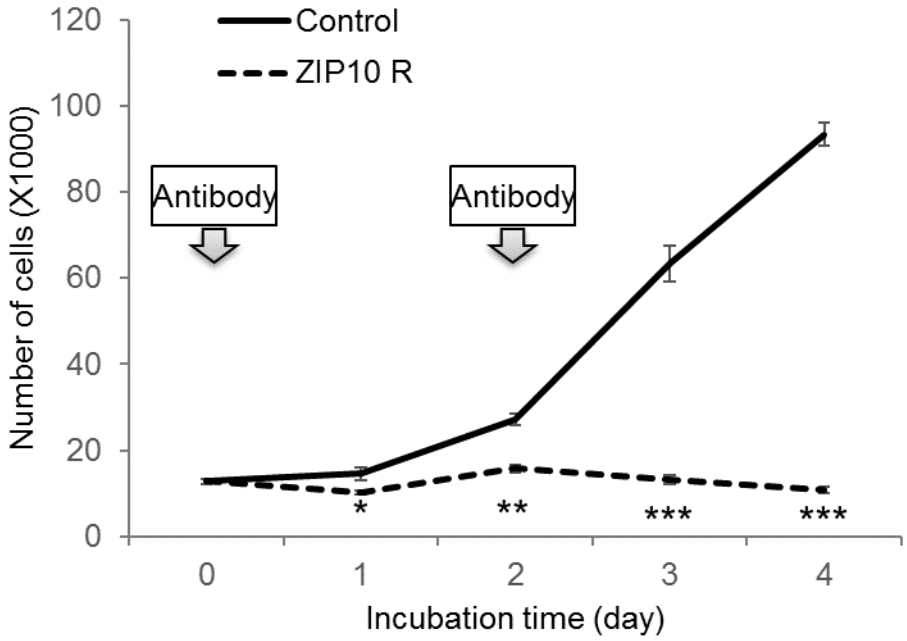

MCF−7 cells were seeded in a 24−well plate, and were treated with a 1:20 dilution of the ZIP10 R antibody at 24 hours (day 0). The cells were counted every 24 hours for 4 days. The medium with the antibody was refreshed on day 2. The number of the cells from each counting is presented in a line graph as mean ± standard error (n = 3). Statistical significance is compared to the cells without antibody treatment (control).
* $p < 0.05$, ** $p < 0.01$, *** $p < 0.001$.

The ZIP10 R antibody without a preservative added was also made and used to investigate the growth suppression effect of sodium azide, which was added to all the antibodies made in−house, including the ZIP6 Y and ZIP10 R antibodies. The cytostatic effect of sodium azide has been reported in various cell types (Slamenova and Gabelova 1980), but this effect on MCF−7 cells has not been reported. To exclude the cytostatic effect of sodium azide, MCF−7 cells were treated with the ZIP10 R antibody without any preservative added and compared to those treated with the ZIP10 R antibody with sodium azide added. Mitotic cells were identified by immunofluorescence using a pS10 histone H3 antibody. The mitotic cell count demonstrated that the nocodazole−induced mitotic cells were significantly reduced from 21% to 3% as a result of the treatment with the ZIP10 R antibody with sodium azide added, and to 4.5% as a result of the treatment with the ZIP10 R antibody without any preservative added (Fig. 7.10). No statistical significance was detected between the treatment with the ZIP10 R antibody with and without sodium azide added

(Fig. 7.10). These data proved that the inhibitory effect of the ZIP10 R antibody on mitosis was genuinely attributed to the binding of the antibody to ZIP10 and not due to cell toxicity of sodium azide.

Figure 7.10 Exclusion of preservative−induced cytotoxic effects

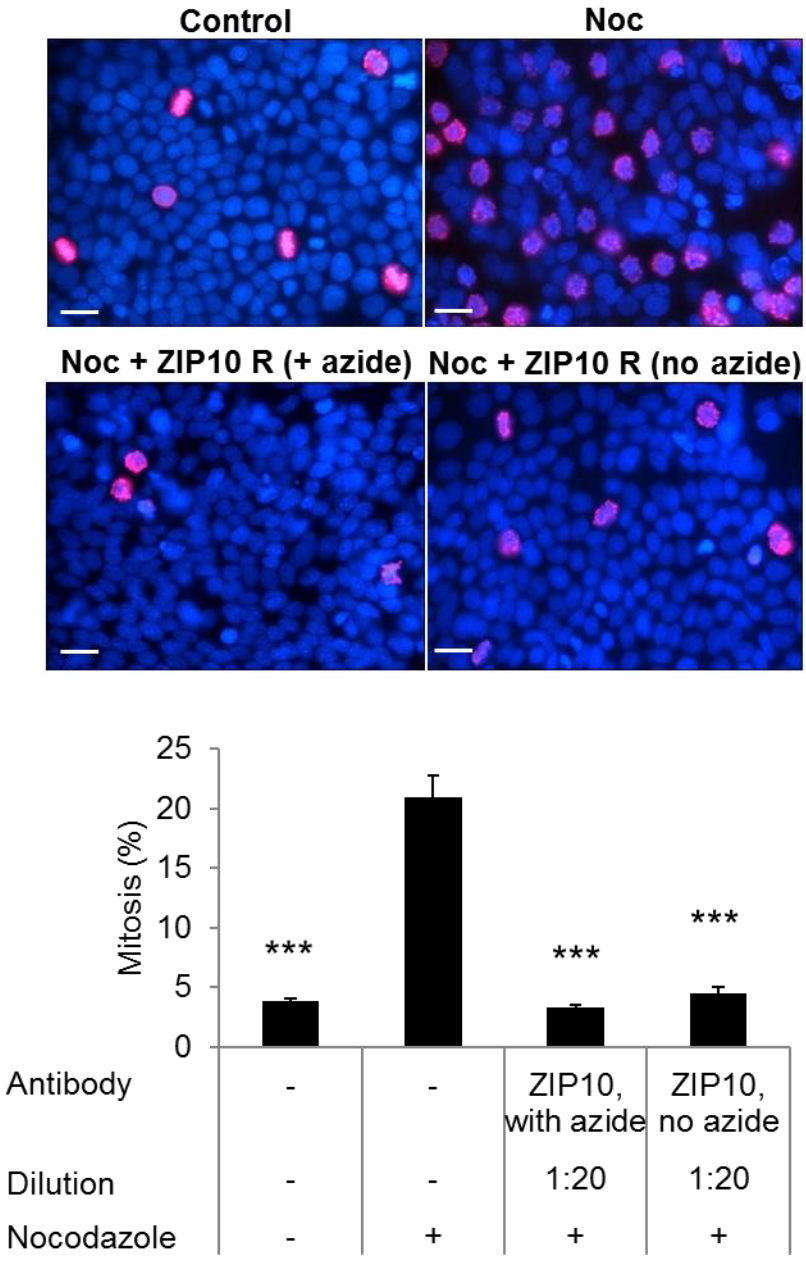

MCF−7 cells were treated with 100 nM nocodazole (Noc) and incubated with either the ZIP10 R antibody with 0.02% sodium azide or the ZIP10 R antibody without sodium azide for 20 hours. The cells were immunostained with a rabbit pS10 histone H3 antibody, which was conjugated to Alexa Fluor 594 (red). The nuclei were stained with DAPI (blue). A representative image for each sample is shown. Percentages of the mitotic cells are presented in a bar graph as mean ± standard error (n = 3). Statistical significance is compared to the nocodazole−treated cells without antibody treatment.
Scale bar, 25 μm. *** $p < 0.001$.

7.3.3 ZIP6/10 antibodies inhibit mitosis in other breast cancer cell lines

Mitosis in the hormone−responsive MCF−7 cells was successfully suppressed by the treatment with the antibodies that bind to the N−terminus of ZIP6 or ZIP10. To investigate the inhibitory effect of the antibodies on mitosis in other hormone−irresponsive breast cancer cells, we performed experiments in three additional cell lines: MDA−231 cells, MDA−436 cells, and TAMR cells. MDA−231 cells and MDA−436 cells are triple negative (ER−negative, PR−negative, and HER2−negative) breast cancer cell lines. TAMR cells are tamoxifen−resistant breast cancer cells that are derived from MCF−7 cells and known to have acquired a more aggressive phenotype than its endocrine−responsive parental cells (Knowlden et al. 2003).

Immunofluorescence using a pS10 histone H3 antibody was performed in MDA−231 cells (Fig. 7.11) and MDA−436 cells (Fig. 7.12) that had been treated with the ZIP6 Y or ZIP10 (Sigma−Aldrich, SAB2102209) antibody in the presence of nocodazole. The nocodazole treatment successfully increased the mitotic cell population in both the cell lines (Fig. 7.11 and 7.12). Concentration−dependent mitosis inhibition as a result of the treatment with the ZIP6 Y or ZIP10 (Sigma−Aldrich, SAB2102209) antibody was observed in both MDA−231 and MDA−436 cells (Fig. 7.11 and 7.12) in the same manner as that seen for MCF−7 cells. Using the same concentrations of these antibodies, the nocodazole−induced mitosis was inhibited in MDA−231 cells to a greater extent than MDA−436 cells (Fig. 7.11 and 7.12). These results revealed that the ZIP6 Y and ZIP10 antibodies were able to inhibit nocodazole−induced mitosis in these two triple negative breast cancer cells as well as the hormone receptor−positive MCF−7 cells. Triple negative breast cancer is highly aggressive and does not respond to either hormonal or HER2−targeted therapy. A study in mice with severe combined immunodeficiency revealed that 100% and 90% of the mice that were injected with MDA−231 and MDA−436 cells developed lung macro−metastases 53 and 43 days after injection, respectively (Iorns *et al.* 2012). In contrast, the same study revealed that only 25% of the mice injected with MCF−7 cells developed lung macro−metastases 184 days after injection. The ZIP6 Y or ZIP10 antibody treatment could therefore become a potential therapeutic means to control growth of triple−negative breast cancer,

both at the primary site and at distant organs, thereby improving clinical outcomes in patients with this highly aggressive disease.

Our group have demonstrated that TAMR cells have reduced mRNA expression of both ZIP6 and ZIP10 when compared to its parental MCF−7 cells, even though the decrease was not statistically significant (Taylor et al. 2007). It was therefore interesting to determine whether the treatment with the ZIP6 Y or ZIP10 R antibody could supress growth of TAMR cells as well as the parental MCF−7 cells. A growth assay was performed in TAMR cells that were treated with either the ZIP6 Y or the ZIP10 R antibody for 72 hours to determine the long−term effect of the treatment on growth of TAMR cells. To prevent nutrient starvation of the cells or degradation of the antibodies, the medium with the antibodies were replaced on day 2. TAMR cells without antibody treatment were increased 2−fold and 3−fold at day 1 and day 2, respectively, with no further increase observed at day 3 (Fig. 7.13). In the presence of a 1:20 dilution of the ZIP6 Y antibody, no increase was observed until day 3 when a 1.5−fold rise was detected (Fig. 7.13), suggesting that the antibody partially inhibited the growth of this cell line, and with enough time, the cells might grow again. On the contrary, in the presence of a 1:20 dilution of the ZIP10 R antibody, declines in cell numbers were observed at day 2 and day 3 (Fig. 7.13), suggesting that the antibody might also induce cell death in this cell line. The difference in cell numbers between the cells treated with either of the antibodies and the non−treated TAMR cells became statistically significant at day 1 (Fig. 7.13), suggesting a potent cytostatic effect of these antibodies in TAMR cells. Interestingly, this result also demonstrated a superior cytostatic effect of the ZIP10 R antibody treatment to the ZIP6 Y antibody treatment, as seen for MCF−7 cells, again suggesting either a more crucial role for ZIP10 in the mitotic process than ZIP6 or a higher concentration of the ZIP10R antibody than the ZIP6 Y antibody.

Figure 7.11 Mitosis inhibition by ZIP6 and ZIP10 antibodies in MDA−231

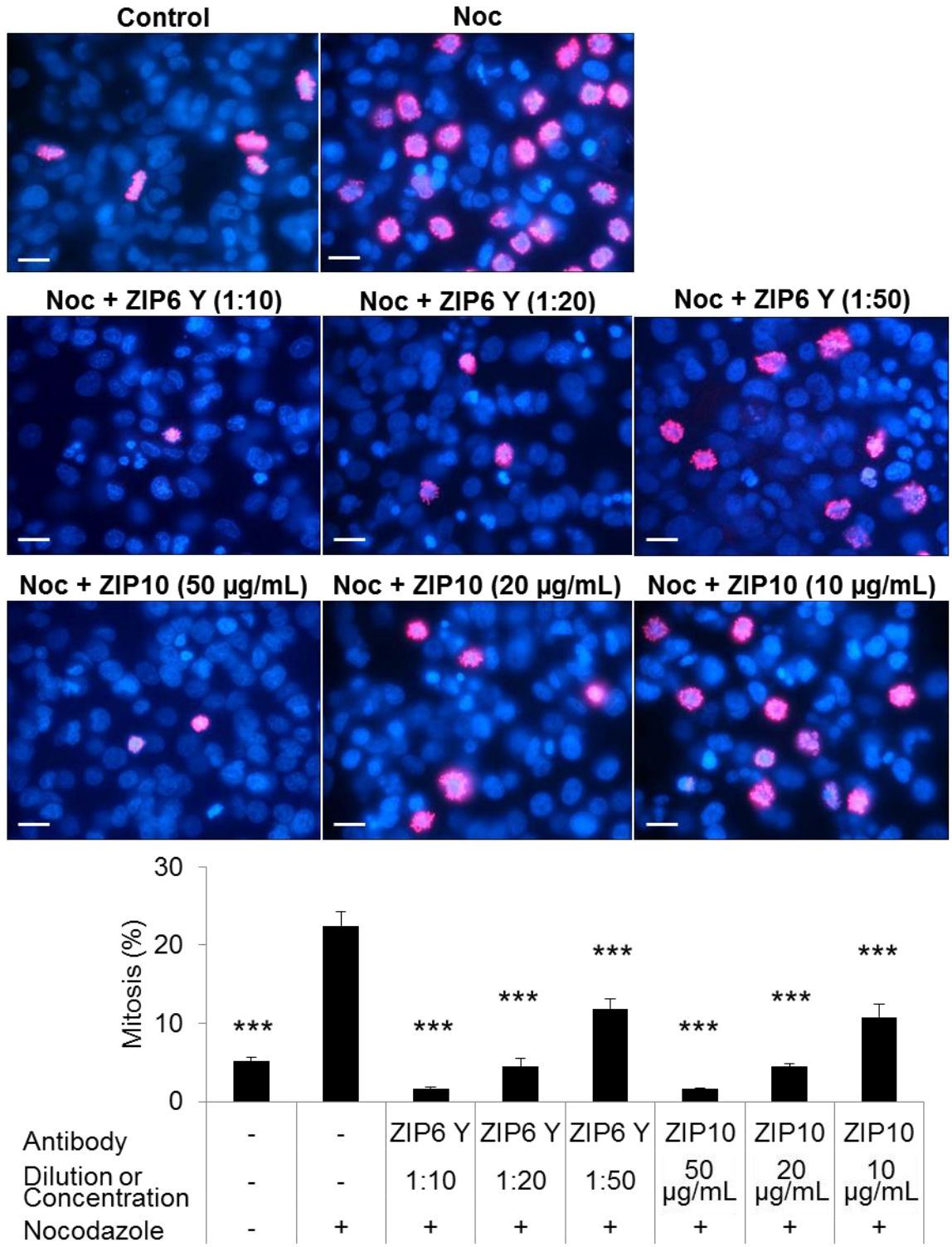

MDA−231 cells were treated with 100 nM nocodazole (Noc) and incubated with either the ZIP6 Y antibody or the ZIP10 antibody (Sigma−Aldrich, SAB2102209) for 20 hours. The cells were immunostained with a rabbit pS10 histone H3 antibody, which was conjugated to Alexa Fluor 594 (red). The nuclei were stained with DAPI (blue). A representative image for each sample is shown. Percentages of the mitotic cells are presented in a bar graph as mean ± standard error (n = 3). Statistical significance is compared to the nocodazole−treated cells without antibody treatment.
Scale bar, 25 µm. *** $p < 0.001$.

Figure 7.12 Mitosis inhibition by ZIP6 and ZIP10 antibodies in MDA−436

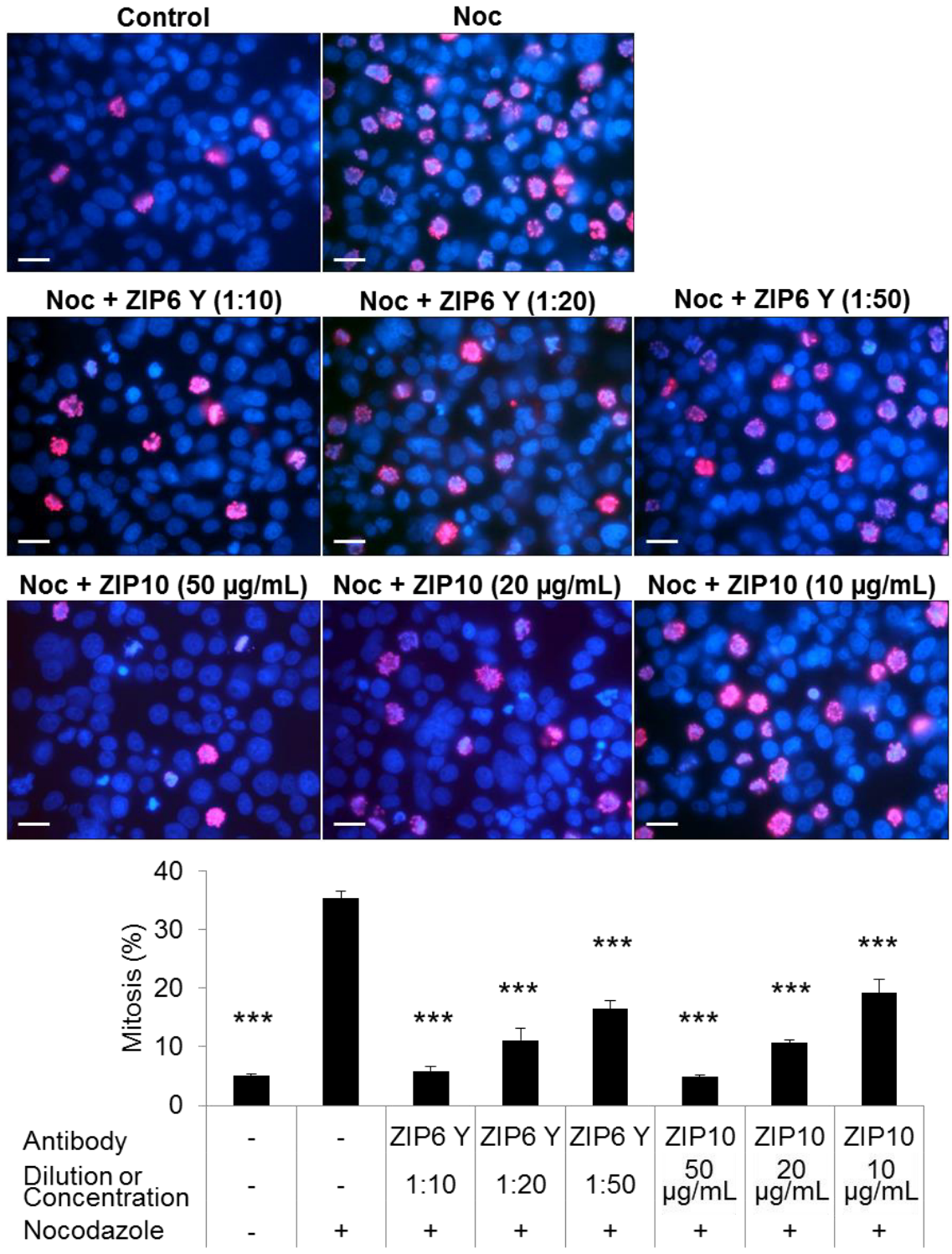

MDA−436 cells were treated with 100 nM nocodazole (Noc) and incubated with either the ZIP6 Y antibody or the ZIP10 antibody (Sigma−Aldrich, SAB2102209) for 20 hours. The cells were immunostained with a rabbit pS10 histone H3 antibody, which was conjugated to Alexa Fluor 594 (red). The nuclei were stained with DAPI (blue). A representative image for each sample is shown. Percentages of the mitotic cells are presented in a bar graph as mean ± standard error (n = 3). Statistical significance is compared to the nocodazole−treated cells without antibody treatment.
Scale bar, 25 µm. *** $p < 0.001$.

Figure 7.13 TAMR cell growth suppression by ZIP6 and ZIP10 antibodies

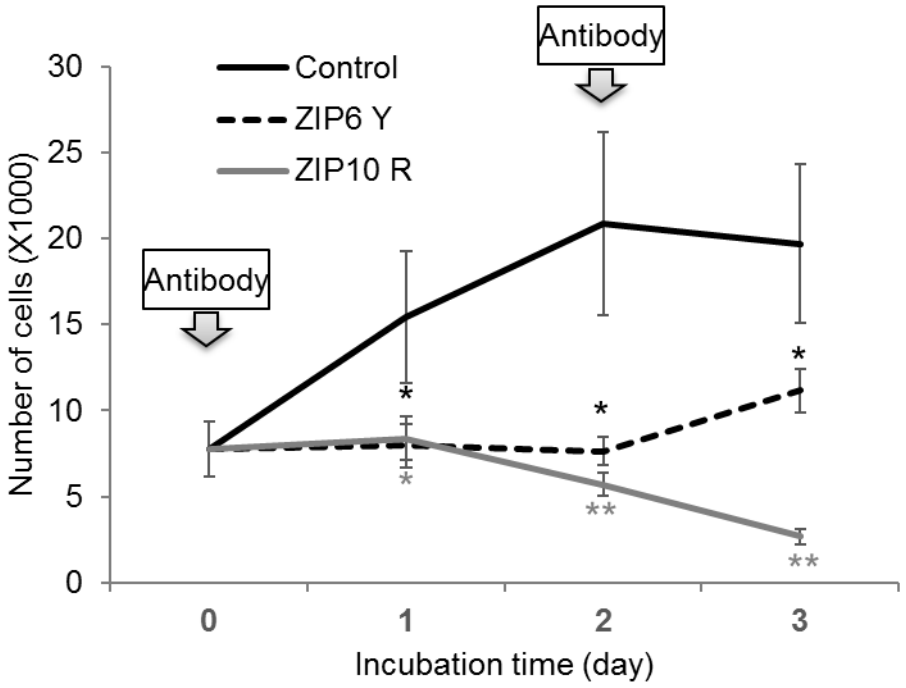

Tamoxifen-resistant MCF-7 cells (TAMR cells) were seeded in a 24-well plate, and were treated with a 1:20 dilution of either the ZIP6 Y or ZIP10 R antibody at 24 hours (day 0). The cells were counted every 24 hours for 3 days. The number of the cells from each counting is presented in a line graph as mean ± standard error. Statistical significance is compared to the cells without antibody treatment (control).
* $p < 0.05$, ** $p < 0.01$.

7.3.4 ZIP6 knockout decreases mitosis in NMuMg cells

ZIP6 knockout using clustered regularly-interspaced short palindromic repeats (CRISPR) technology was performed in NMuMg (mouse mammary glandular) cells by Dr. Gerold Schmitt-Ulms, University of Toronto. To determine the need for ZIP6 in the mitotic process, experiments were performed in this cell model. To characterise this cell line, zinc assays were performed using Fluozin-3. Imaging demonstrated that the green fluorescence of Fluozin-3 was decreased in the ZIP6-knockout NMuMg cells when compared to the wild-type NMuMg cells (Fig. 7.14). The calculation of the corrected total cell fluorescence in the representative fluorescence images revealed a 22% decrease in fluorescence intensity in the ZIP6-knockout cells when compared to the wild-type cells (Fig. 7.14). Furthermore, FACS analysis in cells loaded with the zinc-sensitive dye demonstrated a 35% decrease in the ZIP6-knockout cells compared to the wild-type cells (Fig. 7.15). These findings were consistent with the absence of ZIP6 in the ZIP6-knockout cells.

Nevertheless, a considerable amount of zinc was also present in the ZIP6−knockout cells, suggesting that zinc−import function of ZIP6 could be compensated for by other plasma membrane−located ZIP channels.

Figure 7.14 Decreased zinc levels in ZIP6−knockout cells

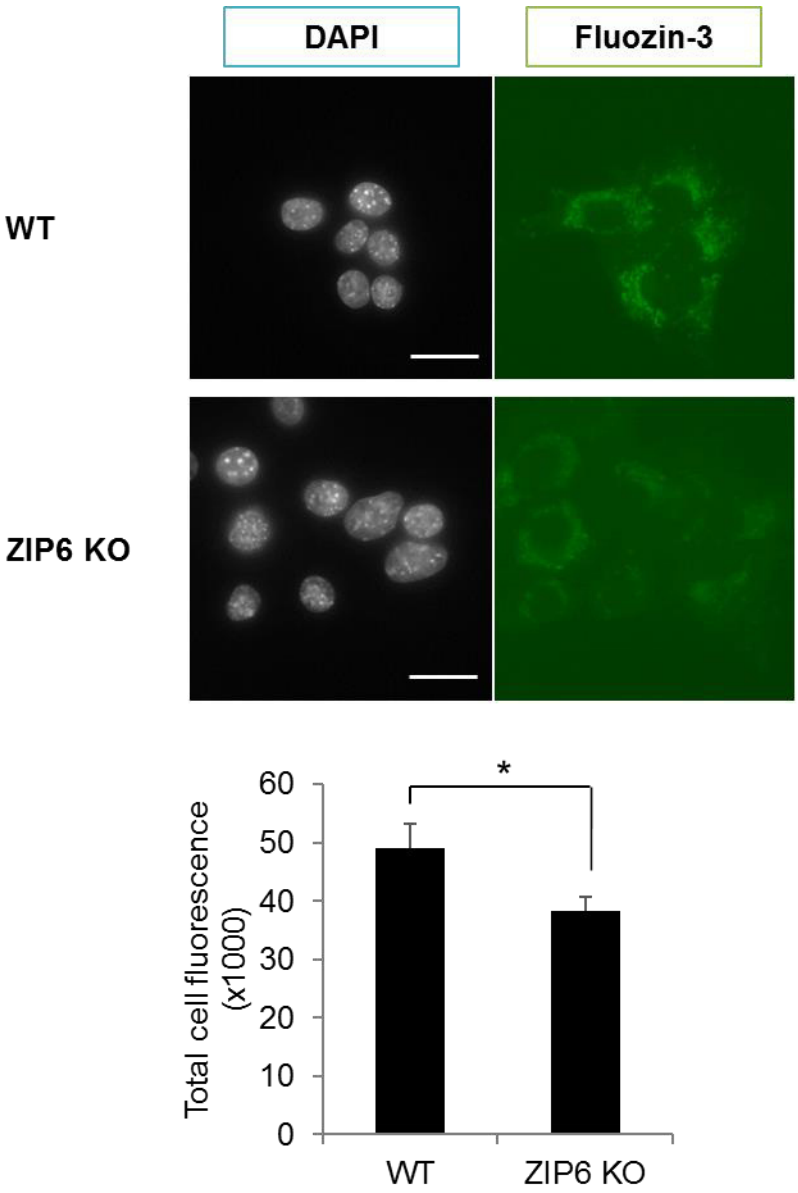

Wild−type (WT) and ZIP6−knockout (ZIP6 KO) NMuMg cells were stained with Fluozin−3 (green), and fixed in 4% formaldehyde. The nuclei were stain with DAPI. A representative microscopic view captured with 63x magnification lens is shown. The total cell fluorescence was calculated from the images taken from the Fluozin−3−stained slides using ImageJ software (Schneider et al. 2012), and is presented in a bar graph as mean ± standard error. Statistical significance is compared between the wild−type and the ZIP6−knockout cells.
Scale bar, 25 μm. * $p < 0.05$.

Figure 7.15 Decreased zinc levels in ZIP6-knockout cells

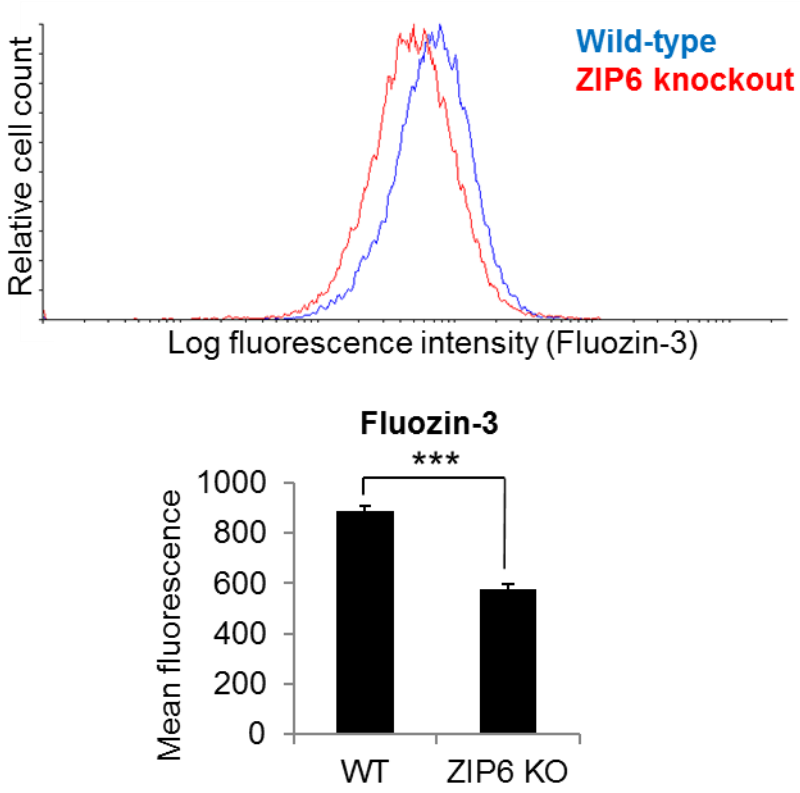

Wild-type (WT) and ZIP6-knockout (ZIP6 KO) NMuMg cells were stained with Fluozin-3 (green). FACS analysis was performed. The data are shown in an overlay histogram. The mean fluorescence is demonstrated in a bar graph as mean ± standard error (n = 3). Statistical significance is compared between the wild-type and the ZIP6-knockout cells.
*** $p < 0.001$.

To determine the effect of ZIP6 knockout on mitosis, FACS was performed in wild-type and ZIP6-knockout NMuMg cells stained with propidium iodide. The overlapping histogram revealed a decrease in the 4n peak, which represents cells in the G2/M phase, and the area between the two peaks, which represents cells in the S phase, with no change in the 2n peak, which represents cells in the G0/G1 phase (Fig. 7.16A). Further analysis in the ZIP6-knockout cells using the Watson Pragmatic algorithm revealed a 1.9% decrease in the percentage of the G2/M cells and a 16.6% decrease in the percentage of the S-phase cells when compared to the wild-type cells (Fig. 7.16B). Even though the decrease in the G2/M cells was relatively small, the decrease was statistically significant for both the G2/M cells (Fig. 7.16C) and the S-phase cells (Fig. 7.16D). The decrease in the S-phase fraction in the ZIP6-knockout cells suggested that ZIP6 might play a role in cell cycle progression even prior to cell entry into the mitotic phase. This early blockade of

the cell cycle was not detected in the ZIP6 antibody treatment experiment (Fig. 7.1), possibly because of the intracellular location of ZIP6 in the interphase cells and thereby lack of approachability of ZIP6 to the ZIP6 antibody. Given that the S−phase fraction has long been known as a biomarker of clinically aggressive tumours (Johnson 1994), this effect of the ZIP6 knockout supported ZIP6 as a potential target for cancer treatment.

Figure 7.16 Decreased S and G2/M population in ZIP6−knockout cells

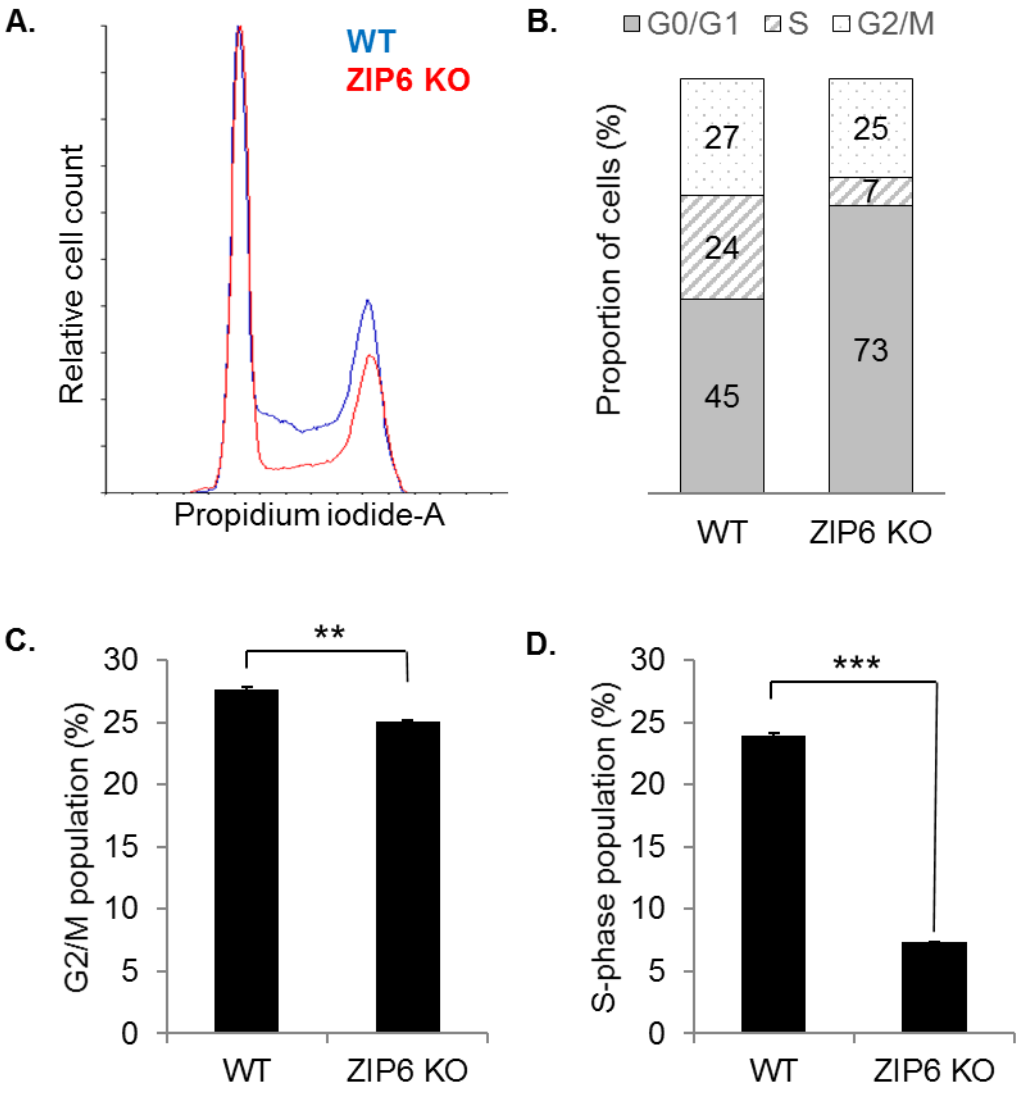

Wild−type (WT) and ZIP6−knockout (ZIP6 KO) NMuMg cells were stained with propidium iodide. DNA content was measured using FACS analysis. An overlapping histogram was generated using Flowing Software (A). Percentages of the cells in the G0/G1, S and G2/M phases determined using FlowJo Software are presented as a 100% stacked column chart (B). The percentages of the cells in the G2M phase (C) and S phase (D) are individually presented in bar graphs as mean ± standard error (n = 3). Statistical significance is compared between the wild−type and the ZIP6−knockout cells.
** $p < 0.01$, *** $p < 0.001$.

A 96-hour growth assay was performed to determine long-term growth of the ZIP6-knockout cells. Rapid proliferation was observed for the wild-type cells until day 4, whereas a slower increase in cell number was observed in the ZIP6-knockout cells until day 3, with statistical significance observed from day 1 to day 3 when compared to the wild-type cells (Fig. 7.17). Unexpectedly, the growth of the ZIP6-knockout cells accelerated at day 4, when the cell numbers reached the levels comparable to the wild-type cells (Fig. 7.17). These data suggested that ZIP6 played important roles in mitosis, since the absence of ZIP6 resulted in the decrease in cell growth. Nevertheless, the ability of the ZIP6-knockout cells to grow with rapid acceleration at day 4 suggested that the role of ZIP6 in mitosis was dispensable, and ZIP6 might be compensated for by other ZIP channels, especially in long-term absence of ZIP6. The dispensability of the role for ZIP6 in cell proliferation was consistent with a recent report that shRNA-mediated suppression of ZIP6 gene expression by 80% did not have any effect on cell proliferation in pancreatic cancer cells (Unno *et al.* 2014).

Figure 7.17 Cell growth suppression in ZIP6-knockout cells

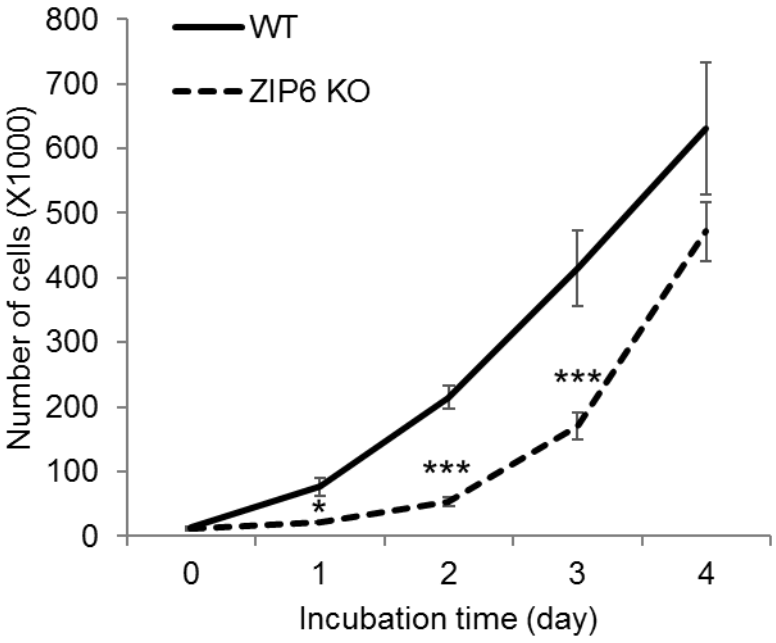

Wild-type (WT) and ZIP6-knockout (ZIP6 KO) NMuMg cells were seeded in a 24-well plate. The cells were counted every 24 hours for 4 days. The number of the cells from each counting is presented in a line graph as mean ± standard error (n = 3). Statistical significance is compared between the wild-type and the ZIP6-knockout cells.
* $p < 0.05$, *** $p < 0.001$.

7.4 Chapter summary

In this chapter, inhibition of ZIP6 and ZIP10 by treating cells with the antibodies that target the ectodomain of ZIP6 and ZIP10 was demonstrated to result in a decrease in mitosis and cell growth. These antibodies were shown to suppress both nocodazole−induced mitosis and endogenous mitosis in MCF−7 cells, with a concentration−dependent manner demonstrated for the inhibition of nocodazole−induced mitosis (Fig. 7.1−7.9). Furthermore, inhibitory effects of the antibodies on mitosis were also seen in endocrine−resistant breast cancer cell lines, consisting of MDA−231 (Fig. 7.11), MDA−436 (Fig. 7.12), and TAMR cells (Fig. 7.13), as well as hormone−sensitive MCF−7 cells. Additionally, crucial involvement of ZIP6 in mitosis was supported by a decrease in cell proliferation in ZIP6−knockout NMuMg cells when compared to wild−type NMuMg cells (Fig. 7.16 and 7.17). These findings collectively confirmed the important role of ZIP6 and ZIP10 in the mitotic process and introduced ZIP6 and ZIP10 antibody treatment as a novel modality for cancer treatment.

Chapter 8:
General discussion

An increasing number of human diseases, which include cancer, have been attributed to increases or decreases in zinc transport function of ZIP channels (Taylor et al. 2011). It is therefore crucial to comprehend functional control of ZIP channels in order to discover a novel therapeutic strategy for diseases that are associated with ZIP channel dysfunctions. To obtain some basic understanding about the predicted structure of ZIP channels, amino acid sequences were analysed, and potential phosphorylation sites in the cytosolic loop between TM3 and TM4 were explored in all members of the ZIP family of zinc transport proteins (Chapter 3). Post-translational mechanisms of ZIP7 were further deciphered by determining usefulness of the pZIP7 antibody in indicating the modification and function of ZIP7 (Chapter 4) and exploring cellular kinases phosphorylated as a result of ZIP7-mediated zinc release from cellular stores (Chapter 5). To expand the insight into the ZIP channel functional control, the investigation was extended to post-translational mechanisms of ZIP6, another member of the LIV-1 subfamily in which a STAT3-binding site and multiple phosphorylation sites were detected (Chapter 6). Following the discovery of ZIP6 and ZIP10 mechanisms during mitosis in Chapter 6, the essentiality of these ZIP channels for the mitotic process was proved by inhibiting their function using specific ZIP6 and ZIP10 antibodies (Chapter 7).

The most prominent discovery in this project was the post-translational mechanisms of ZIP6 and ZIP10 in mitosis with the application of ZIP6 and ZIP10 antibodies to inhibit mitosis. These two topics will therefore be discussed first in this chapter, followed by a separate discussion on the investigation of ZIP6 phosphorylation in mitosis. The discussion will then be focused on ZIP7, starting from an analysis of the kinases that were detected as downstream effectors of ZIP7-mediated zinc release from cellular stores. Finally, the potential usefulness of the pZIP7 antibody and the essential role of ZIP7 in human immunity will be discussed.

8.1 ZIP6 and ZIP10 play important roles in mitosis

It has been recognised for decades that zinc is essential for cell division, and the absence of zinc in the medium results in cell proliferation arrest (Falchuk *et al.* 1975). The importance of zinc homeostasis in cell division is underlined by the demonstration of transient fluctuations of intracellular zinc levels during the mitotic cell cycle (Li and Maret 2009) as well as the meiotic cell cycle (Kim *et al.* 2010). However, little is known about the direct role of zinc in mitosis. It has been proposed that zinc is involved in mitosis because of its major involvement in DNA synthesis through its association with various metalloenzymes and zinc-finger proteins and how zinc affects the G1/S phase transition by an undefined mechanism (MacDonald 2000). Furthermore, zinc signalling has been linked to cell growth in prostatic cancer in a recent study (Zhang *et al.* 2010). In this study, ZIP4 overexpression was seen to activate CREB by phosphorylation, resulting in increases in IL-6 transcription, STAT3 activation, cyclin D1 expression, and cell proliferation. However, these effects of ZIP4 overexpression might be attributed solely to the increase in cytosolic zinc, since no molecular association of ZIP4 with other molecules was indicated.

According to the data in Chapter 6, the mechanism of how ZIP6 is involved in mitosis can be summarised in a schematic shown in Fig. 8.1. ZIP6 is transcriptionally activated by STAT3 (Yamashita et al. 2004; Hogstrand et al. 2013) in its active tyrosine-phosphorylated form, pY705 STAT3 (Abroun et al. 2015). ZIP6 is produced as a pro-protein, which is stored in the ER and represented by a 103 kDa band on a Western blot (Hogstrand et al. 2013) (Fig. 6.8). A recent study in our group detected that ZIP6 forms a heterodimer with ZIP10 in the ER (Taylor *et al.* 2016). When the cell is triggered by a mitosis-promoting factor, the ZIP6 pro-protein is N-terminally cleaved at a strong PEST site (Fig. 3.7) and relocated to the plasma membrane. This active form of ZIP6 on the plasma membrane is represented by a 68 kDa band on a Western blot (Hogstrand et al. 2013) (Fig. 6.8). At this stage, ZIP6 might be regulated by phosphorylation on the predicted sites in the cytosolic loop between TM3 and TM4, which could possibly be mediated by CK2, GSK-3β, CK1, or PLK1 (Fig. 6.29-6.38). Noteworthy, it is still not known whether ZIP10 is also post-translationally regulated by phosphorylation.

Figure 8.1 ZIP6 and ZIP10 involvement in mitosis

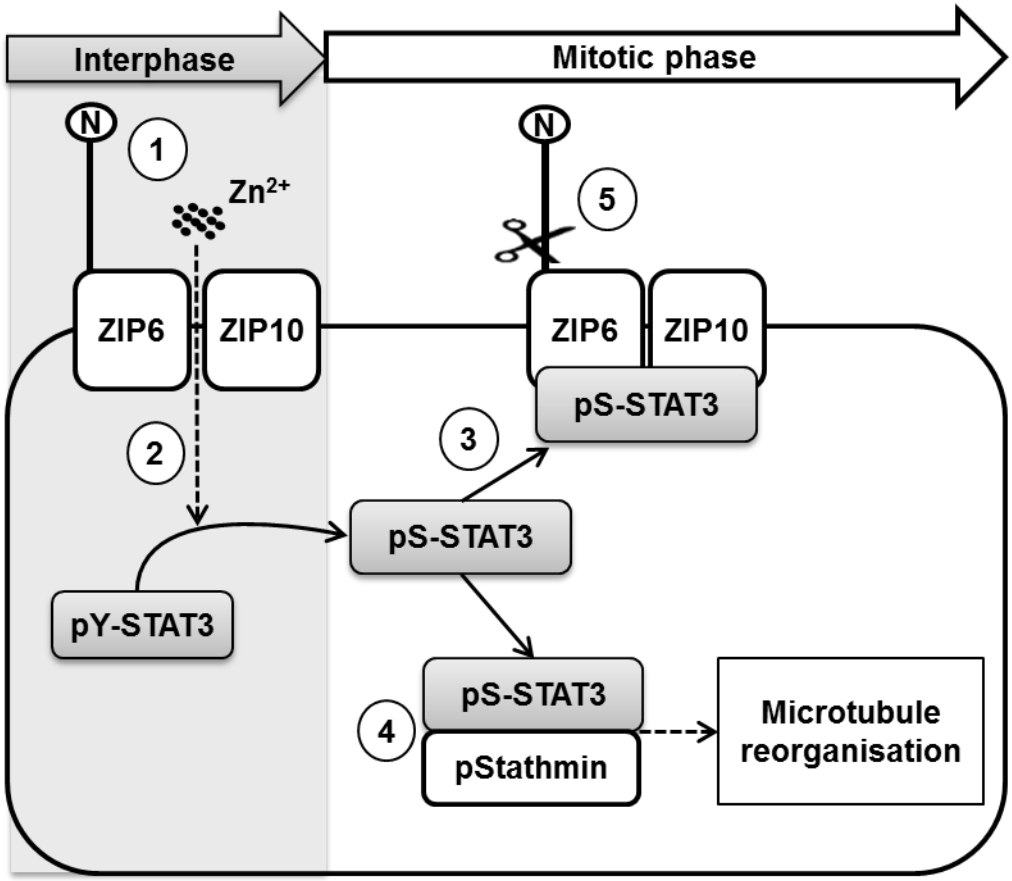

This schematic demonstrates a model of ZIP6 and ZIP10 involvement in mitosis based on the findings in this project.

1. ZIP6 forms a heteromer with ZIP10 in the ER (Taylor et al. 2016), and the heteromer relocates to the plasma membrane in mitosis.
2. The ZIP6/ZIP10 heterodimer mediates zinc influx into the cytosol, resulting in phosphorylation of STAT3 on residue S727.
3. The serine−phosphorylated STAT3 (pS727 STAT3) binds to ZIP6 on residue Y473, which is in the intracytosolic loop between TM3 and TM4. pS727 STAT3 also binds to ZIP10 on an unidentified site.
4. pS727 STAT3 binds to pS38 Stathmin, which is required for microtubule reorganisation during mitosis (Rubin and Atweh 2004).
5. ZIP6 undergoes an additional N−terminal cleavage during early mitosis.

When ZIP6 or ZIP10 on the plasma membrane is activated, the ZIP6/ZIP10 heteromer mobilises zinc into the cell (Fig. 8.1, step 1), resulting in conversion of pY705 STAT3 to pS727 STAT3 (Fig. 8.1, step 2), the form of STAT3 which is present in all mitotic cells (Nimmanon et al., manuscript in preparation). During mitosis, pS727 STAT3 binds to the ZIP6/ZIP10 heterodimer on the plasma membrane (Fig. 8.1, step 3). This binding was shown to be at the predicted STAT3−binding motif in ZIP6 (sequence YESQ, positions 473−476) (Fig. 6.15−6.17) and at an unknown site in ZIP10 (Fig. 6.21). Additionally, pS727 STAT3 also binds to pStathmin (Fig. 6.18;

Fig. 8.1, step 4), which is required for microtubule reorganisation, an essential process for mitotic progression (Rubin and Atweh 2004). During early mitosis, before the transition from prophase to metaphase, the extracellular N-terminus of ZIP6 is cleaved again just upstream of TM1 (Fig. 6.22; Fig. 8.1, step 5). The role of this second cleavage still needs to be investigated. Altogether, the findings in this project have introduced at least five molecules that are actively involved in the mitotic process according to this model: zinc, ZIP6, ZIP10, pS727 STAT3, and pStathmin. These molecules might therefore become interesting targets for treatment of proliferative diseases such as cancer.

Tyrosine phosphorylation on a C-terminal tyrosine residue, Y705, is a crucial step for the formation of a STAT3 dimer (Rawlings et al. 2004). As a result, most studies on STAT3 have been focussed on pY705 STAT3, which is generally regarded as the transcriptionally-active form of STAT3 (Abroun et al. 2015). However, phosphorylation on an evolutionarily-conserved serine residue, S727, which is located in the C-terminal tail distal to residue Y705, has also been reported (Decker and Kovarik 2000). In response to interferon-alpha, a luciferase assay in cells transfected with the interferon regulatory factor-1 promoter demonstrated a 50% decrease in transcriptional activity when co-transfected with a STAT3 S727A mutant, compared to the wild type, even though a gel mobility shift assay could not show a decrease in DNA binding (Wen *et al.* 1995). Consistent with this finding, transfection with the STAT3 S727A mutant was shown to reduce transcription of the interleukin-6 response element of the ICAM-1 promoter upon interleukin-6 induction by 50%, compared to wild-type STAT3 (Schuringa *et al.* 2000). Importantly, the relevance of this S727 phosphorylation in physiology has been underlined by an in vivo study, showing that SA/- mice (one allele having the STAT3 S727A mutation and the other having no STAT3 gene) had a significant reduction in birth weight with 75% mortality rate soon after birth (Shen *et al.* 2004). Both the reduced birth weight and the mortality seen in these SA/- mice were correlated with a reduction in serum levels of IGF-1. Given the transcription-stimulating role of pS727 STAT3, this modification has been implicated in carcinogenesis. For example, in prostate cancer cells, when residue S727 of STAT3 is mutated to glutamate, which is a phosphomimetic amino acid, the cells were shown to have increased growth, tumorigenic potential, and invasion (Qin *et al.* 2008).

These aggressive characteristics were attributed to pS727 STAT3-mediated transcriptional activation of proto-oncogenes, such as mcl-1, surviving, and c-myc, independently of Y705 phosphorylation. In addition, the constitutively-present pS727 STAT3 was shown in chronic lymphoid leukaemia cells to bind to DNA and thereby activate transcription, suggesting pS727 STAT3 as a salient feature and a potential therapeutic target for this lymphoid neoplasm (Hazan-Halevy *et al.* 2010).

Nevertheless, there are a few pieces of evidence contradicting these positive effects of pS727 STAT3 on transcriptional activity (Decker and Kovarik 2000). In HepG2 hepatoma cells, investigations using a STAT3 S727A mutant as well as a STAT3 mutant with the distal 55 amino acids removed from the C-terminus proved a requirement of the C-terminus, but not residue S727, in transcription-activating function of STAT3 (Kim and Baumann 1997). Furthermore, a decrease in transcriptional activity has been demonstrated when residue S727 was phosphorylated by ERKs (Jain *et al.* 1998; Sengupta *et al.* 1998), protein kinase C delta (Jain *et al.* 1999), or c-Jun N-terminal kinase 1 (JNK1) (Lim and Cao 1999). Indirectly supporting this negative role of pS727 STAT3 in transcriptional activity, the phosphorylation on residue S727 of STAT3 in nocodazole-treated cells was shown to suppress gene expression of $p21^{CIP1/WAF1}$ and $p27^{Kip1}$, which are negative regulators of the cell cycle (Shi et al. 2006). The suppression of these cell cycle regulators therefore resulted in unopposed activation of cyclin-dependent kinase 1, which is required for mitotic progression. This study also demonstrated an inverse relationship between pY725 STAT3 and pS705 STAT3 in mitotic cells, and introduced pS727 STAT3 as a positive regulator of the mitotic process. Collectively, these controversial data suggest that pS727 STAT3 can either activate or suppress gene expression, depending on cell types and circumstances.

Importantly, zinc was shown to bind to STAT3, resulting in inhibition of STAT3 transcriptional function, as suggested by a decrease in the pY705 STAT3 levels (Kitabayashi et al. 2010). Furthermore, a recent investigation in our group confirmed this and further demonstrated in the context of mitosis that ZIP6-mediated zinc influx resulted in not only a decrease in pY705 STAT3, but also an increase in pS727 STAT3 (Nimmanon et al.,

manuscript in preparation). Noteworthy, these effects of zinc on the two STAT3 modifications were consistent with the inverse relationship between pY725 STAT3 and pS705 STAT3, which was seen in nocodazole-induced mitotic cells (Shi et al. 2006) and cells overexpressing ZIP6 (Hogstrand et al. 2013). As previously mentioned, the binding of pS727 STAT3 to pStathmin provided a clear link between ZIP6-mediated zinc signalling and mitosis through the crucial role of pStathmin in facilitating microtubule reorganisation during mitosis (Rubin and Atweh 2004). In contrast to this binding of pS727 STAT3 to pStathmin, the role of the ZIP6/pS727 STAT3 complex formation was rather inconclusive. Interestingly, ZIP6 has been reported to associate with histone demethylase Jarid1B (Zhou *et al.* 2009a), which was previously demonstrated by our group to bind to histone H3, but not ZIP6, in mitotic cells (Nimmanon et al., manuscript in preparation). It is interesting to speculate that the ZIP6/pS727 STAT3 complex formation resulted in dislodging of Jarid1B from ZIP6, and the freed Jarid1B would then bind and activate histone H3, which is responsible for chromosome condensation (Wei *et al.* 1999). Additionally, given that the cytosolic loop between TM3 and TM4 contains histidine-rich regions that are required for zinc transport across the plasma membrane (Milon *et al.* 2006), the binding of pS727 STAT3 at this loop might in fact prevent excessive zinc influx, which could be toxic to the cell. This hypothesis is partly supported by the constant zinc levels observed throughout different mitotic stages (Fig. 6.14). Altogether, the unique presence of pS727 STAT3 and its binding to ZIP6 and pStathmin provided a mechanistic link between zinc signalling and mitotic control and suggested the importance of these proteins and their potential to become cancer therapeutic targets.

The speculated involvement of Jarid1B in the ZIP6/pS727 STAT3 complex-driven mitotic progression is intriguing. Jarid1B, previously known as PLU-1, is a histone demethylase that is specific for histone H3 with tri- and di-methylation on residue lysine 4 (Christensen *et al.* 2007). Using Northern blotting, the Jarid1B gene was highly expressed in different breast cancer cells when compared to non-malignant mammary glandular cells, with restricted expression in various non-cancerous adult tissues (Lu *et al.* 1999). Consistent with this gene expression profile, protein expression of Jarid1B was also shown using Western blotting to be increased in both breast cancer cells and breast

cancer tissue extracts, but not detectable in extracts from various normal adult tissues (Barrett *et al.* 2002). Through the demethylase activity of Jarid1B, which results in transcriptional repression of tumour suppressor genes such as BRCA1, this protein has been demonstrated to promote cell proliferation both in MCF-7 cells and in a mouse breast tumour model (Yamane *et al.* 2007). The speculation that the ZIP6/pS727 STAT3 complex formation resulted in binding of the freed Jarid1B to histone H3 during mitosis (Nimmanon et al., manuscript in preparation) therefore suggests another possible post-translational mechanism for Jarid1B in promoting cell proliferation independently of its demethylase activity. Interestingly, in contrast to the role of Jarid1B in enhancing cell proliferation, this protein has been reported to be a biomarker of the slow-growing subpopulation of melanoma cells, which is relatively small in number when compared to the rapidly growing population of melanoma cells (Roesch *et al.* 2010). Regardless of the apparently low proliferation rate of this subpopulation, these Jarid1B-positive melanoma cells were shown to be capable of continuously growing and highly tumorigenic, fulfilling a major criterion for cancer stem cells (Bruttel and Wischhusen 2014). Similar to Jarid1B, ZIP6 has also been revealed responsible for the stem cell properties in pancreatic cancer cells (Unno et al. 2014). In this study, ZIP6 knockdown in Panc-1 human pancreatic cancer cells was shown to result in decreased expression of stemness-related genes, spheroid-forming ability, invasiveness, and tumorigenicity in nude mice, thereby introducing ZIP6 as a regulator of pancreatic cancer cell stemness. Given the molecular link between Jarid1B and ZIP6 (Nimmanon et al., manuscript in preparation), it is plausible that both these molecules might work together to promote stemness of both melanoma cells and pancreatic cancer cells.

ZIP6 and ZIP10 are grouped into the same sub-branch of the phylogenetic tree of the ZIP family of zinc transport proteins (Fig. 3.1), and share many common characteristics in terms of both gene sequences and biological roles. Both the ZIP6 and ZIP10 genes have been shown to contain a prion-like ectodomain (Schmitt-Ulms et al. 2009) and proteolytic cleavage sites (Fig. 3.7) with a STAT3-binding motif (Shao et al. 2004; Keshava Prasad et al. 2009). Furthermore, both ZIP6 and ZIP10 are associated with cell migration in breast cancer (Kagara et al. 2007; Hogstrand et al. 2013). Interestingly, both

ZIP6 and ZIP10 are enriched in the cortex of mammalian oocytes, and disruption of their functions has been shown to result in meiotic cell cycle arrest during oogenesis (Kong et al. 2014). Importantly, ZIP6 was demonstrated to form a heteromer with ZIP10 (Taylor et al. 2016) (Fig. 6.19 and 6.20), the phenomenon previously reported for zinc exporters ZnT5 and ZnT6 (Fukunaka et al. 2009). This ZIP6/ZIP10 heteromer formation is contrary to ZIP5 (Pocanschi *et al.* 2013) and ZIP13 (Bin et al. 2011), which were shown to form a homodimer. These data suggested that both ZIP6 and ZIP10 might be needed for mitotic progression, and blocking only one of the two would therefore not be sufficient to stop mitosis.

8.2 ZIP6 and ZIP10 antibodies successfully inhibit mitosis

To prove that ZIP6 and ZIP10 were required for initiation of mitosis, we employed different antibodies that target the N−terminus of either ZIP6 or ZIP10, expecting that the binding of the antibodies could inhibit the function of these ZIP channels. We were able to exhibit in Chapter 7 that treatment with either the ZIP6 or the ZIP10 antibody successfully inhibited mitosis in a concentration−dependent manner. This inhibition was observed in different breast cancer cell lines and seen for both endogenous mitosis and nocodazole−induced mitosis (Fig. 7.1−7.13). Incubation with a monoclonal antibody to inhibit its target protein has previously been performed in an investigation of the Wnt−1 pathway, showing that treatment with an antibody against the Wnt−1 protein successfully induced apoptosis and had the same effect as when Wnt−1 siRNA was used (He et al. 2004). The mitosis inhibition by the ZIP6 and ZIP10 antibodies supported that both these channels were essential for initiation of the mitotic process. However, it could be questioned that the reduction in mitotic cells might have been confounded by toxicity of chemicals added to the antibodies, such as the highly−toxic sodium azide. Sodium azide has differential cytostatic effects on various types of cells (Slamenova and Gabelova 1980), even though these effects have not been specifically reported for MCF−7 cells. This could be argued that the concentration of azide in the treatment solution was very low. Importantly, it was demonstrated using the ZIP10 R antibody with and without sodium azide that this preservative did not significantly influence the mitosis−inhibitory effect of the antibody (Fig. 7.10). The confounding effect of sodium azide could therefore

be excluded. An alternative potential mechanism of the mitotic cell reduction observed as a result of the antibody treatment is prolonged mitotic arrest, resulting in activation of caspase-dependent apoptosis (Hain *et al.* 2016). However, a follow−up investigation in our group using an apoptosis Western blot cocktail disproved this hypothesis by exhibiting no change in the apoptotic rate as a result of the antibody treatment (Nimmanon et al., manuscript in preparation). Noteworthy, IgG negative controls also produced some inhibition of mitosis (data not shown), the mechanism of which is currently unexplained. Comparison between the antibody−treated samples and the IgG control was also limited, because the exact ZIP6/10 antibody concentrations were not known. Nevertheless, a recent publication demonstrated the ability of IgG to bind zinc (Yamanaka et al. 2016), providing an explanation for the observed mitosis inhibition effect of IgG. Further investigation is now needed to explore the manipulation of zinc to confirm this effect.

If ZIP6 is indispensably needed for mitosis, one point to consider is why some cells were able to escape the blockade by the ZIP6 antibody, since the antibodies did not completely inhibit mitosis. This question is confirmed to be legitimate by the finding that the ZIP6−knockout cells were able to proliferate, even though they did not grow as quickly as the wild type (Fig. 7.17). We might reasonably speculate that its function could be compensated for by other ZIP channels, such as ZIP10. It is therefore interesting to investigate whether the cells could still proliferate when both ZIP6 and ZIP10 are deleted. Nevertheless, we could exploit this imperfect mitosis inhibition of the ZIP6 antibody treatment. When using the antibody for treating a patient with a proliferative disease such as cancer, the antibody might cause less adverse effects related to its toxicity to normal cells, given that a small extent of mitosis would still be allowed in normal tissues. Additionally, given that ZIP6 was increased and present on the plasma membrane only in mitotic cells (Fig. 6.7, 6.9 and 6.10) and migrating cells (Hogstrand et al. 2013), this antibody would specifically target the highly aggressive cancer cell population that are actively dividing, invading, circulating, and metastasising. Hence, it is highly probable that this antibody could effectively prevent cancer progression with fewer side effects.

Importantly, exploiting the increased ZIP6 protein expression in the majority of breast cancer, prostate cancer, and melanoma cases detected using immunohistochemistry in tissue sections, an antibody–drug conjugate that targets ZIP6, SGN-LIV1A, has been developed (Sussman *et al.* 2014). Noteworthy, antibody-drug conjugates are a novel class of cancer chemotherapeutic drugs. Each antibody-drug conjugate has 3 components: a cancer-specific monoclonal antibody, a cytotoxic agent covalently attached to the antibody, and a linker (Peters and Brown 2015). Mechanistically, when an antibody-drug conjugate binds to its target, it is endocytosed, trafficked, and degraded, resulting in release of the active cytotoxic component into the cytosol where its intracellular target is located (Bouchard *et al.* 2014). Compared to treatments with naked antibodies, antibody-drug conjugates are believed to have higher clinical efficacy, because they have both high selectivity of the monoclonal antibodies and high potency of the cytotoxic drugs (Sassoon and Blanc 2013). The SGN-LIV1A antibody-drug conjugate is composed of a ZIP6 monoclonal antibody conjugated to monomethyl auristatin E, an anti-cancer drug that inhibits mitosis by blocking tubulin polymerisation (Sussman et al. 2014). In contrast to the results in Chapter 7 using the ZIP6 antibody that was developed in our group, this study on SGN-LIV1A demonstrated using a growth assay that MCF-7 cells were insensitive to the naked antibody used in the investigation, but were highly sensitive to SGN-LIV1A. The same study also revealed in immunodeficient mice with breast cancer xenografts that SGN-LIV1A was effective and well-tolerated at the dosage used with no serious side effect reported. Noteworthy, SGN-LIV1A is currently evaluated in a phase 1 clinical trial for its safety and anti-tumour activity in patients with ZIP6-positive metastatic breast cancer (Forero *et al.* 2014). Collectively, not only does the ZIP6 Y antibody, either in its naked or conjugated form, have high potential to be used as an anti-cancer agent, but these data on SGN-LIV1A (Sassoon and Blanc 2013) have also suggested good tolerability of this antibody.

8.3 ZIP6 is phosphorylated in mitosis

Given the importance of ZIP7 phosphorylation on residues S275 and S276 in ZIP7 activation (Taylor et al. 2012), other potential phosphorylation sites in ZIP7 and other ZIP channels were explored, using data from whole

genome phosphoscreens and online predictive software. Potential phosphorylation sites were detected in multiple ZIP channels besides ZIP7, including ZIP3, ZIP4, ZIP6, and ZIP10, suggesting the potential role of phosphorylation in their post-translational functional control (Table 3.2; Fig. 3.11). Interestingly, sites predicted to be phosphorylated by CK2 were also present in ZIP3 at S129, ZIP6 at S478, and ZIP10 at T573 and S583 (Table 3.2; Fig. 3.11). The sequences of these sites match the consensus sequence motif for CK2 phosphorylation (Pinna 1990; Meggio and Pinna 2003). Given that CK2 plays important roles in cell growth and proliferation, oncogenesis, and pathobiological features of cancer (Tawfic et al. 2001), either ZIP7 alone or together with these other ZIP channels might be among the substrates of this kinase that are responsible for the CK2-associated cancer-promoting effects.

In ZIP6, residue S478 was expected to be a key CK2-phosphorylated site for ZIP6, given that this kinase was ranked top as the potential kinase that phosphorylates this site (Hornbeck et al. 2012). Furthermore, this residue was shown to be highly-conserved across all mammalian species (Fig. 3.15), suggesting its potential importance in ZIP6 functional control. ZIP6 phosphorylation was further investigated in Chapter 6, in which ZIP6 was demonstrated for the first time to be serine-phosphorylated as a result of zinc treatment (Fig. 6.26), the same activation method that has been proved to trigger the CK2-mediated ZIP7 phosphorylation (Taylor et al. 2012). This serine phosphorylation of ZIP6 was detected at 2 minutes after zinc treatment, which was as early as the phosphorylation of ZIP7 (Fig. 4.9). Importantly, residue S478 of ZIP6 was confirmed to be an important site that was phosphorylated by zinc treatment, since the S478A mutant successfully prevented this serine phosphorylation of ZIP6 (Fig. 6.27). According to these findings, it is interesting to speculate that CK2 might simultaneously stimulate ZIP7, which releases zinc from the stores, and other plasma membrane-located ZIP channels, especially ZIP6, which import zinc into the cell.

In a previous investigation, ZIP6-mediated zinc influx into the subsynaptic compartment of the cytosol of T cells was detected within 1 minute after T-cell receptor stimulation by exposure of the cells to superantigen, which was presented by myeloid dendritic cells (Yu et al. 2011). Noteworthy,

according to the concept of immunological synaptic communication between a T cell and an antigen-presenting cell, this subsynaptic compartment was defined as the area in the cytosol of a T cell underneath the synapse with a dendritic cell (Huppa and Davis 2003). This ZIP6-mediated zinc influx was shown to result in increased ZAP70 phosphorylation, sustained calcium influx, and inhibition of Src homology region 2 domain-containing phosphatase-1 recruitment (Yu et al. 2011). Based on this report of early ZIP6 activation in T cells, serine phosphorylation of ZIP6 could also occur within 1 minute after zinc treatment in MCF-7 cells, even though the different cell types and treatment methods also needed to be considered. This further raised the question whether ZIP6 or ZIP7 was activated first and whether ZIP6 was necessary for zinc influx into the cytosol prior to ZIP7-mediated zinc release from the stores. If ZIP6 phosphorylation preceded ZIP7 phosphorylation, ZIP6-mediated zinc influx might act as an upstream signalling event that led to ZIP7 activation as well as a means of zinc supply to the stores. This zinc uptake might result in immediate activation of ERK1/2, which is required for zinc wave production (Yamasaki et al. 2007; Ho *et al.* 2008). Alternatively, zinc itself might be a trigger of zinc release from cellular stores, mimicking the well-known mechanism of calcium release from its stores called “calcium-induced calcium release” (Endo 2009).

Calcium-induced calcium release was first described in skeletal muscle as a physiological mechanism by which a small amount of free calcium that was initially released from the sarcoplasmic reticulum triggered further calcium release from the stores (Ford and Podolsky 1970). This mechanism has been observed not only in skeletal muscle, but also in smooth muscle (Kotlikoff 2003), cardiac muscle (Zahradníková and Zahradník 1999), and pyramidal neurons (Sandler and Barbara 1999). Supporting this mechanism in cardiac myocytes, it was demonstrated using computer simulations that in response to calcium influx via L-type voltage-dependent calcium channels, ryanodine receptors on the sarcoplasmic reticulum were rapidly activated, resulting in calcium release from the sarcoplasmic reticulum within 0.4 milliseconds after calcium influx (Cannell and Soeller 1997). In the light of this calcium-induced calcium release, there might also be a similar mechanism for zinc, which could be called zinc-induced zinc release. In parallel with the calcium-induced calcium release in cardiac myocytes, in response to zinc influx via a ZIP

channel on the plasma membrane such as ZIP6, ZIP7 was triggered, resulting zinc release from intracellular stores such as the ER. Noteworthy, cytosolic zinc, even at a physiological level, has been shown in cardiac myocytes to be able to activate the ryanodine receptor 2 and thereby induce calcium release in the absence of activating levels of calcium in the cytosol (Woodier *et al.* 2015). Zinc influx into cells might therefore trigger not only zinc release, but also calcium release from intracellular stores. Additionally, given the presence of potential tyrosine phosphorylation sites in ZIP3, ZIP6, and ZIP10 (Table 3.2; Fig. 3.11) and the known potent inhibitory effect of zinc on protein tyrosine phosphatases (Wilson et al. 2012), zinc release from cellular stores might also result in tyrosine phosphorylation of these ZIP channels. This phenomenon could therefore provide a positive−feedback mechanism by which zinc itself potentiated zinc signalling.

According to the cellular homeostatic mechanisms of zinc that have previously been reported, the proposed mechanism of zinc−induced zinc release can still be challenged. The effects of ZIP7 activation as a result of CK2−mediated phosphorylation were shown to be independent of the activity of other ZIP channels that are located on the plasma membrane (Taylor et al. 2012). This fact was proved in this study by demonstrating using a Fluozin−3 assay that no apparent cytosolic free zinc was detected following zinc treatment until zinc was released from the ER. Furthermore, stimulation with EGF plus ionomycin produced cellular effects similar to those observed as a result of treatment with zinc plus pyrithione, proving that the rise in cytosolic free zinc levels resulted from the release of endogenous zinc from the ER, not from the influx of exogenous zinc added to the cells. These previous findings are consistent with the muffler model, which highlights the effectiveness of zinc−binding proteins such as the metallothioneins in controlling cytosolic free zinc levels within a narrow physiological range (Colvin et al. 2010). According to these data, the proposed simultaneous activation of ZIP6 at 2 minutes after the stimulation might not be important for the early effects of ZIP7 activation. However, ZIP6 might instead be necessary for the prolonged effects of ZIP7 activation, since ZIP6 could provide zinc supply to cellular stores and prevent the stores from being depleted of zinc. Given that carcinogenesis is a chronic process, it is plausible that ZIP6 as well as other plasma membrane−located

ZIP channels could synergistically work with ZIP7 in sustaining the activation of ZIP7 downstream effectors and thereby promoting cancer phenotype.

Regardless of the potential importance of residue S478 in ZIP6 serine phosphorylation, this residue showed no preference to other sites in binding to CK2 (Fig. 6.30). The specific binding residues in ZIP6 for the binding of CK1 (Fig. 6.34) and PLK1 (Fig. 6.36) were also not detected. This might be because the sites that were investigated did not serve as major binding sites for these kinases. Alternatively, these sites might be notably activated only in mitotic cells, which were the minority of the cells in the samples tested, since the experiment was performed in the absence of a mitosis inducer such as nocodazole. Noteworthy, the combination of ZIP6 transfection and nocodazole treatment was not performed in the investigation due to our concern that the presence of nocodazole might adversely affect the transfection efficiency. Another possible explanation that a specific binding site was not detected for CK2, CK1, and PLK1 is that these three kinases bound to more than one residue in ZIP6, in as much as there are multiple potential sites on ZIP6 for which these kinases were predicted to be the responsible kinases. Additionally, multiple tyrosine residues have recently been reported as potential phosphorylation sites on ZIP6, consisting of residues Y493, Y528, and Y531 (Palacios-Moreno et al. 2015). In consideration of the theory of hierarchical phosphorylation (Ayuso et al. 2010), another possibility is that these tyrosine residues needed to be phosphorylated first, and phosphorylation of the investigated sites would then follow.

Importantly, residue S471 was the only residue in ZIP6 detected to be a specific phosphorylation site for a kinase, GSK−3β (Fig. 6.32). GSK−3β is a negative regulator of Snail (Zhou et al. 2004), which functions as a transcription repressor of E−cadherin (Peinado *et al.* 2007), thereby playing a major role in EMT control. Recently, our group have demonstrated that the ZIP6−mediated zinc signalling pathway in EMT involves inhibitory phosphorylation of GSK−3β (Hogstrand et al. 2013), which is driven by either zinc itself (Ilouz et al. 2002) or zinc−activated AKT (Lee et al. 2009). It is therefore interesting to discover that this kinase bound to ZIP6 on residue S471 during mitosis (Fig. 6.32). In the light of the discovery in this project, GSK−3β could be either an upstream activator of

ZIP6 or a downstream effector of ZIP6−mediated cellular zinc influx. In so far as ZIP6 function could be regulated by GSK−3β−mediated phosphorylation, a threefold implication could be drawn. Firstly, since ZIP6−mediated zinc influx results in inhibitory phosphorylation of GSK−3β (Hogstrand et al. 2013), this might be the mechanism whereby GSK−3β negatively controlled its own function. Secondly, because ZIP6 causes cell rounding prior to EMT (Hogstrand et al. 2013) or mitosis (Chapters 6), phosphorylation of GSK−3β might provide a switch mechanism by which the cell was predestined whether to migrate (when the phosphorylated form of GSK−3β predominated) or divide (when the active non−phosphorylated form of GSK−3β predominated). Thirdly, given that ZIP6 might also be phosphorylated by other protein kinases, particularly CK2, this could also suggest a possibility of hierarchical phosphorylation for ZIP6, in which not until residue S471 had been phosphorylated could the other residues such as S478 be post−translationally modified, or vice versa (Ayuso et al. 2010). Nevertheless, more investigations are needed to confirm this reciprocal interaction between GSK−3β and ZIP6 and its role in ZIP6 regulation.

8.4 ZIP7 signalling is involved in diverse kinase pathways

In order to investigate downstream effectors of ZIP7−mediated zinc release from cellular stores, three types of antibody arrays were employed, namely the phospho−receptor tyrosine kinase (RTK) arrays (Fig. 5.1−5.4, Table 5.1), the phospho−kinase arrays (Fig. 5.5−5.8, Table 5.2), and the phospho−mitogen−activated protein kinase array (MAPK) arrays (Fig. 5.9−5.12, Table 5.3). Two methods of increasing ZIP7 function were employed: transfection with wild−type ZIP7 and zinc treatment for 10 minutes, which activates ZIP7 by CK2−mediated phosphorylation on residues S275 and S276 (Taylor et al. 2012). Only the kinases that were phosphorylated by both of these two ZIP7−activating methods were further analysed for potential downstream cascades triggered by ZIP7−mediated zinc release from cellular stores. A list of all these kinases is shown in Table 8.1. These kinases were linked together according to their common signalling pathways using different online platforms, including the Database for Annotation, Visualization, and Integrated Discovery (DAVID) (Huang *et al.* 2009) and WikiPathways (Kutmon *et al.* 2016). Interestingly, 15 out of the 21 kinases that were phosphorylated as a result of

both ZIP7 transfection and zinc treatment regardless of their different isoforms were detected as signalling molecules involved in an integrated network of cancer signalling pathways (Fig. 8.2).

According to the integrated network of the kinases phosphorylated as a result of ZIP7−mediated zinc release (Fig. 8.2), when different RTKs, including EGFR, ErbB2, IGF−1R, FGFR3, Flt−3, and RET, are activated by tyrosine phosphorylation, they can exert their effects on gene expression through activation of the RAS/RAF/MEK/ERK pathway (Fig. 8.2). The activation of this ERK pathway in turn regulates genes through transcription factors MYC, ELK, or CREB or through activation of the RAS/JNK pathway, which subsequently regulates genes through transcription factor JUN (Fig. 8.2). Alternatively, EGFR and ErbB2 are also able to trigger transcription factor STAT5, whereas IGF−1R, FGFR3, and Flt−3 are also known as upstream activators of the PI3K/AKT pathway (Fig. 8.2). The PI3K/AKT pathway can in turn either activate transcription factors β−catenin and CREB through inhibitory phosphorylation of GSK−3β or regulate protein synthesis through activation of the MTOR pathway, which eventually triggers p70 S6 kinase (Fig. 8.2).

Table 8.1 Downstream effectors of ZIP7−mediated zinc release

Receptor−tyrosine kinases (RTK)	
c−Ret	FGFR3
EGFR	Flt−3
EphA7	IGF−1R
ErbB2	
Kinases including mitogen−activated protein kinases (MAPKs)	
AKT	p38α MAPK
c−Jun	p70 S6
CREB	PRAS40
ERK1/2	STAT2
GSK−3α/β	STAT5a
HSP27	STAT6
JNK	WNK1

MCF−7 cells were transfected with wild−type ZIP7 and treated with 20 µM zinc plus 10 µM sodium pyrithione for 10 minutes. Phosphorylation of selected kinases was determined using the human phospho−RTK, the human phospho−kinase and the human phospho−MAPK antibody arrays (R&D Systems). The kinases that were phosphorylated by both wild−type ZIP7 transfection and zinc treatment are shown in this table. The kinases with more than one isoform or modification are merged together.

Figure 8.2 Potential downstream pathways of ZIP7−mediated zinc release from cellular stores

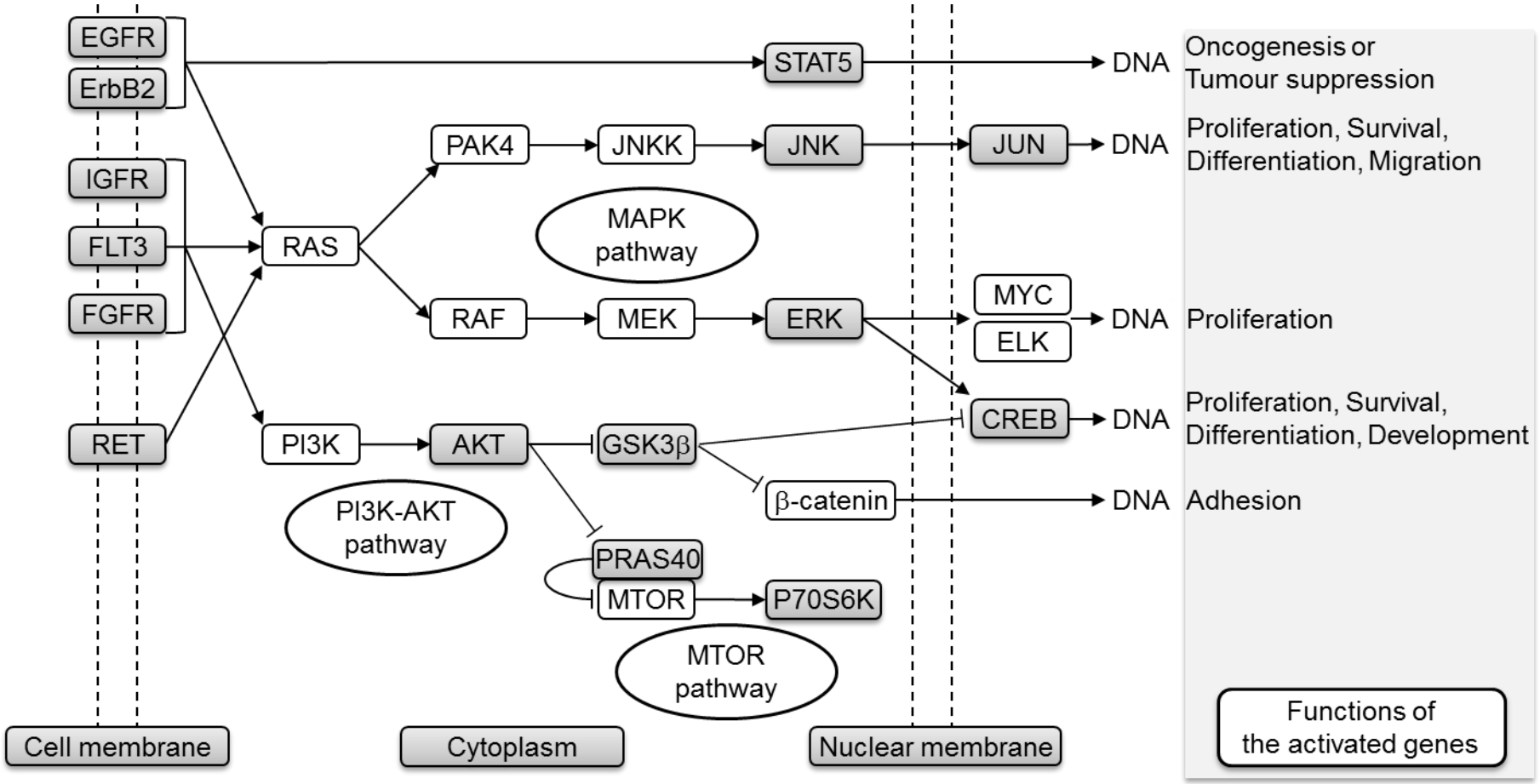

This schematic reveals signalling pathways that include most of the kinases that were phosphorylated as a result of both ZIP7 overexpression and zinc treatment according to the phospho−receptor tyrosine kinase, phospho−kinase, and phospho−mitogen−activated protein kinase array data (grey boxes). The major pathways in which these kinases are involved include the MAPK pathway, the PI3K-AKT pathway and the MTOR pathway.

This network of the signalling pathways downstream of ZIP7−mediated zinc release from cellular stores (Fig. 8.2) has highlighted the diverse roles for ZIP7 in different cellular processes. All of these pathways have been reported to play pivotal roles in carcinogenesis. STAT5−regulated signalling, which can be triggered by the EGFR/ErbB pathway (Kloth *et al.* 2002), is important for both breast development and oncogenesis, in spite of its conflicting role in carcinogenesis as both a tumour suppressor and an oncogene (Ferbeyre and Moriggl 2011). The JNK pathway, with its crosstalk with p38α MAPK, orchestrates regulation of cell cycle progression, either dependently on or independently of gene transcription, and modulation of cell survival, differentiation, and migration (Wagner and Nebreda 2009). Uncontrolled activation of the Raf/MEK/ERK pathway (Friday and Adjei 2008), the PI3K/AKT pathway (Falasca 2010), and the MTOR pathway (Pópulo *et al.* 2012) has been implicated in various types of cancer and shown to participate in many carcinogenetic processes, such as cell proliferation, cell survival (through modulation of apoptosis), and cell migration (through inhibition of cell adhesion). Notably, many cancer−therapeutic drugs have been designed to target components of these cascades. Given that ZIP7 is capable of inducing phosphorylation of multiple signalling molecules in these cancer−related pathways through mobilisation of zinc from cellular stores, ZIP7−mediated zinc signalling has inevitably become an interesting target for cancer treatment.

The additional kinases that were phosphorylated as a result of ZIP7−mediated zinc release from cellular stores but were not included in any of the cancer−related pathways in Fig. 8.2 consist of EphA7, HSP27, p38α MAPK, STAT2, STAT6, and WNK1. EphA7 signalling has been known for its significant roles in development of the central nervous system (Clifford *et al.* 2014). The p38α MAPK pathway, which has HSP27 as a downstream effector, is actively involved in cellular responses to various stimuli, such as inflammatory cytokines, environmental stressors, and growth factors (Cuadrado and Nebreda 2010). The p38α MAPK pathway has a regulatory interplay with different MAPK pathways with, for example, p38α MAPK exerting its inhibitory action on EGFR and GSK−3β (Cuadrado and Nebreda 2010). In response to type 1 interferons, STAT2 and STAT6 form a heterodimer and mediate cytokine signalling in B cells (Delgoffe and Vignali 2013). WNK1 is phosphorylated upon cellular

exposure to EGF or different types of stress, resulting in activation of ERK5, which has significant roles in neuronal survival and cell proliferation (Xu *et al.* 2005). Noteworthy, the activating phosphorylation on WNK1 also results in marginal activation of p38α MAPK (Xu et al. 2005). The link between ZIP7 and activation of these signalling pathways has therefore suggested potential involvement of ZIP7 in the non-carcinogenesis-related cellular processes that have not previously been associated with ZIP7 function, such as nervous system development, inflammation, stress response, and cell proliferation.

Zinc is a competent inhibitor of protein tyrosine phosphatases, such as protein tyrosine phosphatase 1B (Haase and Maret 2005; Bellomo et al. 2014), and can effectively inhibit these enzymes even at the physiologically-relevant nanomolar levels (Wilson et al. 2012). Through this zinc inhibitory effect on protein tyrosine phosphatases, our group have experimentally demonstrated that ZIP7-mediated zinc release from cellular stores results in activation of various RTKs, such as EGFR (ErbB1), ErbB2, and IGF-1R, as well as non-RTKs, such as Src (Taylor et al. 2008b). EGFR, ErbB2, and IGF-1R were also confirmed to be phosphorylated as a result of ZIP7-mediated zinc release from cellular stores using the phospho-RTK arrays in this project (Fig. 5.1-5.4, Table 5.1). However, many other cellular kinases that were phosphorylated as a result of ZIP7-mediated zinc release from cellular stores are serine/threonine kinases, such as AKT or GSK-3β. These serine/threonine kinases are not tyrosine-phosphorylated and are therefore not dephosphorylated by tyrosine phosphatases. Consequently, it is reasonable to question whether activation of these serine/threonine kinases was directly induced by zinc or indirectly induced by zinc-activated RTKs. In H9C2 rat myoblast cells, zinc ions were shown to activate AKT either directly through the zinc inhibitory effect on serine/threonine phosphatases or indirectly through activation of IGF-1R (Lee et al. 2009). The direct inhibition by zinc ions has also been reported in HEK293 human embryonic kidney cells for GSK-3β (Ilouz et al. 2002), a downstream effector of serine/threonine kinase AKT. Noteworthy, a recent investigation in our group revealed that GSK-3β was phosphorylated on residue S9 10 minutes after zinc treatment (Nimmanon et al., manuscript in preparation), compared to AKT which was phosphorylated on residue S473 5 minutes after zinc treatment

(Fig. 4.7). The activation of AKT in advance of the inhibitory phosphorylation of GSK−3β following zinc treatment suggested that in this context, GSK−3β was likely to be indirectly phosphorylated by zinc−activated AKT, rather than directly phosphorylated by zinc itself. Nevertheless, the exact activation mechanism of the cellular kinases other than AKT and GSK−3β is yet to be investigated.

According to the antibody array data, zinc treatment was generally shown to result in activation of a greater variety of tyrosine kinases than wild−type ZIP7 transfection. This might be due to a relatively low transfection rate of ZIP7, which was approximately 20−30% (Fig. 4.3A and 4.4A). In spite of this low transfection rate, a 1.7−fold increase in pZIP7 levels as a result of wild−type ZIP7 transfection was seen on a Western blot (Fig. 5.13), which was compatible with a 50% increase in zinc levels observed in the transfected cells when compared to the non−transfected cells (Taylor et al. 2008b). Alternatively, zinc treatment might have activated kinases via an alternative ZIP7−independent signalling pathway that has not been reported. Nevertheless, this hypothesis of an alternative ZIP7−independent pathway is less possible, given the fact that the cellular effects of zinc treatment are mediated by the endogenous zinc that has been released from cellular stores via ZIP7 rather than the exogenous zinc that has been added to the cell (Taylor et al. 2012). Furthermore, according to the muffler model, zinc influx into the cell is immediately bound to the mufflers such as metallothioneins, so that the desired physiological levels of free zinc ions are well maintained (Colvin et al. 2008). Notwithstanding, there is a possibility that the intracellular kinases localised in the proximity of plasma−membrane−located zinc influx channels, such as ZIP6, are instantly activated by the imported zinc before zinc is muffled by the mufflers (Yu et al. 2011).

Interestingly, some kinases, such as AMPKα1, were phosphorylated specifically by zinc treatment without a detectable increase in phosphorylation following ZIP7 overexpression (Fig. 5.5−5.8, Table 5.2). AMPK functions as an energy sensor as well as a signal transducer, which can be activated by various forms of energetic stress (Inoki *et al.* 2012). Activation of AMPK results in phosphorylation of various substrates that are involved in energy metabolism, cell growth, and transcription regulation, suggesting its crucial roles in these

important cellular processes (Mihaylova and Shaw 2011). Importantly, consistent with our phospho-kinase array results, an exposure of mouse cortical neuronal cultures to 300 µM zinc in a serum-free solution for 10 minutes resulted in delayed AMPK activation, which was detected 2 hours following the exposure (Eom *et al.* 2016). This zinc-induced AMPK activation was shown to induce the apoptotic pathway, explaining the role of zinc in neuronal cell death after an acute brain injury, such as ischemia, epilepsy, or trauma (Frederickson *et al.* 2005). This zinc-induced AMPK activation in neuronal cells was selectively mediated by activation of liver kinase B1 (Eom et al. 2016). Noteworthy, even though a much higher dose of zinc was used in this previous study in cortical neuronal cultures, the AMPK activation was apparently delayed compared to our phospho-kinase array results, which detected the AMPK activation as soon as 10 minutes after zinc treatment (Fig. 5.5-5.8, Table 5.2). The relatively delayed AMPK activation in this previous study might be due to the different types of cells in the study or the absence of an ionophore in the treatment solution (Huang et al. 2005). Given that the endogenous ZIP7 gene and protein expression has been demonstrated in mouse brain tissue using both Northern and Western blotting techniques, respectively (Huang et al. 2005), it is possible that ZIP7 might also play a role in this zinc-induced AMPK-mediated neuronal injury.

In contrast to our findings of AMPK activation by zinc, a previous study in a mouse model demonstrated transient activation of hepatic AMPK that resulted from loss of function of intestinal ZIP4, which prevented zinc absorption by intestinal epithelial cells and caused a severe form of zinc deficiency called acrodermatitis enteropathica (Geiser *et al.* 2012). This discrepancy suggested that zinc signalling could be involved in regulation of AMPK in a tissue- or cell type-specific manner. Notwithstanding, no mechanistic link between the intestinal loss of ZIP4 and the increased hepatic AMPK activation was investigated in the study. This decrease in the hepatic AMPK activation might not be related to the decrease in hepatocellular zinc levels. Given that zinc deficiency is frequently associated with reduced food intake and thereby energy deficit (MacDonald 2000), the reduced AMPK activation might instead be induced by the hepatocellular increase in the AMP/ATP ratio, a condition which results in AMPK activation (Hardie 2015).

Another interesting observation is the phosphorylation of p53 as a result of ZIP7 overexpression, particularly the S46-phosphorylated form, which was clearly detected by both the phospho-kinase and the phospho-MAPK arrays, with no change observed following zinc treatment alone (Fig. 5.5-5.12, Table 5.2-5.3). This modification of p53 has been known to have a role in apoptosis (Smeenk et al. 2011). This finding might therefore be suggestive of activation of programmed cell death induced by either ZIP7 overexpression or the transfection procedure. Importantly, it has been established that differential post-translational modifications of EGFR at different sites in the molecule lead to activation of site-specific downstream signalling cascades (Tong *et al.* 2009). It has been established that ZIP7 is phosphorylated on residues S275 and S276 as a result of zinc treatment (Taylor et al. 2012), whereas the role for other potential phosphorylation sites, such as residues S293 and T294, has not been fully investigated. Hypothetically, in so far as this modification of p53 resulted from the activation of ZIP7 independently of the phosphorylation on residues S275 and S276, our findings suggested that ZIP7 function might be regulated in the same way as EGFR, whereby ZIP7 post-translational modifications at different sites resulted in activation of different signalling pathways.

It is noteworthy that many stress-related proteins, such as p38α MAPK (Coulthard et al. 2009) and HSP27 (Vidyasagar et al. 2012), were activated by both ZIP7 overexpression and zinc treatment (Fig. 5.5-5.8, Table 5.2). This could suggest that cell stress response was triggered by the increase in ZIP7 function or the treatment with a supra-physiologic amount of zinc. Exposure of cells to a high amount of zinc could induce excessive production of reactive oxygen species, thereby causing oxidative stress (Morina *et al.* 2010). Nevertheless, these stress-related proteins are involved not only in stress responses, but also in other crucial cellular mechanisms. For example, p38α MAPK can also be activated by growth factors and cytokines, resulting in phosphorylation of a great variety of substrates that are involved in diverse cellular processes, such as nuclear transcription, chromatin remodelling, cell survival, cytoskeletal change, and cell migration (Cuadrado and Nebreda 2010). Not surprisingly, p38α MAPK has been shown to promote breast cancer metastasis (Hong et al. 2014). Moreover, HSP27 is also involved in cellular

cytoprotective functions and prevention of apoptosis (Wang *et al.* 2014) as well as promotion of breast cancer EMT (Wei et al. 2011). The activation of these proteins might therefore not necessarily be indicative of cell stress caused by the treatment, but it could again further support the involvement of ZIP7−mediated zinc signalling in various cellular processes and carcinogenesis.

8.5 ZIP7 activity is accurately indicated by the pZIP7 antibody

It has been established that ZIP7 is highly expressed in various anti−hormone−resistant breast cancer cell models (Taylor et al. 2007) and responsible for aggressive behaviours seen in these cell models (Taylor et al. 2012). These aggressive behaviours have been attributed to ZIP7−mediated zinc release from the stores and consequential activation of multiple cellular signalling pathways (Taylor et al. 2008b). An antibody that recognises the non−phosphorylated form of ZIP7 is therefore potentially useful for evaluating ZIP7 expression in clinical samples, as it can provide helpful prognostic and predictive information for a clinician to make a therapeutic decision. Nevertheless, the usefulness of this antibody might be limited due to its inability to distinguish between the total levels of ZIP7 and the levels of the actively functioning ZIP7. Following the discovery of the ZIP7 activation mechanism by phosphorylation on residues S275 and S276 (Taylor et al. 2012), a monoclonal antibody recognising ZIP7 when phosphorylated on both these residues has been developed in our group and was characterised in Chapter 3. This antibody sensitively and specifically recognised the activated form of ZIP7 and accurately indicated the ZIP7 activity. It could therefore be implied that this pZIP7 antibody, either alone or together with the total ZIP7 antibody, would make a useful clinical biomarker, particularly for anti−hormone resistant breast cancer. Additionally, since there is currently no available reliable biomarker for assessing total body zinc status (Wieringa et al. 2015), this pZIP7 antibody also has potential to be used for this purpose, which might also benefit patients with subclinical zinc deficiency.

8.6 ZIP7 is needed for human immunity

An interesting fact about ZIP7 is that this zinc channel is encoded by a gene in the human leukocyte antigen (HLA) region on chromosome 6 (Ando et al. 1996). This chromosome region is a highly gene−dense area, which contains

at least 253 gene loci, with many these gene loci encoding proteins that are known to be involved in regulation of the immune system (Shiina *et al.* 2009). It is therefore possible that ZIP7 also participated in the immune system. Importantly, two ZIP7 mutants, P190A and E363K, have been detected in two young siblings by Doctor Sophie Hambleton at Newcastle University. These two siblings were shown to have immunodeficiency without clinically detectable zinc deficiency. In this project, these two mutant constructs were investigated for their ability to mobilise zinc from intracellular stores. Both the ZIP7 P190A and E363K mutants were shown to have impaired zinc-transport function, as suggested by their inability to significantly produce a zinc wave and the decrease in ZIP7 phosphorylation on residues S275 and S276 (Fig. 4.15-4.19; Table 4.2). The findings in this project therefore suggested that human immunity requires not only adequate zinc intake (Haase and Rink 2014a), but also proper cellular zinc homeostasis, which largely depends upon intact functions of zinc transport proteins, especially ZIP7.

ZIP7 is known to be a gatekeeper of zinc release from intracellular stores (Hogstrand et al. 2009), which might be essential for an immune cell to function properly. Nevertheless, this zinc channel might also indirectly participate in the humoral immune system independently of its canonical role in cellular zinc transport. This speculation is based on a large-scale mass spectrometry-based investigation of protein-protein interactions in human embryonic kidney cells, showing an interaction between ZIP7 and CD40 (Ewing *et al.* 2007). In this proteomic study, CD40 (bait) tagged with a FLAG epitope was immunoprecipitated, and a high-throughput mass spectrometry analysis listed ZIP7 (prey) as a protein interacting with CD40 with an assigned confidence score of 0.309. Confirming this binding, we performed a preliminary proximity ligation assay using pZIP7 and CD40 antibodies, demonstrating 60 signals per cell, signifying strong binding between the two proteins (Fig. 8.3). CD40 is a member of the tumour necrosis factor receptor superfamily, which can be found on the surface of antigen-presenting cells including B lymphocytes (Elgueta *et al.* 2009). CD40 crucially engages in the adaptive immunity, both cell-mediated and humoral (Elgueta et al. 2009). In the humoral immune response, CD40/CD40L interactions are required for B-cell differentiation into plasmablasts upon induction by activated T helper cells as well as germinal

centre formation and progression (Elgueta et al. 2009). This preliminary finding of pZIP7 binding to CD40 (Fig. 8.3) therefore suggested that ZIP7 might be additionally involved in the regulation of the humoral response through its interaction with CD40, independently of its function as a zinc transport protein.

Figure 8.3 Binding of pZIP7 to CD40

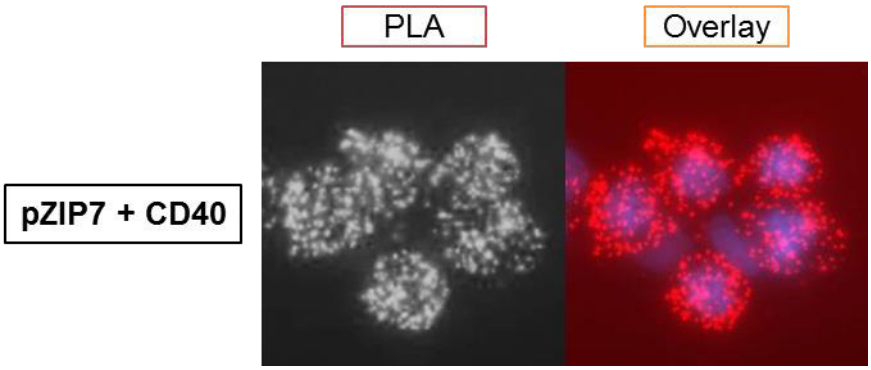

A proximity ligation assay was performed in MCF−7 cells, using pZIP7 and CD40 antibodies (red fluorescent dots), with DAPI nuclear staining (blue). A preliminary result shows 60 signals per cells, signifying spatial proximity of the two proteins.

The link between ZIP7 and the immune system has not been reported. However, ZIP10, another member of the LIV−1 subfamily of ZIP channels, has been shown to play an indispensable role in the immune system, particularly in humoral immunity. Ablation of the ZIP10 gene was shown to severely decrease survival of B cells in bone marrow through activation of apoptotic cascades, an effect similarly found as a result of zinc chelation (Miyai et al. 2014). In ZIP10−conditional knockout mice, B cells were not able to form a germinal centre, a defect also detected in zinc−deficient mice (Hojyo *et al.* 2014). Furthermore, B cells in these ZIP10−knockout mice also intrinsically failed to produce specific IgM and IgG1 in response to immunisation with 4−hydroxy−3−nitrophenylacetyl chicken gamma globulin. Additionally, B−cell receptor signalling was demonstrated in the same study to be severely dysregulated in ZIP10−conditional knockout B cells. Collectively, these reports have suggested that ZIP10−mediated signalling is needed for B−cell survival, activation, immunoglobulin production, and receptor signalling. Even though no direct association of ZIP7 with immune function has been studied, it is plausible

that ZIP7 dysfunction could result in impaired immunity, since ZIP7 is the key zinc channel mobilising zinc from the stores (Taylor et al. 2012). In the light of the muffler model (Colvin et al. 2010), ZIP7 might even participate in the reported ZIP10-mediated signalling, given that zinc ions were likely to be muffled by zinc-binding proteins such as the metallothioneins immediately after the influx via ZIP10, and the action of zinc might require its release from cellular stores via ZIP7. Noteworthy, these two siblings with the ZIP7 mutants had a blood profile showing increased T-cell population and absent B-cell population, which was reminiscent of an X-linked genetic disorder called Bruton agammaglobulinemia (Ochs and Smith 1996). This blood profile was consistent with the decreased B-cell survival in ZIP10-conditional knockout B cells (Hojyo et al. 2014), further suggesting the involvement of ZIP7 in this ZIP10 axis.

8.7 Conclusion

In conclusion, the data in this project have advanced the insight into the post-translational mechanisms of ZIP channels, particularly ZIP7, ZIP6, and ZIP10. The knowledge of the signalling pathways that are triggered by zinc release mediated by ZIP7 has also been expanded, introducing ZIP7 as a prime potential target for modulating these oncogenesis-related signalling pathways and providing multiple research opportunities to decipher the individual pathways. Importantly, our pZIP7 antibody has been introduced as a potential predictive or prognostic biomarker various types of cancer. Furthermore, the N-terminal ZIP6 and ZIP10 antibodies have been proposed to be potential therapeutic agents for treatment of proliferative diseases such as cancer. It is therefore crucial to continue the investigation on these antibodies to determine their actual clinical usefulness when used in clinical samples or even in real clinical settings. If successful, these antibodies will inevitably benefit numerous patients worldwide who are suffering from cancer.

Chapter 9:
References

Abroun, S., Saki, N., Ahmadvand, M., Asghari, F., Salari, F. and Rahim, F. (2015). STATs: An Old Story, Yet Mesmerizing. *Cell J* **17:**395-411.

Akira, S. (1999). Functional roles of STAT family proteins: lessons from knockout mice. *Stem Cells* **17:**138-146.

Alam, S. and Kelleher, S. L. (2012). Cellular mechanisms of zinc dysregulation: a perspective on zinc homeostasis as an etiological factor in the development and progression of breast cancer. *Nutrients* **4:**875-903.

Aley, P. K., Singh, N., Brailoiu, G. C., Brailoiu, E. and Churchill, G. C. (2013). Nicotinic acid adenine dinucleotide phosphate (NAADP) is a second messenger in muscarinic receptor-induced contraction of guinea pig trachea. *J Biol Chem* **288:**10986-10993.

Altmeppen, H. C., Puig, B., Dohler, F., Thurm, D. K., Falker, C., Krasemann, S. and Glatzel, M. (2012). Proteolytic processing of the prion protein in health and disease. *Am J Neurodegener Dis* **1:**15-31.

An, W. L., Bjorkdahl, C., Liu, R., Cowburn, R. F., Winblad, B. and Pei, J. J. (2005). Mechanism of zinc-induced phosphorylation of p70 S6 kinase and glycogen synthase kinase 3beta in SH-SY5Y neuroblastoma cells. *J Neurochem* **92:**1104-1115.

Ando, A., Kikuti, Y. Y., Shigenari, A., Kawata, H., Okamoto, N., Shiina, T., Chen, L. *et al.* (1996). cDNA cloning of the human homologues of the mouse Ke4 and Ke6 genes at the centromeric end of the human MHC region. *Genomics* **35:**600-602.

Andreini, C., Banci, L., Bertini, I. and Rosato, A. (2006). Counting the zinc-proteins encoded in the human genome. *J Proteome Res* **5:**196-201.

Andrews, G. K. (2008). Regulation and function of Zip4, the acrodermatitis enteropathica gene. *Biochem Soc Trans* **36:**1242-1246.

Arinola, O. G. and Charles-Davies, M. A. (2008). Micronutrient levels in the plasma of Nigerian females with breast cancer. *Afr J Biotechnol* **7:**1620-1623.

Ayuso, M. I., Hernández-Jiménez, M., Martín, M. E., Salinas, M. and Alcázar, A. (2010). New hierarchical phosphorylation pathway of the translational repressor eIF4E-binding protein 1 (4E-BP1) in ischemia-reperfusion stress. *J Biol Chem* **285:**34355-34363.

Barrett, A., Madsen, B., Copier, J., Lu, P. J., Cooper, L., Scibetta, A. G., Burchell, J. *et al.* (2002). PLU-1 nuclear protein, which is upregulated in breast cancer, shows restricted expression in normal human adult tissues: a new cancer/testis antigen? *Int J Cancer* **101:**581-588.

Barrett, A. J. and McDonald, J. K. (1986). Nomenclature: protease, proteinase and peptidase. *Biochem J* **237:**935.

Bauer, K., Dowejko, A., Bosserhoff, A. K., Reichert, T. E. and Bauer, R. J. (2009). P-cadherin induces an epithelial-like phenotype in oral squamous cell carcinoma by GSK-3beta-mediated Snail phosphorylation. *Carcinogenesis* **30:**1781-1788.

Bellomo, E., Massarotti, A., Hogstrand, C. and Maret, W. (2014). Zinc ions modulate protein tyrosine phosphatase 1B activity. *Metallomics* **6:**1229-1239.

Bin, B. H., Fukada, T., Hosaka, T., Yamasaki, S., Ohashi, W., Hojyo, S., Miyai, T. *et al.* (2011). Biochemical characterization of human ZIP13 protein: a homo-dimerized zinc transporter involved in the spondylocheiro dysplastic Ehlers-Danlos syndrome. *J Biol Chem* **286:**40255-40265.

Blanco, M. J., Moreno-Bueno, G., Sarrio, D., Locascio, A., Cano, A., Palacios, J. and Nieto, M. A. (2002). Correlation of Snail expression with histological grade and lymph node status in breast carcinomas. *Oncogene* **21:**3241-3246.

BMJ Best Practice. (2015). Zinc deficiency: Step-by-step diagnostic approach [Online]. Available at: http://bestpractice.bmj.com/best-practice/monograph/1195/diagnosis/step-by-step.html [Accessed: 26th January 2016].

Bornfeldt, K. E. (2006). A single second messenger: several possible cellular responses depending on distinct subcellular pools. *Circ Res* **99:**790-792.

Bouchard, H., Viskov, C. and Garcia-Echeverria, C. (2014). Antibody-drug conjugates—a new wave of cancer drugs. *Bioorg Med Chem Lett* **24:**5357-5363.

Bourdeau, A., Dube, N. and Tremblay, M. L. (2005). Cytoplasmic protein tyrosine phosphatases, regulation and function: the roles of PTP1B and TC-PTP. *Curr Opin Cell Biol* **17:**203-209.

Boz, A., Evliyaoglu, O., Yildirim, M., Erkan, N. and Karaca, B. (2005). The value of serum zinc, copper, ceruloplasmin levels in patients with gastrointestinal tract cancers. *Turk J Gastroenterol* **16:**81-84.

Brill, L. M., Xiong, W., Lee, K. B., Ficarro, S. B., Crain, A., Xu, Y., Terskikh, A. *et al.* (2009). Phosphoproteomic analysis of human embryonic stem cells. *Cell Stem Cell* **5:**204-213.

Brown, K. H., Peerson, J. M., Rivera, J. and Allen, L. H. (2002). Effect of supplemental zinc on the growth and serum zinc concentrations of prepubertal children: a meta-analysis of randomized controlled trials. *Am J Clin Nutr* **75:**1062-1071.

Bruinsma, J. J., Jirakulaporn, T., Muslin, A. J. and Kornfeld, K. (2002). Zinc ions and cation diffusion facilitator proteins regulate Ras-mediated signaling. *Dev Cell* **2:**567-578.

Bruttel, V. S. and Wischhusen, J. (2014). Cancer stem cell immunology: key to understanding tumorigenesis and tumor immune escape? *Front Immunol* **5:**360.

Buntzel, J., Bruns, F., Glatzel, M., Garayev, A., Mucke, R., Kisters, K., Schafer, U. *et al.* (2007). Zinc concentrations in serum during head and neck cancer progression. *Anticancer Res* **27:**1941-1943.

Cannell, M. B. and Soeller, C. (1997). Numerical analysis of ryanodine receptor activation by L-type channel activity in the cardiac muscle diad. *Biophys J* **73:**112-122.

Chaipan, C., Kobasa, D., Bertram, S., Glowacka, I., Steffen, I., Tsegaye, T. S., Takeda, M. *et al.* (2009). Proteolytic activation of the 1918 influenza virus hemagglutinin. *J Virol* **83:**3200-3211.

Chang, E. T., Hedelin, M., Adami, H. O., Gronberg, H. and Balter, K. A. (2004). Re: Zinc supplement use and risk of prostate cancer. *J Natl Cancer Inst* **96:**1108; author reply 1108-1109.

Chaudhry, A. A., Warthan, M. M., Pariser, R. J. and Hood, A. F. (2008). Acquired acrodermatitis enteropathica secondary to alcoholism. *Cutis* **82:**60-62.

Chen, P., Chakraborty, S., Mukhopadhyay, S., Lee, E., Paoliello, M. M., Bowman, A. B. and Aschner, M. (2015). Manganese homeostasis in the nervous system. *J Neurochem* **134:**601-610.

Cheng, H. C., Qi, R. Z., Paudel, H. and Zhu, H. J. (2011). Regulation and function of protein kinases and phosphatases. *Enzyme Res* **2011:**794089.

Chesters, J. K. and Petrie, L. (1999). A possible role for cyclins in the zinc requirements during G1 and G2 phases of the cell cycle. *J Nutr Biochem* **10:**279-290.

Chesters, J. K., Petrie, L. and Vint, H. (1989). Specificity and timing of the Zn2+ requirement for DNA synthesis by 3T3 cells. *Exp Cell Res* **184:**499-508.

Choi, K. H., Basma, H., Singh, J. and Cheng, P. W. (2005). Activation of CMV promoter-controlled glycosyltransferase and beta -galactosidase glycogenes by butyrate, tricostatin A, and 5-aza-2'-deoxycytidine. *Glycoconj J* **22:**63-69.

Chowanadisai, W., Lonnerdal, B. and Kelleher, S. L. (2006). Identification of a mutation in SLC30A2 (ZnT-2) in women with low milk zinc concentration that results in transient neonatal zinc deficiency. *J Biol Chem* **281:**39699-39707.

Christensen, J., Agger, K., Cloos, P. A., Pasini, D., Rose, S., Sennels, L., Rappsilber, J. *et al.* (2007). RBP2 belongs to a family of demethylases, specific for tri-and dimethylated lysine 4 on histone 3. *Cell* **128:**1063-1076.

Clifford, M. A., Athar, W., Leonard, C. E., Russo, A., Sampognaro, P. J., Van der Goes, M. S., Burton, D. A. *et al.* (2014). EphA7 signaling guides cortical dendritic development and spine maturation. *Proc Natl Acad Sci U S A* **111:**4994-4999.

Cohen, P. (2002). The origins of protein phosphorylation. *Nat Cell Biol* **4:**E127-130.

Coleman, J., Inukai, M. and Inouye, M. (1985). Dual functions of the signal peptide in protein transfer across the membrane. *Cell* **43:**351-360.

Colvin, R. A., Bush, A. I., Volitakis, I., Fontaine, C. P., Thomas, D., Kikuchi, K. and Holmes, W. R. (2008). Insights into Zn2+ homeostasis in neurons from experimental and modeling studies. *Am J Physiol Cell Physiol* **294:**C726-742.

Colvin, R. A., Holmes, W. R., Fontaine, C. P. and Maret, W. (2010). Cytosolic zinc buffering and muffling: their role in intracellular zinc homeostasis. *Metallomics* **2:**306-317.

Corniola, R. S., Tassabehji, N. M., Hare, J., Sharma, G. and Levenson, C. W. (2008). Zinc deficiency impairs neuronal precursor cell proliferation and induces apoptosis via p53-mediated mechanisms. *Brain Res* **1237:**52-61.

Coulthard, L. R., White, D. E., Jones, D. L., McDermott, M. F. and Burchill, S. A. (2009). p38(MAPK): stress responses from molecular mechanisms to therapeutics. *Trends Mol Med* **15:**369-379.

Cousins, R. J., Liuzzi, J. P. and Lichten, L. A. (2006). Mammalian zinc transport, trafficking, and signals. *J Biol Chem* **281:**24085-24089.

Cuadrado, A. and Nebreda, A. R. (2010). Mechanisms and functions of p38 MAPK signalling. *Biochem J* **429:**403-417.

Cunha, S. F. D., Goncalves, G. A. P., Marchini, J. S. and Roselino, A. M. F. (2012). Acrodermatitis due to zinc deficiency after combined vertical gastroplasty with jejunoileal bypass: case report. *Sao Paulo Medical Journal* **130:**330-335.

Dai, C. and Gu, W. (2010). p53 post-translational modification: deregulated in tumorigenesis. *Trends Mol Med* **16:**528-536.

Dalton, T. P., He, L., Wang, B., Miller, M. L., Jin, L., Stringer, K. F., Chang, X. Q. *et al.* (2005). Identification of mouse SLC39A8 as the transporter responsible for cadmium-induced toxicity in the testis. *Proc Natl Acad Sci U S A* **102:**3401-3406.

Danbolt, N. and Closs, K. (1942). Acrodermatitis enteropathica. *Acta Derm Venereol* **23:**127-169.

Dani, V., Goel, A., Vaiphei, K. and Dhawan, D. K. (2007). Chemopreventive potential of zinc in experimentally induced colon carcinogenesis. *Toxicol Lett* **171:**10-18.

Darnell, J. E., Jr. (1997). STATs and gene regulation. *Science* **277:**1630-1635.

David, R. (2012). Antimicrobials: Why zinc is bad for bacteria. *Nat Rev Micro* **10:**4-4.

de Benoist, B., Darnton-Hill, I., Davidsson, L. and Fontaine, O. (2007). Report of a WHO/UNICEF/IAEA/IZiNCG interagency meeting on zinc status indicators, held in IAEA headquarters, Vienna, December 9, 2005 - Foreword. *Food and Nutrition Bulletin* **28:**S401-S402.

de Poorter, J. J., Lipinski, K. S., Nelissen, R. G., Huizinga, T. W. and Hoeben, R. C. (2007). Optimization of short-term transgene expression by sodium butyrate and ubiquitous chromatin opening elements (UCOEs). *J Gene Med* **9:**639-648.

Decker, T. and Kovarik, P. (2000). Serine phosphorylation of STATs. *Oncogene* **19:**2628-2637.

Delgoffe, G. M. and Vignali, D. A. (2013). STAT heterodimers in immunity: A mixed message or a unique signal? *JAKSTAT* **2:**e23060.

Dereeper, A., Guignon, V., Blanc, G., Audic, S., Buffet, S., Chevenet, F., Dufayard, J. F. *et al.* (2008). Phylogeny.fr: robust phylogenetic analysis for the non-specialist. *Nucleic Acids Res* **36:**W465-469.

Devarajan, E. and Huang, S. (2009). STAT3 as a Central Regulator of Tumor Metastases. *Current Molecular Medicine* **9:**626-633.

Dhawan, D. K. and Chadha, V. D. (2010). Zinc: a promising agent in dietary chemoprevention of cancer. *Indian J Med Res* **132:**676-682.

Dinkel, H., Chica, C., Via, A., Gould, C. M., Jensen, L. J., Gibson, T. J. and Diella, F. (2011). Phospho.ELM: a database of phosphorylation sites--update 2011. *Nucleic Acids Res* **39:**D261-267.

Ehsani, S., Salehzadeh, A., Huo, H., Reginold, W., Pocanschi, C. L., Ren, H., Wang, H. *et al.* (2012). LIV-1 ZIP ectodomain shedding in prion-infected mice resembles cellular response to transition metal starvation. *J Mol Biol* **422:**556-574.

Elgueta, R., Benson, M. J., de Vries, V. C., Wasiuk, A., Guo, Y. and Noelle, R. J. (2009). Molecular mechanism and function of CD40/CD40L engagement in the immune system. *Immunol Rev* **229:**152-172.

Elomaa, O., Pulkkinen, K., Hannelius, U., Mikkola, M., Saarialho-Kere, U. and Kere, J. (2001). Ectodysplasin is released by proteolytic shedding and binds to the EDAR protein. *Human Molecular Genetics* **10:**953-962.

Endo, M. (2009). Calcium-induced calcium release in skeletal muscle. *Physiol Rev* **89:**1153-1176.

Eom, J. W., Lee, J. M., Koh, J. Y. and Kim, Y. H. (2016). AMP-activated protein kinase contributes to zinc-induced neuronal death via activation by LKB1 and induction of Bim in mouse cortical cultures. *Mol Brain* **9:**14.

Ewing, R. M., Chu, P., Elisma, F., Li, H., Taylor, P., Climie, S., McBroom-Cerajewski, L. *et al.* (2007). Large-scale mapping of human protein-protein interactions by mass spectrometry. *Mol Syst Biol* **3:**89.

Falasca, M. (2010). PI3K/Akt signalling pathway specific inhibitors: a novel strategy to sensitize cancer cells to anti-cancer drugs. *Curr Pharm Des* **16:**1410-1416.

Falchuk, K. H., Fawcett, D. W. and Vallee, B. L. (1975). Role of zinc in cell division of Euglena gracilis. *J Cell Sci* **17:**57-78.

FAO/WHO. (2002). Zinc.*FAO/WHO expert consultation on human vitamin and mineral requirements*. Rome, pp. 257-270.

Farquharson, M. J., Al-Ebraheem, A., Geraki, K., Leek, R., Jubb, A. and Harris, A. L. (2009). Zinc presence in invasive ductal carcinoma of the breast and its correlation with oestrogen receptor status. *Phys Med Biol* **54:**4213.

Fashner, J., Ericson, K. and Werner, S. (2012). Treatment of the common cold in children and adults. *Am Fam Physician* **86:**153-159.

Ferbeyre, G. and Moriggl, R. (2011). The role of Stat5 transcription factors as tumor suppressors or oncogenes. *Biochim Biophys Acta* **1815:**104-114.

Fink, K. and Grandvaux, N. (2013). STAT2 and IRF9: Beyond ISGF3. *JAKSTAT* **2:**e27521.

Fong, L. Y., Nguyen, V. T. and Farber, J. L. (2001). Esophageal cancer prevention in zinc-deficient rats: rapid induction of apoptosis by replenishing zinc. *J Natl Cancer Inst* **93:**1525-1533.

Ford, L. E. and Podolsky, R. J. (1970). Regenerative calcium release within muscle cells. *Science* **167:**58-59.

Forero, A., Burris III, H., LoRusso, P., Specht, J., Miller, K., Mita, M., Liu, M. C. *et al.* eds. (2014). *SGN-LIV1A: A phase 1 trial evaluating a novel antibody-drug conjugate in patients with LIV-1-positive breast cancer [abstract]*. Proceedings of the Thirty-Seventh

Annual CTRC-AACR San Antonio Breast Cancer Symposium. San Antonio, TX. Cancer Res.

Fraker, P. J. (2005). Roles for cell death in zinc deficiency. *J Nutr* **135:**359-362.

Franz-Wachtel, M., Eisler, S. A., Krug, K., Wahl, S., Carpy, A., Nordheim, A., Pfizenmaier, K. *et al.* (2012). Global detection of protein kinase D-dependent phosphorylation events in nocodazole-treated human cells. *Mol Cell Proteomics* **11:**160-170.

Frederickson, C. J., Koh, J. Y. and Bush, A. I. (2005). The neurobiology of zinc in health and disease. *Nat Rev Neurosci* **6:**449-462.

Friday, B. B. and Adjei, A. A. (2008). Advances in targeting the Ras/Raf/MEK/Erk mitogen-activated protein kinase cascade with MEK inhibitors for cancer therapy. *Clin Cancer Res* **14:**342-346.

Fujioka, M. and Lieberman, I. (1964). A Zn++ requirement for synthesis of deoxyribonucleic acid by rat liver. *J Biol Chem* **239:**1164-1167.

Fukunaka, A., Suzuki, T., Kurokawa, Y., Yamazaki, T., Fujiwara, N., Ishihara, K., Migaki, H. *et al.* (2009). Demonstration and characterization of the heterodimerization of ZnT5 and ZnT6 in the early secretory pathway. *J Biol Chem* **284:**30798-30806.

Gee, K. R., Zhou, Z. L., Qian, W. J. and Kennedy, R. (2002). Detection and imaging of zinc secretion from pancreatic beta-cells using a new fluorescent zinc indicator. *J Am Chem Soc* **124:**776-778.

Geiser, J., Venken, K. J., De Lisle, R. C. and Andrews, G. K. (2012). A mouse model of acrodermatitis enteropathica: loss of intestine zinc transporter ZIP4 (Slc39a4) disrupts the stem cell niche and intestine integrity. *PLoS Genet* **8:**e1002766.

Girijashanker, K., He, L., Soleimani, M., Reed, J. M., Li, H., Liu, Z., Wang, B. *et al.* (2008). Slc39a14 gene encodes ZIP14, a metal/bicarbonate symporter: similarities to the ZIP8 transporter. *Mol Pharmacol* **73:**1413-1423.

Gnad, F., Gunawardena, J. and Mann, M. (2011). PHOSIDA 2011: the posttranslational modification database. *Nucleic Acids Res* **39:**D253-260.

Gnad, F., Ren, S., Cox, J., Olsen, J. V., Macek, B., Oroshi, M. and Mann, M. (2007). PHOSIDA (phosphorylation site database): management, structural and evolutionary investigation, and prediction of phosphosites. *Genome Biol* **8:**R250.

Gonzalez, A., Peters, U., Lampe, J. W. and White, E. (2009). Zinc intake from supplements and diet and prostate cancer. *Nutr Cancer* **61:**206-215.

Guerinot, M. L. (2000). The ZIP family of metal transporters. *Biochim Biophys Acta* **1465:**190-198.

Gullberg, M. and Andersson, A.-C. (2010). Visualization and quantification of protein-protein interactions in cells and tissues. *Nat Methods*.

Gumulec, J., Masarik, M., Adam, V., Eckschlager, T., Provaznik, I. and Kizek, R. (2014). Serum and tissue zinc in epithelial malignancies: a meta-analysis. *PLoS One* **9:**e99790.

Gupta, S. K., Singh, S. P. and Shukla, V. K. (2005). Copper, zinc, and Cu/Zn ratio in carcinoma of the gallbladder. *J Surg Oncol* **91:**204-208.

Haase, H. and Maret, W. (2005). Protein tyrosine phosphatases as targets of the combined insulinomimetic effects of zinc and oxidants. *Biometals* **18:**333-338.

Haase, H. and Rink, L. (2014a). Multiple impacts of zinc on immune function. *Metallomics* **6:**1175-1180.

Haase, H. and Rink, L. (2014b). Zinc signals and immune function. *Biofactors* **40:**27-40.

Hain, K. O., Colin, D. J., Rastogi, S., Allan, L. A. and Clarke, P. R. (2016). Prolonged mitotic arrest induces a caspase-dependent DNA damage response at telomeres that determines cell survival. *Sci Rep* **6:**26766.

Hambidge, K. M. and Krebs, N. F. (2007). Zinc deficiency: a special challenge. *J Nutr* **137:**1101-1105.

Hambidge, M. (2000). Human zinc deficiency. *J Nutr* **130:**1344S-1349S.

Hanahan, D. and Weinberg, R. A. (2011). Hallmarks of cancer: the next generation. *Cell* **144:**646-674.

Hardie, D. G. (2015). AMPK: positive and negative regulation, and its role in whole-body energy homeostasis. *Curr Opin Cell Biol* **33:**1-7.

Hazan-Halevy, I., Harris, D., Liu, Z., Liu, J., Li, P., Chen, X., Shanker, S. *et al.* (2010). STAT3 is constitutively phosphorylated on serine 727 residues, binds DNA, and activates transcription in CLL cells. *Blood* **115:**2852-2863.

He, B., You, L., Uematsu, K., Xu, Z., Lee, A. Y., Matsangou, M., McCormick, F. *et al.* (2004). A monoclonal antibody against Wnt-1 induces apoptosis in human cancer cells. *Neoplasia* **6:**7-14.

He, L., Girijashanker, K., Dalton, T. P., Reed, J., Li, H., Soleimani, M. and Nebert, D. W. (2006). ZIP8, member of the solute-carrier-39 (SLC39) metal-transporter family: characterization of transporter properties. *Mol Pharmacol* **70:**171-180.

Heim, M. H., Kerr, I. M., Stark, G. R. and Darnell, J. E. (1995). Contribution of STAT SH2 groups to specific interferon signaling by the Jak-STAT pathway. *Science* **267:**1347-1349.

Henkes, M., van der Kuip, H. and Aulitzky, W. E. (2008). Therapeutic options for chronic myeloid leukemia: focus on imatinib (Glivec, Gleevectrade mark). *Ther Clin Risk Manag* **4:**163-187.

Hirano, T., Murakami, M., Fukada, T., Nishida, K., Yamasaki, S. and Suzuki, T. (2008). Roles of zinc and zinc signaling in immunity: zinc as an intracellular signaling molecule. *Adv Immunol* **97:**149-176.

Hiscox, S., Morgan, L., Barrow, D., Dutkowski, C., Wakeling, A. and Nicholson, R. I. (2004). Tamoxifen resistance in breast cancer cells is accompanied by an enhanced motile and invasive phenotype: Inhibition by gefitinib ('Iressa', ZD1839). *Clin Exp Metastas* **21:**201-212.

Hiscox, S., Morgan, L., Green, T. P., Barrow, D., Gee, J. and Nicholson, R. I. (2006). Elevated Src activity promotes cellular invasion and motility in tamoxifen resistant breast cancer cells. *Breast Cancer Res Treat* **97:**263-274.

Ho, E. and Ames, B. N. (2002). Low intracellular zinc induces oxidative DNA damage, disrupts p53, NFkappa B, and AP1 DNA binding, and affects DNA repair in a rat glioma cell line. *Proc Natl Acad Sci U S A* **99:**16770-16775.

Ho, E., Courtemanche, C. and Ames, B. N. (2003). Zinc deficiency induces oxidative DNA damage and increases p53 expression in human lung fibroblasts. *J Nutr* **133:**2543-2548.

Ho, Y., Samarasinghe, R., Knoch, M. E., Lewis, M., Aizenman, E. and DeFranco, D. B. (2008). Selective inhibition of mitogen-activated protein kinase phosphatases by zinc accounts for extracellular signal-regulated kinase 1/2-dependent oxidative neuronal cell death. *Mol Pharmacol* **74:**1141-1151.

Hoch, E., Lin, W., Chai, J., Hershfinkel, M., Fu, D. and Sekler, I. (2012). Histidine pairing at the metal transport site of mammalian ZnT transporters controls Zn2+ over Cd2+ selectivity. *Proc Natl Acad Sci U S A* **109:**7202-7207.

Hofmann, K. and Baron, M. D. (1996). BOXSHADE 3.21: Pretty Printing and Shading of Multiple-Alignment files [Online]. Available at: http://www.ch.embnet.org/software/BOX_form.html [Accessed: 6th November 2015].

Hogstrand, C., Kille, P., Ackland, M. L., Hiscox, S. and Taylor, K. M. (2013). A mechanism for epithelial-mesenchymal transition and anoikis resistance in breast cancer triggered by zinc channel ZIP6 and STAT3 (signal transducer and activator of transcription 3). *Biochem J* **455:**229-237.

Hogstrand, C., Kille, P., Nicholson, R. I. and Taylor, K. M. (2009). Zinc transporters and cancer: a potential role for ZIP7 as a hub for tyrosine kinase activation. *Trends Mol Med* **15:**101-111.

Hojyo, S., Miyai, T., Fujishiro, H., Kawamura, M., Yasuda, T., Hijikata, A., Bin, B. H. *et al.* (2014). Zinc transporter SLC39A10/ZIP10 controls humoral immunity by modulating B-cell receptor signal strength. *Proc Natl Acad Sci U S A* **111:**11786-11791.

Hong, B., Li, H., Zhang, M., Xu, J., Lu, Y., Zheng, Y., Qian, J. *et al.* (2014). p38 MAPK inhibits breast cancer metastasis through regulation of stromal expansion. *Int J Cancer*.

Hooper, N. M. (1994). Families of zinc metalloproteases. *FEBS Lett* **354:**1-6.

Horn, H., Schoof, E. M., Kim, J., Robin, X., Miller, M. L., Diella, F., Palma, A. *et al.* (2014). KinomeXplorer: an integrated platform for kinome biology studies. *Nat Methods* **11:**603-604.

Hornbeck, P. V., Kornhauser, J. M., Tkachev, S., Zhang, B., Skrzypek, E., Murray, B., Latham, V. *et al.* (2012). PhosphoSitePlus: a comprehensive resource for investigating the structure and function of experimentally determined post-translational modifications in man and mouse. *Nucleic Acids Res* **40:**D261-270.

Hornbeck, P. V., Zhang, B., Murray, B., Kornhauser, J. M., Latham, V. and Skrzypek, E. (2015). PhosphoSitePlus, 2014: mutations, PTMs and recalibrations. *Nucleic Acids Res* **43:**D512-520.

Huang, d. W., Sherman, B. T. and Lempicki, R. A. (2009). Systematic and integrative analysis of large gene lists using DAVID bioinformatics resources. *Nat Protoc* **4:**44-57.

Huang, L. and Kirschke, C. P. (2007). A di-leucine sorting signal in ZIP1 (SLC39A1) mediates endocytosis of the protein. *FEBS J* **274:**3986-3997.

Huang, L., Kirschke, C. P. and Zhang, Y. (2006). Decreased intracellular zinc in human tumorigenic prostate epithelial cells: a possible role in prostate cancer progression. *Cancer Cell Int* **6:**10.

Huang, L., Kirschke, C. P., Zhang, Y. and Yu, Y. Y. (2005). The ZIP7 gene (Slc39a7) encodes a zinc transporter involved in zinc homeostasis of the Golgi apparatus. *J Biol Chem* **280:**15456-15463.

Humphrey, S. J., James, D. E. and Mann, M. (2015). Protein Phosphorylation: A Major Switch Mechanism for Metabolic Regulation. *Trends Endocrinol Metab* **26:**676-687.

Huppa, J. B. and Davis, M. M. (2003). T-cell-antigen recognition and the immunological synapse. *Nat Rev Immunol* **3:**973-983.

Ilouz, R., Kaidanovich, O., Gurwitz, D. and Eldar-Finkelman, H. (2002). Inhibition of glycogen synthase kinase-3β by bivalent zinc ions: insight into the insulin-mimetic action of zinc. *Biochem Biophys Res Commun* **295:**102-106.

Inoki, K., Kim, J. and Guan, K. L. (2012). AMPK and mTOR in cellular energy homeostasis and drug targets. *Annu Rev Pharmacol Toxicol* **52:**381-400.

Iorns, E., Drews-Elger, K., Ward, T. M., Dean, S., Clarke, J., Berry, D., El Ashry, D. *et al.* (2012). A new mouse model for the study of human breast cancer metastasis. *PLoS One* **7:**e47995.

Izawa, D. and Pines, J. (2015). The mitotic checkpoint complex binds a second CDC20 to inhibit active APC/C. *Nature* **517:**631-634.

Jain, N., Zhang, T., Fong, S. L., Lim, C. P. and Cao, X. (1998). Repression of Stat3 activity by activation of mitogen-activated protein kinase (MAPK). *Oncogene* **17:**3157-3167.

Jain, N., Zhang, T., Kee, W. H., Li, W. and Cao, X. (1999). Protein kinase C delta associates with and phosphorylates Stat3 in an interleukin-6-dependent manner. *J Biol Chem* **274:**24392-24400.

Jenkitkasemwong, S., Wang, C. Y., Coffey, R., Zhang, W., Chan, A., Biel, T., Kim, J. S. *et al.* (2015). SLC39A14 Is Required for the Development of Hepatocellular Iron Overload in Murine Models of Hereditary Hemochromatosis. *Cell Metabolism* **22:**138-150.

Jeong, J., Walker, J. M., Wang, F., Park, J. G., Palmer, A. E., Giunta, C., Rohrbach, M. *et al.* (2012). Promotion of vesicular zinc efflux by ZIP13 and its implications for spondylocheiro dysplastic Ehlers-Danlos syndrome. *Proc Natl Acad Sci U S A* **109:**E3530-3538.

Jin, R., Bay, B., Tan, P. and Tan, B. K. (1999). Metallothionein expression and zinc levels in invasive ductal breast carcinoma. *Oncol Rep* **6:**871-875.

Johnson, H. A. (1994). On the clinical significance of the S-phase fractions of tumors. *Ann Clin Lab Sci* **24:**431-435.

Jones, H. E., Goddard, L., Gee, J. M., Hiscox, S., Rubini, M., Barrow, D., Knowlden, J. M. *et al.* (2004). Insulin-like growth factor-I receptor signalling and acquired resistance to gefitinib (ZD1839; Iressa) in human breast and prostate cancer cells. *Endocr Relat Cancer* **11:**793-814.

Kagara, N., Tanaka, N., Noguchi, S. and Hirano, T. (2007). Zinc and its transporter ZIP10 are involved in invasive behavior of breast cancer cells. *Cancer Sci* **98:**692-697.

Kaler, P. and Prasad, R. (2007). Molecular cloning and functional characterization of novel zinc transporter rZip10 (Slc39a10) involved in zinc uptake across rat renal brush-border membrane. *Am J Physiol Renal Physiol* **292:**F217-229.

Kambe, T. and Andrews, G. K. (2009). Novel proteolytic processing of the ectodomain of the zinc transporter ZIP4 (SLC39A4) during zinc deficiency is inhibited by acrodermatitis enteropathica mutations. *Mol Cell Biol* **29:**129-139.

Kambe, T., Suzuki, T., Nagao, M. and Yamaguchi-Iwai, Y. (2006). Sequence Similarity and Functional Relationship Among Eukaryotic ZIP and CDF Transporters. *Genomics Proteomics Bioinformatics* **4:**1-9.

Kambe, T., Tsuji, T., Hashimoto, A. and Itsumura, N. (2015). The Physiological, Biochemical, and Molecular Roles of Zinc Transporters in Zinc Homeostasis and Metabolism. *Physiol Rev* **95:**749-784.

Karn, T., Metzler, D., Ruckhaberle, E., Hanker, L., Gatje, R., Solbach, C., Ahr, A. *et al.* (2010). Data-driven derivation of cutoffs from a pool of 3,030 Affymetrix arrays to stratify distinct clinical types of breast cancer. *Breast Cancer Res Treat* **120:**567-579.

Kasper, G., Weiser, A. A., Rump, A., Sparbier, K., Dahl, E., Hartmann, A., Wild, P. *et al.* (2005). Expression levels of the putative zinc transporter LIV-1 are associated with a better outcome of breast cancer patients. *Int J Cancer* **117:**961-973.

Kavurma, M. M. and Khachigian, L. M. (2003). Sp1 inhibits proliferation and induces apoptosis in vascular smooth muscle cells by repressing p21WAF1/Cip1 transcription and cyclin D1-Cdk4-p21WAF1/Cip1 complex formation. *J Biol Chem* **278:**32537-32543.

Kawachi, M., Kobae, Y., Mimura, T. and Maeshima, M. (2008). Deletion of a histidine-rich loop of AtMTP1, a vacuolar Zn(2+)/H(+) antiporter of Arabidopsis thaliana, stimulates the transport activity. *J Biol Chem* **283:**8374-8383.

Kay, A. R. and Tóth, K. (2008). Is zinc a neuromodulator? *Sci Signal* **1:**re3.

Keshava Prasad, T. S., Goel, R., Kandasamy, K., Keerthikumar, S., Kumar, S., Mathivanan, S., Telikicherla, D. *et al.* (2009). Human Protein Reference Database--2009 update. *Nucleic Acids Res* **37:**D767-772.

Kettenbach, A. N., Schweppe, D. K., Faherty, B. K., Pechenick, D., Pletnev, A. A. and Gerber, S. A. (2011). Quantitative phosphoproteomics identifies substrates and functional modules of Aurora and Polo-like kinase activities in mitotic cells. *Sci Signal* **4:**rs5.

Kikuchi, K., Komatsu, K. and Nagano, T. (2004). Zinc sensing for cellular application. *Curr Opin Chem Biol* **8:**182-191.

Kim, A. M., Vogt, S., O'Halloran, T. V. and Woodruff, T. K. (2010). Zinc availability regulates exit from meiosis in maturing mammalian oocytes. *Nat Chem Biol* **6:**674-681.

Kim, H. and Baumann, H. (1997). The carboxyl-terminal region of STAT3 controls gene induction by the mouse haptoglobin promoter. *J Biol Chem* **272:**14571-14579.

Kim, H. S., Park, I., Cho, H. J., Gwak, G., Yang, K., Bae, B. N., Kim, K. W. *et al.* (2012). Analysis of the potent prognostic factors in luminal-type breast cancer. *J Breast Cancer* **15:**401-406.

Kim, Y. H., Kim, E. Y., Gwag, B. J., Sohn, S. and Koh, J. Y. (1999). Zinc-induced cortical neuronal death with features of apoptosis and necrosis: mediation by free radicals. *Neuroscience* **89:**175-182.

Kinexus Bioinformatics Corporation. PhosphoNET: Human Phospho-Site KnowledgeBase [Online]. Available at: http://www.phosphonet.ca [Accessed: 15th August 2015].

King, J. C. (2011). Zinc: an essential but elusive nutrient. *Am J Clin Nutr* **94:**679S-684S.

King, J. C., Shames, D. M. and Woodhouse, L. R. (2000). Zinc homeostasis in humans. *J Nutr* **130:**1360S-1366S.

Kitabayashi, C., Fukada, T., Kanamoto, M., Ohashi, W., Hojyo, S., Atsumi, T., Ueda, N. *et al.* (2010). Zinc suppresses Th17 development via inhibition of STAT3 activation. *Int Immunol* **22:**375-386.

Kloth, M. T., Catling, A. D. and Silva, C. M. (2002). Novel activation of STAT5b in response to epidermal growth factor. *J Biol Chem* **277:**8693-8701.

Knowlden, J. M., Hutcheson, I. R., Jones, H. E., Madden, T., Gee, J. M., Harper, M. E., Barrow, D. *et al.* (2003). Elevated levels of epidermal growth factor receptor/c-erbB2 heterodimers mediate an autocrine growth regulatory pathway in tamoxifen-resistant MCF-7 cells. *Endocrinology* **144:**1032-1044.

Kolonel, L. N., Yoshizawa, C. N. and Hankin, J. H. (1988). Diet and prostatic cancer: a case-control study in Hawaii. *Am J Epidemiol* **127:**999-1012.

Kong, B. Y., Duncan, F. E., Que, E. L., Kim, A. M., O'Halloran, T. V. and Woodruff, T. K. (2014). Maternally-derived zinc transporters ZIP6 and ZIP10 drive the mammalian oocyte-to-egg transition. *Mol Hum Reprod* **20:**1077-1089.

Kornreich, B. G. (2007). The patch clamp technique: principles and technical considerations. *J Vet Cardiol* **9:**25-37.

Kotlikoff, M. I. (2003). Calcium-induced calcium release in smooth muscle: the case for loose coupling. *Prog Biophys Mol Biol* **83:**171-191.

Krause, M. and Gautreau, A. (2014). Steering cell migration: lamellipodium dynamics and the regulation of directional persistence. *Nat Rev Mol Cell Biol* **15:**577-590.

Krezel, A. and Maret, W. (2006). Zinc-buffering capacity of a eukaryotic cell at physiological pZn. *J Biol Inorg Chem* **11:**1049-1062.

Kristal, A. R., Stanford, J. L., Cohen, J. H., Wicklund, K. and Patterson, R. E. (1999). Vitamin and mineral supplement use is associated with reduced risk of prostate cancer. *Cancer Epidem Biomar* **8:**887-892.

Kumar, P., Lal, N. R., Mondal, A. K., Mondal, A., Gharami, R. C. and Maiti, A. (2012). Zinc and skin: a brief summary. *Dermatol Online J* **18:**1.

Kumar, R. and Prasad, R. (1999). Purification and characterization of a major zinc binding protein from renal brush border membrane of rat. *Biochim Biophys Acta* **1419:**23-32.

Kumar, R. and Prasad, R. (2000). Functional characterization of purified zinc transporter from renal brush border membrane of rat. *Biochim Biophys Acta* **1509:**429-439.

Kumánovics, A., Poruk, K. E., Osborn, K. A., Ward, D. M. and Kaplan, J. (2006). YKE4 (YIL023C) encodes a bidirectional zinc transporter in the endoplasmic reticulum of Saccharomyces cerevisiae. *J Biol Chem* **281:**22566-22574.

Kutmon, M., Riutta, A., Nunes, N., Hanspers, K., Willighagen, E. L., Bohler, A., Mélius, J. *et al.* (2016). WikiPathways: capturing the full diversity of pathway knowledge. *Nucleic Acids Res* **44:**D488-494.

Küry, S., Dréno, B., Bézieau, S., Giraudet, S., Kharfi, M., Kamoun, R. and Moisan, J. P. (2002). Identification of SLC39A4, a gene involved in acrodermatitis enteropathica. *Nat Genet* **31:**239-240.

LaBaer, J., Garrett, M. D., Stevenson, L. F., Slingerland, J. M., Sandhu, C., Chou, H. S., Fattaey, A. *et al.* (1997). New functional activities for the p21 family of CDK inhibitors. *Genes Dev* **11:**847-862.

Laemmli, U. K. (1970). Cleavage of structural proteins during the assembly of the head of bacteriophage T4. *Nature* **227:**680-685.

Lai, Z. W., Petrera, A. and Schilling, O. (2015). Protein amino-terminal modifications and proteomic approaches for N-terminal profiling. *Curr Opin Chem Biol* **24:**71-79.

Lansdown, A. B., Mirastschijski, U., Stubbs, N., Scanlon, E. and Agren, M. S. (2007). Zinc in wound healing: theoretical, experimental, and clinical aspects. *Wound Repair Regen* **15:**2-16.

Larner, F., Woodley, L. N., Shousha, S., Moyes, A., Humphreys-Williams, E., Strekopytov, S., Halliday, A. N. *et al.* (2015). Zinc isotopic compositions of breast cancer tissue. *Metallomics* **7:**112-117.

Lawrenson, J. G. and Grzybowski, A. (2015). Controversies in the use of nutritional supplements in ophthalmology. *Curr Pharm Des*.

Lee, S., Chanoit, G., McIntosh, R., Zvara, D. A. and Xu, Z. (2009). Molecular mechanism underlying Akt activation in zinc-induced cardioprotection. *Am J Physiol Heart Circ Physiol* **297:**H569-575.

Leitzmann, M. F., Stampfer, M. J., Wu, K. N., Colditz, G. A., Willett, W. C. and Giovannucci, E. L. (2003). Zinc supplement use and risk of prostate cancer. *J Natl Cancer I* **95:**1004-1007.

Lemaire, K., Ravier, M. A., Schraenen, A., Creemers, J. W., Van de Plas, R., Granvik, M., Van Lommel, L. *et al.* (2009). Insulin crystallization depends on zinc transporter ZnT8 expression, but is not required for normal glucose homeostasis in mice. *Proc Natl Acad Sci U S A* **106:**14872-14877.

Li, Y. and Maret, W. (2009). Transient fluctuations of intracellular zinc ions in cell proliferation. *Exp Cell Res* **315:**2463-2470.

Lichten, L. A. and Cousins, R. J. (2009). Mammalian zinc transporters: nutritional and physiologic regulation. *Annu Rev Nutr* **29:**153-176.

Lieberman, I., Abrams, R., Hunt, N. and Ove, P. (1963). Levels of Enzyme Activity and Deoxyribonucleic Acid Synthesis in Mammalian Cells Cultured from the Animal. *J Biol Chem* **238:**3955-3962.

Lim, C. P. and Cao, X. (1999). Serine phosphorylation and negative regulation of Stat3 by JNK. *J Biol Chem* **274:**31055-31061.

Lim, Y. P. (2005). Mining the tumor phosphoproteome for cancer markers. *Clin Cancer Res* **11:**3163-3169.

Lin, W., Chai, J., Love, J. and Fu, D. (2010). Selective electrodiffusion of zinc ions in a Zrt-, Irt-like protein, ZIPB. *J Biol Chem* **285:**39013-39020.

Lindqvist, A., Rodríguez-Bravo, V. and Medema, R. H. (2009). The decision to enter mitosis: feedback and redundancy in the mitotic entry network. *J Cell Biol* **185:**193-202.

Liuzzi, J. P., Aydemir, F., Nam, H., Knutson, M. D. and Cousins, R. J. (2006). Zip14 (Slc39a14) mediates non-transferrin-bound iron uptake into cells. *Proc Natl Acad Sci U S A* **103:**13612-13617.

Lizio, M., Harshbarger, J., Shimoji, H., Severin, J., Kasukawa, T., Sahin, S., Abugessaisa, I. *et al.* (2015). Gateways to the FANTOM5 promoter level mammalian expression atlas. *Genome Biol* **16:**22.

Lodish, H., Berk, A., Zipursky, S. L., Matsudaira, P., Baltimore, D. and Darnell, J. (2000). Hierarchical Structure of Proteins. [Online]. New York: W. H. Freeman. Available at: http://www.ncbi.nlm.nih.gov/books/NBK21581 [Accessed: 12th November 2015].

Loh, S. N. (2010). The missing zinc: p53 misfolding and cancer. *Metallomics* **2:**442-449.

Lowe, N. M., Fekete, K. and Decsi, T. (2009). Methods of assessment of zinc status in humans: a systematic review. *Am J Clin Nutr* **89:**2040S-2051S.

Lu, P. J., Sundquist, K., Baeckstrom, D., Poulsom, R., Hanby, A., Meier-Ewert, S., Jones, T. *et al.* (1999). A novel gene (PLU-1) containing highly conserved putative DNA/chromatin binding motifs is specifically up-regulated in breast cancer. *J Biol Chem* **274:**15633-15645.

Lue, H. W., Yang, X., Wang, R., Qian, W., Xu, R. Z., Lyles, R., Osunkoya, A. O. *et al.* (2011). LIV-1 promotes prostate cancer epithelial-to-mesenchymal transition and metastasis through HB-EGF shedding and EGFR-mediated ERK signaling. *PLoS One* **6:**e27720.

Luk, S. C.-W., Siu, S. W.-F., Lai, C.-K., Wu, Y.-J. W. and Pang, S.-F. (2009). Cell Cycle Arrest by a Natural Product via G2/M Checkpoint. *Int J Med Sci* **2:**64-69.

López-Otín, C. and Bond, J. S. (2008). Proteases: multifunctional enzymes in life and disease. *J Biol Chem* **283:**30433-30437.

Macdonald, J. B., Connolly, S. M. and DiCaudo, D. J. (2012). Think Zinc Deficiency: Acquired Acrodermatitis Enteropathica Due to Poor Diet and Common Medications. *Archives of Dermatology* **148:**961-963.

MacDonald, R. S. (2000). The role of zinc in growth and cell proliferation. *J Nutr* **130:**1500S-1508S.

Madden, T. (2002). The BLAST Sequence Analysis Tool. In: McEntyre, J. and Ostell, J. eds. *The NCBI Handbook [Internet].* Maryland: National Center for Biotechnology Information (US).

Manning, D. L., Daly, R. J., Lord, P. G., Kelly, K. F. and Green, C. D. (1988). Effects of oestrogen on the expression of a 4.4 kb mRNA in the ZR-75-1 human breast cancer cell line. *Mol Cell Endocrinol* **59:**205-212.

Manning, D. L., McClelland, R. A., Gee, J. M., Chan, C. M., Green, C. D., Blamey, R. W. and Nicholson, R. I. (1993). The role of four oestrogen-responsive genes, pLIV1, pS2, pSYD3 and pSYD8, in predicting responsiveness to endocrine therapy in primary breast cancer. *Eur J Cancer* **29A:**1462-1468.

Manning, D. L., McClelland, R. A., Knowlden, J. M., Bryant, S., Gee, J. M., Green, C. D., Robertson, J. F. *et al.* (1995). Differential expression of oestrogen regulated genes in breast cancer. *Acta Oncol* **34:**641-646.

Manning, D. L., Robertson, J. F., Ellis, I. O., Elston, C. W., McClelland, R. A., Gee, J. M., Jones, R. J. *et al.* (1994). Oestrogen-regulated genes in breast cancer: association of pLIV1 with lymph node involvement. *Eur J Cancer* **30A:**675-678.

Manning, G., Whyte, D. B., Martinez, R., Hunter, T. and Sudarsanam, S. (2002). The protein kinase complement of the human genome. *Science* **298:**1912-1934.

Maret, W. (2008). Metallothionein redox biology in the cytoprotective and cytotoxic functions of zinc. *Exp Gerontol* **43:**363-369.

Maret, W. (2013). Zinc biochemistry: from a single zinc enzyme to a key element of life. *Adv Nutr* **4:**82-91.

Margalioth, E. J., Schenker, J. G. and Chevion, M. (1983). Copper and zinc levels in normal and malignant tissues. *Cancer* **52:**868-872.

Marino, G., Eckhard, U. and Overall, C. M. (2015). Protein Termini and Their Modifications Revealed by Positional Proteomics. *ACS Chem Biol* **10:**1754-1764.

Martin-Lagos, F., Navarro-Alarcon, M., Terres-Martos, C., Lopez, G. d. l. S. H. and Lopez-Martinez, M. C. (1997). Serum copper and zinc concentrations in serum from patients with cancer and cardiovascular disease. *Sci Total Environ* **204:**27-35.

Matsuura, W., Yamazaki, T., Yamaguchi-Iwai, Y., Masuda, S., Nagao, M., Andrews, G. K. and Kambe, T. (2009). SLC39A9 (ZIP9) regulates zinc homeostasis in the secretory

pathway: characterization of the ZIP subfamily I protein in vertebrate cells. *Biosci Biotechnol Biochem* **73:**1142-1148.

McCall, K. A., Huang, C. and Fierke, C. A. (2000). Function and mechanism of zinc metalloenzymes. *J Nutr* **130:**1437S-1446S.

McCloy, R. A., Rogers, S., Caldon, C. E., Lorca, T., Castro, A. and Burgess, A. (2014). Partial inhibition of Cdk1 in G 2 phase overrides the SAC and decouples mitotic events. *Cell Cycle* **13:**1400-1412.

Meggio, F. and Pinna, L. A. (2003). One-thousand-and-one substrates of protein kinase CK2? *FASEB J* **17:**349-368.

Memon, A. U., Kazi, T. G., Afridi, H. I., Jamali, M. K., Arain, M. B., Jalbani, N. and Syed, N. (2007). Evaluation of zinc status in whole blood and scalp hair of female cancer patients. *Clin Chim Acta* **379:**66-70.

Meyer, F., Galan, P., Douville, P., Bairati, I., Kegle, P., Bertrais, S., Estaquio, C. *et al.* (2005). Antioxidant vitamin and mineral supplementation and prostate cancer prevention in the SU.VI.MAX trial. *Int J Cancer* **116:**182-186.

Meyer, R. D., Srinivasan, S., Singh, A. J., Mahoney, J. E., Gharahassanlou, K. R. and Rahimi, N. (2011). PEST motif serine and tyrosine phosphorylation controls vascular endothelial growth factor receptor 2 stability and downregulation. *Mol Cell Biol* **31:**2010-2025.

Mihaylova, M. M. and Shaw, R. J. (2011). The AMPK signalling pathway coordinates cell growth, autophagy and metabolism. *Nat Cell Biol* **13:**1016-1023.

Milon, B., Wu, Q., Zou, J., Costello, L. C. and Franklin, R. B. (2006). Histidine residues in the region between transmembrane domains III and IV of hZip1 are required for zinc transport across the plasma membrane in PC-3 cells. *Biochimica Et Biophysica Acta-Biomembranes* **1758:**1696-1701.

Miyai, T., Hojyo, S., Ikawa, T., Kawamura, M., Irié, T., Ogura, H., Hijikata, A. *et al.* (2014). Zinc transporter SLC39A10/ZIP10 facilitates antiapoptotic signaling during early B-cell development. *Proc Natl Acad Sci U S A* **111:**11780-11785.

Moore, S. F., van den Bosch, M. T., Hunter, R. W., Sakamoto, K., Poole, A. W. and Hers, I. (2013). Dual regulation of glycogen synthase kinase 3 (GSK3)α/β by protein kinase C (PKC)α and Akt promotes thrombin-mediated integrin αIIbβ3 activation and granule secretion in platelets. *J Biol Chem* **288:**3918-3928.

Mori, H., Tomari, T., Koshikawa, N., Kajita, M., Itoh, Y., Sato, H., Tojo, H. *et al.* (2002). CD44 directs membrane-type 1 matrix metalloproteinase to lamellipodia by associating with its hemopexin-like domain. *EMBO J* **21:**3949-3959.

Morina, F., Jovanovic, L., Mojovic, M., Vidovic, M., Pankovic, D. and Veljovic Jovanovic, S. (2010). Zinc-induced oxidative stress in Verbascum thapsus is caused by an accumulation of reactive oxygen species and quinhydrone in the cell wall. *Physiol Plant* **140:**209-224.

Moynahan, E. J. (1974). Letter: Acrodermatitis enteropathica: a lethal inherited human zinc-deficiency disorder. *Lancet* **2:**399-400.

Mulay, I. L., Roy, R., Knox, B. E., Suhr, N. H. and Delaney, W. E. (1971). Trace-metal analysis of cancerous and noncancerous human tissues. *J Natl Cancer Inst* **47:**1-13.

Naidu, M. S., Suryakar, A. N., Swami, S. C., Katkam, R. V. and Kumbar, K. M. (2007). Oxidative stress and antioxidant status in cervical cancer patients. *Indian J Clin Biochem* **22:**140-144.

Nakamura, N., Rabouille, C., Watson, R., Nilsson, T., Hui, N., Slusarewicz, P., Kreis, T. E. *et al.* (1995). Characterization of a cis-Golgi matrix protein, GM130. *J Cell Biol* **131:**1715-1726.

Nelson, D. L. and Cox, M. M. (2013). Biological membranes and transport.*CourseSmart International E-Book for Principles of Biochemistry*. 6th ed. Palgrave Macmillan, pp. 385-432.

Nimmanon, T. and Taylor, K. M. (2015). Cellular Zinc Signalling Is Triggered by CK2. In: Ahmed, K. and Issinger, O.-G. and Szyszka, R. (eds.) *Protein Kinase CK2 Cellular Function in Normal and Disease States*. Switzerland: Springer International Publishing, pp. 141-157.

Nordle Gilliver, A., Griffin, S. and Harris, M. (2010). Identification of a novel phosphorylation site in hepatitis C virus NS5A. *J Gen Virol* **91:**2428-2432.

Noseda, M., Chang, L., McLean, G., Grim, J. E., Clurman, B. E., Smith, L. L. and Karsan, A. (2004). Notch activation induces endothelial cell cycle arrest and participates in contact inhibition: role of p21Cip1 repression. *Mol Cell Biol* **24:**8813-8822.

Notredame, C., Higgins, D. G. and Heringa, J. (2000). T-Coffee: A novel method for fast and accurate multiple sequence alignment. *J Mol Biol* **302:**205-217.

Ochs, H. D. and Smith, C. I. (1996). X-linked agammaglobulinemia. A clinical and molecular analysis. *Medicine (Baltimore)* **75:**287-299.

Ohana, E., Hoch, E., Keasar, C., Kambe, T., Yifrach, O., Hershfinkel, M. and Sekler, I. (2009). Identification of the Zn2+ binding site and mode of operation of a mammalian Zn2+ transporter. *J Biol Chem* **284:**17677-17686.

Ohashi, K., Nagata, Y., Wada, E., Zammit, P. S., Shiozuka, M. and Matsuda, R. (2015). Zinc promotes proliferation and activation of myogenic cells via the PI3K/Akt and ERK signaling cascade. *Exp Cell Res* **333:**228-237.

Olsen, J. V., Vermeulen, M., Santamaria, A., Kumar, C., Miller, M. L., Jensen, L. J., Gnad, F. *et al.* (2010). Quantitative phosphoproteomics reveals widespread full phosphorylation site occupancy during mitosis. *Sci Signal* **3:**ra3.

Ortega, C. E., Seidner, Y. and Dominguez, I. (2014). Mining CK2 in cancer. *PLoS One* **9:**e115609.

Oteiza, P. I. (2012). Zinc and the modulation of redox homeostasis. *Free Radic Biol Med* **53:**1748-1759.

Palacios-Moreno, J., Foltz, L., Guo, A., Stokes, M. P., Kuehn, E. D., George, L., Comb, M. *et al.* (2015). Neuroblastoma tyrosine kinase signaling networks involve FYN and LYN in endosomes and lipid rafts. *PLoS Comput Biol* **11:**e1004130.

Pandey, N. R., Vardatsikos, G., Mehdi, M. Z. and Srivastava, A. K. (2010). Cell-type-specific roles of IGF-1R and EGFR in mediating Zn2+-induced ERK1/2 and PKB phosphorylation. *J Biol Inorg Chem* **15:**399-407.

Passerini, A., Andreini, C., Menchetti, S., Rosato, A. and Frasconi, P. (2007). Predicting zinc binding at the proteome level. *BMC Bioinformatics* **8:**39.

Peinado, H., Olmeda, D. and Cano, A. (2007). Snail, Zeb and bHLH factors in tumour progression: an alliance against the epithelial phenotype? *Nat Rev Cancer* **7:**415-428.

Perfettini, J. L., Castedo, M., Nardacci, R., Ciccosanti, F., Boya, P., Roumier, T., Larochette, N. *et al.* (2005). Essential role of p53 phosphorylation by p38 MAPK in apoptosis induction by the HIV-1 envelope. *J Exp Med* **201:**279-289.

Peters, C. and Brown, S. (2015). Antibody-drug conjugates as novel anti-cancer chemotherapeutics. *Biosci Rep* **35**.

Phanstiel, D. H., Brumbaugh, J., Wenger, C. D., Tian, S., Probasco, M. D., Bailey, D. J., Swaney, D. L. *et al.* (2011). Proteomic and phosphoproteomic comparison of human ES and iPS cells. *Nat Methods* **8:**821-827.

Pinna, L. A. (1990). Casein kinase 2: an 'eminence grise' in cellular regulation? *Biochim Biophys Acta* **1054:**267-284.

Pinto, A. C., Ades, F., de Azambuja, E. and Piccart-Gebhart, M. (2013). Trastuzumab for patients with HER2 positive breast cancer: delivery, duration and combination therapies. *Breast* **22 Suppl 2:**S152-155.

Pocanschi, C. L., Ehsani, S., Mehrabian, M., Wille, H., Reginold, W., Trimble, W. S., Wang, H. *et al.* (2013). The ZIP5 ectodomain co-localizes with PrP and may acquire a PrP-like fold that assembles into a dimer. *PLoS One* **8:**e72446.

Podar, D., Scherer, J., Noordally, Z., Herzyk, P., Nies, D. and Sanders, D. (2012). Metal selectivity determinants in a family of transition metal transporters. *J Biol Chem* **287:**3185-3196.

Prasad, A. S., Halsted, J. A. and Nadimi, M. (1961). Syndrome of iron deficiency anemia, hepatosplenomegaly, hypogonadism, dwarfism and geophagia. *Am J Med* **31:**532-546.

Prasad, A. S., Miale, A., Jr., Farid, Z., Sandstead, H. H., Schulert, A. R. and Darby, W. J. (1963). Biochemical studies on dwarfism, hypogonadism, and anemia. *Arch Intern Med* **111:**407-428.

Puente, X. S., Sánchez, L. M., Overall, C. M. and López-Otín, C. (2003). Human and mouse proteases: a comparative genomic approach. *Nat Rev Genet* **4:**544-558.

Pópulo, H., Lopes, J. M. and Soares, P. (2012). The mTOR signalling pathway in human cancer. *Int J Mol Sci* **13:**1886-1918.

Qin, H. R., Kim, H. J., Kim, J. Y., Hurt, E. M., Klarmann, G. J., Kawasaki, B. T., Duhagon Serrat, M. A. *et al.* (2008). Activation of signal transducer and activator of transcription 3 through a phosphomimetic serine 727 promotes prostate tumorigenesis independent of tyrosine 705 phosphorylation. *Cancer Res* **68:**7736-7741.

Qin, Y., Miranda, J. G., Stoddard, C. I., Dean, K. M., Galati, D. F. and Palmer, A. E. (2013). Direct comparison of a genetically encoded sensor and small molecule indicator: implications for quantification of cytosolic Zn(2+). *ACS Chem Biol* **8:**2366-2371.

Radivojac, P., Baenziger, P. H., Kann, M. G., Mort, M. E., Hahn, M. W. and Mooney, S. D. (2008). Gain and loss of phosphorylation sites in human cancer. *Bioinformatics* **24:**i241-247.

Ramakrishna, S., Suresh, B., Lim, K. H., Cha, B. H., Lee, S. H., Kim, K. S. and Baek, K. H. (2011). PEST motif sequence regulating human NANOG for proteasomal degradation. *Stem Cells Dev* **20:**1511-1519.

Rawlings, J. S., Rosler, K. M. and Harrison, D. A. (2004). The JAK/STAT signaling pathway. *J Cell Sci* **117:**1281-1283.

Rawlings, N. D., Waller, M., Barrett, A. J. and Bateman, A. (2014). MEROPS: the database of proteolytic enzymes, their substrates and inhibitors. *Nucleic Acids Res* **42:**D503-509.

Rechsteiner, M. and Rogers, S. W. (1996). PEST sequences and regulation by proteolysis. *Trends Biochem Sci* **21:**267-271.

Reeder, N. L., Kaplan, J., Xu, J., Youngquist, R. S., Wallace, J., Hu, P., Juhlin, K. D. *et al.* (2011). Zinc pyrithione inhibits yeast growth through copper influx and inactivation of iron-sulfur proteins. *Antimicrob Agents Chemother* **55:**5753-5760.

Rhodes, D. R., Yu, J., Shanker, K., Deshpande, N., Varambally, R., Ghosh, D., Barrette, T. *et al.* (2004). ONCOMINE: a cancer microarray database and integrated data-mining platform. *Neoplasia* **6:**1-6.

Roesch, A., Fukunaga-Kalabis, M., Schmidt, E. C., Zabierowski, S. E., Brafford, P. A., Vultur, A., Basu, D. *et al.* (2010). A temporarily distinct subpopulation of slow-cycling melanoma cells is required for continuous tumor growth. *Cell* **141:**583-594.

Rogers, L. D. and Overall, C. M. (2013). Proteolytic post-translational modification of proteins: proteomic tools and methodology. *Mol Cell Proteomics* **12:**3532-3542.

Rogers, S., Wells, R. and Rechsteiner, M. (1986). Amino acid sequences common to rapidly degraded proteins: the PEST hypothesis. *Science* **234:**364-368.

Roohani, N., Hurrell, R., Kelishadi, R. and Schulin, R. (2013). Zinc and its importance for human health: An integrative review. *J Res Med Sci* **18:**144-157.

Rosner, M., Schipany, K. and Hengstschlager, M. (2013). Merging high-quality biochemical fractionation with a refined flow cytometry approach to monitor nucleocytoplasmic protein expression throughout the unperturbed mammalian cell cycle. *Nat Protoc* **8:**602-626.

Rubin, C. I. and Atweh, G. F. (2004). The role of stathmin in the regulation of the cell cycle. *J Cell Biochem* **93:**242-250.

Ruttkay-Nedecky, B., Nejdl, L., Gumulec, J., Zitka, O., Masarik, M., Eckschlager, T., Stiborova, M. *et al.* (2013). The role of metallothionein in oxidative stress. *Int J Mol Sci* **14:**6044-6066.

Sadeghian, G., Ziaei, H. and Nilforoushzadeh, M. A. (2011). Treatment of localized psoriasis with a topical formulation of zinc pyrithione. *Acta Dermatovenerol Alp Pannonica Adriat* **20:**187-190.

Sandler, V. M. and Barbara, J. G. (1999). Calcium-induced calcium release contributes to action potential-evoked calcium transients in hippocampal CA1 pyramidal neurons. *J Neurosci* **19:**4325-4336.

Sandoval, A., Oviedo, N., Tadmouri, A., Avila, T., De Waard, M. and Felix, R. (2006). Two PEST-like motifs regulate Ca2+/calpain-mediated cleavage of the CaVbeta3 subunit and provide important determinants for neuronal Ca2+ channel activity. *Eur J Neurosci* **23:**2311-2320.

Sassoon, I. and Blanc, V. (2013). Antibody-drug conjugate (ADC) clinical pipeline: a review. *Methods Mol Biol* **1045:**1-27.

Satoh, M., Kondo, Y., Mita, M., Nakagawa, I., Naganuma, A. and Imura, N. (1993). Prevention of carcinogenicity of anticancer drugs by metallothionein induction. *Cancer Res* **53:**4767-4768.

Sauve, D. M., Anderson, H. J., Ray, J. M., James, W. M. and Roberge, M. (1999). Phosphorylation-induced rearrangement of the histone H3 NH2-terminal domain during mitotic chromosome condensation. *J Cell Biol* **145:**225-235.

Schindler, C. and Darnell, J. E., Jr. (1995). Transcriptional responses to polypeptide ligands: the JAK-STAT pathway. *Annu Rev Biochem* **64:**621-651.

Schindler, C., Shuai, K., Prezioso, V. R. and Darnell, J. E., Jr. (1992). Interferon-dependent tyrosine phosphorylation of a latent cytoplasmic transcription factor. *Science* **257:**809-813.

Schmitt-Ulms, G., Ehsani, S., Watts, J. C., Westaway, D. and Wille, H. (2009). Evolutionary descent of prion genes from the ZIP family of metal ion transporters. *PLoS One* **4:**e7208.

Schneider, C. A., Rasband, W. S. and Eliceiri, K. W. (2012). NIH Image to ImageJ: 25 years of image analysis. *Nat Methods* **9:**671-675.

Schneider, J., Ruschhaupt, M., Buness, A., Asslaber, M., Regitnig, P., Zatloukal, K., Schippinger, W. *et al.* (2006). Identification and meta-analysis of a small gene expression signature for the diagnosis of estrogen receptor status in invasive ductal breast cancer. *Int J Cancer* **119:**2974-2979.

Schnitt, S. J. (2010). Classification and prognosis of invasive breast cancer: from morphology to molecular taxonomy. *Mod Pathol* **23 Suppl 2:**S60-64.

Schuringa, J. J., Jonk, L. J., Dokter, W. H., Vellenga, E. and Kruijer, W. (2000). Interleukin-6-induced STAT3 transactivation and Ser727 phosphorylation involves Vav, Rac-1 and the kinase SEK-1/MKK-4 as signal transduction components. *Biochem J* **347 Pt 1:**89-96.

Schwartz, J. R., Bacon, R. A., Shah, R., Mizoguchi, H. and Tosti, A. (2013). Therapeutic efficacy of anti-dandruff shampoos: a randomized clinical trial comparing products based on potentiated zinc pyrithione and zinc pyrithione/climbazole. *Int J Cosmet Sci* **35:**381-387.

Schwingshackl, L., Hoffmann, G., Buijsse, B., Mittag, T., Stelmach-Mardas, M., Boeing, H., Gottschald, M. *et al.* (2015). Dietary supplements and risk of cause-specific death, cardiovascular disease, and cancer: a protocol for a systematic review and network meta-analysis of primary prevention trials. *Syst Rev* **4:**34.

Sciaky, N., Presley, J., Smith, C., Zaal, K. J., Cole, N., Moreira, J. E., Terasaki, M. *et al.* (1997). Golgi tubule traffic and the effects of brefeldin A visualized in living cells. *J Cell Biol* **139:**1137-1155.

Sengupta, T. K., Talbot, E. S., Scherle, P. A. and Ivashkiv, L. B. (1998). Rapid inhibition of interleukin-6 signaling and Stat3 activation mediated by mitogen-activated protein kinases. *Proc Natl Acad Sci U S A* **95:**11107-11112.

Shao, H., Xu, X., Mastrangelo, M. A., Jing, N., Cook, R. G., Legge, G. B. and Tweardy, D. J. (2004). Structural requirements for signal transducer and activator of transcription 3 binding to phosphotyrosine ligands containing the YXXQ motif. *J Biol Chem* **279:**18967-18973.

Sharma, K., D'Souza, R. C., Tyanova, S., Schaab, C., Wiśniewski, J. R., Cox, J. and Mann, M. (2014). Ultradeep human phosphoproteome reveals a distinct regulatory nature of Tyr and Ser/Thr-based signaling. *Cell Rep* **8:**1583-1594.

Shen, Y., Schlessinger, K., Zhu, X., Meffre, E., Quimby, F., Levy, D. E. and Darnell, J. E. (2004). Essential role of STAT3 in postnatal survival and growth revealed by mice lacking STAT3 serine 727 phosphorylation. *Mol Cell Biol* **24:**407-419.

Shi, X., Zhang, H., Paddon, H., Lee, G., Cao, X. and Pelech, S. (2006). Phosphorylation of STAT3 serine-727 by cyclin-dependent kinase 1 is critical for nocodazole-induced mitotic arrest. *Biochemistry* **45:**5857-5867.

Shiina, T., Hosomichi, K., Inoko, H. and Kulski, J. K. (2009). The HLA genomic loci map: expression, interaction, diversity and disease. *J Hum Genet* **54:**15-39.

Shiromizu, T., Adachi, J., Watanabe, S., Murakami, T., Kuga, T., Muraoka, S. and Tomonaga, T. (2013). Identification of missing proteins in the neXtProt database and unregistered phosphopeptides in the PhosphoSitePlus database as part of the Chromosome-centric Human Proteome Project. *J Proteome Res* **12:**2414-2421.

Slamenova, D. and Gabelova, A. (1980). The effects of sodium azide on mammalian cells cultivated in vitro. *Mutat Res* **71:**253-261.

Smeenk, L., van Heeringen, S. J., Koeppel, M., Gilbert, B., Janssen-Megens, E., Stunnenberg, H. G. and Lohrum, M. (2011). Role of p53 serine 46 in p53 target gene regulation. *PLoS One* **6:**e17574.

Sussman, D., Smith, L. M., Anderson, M. E., Duniho, S., Hunter, J. H., Kostner, H., Miyamoto, J. B. *et al.* (2014). SGN-LIV1A: a novel antibody-drug conjugate targeting LIV-1 for the treatment of metastatic breast cancer. *Mol Cancer Ther* **13:**2991-3000.

Sutherland, E., Robison, G. and Butcher, R. (1968). Some aspects of the biological role of adenosine 3', 5'-monophosphate (cyclic AMP). *Circulation* **37:**279-306.

Suzuki, A. and Endo, T. (2002). Ermelin, an endoplasmic reticulum transmembrane protein, contains the novel HELP domain conserved in eukaryotes. *Gene* **284:**31-40.

Suzuki, T., Ishihara, K., Migaki, H., Ishihara, K., Nagao, M., Yamaguchi-Iwai, Y. and Kambe, T. (2005). Two different zinc transport complexes of cation diffusion facilitator proteins localized in the secretory pathway operate to activate alkaline phosphatases in vertebrate cells. *J Biol Chem* **280:**30956-30962.

Takeda, A., Nakamura, M., Fujii, H. and Tamano, H. (2013). Synaptic Zn(2+) homeostasis and its significance. *Metallomics* **5:**417-423.

Tanaka, N., Fujiwara, T., Tomioka, R., Kramer, U., Kawachi, M. and Maeshima, M. (2015). Characterization of the histidine-rich loop of arabidopsis vacuolar membrane zinc transporter AtMTP1 as a sensor of zinc level in the cytosol. *Plant Cell Physiol* **56:**510-519.

Tanaka, N., Kawachi, M., Fujiwara, T. and Maeshima, M. (2013). Zinc-binding and structural properties of the histidine-rich loop of Arabidopsis thaliana vacuolar membrane zinc transporter MTP1. *FEBS Open Bio* **3:**218-224.

Taniguchi, M., Fukunaka, A., Hagihara, M., Watanabe, K., Kamino, S., Kambe, T., Enomoto, S. *et al.* (2013). Essential role of the zinc transporter ZIP9/SLC39A9 in regulating the activations of Akt and Erk in B-cell receptor signaling pathway in DT40 cells. *PLoS One* **8:**e58022.

Tawfic, S., Yu, S., Wang, H., Faust, R., Davis, A. and Ahmed, K. (2001). Protein kinase CK2 signal in neoplasia. *Histol Histopathol* **16:**573-582.

Taylor, J. T., Zeng, X. B., Pottle, J. E., Lee, K., Wang, A. R., Yi, S. G., Scruggs, J. A. *et al.* (2008a). Calcium signaling and T-type calcium channels in cancer cell cycling. *World J Gastroenterol* **14:**4984-4991.

Taylor, K. M., Gee, J. M. W. and Kille, P. (2011). Zinc and Cancer. In: Rink, L. (ed.) *Zinc in Human Health*. Vol. 76. Amsterdam: IOS Press, pp. 283-304.

Taylor, K. M., Hiscox, S., Nicholson, R. I., Hogstrand, C. and Kille, P. (2012). Protein kinase CK2 triggers cytosolic zinc signaling pathways by phosphorylation of zinc channel ZIP7. *Sci Signal* **5:**ra11.

Taylor, K. M., Morgan, H. E., Johnson, A., Hadley, L. J. and Nicholson, R. I. (2003). Structure-function analysis of LIV-1, the breast cancer-associated protein that belongs to a new subfamily of zinc transporters. *Biochem J* **375:**51-59.

Taylor, K. M., Morgan, H. E., Johnson, A. and Nicholson, R. I. (2004). Structure-function analysis of HKE4, a member of the new LIV-1 subfamily of zinc transporters. *Biochem J* **377:**131-139.

Taylor, K. M., Morgan, H. E., Smart, K., Zahari, N. M., Pumford, S., Ellis, I. O., Robertson, J. F. *et al.* (2007). The emerging role of the LIV-1 subfamily of zinc transporters in breast cancer. *Mol Med* **13:**396-406.

Taylor, K. M., Muraina, I., Brethour, D., Schmitt-Ulms, G., Nimmanon, T., Ziliotto, S., Kille, P. *et al.* (2016). Zinc transporter ZIP10 forms a heteromer with ZIP6 which regulates embryonic development and cell migration. *Biochem J*.

Taylor, K. M. and Nicholson, R. I. (2003). The LZT proteins; the LIV-1 subfamily of zinc transporters. *Biochim Biophys Acta* **1611:**16-30.

Taylor, K. M., Vichova, P., Jordan, N., Hiscox, S., Hendley, R. and Nicholson, R. I. (2008b). ZIP7-mediated intracellular zinc transport contributes to aberrant growth factor signaling in antihormone-resistant breast cancer Cells. *Endocrinology* **149:**4912-4920.

The UniProt Consortium. (2015). UniProt: a hub for protein information. *Nucleic Acids Res* **43:**D204-212.

Thery, M. and Bornens, M. (2008). Get round and stiff for mitosis. *HFSP J* **2:**65-71.

Thiery, J. P., Acloque, H., Huang, R. Y. and Nieto, M. A. (2009). Epithelial-mesenchymal transitions in development and disease. *Cell* **139:**871-890.

Thornton, J. K., Taylor, K. M., Ford, D. and Valentine, R. A. (2011). Differential subcellular localization of the splice variants of the zinc transporter ZnT5 is dictated by the different C-terminal regions. *PLoS One* **6:**e23878.

Tong, J., Taylor, P., Peterman, S. M., Prakash, A. and Moran, M. F. (2009). Epidermal growth factor receptor phosphorylation sites Ser991 and Tyr998 are implicated in the regulation of receptor endocytosis and phosphorylations at Ser1039 and Thr1041. *Mol Cell Proteomics* **8:**2131-2144.

Tozlu, S., Girault, I., Vacher, S., Vendrell, J., Andrieu, C., Spyratos, F., Cohen, P. *et al.* (2006). Identification of novel genes that co-cluster with estrogen receptor alpha in breast tumor biopsy specimens, using a large-scale real-time reverse transcription-PCR approach. *Endocr Relat Cancer* **13:**1109-1120.

Trzaskowski, B., Adamowicz, L. and Deymier, P. A. (2008). A theoretical study of zinc(II) interactions with amino acid models and peptide fragments. *J Biol Inorg Chem* **13:**133-137.

Turk, B. (2006). Targeting proteases: successes, failures and future prospects. *Nat Rev Drug Discov* **5:**785-799.

Unno, J., Masamune, A., Hamada, S. and Shimosegawa, T. (2014). The zinc transporter LIV-1 is a novel regulator of stemness in pancreatic cancer cells. *Scand J Gastroenterol* **49:**215-221.

Unno, J., Satoh, K., Hirota, M., Kanno, A., Hamada, S., Ito, H., Masamune, A. *et al.* (2009). LIV-1 enhances the aggressive phenotype through the induction of epithelial to mesenchymal transition in human pancreatic carcinoma cells. *Int J Oncol* **35:**813-821.

Valentine, R. A., Jackson, K. A., Christie, G. R., Mathers, J. C., Taylor, P. M. and Ford, D. (2007). ZnT5 variant B is a bidirectional zinc transporter and mediates zinc uptake in human intestinal Caco-2 cells. *J Biol Chem* **282:**14389-14393.

Vallee, B. L. and Galdes, A. (1984). The metallobiochemistry of zinc enzymes. *Adv Enzymol Relat Areas Mol Biol* **56:**283-430.

van Vugt, M. A. and Medema, R. H. (2005). Getting in and out of mitosis with Polo-like kinase-1. *Oncogene* **24:**2844-2859.

Vasquez, R. J., Howell, B., Yvon, A. M., Wadsworth, P. and Cassimeris, L. (1997). Nanomolar concentrations of nocodazole alter microtubule dynamic instability in vivo and in vitro. *Mol Biol Cell* **8:**973-985.

Vidyasagar, A., Wilson, N. A. and Djamali, A. (2012). Heat shock protein 27 (HSP27): biomarker of disease and therapeutic target. *Fibrogenesis Tissue Repair* **5:**7.

Wagner, E. F. and Nebreda, A. R. (2009). Signal integration by JNK and p38 MAPK pathways in cancer development. *Nat Rev Cancer* **9:**537-549.

Walker, C. L., Taneja, S., LeFevre, A., Black, R. E. and Mazumder, S. (2015). Appropriate Management of Acute Diarrhea in Children Among Public and Private Providers in Gujarat, India: A Cross-Sectional Survey. *Glob Health Sci Pract* **3:**230-241.

Walker, S. R., Xiang, M. and Frank, D. A. (2014). Distinct roles of STAT3 and STAT5 in the pathogenesis and targeted therapy of breast cancer. *Mol Cell Endocrinol* **382:**616-621.

Walsh, C. T., Garneau-Tsodikova, S. and Gatto, G. J. (2005). Protein posttranslational modifications: the chemistry of proteome diversifications. *Angew Chem Int Ed Engl* **44:**7342-7372.

Wang, C. Y., Jenkitkasemwong, S., Duarte, S., Sparkman, B. K., Shawki, A., Mackenzie, B. and Knutson, M. D. (2012). ZIP8 Is an Iron and Zinc Transporter Whose Cell-surface Expression Is Up-regulated by Cellular Iron Loading. *J Biol Chem* **287:**34032-34043.

Wang, K., Zhou, B., Kuo, Y. M., Zemansky, J. and Gitschier, J. (2002). A novel member of a zinc transporter family is defective in acrodermatitis enteropathica. *Am J Hum Genet* **71:**66-73.

Wang, N., Chen, W., Linsel-Nitschke, P., Martinez, L. O., Agerholm-Larsen, B., Silver, D. L. and Tall, A. R. (2003). A PEST sequence in ABCA1 regulates degradation by calpain protease and stabilization of ABCA1 by apoA-I. *J Clin Invest* **111:**99-107.

Wang, X., Chen, M., Zhou, J. and Zhang, X. (2014). HSP27, 70 and 90, anti-apoptotic proteins, in clinical cancer therapy (Review). *Int J Oncol* **45:**18-30.

Watson, J. V., Chambers, S. H. and Smith, P. J. (1987). A pragmatic approach to the analysis of DNA histograms with a definable G1 peak. *Cytometry* **8:**1-8.

Watts, J. C., Huo, H., Bai, Y., Ehsani, S., Jeon, A. H., Won, A. H., Shi, T. *et al.* (2009). Interactome analyses identify ties of PrP and its mammalian paralogs to oligomannosidic N-glycans and endoplasmic reticulum-derived chaperones. *PLoS Pathog* **5:**e1000608.

Weber, C., Schreiber, T. B. and Daub, H. (2012). Dual phosphoproteomics and chemical proteomics analysis of erlotinib and gefitinib interference in acute myeloid leukemia cells. *J Proteomics* **75:**1343-1356.

Wei, L., Liu, T. T., Wang, H. H., Hong, H. M., Yu, A. L., Feng, H. P. and Chang, W. W. (2011). Hsp27 participates in the maintenance of breast cancer stem cells through regulation of epithelial-mesenchymal transition and nuclear factor-κB. *Breast Cancer Res* **13:**R101.

Wei, Y., Yu, L. L., Bowen, J., Gorovsky, M. A. and Allis, C. D. (1999). Phosphorylation of histone H3 is required for proper chromosome condensation and segregation. *Cell* **97:**99-109.

Wen, Z., Zhong, Z. and Darnell Jr, J. E. (1995). Maximal activation of transcription by statl and stat3 requires both tyrosine and serine phosphorylation. *Cell* **82:**241-250.

Wessells, K. R. and Brown, K. H. (2012). Estimating the global prevalence of zinc deficiency: results based on zinc availability in national food supplies and the prevalence of stunting. *PLoS One* **7:**e50568.

Wieringa, F. T., Dijkhuizen, M. A., Fiorentino, M., Laillou, A. and Berger, J. (2015). Determination of zinc status in humans: which indicator should we use? *Nutrients* **7:**3252-3263.

Wilson, M., Hogstrand, C. and Maret, W. (2012). Picomolar concentrations of free zinc(II) ions regulate receptor protein-tyrosine phosphatase β activity. *J Biol Chem* **287:**9322-9326.

Wong, S. H., Zhao, Y., Schoene, N. W., Han, C. T., Shih, R. S. and Lei, K. Y. (2007). Zinc deficiency depresses p21 gene expression: inhibition of cell cycle progression is independent of the decrease in p21 protein level in HepG2 cells. *Am J Physiol Cell Physiol* **292:**C2175-2184.

Woodier, J., Rainbow, R. D., Stewart, A. J. and Pitt, S. J. (2015). Intracellular Zinc Modulates Cardiac Ryanodine Receptor-mediated Calcium Release. *J Biol Chem* **290:**17599-17610.

Wu, F., Wang, P., Zhang, J., Young, L. C., Lai, R. and Li, L. (2010). Studies of phosphoproteomic changes induced by nucleophosmin-anaplastic lymphoma kinase (ALK) highlight deregulation of tumor necrosis factor (TNF)/Fas/TNF-related apoptosis-induced ligand signaling pathway in ALK-positive anaplastic large cell lymphoma. *Mol Cell Proteomics* **9:**1616-1632.

Wu, X., Tang, J. and Xie, M. (2015). Serum and hair zinc levels in breast cancer: a meta-analysis. *Sci Rep* **5:**12249.

Xiong, Y., Luo, D. J., Wang, X. L., Qiu, M., Yang, Y., Yan, X., Wang, J. Z. *et al.* (2015). Zinc binds to and directly inhibits protein phosphatase 2A in vitro. *Neurosci Bull* **31:**331-337.

Xu, B. E., Lee, B. H., Min, X., Lenertz, L., Heise, C. J., Stippec, S., Goldsmith, E. J. *et al.* (2005). WNK1: analysis of protein kinase structure, downstream targets, and potential roles in hypertension. *Cell Res* **15:**6-10.

Yamanaka, Y., Matsugano, S., Yoshikawa, Y. and Orino, K. (2016). Binding Analysis of Human Immunoglobulin G as a Zinc-Binding Protein. *Antibodies* **5:**13.

Yamane, K., Tateishi, K., Klose, R. J., Fang, J., Fabrizio, L. A., Erdjument-Bromage, H., Taylor-Papadimitriou, J. *et al.* (2007). PLU-1 is an H3K4 demethylase involved in transcriptional repression and breast cancer cell proliferation. *Mol Cell* **25:**801-812.

Yamasaki, S., Sakata-Sogawa, K., Hasegawa, A., Suzuki, T., Kabu, K., Sato, E., Kurosaki, T. *et al.* (2007). Zinc is a novel intracellular second messenger. *J Cell Biol* **177:**637-645.

Yamashita, S., Miyagi, C., Fukada, T., Kagara, N., Che, Y. S. and Hirano, T. (2004). Zinc transporter LIVI controls epithelial-mesenchymal transition in zebrafish gastrula organizer. *Nature* **429:**298-302.

Yanagisawa, H. (2008). Zinc deficiency and clinical practice--validity of zinc preparations. *Yakugaku Zasshi* **128:**333-339.

Yohannan, S., Faham, S., Yang, D., Whitelegge, J. P. and Bowie, J. U. (2004). The evolution of transmembrane helix kinks and the structural diversity of G protein-coupled receptors. *Proc Natl Acad Sci U S A* **101:**959-963.

Yu, H., Lee, H., Herrmann, A., Buettner, R. and Jove, R. (2014). Revisiting STAT3 signalling in cancer: new and unexpected biological functions. *Nature Reviews Cancer* **14:**736-746.

Yu, M., Lee, W. W., Tomar, D., Pryshchep, S., Czesnikiewicz-Guzik, M., Lamar, D. L., Li, G. *et al.* (2011). Regulation of T cell receptor signaling by activation-induced zinc influx. *J Exp Med* **208:**775-785.

Yu, Y., Wu, A., Zhang, Z., Yan, G., Zhang, F., Zhang, L., Shen, X. *et al.* (2013). Characterization of the GufA subfamily member SLC39A11/Zip11 as a zinc transporter. *J Nutr Biochem* **24:**1697-1708.

Zahradníková, A. and Zahradník, I. (1999). Analysis of calcium-induced calcium release in cardiac sarcoplasmic reticulum vesicles using models derived from single-channel data. *Biochim Biophys Acta* **1418:**268-284.

Zhang, Y., Bharadwaj, U., Logsdon, C. D., Chen, C., Yao, Q. and Li, M. (2010). ZIP4 regulates pancreatic cancer cell growth by activating IL-6/STAT3 pathway through zinc finger transcription factor CREB. *Clin Cancer Res* **16:**1423-1430.

Zhao, J., Bertoglio, B. A., Gee, K. R. and Kay, A. R. (2008). The zinc indicator FluoZin-3 is not perturbed significantly by physiological levels of calcium or magnesium. *Cell Calcium* **44:**422-426.

Zhao, L., Chen, W., Taylor, K. M., Cai, B. and Li, X. (2007). LIV-1 suppression inhibits HeLa cell invasion by targeting ERK1/2-Snail/Slug pathway. *Biochem Biophys Res Commun* **363:**82-88.

Zhao, N., Zhang, A. S., Worthen, C., Knutson, M. D. and Enns, C. A. (2014). An iron-regulated and glycosylation-dependent proteasomal degradation pathway for the plasma membrane metal transporter ZIP14. *Proc Natl Acad Sci U S A* **111:**9175-9180.

Zhou, B. P., Deng, J., Xia, W., Xu, J., Li, Y. M., Gunduz, M. and Hung, M. C. (2004). Dual regulation of Snail by GSK-3beta-mediated phosphorylation in control of epithelial-mesenchymal transition. *Nat Cell Biol* **6:**931-940.

Zhou, H., Di Palma, S., Preisinger, C., Peng, M., Polat, A. N., Heck, A. J. and Mohammed, S. (2013). Toward a comprehensive characterization of a human cancer cell phosphoproteome. *J Proteome Res* **12:**260-271.

Zhou, W., Chen, H. and Zhang, L. (2009a). The PcG protein hPc2 interacts with the N-terminus of histone demethylase JARID1B and acts as a transcriptional co-repressor. *BMB Rep* **42:**154-159.

Zhou, X. W., Winblad, B., Guan, Z. and Pei, J. J. (2009b). Interactions between glycogen synthase kinase 3beta, protein kinase B, and protein phosphatase 2A in tau phosphorylation in mouse N2a neuroblastoma cells. *J Alzheimers Dis* **17:**929-937.

Zhu, Z. Y. and Karlin, S. (1996). Clusters of charged residues in protein three-dimensional structures. *Proc Natl Acad Sci U S A* **93:**8350-8355.

Zhuang, X. L., Northup, J. K. and Ray, K. (2012). Large Putative PEST-like Sequence Motif at the Carboxyl Tail of Human Calcium Receptor Directs Lysosomal Degradation and Regulates Cell Surface Receptor Level. *Journal of Biological Chemistry* **287:**4165-4176.